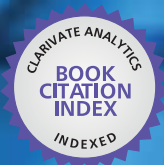


IntechOpen

# Biomaterials

Physics and Chemistry

*Edited by Rosario Pignatello*



WEB OF SCIENCE™



---

# **BIOMATERIALS – PHYSICS AND CHEMISTRY**

---

Edited by **Rosario Pignatello**

**INTECHOPEN.COM**

## Biomaterials - Physics and Chemistry

<http://dx.doi.org/10.5772/914>

Edited by Rosario Pignatello

### Contributors

Osvaldo Campanella, Behic Mert, Patel K Bhavesh, Hartono Sumali, Rong-Sen Yang, Tsang-Hai Huang, Ming-Yao Chang, Kung-Tung Chen, Sandy Hsieh, Ben Ayed Foued, Nobuhiro Nagai, Ryosuke Kubota, Ryohei Okahashi, Masanobu Munekata, Baoping Zhang, You Wang, Lin Geng, Serpil Ünver Saraydin, Dursun Saraydin, Mitsugu Todo, Tetsuo Takayama, Ben Chew, Dirk Lange, Chelsea Elwood, Mar Diez, Vera Schulte, Marga Lensen, Philippe Courtois, Leif Hermansson, Lothar Elling, Christiane Elisabeth Römer, Gabriel Katana, Wycliffe Kipnusu, Federica Chiellini, Andrea Morelli, Gary Rayson, Patrick Williams, Sang Hyuk Park, Eun Mi Rhim, Sun-Young Kim, Su-Jin Ahn, Kyung Lhi Kang, Duck Su Kim, Sungyoon Huh, Piero Ugliengo, Marta Corno, Fabio Chiatti, Alfonso Pedone, Miroslav Petrtyl, Jaroslav Lisal, Jana Danesova, Jessem Landoulsi, Michel J. Genet, Karim El Kirat, Caroline Richard, Sylviane Pulvin, Paul Rouxhet, Masaru Murata, Toshiyuki Akazawa, Masaharu Mitsugi, In-Woong Um, Kyung-Wook Kim, Young-Kyun Kim, Luca Maria Moricca, Giuseppina Fini, Alessandra Leonardi, Sara Buonaccorsi, Valentina Pellacchia, Luciano D, Elidon Mici, Laura Frontero, Yan Lu, Zhao Xia, Jiao Wei, John Ramshaw, Juan Valerio Cauich-Rodríguez, Birzabith Mendoza-Novelo

### © The Editor(s) and the Author(s) 2011

The moral rights of the and the author(s) have been asserted.

All rights to the book as a whole are reserved by INTECH. The book as a whole (compilation) cannot be reproduced, distributed or used for commercial or non-commercial purposes without INTECH's written permission.

Enquiries concerning the use of the book should be directed to INTECH rights and permissions department ([permissions@intechopen.com](mailto:permissions@intechopen.com)).

Violations are liable to prosecution under the governing Copyright Law.



Individual chapters of this publication are distributed under the terms of the Creative Commons Attribution 3.0 Unported License which permits commercial use, distribution and reproduction of the individual chapters, provided the original author(s) and source publication are appropriately acknowledged. If so indicated, certain images may not be included under the Creative Commons license. In such cases users will need to obtain permission from the license holder to reproduce the material. More details and guidelines concerning content reuse and adaptation can be found at <http://www.intechopen.com/copyright-policy.html>.

### Notice

Statements and opinions expressed in the chapters are those of the individual contributors and not necessarily those of the editors or publisher. No responsibility is accepted for the accuracy of information contained in the published chapters. The publisher assumes no responsibility for any damage or injury to persons or property arising out of the use of any materials, instructions, methods or ideas contained in the book.

First published in Croatia, 2011 by INTECH d.o.o.

eBook (PDF) Published by IN TECH d.o.o.

Place and year of publication of eBook (PDF): Rijeka, 2019. IntechOpen is the global imprint of IN TECH d.o.o.

Printed in Croatia

Legal deposit, Croatia: National and University Library in Zagreb

Additional hard and PDF copies can be obtained from [orders@intechopen.com](mailto:orders@intechopen.com)

Biomaterials - Physics and Chemistry

Edited by Rosario Pignatello

p. cm.

ISBN 978-953-307-418-4

eBook (PDF) ISBN 978-953-51-4403-8

# We are IntechOpen, the first native scientific publisher of Open Access books

**3,400+**

Open access books available

**109,000+**

International authors and editors

**115M+**

Downloads

**151**

Countries delivered to

Our authors are among the  
**Top 1%**

most cited scientists

**12.2%**

Contributors from top 500 universities



**WEB OF SCIENCE™**

Selection of our books indexed in the Book Citation Index  
in Web of Science™ Core Collection (BKCI)

Interested in publishing with us?  
Contact [book.department@intechopen.com](mailto:book.department@intechopen.com)

Numbers displayed above are based on latest data collected.  
For more information visit [www.intechopen.com](http://www.intechopen.com)





# Meet the editor



Professor Rosario Pignatello is Professor of Pharmaceutical Technology and Legislation at the Faculty of Pharmacy, University of Catania (Italy). He is a member of the Scientific Committee of the Inter-University Research Consortium TEFARCO Innova (Parma, Italy) and acts as an Independent Expert of the European Commission for evaluation of F6 and F7 projects under different thematic areas: Health; ICT for Health; NMP - Nanomaterials and Nanotechnologies. Rosario Pignatello is the author of about 105 scientific publications in peer-reviewed journals, 15 lectures and about 140 oral and poster communications. Focus of his research activity is in the area of innovative pharmaceutical technologies in particular regards the production, physico-chemical characterization and biological evaluation of polymer micro- and nanoparticles as modified drug delivery systems, lipophilic prodrugs and conjugates, chemically engineered polymers for drug delivery and targeting, colloidal drug carriers (liposomes, SLN/NCL, and micelles) and calorimetry (DSC) studies on vesicular biomembrane models for the analysis of drug-membrane interactions, with special applications to anti-cancer drug delivery and targeting, brain delivery, and ophthalmic nanotechnology.





---

# Contents

---

**Preface XIII**

- Part 1 New Materials for Biomedical Applications:  
Chemical and Engineering Interventions 1**
- Chapter 1 **Galectins: Structures, Binding  
Properties and Function in Cell Adhesion 3**  
Christiane E. Römer and Lothar Elling
- Chapter 2 **Biomaterials and Epithesis,  
Our Experience in Maxillo Facial Surgery 29**  
G. Fini, L.M. Moricca, A. Leonardi,  
S. Buonaccorsi and V. Pellacchia
- Chapter 3 **Nanostructural Chemically Bonded  
Ca-Aluminate Based Bioceramics 47**  
Leif Hermansson
- Chapter 4 **Ulvan: A Versatile Platform of  
Biomaterials from Renewable Resources 75**  
Federica Chiellini and Andrea Morelli
- Chapter 5 **Silanization with APTES for Controlling  
the Interactions Between Stainless Steel  
and Biocomponents: Reality vs Expectation 99**  
Jessem Landoulsi, Michel J. Genet, Karim El Kirat,  
Caroline Richard, Sylviane Pulvin and Paul G. Rouxhet
- Chapter 6 **Human Dentin as Novel  
Biomaterial for Bone Regeneration 127**  
Masaru Murata, Toshiyuki Akazawa, Masaharu Mitsugi,  
In-Woong Um, Kyung-Wook Kim and Young-Kyun Kim
- Chapter 7 **Comparative Metal Ion Binding to  
Native and Chemically Modified  
*Datura innoxia* Immobilized Biomaterials 141**  
Gary D. Rayson and Patrick A. Williams

- Chapter 8 **Decellularization, Stabilization and Functionalization of Collagenous Tissues Used as Cardiovascular Biomaterials** 159  
Birzabith Mendoza-Novelo and Juan Valerio Cauich-Rodríguez
- Chapter 9 **Research on Mg-Zn-Ca Alloy as Degradable Biomaterial** 183  
B.P. Zhang, Y. Wang and L. Geng
- Part 2 Biomechanical and Physical Studies** 205
- Chapter 10 **Biomechanical Properties of Synovial Fluid in/Between Peripheral Zones of Articular Cartilage** 207  
Miroslav Petrtyl, Jaroslav Lisal and Jana Danesova
- Chapter 11 **Charge Transport and Electrical Switching in Composite Biopolymers** 225  
Gabriel Katana and Wycliffe Kipnusu
- Chapter 12 **Biomimetic Materials as Potential Medical Adhesives – Composition and Adhesive Properties of the Material Coating the Cuvierian Tubules Expelled by *Holothuria dofleinii*** 245  
Yong Y. Peng, Veronica Glattauer, Timothy D. Skewes, Jacinta F. White, Kate M. Nairn, Andrew N. McDevitt, Christopher M. Elvin, Jerome A. Werkmeister, Lloyd D. Graham and John A.M. Ramshaw
- Chapter 13 **Mechanical and Biological Properties of Bio-Inspired Nano-Fibrous Elastic Materials from Collagen** 259  
Nobuhiro Nagai, Ryosuke Kubota, Ryohei Okahashi and Masanobu Munekata
- Chapter 14 ***In Silico* Study of Hydroxyapatite and Bioglass®: How Computational Science Sheds Light on Biomaterials** 275  
Marta Corno, Fabio Chiatti, Alfonso Pedone and Piero Ugliengo
- Chapter 15 **The Use of Vibration Principles to Characterize the Mechanical Properties of Biomaterials** 299  
Osvaldo H. Campanella, Hartono Sumali, Behic Mert and Bhavesh Patel
- Chapter 16 **The Effects of Endurance Running Training on Young Adult Bone: Densitometry vs. Biomaterial Properties** 329  
Tsang-Hai Huang, Ming-Yao Chang, Kung-Tung Chen, Sandy S. Hsieh and Rong-Sen Yang

- Chapter 17 **Effect of the Er, Cr: YSGG Laser Parameters on Shear Bond Strength and Microstructure on Human Dentin Surface 347**  
Eun Mi Rhim, Sungyoon Huh, Duck Su Kim, Sun-Young Kim, Su-Jin Ahn, Kyung Lhi Kang and Sang Hyuk Park
- Chapter 18 **Elaboration and Characterization of Calcium Phosphate Biomaterial for Biomedical Applications 357**  
Foued Ben Ayed
- Chapter 19 **Fracture Mechanisms of Biodegradable PLA and PLA/PCL Blends 375**  
Mitsugu Todo and Tetsuo Takayama
- Part 3 Evaluation of the Interaction and Compatibility of Biomaterials with Biological Media 395**
- Chapter 20 **Cell Adhesion and Spreading on an Intrinsically Anti-Adhesive PEG Biomaterial 397**  
Marga C. Lensen, Vera A. Schulte and Mar Diez
- Chapter 21 **A Preliminary In Vivo Study on the Histocompatibility of Silk Fibroin 415**  
Lu Yan, Zhao Xia, Shao Zhengzhong, Cao Zhengbing and Cai Lihui
- Chapter 22 **Histopatological Effect Characteristics of Various Biomaterials and Monomers Used in Polymeric Biomaterial Production 425**  
Serpil Ünver Saraydin and Dursun Saraydin
- Chapter 23 **Facial Remodelling and Biomaterial 445**  
G. Fini, L.M. Moricca, A. Leonardi, S. Buonaccorsi and V. Pellacchia
- Part 4 Prevention and Management of Biological Phenomena at Biomaterial/Cell Surfaces 457**
- Chapter 24 **Biomaterials in Urology - Beyond Drug Eluting and Degradable - A Rational Approach to Ureteral Stent Design 459**  
Dirk Lange, Chelsea N. Elwood and Ben H. Chew
- Chapter 25 **Candida Biofilms on Oral Biomaterials 475**  
Philippe Courtois



---

## Preface

---

Scientists who dedicate their research activity to biomaterials pass through the typical dichotomy that often characterizes the basic research. On one side is the wish of exploring new frontiers of chemistry, physics, biology, medicine, pharmaceuticals and all other disciplines to which biomaterials can be applied. The constantly improving scientific knowledge would feed the freedom of attempting new strategies for producing materials with always tailored and improved characteristics. On the other side, one should one have a look to the different 'official' definitions given for biomaterials. It is evident how the restriction imposed by words would limit the fantasy and effectiveness of fundamental scientific research. Just as an example-biomaterials are defined as a 'nonviable material used in a medical device, intended to interact with biological systems' (Consensus Conference of the European Society for Biomaterials, 1986), or as 'any substance (other than a drug) or combination of substances, synthetic or natural in origin, which can be used (...) as a whole or as a part of a system which treats, augments, or replaces any tissue, organ, or function of the body (NIH), or even 'a systematically and pharmacologically inert substance designed for implantation within or incorporation with living systems' (Clemson University Advisory Board for Biomaterials). Essentially, the only common property is that a biomaterial would be different from a biological material, that is produced by a biological system. Clearly, none of the proposed definitions can succeed to cover the whole landscape of properties and applications of these peculiar compounds, but they can only enlighten a particular aspect of their potentials. A similar situation can be applied for nanomedicine – a research field with which the field of biomaterials actually often shares technologies and applications – and for which is the gap between 'official' definitions and the originality of published researches even larger.

These considerations have been one of the basis of the present editorial task, that will comprehend three volumes focused on the recent developments and applications of biomaterials. These books collect review articles, original researches and experimental reports from eminent experts from all over the world, who have been working in this scientific area for a long time. The chapters are covering the interdisciplinary arena which is necessary for an effective development and usage of biomaterials. Contributors were asked to give their personal and recent experience on biomaterials, regardless any specific limitation due to fit into one definition or the other. In our

opinion, this will give readers a wider idea on the new and ongoing potentials of different synthetic and engineered macromolecular materials.

In the meantime, another editorial guidance was not to force the selection of papers concerning the market or clinical applications or biomaterial products. The aim of the book was to gather all results coming from very fundamental studies. Again, this will allow to gain a more general view of what and how the various biomaterials can do and work for, along with the methodologies necessary to design, develop and characterize them, without the restrictions necessarily imposed by industrial or profit concerns.

The chapters have been arranged to give readers an organized view of this research field. In particular, this book contains 25 chapters related to recent research on new materials, with a particular attention to their physical, mechanical and chemical characterization. The first section of the volume contains 9 reviews and articles focused on chemical and engineering modification of biomaterials for specific applications. The following 10 chapters deal with physical and biomechanical studies on biomaterials, followed by two sections which report some recent studies on the interactions and compatibility of biomaterials with biological media, as well as on the management of the phenomena that can occur at the biomaterial/tissue interfaces, such as biofilm formation.

I am sure that readers will gain an improved understanding of the full range of disciplines and design methodologies that are used to develop biomaterials with the physical and biological properties needed for specific clinical applications.

I hope that you will find all these contributions interesting, and that you will be inspired from their reading to broaden your own research towards the exciting field of biomaterial development and applications.

**Prof. Rosario Pignatello**  
Department of Pharmaceutical Sciences  
Faculty of Pharmacy  
University of Catania  
Italy

## **Part 1**

# **New Materials for Biomedical Applications: Chemical and Engineering Interventions**





# Galectins: Structures, Binding Properties and Function in Cell Adhesion

Christiane E. Römer and Lothar Elling

*Helmholtz-Institute for Biomedical Engineering, RWTH Aachen University  
Germany*

## 1. Introduction

Galectins are nearly ubiquitous distributed  $\beta$ -galactoside binding proteins which share a common amino acid sequence, the carbohydrate recognition domain (CRD) (Barondes et al., 1994a; Cooper, 2002; Elola et al., 2007; Hirabayashi & Kasai, 1993; Hughes, 2001; Klyosov et al., 2008; Leffler et al., 2004). They are evident in vertebrates, invertebrates and also protists, implying fundamental functions of these lectins (Hirabayashi & Kasai, 1993). Some galectins are distributed in a variety of different tissues, others are more specifically expressed (Cooper, 2002).

Galectins are known to perform high diversity of functions inside the cells and in the extracellular space. They are regulators of cell cycle, inflammation, immune responses, cancer progression, cell adhesion, cell signalling events and so on. The different functions are performed either by protein-protein or by protein-glycan interactions (Almkvist & Karlsson, 2004; Danguy et al., 2002; Elola et al., 2007; Hernandez & Baum, 2002; Hughes, 2001; Ilarregui et al., 2005; Liu et al., 2002; Liu & Rabinovich, 2005; Rabinovich et al., 2002b; Rabinovich & Toscano, 2009; Vasta, 2009).

Different excellent reviews focus on the wide-spread functions of galectins such as tumor progression, cell signalling or inflammation (Garner & Baum, 2008; Hernandez & Baum, 2002; Liu et al., 2002; Liu & Rabinovich, 2005; Nangia-Makker et al., 2008; Rabinovich et al., 2002a; Rabinovich & Toscano, 2009; van den Brule et al., 2004; Vasta, 2009). Review articles discussing functions of galectins in cell adhesion events and their role as matricellular proteins for the crosslinking of extracellular matrix components have also been published (Elola et al., 2007; Hughes, 2001). The function of galectins in the assembly of the extracellular matrix as well as in cell adhesion and cell signalling processes shows their potential as mediators for cell adhesion and proliferation on biomaterial surfaces. Galectins are interesting candidates for the functionalisation of biomaterial surfaces as they can promote the primary binding event of cells to foreign materials and influence specific signalling processes. In this article we want to analyse the potential use of galectins (explained by the examples of galectin-1, -3 and -8) in biomaterial research and application.

## 2. Families and structures of galectins

Galectins are defined by their  $\beta$ -galactoside binding ability and their common sequence of about 130 conserved amino acids. This sequence homology results in a similar overall three-

dimensional structure of the carbohydrate recognition domain (CRD) (Barondes et al., 1994a; Barondes et al., 1994b). Several human galectin CRDs have been characterised by crystallography, including those of human galectin-1, galectin-3 and the N-terminal domain of galectin-8 (Ideo et al., 2011; Kishishita et al., 2008; Lobsanov et al., 1993; Lopez-Lucendo et al., 2004; Seetharaman et al., 1998). The C-terminal domain of galectin-8 has been investigated by NMR (Tomizawa et al., 2008). All of them show a globular fold consisting of two anti-parallel  $\beta$ -sheets with five to six strands respectively (Ideo et al., 2011; Kishishita et al., 2008; Lobsanov et al., 1993; Lopez-Lucendo et al., 2004; Seetharaman et al., 1998; Tomizawa et al., 2008). The CRDs analysed so far consist of three consecutive exons, with most of the conserved amino acids encoded on the middle one (Cooper & Barondes, 1999; Houzelstein et al., 2004).

## 2.1 Galectin families

Regarding their overall structure galectins are clustered in three families: a) prototype galectins consisting of one CRD, b) chimera-type galectins with one CRD and a non-lectin domain whose only member known so far is galectin-3, and c) tandem-repeat galectins which have two different CRDs linked by a short peptide (see Fig. 1) (Hirabayashi & Kasai, 1993; Leffler et al., 2004).

In this review we want to focus on galectin-1, -3 and -8 as representatives of the three galectin families.

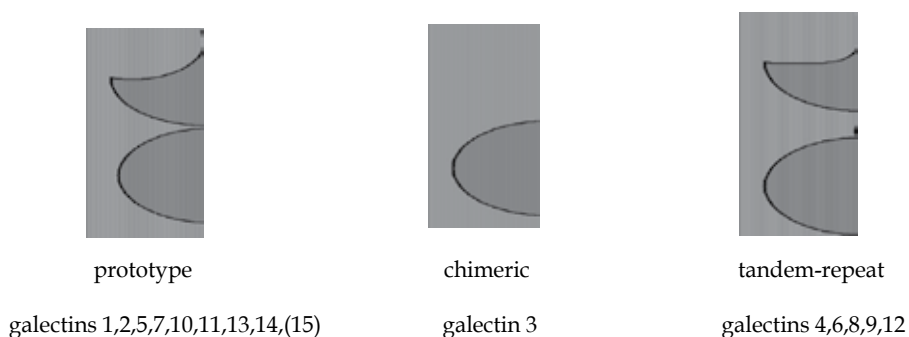


Fig. 1. Galectin families regarding their overall structure (modified from Barondes et al. 1994) (Al-Ansari et al., 2009).

Galectins are either divalent regarding their intrinsic protein structure (tandem-repeat galectins such as galectin-8) or form homotypic di- to oligomers through site-specific interactions (prototype and chimera galectins such as galectin-1 and -3). Different galectin-8 isoforms represent either prototypic or tandem-repeat type galectins depending on splice variants. Some galectin-8 splice variants consist only of the N-terminal CRD and different elongations without a second CRD. Those variants can rather be grouped to the prototypic galectins (Bidon et al., 2001; Al-Ansari et al., 2009; Zick et al., 2004). Prototype galectins such as galectin-1 form homodimers through hydrophobic interactions at the N-terminal amino acid residues (Cho & Cummings, 1997; Lobsanov et al., 1993). Dimerisation occurs as equilibrium reaction depending on protein concentration but independent of available soluble ligands (Cho & Cummings, 1995). In contrast the chimeric galectin-3 forms oligomers (most likely pentamers) via its N-terminal collagen-like extension after ligand-binding (Ahmad et al., 2004a; Birdsall et al., 2001; Nieminen et al., 2008).

## 2.2 Carbohydrate recognition domains

The carbohydrate recognition domain is highly conserved throughout different galectins and organisms.

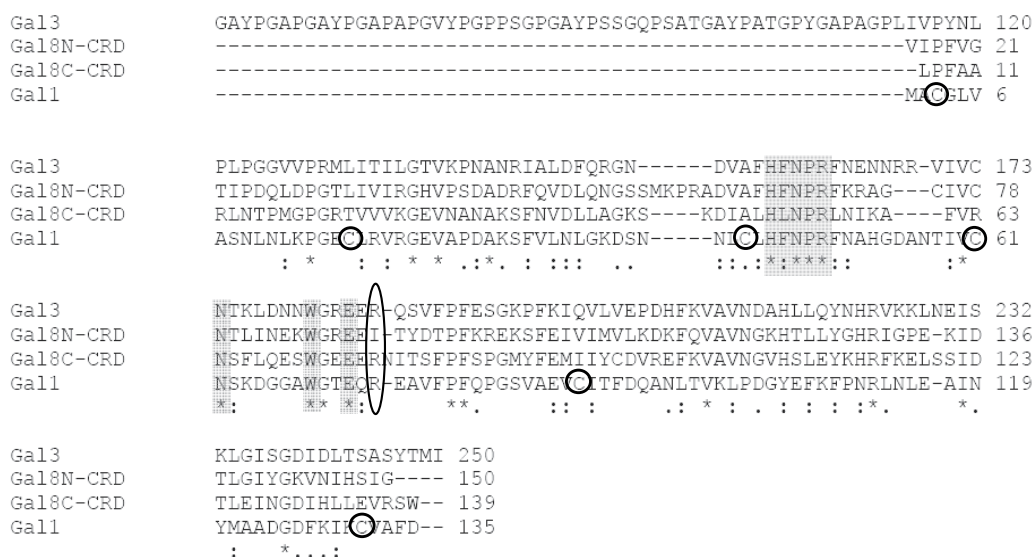


Fig. 2. Sequence alignment of human galectin-1, -3 and the single carbohydrate recognition domains of galectin-8 (residues 1-150 and 221-359 of isoform a). Used sequences are galectin-1 (NP\_002296), galectin-3 (P17931) and galectin-8 isoform a (NP\_963839) as published on <http://www.ncbi.nlm.nih.gov/protein>. Completely conserved amino acids are marked with an asterisk, conserved substitutions are marked with a colon and semi-conserved substitutions with a simple dot. Important amino acids mentioned in the following text are additionally highlighted: Conserved amino acids of the binding pocket are highlighted in grey; residues with importance for the binding are labelled in an ellipse; galectin-1 cysteine residues are marked with circles. The alignment has been performed using ClustalW2 at <http://www.ebi.ac.uk> using the default settings (Chenna et al., 2003; Larkin et al., 2007).

The conserved amino acids are directly involved in carbohydrate binding either by the formation of hydrogen bonds or van der Waals interactions with the sugar moiety. Most of the conserved amino acids form hydrogen bonds with the bound sugar unit. An important sequence motif in this context is His(158)-Asn(160)-Arg(162) (numbering according to human galectin-3, see Fig. 2). Those three amino acids have been found to form hydrogen bonds with the bound galactose residue for example in galectin-1 (Lobsanov et al., 1993), galectin-3 (Diehl et al., 2010; Seetharaman et al., 1998), and galectin-8 N-CRD (Ideo et al., 2011; Kishishita et al., 2008) (see Fig. 3). The sequence motif can also be found in galectin-8

C-CRD but as no x-ray crystallography is available for this CRD the hydrogen bridges have not been verified yet. Additional residues are involved in the conserved binding process either by hydrogen bonding (Glu184, Asn174, numbering according to human galectin-3, see Fig. 3) or van-der-Waals interaction (Trp181, numbering according to human galectin-3) (Di Lella et al., 2009; Diehl et al., 2010; Lobsanov et al., 1993; Seetharaman et al., 1998).

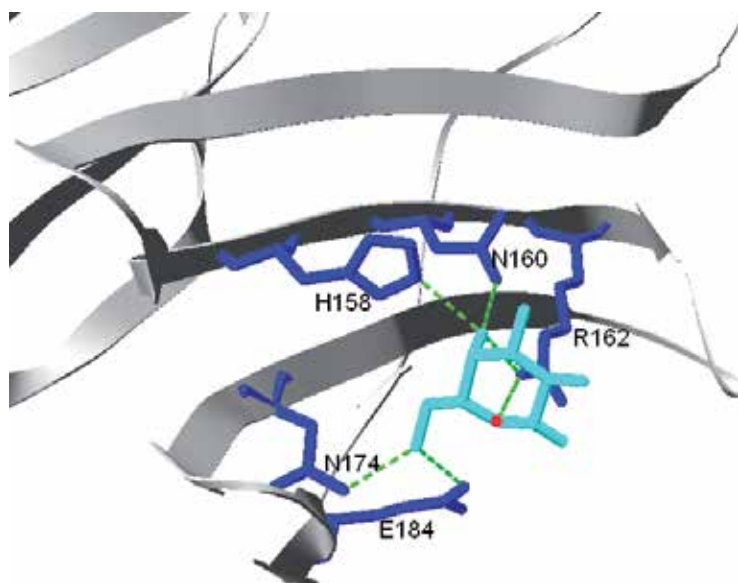


Fig. 3. Human galectin-3 with bound galactose unit of LacNAc **PDB 1KJL**. H-bondings are shown as dotted lines for residues H158 (C4-OH), N160 (C4-OH), R162 (C4-OH and intramolecular O-atom), N174 (C6-OH), E184 (C6-OH) (Seetharaman et al., 1998; Sörme et al., 2005). Picture made with SwissProt pdb viewer (Guex & Peitsch, 1997).

The importance of the mentioned H-bonding amino acids has been proven by site-directed mutagenesis performed with human galectin-1. In those experiments the change of single amino acids involved in H-bonding eliminates the binding to lactose-sepharose and/or asialofetuin (Hirabayashi & Kasai, 1991; Hirabayashi & Kasai, 1994). Although binding is not completely abolished, significant influence of the conserved Trp residue for sugar binding was also proven in bovine and human galectin-1 (Abbott & Feizi, 1991; Hirabayashi & Kasai, 1991).

Arg186 is not completely conserved throughout the different galectins (see Fig. 2, ellipse). The N-terminal domain of galectin-8 for example presents an Ile at the corresponding position resulting in a differing fine specificity for glycans. Due to this mutation galectin-8 N-CRD favours lactose structures over LacNAc type II structures in the binding site. Thereby different biological functions of galectin-8 in contrast to other galectins such as galectin-3 are regulated (Salomonsson et al., 2010). Specific binding preferences resulting from the differences in amino acid sequence will be discussed in chapter 4 in more detail.

## **2.3 Other specific features of galectins**

### **2.3.1 Secretion**

Different tissues are known to produce galectins and most of them secrete parts of the cytosolic galectin pool. The amount of secreted galectin depends on cell type, differentiation status and can be regulated by external triggers (Cooper, 2002; Hughes, 1999). Examples of galectin producing cells with relevance for regenerative medicine are besides others neurons, epithelial cells of several tissues and liver cells, which produce either several different galectins or a specific subset of galectins (Dumic et al., 2006; Hughes, 1999).

Galectins act intra- and extracellularly. As known so far they are secreted via a non-classical mechanism which is not fully understood yet. They lack classical signalling sequences for specific localisation but can be found in the outer cellular space as well as inside the cells even located in the nucleus (Hughes, 1999). Although the complex regulation of secretion remains still elusive some explanations have been found: Galectin-1 secretion depends on the binding to a counter-receptor molecule and does not involve plasma membrane blebbing (Seelenmeyer et al., 2005; Seelenmeyer et al., 2008). Galectin-3 secretion seems also to be regulated by binding to other proteins such as chaperons and subsequent vesicular secretion (Hughes, 1999; Mehul & Hughes, 1997). The N-terminal-domain of galectin-3 is important for subcellular translocation and secretion of the protein (Gong et al., 1999).

### **2.3.2 Galectin-1: Importance of reducing conditions**

The lectin activity of galectin-1 depends on reduced cysteine residues. Oxidised galectin-1 has no lectin activity but functions in the regeneration of nerve axons (Horie et al., 2004). Galectin-1 has six cysteine residues which are accessible to the solvent (see Fig. 2). The removal of the most accessible cysteine (Cys2) (Lopez-Lucendo et al., 2004) - or better all cysteine residues - enhances protein stability under both reducing and non-reducing conditions significantly (Cho & Cummings, 1995; Nishi et al., 2008), while none of them is necessary for lactose binding as shown by site directed mutagenesis and x-ray crystallography (Hirabayashi & Kasai, 1991; Lopez-Lucendo et al., 2004).

### **2.3.3 Galectin-3: The only known chimera type galectin**

Galectin-3 has some specific properties due to its unique structure. Galectin-3 consists of three parts: 1) a N-terminal 12 amino acid leader sequence containing two phosphorylation sites, 2) a proline and glycine rich collagen like domain necessary for oligomerisation and 3) the carbohydrate recognition domain (Ahmad et al., 2004a; Dumic et al., 2006; Kubler et al., 2008; Mehul & Hughes, 1997; Nieminen et al., 2008). The first few amino acids forming the leader peptide are important for the subcellular localisation and secretion of the protein (Gong et al., 1999). Moreover phosphorylation of Ser6 seems to regulate affinity for different ligands and thereby cellular activity of galectin-3 (Dumic et al., 2006; Mazurek et al., 2000; Szabo et al., 2009; Yoshii et al., 2002). Galectin-3 can be cleaved by different proteases such as metalloproteinases-2 and -9 (gelatinases A and B respectively), metalloproteinase-13 (collagenase-3) and with low activity metalloproteinase-1 (collagenase-1) separating the full-length CRD from the N-terminal extension (Guévremont et al., 2004; Ochieng et al., 1994). The main cleavage position is located between Ala62 and Tyr63 while other cleaving sites are only recognised by some specific proteases to lesser extend (Dumic et al., 2006;

Guévremont et al., 2004; Ochieng et al., 1994). The single CRD is mainly described to have an increased affinity for different carbohydrates such as *N*-acetyllactosamine, the glycoprotein asialofetuin or glycans presented on endothelial cells but to have less biological activity as it loses the ability to form oligomers. This reveals the possible regulatory function of galectin-3 cleavage (Dam et al., 2005; Dumic et al., 2006; Ochieng et al., 1998a; Shekhar et al., 2004). In terms of this regulation it is suggested that the single galectin-3-CRD binds with high affinity to glycans on cell surfaces thereby blocking these interaction partners for full-length galectin-3 binding. After this blockage the full-length protein cannot perform its physiological functions anymore. In this way galectin-3 cleavage could act as down-regulation of galectin-3 function (John et al., 2003; Shekhar et al., 2004).

#### **2.3.4 Galectin-8: Several isoforms of a tandem-repeat galectin**

The specific properties of galectin-8 are also implied in its structure and the different isoforms arising from it. At least 6 different isoforms are described so far of which some only consist of the N-terminal CRD with an extension and others consist of both CRDs linked by different hinge domains (Bidon et al., 2001; Delgado et al., 2011; Zick et al., 2004). The two galectin-8 CRDs show approximately 35% sequence similarity but reveal different fine specificity for glycan structures. Therefore galectin-8 can act as “hetero-bifunctional crosslinking agent” (Zick et al., 2004). The length and structure of the linker domain has direct influence on the biological function (Levy et al., 2006). Moreover the linker domain regulates susceptibility to protease cleavage. It was for example shown that a long linker can be cleaved by thrombin while shorter linker variants are not substrate for this protease (Nishi et al., 2006).

### **3. Glycan binding assays for galectins**

As galectins play a fundamental role in cell adhesion, cell signalling, inflammation, tumor progression etc. there is an enormous interest in the evaluation of galectin-glycan interactions regulating those functions.

#### **3.1 Comparison of different common assays**

Various assay set-ups have been designed to analyse the binding behaviour of different galectins to specific glycan structures. Binding assays can be subdivided regarding the presentation of the different binding partners: 1) the glycan structure is immobilised, 2) the galectin is immobilised and 3) both binding partners are soluble.

The chosen assay format influences the data generated as each assay set-up has its own advantages and disadvantages (Rapoport et al., 2008):

Assays in which one of the binding partners is immobilised raise the problem that the amount of this ligand is not completely known. Moreover it is possible that side interactions with the surface occur or that the conformation and flexibility of the bound partner differ slightly from its soluble parameters. The natural oligomerisation of galectins is blocked after immobilisation. Beside this the presentation of the immobilised binding partner is multivalent which influences the binding (Sörme et al., 2004). This can be useful for the glycan structures, as they are multivalently presented in nature as well, but not for galectins. Examples for studies with immobilised glycans or glycoproteins are glycan arrays, ELISA

assays and surface plasmon resonance (Appukuttan, 2002; Blixt et al., 2004; Bohorov et al., 2006; Ideo et al., 2003; Munoz et al., 2010; Song et al., 2009b; Stowell et al., 2008a). For glycan arrays it can be important which linker is used to bind the glycan epitopes to the surface (length, chemical structure). Moreover it is possible to use chemically and/or enzymatically produced ligands as well as glycans from natural compounds like glycopeptides and glycolipids (Blixt et al., 2004; Bohorov et al., 2006). The latter allows the analysis of complex and even unknown glycan structures of different cells (Song et al., 2009a; Song et al., 2009b; Song et al., 2010). Immobilised galectins are for example used in frontal affinity approaches and ELISA assays (Hirabayashi et al., 2002; Sörme et al., 2002).

Variations of binding assays with immobilised partners are assays in which the surface binding is inhibited by a soluble ligand. Such inhibition studies of surface interactions allow a direct read-out of IC<sub>50</sub> values and thereby the direct comparison of relative affinities (Sörme et al., 2002). For the calculation of affinity constants assumptions have to be made to simplify calculations which might not be correct for each single interaction measurement. Additionally the problems mentioned before still persist (Sörme et al., 2004).

Most assays with one immobilised component as well as some direct interaction assays are based on the read-out of a fluorescence signal or other labels. Therefore either the galectin or the glycan structures have to be labelled. This leads to some additional problems: If the glycan is chemically labelled the linker or label itself can alter the binding affinity with specific effects for different galectins (Sörme et al., 2004). Therefore the affinity constants measured do not exactly fit to the unmodified glycan structures. Moreover the labelling of glycans is time-consuming. The labelling of galectins can also alter the binding specificities. It is in most cases done by random chemical modification of specific functional groups such as amino or thiol functionalities (Carlsson et al., 2007; Patnaik et al., 2006; Rapoport et al., 2008; Salomonsson et al., 2010; Song et al., 2009b; Stowell et al., 2008a; Stowell et al., 2008b). Although this labelling is assumed not to influence binding specificity or inactive galectins are removed after the labelling reaction, binding and oligomerisation still might be slightly affected. Moreover lot-specific aberrations between different labelling reactions occur. Labelled galectins are for example used for glycan arrays and ELISA-type set-ups (Blixt et al., 2004; Carlsson et al., 2007; Rapoport et al., 2008; Salomonsson et al., 2010; Song et al., 2009b; Stowell et al., 2008a) while fluorescence labelled glycans are used in frontal affinity chromatography or fluorescence polarisation (Carlsson et al., 2007; Hirabayashi et al., 2002; Salomonsson et al., 2010; Sörme et al., 2004).

Assays using both binding partners in its soluble form overcome most of the mentioned problems. But although those assays have different advantages the results cannot directly be compared with the natural set-up in which the glycans are immobilised on glycoproteins or glycolipids and thereby multivalently presented. Fluorescence polarisation is one of these methods measuring direct interactions of ligands in solution, but facing negative side effects of glycan labelling. Similarly, titration calorimetry also measures the interaction of two soluble binding partners. As for titration calorimetry no labelling reaction has to be performed this assay set-up might be considered as the one with fewest problems. But needed galectin concentrations for this test are usually (but not always) in high micromolar ranges and therefore above the physiological range. In this concentration range galectins tend to oligomerise, aggregate or precipitate (Ahmad et al., 2004b; Bachhawat-Sikder et al., 2001; Cho & Cummings, 1995; Dam et al., 2005; Sörme et al., 2004). Moreover titration

calorimetry experiments are suitable for comparative studies of different glycans but do not lead to accurate calculation of affinity constants (Ahmad et al., 2004b). Another way to determine the direct interaction of soluble galectins and glycans is the use of hemagglutination assays, but those are limited to multivalent glycans or the inhibition of interactions between galectins and multivalent glycans or erythrocytes (Ahmad et al., 2004a; Ahmad et al., 2004b; Appukuttan, 2002; Giguere et al., 2008).

### 3.2 Determined fine specificity of galectin-1, -3 and the two galectin-8 CRDs

Although the general fold of all galectins is highly conserved, single galectins are characterised by specific binding interactions with single carbohydrate ligands. Differences in fine specificity have been analysed using different binding assays (as mentioned above). Moreover extensive theoretical evaluation of the putative interactions between single amino acids and functional groups of the bound glycan has been done by modelling and calculation. Some specific ligands with high affinity for the single galectin CRDs are mentioned in Table 1.

The recognition of galactose is common for all galectins but the interaction with the monosaccharide alone is very weak (Carlsson et al., 2007; Knibbs et al., 1993; Salameh et al., 2010). Disaccharides containing galactose  $\beta$ -glycosidic bound to GlcNAc, Glc or GalNAc are bound with significantly increased affinities. Different galectins thereby show high affinity to specific disaccharides. Galectin-3, galectin-1 and the C-terminal CRD of galectin-8 bind preferentially LacNAc units of type I and type II while the N-terminal CRD of galectin-8 shows highest affinity for lactose (Carlsson et al., 2007; Ideo et al., 2011; Salomonsson et al., 2010).

Extensions of the bound galactose moiety effect glycan binding in dependence on the galectin. Galectin-3 tolerates due to its enlarged binding pocket extensions at the galactose 3'-OH-group for example repetitive LacNAc (type II) -structures (poly-LacNAc), showing even higher affinities for repetitive LacNAc structures compared to single LacNAc units (Hirabayashi et al., 2002; Rapoport et al., 2008; Salomonsson et al., 2010). In contrast galectin-1 recognises single LacNAc units presented at the non-reducing terminus of glycans not showing preference for extended poly-LacNAc glycans (Leppänen et al., 2005). Most authors agree that galectin-1 is not able to bind internal galactose moieties in poly-LacNAc-glycans (GlcNAc- $\beta$ -Gal- $\beta$ 4-GlcNAc) (Leppänen et al., 2005; Stowell et al., 2004; Stowell et al., 2008a) but depending on the assay set-up some publications report affinity to this sugar unit (Di Virgilio et al., 1999; Zhou & Cummings, 1993). These different results prove the importance of evaluation of the test set-up and critical examination of the measured binding data.

Other extensions at the 3'-OH-group of galactose such as sulphate or neuraminic acid increase the affinity of galectin-3, galectin-1 and especially galectin-8 N-CRD to the core disaccharide (Carlsson et al., 2007; Sörme et al., 2002; Stowell et al., 2008a). In contrast the C-terminal galectin-8 domain fails to bind 3'-sulfated or 3'-sialylated galactose (Ideo et al., 2003).

Modification at the 6'-OH-group for example with neuraminic acid reduces binding of all four discussed galectin CRDs (Ideo et al., 2003; Stowell et al., 2008a). Therefore  $\alpha$ 6-sialylation is discussed as regulatory modification for galectin-mediated functions (Zhuo & Bellis, 2011). Galectin-3 and galectin-8 C-CRD show high affinity for blood-group antigens (Hirabayashi et al., 2002; Yamamoto et al., 2008)







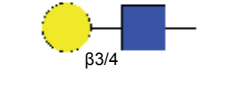
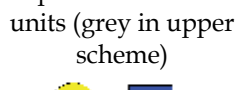



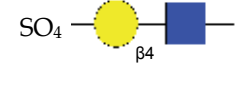
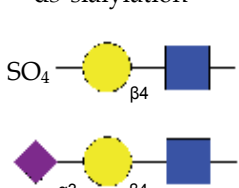
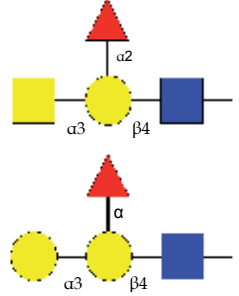
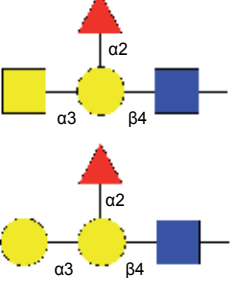
Galectin-1	Galectin-3	Galectin-8 N-CRD	Galectin-8 C-CRD
<p>Complex <i>N</i>-glycans Increasing affinity with increasing number of antennas</p> 	<p><i>N</i>-glycans, preferred poly-LacNAc</p> 	<p><i>N</i>-glycans and glycosphingolipids (e.g. GM3 and GD1a)</p> 	<p><i>N</i>-glycans, preferred poly-LacNAc</p> 
<p>Non-reducing terminal LacNAc type I or II (grey in upper scheme)</p> 	<p>Non-reducing terminal and internal LacNAc, high affinity for repetitive LacNAc-units (grey in upper scheme)</p> 	<p>Preference for lactose (but also binding to LacNAc-units)</p> 	<p>LacNAc type I or II high affinity for repetitive LacNAc-units (grey in upper scheme)</p> 
<p>3-O-sulfation</p> 	<p>3 O-sulfation</p> 	<p>3 O-sulfation and <math>\alpha</math>3-sialylation</p> 	
	<p>Blood group A and B antigens</p> 		<p>Blood group A and B antigens</p> 

Table 1. Preferred ligands of the single carbohydrate recognition domains of galectin-1, -3 and -8 following Rapoport et al. 2002. Symbols according to the consortium of functional glycomics (Brewer, 2004; Carlsson et al., 2007; Dell, 2002; Hirabayashi et al., 2002; Ideo et al., 2003; Ideo et al., 2011; Leppänen et al., 2005; Patnaik et al., 2006; Rabinovich & Toscano, 2009; Rapoport et al., 2008; Salomonsson et al., 2010; Stowell et al., 2004; Stowell et al., 2008a; Yamamoto et al., 2008)

## 4. Glycoproteins as binding partners of galectins

Galectins can act intracellular or in the extracellular space, where they have different functions regulated by protein-protein or protein-glycan interactions. In the extracellular space they interact with different glycoproteins influencing cell adhesion, signalling and proliferation events. Thereby they interact with ECM-glycoproteins forming the extracellular matrix and with glycosylated transmembrane or membrane associated proteins on the cell surface (table 2). Following we present some selected binding partners of the three different galectins discussed so far.

### 4.1 ECM glycoproteins as binding partners of galectins

Different extracellular matrix proteins contribute to structural and functional aspects of the extracellular space. Galectin-1 interacts strongly with different extracellular matrix proteins. It has affinity to several glycoproteins as with increasing affinity osteopontin, vitronectin, thrombospondin, cellular fibronectin and laminin (Moiseeva et al., 2003). Most of these interactions depend on the carbohydrate recognition domain and can be inhibited with soluble glycan ligands (Cooper, 1997; Moiseeva et al., 2003; Ozeki et al., 1995; Zhou & Cummings, 1993). Galectin-3 also shows high affinity for some ECM-glycoproteins (Dumic et al., 2006; Kuwabara & Liu, 1996; Massa et al., 1993; Matarrese et al., 2000; Ochieng et al., 1998b; Sato & Hughes, 1992). The best binding candidates fibronectin and laminin are heavily glycosylated (5-7% and at least 12-15% respectively), carrying mainly *N*-glycans (Paul & Hynes, 1984; Tanzer et al., 1993). *N*-glycans are among the main binding partners of galectin-1, -3 and -8 (Patnaik et al., 2006) (although galectin-8 also shows high affinity to some glycosphingolipids (Ideo et al., 2003; Yamamoto et al., 2008)). One third of laminin *N*-glycans is composed of repetitive “*N*-acetylglucosamine” units (shown for mouse EHS-laminin) which are preferentially recognised by galectin-3 but also by galectin-1 and to less extent galectin-8 (Arumugham et al., 1986; Hirabayashi et al., 2002; Knibbs et al., 1989; Sato & Hughes, 1992; Zhou & Cummings, 1993). The other ECM-glycoproteins carry also *N*-glycans but are less glycosylated (Bunkenborg et al., 2004; Chen et al., 2009; Liu et al., 2005). For example osteopontin from human bone shows only two *N*-glycans with binding sites which are partially blocked by  $\alpha$ 6-bound sialic acid (Ideo et al., 2003; Masuda et al., 2000; Stowell et al., 2008a). Another extracellular matrix protein interacting with galectin-1 and -3 is the Mac-2 binding protein or 90K antigen which influences adhesion processes (Sasaki et al., 1998; Tinari et al., 2001).

The different ECM-proteins which are bound by galectins can interact with other ECM-glycoproteins and/or integrins (Adams, 2001; Janik et al., 2010; Kariya et al., 2008; Singh et al., 2010). These interactions can lead to regulatory effects, lattice formation and signalling cascades.

### 4.2 Cell-surface glycoproteins as binding partners of galectins

Beside these soluble ECM components also some membrane-bound proteins are recognised by galectins. One of these is the lysosome associated membrane glycoprotein 1 (LAMP-1) which is known to carry several *N*-glycans partly presenting poly-lactosamine glycans recognised by galectin-3 and -1 (Chen et al., 2009; Do et al., 1990; Dong & Hughes, 1997). LAMP-1 is also known as CD107a. Several other membrane proteins associated in the cluster of differentiation such as CD3, 4, 7, 8, 43 and 45 which are presented on T-cells are

also recognised by galectin-1, showing the function of galectin-1 in immune response and inflammation (Liu, 2005; Nishi et al., 2008; Pace et al., 1999; Rabinovich et al., 2002a; Rabinovich et al., 2002b).

Binding partner	Gal	Cell type	Process	Reference
Integrin $\alpha 7\beta 1$	1	Skeletal muscle cells; Myoblasts	Influences integrin-laminin interaction	(Gu et al., 1994)
Integrin $\alpha 1\beta 1$	1	Vascular smooth muscle cells	Influences adhesion and migration	(Moiseeva et al., 1999)
Integrin $\alpha 3\beta 1$	8	e.g. endothelial cells	Influences cell adhesion and survival by modulating integrin-ECM interaction	(Hadari et al., 2000)
Cell recognition molecule L1; Myelin associated glycoprotein (MAG) Neural cell adhesion molecule (NCAM)	3	Neural tissue	Likely influences cell adhesion and signalling processes	(Probstmeier et al., 1995)
NG2 proteoglycan	3	Microvascular pericytes	Influences endothelial cell motility and morphogenesis	(Wen et al., 2006)

Table 2. Examples of cell-surface-glycoproteins interacting with galectins

This does not constitute a comprehensive list of cell-bound galectin-binding-glycoproteins, but just intends to show some examples which might be interesting for tissue engineering. Immune and tumor cells are not included in the list.

Similarly galectin-3 binds to CD98 on macrophages, CD66 on neutrophils and the T-cell receptor also showing functions in immune response and inflammation (Demetriou et al., 2001; Dong & Hughes, 1997; Dumic et al., 2006; Hughes, 2001). Other cell surface markers involved in cell-adhesion processes such as CD44 are bound by galectin-8 in a glycan-dependent manner underlining the importance of galectin-8 as matricellular protein involved in the regulation of cell-adhesion (Sebban et al., 2007).

All three galectins mentioned in this review are able to bind different integrin subunits. All bind to  $\beta 1$ -integrins (Dumic et al., 2006; Furtak et al., 2001; Hughes, 2001; Sakaguchi et al., 2010; Zick et al., 2004). In this context galectin-3 binding to  $\beta 1$ -integrins leads to an internalisation signal, regulating receptor amount on the cell surface and thereby influencing cell signalling aspects (Furtak et al., 2001). Other integrins such as  $\alpha v\beta 3$  integrin on endothelial cells or the  $\alpha M$  subunit on macrophages are also bound by galectin-3 (Dong & Hughes, 1997; Markowska et al., 2010). Galectin-8 is known to have a major function in integrin-binding and integrin-mediated signalling (Zick et al., 2004). The binding of galectin-8 N-CRD to the  $\beta 1$ -integrin-subunit is especially good as high affinity  $\alpha 2$ -3-

sialylated ligands are presented on this subunit (Diskin et al., 2009). Beside the  $\beta$ 1-subunit galectin-8 N-CRD also binds  $\alpha$ 5 and some other integrin-subunits, but literature does not give a clear picture about the exact integrin binding partners. For example *N*-glycans on the  $\alpha$ 4-subunit are once mentioned as main binding partner while other authors do not report binding to this subunit. Similar discrepancies were noticed for other subunits (Cárcamo et al., 2006; Diskin et al., 2009; Hadari et al., 2000; Nishi et al., 2003; Yamamoto et al., 2008). This might be explained by tissue- or cell-specific glycosylation patterns of the single subunits. In contrast to most interactions which are performed by the N-terminal galectin-8 CRD binding to the  $\alpha$ M-subunit is performed by the C-terminal CRD (Nishi et al., 2003).

## 5. Galectin function in cell adhesion and cell migration

### 5.1 Principle function

Galectins can act pro- or antiadhesive for different cell types. They can either facilitate or reduce adhesion to other cells depending on different factors. Cell adhesion is enhanced if galectins crosslink glycosylated structures on one cell with glycans on other cells or the extracellular matrix. In contrast the adhesion is reduced if soluble galectins block available receptors for other binding interactions. This depends on one hand on galectin concentration. At high concentrations galectins may block all available receptors without interaction with each other which is necessary for crosslinking and therefore for adhesion (Elola et al., 2007). It is for example discussed that galectin-3 outbursts can lead to detachment of cells from the extracellular matrix as galectin-3 blocks integrin binding to ECM glycoproteins (Ochieng et al., 1998b). On the other hand it is important which receptors are available on the specific cell type used in the experiment and if those receptors interact more easily with the soluble galectins or with receptors on the surface the cell attaches to (Elola et al., 2007). Additionally the oligomerisation state of the galectins plays an important role as they can either block receptors or crosslink molecules depending on their valency (Hughes, 2001). The oligomerisation is in case of galectin-1 depending on galectin concentration while galectin-3 stays monomeric in solution without ligand binding and builds pentamers after the binding reaction (Ahmad et al., 2004a; Cho & Cummings, 1995; Cho & Cummings, 1997; Morris et al., 2004; Nieminen et al., 2008). Moreover effects of single galectins can hardly be determined as most cell types co-express different galectins which might at least partially result in overlapping or opposite effects (Cooper & Barondes, 1999; Liu & Rabinovich, 2005).

In addition to direct binding of galectins to glycan structures on either membrane-bound receptors or ECM-glycoproteins, regulation of integrin amount, availability and affinity by galectin binding also contributes to adhesion events. Galectin-3 for example is able to increase amount and/or affinity of  $\beta$ 2-integrins on the cell surface on neutrophils, thereby regulating the binding to ECM glycoproteins recognised by integrins (Hughes, 2001; Kuwabara & Liu, 1996). Overexpression of galectin-3 correlates with enhanced surface expression of  $\alpha$ 4 $\beta$ 7 integrins resulting in increased cell adhesion (Matarrese et al., 2000). In contrast binding of galectin-3 leads to internalisation of  $\beta$ 1-integrins in breast carcinoma cells (Furtak et al., 2001). Moreover the clustering and residence time of other receptors on the cell surface is regulated by the formation of glycan-galectin lattices thereby regulating different signalling processes (Garner & Baum, 2008; Lau & Dennis, 2008; Rabinovich et al., 2007).

## 5.2 Selected examples of cell adhesion and motility regulated by galectins-1, -3 and -8

We here present only few examples of galectin function in cell adhesion and motility processes. The list is by far not complete. Other review articles focus more detailed on cell adhesion events mediated by galectins (Elola et al., 2007; Hughes, 2001).

Galectin-1 is an important factor for the adhesion and proliferation of neural stem cells and neural progenitor cells. The adhesion is mediated by the carbohydrate recognition domain and interaction of this binding domain with integrin  $\beta 1$  subunit (Sakaguchi et al., 2006; Sakaguchi et al., 2010). Moreover galectin-1 can reduce the motility of immune cells which might explain parts of its anti-inflammatory effects (Elola et al., 2007; Liu, 2005; Rabinovich et al., 2002a; Rabinovich et al., 2002b).

One important function of galectin-3 is associated with angiogenesis (Nangia-Makker et al., 2000a; Nangia-Makker et al., 2000b). Galectin-3 increases for example angiogenesis by forming integrin  $\alpha \beta 3$  lattices on the cell-surface leading to FAK regulated downstream signalling. Galectin-3 mediated angiogenesis depends on the growth factors VEGF and bFGF (Markowska et al., 2010). Another interesting function of galectin-3 is the chemotraction of monocytes via a G-protein coupled receptor pathway and the role in eosinophil rolling to sites of inflammation (Rao et al., 2007; Sano et al., 2000). Most of those functions can only be performed by full length galectin-3 showing the importance of glycan binding and oligomerisation of the protein (Markowska et al., 2010; Sano et al., 2000). Different other biological activities are also depending on both N- and C-terminal domain (Nieminen et al., 2005; Ochieng et al., 1998a; Sano et al., 2000; Sato et al., 2002; Yamaoka et al., 1995). This proves the possibility of regulating galectin-3 function by protease cleavage as mentioned in chapter 2.3.3.

Galectin-8 has been assigned to matricellular proteins which are able to promote cell adhesion. CHO-cells on galectin-8 show similar binding kinetics as on fibronectin but differ in their formation of cytoskeleton (Boura-Halfon et al., 2003). Moreover the binding to galectin-8 triggers specific signalling cascades as Ras, MAPK and Erk pathway (Levy et al., 2003). A physiological function in human might be the modulation of neutrophil function. Galectin-8 promotes neutrophil adhesion by binding  $\alpha M$  integrin and promatrix metalloproteinase-9. Moreover superoxide production which is essential for neutrophil function is triggered by galectin-8 C-terminal CRD (Nishi et al., 2003). Another galectin-8 function might be the promotion of angiogenesis as it was also shown for galectin-3. Galectin-8 increases tube formation *in vitro* and angiogenesis *in vivo* in dependence of its specific carbohydrate affinity at physiological concentrations. This regulatory function is at least partially depending on CD 166 (Delgado et al., 2011).

## 6. Galectins in biomaterial research

As discussed in chapter 5.1 galectins can act pro- and antiadhesive which *in vivo* seems to be mainly regulated by concentration and oligomerisation status of the galectins. In the context of biomaterial research it is also of huge importance if the galectins are immobilised or soluble presented. Immobilised galectins act mainly proadhesive as they crosslink the surface they are immobilised on with glycosylated structures on the cell-membrane. Soluble galectins can either facilitate or reduce adhesion for example to functionalised surfaces as discussed for the *in vivo* situation in chapter 5.1 depending on concentration, oligomerisation and cell type (respectively receptor availability on this cell type) (Elola et al., 2007).

The pro-adhesive properties of galectins have been shown several times. But only few efforts have been done to elucidate the potential of galectins as coatings for biomaterial surfaces. In contrast other components of the extracellular matrix are often used. Coatings with peptides from ECM proteins such as RGD or YIGSR peptide are one of the most common methods to modify biomaterial surfaces. Also coatings with complete ECM proteins or specific adhesion proteins have been investigated. Another important molecule class used in biomaterial research today are growth factors (Chan & Mooney, 2008; Shekaran & Garcia, 2011; Straley et al., 2010). The functionalisation with glycans or lectins seems to be underrepresented although their function in natural processes is well known. Only few studies show the potential of galectins and glycans as biomaterial coatings: The positive influence of galectins was shown for example as the coating of PLGA scaffolds with recombinant galectin-1 promotes adhesion and growth of immortal rat chondrocytes. Therefore this surface is mentioned to have potential as biomaterial in tissue engineering (Chen et al., 2005). The potential of glycans in biomaterial coatings has also been shown. For example galactose derivatives immobilised on material surfaces were proven to influence the growth and function of liver cells positively. But in this study the receptor molecules and mechanisms of signal transduction were not investigated and binding of an asialoglycoprotein receptor (and not galectin mediated binding) is assumed (De Bartolo et al., 2006). Another study shows combined use of immobilised glycans with galectins as it evidences positive effects of endogenous galectin-1 for adhesion of chondrocytes to a lactose-modified surface (Marcon et al., 2005). These findings prove the possible use of glycan and/or galectin modified materials for improved cell adhesion.

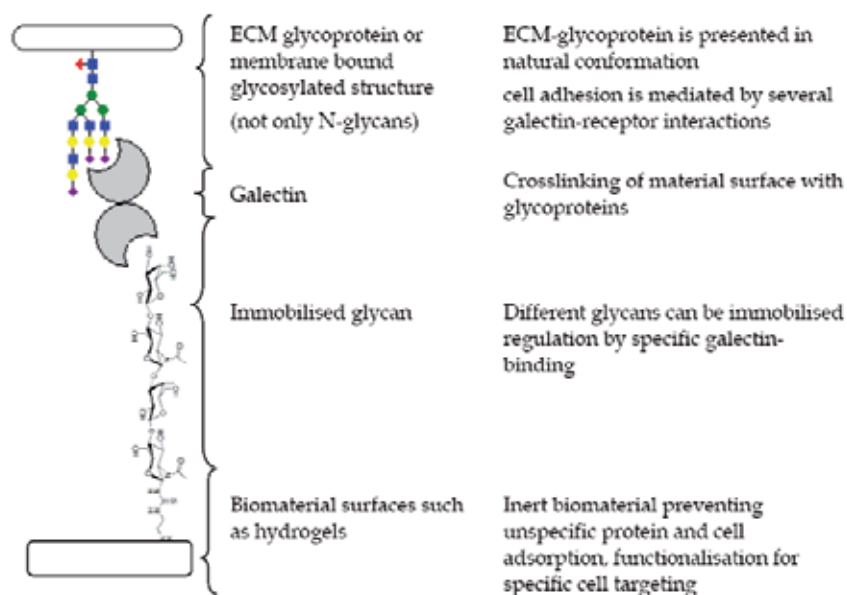


Fig. 4. Schematic representation of a possible biomaterial set-up using immobilised glycans as scaffold for subsequent galectin-mediated protein and cell-adhesion

Our recent work shows the potential of galectins and glycans in the preparation of biomaterial surfaces (figure 4). The assembly of an artificial extracellular matrix consisting of immobilised glycans, galectins and other extracellular matrix components was proven with a fungal model lectin (CGL2) (Sauerzapfe et al., 2009). In this approach poly-*N*-acetyllactosamine structures which are well known ligands for galectins (see chapter 3.2) are enzymatically produced. Those structures can be immobilised to different functionalised materials by a free amino group coupled to the reducing sugar. Concentration dependent binding of lectins to immobilised glycans was proven showing differences for specific glycan ligands. Lectin-mediated crosslinking of the surface with ECM-glycoproteins was also shown (Sauerzapfe et al., 2009). This galectin-mediated binding of ECM-glycoproteins leads to a natural presentation of these structures for subsequent adhesion of cells.

Our ongoing work focuses on the transfer of this set-up to applicable biomaterial surfaces. On the one hand recombinant human galectins are used instead of the fungal lectin to provide a more natural set-up (unpublished data). On the other hand the assembly of this artificial extracellular matrix is transferred to a special hydrogel surface. Star shaped NCO-sP(EO-stat-PO) is used as inert biomaterial which prevents unspecific protein adsorption and can be further functionalised with specific structures such as sugar molecules (Bruellhoff et al., 2010; Grafahrend et al., 2011). On the basis of these glycans an artificial extracellular matrix composed of galectins and ECM-glycoproteins can be built up. Fibroblasts show excellent adhesion and cell spreading on these surfaces (Rech, Beer, Elling, Groll, manuscript in preparation).

## 7. Conclusion

The importance of galectins in cell adhesion and signal transduction has been shown in several investigations. Therefore a possible application of galectins in the assembly of a biomaterial surface mimicking the natural microenvironment seems to be obvious. Anyhow only few articles regarding the use of galectins in biomaterial research have been published. This might be explained by the fact that the fine regulation of galectin mediated cell adhesion and signalling is still not fully understood yet. Therefore it is important to evaluate galectin function under specified conditions to reduce or exclude the risk of unwanted inflammatory or carcinogenic effects.

Taking the presented literature and our own work regarding the biofunctionalisation of surfaces with glycans and galectins together, there is clear evidence that galectins play an important role in cell adhesion and proliferation on specifically functionalised biomaterial surfaces. However, further research has to be done to adopt the fundamental understanding of galectin-glycan mediated cell adhesion processes to an applicable biomaterial surface.

## 8. Acknowledgements

The authors acknowledge financial support by the DFG (Deutsche Forschungsgemeinschaft) within the Research Training Group 1035 "Biointerface", by the DFG (project EL 135/10-1), and by the excellence initiative of the German federal and state governments through ERS@RWTH Aachen University.

## 9. References

Abbott, W. M. & Feizi, T. (1991). Soluble 14-kDa beta-galactoside-specific bovine lectin - evidence from mutagenesis and proteolysis that almost the complete polypeptide-

- chain is necessary for integrity of the carbohydrate recognition domain. *The Journal of Biological Chemistry*, 266, pp. 5552-5557.
- Adams, J. C. (2001). Thrombospondins: Multifunctional Regulators of Cell Interactions. *Annual Review of Cell and Developmental Biology*, 17, pp. 25-51.
- Ahmad, N., Gabius, H. J., Andre, S., Kaltner, H., Sabesan, S., Roy, R., Liu, B. C., Macaluso, F. & Brewer, C. F. (2004a). Galectin-3 precipitates as a pentamer with synthetic multivalent carbohydrates and forms heterogeneous cross-linked complexes. *The Journal of Biological Chemistry*, 279, pp. 10841-10847.
- Ahmad, N., Gabius, H. J., Sabesan, S., Oscarson, S. & Brewer, C. F. (2004b). Thermodynamic binding studies of bivalent oligosaccharides to galectin-1, galectin-3, and the carbohydrate recognition domain of galectin-3. *Glycobiology*, 14, pp. 817-25.
- Al-Ansari, S., Zeebregts, C. J., Slart, R., Peppelenbosch, M. & Tio, R. A. (2009). Galectins in atherosclerotic disease. *Trends in Cardiovascular Medicine*, 19, pp. 164-169.
- Almkvist, J. & Karlsson, A. (2004). Galectins as inflammatory mediators. *Glycoconjugate Journal*, 19, pp. 575-581.
- Appukkuttan, P. S. (2002). Terminal alpha-linked galactose rather than N-acetyl lactosamine is ligand for bovine heart galectin-1 in N-linked oligosaccharides of glycoproteins. *Journal of Molecular Recognition*, 15, pp. 180-187.
- Arumugham, R. G., Hsieh, T. C., Tanzer, M. L. & Laine, R. A. (1986). Structures of the asparagine-linked sugar chains of laminin. *Biochimica et Biophysica Acta*, 883, pp. 112-126.
- Bachhawat-Sikder, K., Thomas, C. J. & Surolia, A. (2001). Thermodynamic analysis of the binding of galactose and poly-N-acetyllactosamine derivatives to human galectin-3. *FEBS Letters*, 500, pp. 75-79.
- Barondes, S. H., Castronovo, V., Cooper, D. N. W., Cummings, R. D., Drickamer, K., Felzi, T., Gitt, M. A., Hirabayashi, J., Hughes, C., Kasai, K.-i., Leffler, H., Liu, F.-T., Lotan, R., Mercurio, A. M., Monsigny, M., Pillai, S., Poirer, F., Raz, A., Rigby, P. W. J., Rini, J. M. & Wang, J. L. (1994a). Galectins: A family of animal  $\beta$ -galactoside-binding lectins. *Cell*, 76, pp. 597-598.
- Barondes, S. H., Cooper, D. N. W., Gitt, M. A. & Leffler, H. (1994b). Galectins - structure and function of a large family of animal lectins. *The Journal of Biological Chemistry*, 269, pp. 20807-20810.
- Bidon, N., Brichory, F., Bourguet, P., Le Pennec, J. P. & Dazord, L. (2001). Galectin-8: A complex sub-family of galectins. *International Journal of Molecular Medicine*, 8, pp. 245-250.
- Birdsall, B., Feeney, J., Burdett, I. D. J., Bawumia, S., Barboni, E. A. M. & Hughes, R. C. (2001). NMR solution studies of hamster galectin-3 and electron microscopic visualization of surface-adsorbed complexes: Evidence for interactions between the N- and C-terminal domains. *Biochemistry*, 40, pp. 4859-4866.
- Blixt, O., Head, S., Mondala, T., Scanlan, C., Huflejt, M. E., Alvarez, R., Bryan, M. C., Fazio, F., Calarese, D., Stevens, J., Razi, N., Stevens, D. J., Skehel, J. J., van Die, I., Burton, D. R., Wilson, I. A., Cummings, R., Bovin, N., Wong, C. H. & Paulson, J. C. (2004). Printed covalent glycan array for ligand profiling of diverse glycan binding proteins. *Proceedings of the National Academy of Sciences of the United States of America*, 101, pp. 17033-17038.



- Bohorov, O., Andersson-Sand, H., Hoffmann, J. & Blixt, O. (2006). Arraying glycomics: a novel bi-functional spacer for one-step microscale derivatization of free reducing glycans. *Glycobiology*, 16, pp. 21C-27C.
- Boura-Halfon, S., Voliovitch, H., Feinstein, R., Paz, K. & Zick, Y. (2003). Extracellular matrix proteins modulate endocytosis of the insulin receptor. *The Journal of Biological Chemistry*, 278, pp. 16397-16404.
- Brewer, C. F. (2004). Thermodynamic binding studies of galectin-1, -3 and -7. *Glycoconjugate Journal*, 19, pp. 459-465.
- Bruellhoff, K., Fiedler, J., Moller, M., Groll, J. & Brenner, R. E. (2010). Surface coating strategies to prevent biofilm formation on implant surfaces. *International Journal of Artificial Organs*, 33, pp. 646-653.
- Bunkenborg, J., Pilch, B. J., Podtelejnikov, A. V. & Wiśniewski, J. R. (2004). Screening for N-glycosylated proteins by liquid chromatography mass spectrometry. *PROTEOMICS*, 4, pp. 454-465.
- Cárcamo, C., Pardo, E., Oyanadel, C., Bravo-Zehnder, M., Bull, P., Cáceres, M., Martínez, J., Massardo, L., Jacobelli, S., González, A. & Soza, A. (2006). Galectin-8 binds specific beta1 integrins and induces polarized spreading highlighted by asymmetric lamellipodia in Jurkat T cells. *Experimental Cell Research*, 312, pp. 374-386.
- Carlsson, S., Oberg, C. T., Carlsson, M. C., Sundin, A., Niisson, U. J., Smith, D., Cummings, R. D., Almkvist, J., Karlsson, A. & Leffler, H. (2007). Affinity of galectin-8 and its carbohydrate recognition domains for ligands in solution and at the cell surface. *Glycobiology*, 17, pp. 663-676.
- Chan, G. & Mooney, D. J. (2008). New materials for tissue engineering: towards greater control over the biological response. *Trends in Biotechnology*, 26, pp. 382-392.
- Chen, R., Jiang, X., Sun, D., Han, G., Wang, F., Ye, M., Wang, L. & Zou, H. (2009). Glycoproteomics analysis of human liver tissue by combination of multiple enzyme digestion and hydrazide chemistry. *Journal of Proteome Research*, 8, pp. 651-661.
- Chen, S. J., Lin, C. C., Tuan, W. C., Tseng, C. S. & Huang, R. N. (2005). Effect of recombinant galectin-1 on the growth of immortal rat chondrocyte on chitosan-coated PLGA scaffold. *Journal of Biomedical Materials Research Part A*, 93A, pp. 1482-1492.
- Chenna, R., Sugawara, H., Koike, T., Lopez, R., Gibson, T. J., Higgins, D. G. & Thompson, J. D. (2003). Multiple sequence alignment with the Clustal series of programs. *Nucleic Acids Research*, 31, pp. 3497-3500.
- Cho, M. & Cummings, R. D. (1995). Galectin-1, a beta-galactoside-binding lectin in Chinese hamster ovary cells. I. Physical and chemical characterization. *The Journal of Biological Chemistry*, 270, pp. 5198-5206.
- Cho, M. J. & Cummings, R. D. (1997). Galectin-1: Oligomeric structure and interactions with poly-lactosamine. *Trends in Glycoscience and Glycotechnology*, 9, pp. 47-56.
- Cooper, D. N. W. (1997). Galectin-1: Secretion and modulation of cell interactions with laminin. *Trends in Glycoscience and Glycotechnology*, 9, pp. 57-67.
- Cooper, D. N. W. & Barondes, S. H. (1999). God must love galectins; He made so many of them. *Glycobiology*, 9, pp. 979-984.
- Cooper, D. N. W. (2002). Galectinomics: finding themes in complexity. *Biochimica et Biophysica Acta - General Subjects*, 1572, pp. 209-231.

- Dam, T. K., Gabius, H. J., Andre, S., Kaltner, H., Lensch, M. & Brewer, C. F. (2005). Galectins bind to the multivalent glycoprotein asialofetuin with enhanced affinities and a gradient of decreasing binding constants. *Biochemistry*, 44, pp. 12564-12571.
- Danguy, A., Camby, I. & Kiss, R. (2002). Galectins and cancer. *Biochimica et Biophysica Acta - General Subjects*, 1572, pp. 285-293.
- De Bartolo, L., Morelli, S., Rende, M., Salerno, S., Giorno, L., Lopez, L. C., Favia, P., d'Agostino, R. & Drioli, E. (2006). Galactose derivative immobilized glow discharge processed polyethersulfone membranes maintain the liver cell metabolic activity. *Journal of Nanoscience and Nanotechnology*, 6, pp. 2344-2353.
- Delgado, V. M. C., Nugnes, L. G., Colombo, L. L., Troncoso, M. F., Fernandez, M. M., Malchiodi, E. L., Frahm, I., Croci, D. O., Compagno, D., Rabinovich, G. A., Wolfenstein-Todel, C. & Elola, M. T. (2011). Modulation of endothelial cell migration and angiogenesis: a novel function for the "tandem-repeat" lectin galectin-8. *The FASEB Journal*, 25, pp. 242-254.
- Dell, A. (2002). Structures of Glycoprotein Glycans. *Australian Journal of Chemistry*, 55, pp. 27-37.
- Demetriou, M., Granovsky, M., Quaggin, S. & Dennis, J. W. (2001). Negative regulation of T-cell activation and autoimmunity by Mgat5 N-glycosylation. *Nature*, 409, pp. 733-739.
- Di Lella, S., Ma, L., Díaz Ricci, J. C., Rabinovich, G. A., Asher, S. A. & Álvarez, R. M. S. (2009). Critical role of the solvent environment in galectin-1 binding to the disaccharide lactose. *Biochemistry*, 48, pp. 786-791.
- Di Virgilio, S., Glushka, J., Moremen, K. & Pierce, M. (1999). Enzymatic synthesis of natural and C-13 enriched linear poly-N-acetylglucosamines as ligands for galectin-1. *Glycobiology*, 9, pp. 353-364.
- Diehl, C., Engstrom, O., Delaine, T., Hakansson, M., Genheden, S., Modig, K., Leffler, H., Ryde, U., Nilsson, U. J. & Akke, M. (2010). Protein flexibility and conformational entropy in ligand design targeting the carbohydrate recognition domain of galectin-3. *Journal of the American Chemical Society*, 132, pp. 14577-14589.
- Diskin, S., Cao, Z. Y., Leffler, H. & Panjwani, N. (2009). The role of integrin glycosylation in galectin-8-mediated trabecular meshwork cell adhesion and spreading. *Glycobiology*, 19, pp. 29-37.
- Do, K.-Y., Smith, D. F. & Cummings, R. D. (1990). LAMP-1 in CHO cells is a primary carrier of poly-N-acetylglucosamine chains and is bound preferentially by a mammalian S-type lectin. *Biochemical and Biophysical Research Communications*, 173, pp. 1123-1128.
- Dong, S. & Hughes, R. C. (1997). Macrophage surface glycoproteins binding to galectin-3 (Mac-2-antigen). *Glycoconjugate Journal*, 14, pp. 267-274.
- Dumic, J., Dabelic, S. & Flogel, M. (2006). Galectin-3: An open-ended story. *Biochimica Et Biophysica Acta-General Subjects*, 1760, pp. 616-635.
- Elola, M. T., Wolfenstein-Todel, C., Troncoso, M. F., Vasta, G. R. & Rabinovich, G. A. (2007). Galectins: matricellular glycan-binding proteins linking cell adhesion, migration, and survival. *Cellular and Molecular Life Sciences*, 64, pp. 1679-1700.
- Furtak, V., Hatcher, F. & Ochieng, J. (2001). Galectin-3 mediates the endocytosis of beta-1 integrins by breast carcinoma cells. *Biochemical and Biophysical Research Communications*, 289, pp. 845-850.

- Garner, O. B. & Baum, L. G. (2008). Galectin-glycan lattices regulate cell-surface glycoprotein organization and signalling. *Biochemical Society Transactions*, 36, pp. 1472-1477.
- Giguere, D., Bonin, M. A., Cloutier, P., Patnam, R., St-Pierre, C., Sato, S. & Roy, R. (2008). Synthesis of stable and selective inhibitors of human galectins-1 and-3. *Bioorganic & Medicinal Chemistry*, 16, pp. 7811-7823.
- Gong, H. C., Honjo, Y., Nangia-Makker, P., Hogan, V., Mazurak, N., Bresalier, R. S. & Raz, A. (1999). The NH<sub>2</sub> terminus of galectin-3 governs cellular compartmentalization and functions in cancer cells. *Cancer Research*, 59, pp. 6239-6245.
- Grafahrend, D., Heffels, K. H., Beer, M. V., Gasteier, P., Moller, M., Boehm, G., Dalton, P. D. & Groll, J. (2011). Degradable polyester scaffolds with controlled surface chemistry combining minimal protein adsorption with specific bioactivation. *Nature Materials*, 10, pp. 67-73.
- Gu, M., Wang, W., Song, W. K., Cooper, D. N. W. & Kaufman, S. J. (1994). Selective modulation of the interaction of alpha7beta1 integrin with fibronectin and laminin by L-14 lectin during skeletal muscle differentiation. *Journal of Cell Science*, 107, pp. 175-181.
- Guévremont, M., Martel-Pelletier, Boileau, C., Liu, F.-T., Richard, M., Fernandes, J.-C., Pelletier, J.-P. & Reboul, P. (2004). Galectin-3 surface expression on human adult chondrocytes: a potential substrate for collagenase-3. *Annals of the Rheumatic Diseases*, pp. 636-643.
- Gueux, N. & Peitsch, M. C. (1997). Swiss-Model and the swiss-pdb viewer: an environment for comparative protein modeling. *Electrophoresis*, 18, pp. 2714-2723.
- Hadari, Y. R., Arbel-Goren, R., Levy, Y., Amsterdam, A., Alon, R., Zakut, R. & Zick, Y. (2000). Galectin-8 binding to integrins inhibits cell adhesion and induces apoptosis. *Journal of Cell Science*, 113, pp. 2385-2397.
- Hernandez, J. D. & Baum, L. G. (2002). Ah, sweet mystery of death! Galectins and control of cell fate. *Glycobiology*, 12, pp. 127R-136.
- Hirabayashi, J. & Kasai, K. (1991). Effect of amino acid substitution by site-directed mutagenesis on the carbohydrate recognition and stability of human 14-kDa beta-galactoside-binding lectin. *The Journal of Biological Chemistry*, 266, pp. 23648-23653.
- Hirabayashi, J. & Kasai, K. (1993). The family of metazoan metal-independent beta-galactoside-binding lectins: structure, function and molecular evolution. *Glycobiology*, 3, pp. 297-304.
- Hirabayashi, J. & Kasai, K. I. (1994). Further evidence by site-directed mutagenesis that conserved hydrophilic residues form a carbohydrate-binding site of human galectin-1. *Glycoconjugate Journal*, 11, pp. 437-442.
- Hirabayashi, J., Hashidate, T., Arata, Y., Nishi, N., Nakamura, T., Hirashima, M., Urashima, T., Oka, T., Futai, M., Muller, W. E. G., Yagi, F. & Kasai, K.-i. (2002). Oligosaccharide specificity of galectins: a search by frontal affinity chromatography. *Biochimica et Biophysica Acta - General Subjects*, 1572, pp. 232-254.
- Horie, H., Kadoya, T., Hikawa, N., Sango, K., Inoue, H., Takeshita, K., Asawa, R., Hiroi, T., Sato, M., Yoshioka, T. & Ishikawa, Y. (2004). Oxidized galectin-1 stimulates macrophages to promote axonal regeneration in peripheral nerves after axotomy. *The Journal of Neuroscience*, 24, pp. 1873-1880.

- Houzelstein, D., Goncalves, I. R., Fadden, A. J., Sidhu, S. S., Cooper, D. N. W., Drickamer, K., Leffler, H. & Poirier, F. (2004). Phylogenetic analysis of the vertebrate galectin family. *Molecular Biology and Evolution*, 21, pp. 1177–1187.
- Hughes, R. C. (1999). Secretion of the galectin family of mammalian carbohydrate-binding proteins. *Biochimica et Biophysica Acta*, 1473, pp. 172–185.
- Hughes, R. C. (2001). Galectins as modulators of cell adhesion. *Biochimie*, 83, pp. 667–676.
- Ideo, H., Seko, A., Ishizuka, I. & Yamashita, K. (2003). The N-terminal carbohydrate recognition domain of galectin-8 recognizes specific glycosphingolipids with high affinity. *Glycobiology*, 13, pp. 713–723.
- Ideo, H., Matsuzaka, T., Nonaka, T., Seko, A. & Yamashita, K. (2011). Galectin-8-N-domain recognition mechanism for sialylated and sulfated glycans. *The Journal of Biological Chemistry*, pp.11346–11355
- Ilarregui, J. M., Bianco, G. A., Toscano, M. A. & Rabinovich, G. A. (2005). The coming of age of galectins as immunomodulatory agents: impact of these carbohydrate binding proteins in T cell physiology and chronic inflammatory disorders. *Annals of the Rheumatic Diseases*, 64, pp. 96–103.
- Janik, M. E., Litynska, A. & Vereecken, P. (2010). Cell migration-The role of integrin glycosylation. *Biochimica et Biophysica Acta- General Subjects*, 1800, pp. 545–555.
- John, C. M., Leffler, H., Kahl-Knutsson, B., Svensson, I. & Jarvis, G. A. (2003). Truncated galectin-3 inhibits tumor growth and metastasis in orthotopic nude mouse model of human breast cancer. *Clinical Cancer Research*, 9, pp. 2374–2383.
- Kariya, Y., Kato, R., Itoh, S., Fukuda, T., Shibukawa, Y., Sanzen, N., Sekiguchi, K., Wada, Y., Kawasaki, N. & Gu, J. G. (2008). N-Glycosylation of laminin-332 regulates its biological functions: A novel function of the bisecting GlcNAc. *The Journal of Biological Chemistry*, 283, pp. 33036–33045.
- Kishishita, S., Nishino, A., Murayama, K., Terada, T., Shirouzu, M. & Yokoyama, S. (2008). pdb database 2YXS.
- Klyosov, A. A., Zbigniew, J. W. & Platt, D. (2008). *Galectins*. Wiley, ISBN 978-0-470-37318, Hoboken.
- Knibbs, R. N., Perini, F. & Goldstein, I. J. (1989). Structure of the Major Concanavalin-a Reactive Oligosaccharides of the Extracellular-Matrix Component Laminin. *Biochemistry*, 28, pp. 6379–6392.
- Knibbs, R. N., Agrwal, N., Wang, J. L. & Goldstein, I. J. (1993). Carbohydrate-binding protein-35 2. Analysis of the interaction of the recombinant polypeptide with saccharides. *The Journal of Biological Chemistry*, 268, pp. 14940–14947.
- Kubler, D., Hung, C. W., Dam, T. K., Kopitz, J., Andre, S., Kaltner, H., Lohr, M., Manning, J. C., He, L. Z., Wang, H., Middelberg, A., Brewer, C. F., Reed, J., Lehmann, W. D. & Gabius, H. J. (2008). Phosphorylated human galectin-3: Facile large-scale preparation of active lectin and detection of structural changes by CD spectroscopy. *Biochimica et Biophysica Acta- General Subjects*, 1780, pp. 716–722.
- Kuwabara, I. & Liu, F. T. (1996). Galectin-3 promotes adhesion of human neutrophils to laminin. *Journal of Immunology*, 156, pp. 3939–3944.
- Larkin, M. A., Blackshields, G., Brown, N. P., Chenna, R., McGettigan, P. A., McWilliam, H., Valentin, F., Wallace, I. M., Wilm, A., Lopez, R., Thompson, J. D., Gibson, T. J. & Higgins, D. G. (2007). Clustal W and clustal X version 2.0. *Bioinformatics*, 23, pp. 2947–2948.

- Lau, K. S. & Dennis, J. W. (2008). N-Glycans in cancer progression. *Glycobiology*, 18, pp. 750-760.
- Leffler, H., Carlsson, S., Hedlund, M., Qian, Y. & Poirier, F. (2004). Introduction to galectins. *Glycoconjugate Journal*, 19, pp. 433-440.
- Leppänen, A., Stowell, S., Blixt, O. & Cummings, R. D. (2005). Dimeric galectin-1 binds with high affinity to alpha2,3-sialylated and non-sialylated terminal N-Acetylglucosamine units on surface-bound extended glycans. *The Journal of Biological Chemistry*, 280, pp. 5549-5562.
- Levy, Y., Ronen, D., Bershadsky, A. D. & Zick, Y. (2003). Sustained induction of ERK, protein kinase B, and p70 S6 kinase regulates cell spreading and formation of F-actin microspikes upon ligation of integrins by galectin-8, a mammalian lectin. *The Journal of Biological Chemistry*, 278, pp. 14533-14542.
- Levy, Y., Auslender, S., Eisenstein, M., Vidavski, R. R., Ronen, D., Bershadsky, A. D. & Zick, Y. (2006). It depends on the hinge: a structure-functional analysis of galectin-8, a tandem-repeat type lectin. *Glycobiology*, 16, pp. 463-476.
- Liu, F.-T., Patterson, R. J. & Wang, J. L. (2002). Intracellular functions of galectins. *Biochimica et Biophysica Acta (BBA) - General Subjects*, 1572, pp. 263-273.
- Liu, F.-T. (2005). Regulatory Roles of Galectins in the Immune Response. *International Archives of Allergy and Immunology*, 136, pp. 385-400.
- Liu, F.-T. & Rabinovich, G. A. (2005). Galectins as modulators of tumour progression. *Nature Reviews Cancer*, 5, pp. 29-41.
- Liu, T., Qian, W.-J., Gritsenko, M. A., Camp, D. G., Monroe, M. E., Moore, R. J. & Smith, R. D. (2005). Human Plasma N-Glycoproteome Analysis by Immunoaffinity Subtraction, Hydrazide Chemistry, and Mass Spectrometry. *Journal of Proteome Research*, 4, pp. 2070-2080.
- Lobsanov, Y. D., Gitt, M. A., Leffler, H., Barondes, S. H. & Rini, J. M. (1993). X-ray crystal structure of the human dimeric S-Lac lectin, L-14-II, in complex with lactose at 2.9-Å resolution. *The Journal of Biological Chemistry*, 268, pp. 27034-27038.
- Lopez-Lucendo, M. F., Solis, D., Andre, S., Hirabayashi, J., Kasai, K., Kaltner, H., Gabius, H. J. & Romero, A. (2004). Growth-regulatory human galectin-1: crystallographic characterisation of the structural changes induced by single-site mutations and their impact on the thermodynamics of ligand binding. *The Journal of Molecular Biology*, 343, pp. 957-970.
- Marcon, P., Marsich, E., Vetere, A., Mozetic, P., Campa, C., Donati, I., Vittur, F., Gamini, A. & Paoletti, S. (2005). The role of Galectin-1 in the interaction between chondrocytes and a lactose-modified chitosan. *Biomaterials*, 26, pp. 4975-4984.
- Markowska, A. I., Liu, F. T. & Panjwani, N. (2010). Galectin-3 is an important mediator of VEGF- and bFGF-mediated angiogenic response. *Journal of Experimental Medicine*, 207, pp. 1981-1993.
- Massa, S. M., Cooper, D. N. W., Leffler, H. & Barondes, S. H. (1993). L-29, an endogenous lectin, binds to glycoconjugate ligands with positive cooperativity. *Biochemistry*, 32, pp. 260-267.
- Masuda, K., Takahashi, N., Tsukamoto, Y., Honma, H. & Kohri, K. (2000). N-Glycan structures of an osteopontin from human bone. *Biochemical and Biophysical Research Communications*, 268, pp. 814-817.

- Matarrese, P., Fusco, O., Tinari, N., Natoli, C., Liu, F. T., Semeraro, M. L., Malorni, W. & Iacobelli, S. (2000). Galectin-3 overexpression protects from apoptosis by improving cell adhesion properties. *International Journal of Cancer*, 85, pp. 545-554.
- Mazurek, N., Conklin, J., Byrd, J. C., Raz, A. & Bresalier, R. S. (2000). Phosphorylation of the beta-galactoside-binding protein galectin-3 modulates binding to its ligands. *The Journal of Biological Chemistry*, 275, pp. 36311-36315.
- Mehul, B. & Hughes, R. C. (1997). Plasma membrane targeting, vesicular budding and release of galectin 3 from the cytoplasm of mammalian cells during secretion. *Journal of Cell Science*, 110, pp. 1169-1178.
- Moiseeva, E. P., Spring, E. L., Baron, J. H. & de Bono, D. P. (1999). Galectin 1 modulates attachment, spreading and migration of cultured vascular smooth muscle cells via interactions with cellular receptors and components of extracellular matrix. *Journal of Vascular Research*, 36, pp. 47-58.
- Moiseeva, E. P., Williams, B. & Samani, N. J. (2003). Galectin 1 inhibits incorporation of vitronectin and chondroitin sulfate B into the extracellular matrix of human vascular smooth muscle cells. *Biochimica et Biophysica Acta*, 1619, pp. 125-132.
- Morris, S., Ahmad, N., Andre, S., Kaltner, H., Gabius, H. J., Brenowitz, M. & Brewer, F. (2004). Quaternary solution structures of galectins-1, -3, and -7. *Glycobiology*, 14, pp. 293-300.
- Munoz, F. J., Santos, J. I., Arda, A., Andre, S., Gabius, H. J., Sinisterra, J. V., Jimenez-Barbero, J. & Hernaiz, M. J. (2010). Binding studies of adhesion/growth-regulatory galectins with glycoconjugates monitored by surface plasmon resonance and NMR spectroscopy. *Organic & Biomolecular Chemistry*, 8, pp. 2986-2992.
- Nangia-Makker, P., Baccarini, S. & Raz, A. (2000a). Carbohydrate-recognition and angiogenesis. *Cancer and Metastasis Reviews*, 19, pp. 51-57.
- Nangia-Makker, P., Honjo, Y., Sarvis, R., Akahani, S., Hogan, V., Pienta, K. J. & Raz, A. (2000b). Galectin-3 induces endothelial cell morphogenesis and angiogenesis. *American Journal of Pathology*, 156, pp. 899-909.
- Nangia-Makker, P., Balan, V. & Raz, A. (2008). Regulation of tumor progression by extracellular Galectin-3. *Cancer Microenvironment*, 1, pp.43-51
- Nieminen, J., St-Pierre, C. & Sato, S. (2005). Galectin-3 interacts with naive and primed neutrophils, inducing innate immune responses. *Journal of Leukocyte Biology*, 78, pp. 1127-1135.
- Nieminen, J., Kuno, A., Hirabayashi, J. & Sato, S. (2008). Visualization of Galectin-3 Oligomerization on the Surface of Neutrophils and Endothelial Cells Using Fluorescence Resonance Energy Transfer. *The Journal of Biological Chemistry*, 282, pp. 1374-1383.
- Nishi, N., Shoji, H., Seki, M., Itoh, A., Miyataka, H., Yuube, K., Hirashima, M. & Nakamura, T. (2003). Galectin-8 modulates neutrophil function via interaction with integrin alpha M. *Glycobiology*, 13, pp. 755-763.
- Nishi, N., Itoh, A., Shoji, H., Miyataka, H. & Nakamura, T. (2006). Galectin-8 and galectin-9 are novel substrates for thrombin. *Glycobiology*, 16, pp. 15C-20C.
- Nishi, N., Abe, A., Iwaki, J., Yoshida, H., Itoh, A., Shoji, H., Kamitori, S., Hirabayashi, J. & Nakamura, T. (2008). Functional and structural bases of a cysteine-less mutant as a long-lasting substitute for galectin-1. *Glycobiology*, pp. 1065-1073.

- Ochieng, J., Fridman, R., Nangiamakker, P., Kleiner, D. E., Liotta, L. A., Stetlerstevenson, W. G. & Raz, A. (1994). Galectin-3 is a novel substrate for human matrix metalloproteinase-2 and metalloproteinase-9. *Biochemistry*, 33, pp. 14109-14114.
- Ochieng, J., Green, B., Evans, S., James, O. & Warfield, P. (1998a). Modulation of the biological functions of galectin-3 by matrix metalloproteinases. *Biochimica et Biophysica Acta- General Subjects*, 1379, pp. 97-106.
- Ochieng, J., Leite-Browning, M. L. & Warfield, P. (1998b). Regulation of cellular adhesion to extracellular matrix proteins by galectin-3. *Biochemical and Biophysical Research Communications*, 246, pp. 788-791.
- Ozeki, Y., Matsui, T., Yamamoto, Y., Funahashi, M., Hamako, J. & Titani, K. (1995). Tissue fibronectin is an endogenous ligand for galectin-1. *Glycobiology*, 5, pp. 255-261.
- Pace, K. E., Lee, C., Stewart, P. L. & Baum, L. G. (1999). Restricted receptor segregation into membrane microdomains occurs on human T cells during apoptosis induced by galectin-1. *Journal of Immunology*, 163, pp. 3801-3811.
- Patnaik, S. K., Potvin, B., Carlsson, S., Sturm, D., Leffler, H. & Stanley, P. (2006). Complex N-glycans are the major ligands for galectin-1, -3, and -8 on Chinese hamster ovary cells. *Glycobiology*, 16, pp. 305-317.
- Paul, J. I. & Hynes, R. O. (1984). Multiple fibronectin subunits and their post-translational modifications. *The Journal of Biological Chemistry*, 259, pp. 13477-13487.
- Probstmeier, R., Montag, D. & Schachner, M. (1995). Galectin-3, a beta-galactoside-binding animal lectin, binds to neural recognition molecules. *Journal of Neurochemistry*, 64, pp. 2465-2472.
- Rabinovich, G. A., Baum, L. G., Tinari, N., Paganelli, R., Natoli, C., Liu, F. T. & Iacobelli, S. (2002a). Galectins and their ligands: amplifiers, silencers or tuners of the inflammatory response? *Trends in Immunology*, 23, pp. 313-320.
- Rabinovich, G. A., Rubinstein, N. & Toscano, M. A. (2002b). Role of galectins in inflammatory and immunomodulatory processes. *Biochimica et Biophysica Acta- General Subjects*, 1572, pp. 274-284.
- Rabinovich, G. A., Toscano, M. A., Jackson, S. S. & Vasta, G. R. (2007). Functions of cell surface galectin-glycoprotein lattices. *Current Opinion in Structural Biology*, 17, pp. 513-520.
- Rabinovich, G. A. & Toscano, M. A. (2009). Turning 'sweet' on immunity: galectin-glycan interactions in immune tolerance and inflammation. *Nature Reviews Immunology*, 9, pp. 338-352.
- Rao, S. P., Wang, Z. Z., Zuberi, R. I., Sikora, L., Bahaie, N. S., Zuraw, B. L., Liu, F. T. & Sriramarao, P. (2007). Galectin-3 functions as an adhesion molecule to support eosinophil rolling and adhesion under conditions of flow. *The Journal of Immunology*, 179, pp. 7800-7807.
- Rapoport, E. M., Andre, S., Kurmyshkina, O. V., Pochechueva, T. V., Severov, V. V., Pazynina, G. V., Gabius, H.-J. & Bovin, N. V. (2008). Galectin-loaded cells as a platform for the profiling of lectin specificity by fluorescent neoglycoconjugates: A case study on galectins-1 and -3 and the impact of assay setting. *Glycobiology*, 18, pp. 315-324.
- Sakaguchi, M., Shingo, T., Shimazaki, T., Okano, H. J., Shiwa, M., Ishibashi, S., Oguro, H., Ninomiya, M., Kadoya, T., Horie, H., Shibuya, A., Mizusawa, H., Poirier, F., Nakauchi, H., Sawamoto, K. & Okano, H. (2006). A carbohydrate-binding protein,

- Galectin-1, promotes proliferation of adult neural stem cells. *Proceedings of the National Academy of Sciences of the United States of America*, 103, pp. 7112-7117.
- Sakaguchi, M., Imaizumi, Y., Shingo, T., Tada, H., Hayama, K., Yamada, O., Morishita, T., Kadoya, T., Uchiyama, N., Shimazaki, T., Kuno, A., Poirier, F., Hirabayashi, J., Sawamoto, K. & Okano, H. (2010). Regulation of adult neural progenitor cells by Galectin-1/ $\beta$ 1 Integrin interaction. *Journal of Neurochemistry*, 113, pp. 1516-1524.
- Salameh, B. A., Cumpstey, I., Sundin, A., Leffler, H. & Nilsson, U. J. (2010). 1H-1,2,3-Triazol-1-yl thiodigalactoside derivatives as high affinity galectin-3 inhibitors. *Bioorganic & Medicinal Chemistry*, 18, pp. 5367-5378.
- Salomonsson, E., Carlsson, M. C., Osla, V., Hendus-Altenburger, R., Kahl-Knutson, B., Oberg, C. T., Sundin, A., Nilsson, R., Nordberg-Karlsson, E., Nilsson, U. J., Karlsson, A., Rini, J. M. & Leffler, H. (2010). Mutational tuning of galectin-3 specificity and biological function. *The Journal of Biological Chemistry*, 285, pp. 35079-35091.
- Sano, H., Hsu, D. K., Yu, L., Apgar, J. R., Kuwabara, I., Yamanaka, T., Hirashima, M. & Liu, F.-T. (2000). Human galectin-3 is a novel chemoattractant for monocytes and macrophages. *The Journal of Immunology*, 165, pp. 2156-2164.
- Sasaki, T., Brakebusch, C., Engel, J. & Timpl, R. (1998). Mac-2 binding protein is a cell-adhesive protein of the extracellular matrix which self-assembles into ring-like structures and binds  $\beta$ 1 integrins, collagens and fibronectin. *The EMBO Journal*, 17, pp. 1606-1613.
- Sato, S. & Hughes, R. C. (1992). Binding-specificity of a baby hamster-kidney lectin for H type-I and type-II chains, poly-lactosamine glycans, and appropriately glycosylated forms of laminin and fibronectin. *The Journal of Biological Chemistry*, 267, pp. 6983-6990.
- Sato, S., Ouellet, N., Pelletier, I., Simard, M., Rancourt, A. & Bergeron, M. G. (2002). Role of galectin-3 as an adhesion molecule for neutrophil extravasation during streptococcal pneumonia. *Journal of Immunology*, 168, pp. 1813-1822.
- Sauerzapfe, B., Krenek, K., Schmiedel, J., Wakarchuk, W. W., Pelantová, H., Kren, V. & Elling, L. (2009). Chemo-enzymatic synthesis of poly-N-acetyl-lactosamine (poly-LacNAc) structures and their characterization for CGL2-galectin-mediated binding of ECM glycoproteins to biomaterial surfaces. *Glycoconjugate Journal*, 26, pp. 141-159.
- Sebban, L. E., Ronen, D., Levartovsky, D., Elkayam, O., Caspi, D., Amar, S., Amital, H., Rubinow, A., Golan, I., Naor, D., Zick, Y. & Golan, I. (2007). The involvement of CD44 and its novel ligand galectin-8 in apoptotic regulation of autoimmune inflammation. *Journal of Immunology*, 179, pp. 1225-1235.
- Seelenmeyer, C., Wegehingel, S., Tews, I., Kunzler, M., Aebi, M. & Nickel, W. (2005). Cell surface counter receptors are essential components of the unconventional export machinery of galectin-1. *The Journal of Cell Biology*, 171, pp. 373-381.
- Seelenmeyer, C., Stegmayer, C. & Nickel, W. (2008). Unconventional secretion of fibroblast growth factor 2 and galectin-1 does not require shedding of plasma membrane-derived vesicles. *FEBS Letters*, 582, pp. 1362-1368.
- Seetharaman, J., Kanigsberg, A., Slaaby, R., Leffler, H., Barondes, S. H. & Rini, J. R. (1998). X-ray crystal structure of the human galectin-3 carbohydrate recognition domain at 2.1-Å resolution. *The Journal of Biological Chemistry*, 273, pp. 13047-13052.



- Shekaran, A. & Garcia, A. J. (2011). Extracellular matrix-mimetic adhesive biomaterials for bone repair. *Journal of Biomedical Materials Research Part A*, 96A, pp. 261-272.
- Shekhar, M. P. V., Nangia-Makker, P., Tait, L., Miller, F. & Raz, A. (2004). Alterations in galectin-3 expression and distribution correlate with breast cancer progression - Functional analysis of galectin-3 in breast epithelial-endothelial interactions. *American Journal of Pathology*, 165, pp. 1931-1941.
- Singh, P., Carraher, C. & Schwarzbauer, J. E. (2010). Assembly of fibronectin extracellular matrix. In: *Annual Review of Cell and Developmental Biology*, vol. 26, pp. 397-419, ISBN 1081-0706.
- Song, X. Z., Lasanajak, Y., Xia, B. Y., Smith, D. & Cummings, R. (2009a). Fluorescent glycosylamides produced by microscale derivatization of free glycans for natural glycan microarrays. *ACS Chemical Biology*, vol. 4, no. 9, 741-750.
- Song, X. Z., Xia, B. Y., Stowell, S. R., Lasanajak, Y., Smith, D. F. & Cummings, R. D. (2009b). Novel fluorescent glycan microarray strategy reveals ligands for galectins. *Chemistry & Biology*, 16, pp. 36-47.
- Song, X. Z., Lasanajak, Y., Xia, B. Y., Heimbürg-Molinari, J., Rhea, J., Ju, H., Zhao, C. M., Molinari, R., Cummings, R. & Smith, D. (2010). Shotgun glycomics: Functional identification of glycan determinants through a microarray strategy using fluorescently tagged glycans. *Glycobiology*, 20, pp. 54.
- Sörme, P., Qian, Y. N., Nyholm, P. G., Leffler, H. & Nilsson, U. J. (2002). Low micromolar inhibitors of galectin-3 based on 3'-derivatization of N-acetylglucosamine. *Chembiochem*, 3, pp. 183-189.
- Sörme, P., Kahl-Knutsson, B., Huflejt, M., Nilsson, U. J. & Leffler, H. (2004). Fluorescence polarization as an analytical tool to evaluate galectin-ligand interactions. *Analytical Biochemistry*, 334, pp. 36-47.
- Sörme, P., Arnoux, P., Kahl-Knutsson, B., Leffler, H., Rini, J. M. & Nilsson, U. J. (2005). Structural and thermodynamic studies on cation-II interactions in lectin-ligand complexes: High-affinity galectin-3 inhibitors through fine-tuning of an arginine-arene interaction. *Journal of the American Chemical Society*, 127, pp. 1737-1743.
- Stowell, S. R., Dias-Baruffi, M., Penttilä, L., Renkonen, O., Nyame, A. K. & Cummings, R. D. (2004). Human galectin-1 recognition of poly-N-acetylglucosamine and chimeric polysaccharides. *Glycobiology*, 14, pp. 157-67.
- Stowell, S. R., Arthur, C. M., Mehta, P., Slanina, K. A., Blixt, O., Leffler, H., Smith, D. F. & Cummings, R. D. (2008a). Galectin-1,-2, and-3 exhibit differential recognition of sialylated glycans and blood group antigens. *The Journal of Biological Chemistry*, 283, pp. 10109-10123.
- Stowell, S. R., Arthur, C. M., Slanina, K. A., Horton, J. R., Smith, D. F. & Cummings, R. D. (2008b). Dimeric galectin-8 induces phosphatidylserine exposure in leukocytes through polyglucosamine recognition by the C-terminal domain. *The Journal of Biological Chemistry*, 283, pp. 20547-20559.
- Straley, K. S., Foo, C. W. P. & Heilshorn, S. C. (2010). Biomaterial Design Strategies for the Treatment of Spinal Cord Injuries. *Journal of Neurotrauma*, 27, pp. 1-19.
- Szabo, P., Dam, T. K., Smetana, K., Dvorankova, B., Kurbler, D., Brewer, C. F. & Gabius, H. J. (2009). Phosphorylated Human Lectin Galectin-3: Analysis of Ligand Binding by Histochemical Monitoring of Normal/Malignant Squamous Epithelia and by Isothermal Titration Calorimetry. *Anatomia Histologia Embryologia*, 38, pp. 68-75.

- Tanzer, M. L., Chandrasekaran, S., Dean, J. W., 3rd & Giniger, M. S. (1993). Role of laminin carbohydrates on cellular interactions. *Kidney International*, 43, pp. 66-72.
- Tinari, N., Kuwabara, I., Huflejt, M. E., Shen, P. F., Iacobelli, S. & Liu, F.-T. (2001). Glycoprotein 90K/Mac-2BP interacts with galectin-1 and mediates galectin-1-induced cell aggregation. *International Journal of Cancer*, 91, pp. 167-172.
- Tomizawa, T., Koshiba, S., Inoue, M., Kigawa, T., Yokoyama, S. & Initiative, R. S. G. P. (2008). pdb database 2YRO.
- van den Brule, F., Califice, S. & Castronovo, V. (2004). Expression of galectins in cancer: A critical review. *Glycoconjugate Journal*, 19, pp. 537-542.
- Vasta, G. R. (2009). Roles of galectins in infection. *Nature Reviews Microbiology* 7, pp. 424-438.
- Wen, Y. F., Makagiansar, I. T., Fukushi, J., Liu, F. T., Fukuda, M. N. & Stallcup, W. B. (2006). Molecular basis of interaction between NG2 proteoglycan and galectin-3. *Journal of Cellular Biochemistry*, 98, pp. 115-127.
- Yamamoto, H., Nishi, N., Shoji, H., Itoh, A., Lu, L. H., Hirashima, M. & Nakamura, T. (2008). Induction of cell adhesion by galectin-8 and its target molecules in Jurkat T-cells. *Journal of Biochemistry*, 143, pp. 311-324.
- Yamaoka, A., Kuwabara, I., Frigeri, L. G. & Liu, F. T. (1995). A Human Lectin, Galectin-3 (Epsilon-Bp/Mac-2), Stimulates Superoxide Production by Neutrophils. *Journal of Immunology*, 154, pp. 3479-3487.
- Yoshii, T., Fukumori, T., Honjo, Y., Inohara, H., Kim, H.-R. C. & Raz, A. (2002). Galectin-3 phosphorylation is required for its anti-apoptotic function and cell cycle arrest. *The Journal of Biological Chemistry*, 277, pp. 6852-6857.
- Zhou, Q. & Cummings, R. D. (1993). L-14 lectin recognition of laminin and its promotion of in vitro cell adhesion. *Arch Biochem Biophys*, 300, pp. 6-17.
- Zhuo, Y. & Bellis, S. L. (2011). Emerging Role of alpha 2,6-Sialic Acid as a Negative Regulator of Galectin Binding and Function. *The Journal of Biological Chemistry*, 286, pp. 5935-5941.
- Zick, Y., Eisenstein, M., Goren, R. A., Hadari, Y. R., Levy, Y. & Ronen, D. (2004). Role of galectin-8 as a modulator of cell adhesion and cell growth. *Glycoconjugate Journal*, 19, pp. 517-526.

# Biomaterials and Epithesis, Our Experience in Maxillo Facial Surgery

G. Fini, L.M. Moricca, A. Leonardi,  
S. Buonaccorsi and V. Pellacchia  
*La Sapienza/ Roma  
Italy*

## 1. Introduction

Maxillofacial prosthetics is considered in literature as "... the art and science of anatomic, functional and cosmetic reconstruction, by the use of non-living substitutes, of those regions in the maxillae, mandible and face that are missing or defective..." 1. In the maxillofacial surgery where malformative, oncologic traumatologic pathology and the plastic surgery are treated, the maxillofacial prostheses, in selected cases, can reach a satisfactory therapeutic result from functional, aesthetic, psychologic, and social point of views. In a delicate district, such as the face, where a heavy deficit can determine huge psychologic and social problems, the conventional reconstructive surgery intervenes with reconstructive techniques and with the biomaterials insertion, often insufficient to guarantee the restoration of the harmony of the face. When these conditions are verified, the solution resides in the osteointegration concept and in the application of the epithesis. There are certainly some limits of application of these prostheses, first, the ethics limits: the epithesis constitute in fact an alternative only when the conventional reconstructive surgery cannot be applied, but inside these limits, it is really possible to find an excellent therapeutic resource in patients who cannot undergo surgical interventions. In literature, it is possible to find different kinds of reconstruction of missing body parts by the application of prothesis<sup>2</sup>. The osteointegration concept was introduced at first time by Professor Branemark in 1960 to describe the "direct structural and functional connection between living bone and the surface of a plant exposed to load, understood as a not static but dynamic process<sup>3</sup>. According to his school of thought, the technique of positioning of the implant is fundamental, to take place in the most complete precision and to allow the initial stability of one's self. Other elements conditioning the success of the osteointegration are the material of the implant, the form, the areas of the application, and the patient's clinical conditions. The first titanium osteointegration implant was positioned in 1965 in the jaw without dental elements 4; in 1977, implants were positioned in mastoid areas for the application of an acoustic translator. In 1979, implants for the fixation of epithesis of ears, noses, and eyes were positioned. At present, the indication to the position of epithesis as the first choice of treatment is when the conventional reconstructive interventions turn out to be inapplicable or ineffective. The epithesis is a good resolution for the patient because it is not traumatic and has short-time result, removing every psychologic physique obstacle for the inclusion in a normal social life.

## 2. Our experience

From May 2002 to December 2010, 415 facial prosthesis (1117 implants) have been positioned in our Ephitesy Center. Defects were congenital (N = 142), consequent to trauma (N = 95) and to demolitive surgery for malignant tumors (N = 95), and infection (N = 83). In 40 patients, implants were placed in previously irradiated areas. A total of 1117 titanium implants were placed to support 187 auricular prostheses (bilateral in 29 cases), 126 orbital prostheses, 89 nasal prostheses, and 13 complex midfacial prostheses.

Clinical Case 1 U.G., 57-year-old patient, came to our observation with ethmoidal-sphenoidal-orbital-hemimaxillary resection and reconstruction with pectoral flap complicated in the same year by cerebral abscess of *Eikenella*. The patient was presenting the absence of the skeleton structures and the soft tissues of the third middle of the right emi-face with involvement of the nose and of the hard palate. The pectoral flap was causing deficit in the movements of extent and left rotation of the head. As a consequence of a cerebral ictus and for the detachment of septic carotid plaque embolus, the patient presented with hemiplegy. Heavy deficits were furthermore present to deglutition and masticatory function. The patient was arriving to our observation in order to restore the symmetry of the face and the integrity of the hard palate and to recover the motility of the cervical stroke. A surgical intervention of positioning of epithesis to rebuild the third middle and superior of the face and of the revision of the pectoral flap was therefore planned. Four fixtures with related abutments were placed to support anchoration for the midfacial prosthesis (Figs 3 and 4). In addition, a dental implant was placed in the right tuber maxillae to support a palatal obturator (Fig 5). Finally, a surgical revision of the pectoral flap was performed. Ten months after surgery, a palatal obturator was placed so that it was possible to remove percutaneous endoscopicgastrostomy (PEG).

Clinical Case 2, R.A., a 40-year-old man affected by the Goldenhar syndrome, underwent different reconstructive surgical treatments to restore the normal symmetry of the face soft tissues. The patient came to our center presenting a facial asymmetry characterized by atrophy of the right hemifacial soft tissues, associated to auricular agenesis and to esterior uditive conduct and “anteroposizione” of the left auricular (Figs 6 and 7). Clinical and radiologic examinations with computer tomography dental scan and Telecranium x-ray in 2 projections with cefalometric study were performed to evaluate the bone and the soft tissues. After 1 month, a surgery has been performed to remove the residual cartilage planted in the site corresponding to porous polyethylene prosthesis, positioned during the previous surgical treatment. In addition, 2 fixtures with abutment have been positioned in the right mastoid bone. Then the left auricular was positioned to reestablish the normal structures of the face. In the same surgical time, 2 porous polyethylene prostheses were implanted in the malar region to restore the sagittal diameter of the middle third of the face; then 2 porous polyethylene prostheses were implanted in the mandibular angle, and 1 prosthesis was implanted on the mandibulae, to restore the transversal and sagittal diameter of the third inferior of the face. After 3 months, an auricular prosthesis associated to polyacrylamide implant was positioned in bilateral preauricular area (Figs 8 and 9). Clinical and radiologic follow-up demonstrated a good integration of implants and the biomaterial

Clinical Case 3 A.S., a 51-year-old man affected with posttraumatic anophthalmia, sequelae of left orbit exenteration and reconstruction of the eye socket with a titanium mesh covered by dermo-adipose flap, came to our observation with anophthalmia O.S. and fibrotic scars. Clinical and radiologic examinations with three-dimensional computed tomography were

performed to evaluate the bone and the soft tissues (Figs 10 and 11). After the clinical and radiologic evaluation and the patient's agreement, 4 fixtures with corresponding abutments were placed to support the anchor of the orbital epithesis. Nasal and orbital scars were corrected by little flaps (Figs 12 and 13).

Clinical Case 4 F.M., a 61-year-old man, was referred with a nose extirpation for a squamocellular cancer on the nasal tip, involving all nasal structure, 7 years before (Fig 14). The patient and his family declined any kind of reconstructive operative interventions, so the patient underwent nasal movable prosthesis resting. Based on this situation, we had proposed to him nasal removable prosthesis fixed with bone paranasal implants. For this reason, the patient had undergone computed tomography scan of the head and neck to study bone density and then 2 implants (4 mm) were placed. Follow-up at 3, 6, and 12 months with clinical visits and computed tomography scan revealed correct implant bone integration (Fig 15).

Clinical Case 5 P.D., a 25-year-old woman, underwent surgical exenteration orbitae because of retinoblastoma. The orbital cavity was restored by temporal muscle flap and dermal-free flap. The patient underwent many reconstructive surgical treatments through the use of fillers of biomaterials in frontal-temporal-cheek side, to reconstitute the anatomic structure. She arrived in our observation with a moving orbital prosthesis (Fig 16). Clinical and radiologic examinations with three-dimensional computed tomography were performed to evaluate the bone and the soft tissues. In accordance with the patient's desire, 3 titanium fixtures with abutments were implanted to position the orbital prosthesis (Fig 17).

Clinical Case 6 M.N., a 56-year-old woman, was referred with a partial auricular extirpation for a basocellular cancer on the auricular left elice. The 2/3 superiors of the auricular pavilion have been removed, with a partial deficit of the pavilion itself, which has caused psychologic problems to the patient. In agreement with the patient, a second surgical treatment was performed, modeling porous polyethylene peace with Nagata technique and covered by temporoparietal fascia and dermo-epidermic flap to fill the auricular fault. The biomaterial is not osteointegrated, so it has been removed. For such reason, in agreement with the patient justified strongly to an immediate and no invasive aesthetic rehabilitation, 2 fixtures with abutments have been positioned that support auricular epithesis (Figs 18Y20). The clinical and radiologic follow-up has shown a correct osteointegration of the implants reaching psychologic stability of the patient.

Clinical Case 7 G.B., a 68-year-old woman, with epatotrasplanting and hepatitis C virus has arrived in our observation with a necrotic lesion of the nasal tip resulting to immunosuppressive therapy. She was referring to have noticed the appearance of the necrosy and his progressive growth soon after the end of the therapy. The patient was presenting exposure of the cartilaginous septum with erosion and cutaneous necrosy to the nasal base (Fig 21). Because of the clinical conditions of the patient, a fixture's implant has been made for the positioning of an epithesis in order to obtain an effective reconstruction. Three fixtures with abutments have been applied. A fixture was removed approximately 2 months after the installing because it is not integrated. The other 2 implants seemed to be well supplemented to allow the positioning of the bar that supports the epithesis, but after 2 months, 1 fixture has been removed because of missed osteointegration. Therefore, it was decided to position some magnets to anchorage the epithesis (Fig 22).



Fig. 1. Preoperative frontal view of the patient.

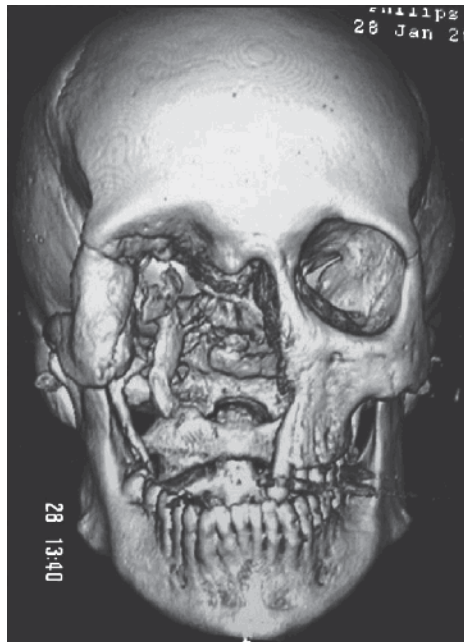


Fig. 2. Preoperative three-dimensional computed. TomographyVfrontal view of the patient.

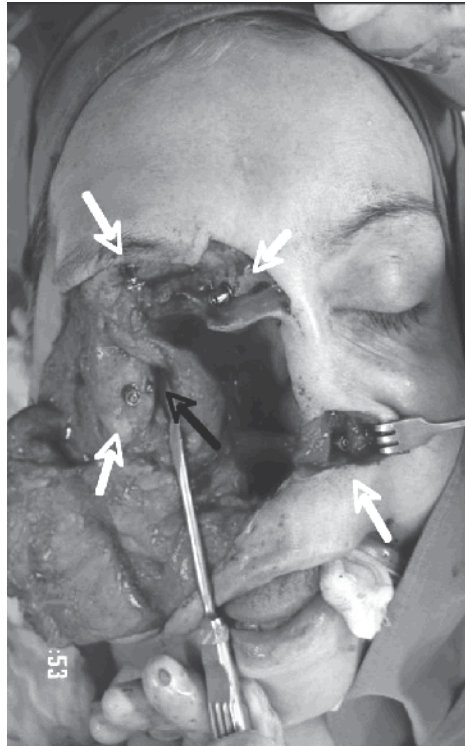


Fig. 3. Intraoperative point of view.

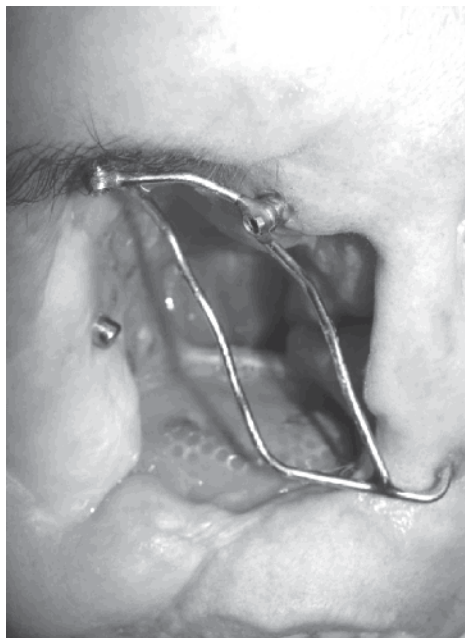


Fig. 4. Anchoration for the midfacial prosthesis.



Fig. 5. The palatal obturator.

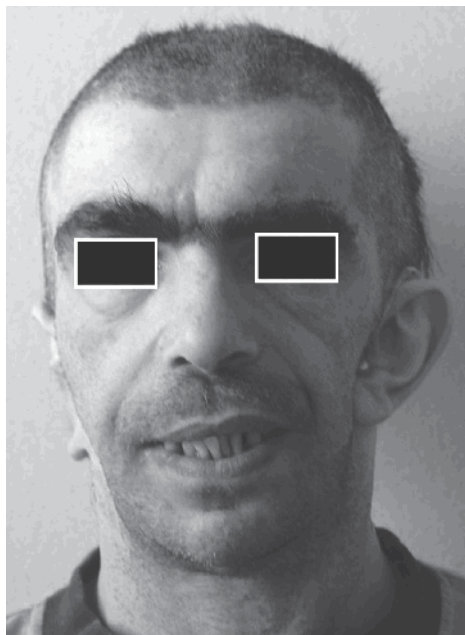


Fig. 6. Preoperative frontal view of the patient.



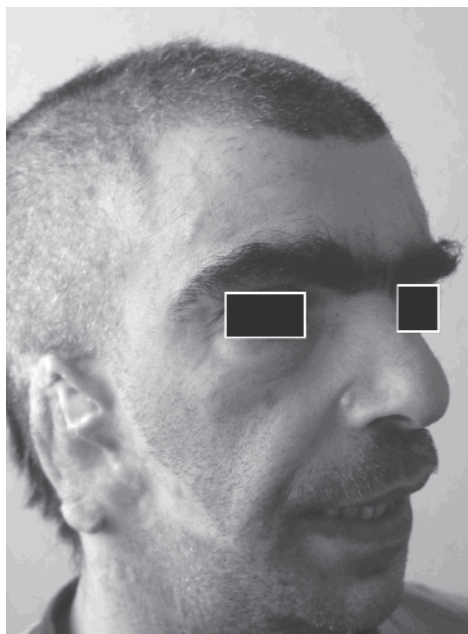


Fig. 7. Preoperative lateral view of the patient.

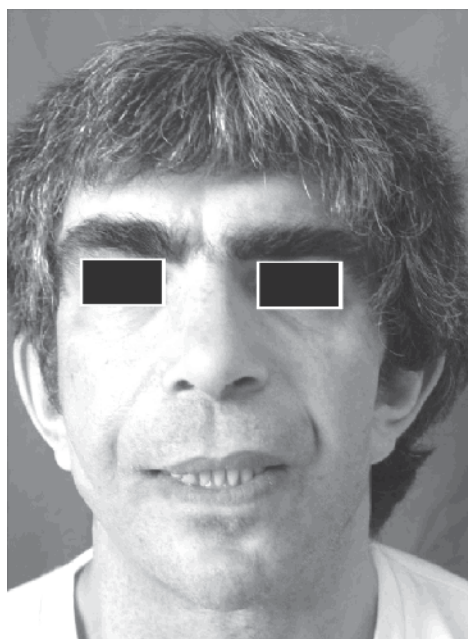


Fig. 8. Postoperative frontal view of the patient.



Fig. 9. Postoperative lateral view of the patient.

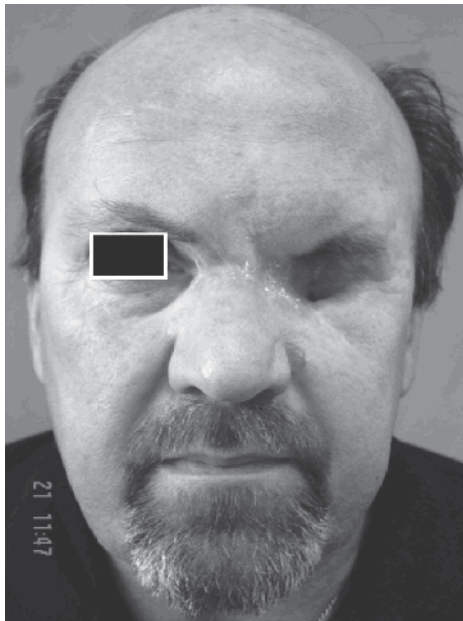


Fig. 10. Preoperative frontal view of the patient.

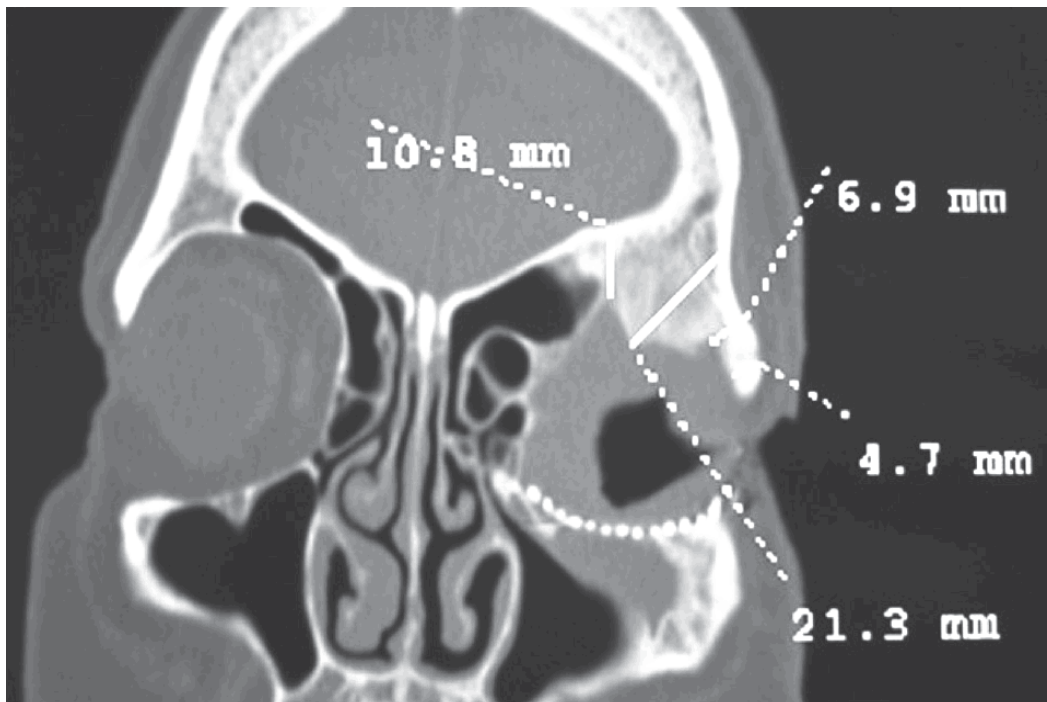


Fig. 11. Preoperative computer tomographyVfrontal view.



Fig. 12. Postoperative frontal view of the patient.



Fig. 13. Postoperative computer tomography frontal view.

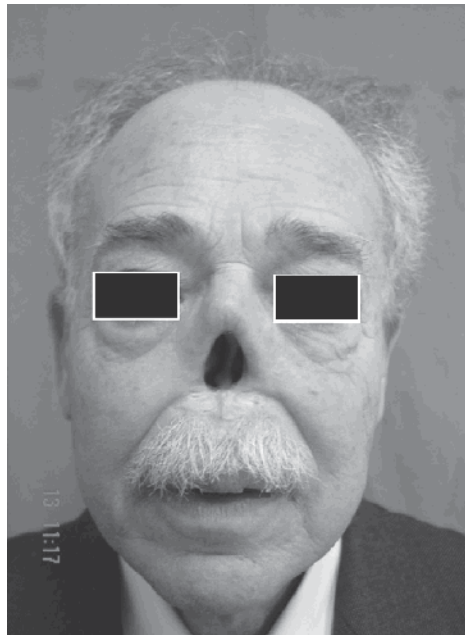


Fig. 14. Preoperative frontal view of the patient.

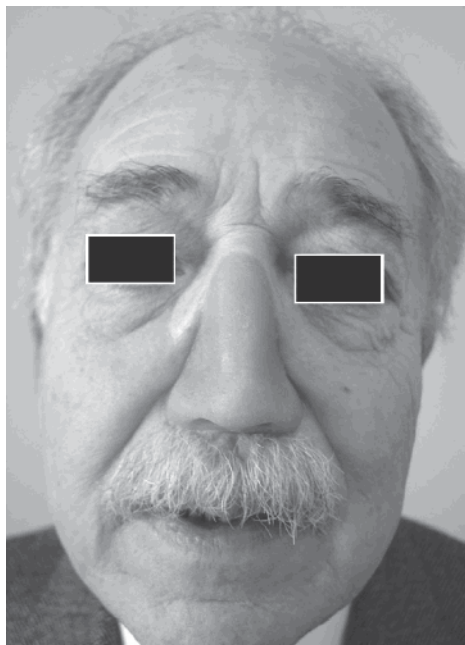


Fig. 15. Postoperative frontal view of the patient.



Fig. 16. Preoperative frontal view of the patient.



Fig. 17. Postoperative frontal view of the patient.

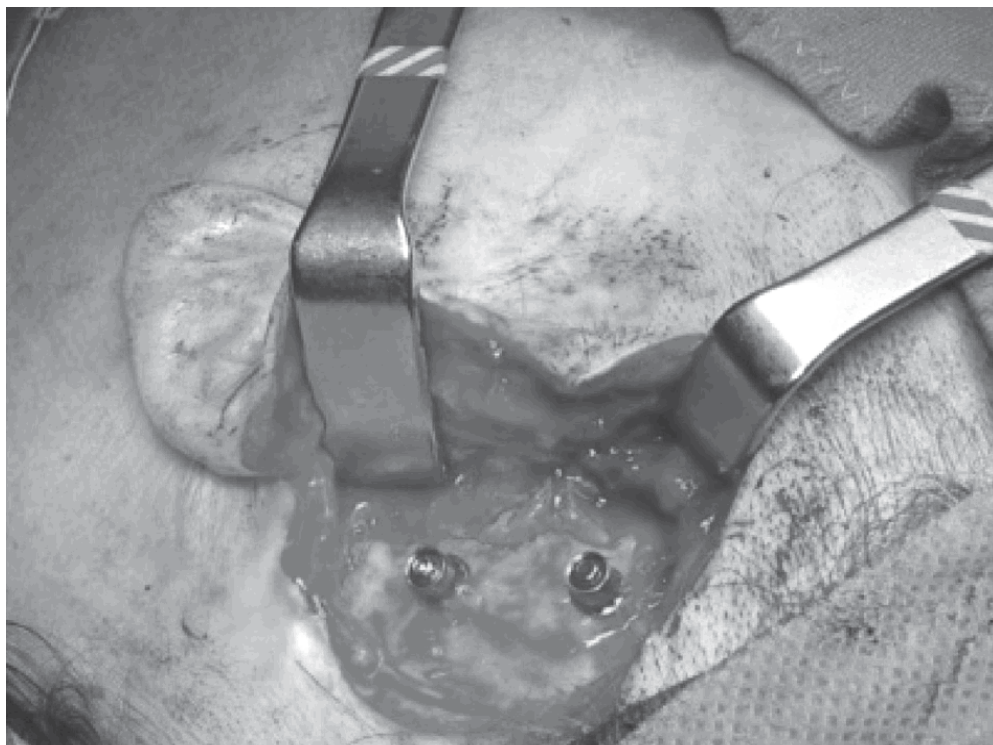


Fig. 18. Fixtures positioning.

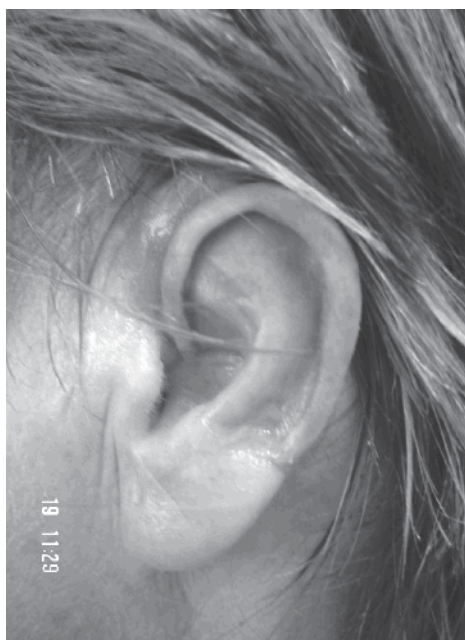


Fig. 19. Patient with auricular epithesis.

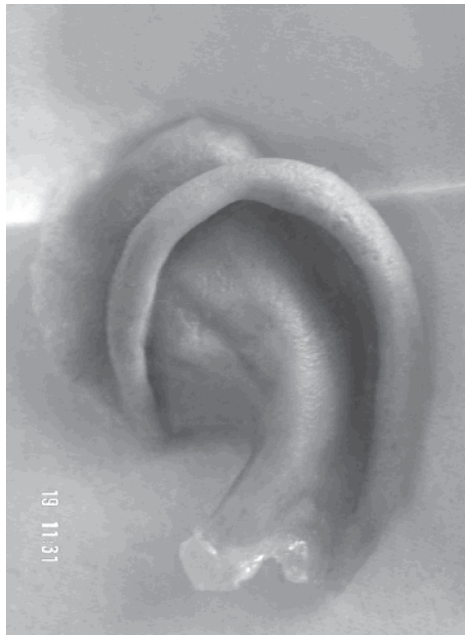


Fig. 20. Auricular epithesis.

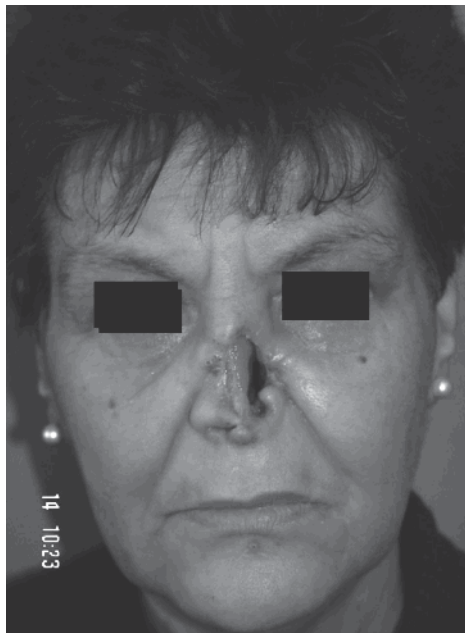


Fig. 21. Preoperative frontal view of the patient.





Fig. 22. Postoperative frontal view of the patient.

### 3. Conclusion

The facial prosthetic rehabilitation is a valid alternative when the conventional reconstructive surgical techniques cannot be applied either because of the psychophysical conditions of the patient or because of an excessive substance loss. The surgical technique with prosthesis has several applications: malformative, infective, traumatic pathology, results of oncologic surgery and radiant therapy, and particular clinical conditions such as diabetes, leukemia, and others. The position of epithesis, as described in the literature<sup>5,6</sup> and confirmed by the experience of our epithesis Center, is suitable in selected cases:

- reconstruction with patient's own tissue, which is uneventful or impossible;
- "Reversible" intervention to operate clinically;
- Surveillance in oncologic patients;
- Advanced age or poor health; and poor tissues quality patient's choice

The described technique presents absolute limits such as osteolytic process, leukemia-lymphoma, and terminal cirrhosis and relative limits such as ending life, hygienic deficiency, and psychological refuse. Another important limit is the radiotherapy treatment; the skeletal structure of persons who undergone radiotherapy react to the osteointegration process with a lower success percent. It goes, in fact, to consider that if the combined application of the chemotherapy and radiotherapy treatments with demolitive surgery increases the life on average, the survival of the subject with surgical cancer ablation increases, compromising the quality of life.<sup>7</sup> The results of the osteointegration in patients who have underwent chemotherapy are very variable, approximately 60% and 100%.<sup>8</sup> In accordance with the literature, we can affirm that the radiotherapy compromises the human tissues, hindering the osteointegration process, when the irradiation is around 5000 Gy. Besides the site and the radiation dose, the time existing between the radiant treatment and the positioning of the implant is another determinant factor for the success of osteointegration process. In particular, 6 months should exist between the term of the radiant treatment and the positioning of the implant period in which the tissue alteration produced by the radiations are in regression. According to the oncologic guideline, it would

be more opportune to wait 1 year to avoid the recidivism risk.<sup>8</sup> Furthermore, the treatment in the hyperbaric room is effective in the bone life, with higher success percents.<sup>8,9</sup> Another fundamental aspect is the epithesis stability, which depends from many circumstances such as hygienic condition, material quality, and the correct method of the epithesis production; when these conditions are respected, the epithesis can resist for 2 years. The application of an epithesis happens with no invasive and immediate results, both from the aesthetic and psychologic point of views, allowing to get around with the heavy social insertion problems derived from his facial deformation. The therapeutic iter in the reconstructive treatment with epithesis foresees a dynamic study with few fundamental stages:

- clinical, radiologic, and psychologic evaluation;
- surgical planning;
- positioning of the fixtures;
- templating;
- preparation of the epithesis;
- fixtures; and epithesis exposure.

Beyond the application of bone implants, several retention methods are possible: anatomic, exploiting the premade cavity getting to the deficit (ocular epithesis), and mechanical, exploiting outside anchorage strengths (sight glasses) and adhesive, by glue.<sup>10</sup> Thanks to the use of the bone implants, it has been able to get around the problems caused by the use of adhesives like decoloration, the precocious deterioration of the epithesis, and inflammatory phenomena of the skin in contact with epithesis' materials. Under the point of view of the aesthetic result, the margins of an epithesis can be easily hidden, and the prosthesis is more stable, is easy to wear, and keeps under a hygienic point of view. Furthermore, the psychologic appearance should not be neglected because, unlike traditional prosthesis, the epithesis fixed with implants are not considered as an extraneous object, with the consequent improvement of a good quality of life. At present, our experience teaches us that the indication to the position of epithesis as the first choice of treatment is when the conventional reconstructive interventions turn out to be inapplicable or ineffective

#### 4. References

- Bulbulian AH. Maxillofacial prosthetics: evolution and practical application in patient rehabilitation. *J Prosthet Dent* 1965; 15:554Y569
- Fini Hatzikiriakos G. Uno sguardo al passato, curiosita` sulle protesi nasali. *Il Valsala* 1985;61:61Y64
- Tjellstrom A. Osteointegrated implants for replacement of absent or defective ears. *Clin Plast Surg* 1990;17:355Y366
- Tjellstrom A, Granstrom G. One stage procedure to establish osteointegration: a zero to five years follow-up report. *J Laryngol Otol* 1995;109:593Y598
- Schaaf NG. Maxillofacial prosthetics and the head and neck cancer patients. *Cancer* 1984;54:2682Y2690
- Labbe` D, Be`nateau H, Compe`re JF, et al. Implants extra-oraux: indications et contre-indications. *Rev Stomatol Chir Maxillofac* 2001;102:239Y242

- Be´nateau H, Crasson F, Labbe´ D, et al. Implants extra-oraux et irradiation: tendances actuelles. *Rev Stomatol Chir Maxillofac* 2001;102:266Y269
- Granstrom G, Jacobsson M, Tjellstrom A. Titanium implants in irradiated tissue: benefits from hyperbaric oxygenation. *Int J Oral Maxillofac Implants* 1992;7:15Y25
- Markt JC, Lemon JC. Extraoral maxillofacial prosthetic rehabilitation at the M.D. Anderson Cancer Center: a survey of patient attitudes and opinions. *J Prosthet Dent* 2001;85:608Y613
- Tjellstrom A, Granstrom G. One-stage procedure to establish osteointegration: a zero to five years follow-up report. *J Laryngol Otol* 1995;109:593Y598
- Ramires PA, Miccoli MA, Panzarini E, Dini L, Protopapa C. In vitro and in vivo biocompatibility of a Polykymide Hydrogel for soft tissue augmentation. *J.Biomed.Mater.Res.Part.*2004; 72: 230-238. 2004.
- Christensen LC, Breiting VB, Aasted A, Jorgensen A, Kebuladze I. Long-Term effects of polyacrylamide hydrogel in human breast tissue. *Plast.Reconstr.Surg.*2003; 11:1883-1890
- Rees TD, Ashlet FL, Delgado JP. Silicone fluid injectons for facial atrophy: a 10 years study.*Plast.Reconstr.Surgery.* 1985;52: 118-125.
- Greenwald AS,bBoden SD, goldberg VM et al.Bone graft substitutes: Facts, fictions and applications. *J. Bone Joint Surg Am* 2001; 83-A:598-S103
- Bauer TW, Muschler GF. Bone Graft Materials. An overview of The basic science. *Clin Orthop.* 2000; 371:10-27.
- Oka Y, Ikeda M. Treatment of severe osteochondritis dissecans of the elbow using osteochondral grafts from a rib. *J Bone Joint Surg Am.* 2001 83-b: 738-739
- Stevenson S. Biology of bone grafts. *Orthoped Clin North Am.* 1999; 30:543-552.
- Skowronski PP, An Yh. Bone graft materials in orthopaedics.MUSC *Orthopaed J.* 2003;6:58-66
- Betz RR. Limitation of autograft and allograft: new synthetic solutions. *Orthopedics* 2002;25(Suppl):S561-S560
- Hollinger JO, Mark DE, Goco P, et al. A comparison of four particulate bone derivatives. *Clin*
- Pietrzak WS, MillervSD, Kucharzyk DW, et al. Demineralized bone graftvformulations: Design, development, and a novel exemple. *Proceedings of the Pittsburg BonevSymposium, Pittsburgh, PA, August 19-23,"003,557-575.*
- Davy DT.Biomechanical issues in bone transplantation. *Orthop Clin North Am.*1999;30:553-56 science and technology for the Craniomaxillofacial Surgeon.*J Craniofac. Surg.* 005(16);6:981-988.15
- Mauriello JA, McShane R, Voglino J. Use Vicryl( Polyglactina 910) mesh implant for correcting enophtalmos A study of 16 patients. *Ophthal Plast Reconstr Surg* 1990; 6:247-251.
- S. Ozturk, M Sengezer, S Isik et all. Long Term Outcomes of Ultra Thin Porous Polyethylene Implants used for Reconstruction of Orbital Floor Defects. *J Craniofac Surg.* 2005 (16) 6:973-977.
- S. Buelow, D Heimburg, N. Pallua. Efficacy ad Safety of Polycrylamide Hydrogel for FacialSoft-Tissue Augmentation. *Plast Reconstr Surg* 2005 (15);1137-1146.
- KW Broder, SR Cohen. An Overview of Permanent and Semipermanent Fillers. *Plast Reconstr Surg* 2006 118(3 suppl.) S7\_S14

Biomaterial Implantation in Facial Esthetic Diseases: Ultrasonography Monitor Follow-Up  
Elena Indrizzi, MDS, Luca Maria Moricca, MD, Valentina Pellacchia, MD,  
Alessandra Leonardi, MD, Sara Buonaccorsi, MD, Giuseppina Fini, MDS, PhD. The  
Journal of Craniofacial Surgery -Vol.19, N. 4 -July 2008

# Nanostructural Chemically Bonded Ca-Aluminate Based Bioceramics

Leif Hermansson

*Doxa AB*

*Sweden*

## 1. Introduction

Biomaterials are based on a broad range of materials, such as organic polymers, metals and ceramics including both sintered and chemically bonded ceramics (silicates, aluminates, sulphates and phosphates). The biomaterials can be made prior to use in the body in a conventional preparation of the material. The need for in situ in vivo formed implant materials makes the chemically bonded ceramics especially potential as biomaterials. These ceramics include room/body temperature formed biomaterials with excellent biocompatibility. Ca-aluminate as a biomaterial has been evaluated for over two decades with regard to general physical, mechanical and biocompatible properties. The Ca-aluminate based materials exhibit due to their unique curing/hardening characteristics and related microstructure a great potential within the biomaterial field. The presentation in this chapter aims at giving an overview of the use of Ca-aluminate (CA) as a biomaterial within odontology, orthopaedics and as a carrier material for drug delivery. The examination deals with aspects such as; the chemical composition selected, inert filler particles used, early properties during preparation and handling (working, setting, injection time, translucency, radio-opacity), and final long-term properties such as dimensional stability and mechanical properties (fracture toughness, compressive and flexural strength, hardness and Young's modulus). One specific topic deals with the sealing of the Ca-aluminate biomaterials to tissue - a key in the understanding of the mechanisms of nanostructural integration.

## 2. Overview of properties of chemically bonded ceramics

The Ca-aluminate bioceramics belong to the chemically bonded ceramics, which are usually presented or known as inorganic cements (Mangabhai, 1990). Three different cement systems - Calcium phosphates (CP), Calcium aluminates (CA) and Calcium silicates (CS) are discussed in some details in this section. Ceramic biomaterials are often based on phosphate-containing soluble glasses, and various calcium phosphate salts (Hench, 1998). These salts can be made to cure *in vivo* and are attractive as replacements for the natural calcium phosphates of mineralised tissues. The Ca-phosphate products are gaining ground in orthopaedics as resorbable bone substitutes. Biocements are often based on various calcium phosphate salts - sometimes in combination with Ca-sulphates (Nilsson, 2003). These salts can be made to cure *in vivo* and are attractive as replacements for the natural

mineralised tissues. However, these products have low compression strength values - in the interval 10-40 MPa - and are therefore questioned as load bearing implants.

Materials based on Ca-aluminate (CA) and Ca-silicate (CS) with chemistry similar to that of Ca-phosphates (CP) contribute to some additional features of interest with regard to dental and orthopaedic applications (Scriviner, 1988). The inherent difference in water uptake between the CA/CS-systems and CP gives benefits as:

- Higher mechanical strength.
- Possibility to add fillers, e.g. for improved radio opacity.
- Tuneable handling properties, e.g. rheology.

Materials based on Ca-aluminate and Ca-silicate thus contribute to some additional features of interest with regard to dental and orthopaedic applications. These features are related to the high amount of water involved in the curing process, the early and high mechanical strength obtained, and the biocompatibility profile including *in situ* reactions with phosphates ions of the body fluid. Compressive strength of cements based on Ca-silicate and Ca-aluminate is in the range 50-250 MPa depending on the water to cement ratio. The mechanical properties tested for the three Ca-based cement systems are compiled in Table 1 (Kraft, 2002, Loof et al 2003, Engqvist et al 2006).

Property profile after 7 days	Ca-aluminate based material	Ca-silicate based material	Ca-phosphate based material
Compressive strength (MPa)	100-200	100-150	< 100
Flexural strength (MPa)	30-60	30-40	20-30
Young's modulus (GPa)	Approx. 15	Approx. 11	Approx. 3

Table 1. Mechanical property profile of the Ca-aluminate, Ca-silicate and Ca-phosphate systems

The water content involved in the hydration of the different chemically bonded ceramics are presented in Table 2.

System	Typical phase(s)	Oxide formula	Mol % H <sub>2</sub> O	Weight-% in hydrated product
Ca-phosphate	Apatite	10CaO 3P <sub>2</sub> O <sub>5</sub> H <sub>2</sub> O	7	Approx 5
Ca-aluminate	Katoite + gibbsite	3CaO Al <sub>2</sub> O <sub>3</sub> 6 H <sub>2</sub> O + Al <sub>2</sub> O <sub>3</sub> 2H <sub>2</sub> O	> 60	Approx 25
Ca-silicate	Tobermorite + amorphous phases	5CaO 6SiO <sub>2</sub> 5H <sub>2</sub> O + Ca, Si)H <sub>2</sub> O	> 30	Approx 20

Table 2. The three chemically bonded ceramic systems most used for biomaterials

## 2.1 Materials and basic function

### 2.1.1 Main chemistry

The injectability and handling features of the chemically bonded ceramics is mainly caused by the added water as the reacting phase with the powdered cements. This reaction is an acid-base reaction where water acts as a weak acid and the cement powder as a base. Several cement phases exist in the CaO - Al<sub>2</sub>O<sub>3</sub> (CA) and in the CaO-SiO<sub>2</sub> (CS) systems, see Figure 1, but only a few are suitable as injectable materials. For one of the most attractive phases -

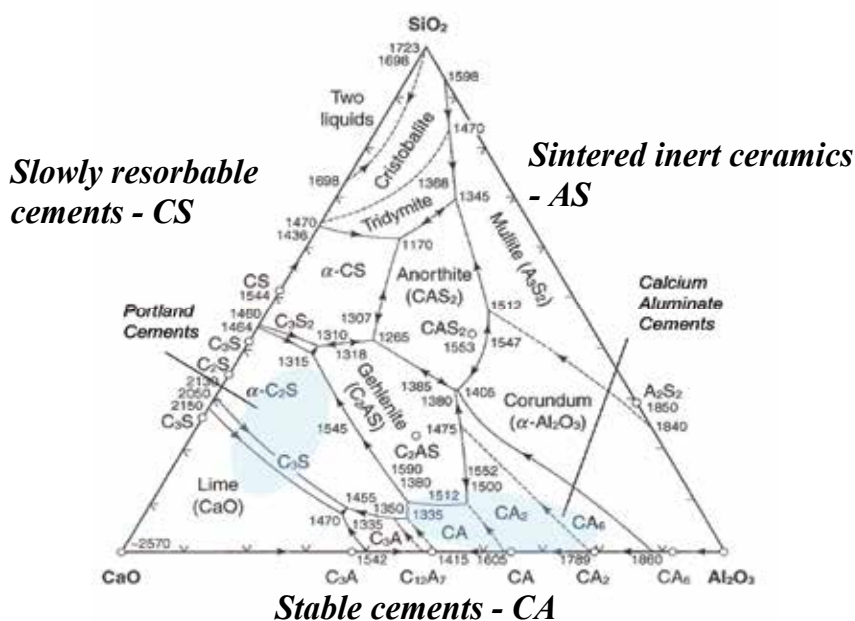
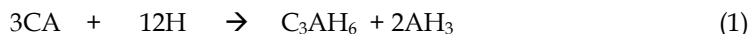
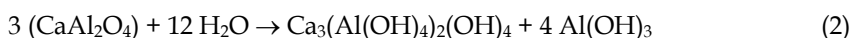


Fig. 1. The phase diagram of the high-strength bioceramic cements (Muan and Osbourne, 1965)

the mono Ca-aluminate,  $\text{CaO}_x\text{Al}_2\text{O}_3$  - the reaction at above 30 °C is described using cement chemical abbreviation as (Mangabhai, 1990);



Or



This example demonstrates 1) the phases obtained,  $\text{C}_3\text{AH}_6$  (katoite) and  $\text{AH}_3$  (gibbsite), and 2) the amount water consumed in the reaction. The technological importance of this is that all the water needed for paste like consistency or injectability can be consumed in the formation of solid phases yielding products with low porosity, one of the requirements for high strength. As can be seen in Eq. (1) three  $\text{CaAl}_2\text{O}_4$  units consume twelve water molecules during hardening. This can be compared with the hardening of Calcium Phosphate Cement (CPC) where practically no extra water is consumed. In the case of CPC, the reaction liquid is only used as a vehicle for the reaction to take place. In both cases the hardening and formation of a solid body are driven by the precipitation of small hydrates, nano-size crystals of katoite and gibbsite for CA, and apatite or brushite for CPC. The amount required water is as high as 28% for CA. The water content of apatite,  $\text{Ca}_5(\text{PO}_4)_3\text{OH}$ , or  $10\text{CaO} \cdot 3\text{P}_2\text{O}_5 \cdot \text{H}_2\text{O}$  ( $\text{C}_{10}\text{P}_3\text{H}$ ) is 2%. The CPC-system may contain some additional Ca-sulphate which can pick up some extra water. An additional 30 % Gypsum,  $\text{CaSO}_4 \cdot \frac{1}{2}\text{H}_2\text{O}$  to the CPC-system yields approximately a total water content of 6%.

The rate of the hydration is controlled by 1) the cement phase, 2) the particle size of the cement, 3) the hydration temperature and 4) processing agents including especially accelerators. Typical powder composition data for CA-cements as biomaterials are shown in

Table 3. Zirconia or high-density glasses are added for achievement of increased strength and increased radio-opacity. The glasses are used preferentially in dental applications where translucency is an additional desired feature. The high radiopacity of zirconia or other heavy-element containing phases means that the physician during the injection can follow the paste penetration in bone tissue without risking any possible leakage of the material into the surrounding tissue.

Compound	Formula	Function	Amount (wt-%)	Mean particle size
Ca-aluminate	$\text{CaO} \cdot \text{Al}_2\text{O}_3$	Cement binder	50-70	< 5 $\mu\text{m}$
Zirconium dioxide	$\text{ZrO}_2$	Radiopacifier	20-40	< 1 $\mu\text{m}$
$\mu$ -Silica	$\text{SiO}_2$	Expansion and viscosity controller	< 10	<50 nm

Table 3. Typical composition of an injectable biomaterial cement powder.

Typical processing agents are accelerators/retarders, dispersants, viscosity agents to control reaction rate, temperature and the cohesiveness, and in general the rheology. Examples are lithium chloride, polycarboxylate polymers and cellulose, as well as glass poly-alkeonates. For the CS-system Ca-chloride at high concentrations is normally used as an accelerator. For cements as injectable biomaterials, the reaction rate must be controlled with respect to working time, setting time, curing time and the maximum temperature during hydration. Typical data are presented in Table 4. The cement reactions are all exothermic and the temperature raise is controlled by the specific cement phase selected, and the hydration rate and the amount of material injected. For dental application the temperature raise is limited to a few  $^{\circ}\text{C}$  above 37  $^{\circ}\text{C}$ . For orthopaedic applications where larger amounts (2-10  $\text{cm}^3$ ) are used the temperature raise is more pronounced but lower than that of the conventional PMMA-based materials (Lewis, 2006).

System	Working time at 23 $^{\circ}\text{C}$ , min	Setting time at 37 $^{\circ}\text{C}$ , min	Max reaction temperature, $^{\circ}\text{C}$
Ca-aluminate	Approx. 5	8-12	< 60, (for dental applications < 40)
Ca-silicate	Approx. 10	15-18	< 45
Ca-phosphate	5	10-12	< 40
PMMA	5-10	11	< 90

Table 4. Typical working and setting times and maximum reaction temperature of the systems discussed.

The on-going precipitation of hydrates and the reduction of the amount of liquid phase result in the formation of a material skeleton. This repeating reaction is fast at the beginning, resulting in a hardened product within 4-20 minutes depending on intended application. Strength corresponding to load carrying capacity is reached after approximately one hour.



However, the final strength and in the case of dental applications the translucency (Engqvist et al 2004), are reached after approximately a few days maturing.

It should be noted that for CBC materials, irrespective of chemistry (CA, CS or CPC), the final porosity cannot be zero. When the hydrates precipitate there is a contraction of approximately 10 %. The porosity is in the nanometer range and its exact amount is difficult to determine, but < 10 % of the filled space (the original liquid-phase volume) is estimated to be pores. However, this internal shrinkage related to hydration and precipitation yield no total shrinkage of the bulk material. In contrast, a limited expansion close to zero, may be induced (Kraft 2002). The porosity lowers the mechanical strength (although being in the nanometer range) but also enables liquids to diffuse into, or even through, the hardened CBC materials. This is an important feature when release of loaded drugs is a complementary aspect of the injectable biomaterial.

### 3. Ca-aluminate – general description and property profile

Ca-aluminates comprise double oxides of CaO and Al<sub>2</sub>O<sub>3</sub>. Several intermediate phases exist and these are - using the cement chemistry abbreviation system - C<sub>3</sub>A, C<sub>12</sub>A<sub>7</sub>, CA, CA<sub>2</sub> and CA<sub>6</sub>, where C=CaO and A=Al<sub>2</sub>O<sub>3</sub>. See Fig. 1 above. Table 5 presents typical property data.

Property	Typical value	Interval*
Compression strength, MPa	150	60-270
Young's modulus, GPa	15	10-20
Thermal conductivity, W/mK	0.8	0.7-0.9
Thermal expansion, ppm/K	9.5	9-10
Flexural strength, MPa	50	20-80
Fracture toughness, MPam <sup>1/2</sup>	0.5	0.3-0.8
Corrosion resistance, water jet impinging, reduction in mm	< 0.01	-
Radio-opacity, mm	1.5	1.4-2.5
Process temperature, °C	> 30	30-70
Working time, min	3	< 4
Setting time, min	5	4-7
Curing time, min	20	10-60
Porosity after final hydration, %	15	5-60

The interval is primarily related to the c/w ratio used, and the highest values are achieved with c/w ratio close to that of complete hydration with no excess of water

Table 5. Mean property data of dental Ca-aluminate based materials (Kraft 2002, Lööf 2008, Lööf et al 2004,2005, Hermansson et al 2008)

Due to reduced porosity based on the huge water uptake ability, the Ca-aluminate material exhibit the highest strength among the chemically bonded ceramics. The inherent flexural strength is above 100 MP based on measurement of the fracture toughness, which is about 0.7 - 0.8 MPam<sup>1/2</sup>. The actual flexural strength is controlled by external defects introduced during handling and injection of the material. The thermal and electrical properties of Ca-aluminate based materials are close to those of hard tissue, the reason being that Ca-aluminate hydrates chemically belong to the same group as Ca-phosphates, the hard tissue

of bone. Another important property related to Ca-aluminate materials is the possibility to control the dimensional change during hardening. In contrast to the shrinkage behaviour of many polymer-based biomaterials, the Ca-aluminates exhibit a small expansion, 0.1-0.3 linear-% (Kraft 2002).

### 3.1 Biocompatibility including bioactivity

#### Definitions used

The terms biocompatibility and bioactivity are used in different ways by different categories of scientists. Below are presented the definitions used in this paper, mainly agreeing with the definitions discussed in (Williams, 1987) Biocompatibility: "The ability of a material to perform with an appropriate host response in a specific application".

Bioactivity (bioactive material): "A material which has been designed to induce specific biological activity". Another definition according to (Cao and Hench,1996) "A bioactive material is one that elicits a specific response at the interface of the material which results in the formation of a bond between the tissues and the material".

Thus a material cannot in itself be classified as biocompatible without being related to the specific application, for which it is intended. Bioactivity from a materials viewpoint is frequently divided into *in vitro* and *in vivo* bioactivity. The *in vitro* bioactivity of a material is however only an indication that it might be bioactive in a specific *in vivo* application. Another aspect of bioactivity is that this term can be adequate only when the biomaterial is in contact with a cellular tissue. However, often a material is claimed to be bioactive if it also reacts with body liquids forming an apatite-phase. *In vitro* bioactivity is tested in phosphate buffer systems similar to that of saliva or body liquid, and apatite formation is the claimed sign of bioactivity. A further aspect of bioactivity and also biocompatibility deals with the different curing times and temperatures at which the observation (testing) is performed. This is important to issues such as initial pH-development, cohesiveness and initial strength. Finally the biocompatibility and bioactivity can only be confirmed in clinical situations, with the actual implant/biomaterial in the designed amount or content and shape. This is especially important for injectable biomaterials which are formed (hydrated) and cured *in vivo*, and for implants where movements, even micro-movement, can influence the outcome.

#### Standards and methods

Relating to the definition aspects above, the acceptance of a biomaterial is a crucial issue, and to some extent the question has been solved by relating to the following toxicological endpoints indicating biocompatibility as referred in the harmonized standard ISO 10993:2003, which comprises the following sections:

Cytotoxicity (ISO10993-5), Sensitization (ISO10993-10), Irritation/Intracutaneous reactivity (ISO10993-10), Systemic toxicity (ISO10993-11), Sub-acute, sub-chronic and chronic toxicity (ISO10993-11), Genotoxicity (ISO10993-3), Implantation (ISO10993-6), Carcinogenicity (ISO10993-3) and Hemocompatibility (ISO10993-4).

This will be the main guideline when presenting the status of the biocompatibility of the CASPH-system, but was complemented by corrosion testing, elementary analysis, pH-change and additional cytotoxicity testing.

The corrosion resistance test - using a water jet impinging technique - was conducted according to EN 29917:1994/ISO 9917:1991, where removal of material is expressed as a height reduction using 0.1 M lactic acid as solution, pH 2.7. The duration time of the test is

24 h. The test starts after 24 h hydration. The test probe accuracy was 0.01 mm. Values below 0.05 mm per 24 h solution impinging are judged as acid resistant.

Determination of Ca and Al in the solution during the hydration process of the Ca-aluminate based material was performed using atomic absorption spectrometry (Liu et al 2002). Standard solutions of different concentrations of Ca and Al were prepared according to the manual. Samples were prepared with a size of 10mm x 2mm height using a wet-press method, corresponding to a surface area of 224 mm<sup>2</sup>. The test pieces were placed in plastic bottles in inorganic saliva solution of pH 7. The amount of liquid was 10 ml in each bottle. The temperature selected was 37 °C. The inorganic saliva solution contained calcium chloride, magnesium chloride, sodium chloride, a phosphate buffer, hydro-carbonate and citric acid. The Ca-content in the saliva solution corresponded to 68 ppm. 1 ml solution was removed at 1, 7 and 28 days for analyses, and saliva was exchanged at 1, 7 and 28 days after every measurement. For the 28 days test additional samples were also taken 1 h after new solution was added.

Measurement of pH development during hydration of the material was conducted using a standard pH-meter. Samples were prepared according to the procedure for atomic absorption described above. The pH-testing was conducted in two separate ways. First the samples were immersed in saliva solution (pH =7) at 37 °C, and pH was measured continually over the whole experiment period (Test 1). 1 ml solution was removed at 1, 7, 14 and 28 days for pH measurement. The second type of measurement comprised immersion in 10 ml saliva solution at 37 °C, where the saliva was exchanged at 1, 7, 14 and 28 days. pH was measured at the time of observation and also after one hour in new saliva (data within brackets), Test 2.

Specimens at different setting stages were subjected to cytotoxicity testing by using primary cultures of human oral fibroblasts. A tissue culture insert retaining tested materials was assembled into a 12-well plate above the fibroblast monolayers. The cytotoxicity was determined by MTT reduction assay after various curing times. Specimens were set and hydrated at 37 °C for different periods of time, i.e. 0, 5, 30, 60 min, 24 h and 1 week and were then placed on tissue culture netwell for a cytotoxicity test. Both acute (1 and 24 h) and long term (1 week) *in vitro* toxicity tests were conducted with MTT assay.

### **3.1.1 Biocompatibility including bioactivity of Ca-aluminate bioceramics**

#### **Biocompatibility evaluation**

Summarized below are the results from several biocompatibility and bioactivity studies (Engqvist 2004, 2005, Faris 2006) where Ca-aluminate is used as a biomaterial in orthopaedic and dental applications. *In vitro* bioactivity studies show apatite formation on the surface of the Ca-aluminate materials exposed to phosphate buffer solution, an example shown in Figure 2 below.

#### **Corrosion resistance**

No height reduction at all was observed for two tested Ca-aluminate materials. Thus, according to the acid corrosion test, Ca-aluminate materials are judged as stable materials. The total absence of material loss, measured as height reduction in the acid corrosion test, is related to the general basic nature of the material, with possibility of neutralization of the acid in the contact zone – especially in the earlier stage of the hydration process.

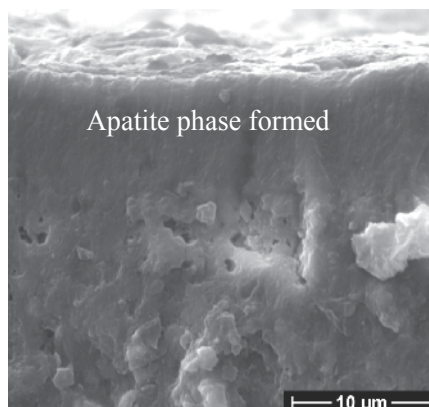


Fig. 2. Cross section of the apatite-containing surface layer formed, SEM (Engqvist et al, 2004)

### Ion release measured by atomic absorption spectrometry

The results of Ca and Al determination in the solution during the hydration process of the Ca-aluminate based material are presented in Table 6.

Ion tested	1h, ppm	24 hrs, ppm	7 days, ppm	28 days, ppm
Ca	66	64	44	50 (70)
Al	11.4	9.3	9.6	8.6 (1.2)

Table 6. Ca and Al dissolution during hardening of the Ca-aluminate material, (The 1h testing at 28 days within brackets)

The release of metal ions in water was below  $5 \times 10^{-2}$  ppm/(mm<sup>2</sup> material) for aluminium and below  $30 \times 10^{-2}$  ppm/(mm<sup>2</sup> material) for calcium, whereas somewhat higher aluminium content was measured in artificial saliva. The ion concentrations detected are generally not time-dependent during hydration. After the initial hydration time the ion concentration (molar) is determined by the solubility product of the phases formed (katoite =  $5 \times 10^{-26}$  and gibbsite =  $3 \times 10^{-24}$ ). Since the concentration of Ca in saliva is higher than what is obtained in the non-physiological aqueous solution (distilled water), it can be assumed that the filling material releases very limited amounts of Ca or Al once the material has hardened. The presence of Ca in saliva will decrease the solubility tendency of the calcium-aluminate-hydrate phases.

Based on a search in the literature, the FAO/WHO Joint Expert Committee on Food Additives (JECFA) has provided a provisional figure for tolerable weekly aluminium intake of 7 mg/kg body weight. This corresponds to 1 mg/kg /day. The daily intake of aluminium via digestion/food is approximately 5 mg per day. For calcium the NIH Consensus Development Conference on Optimal Calcium Intake recommended an intake in the range 800 mg/day for young children to 1000 - 1500 mg/day for adults depending on gender and age. For many people there is a need to supply additional calcium in order to stay healthy. The ion concentrations measured and the amounts of Ca and Al released are far below the concentrations of the elements produced from food intake and should therefore not pose any safety concerns at all.

### Change in pH during hydration

The results of the measurement of pH development during hydration of the Ca-aluminate based are shown in Table 7. The initial *in vitro*-pH is 10.5 in saliva. After 1 week, pH after 1 h dissolution time in saliva is approx. 8.

Test No.	At start	1h	24 hrs	7 days	14 days	28 days
1	10.5	10.3	10.7	10.3	9.9	9.8
2	10.5	10.2	10.2 (7.7)	9.9 (7.8)	9.5 (8.1)	9.2 (8.1)

Table 7. Change of pH during initial hydration of Ca-aluminate based materials

The pH is high during the early stage of the hydration, but decreases with time and approaches neutrality. The reason for the high pH in the beginning is the general basic character of the material and the formation of OH<sup>-</sup> during the hydration process. In the clinical situation saliva is produced in a dynamic way, creating an environment capable of buffering surrounding solution to neutrality. In the clinical studies performed so far no adverse reactions have been reported from a possible elevated pH during the early part of the hydration.

When Ca-aluminate material is combined with glass ionomer system the pH-system becomes initially acidic. However after 10 min the pH is above neutral, but will not exceed pH 9 (Jefferies et al 2009).

### Cytotoxicity testing

The *in vitro* MTT reduction test of the experimental Ca-aluminate dental filling material in human oral fibroblast culture showed no obvious cytotoxicity. The average level of MTT reduction of the experimental dental filling material was close to 100% of the control values. The maximal variation (SD) was less than 30%. Different curing times of the test material did not seem to affect the cytotoxicity test results although one week curing produced the most stable testing results both in the short and long term tests. After a week the material can be considered as fully cured, i.e. stable.

Morphological changes were not observed in any of the test groups at different MTT reduction testing points. As shown in Figure 3, the cell culture was typically fibroblastic with a slender and elongated form in both the control group and the group exposed to the examined material. In the exposed picture B even some precipitated hydrates are seen.

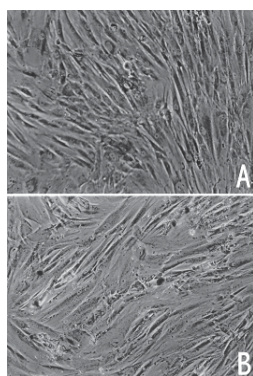


Fig. 3. Morphological observation of human oral fibroblasts on an experimental Ca-aluminate based material. A: Normal control. B: After exposure to the experimental filling material for one week (Liu et al 2002).

The standard for cellular biocompatibility in *in vitro* testing has been stated in the International Organization for Standardization (ISO) standards documents. The standard allows for the contact testing of solid dental materials for cytotoxicity with cell lines. Due to several disadvantages of direct contact testing, indirect testing methods have been developed and compared to the direct testing assays (Tang et al 2002). Introduction of a standard cell culture device, i.e. cell culture insert or transwell, provided an opportunity for such cytotoxicity screening of dental materials with indirect contact between material specimens and cell culture monolayer. It is believed that such a testing system more closely mimics the *in vivo* exposure pattern by providing the test of the material in both its solid and dissolved phases at the same time. It has been shown that this testing system has produced the most stable results as compared to other testing systems, such as direct contact test. In a complementary cytotoxicity test using the pulp derived cell response, the experimental CA-material showed no sign of toxicity (Schmalz 2002).

### Harmonized standard ISO 10993:2003

Further cytotoxicity and other biocompatibility aspects are summarised according to the outline in the harmonized standard ISO 10993:2003. An experimental orthopaedic Ca-aluminate-based material was the test material. This material is judged as mildly cytotoxic during the initial curing, and as non-cytotoxic as cured material. See Table below.

Type of test	Method	Cytotoxicity (scale 0-4 or 100-0%)
During curing, undiluted	ISO 10993-5, § 8.2	2 (mild)
During curing, diluted	ISO 10993-5, § 8.2	0-1 (none-slight)
During curing	XTT-test	60 % (slight)
During curing, diluted	XTT-test	> 70 % (none)
Cured, undiluted	ISO 10993-5, § 8.2	0 (none)
Cured, diluted → diluted	XTT-test	> 70% (none)

Table 8. Cytotoxicity testing of an orthopaedic Ca-aluminate based material

A sensitization test (ISO 10993-10), Guinea Pig Maximization Test was performed with the orthopaedic Ca-aluminate material during curing. No sensitizing potential was obtained. Additional irritation and delayed hypersensitivity testing according to ISO 10993-10:2002 was conducted with both polar and non-polar extract from cured material, and the results showed no discrepancies after intracutaneous injections in the rabbit compared to the blank injections. The acute systemic toxicity study according to ISO 10993-11 was performed with both polar and non-polar extracts from cured Ca-aluminate material (Xeraspine), and the results showed no signs of acute systemic toxicity. Sub-acute, sub-chronic and/or chronic toxicity studies according to ISO 10993-11 were not conducted explicitly, since data from the two implantation studies in rabbit (see below) were judged to support that no long term toxicity is expressed. From the implantation studies histopathological organ and tissue data is available, and no adverse effects were reported.

Additionally, in an *in vivo* genotoxicity assay, the mice micronucleus test of bone marrow was used. The extract (The experimental Ca-aluminate material during curing and cured material) was administered intraperitoneally twice. The results showed no clastogenic effect. Three *in vivo* implantation studies based on ISO 10993-6 have been performed. Two studies in rabbit (femur) and one in sheep (vertebrae). *In vivo* implantation studies are judged as the most relevant studies for documentation of safety of a product. In the rabbit implantation

studies Ca-aluminate material was compared to the PMMA-material CMW 1, and in the sheep study Ca-aluminate material was compared to the PMMA-material Vertebroplastic, and to the Bis-GMA material Cortoss™. The results are summarized in Table 9.

Implantation studies	Species	Reference material	Result
6-week femur	Rabbit	CMW-1	Minimal inflammation, very few inflammatory cells were present in bone, bone marrow and adipose tissues.
6 (12) -month femur	Rabbit	CMW-1	No Al- accumulation
12-week vertebrae	Sheep	Vertebroplastic Cortoss	No inflammation, no Al-accumulation

Table 9. Implantation studies in femur rabbit, and in vertebrae sheep, details in (Hermansson et al 2008)

The 6 months femur study in rabbits included a 12 months subgroup. The amount of aluminium in blood and selected organs was analysed. The main target organs of the animals (kidney, lung, liver) were histopathologically investigated. Granulomatous inflammation in the cavity, pigmented macrophages and new bone formation were the treatment-related observations at 6- and 12-months examination. No difference between Ca-aluminate material and PMMA was detected. There were no signs of aluminium accumulation in the analysed tissues.

In the 12-week study, the histopathology of vertebrae obtained one week after surgery showed the most severe inflammatory reaction to the surgery in the *sham* operated vertebrae. The bone marrow in the vertebrae filled with Ca-aluminate was not reported to be infiltrated by any inflammatory cells. In vertebrae obtained 12 weeks after surgery no inflammatory reactions were reported, and no obvious differences were observed in the pathological reactions to the surgery (*sham*) or the filler materials. Overview of the histological contact zone to the Ca-aluminate based material is shown in Figure 4.

The analysis of serum samples showed low concentrations of aluminum in comparison to what is normal in humans. Since the concentration of aluminum did not increase after surgery and in some instances was lower after surgery than in the 0-samples, one may regard these concentrations as within the normal variation.

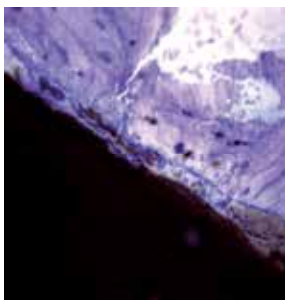


Fig. 4. Histology image of an experimental Ca-aluminate material (black) in close contact with sheep vertebral bone.

Repeated haemocompatibility studies have been performed to evaluate possible reactions in whole human blood as a result of contact with Ca-aluminate materials (Axen et al 2004). Test items were an experimental Ca-aluminate based material and Xeraspine, Vertebroplastic and Norian (Calcium Phosphate Cement, Synthes Inc). A Chandler loop model was used in which circulating human blood was in contact with the test materials for up to 4 hours. For comparison, loops free from test materials were used. Platelet count (PLT), thrombin-antithrombin (TAT) complex, complement factors C3a and C5b-9 (TCC), and TNF- $\alpha$  were assayed. The degree of haemolysis was assessed by the Drabkin method. Norian (a calcium phosphate based material) invariably induced extensive clotting already after 60 minutes, verified macroscopically and also by significantly reduced PLT in comparison to the Control loops, whereas there was no significant reduction in PLT in the loops with Ca-aluminate material or Vertebroplastic, respectively, neither at 60 nor at 240 minutes. The Ca-aluminate material did not induce haemolysis to a greater extent than any of the other materials tested. TCC was activated to a certain degree by the biomaterial, comparable to what is commonly observed for artificial materials. TNF- $\alpha$  generation, indicative of activation of white blood cells, was not enhanced by either Vertebroplastic or the Ca-aluminate material.

Based on all above mentioned data and generated toxicity data, it is considered that there is no reason to expect that the Ca-aluminate biomaterials when used in accordance with the intended clinical use will create any adverse effects. The Ca-aluminate based materials fulfill the requirements of the harmonized standard ISO 10993:2003.

### 3.1.1.1 Complementary reactions of Ca-aluminate in presence of body liquid.

Complementary reactions occur when the Ca-aluminate is in contact with tissue containing body liquid. Several mechanisms have been identified, which control how the Ca-aluminate material is integrated onto tissue. These mechanisms affect the integration differently depending on what type of tissue the biomaterial is in contact with, and in what state (unhydrated or hydrated) the CA is introduced. These mechanisms are summarized as follows and described in more details elsewhere (Hermansson, 2009);

- Mechanism 1: Main reaction, the hydration step of CAC (Eq. 1 above)
- Mechanism 2: Apatite formation in presence of phosphate ions in the biomaterial
- Mechanism 3: Apatite formation in the contact zone in presence of body liquid
- Mechanism 4: Transformation of hydrated Ca-aluminate into apatite and gibbsite
- Mechanism 5: Biological induced integration and ingrowth, i.e. bone formation at the contact zone
- Mechanism 6: Point-welding due to mass increase when in contact with body liquid.

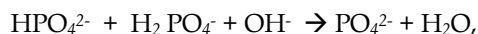
When phosphate ions or water soluble phosphate compounds are present in the biomaterial (powder or liquid) an apatite formation occurs according to the reaction



This complementary reaction to the main reaction occurs due to the presence of Ca-ions and a basic (OH<sup>-</sup>) environment created by the Ca-aluminate material. The solubility product of apatite is very small [ $K_s = 10^{-58}$ ], so apatite is easily precipitated. Body liquid contains among others the following ions HPO<sub>4</sub><sup>2-</sup> and H<sub>2</sub>PO<sub>4</sub><sup>-</sup>. In contact with the Ca-aluminate



system and water during setting and hydration, the presence of Ca-ions and hydroxyl ions, the hydrogen phosphate ions are neutralised according to



whereafter the apatite-formation reaction occurs



This reaction occurs upon the biomaterial surface/periphery towards tissue. The apatite is precipitated as nano-size crystals (Hermansson et al, 2006). See figure 5.

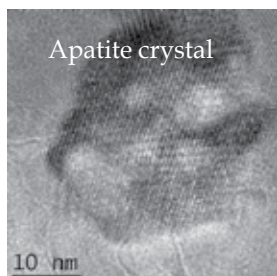
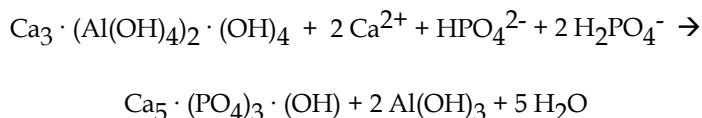


Fig. 5. Nano-size apatite formation in the the contact zone to hard tissue

Katoite is formed as a main phase, and is kept as katoite in the bulk material according to the mechanism 1 above. However, in long-time contact with body liquid containing phosphate ions the katoite is transformed at the interface to body tissue into the at neutral pH even more stable apatite and gibbsite phases according to



When apatite is formed at the interface according to any of the reaction mechanisms 2-4 above, at the periphery of the bulk biomaterial, the biological integration may start. Bone ingrowth towards the apatite allows the new bone structure to come in integrated contact with the biomaterial. This is an established fact for apatite interfaces. For the CA-system the ingrowth is discussed below, 4.4. The transition from tissue to the biomaterial is smooth and intricate.

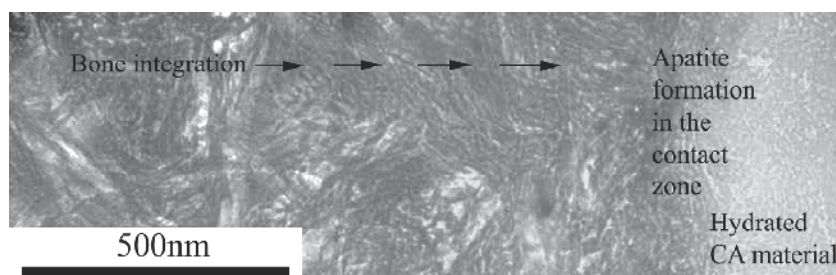


Fig. 6. Integration of CA in tissue – a model using albino adult New Zealand White rabbits (Hermansson et al, 2008).

The actual contact zone developed depends on a combination of the above discussed mechanisms and the tissue. The latter varies from a cellular-free high content apatite tissue in the case of a dental enamel, via dentine to a bone structure with cellular and body liquid contact. Also the material can be in contact with other implant materials as dental crowns, dental screws or coatings on implants. In the tables 10 and 11 are summarized in which applications and specific tissues the demonstrated mechanisms are predominant.

Tissue	Mech 1	Mech 2	Mech 3	Mech 4	Mech 5	Mech 6
Enamel	x	x				
Dentine	x	x	X	x	(x)	
Bone	x	x	X	x	x	x

Table 10. Type of tissue and possible mechanisms.

Application	Mech 1	Mech 2	Mech 3	Mech 4	Mech 5	Mech 6
Cementation						
a. towards tissue	x	x	X	x	x	
b. towards implant	x	(x)				
Dental fillings						
a. towards enamel	x	x				
b. towards dentine	x	x	X	x	(x)	
Endo fillings						
a. orthograde	x	x				
b. retrograde incl bone	x	x	X	x	x	
Coatings and augmentation						
towards implant	x	(x)				
gap filling	x	x	X	x	x	x

Table 11. Applications and possible mechanisms.

### Nanostructure and nano-porosity used in certain applications

The nanostructure including nanoporosity developed in the Ca-aluminate biomaterial system when near complete hydration occurs, yields some unique properties related to how bacteriostatic and antibacterial properties may develop in the biomaterial. The nanoporosity can also be used to control release of drugs incorporated the biomaterial. The background to this is that even if the total porosity is low, all porosity is open, thus allowing transport of molecules in the nanoporosity channels. The nanostructure used in thin film coatings will also be touched upon.

### Antibacterial aspects

The surprising finding in studies recently performed (Doxa patent application 2010) shows that the bacteriostatic and antibacterial properties of the Ca-aluminate biomaterial are not primarily related to pH or specific ions and ion concentration or reducing agents, but to the hydration procedure and the microstructure obtained. This also to some extent is an answer why highly biocompatible and even bioactive biomaterials can combine apparently contradictory features such as biocompatibility, bioactivity and apatite formation and environmental friendliness with bacteriostatic and antibacterial properties.

The bacteriostatic and antibacterial properties are primarily related to the development of the nanostructure and the nano-size porosity during hydration of the Ca-aluminate system. The initial low pH ( $< 8$ ) of the system in the case of the presence of a polycarboxylic acid for cross-linking, is such not a hindrance for the antibacterial properties. The requirements of the microstructure of Ca-aluminate and/or Ca-silicate based biomaterials to achieve antibacterial properties are related to the general nanostructure obtained; A nanoparticle/crystal size of hydrates in the interval 15-40 nm, a nanoporosity size of 1-4 nm and the number of pores per square micrometer of at least 500, preferably  $> 1000$ .

The above mentioned requirements will guarantee that the nanostructure will be free of large pores meaning no escape of bacteria within the original liquid, paste or dental void, during the hydration. The nanocrystals will participate on all walls, within the liquid, and on all inert particles and on bacteria within the original volume. The formation of nanocrystals will continue to all the void is filled. The bacteria will be totally encapsulated and will be chemically dissolved. Also the number of nanopores will be extremely which will have the possibility of catching and fasten bacteria to the hydrate surface - an analogue to how certain peptides may function as antibacterial material due to a structure with nanosize hole within the structure.

#### 4. Materials and biomaterials application

Alternative dental materials and implant materials based on bioceramics are found within all the classical ceramic families: traditional ceramics, special ceramics, glasses, glass-ceramics, coatings and chemically bonded ceramics (CBC) (Ravaglioli and Krajewski, 1992). The CBC-group, also known as inorganic cements, is based on materials in the system  $\text{CaO-Al}_2\text{O}_3\text{-P}_2\text{O}_5\text{-SiO}_2$ , where phosphates, aluminates, and silicates are found. Depending on in vivo chemical and biological stability, the CBC biomaterials can be divided into three groups: stable, slowly resorbable and resorbable. The choice for dental and stable materials is the Ca-aluminate based materials (Hermansson et al 2008). Slowly resorbable materials are found within Ca-silicates and Ca-phosphates, and fast resorbing materials among Ca-sulphates and some Ca-phosphates. The stable biomaterials are suitable for dental applications, long-term load-bearing implants, and osteoporosis-related applications. For trauma and treatment of younger patients, the preferred biomaterial is the slowly resorbable materials, which can be replaced by new bone tissue (Nilsson, 2002). In this section are summarised some of the possible new applications using the strong chemically bonded ceramics based on Ca-aluminate. The presentation is divided in three application areas; dental, orthopaedics and drug delivery.

The following product areas have been identified based on experimental material data, pre-clinical studies, pilot studies and on-going clinical studies (Jefferies et al, 2009). The application areas are; Dental cement, endodontic products (orthograde and retrograde), sealants, restoratives, and pastes for augmentation and dental implant coatings. For low-viscosity and early hardening of the CA, a complementary glass ionomer can preferably be used. Clinical use of the materials is foreseen within the next coming years. The use of CA within odontology is based on the following features; early/rapid anchoring, high strength, long-term stability, no shrinkage, combined bonding and bulk material, biocompatibility and in situ apatite formation ability (nanocrystals formed in the contact zone between material and tissue).

#### 4.1 Dental applications

The existing dental materials are mainly based on amalgam, resin composites or glass ionomers. Amalgam, originating from the Tang dynasty in China, was introduced in the early 19<sup>th</sup> century as the first commercial dental material. It is anchored in the tooth cavity by undercuts in the bottom of the cavity to provide mechanical retention of the metal. Although it has excellent mechanical characteristics it is falling out of favor in most dental markets because of health and environmental concerns. One exception is the US in which amalgam still has a relatively large market share.

The second generation material is the resin composites, first introduced in the late 1950s. These are attached to the tooth using powerful bonding agents that glue them to the tooth structure. After technical problems over several decades, these materials today have developed to a level where they work quite well and provide excellent aesthetic results. Despite the improvements, resin composites have some drawbacks related to shrinkage, extra bonding, irritant components, a risk of post-operative sensitivity, and technique sensitivity in that they require dry field treatment in the inherently moist oral cavity. The key problem, due to shrinkage or possible degradation of the material and the bonding, is the margin between the filler material and tooth, which often fails over time leading to invasion of bacteria and secondary caries. Secondary caries is a leading cause of restorative failure and one of the biggest challenges in dentistry today. As a significant number of dental restorations today are replacement of old, failed tooth fillings, it is clear that tackling this problem is a major market need (Mjör, 2000). Secondary caries occurs not only after filling procedures but also following other restorative procedures such as the cementation of crowns and bridges.

Glass ionomers were first introduced in 1972 and today are an established category for certain restorations and cementations. Their main weakness is the relatively low strength and low resistance to abrasion and wear. Various developments have tried to address this, and in the early 1990s resin-modified ionomers were introduced. They have significantly higher flexural and tensile strength and lower modulus of elasticity and are therefore more fracture-resistant. However, in addition to the problems of resin composites highlighted above, wear resistance and strength properties are still inferior to those of the resin composites.

The nature of the mechanisms utilized by Ca-aluminate materials (especially Mechanism 1 above) when integrating and adhering to tooth tissue and other materials makes these materials compatible with a range of other dental materials, including resin composite, metal, porcelain, zirconia, glass ionomers and gutta-percha. This expands the range of indications for Ca-aluminate based products from not only those involving tooth tissue, e.g. cavity restorations, but also to a range of other indications that involve both tooth tissue and other dental materials. Examples include dental cementation, base and liner and core build-up and endodontic sealer /filler materials, which involve contact with materials such as porcelain, oxides and polymers and metals, and coatings on dental implants such as titanium or zirconia-based materials.

The use of the Ca-aluminate materials may be a first step towards a paradigm shift for dental applications. The features are summarized below.

Nanostructural integration

- Reduced risk of secondary caries and restoration failure
- Excellent biocompatibility

- Reduced/no post-operative sensitivity, environmentally friendly and no allergy
- Optimized consistency and setting properties for the intended application
- Reliable clinical handling performance
- Hydrophilic acid-base system with no extra bonding or no dry field precaution
- Fast and easy clinical handling, no pre-treatment of tooth necessary
- Excellent retentive and mechanical properties, no degradation of properties over time
- Durable tooth-material restoration interface (longevity).

Below are presented in more details the state-of-the-art for different possible applications of Ca-aluminate based materials.

#### 4.1.1 Dental cement

Long-term success after cementation of indirect restorations depends on retention as well as maintenance of the integrity of the marginal seal. Sealing properties of great importance deal with microleakage resistance, the retention developed between the dental cement and the environment, compressive strength and acid resistance. Data presented below support the Ca-aluminate-system as highly relevant for dental cement materials. Integration with tooth tissue is a powerful feature and the foundation of the Ca-aluminate technology platform. Secondary caries occurs not only after filling procedures but also after other restorative procedures such as the cementation of crowns and bridges. The consequence of the difference in the mechanism of action between Ca-aluminate products and conventional products is illustrated by the study presented in details in (Pameijer et al , 2008, 2009), illustrated in Figure 2 below. It shows that the micro leakage, measured by dye penetration after thermo cycling, of a leading dental cement (Ketac Cem®, 3M) was significantly higher, both before and after thermo cycling compared to Ceramir C&B, a Ca-aluminate based product recently approved by FDA. This has also recently been verified using techniques for studying actual bacterial leakage. The above described nanostructural precipitation upon tissue walls, biomaterials and within the original Ca-aluminate paste is the main reason for this, in addition to a high acid corrosion resistance.

General properties of the CAPH-system used as dental cement have been presented (Pameijer et al, 2008), see Fig. 7 and Table 12 below. General features of all the dental cement classes available are presented as a summary in Table 13 below.

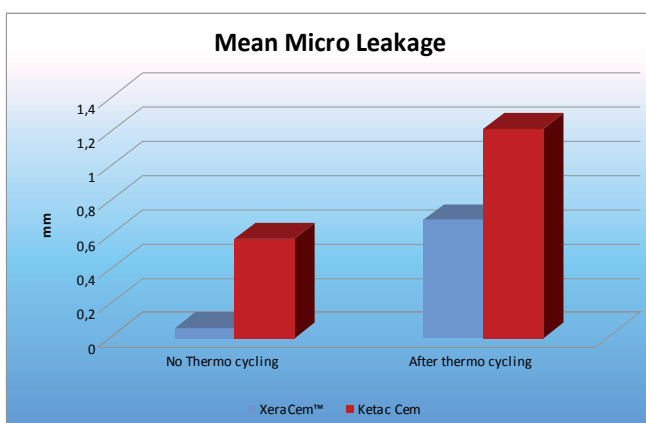


Fig. 7. Micro leakage leakage of a Ca-aluminate based material (blue) and Ketac Cem (red).

Material	Net setting time, min	Film thickness, $\mu\text{m}$	Compressive strength, MPa	Crown retention, Kg/Force
Ca-aluminate based	4.8	15	196 (at 30days)	38.6
Ketac Cem	-	19	-	26.6
RelyX-Unicem	-	-	157	39.4

Table 12. Selected properties, Test methods according to SO 9917-1

Material aspects	Glass Ionomer (GI)	Resin-modified GI	Resin (bonded)	Self-adhesive Resin	Zn-phosphate cement	Ceramir C&B
1. Type of material	Polymer	Monomer	Monomer	Monomer	Inorganic material	Ceramic-polymer
2. Hardening mechanism	Cross-linking	Polymerisation	Polymerisation	Polymerisation	Acid-base reaction	Acid-base + cross-linking
3. pH	Acidic	Acidic	Acidic /neutral	Acidic /neutral	Acidic	Acidic /basic
4. Geometrical stability	Non-shrinking	Non-shrinking	Shrinks	Shrinks	Non-shrinking	Non-shrinking
5. Stability over time	Degrades	Degrades	Degrades	Degrades	Degrades	Stable
6. Extra treatment	-	-	Etching and bonding	-	-	-
7. Hydrophilic / phobic	Hydrophilic	Hydrophilic	Hydrophobic	Initially hydrophilic, Hydrophobic	Hydrophilic	Hydro-philic
8. Integration mechanism	Micro-mechanical retention, Chemical bonding	Micro-mechanical retention / Chemical bonding / Adhesion	Adhesion / Micro-mechanical retention	Adhesion / Micro-mechanical retention	Micro-mechanical retention	Nano-structural integration
9. General behaviour	Irritant	Allergenic	Allergenic	Allergenic	Non-allergenic	Non-allergenic
10. Biocompatibility	Good	OK	OK	OK	Good	Good
11. Bioactivity	No	No	No	No	No	Bioactive
12. Sealing quality	OK	OK	Good but operation sensitive	OK	Acceptable	Excellent

Table 13. Overview of dental luting cements (Hermansson et al, 2010)

Material aspects 4-12 in Table 13 are also relevant for all other Ca-aluminate based dental applications.

A clinical 2-year study comprising 35 cemented crowns was conducted at Kornberg School of Dentistry, Temple University, and follow-up data and feedback from participating dentists were excellent with no failures at all reported (Jefferies et al 2009).

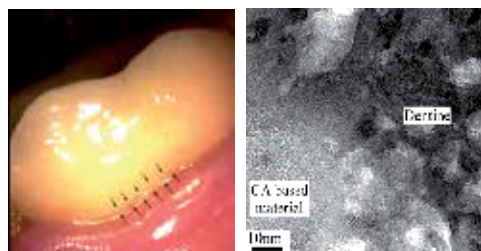


Fig. 8. Cemented ceramic crown (left), and HRTEM of the nanostructure of Ca-aluminate hydrates, hydrates formed in the interval 10-30 nm(right), bar = 10 nm (Hermansson et al, 2010)

#### 4.1.2 Endodontics

In a review of the biocompatibility of dental materials used in contemporary endodontic therapy (Haumann and Love, 2003) amalgam was compared with gutta-percha, zinc oxide-eugenol (ZOE), polymers, glass ionomer cements (GICs), composite resins and mineral trioxide aggregate (MTA). A review (Niedermaier, 2003) of clinical trials of *in vivo* retrograde obturation materials summarized the findings. GIC's appeared to have the same clinical success as amalgam, and orthograde filling with gutta-percha and sealer was more effective than amalgam retrograde filling. Retrograde fillings with composite and Gluma, EBA cement or gold leaf were more effective than amalgam retrograde fillings. However, none of the clinical trials reviewed included MTA. In a 12 week microleakage study, the MTA performance was questioned compared to that of both amalgam and a composite (Alamo et al, 1999).

The Ca-aluminate-based material discussed in this paper belongs to the same material group as MTA, the chemically bonded ceramics. MTA is a calcium silicate (CS) based cement having bismuth oxide as filler material for improved radio-opacity, whereas the Ca-aluminate material consists of Ca-aluminate phases CA and CA<sub>2</sub> with zirconia as filler material. MTA is claimed to prevent microleakage, to be biocompatible, to regenerate original tissues when placed in contact with the dental pulp or periradicular tissues, and to be antibacterial. The product profile of MTA describes the material as a water-based product, which makes moisture contamination a non-issue (Dentsply 2003). The CA-cement materials are more acid resistant than the CS-based materials, and in general show higher mechanical strength than the CS materials. A two-year and a five-year retrospective clinical study of Ca-aluminate based material have been conducted (Pameijer et al, 2004, Kraft et al, 2009). The study involved patients with diagnosis of either chronic per apical osteitis, chronic per apical destruction, or trauma. Surgery microscope was used in all cases. For orthograde therapy the material was mixed with solvent into appropriate consistency and put into a syringe, injected and condensed with coarse gutta-percha points. Machine burs were employed for root canal resection. For the retrograde root fillings, the conventional surgery procedure was performed. The apex was detected with surgery microscope and rinsed and prepared with an ultrasonic device. Crushed water-filled CA-tablets were then inserted and condensed with dental instruments. The patients' teeth were examined with X-

ray, and three questions regarding subjective symptoms were put to patients: 1. Have you had any persistent symptoms? 2. Do you know which tooth was treated? 3. Can you feel any symptoms at the tooth apex?

In 13 of the 17 treated patients the diagnosis was chronic periapical osteitis (c p o). These were treated with retrograde root filling (rf) therapy. Three patients suffered from trauma or chronic periapical destruction, and these patients were treated with orthograde therapy. Out of 17 patients (22 teeth) treated, 16 patients (21 teeth) were examined with follow-up x-ray after treatment and also after two years or more. The additional patient was asked about symptoms. The results of both the clinical examination and the subjective symptoms were graded into different groups related to the success of the therapy. The results of the 2-year and the 5-year study are shown in Table 14.

	1 Complete healing		2 Incomplete healing		3 Uncertain		4 Failure	
	2-year	5-year	2-year	5-year	2 year	5-year	2-year	5-year
Nos. of teeth	18	14	3	2	0	0	1	0
Percentage	82	87	14	13	0	0	4	0

Table 14. Summary of the results (Score 1 and 2 considered successful, score 3 and 4 failure)

Figures 9-10 show examples of the X-ray examination of orthograde and retrograde treatments.

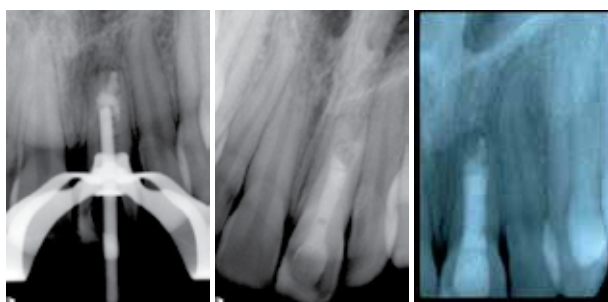


Fig. 9. Tooth 21 (patient14) a) condensing with a Gutta-percha pointer, b) just after treatment and c) at two year control



Fig. 10. Tooth 21 (patient 9) at treatment (left) and at two year control (middle) and at 5 year control (right)

In summary 21 out of 22 treated teeth have acceptable results being either symptom free or judged healed after clinical examination. The single failure can probably not be attributed to



the material, but rather to the difficulty of treating and sealing a multi-channelled tooth. The use of CA's as root canal sealers is indirectly supported in "Introduction to Dental Materials" by van Noort (van Noort, 1994), where the following materials characteristics are looked for; biocompatible, dimensionally stable, antibacterial and bioactive. The results in this study can be interpreted as a success in meeting these materials requirements.

Already in the 1970s, Calcium aluminate (CA) was suggested as a biomaterial and tested *in vivo*. Hentrich et al (Hentrich et al, 1994) compared CA with alumina and zirconia in an evaluation of how the different ceramics influenced the rate of new bone formation in femurs of rhesus monkeys. Hamner et al (Hamner and Gruelich, 1972) presented a study in which 22 CA roots were implanted into fresh natural tooth extraction sites in 10 baboons for periods ranging from 2 weeks to 10 months. In both studies CA successfully met the criteria for tissue adherence and host acceptance.

#### 4.1.3 Dental filling materials

An important feature of the hydration mechanisms of the Ca-aluminate based materials is the nanostructural integration with and the high shear strength developed towards dental tissue. This makes both undercut (retention) technique and bonding techniques redundant. The Ca-aluminate approach to dental filling technique is new. With this technique, the chemical reactions cause integration when the bioceramic material is placed in the oral cavity at body temperature and in a moist treatment field. Figure 11 shows a TEM (transmission electron microscopy) illustration of the interface between the CA-based material and dentine. This establishes a durable seal between bioceramic and tooth. Whereas amalgam attaches to the tooth by mechanical retention and resin-based materials attach by adhesion, using bonding agents, etchants, light-curing or other complementary techniques, the CA-materials integrate with the tooth without any of these, delivering a quicker, simpler and more robust solution.

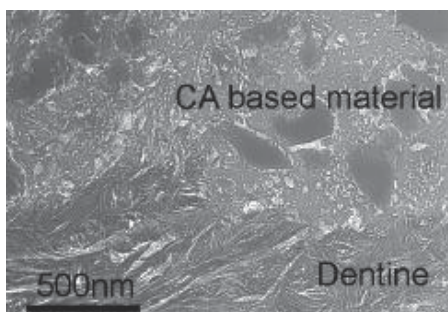


Fig. 11. Nanostructural integration of CAPH-material with dentine (gray particles in the biomaterial are glass particles)

The general aspects of Ca-aluminate based materials have been presented in two Ph D Thesis-publications. Important aspects of Ca-aluminate materials as dental filling materials are dealt with, such as dimensional stability, acid corrosion and wear resistance, and biocompatibility and mechanical properties (Kraft 2002, Lööf et al 2003).

#### 4.1.4 Coatings on dental implant and augmentation

For successful implantation of implants in bone tissue, early stabilisation is of great importance (Ellingsen and Lyngstaadas, 2003). This includes both orthopaedic and dental

implants. Even small gaps may lead to relative micro-motions between implant and the tissue, which increases the risk of implant loosening over time due to formation of zones of fibrous tissues at the implant-tissue interface. Early loading of implants is of particular interest for dental implants (Vercaigne et al, 1998). The use of surface coatings technology is today an established method to reduce the problem with poor interfacial stability for implants. With coatings technology, structural characteristics of the implant (e.g. strength, ductility, low weight or machinability) may be combined with surface properties promoting tissue integration. There are several established coating deposition techniques, e.g. physical vapour deposition (sputtering) and thermal spraying techniques. Coatings based on calcium phosphates are the most used ones.

This section deals with coatings deposited with established methods, with the aim of improving particularly the early stage anchoring of metal implants to bone tissue by exploring *in vivo* hydration of coatings or pastes based on chemically curing ceramics. The study focuses on calcium aluminate in the form of coatings and paste. Results are presented from an implantation study with flame-sprayed coating on titanium implants and uncoated implants augmented with a calcium aluminate paste in the hind legs of rabbits. Implants were applied with the paste composed of a mixture of  $\text{CaO} \cdot \text{Al}_2\text{O}_3$  and  $\text{CaO} \cdot 2\text{Al}_2\text{O}_3$ . The paste was applied manually as a thin layer on the threaded part of the implant just before implantation. The uncoated and coated implants were sterilised with hot dry air at 180 °C for 2 hrs. Female albino adult New Zealand White rabbits with a body weight around 2.5 kg were used. Each animal received four implants, two in each hind leg. Implants were placed in the distal femoral metaphysis as well as in the proximal tibial metaphysis. Surgery followed standard procedure. The implants were screwed into predrilled and threaded cavities. Necropsy took place after 24 hrs, 2 and 6 weeks (Axen et al, 2005).

No negative effects of the implants on the general welfare of the animals were observed. The healing progressed in a normal and favourable way. As for the removal torque recordings, all calcium aluminate coatings types provided an improved implant anchoring to bone tissue after *in vivo* hydration, as compared to that of the pure metal implants. Implants on the tibia and femur side of the knee gave similar removal torques. Table 15 provides average values from both tibia and femur sides.

Implant type	24 hrs	(n)	2 weeks	(n)	6 weeks	(n)
Flame spraying	7.0	(8)	7.0	(8)	25	(6)
Paste augmentation	6.6	(8)	15	(6)	13	(4)
Rf-PVD	12	(4)	-	-	10	(4)
Uncoated reference	3.8	(8)	5.7	(6)	14	(4)

Table 15. Removal torque (Ncm) for dental implants in rabbit hind legs (tibia and femur).

24 hrs after implantation, calcium aluminate in-between the implant and tissue increased the removal torque to about double that of the uncoated reference implants, independently of means of application (coatings or paste). This is considered to be attributable to the point-welding according to integration mechanism 6 above. Two weeks after implantation, implants combined with paste augmentation provide the highest removal torque; flame sprayed coatings also improve the torque relative to the uncoated system. Six weeks after implantation, all systems are relatively similar (considering the uncertainty due to scatter and statistics), apart from the sprayed system which shows significantly higher values.

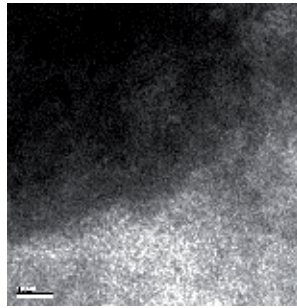


Fig. 12. High-resolution TEM of Ti - CA-paste interface, nano-mechanical integration, bar = 10 nm.

#### 4.2 Orthopaedic applications

Within orthopedics the following areas for Ca-aluminate based materials have been identified; percutaneous vertebroplasty (PVP) and kyphoplasty (KVP), trauma and general augmentation.

The benefits of the injectable ceramic biomaterials based on CA related to orthopaedic applications are

During the surgical procedure (Engqvist et al, 2005, Lööf et al 2008)

- High radiopacity allows for superior visibility of the cement during and increases the probability to detect potential leakages during injection (See Figs. 13-14 below)

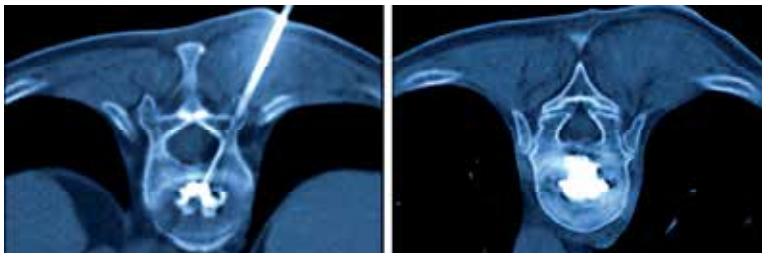


Fig. 13. Percutaneous vertebroplasty using a CA-material.

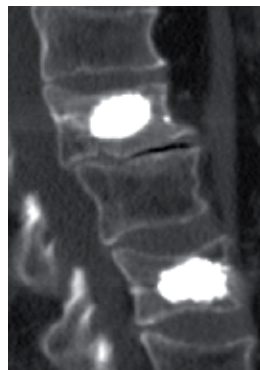


Fig. 14. Vertebral compression fractures, restored by CA-material.

- High and linearly increasing viscosity reduces the risk of leakage and gives a
- predictable handling.
- High cohesiveness optimizes the cement's filling pattern in the vertebra.
- No toxic or smelling fumes

And after the procedure (Jarmar et al, 2008, Engqvist et al 2006)

- Mechanical strength
- Biocompatibility including integration
- Long-term stability i.e. non-resorbable systems.

#### 4.3 Drug carrier for drug delivery

General aspects of ceramics for use in drug delivery of drugs are presented by Ravaglioli et al and by Lasserre and Bajpaj (Ravaglioli et al, 2000, Lasserre and Bajpaj, 1998). A short description of carrier materials for drug delivery using chemically bonded ceramics, especially Ca-aluminate and/or Ca-silicate systems are given below. The CBC carrier material based on CA and CS structures exhibit some attractive features. The manufacturing procedure at low temperatures, where no or limited degradation of the medicaments occur, and the microstructure developed with open porosity as nano-sized channels as described above, are the basic features that open up a possibility for controlled release of medical agents. The precursor powder cures as a result of hydration reactions, between a ceramic oxide powder, primarily Ca-silicates and/or Ca-aluminates, and water. Through the hydration, new phases of hydrates are formed, which to a great part establish the microstructures needed to control the release of drugs incorporated in the injectable precursor material. An injectable material is formed into a paste by mixing it with a water-based hydration liquid, which is then ready to be injected. Directly after the injection, the paste starts to develop the final microstructure. The water-based liquid may also comprise viscosity-controlling additives. These may be loaded with the drug before preparation of the final injectable paste. A couple of unique reaction conditions related to the production of materials yields materials with a variety of possible microstructures with porosities from the nanoscale to the microscale. variety of possible microstructures with porosities from the nanoscale to the microscale. 3) pore size and pore channel size, and 4) combination of different porosity structures (Hermansson, 2010). Porosity generated during the hydration of the Ca-aluminates and Ca-silicates is open porosity due to the reaction mechanism, and can be in the interval of 5-60 vol.-%. The average pore channel size (i.e. the diameter of the pores formed between the particles of the hydrated material) may be 1-10 nm. The crystal size of the reacted hydrates is in the interval 10-50 nm. This was established by BET-measurements, where the specific surface area of dried hydrated CA was determined to be in the interval 400-500 m<sup>2</sup>, corresponding to a particle size of approximately 25 nm, and by HRTEM [7], Fig. 1 below. When short hydration time and/or low amount of water, or moisture at relative humidity > 70 %, are used, additional porosity is achieved with pore sizes in the interval 0.1-1 micrometer due to incomplete reaction. The different pore sizes obtained can be utilized for controlled release of drugs, when the Ca-aluminate implant material also works as a carrier of medicaments.

#### Drug loading and controlled release of drugs

The following properties are of significance with regard to the carrier for controlling the drug release; Type of ceramic precursor for producing the chemically bonded ceramic, grain size distribution of the precursor powder particles and general microstructure of the

material, the microstructure of the additional particles for drug incorporation, and additives to ensure complementary porosity.

The loading of the drug can be performed in several ways. The drug may be included, either partially or fully, in the powder or in the hydration liquid. Time and temperature for hydration are selected with regard to the drug and drug loading and to the selected release criteria. The manufacturing of the carrier can be done completely before or during loading of the drug. This renders a controlled release time to be selected from a few hours to days and months.

The drug is introduced in the carrier by mixing the drug into the precursor powder, or the hydrated CBCs or other porous phases. The material can be formed into a paste by mixing it with a water-based hydration liquid. The powder can also be pressed into pellets, which thereafter are soaked in the liquid. The paste or the soaked pellets start to develop the microstructure that to a great extent will contribute to the controlled release of the drug. The time and temperature after the mixing will determine the degree of hydration, i.e. the porosity obtained. The porosity can be controlled within a broad interval of open porosity.

## 5. Conclusion

The Ca-aluminate technology provides a platform upon which Ca-aluminate based materials may work as a general biomaterial and as a complement to other chemically bonded ceramics based on phosphates, silicates or sulphates. Identified areas are in the first place within the dental and orthopedic areas, where injectable stable biomaterials are required. These include also properties as bioactivity related to apatite formation, antibacterial properties as well as nanostructural features useful for carriers for controlled drug delivery. The studies presented in this paper can be summarised as follows;

- Nano-structural integration and apatite formation provide important benefits to both the dentist and patient, notably minimal micro-leakage, perfect seal at the interface between tooth and material and as a result longer-lasting treatment results.
- The potential use of the Ca-aluminate materials for implant applications is based on the following features: nanostructural integration with tissue, possible apatite formation, and a mass increase yielding early point welding between the biomaterial and surrounding.
- The following product areas have been identified based on experimental material data, pre-clinical studies, pilot studies and on-going clinical studies: dental cement, endodontic products (orthograde and retrograde), sealants, restoratives, underfillings, and pastes for augmentation and dental implant coatings.
- Consequences of nanostructural contact integration of the Ca-aluminate system are reduced risk of secondary caries and restoration failure, and reduced post-operative sensitivity.
- The Ca-aluminate material can be used as a vehicle for transport and delivery of the medicament and as an injectable implant. The combination of the material as carrier and implant material makes site-specific placement of drugs and implants possible. By introducing optional additives, or by changing the w/c ratio, the release time can be controlled from short time periods (a few hours) to prolonged time periods (day and weeks). The release time is also dependant upon where the drug is placed. In cortical bone a release time of months seems possible.

- The Ca-aluminate materials are not degradable and do not induce clotting or haemolysis.
- The first product in a series - a dental luting cement- was recently launched on the European and the US markets.

## 6. Acknowledgment

Results presented in this chapter are mainly based on two decades of research within Doxa AB and the Eng. Sci. Dept., The Angstrom Laboratory, Uppsala University, Sweden.

## 7. References

- Mangabhai, R. J. (1990), Calcium Aluminate Cements, Conf proceedings, Chapman and Hall
- Hench, L (1998) Biomaterials: a forecast for the future, *Biomaterials* Vol 19 1419-1423
- Nilsson, M. (2003) *Ph D Thesis*, Injectable calcium sulphates and calcium phosphates as bone substitutes, Lund University
- Scrivener, K.L. and Capmas A.; (1998) Calcium aluminate cements, In: *Lea's Chemistry of Cement and Concrete*, Ed. Hewett P.C., Arnold: Paris, p 709-771
- Kraft, L. (2002) *Ph D Thesis*, Calcium aluminate based cements as dental restorative materials. Faculty of Science and technology, Uppsala University, Sweden
- Loof, J; Engqvist, H.; Lindqvist, K.; Ahnfelt, N-O.; Hermansson L; (2003), Mechanical properties of a permanent dental restorative material based on calcium aluminate, *Journal of Materials Science: Materials in Medicine*, 14, No. 12 1033-1037
- Engqvist, H.; Edlund S.; Gomez-Ortega, G.; Loof, J.; and Hermansson, L.; (2006) In vitro mechanical properties of a calcium silicate based bone void filler, *Key Eng. Mater.* 361-363 ( 369-376)
- Muan, A.; Osbourne, E. A.; (1965) Phase equilibria among oxides. Adison-Wesley; New York
- Lewis, G.; (2006) *J. Biomed. Matls. Res. PartB: Applied Biomaterials* 76B: 456-468
- H. Engqvist, J. Loof, S. Uppstrom, M. W. Phaneuf, J. C. Jonsson, L. Hermansson, N-O. Ahnfelt, (2004), Transmittance of a bioceramic calcium aluminate based dental restorative material, *Journal of Biomedical materials Research Part B: Applied Biomaterials* vol. 69 no. 1, 94-98
- Lööf, J. (2008) *Ph D Thesis*, Calcium-aluminate as biomaterial: Synthesis, design and evaluation. Faculty of Science and Technology, Uppsala, University, Sweden
- Lööf, J.; Engqvist H.; Gómez-Ortega, G.; Spengler, H.; Ahnfelt, N-O.; Hermansson, L.; (2005) Mechanical property aspects of a biomineral based dental restorative system, *Key Engineering Materials* Vols. 284-286, 741-744
- Loof, J.; Engqvist, H.; Hermansson, L.; Ahnfelt, N-O. (2004) Mechanical testing of chemically bonded bioactive ceramic materials, *Key Engineering Materials* Vols. 254-256, 51-54
- Hermansson, L.; Kraft, L.; Lindqvist, K.; Ahnfelt, N-O.; Engqvist, H.; (2008) Flexural Strength Measurement of Ceramic Dental Restorative Materials, *Key Engineering Materials*, Vols. 361-363, 873-876
- Williams, D.D.; (1987) Definitions in Biomaterials, Chapter 8, pp 66-71, Ed. Elsevier, New York
- Cao, W.; Hench L.L.(1996), Bioactive materials, *Ceramics International*, Vol 22 493-507 ISO 10993:2003 EN 29917:1994/ISO 9917: 1991
- Liu, Y.; Sahlberg, L.; Kraft, L.; Ahnfelt, N-O.; Hermansson, L.; Ekstrand, J. (2002) Aspects of Biocompatibility and Chemical Stability of Calcium-Aluminate-Hydrate Based

- Dental Restorative Material, Paper IX in *Ph D Thesis* by L. Kraft, Uppsala University 2002
- Engqvist, H.; Lööf, J.; Kraft, L.; Hermansson, L.; (2004) Apatite formation on a biomaterial-based dental filling material, *Ceramic Transactions*, Vol 164 , Biomaterials: Materials and Applications, V. 2004;164:37-42.
- Faris, A.; Engqvist, H.; Lööf, J.; Ottosson, M.; Hermansson, L.; (2006) In vitro bioactivity of injectable ceramic orthopaedic cements, *Key Eng. Mater.* 309-11, 1401-1404
- Engqvist, H.; Couillard, M.; Botton, G.A.; Phaneuf, M.P.; Axén, N.; Ahnfelt, N-O. and Hermansson, L.; ( 2005), In vivo bioactivity of a novel mineral based based orthopaedic biocement, *Trends in Biomaterials and Artificial Organs*, 19, 27-32
- Engqvist, H.; Schultz-Walz, J-E.; Lööf, J.; Botton, G.A.; Mayer, D.; Phaneuf, M.W.; Ahnfelt, N-O.; Hermansson, L.; (2004), *Biomaterials* Vol 25, 2781-2787
- FAO/WHO Joint Expert Committee on Food Additives (JECFA)
- Jefferies, S.R.; Appleby, D.; Boston, D.; Pamiejer, C.M.; and Lööf, J.; (2009). Clinical performance of a bioactive dental luting cement- A prospective clinical pilot study. *J. of Clinical Dentristry* XX, No. 7, 231-237 ISO 10993-12: 1992 ISO 10993-5:1992, clause 8.4.1
- Tang, A.T.H.; Li, J.; Ekstrand, J.; and Liu, Y. (2002), Cytotoxicity tests of in situ polymerized resins: Methodological comparisons and introduction of a tissue culture insert as a testing device *J Biomed Mater Res*, 45, 214-222.
- Schmalz, G.; Rietz, M.; Federin, M.; Hiller, H-A.; Schweikl, H.; (2002) Pulp derived cell response to an inorganic direct filling material, Abstact, presented at Cardiff Conference,
- Hermansson, L.; Höglund, U.; Olaisson, E.; Thomsen, P.; Engqvist, H.; (2008) Comparative study of the bevaious of a novel injectable bioceramic in sheep vertebrae, *Trends in Biomater. Artif. Organs*, Vol 22, 134-139
- Axén, N.; Ahnfelt, N-O.; Persson, T.; Hermansson, L.; Sanchez, J. and Larsson, R.; (2004), A comparative evaluation of orthopaedic cements in human whole blood, *Proc. 9th Ceramics: Cells and tissue*, Faenza
- Hermansson, L.; Lööf J. and Jarmar, T.; (2009) Integration mechanisms towards hard tissue of Ca-aluminate based materials, *Key Eng. Mater.* Vol 396-398, 183-186
- Hermansson, L.; Engqvist, H.; Lööf, J.; Gómez-Ortega G. and Björklund, K.; (2006) Nano-size biomaterials based on Ca-aluminate Advances in Science and technology, *Key Eng. Mater.* Vol 49 21-26
- Hermansson, L.; Lööf, J. and Jarmar, T.; (2008) Injectable ceramics as biomaterials today and tomorrow, in *Proc. ICC 2*, Verona 2008
- Ravagliolo, A.; and Krajewski, A.; (1992) *Bioceramics*, Chapman and Hall, Mjör, I.; (2000) *Int Dental Journal*, Vol 50 [6], 50
- Pameijer, C.H.; Jeffries, S.R.; Lööf, J. and Hermansson, L.; (2008) Microleakage Evaluation of XeraCem in Cemented Crowns, *J Dent Res.* 2008;87(B):3098.
- Pameijer, C. H.; Jeffries, S.R; Lööf J. and Hermansson, L.; (2008) Physical properties of XeraCem, *J Dent Res.* 2008; 87(B):3100.
- Pameijer, C. H.; Jeffries, S.R.; Lööf, J.; and Hermansson, L.; (2008) A comparative crown retention test using XeraCem, *J Dent Res.* 2008; 87 (B):3099.
- Jefferies, S.R.; Pameijer, C.H.; Appleby, D.; Boston (2009), One month and six month clinical performance of XeraCem®. *J Dent Res.* 2009;88(A):3146
- Jefferies, S.R.; Pameijer, C.H.; Appleby, D.; Boston D.; Lööf, J.; Glantz, P-O.; (2009), One year clinical performance and post-opreative sensitivity of a bioactive dental luting cement, *Swed. Dent. J.* 2009 Vol 33 193-199

- Hermansson, L.; Faris, A.; Gomez-Ortega, G.; Abrahamsson, E.; Lööf, J.; (2010), Calcium aluminate based dental luting cement with improved properties – an overview, *Advances in Bioceramics and Porous Ceramics*, 34<sup>th</sup> Int Conf on Advanced Ceramics and Composites, , Ed. Wiley, *Ceramic Eng. And Sci. Proc, Vol 31, p 27-38*
- Jefferies, SR.; Pameijer, CH.; Appleby, D.; Boston, D.; Lööf, J.; Glantz, P-O.; (2009) One year clinical performance and post-operative sensitivity of a bioactive dental luting cement – A prospective clinical study. *Swed Dent J.* 2009; 33:193-199.
- Haumann, C.H.J. and R.M. Love, (2003) Biocompatibility of dental materials used in contemporary endodontic therapy: a review. Part 2, Root–canal–filling materials, *International Endo J*, 36: p. 147-160.
- Niederman, R. and J.N. Theodosopoulou, Review: A systematic review of in-vivo retrograde obturation materials. *Int Endo J*, 2003. 36: p. 577-585.
- Alamo, H.L., et al., A Comparison of MTA, Super-EBA, composite and amalgam as root-end filling materials using a bacterial microleakage model, *International Endodontic Journal*, 1999. 32: p. 197-203.
- Kraft, L.; Saksi, M.; Hermansson, L.; Pameijer, CH.; (2009) A five-year retrospective clinical study of a calcium-aluminate in retrograde endodontics. *J Dent Res.* 2009; 88(A):1333.
- Noort, R.v., (1994), *Introduction to Dental Materials*. Mosby Hentricht, R.L.; (1971), An evaluation of inert and resorbable ceramics for future clinical applications, *J. Biom. Res.* 5(1): 25-51
- Hamner, J.E., Reed, M.; and Gruelich, R.C.; Ceramic root implantation in baboons. *J. Biom. Res.* 1972 6 (4): p. 1-13.
- Ellingsen, J-E.;Lyngstadaas, S.P. ; (2003), *Bioimplant interface, improving biomaterials and tissue reactions*, CRC Press LLC. Vercaigne S. et al, (1998) Bone healing capacity of titanium plasma-sprayed and hydroxylapatite coated oral implants, *Clin. Oral Implants Res*, 9, 261
- Axén, N.; Engqvist, H.; Lööf, J.; Thomsen P.; and Hermansson, L.; (2005) , In vivo hydrating calcium aluminate coatings for anchoring of metal implants in bone, *Key Eng. Mater.* Vols. 284-286 831-834 21
- Jarmar, T.; Uhlin, T.; Höglund, U.; Thomsen, P.; Hermansson, L.; and Engqvist, H.; Injectable bone cements for Vertebroplasty studied in sheep vertebrae with electron microscopy, *Key Engineering Materials* Vols. 361-363
- Engqvist, H.; Hermansson, L.; (2006) Chemically bonded nano-size bioceramics based on Ca-aluminates and silicates, *Ceramic Transactions.* 2006; 172: 221-228. Ravaglioli et al, (2000), *J Mater Sci Mater Med.* 2000 11(12):763-7
- Lasserre; and Bajpaj, (1998) *Critical Reviews in Therapeutic Drug Carrier Systems*, Vol 15, 1
- Hermansson, L.; (2010), Chemically bonded bioceramic carrier systems for drug delivery, *Advances in Bioceramics and Porous Ceramics*, Ed. Wiley, 34<sup>th</sup> Int. Conference on Advanced Ceramics and Composites, *Ceramic Eng. and Sci. Proc, Vol 31, p 77-88*



# Ulvan: A Versatile Platform of Biomaterials from Renewable Resources

Federica Chiellini and Andrea Morelli

*Laboratory of Bioactive Polymeric Materials for Biomedical and Environmental Applications (BIOLab) UdR-INSTM – Department of Chemistry and Industrial Chemistry, University of Pisa  
Italy*

## 1. Introduction

Biomass represents an abundant renewable resource for the production of bioenergy and biomaterials and its exploitation could lead to overcome the dependence from petroleum resources. Indeed fossil energy and chemical sources are not unlimited and there is a critical need to turn the current way of life back to a sustainable manner. The conversion of biomasses into high value chemicals, energy and materials is nowadays gaining more and more attention and represents the final goal of the “Industrial Biorefining”. Indeed Biorefinery aims at the optimum exploitation of biomass resources for the production of materials that eventually might replace the conventional products from fossil/non renewable resources, thus decisively contributing to the development of a sustainable system. The great challenge in which Biorefining is involved is the possibility of creating high value products from low value biomasses. In this view, the feasibility of using starting materials obtainable from organic waste sources (agricultural, municipal and industrial waste) or having harmful effects on the environment (algae) as feedstock can represent the strategy of election for the production of sustainable materials.

To this aim algae could represent a potentially advantageous biomass to be explored since they are very abundant and cheap and very often involved in uncontrolled proliferation processes detrimental for marine and aquatic environments (Barghini et al., 2010, Chiellini et al., 2008, 2009, Fletcher, 1996). Today most of the naturally produced and harvested algal biomass is an unused resource and often is left to decompose on the shore creating waste problems (Morand et al., 2006). The current use of this huge underexploited biomass is mainly limited to food consumption and as bio-fertilizer, but its potentiality as renewable and sustainable feedstock for energy and material production is gaining more and more attention (Demirbas A. & Demirbas M.F., 2011). Indeed microalgae have been considered to be an excellent source for biodiesel production since are characterized by high growth rates and high population densities, ideal for intensive agriculture and may contain huge lipid amounts, needed for fuel production (Christi, 2007). Besides biodiesel, algae can be cultivated and can be used as a feedstock for the production of bioethanol (John et al., 2011). In particular macroalgae (seaweed) can produce huge amount of carbohydrates per year

(Matsumoto et al., 2003) that suitably processed through specific fermentation processes would provide renewable and sustainable biofuel.

Algae represent also an advantageous resource of chemicals and building block materials that can be tailored through proper biorefining processes according to the different envisaged applications. The rising demand for natural instead of synthetic materials especially in biomedical applications where high biocompatibility and no adverse effects for the host organism are required (Mano et al., 2007), has led to an outburst of scientific papers involved in the study of biobased materials. Among these, polysaccharides could represent the best candidate since abundant, biocompatible and displaying a pronounced chemical versatility given by the great number of chemical functionalities present in their structures. The list of known natural carbohydrates is continuously growing, owing to new discoveries in animal and plant material (Tsai, 2007). They can be used in their native form or after proper chemical modifications made according to the final applications (d'Ayala et al., 2008). The use of polysaccharides of animal origin (e.g. heparin and hyaluronic acid) in biomedical applications is not straightforward since it can raise concerns about immunogenicity and risk of disease transmission (Stevens, 2008) Indeed these materials require very accurate purification treatments aimed to free them from biological contaminants, in contrary to polysaccharides of plant (e.g. cellulose and starch) or algal origin (e.g. alginate). Polysaccharides of algal origins are gaining particular attention due to their abundance, renewability (Matsumoto et al., 2003) and to their peculiar chemical composition not found in any other organisms. Over the last few years medical and pharmaceutical industries have shown an increasing interest in alginate (d'Ayala et al., 2008), an anionic polysaccharide widely distributed in the cell walls of brown algae. This biopolymer has been largely used for its gel forming properties. Due to its non-toxicity, unique tissue compatibility, and biodegradability, alginate has been studied extensively in tissue engineering, including the regeneration of skin (Hashimoto et al., 2004), cartilage (Bouhadir et al., 2001), bone (Alsberg et al., 2001), liver (Chung et al., 2002) and cardiac tissue (Dar et al., 2002).

A very intriguing feature that distinguishes algal biomass from other resources is that it contains large amounts of sulphated polysaccharides, whose beneficial biological properties (Wijesekara et al., 2011) prompt scientists to increase their use in the biomedical fields. Indeed the presence and the distribution of sulphate groups in these polysaccharides are reported to play an important role in the antiviral (Damonte et al., 2004), anticoagulant (Melo et al., 2004), antioxidant (Rocha de Souza et al., 2007) and anticancer (Athukorala et al., 2009) activity of these materials.

The chemical composition of the sulphated polysaccharides extracted from algae, including the degree and the distribution of the sulphate groups, varies according to the species, and the ecophysiological origin of the algal sources (Rioux et al., 2007). Anyhow, a structural differentiation depending on the different taxonomic classification of the algal origin, has been found. According to the mentioned classification the major sulphated polysaccharides found in marine algae include fucoidan from brown algae, carrageenan from red algae and ulvan obtained from green algae (Figure 1).

Ulvan polysaccharides possess unique structural properties since the repeating unit shares chemical affinity with glycoaminoglycan such as hyaluronan and chondroitin sulphate due to its content of glucuronic acid and sulphate (Figure 2).

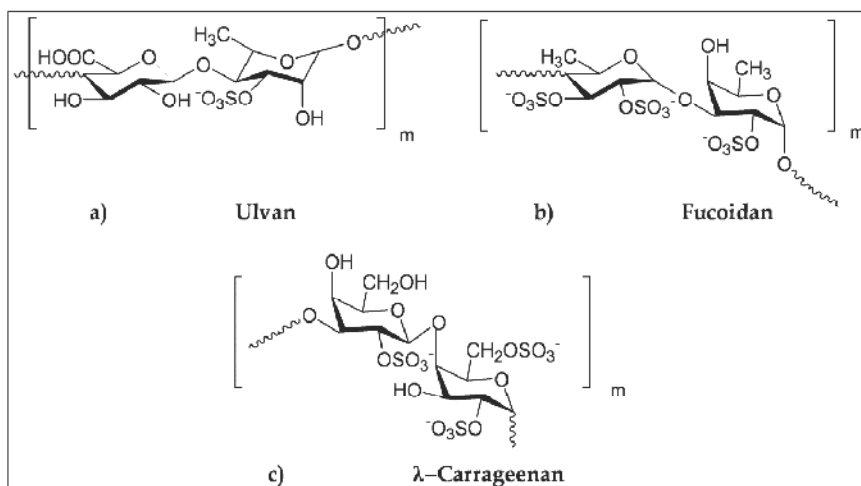


Fig. 1. Chemical structure of the dimeric repeating unit of a) Ulvan, b) Fucoidan, c)  $\lambda$ -Carrageenan.

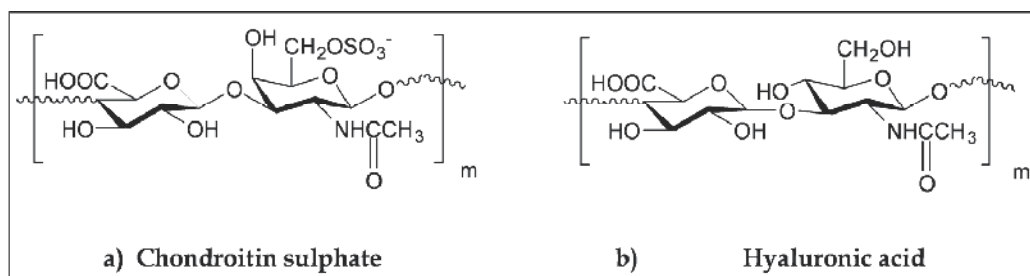


Fig. 2. Chemical structure of the dimeric repeating unit of a) Chondroitin sulphate, b) Hyaluronic acid.

This resemblance and the possibility of obtaining this material from cheap and renewable resources make it worthwhile a deeper investigation on the biological activity and the feasibility of using this polysaccharide for biomedical applications.

## 2. Ulvan properties

Ulvaes (Chlorophyta) are very common seaweeds distributed worldwide. The two main genera *Ulva* and *Enteromorpha* are sadly known for being involved in processes detrimental for the aquatic environment. Indeed this algal biomass proliferates very quickly in eutrophic coastal and lagoon waters in the form of "green tides" leading up to hypoxia and death of most of aquatic organisms (Morand & Brian, 1996). Environmental concerns arise also for the disposal of this huge biomass that is mostly left to degrade on the shore creating nuisance problems, so that its exploitation could represent a remedy to related environmental and economical concerns.

To date, this biomass has very low added value and its use is limited to food consumption (Bobin-Dudigeon et al., 1997) composting (Mazè et al., 1993) and methane production

(Brand & Morand, 1997) but as it will be stressed in the following part of the chapter, the chemicals and polymers of this underexploited biomass along with their abundance, biological properties and “renewability” represent a potential source to be explored.

## 2.1 Chemical-physical properties

### 2.1.1 Ulvan composition

Green algae such as *Ulva sp.* are known to contain high amounts of good-quality protein, carbohydrate, vitamins and minerals (Taboada et al., 2010). Among these, polysaccharides are gaining increasing attention as they possess unique physical and chemical properties representing a versatile material platform for potential biological applications.

Ulvan represents a class of sulphated heteropolysaccharide extracted from the cell wall of green seaweeds belonging to *Ulva sp.* whose composition has been extensively debated (Lahaye & Robic, 2007; Robic et al., 2009;) and showed to vary according to several factors including the period of collection, the ecophysiological growth conditions, the taxonomic origins and the post-collection treatment of the algal sources (Lahaye & Robic, 2007).

Four types of polysaccharides are reported to be contained in the biomass of *Ulva sp.*, including the water soluble Ulvan and insoluble cellulose as major one and an alkali-soluble linear xyloglucan and glucuronan in minor amounts (Lahaye & Robic, 2007). Ulvan represents the major biopolymeric fraction of the cell wall having the function of maintaining the osmolar stability and protection of the cell (Paradossi et al., 2002). As usually found in polysaccharides present into the cell walls, Ulvan is present in close association with proteins and the conventional methods of extraction and purification resulted not completely effective in the removal of the protein fraction even after a specific deproteinization protocol (Alves et al., 2010).

Extraction is conventionally achieved by using warm water solution (80-90°C) containing ammonium oxalate as divalent cation chelator and the recovery of Ulvan is generally obtained by precipitation in ethanol. The yield of extraction usually ranges from 8% to 29% of the algal dry weight depending on the applied purification procedure (Lahaye & Axelos, 1993; Lahaye et al., 1994).

The sugar composition of Ulvan is extremely variable but rhamnose, xylose, glucuronic and iduronic acid and the presence of sulphate groups have been identified as the main constituents of the polymer (Paradossi et al., 2002; Robic et al., 2009). These monomers are arranged in an essentially linear fashion even though a slight degree of branching has been found (Lahaye & Robic, 2007). The chemical heterogeneity of Ulvan is partially striken by a “structural motif” found within the heteropolymer chain essentially given by the presence of repeating dimeric sequences constituted by aldobiuronic acid disaccharides designated as type A (glucurorhamnose 3-sulphate, A<sub>3s</sub>) and type B (iduronorhamnose 3-sulphate, B<sub>3s</sub>) (Figure 3).

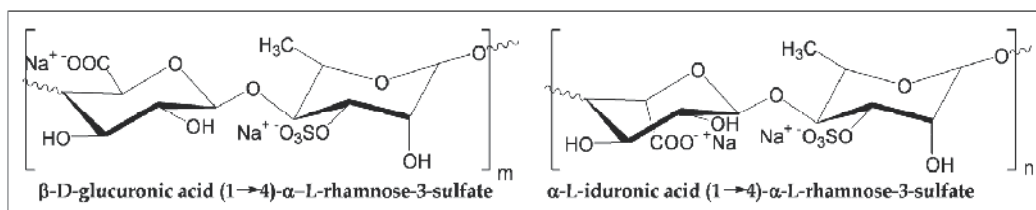


Fig. 3 Structure of the main disaccharide repeating units in Ulvan.

The most striking feature that distinguishes the chemical composition of Ulvan from that of the other polysaccharides of marine origin is, therefore, the presence of uncommon sugar such as iduronic and sulphated rhamnose displaying a close similarity with mammalian glycosaminoglycans. To this view Ulvan and related polysaccharides could represent an abundant and cheap feedstock for the substitution of heparinoid substances commonly used in biomedical applications solving the problems related to their isolation and purification (Alban et al., 2002).

### 2.1.2 Ulvan conformation

The physical properties of polymeric materials are deeply affected by the association and conformation assumed by the constituting chains in the final product. The balance between ordered crystalline and disordered amorphous structures dictates the ultimate mechanical properties of the polymeric material. Indeed the possibility of forming crystalline regions inside a polymeric structure could even generate physical crosslinks between the chains inducing ultimately to the formation of stiff networks, as in the case of polyvinyl alcohol (Ricciardi et al, 2005). The achievement of suitable mechanical properties for a material to be used in biomedical applications, namely tissue engineering, represent a key requirement to fulfil since the final product must provide a physical support for the cell growth and differentiation.

Past investigations on this issue revealed an essentially disordered conformation of Ulvan (Paradossi et al., 1999) mainly induced by the heterogeneous chemical composition of this polysaccharide. The local regularity given by the repeating aldobiuronic units, denominated as  $A_{3s}$  and  $B_{3s}$  (Figure 3), is believed to be sufficient for the formation of transient “junction-zones” responsible for the formation of the weak gel that ulvan is known to perform in nature (Paradossi et al., 2002). The stability of these ordered structures can be affected by the attractive and repulsive interactions that form between the functional groups of the polysaccharide, and in particular by the electrostatic forces. Ulvan is an anionic polyelectrolyte as it contains carboxylic and sulphate groups inside its structure, so that its net charge strongly depends on the pH and ionic strength of the working medium. The net charge on Ulvan is found to affect the conformation of its polymeric chains and ultimately controls the order to disorder transitions given by the locally regular sequences (Paradossi et al., 2002). The conformational change from an ordered structure present in the uncharged chain, i.e. the protonated form of ulvan, toward a disordered state, happens when a critical charge density is reached and is induced only in the chemically regular portions of the chains. The structures of the ordered sequences have been hypothesized on the basis of molecular modelling calculations and are compatible with the formation of helical conformations inside homogeneous portions of the chains containing the repeating units  $A_{3s}$  and  $B_{3s}$  (Paradossi et al., 2002).

The presence of ordered structures limited only in the regular sequences of the Ulvan polymeric chains is not sufficient to provide enough “junction-zones” for the preparation of a material with mechanical properties suitable for biomedical applications. For this purpose Ulvan has to be modified through the introduction of chemical groups or molecules that increase the number of “junction-zones”.

### 2.1.3 Ulvan morphology and solubility

The possibility of chemically modifying Ulvan is strongly dependent on the physical availability of its functional groups so that its solubility and morphology in the working

medium could affect deeply its reactivity. Ulvan has been shown to dissolve only in water due to its charged and highly hydrophilic nature. Nevertheless, the obtained solutions are not transparent, indicating the formation of microaggregates of polymeric material not fully dispersed in the solvent. Indeed TEM analysis of Ulvan revealed the presence of aggregates of spherical shaped forms partially linked by strands-like filaments (Robic et al., 2009). This necklace-like ultrastructure is usually formed by polyelectrolyte material in poor solvent conditions (Dobrynin, 2008) so that even water can not be considered a good solvent for Ulvan. The large presence of methyl groups provided by the rhamnose repeating unit has been considered responsible for the unusual hydrophobic behavior of this highly charged polysaccharide (Robic et al., 2009).

The unusual low intrinsic viscosity of Ulvan in solution can also be ascribed to the presence of condensed spherical shaped aggregates not typical for polyelectrolytes whose conformation usually expands in the form of charged filaments and leads to an increase in the viscosity (Dobrynin et al., 1995). The formation of microaggregates in solution does not allow also a reliable mass analysis of Ulvan, whose different type of aggregation affects deeply the peak distributions usually found on the GPC chromatograms (Robic et al., 2009). Being a polyelectrolyte, both the ionic strength and the pH of the dissolving medium would affect the solubility and the morphology of Ulvan. Indeed the association of the bead-like aggregates in a necklace-type ultrastructure is promoted by the ionic interactions of carboxylated groups as demonstrated by its rupture at pH below the pKa of glucuronic acid (3.28) (Robic et al. 2009). In basic conditions (pH 13) the bead-like structures resulted to collapse into a dense homogeneous network likely prompted by the ionic interactions of carboxylate and sulphate groups. The type and amount of counter-ion in solution could also contribute to chain expansion or condensation as demonstrated by the aggregative propensity of Ulvan at low NaCl concentration observed by light scattering and rheological measurements (Lahaye & Robic, 2007).

The tendency of Ulvan to form aggregates in aqueous solution and its insolubility in almost every organic solvents limit the number of functional groups available for chemical modifications thus hampering its potential versatility. But its great number of reactive groups still present on the “free” surface exposed outside the aggregate and the possibility to optimize the solvent variables (pH and ionic strength) that affect the dispersion of the polymer in solution make Ulvan a suitable reactive platform, tailorable according to the envisaged application.

## 2.2 Biological activity

The possibility of using bio-based materials in almost every technological field and particularly in biomedical applications is challenging and can be considered the strategy of election for limiting environmental concerns and create a virtuous circle of sustainability.

Biomaterials possess the essential prerequisite of renewability and biocompatibility and as such are worth of deep investigations as main candidates for the substitution of synthetic petroleum-based materials, well known for being not renewable and often not biocompatible.

Biodegradability represents also an important property possessed by biomaterials and it is especially required in materials used for biomedical applications with specific reference to tissue engineering and regenerative medicine. Not only the material has to be safe but also the products of degradation should be non-toxic and easily cleared from the body. Biomaterials that other than being renewable, biocompatible and biodegradable are able to

induce a beneficial biological activity on the host organism or on the environment can be considered even more intriguing. This may be the case of Ulvan. Most of the positive health effects induced by this polysaccharide are generated by the presence of sulphate groups in its structure (Wijesekara et al., 2011). A wide list of beneficial biological effects reported by the literature span from antioxidant (Qi et al., 2006) to anticoagulant (Zhang et al., 2008), antitumor (Kaeffer et al., 1998) antihyperlipidemic (Yu et al., 2003) and immunomodulating (Leiro et al., 2007) activities, proved both *in vitro* and *in vivo*.

A brief discussion about the chemical mechanisms that trigger this bioactivity can be worth of mentioning in order to have a deeper insight on the potentiality of using this biomaterial in biomedical applications, and possibly find the “keys” to improve its biological activity.

### 2.2.1 Antioxidant activity

The research of new antioxidant from renewable natural resources able to scavenge free radicals can represent a virtuous strategy for preventing ROS-induced diseases.

In recent years, several classes of sulphated polysaccharides have been demonstrated to show antioxidant activity. Among them Ulvan extracted from *Ulva pertusa* is reported to play an important role as free radical scavenger *in vitro* and displayed antioxidant activity for the prevention of oxidative damage in living organisms (Qi et al., 2005). As found with other sulphated polysaccharides (Wijesekara et al., 2011) the antioxidant activity is deeply affected by the amount and distribution of sulphate groups inside the Ulvan structure.

The possibility to increase the antioxidant activity of Ulvan can be useful according to the envisaged application and has been successfully investigated both by increasing the degree of sulphation through a sulphur trioxide/N,N-dimethylformamide treatment (Qi et al., 2005) and by introducing suitable groups (acetyl and benzoyl) that can boost the activity of the native polysaccharide (Qi et al., 2006).

### 2.2.2 Anticoagulant activity

Heparin, a glycosaminoglycan of animal origin containing carboxylic acid and sulphate groups, has been identified and used for more than fifty years as a commercial anticoagulant and it is widely used for the prevention of venous thromboembolic disorders (Pereira et al., 2002). The heparinoid-like structure of Ulvan makes it also able to provide anticoagulant activity. Indeed this class of polysaccharides displayed the inhibition of both the intrinsic pathways of coagulation or thrombin activity and the conversion of fibrinogen to fibrin (Zhang et al., 2008). The molecular weight of the polysaccharide showed an important effect on the anticoagulant activity indicating that longer chains were necessary to achieve thrombin inhibition.

This behavior has been found to be typical of sulphated polysaccharides of marine origins whose anticoagulant activity has been correlated to the content and position of the sulphate groups inside the polymer chains (Melo et al., 2004).

The importance of finding sources of anticoagulants alternative to heparin has been arising due to the associated harmful side effects and the complex steps of purification required to face the immunological concerns and disease transmission associated with its use (Stevens, 2008). Thus the increasing demand for a safer anticoagulant therapy could be potentially

satisfied by sulphated polysaccharides obtained from abundant and safer origin and Ulvan can represent the ideal material for such purpose.

### 2.2.3 Immunomodulating activity

Some of the polysaccharides obtained from the cell walls of seaweeds appear to exert immunomodulatory activities in mammals as they modify the activity of macrophages. Most classes of carrageenans, sulphated polysaccharide obtained from red algae (Figure 1) are known to induce potent macrophages activation (Nacife et al., 2004.).

The structure of the repeating unit mostly found in Ulvan, resembles that typical of glycosaminoglycan, such as hyaluronic acid and chondroitin sulphate because they all contain glucuronic acid and sulphate. Chondroitin sulphate based proteoglycans are known to be produced by macrophages and human monocytes at inflammatory sites (Uhlen-Hansen et al., 1993) and the structure similarity shared with most of sulphated polysaccharides of algal origin and in particular with Ulvan could represent the trigger of the immunomodulating activity of these materials. Indeed Ulvan from *Ulva rigida* has been reported to modulate the activity of murine macrophages and the presence of sulphate groups has demonstrated to be necessary (Leiro et al., 2007). On the other side, a deeper insight into the structure-immunomodulating effect relationship of these polysaccharides would provide the possibility to obtain an anti-inflammatory effect simply by properly modifying their chemical structure.

### 2.2.4 Antihyperlipidemic activity

Ulvan is known to resist degradation by human endogeneous enzymes thus belonging to the dietary fibers of “sea lettuce” (Taboada et al., 2010). Dietary fibers are considered to be helpful in the prevention of pathologies related to intestinal transit dysfunctions because they act as bulking agents due to their impressive water retention capacity (Bobin-Dubigeon et al., 1997). Dietary fibers are also associated with their ability to lower cholesterol levels (Brown et al., 1999) and the presence of ion charged groups along their structure has shown to improve this beneficial activity (Guillon & Champ, 2000). The ionic groups are thought to complex with bile acids and consequently increase fecal bile acid excretion thus promoting blood cholesterol attenuation (Yu et al., 2003). Ulvan is reported to interact and binding effectively with bile acids due to its high content of negatively charged groups (Lahaye, 1991) thus potentially contributing to the antihyperlipidemic action. Indeed Ulvan has been demonstrated to effectively reduce the level of total and LDL-cholesterol concentrations in the serum and induce an increase in the daily bile excretion in rats (Yu et al., 2003). This activity has been shown to be strongly dependent on the molecular weight of the polysaccharide because a decrease in the viscosity of these materials affected negatively the interaction with bile acids.

## 3. Potential use of ulvan in biomedical applications

A material suitable for biomedical applications, namely tissue engineering, regenerative medicine and drug delivery, is required to be biocompatible and biodegradable and its products of degradation must be safe and easily cleared from the host organisms. Most of the materials obtained from natural resources are able to fulfil these strict requirements but



particular attention are gaining biopolymers of plant and algal origins due to their abundance and minor concerns for purification (Stevens, 2008).

Ulvan could represent an advantageous versatile platform of “unique” sulphated polysaccharides that along with their abundance and renewability would potentially display the properties that match the criteria for biomedical applications. Despite the promising properties related to this material, the use of Ulvan in the biomedical fields is not yet reported and its potentiality still remain unveiled.

A base requirement for a material suitable for tissue engineering, regenerative medicine and/or drug delivery is its insolubility in the physiological fluids not possible with most classes of polysaccharides, whose high hydrophilicity make them very akin to water molecules. Indeed materials used for the regeneration of organs or tissues must avoid dissolution in contact with body fluids thus functioning as chemically and mechanically stable scaffolds during the growth and differentiation of the implanted cells. Also polymeric materials used for drug delivery must preserve their integrity or degrade slowly in order to maintain a controlled release of the loaded drug. The use of polysaccharides in these types of applications is possible only after proper chemical modifications aimed at making them insoluble in aqueous solution. A possible strategy consists in decreasing the hydrophilicity of these materials by introducing hydrophobic groups in their structures, but this often leads to the obtainment of new class of materials, mostly semi-synthetic than naturals and often very different from the original biomaterials. The strategy of election mostly followed by biomaterial scientists in the last 50 years (Hoffmann, 2002) consisted simply in the induction of “junction-zones” between the polymeric chains, inhibiting their dissolution through the formation of permanent or temporary crosslinked networks displaying hydrogel features. These structures maintain almost completely the chemical properties of the original biopolymer comprising their affinity to water giving rise to swollen and not dissolved polymeric scaffolds of natural origins. The maintained hydrophilic character of hydrogels is particularly important in tissue engineering where the overall permeation of nutrients and cellular products into the pores of the gel, determinant for the growth and differentiation of the cells, is determined by the amount of water in the structure (Hoffmann, 2002).

Hydrogels can be chemically or covalently crosslinked and are defined as permanent when the “junction-zones” between the constituting chemical chains are formed by covalent links. If the new bonds are not susceptible to hydrolysis or enzyme recognition the formed hydrogel can be stable indefinitely and not prone to degradation.

The formation of physical or temporary hydrogels is triggered when the “junction-zones” between the polymeric chains are stabilized by weak forces such as electrostatic or hydrophobic interactions. These interactions are reversible, and can be disrupted by changes in physical conditions such as ionic strength, pH, temperature or application of stress. Physical hydrogels are usually not homogeneous, since clusters of molecular entanglements or hydrophobically- or ionically-associated domains can create in-homogeneities (Hoffmann, 2002). This can lead to the formation of hydrogels with weak mechanical properties not suitable for most conventional applications.

Apart from the biological activity displayed by these biomaterials, other important attributes of hydrogels are their mechanical properties and degradation rates that must be tuned according to the final application. The degree of crosslinking along with the chemical

nature of the polymer and of the „junction-zones“ represent the key parameters that mainly affect the above-mentioned properties and can be adjusted according to the addressed applications.

Hydrogels based on polysaccharides are usually characterized by poor mechanical properties due to their impressive water uptake and swelling that lead to the formation of wide opened pore structures that ultimately weakens the scaffold architecture (LaNasa et al., 2010). The presence of charged groups like sulphate and carboxylate in the structure of Ulvan would lead to an even more accentuated absorption of water molecules, hampering the preparation of mechanically stable hydrogels. The strategies for increasing the mechanical properties are several and comprise the preparation of interpenetrating networks with other polymers like polycomplexes formed between oppositely charged polyelectrolytes (Hamman, 2010), the preparation of composite hydrogels mixed with inorganic additives (Pavlyuchenko & Ivanchev, 2009) or the use of hydrophobic comonomers as in the preparation of hydrogels by radical crosslinking (Li et al., 2003).

All these strategies strongly affect the chemical nature of the original biopolymers and the properties of the final hydrogels can be very different from those of the native materials comprising their biocompatibility and bioactivity. A strategy to improve the mechanical properties of polysaccharides and in particular Ulvan is based on a proper choice of the nature and amount of “junction-zones” that crosslink the polymer. Indeed both the increase of the crosslinking or the preference for chemical instead of physical crosslinking would positively affect the mechanical properties of the final hydrogels, leading to more compact structures and dimensionally shaped architecture. Both type of crosslinking have been conducted on Ulvan and are worth of mentioning to get a deeper insight on the possible applications and future developments of using this biopolymer in the biomedical fields.

### 3.1 Ulvan-based physical hydrogels

Ionic gelation is a kind of physical crosslinking based on the ability of polyelectrolytes to give hydrogels in the presence of counter-ions. Alginate is a naturally occurring polysaccharide obtained from marine brown algae that spontaneously form reticulated structures in the presence of divalent or polyvalent cations (Patil et al., 2010). The mechanism involves the cooperative interactions of the carboxylate groups of alginate with the polyvalent cations present in solution to form “junction-zones” between the chains that crosslink the matrix in an insoluble polymeric network.

Due to its polyanionic nature Ulvan is expected to show a similar behavior but its gel formation has the unique characteristic of involving borate esters (Haug, 1976). The optimal conditions for the preparations of the hydrogels requires the presence of boric acid and calcium ions at slightly basic conditions (pH 7.5) giving hydrogels with storage modulus of about 250 Pa (Lahaye & Robic, 2007). Higher ion concentrations, different pH, and even phosphate buffering ions are detrimental to the gel.

The mechanism of gel formation is not yet completely unveiled but is proposed to proceed through the formation of borate esters with Ulvan 1,2-diols followed by crosslinking via  $\text{Ca}^{2+}$  ions (Haug, 1976). Since the gel is thermoreversible the “junction-zones” that crosslink the polymer are thought to involve weak linkages, likely based on labile borate ester groups and ionic interactions easily disrupted by thermal treatments (Lahaye & Robic, 2007). Calcium ions would bridge complexes and/or stabilize the borate esters (Fig. 4a) but also sulphate and carboxylic acid groups were later on proposed to coordinate to  $\text{Ca}^{2+}$  (Figure 3b,c) (Lahaye & Axelos, 1993) and contribute to the gel formation.

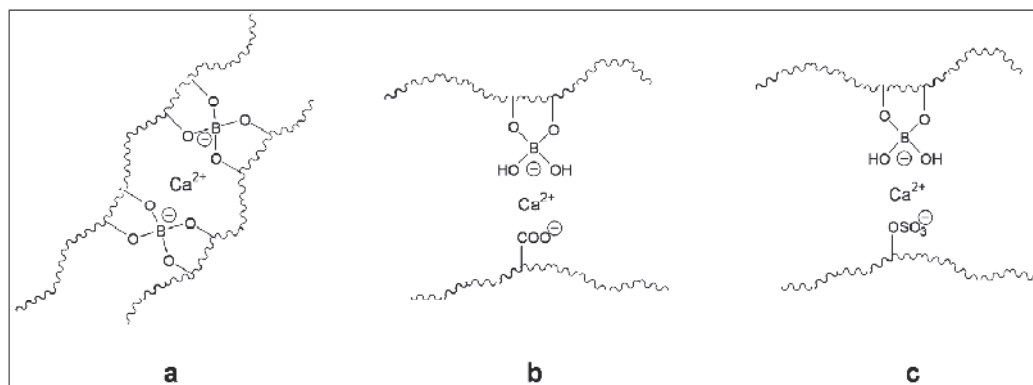


Fig. 4. Proposed mechanisms for the formation of Ulvan-based ionotropic hydrogels through a)  $\text{Ca}^{2+}$  stabilization of borate esters (Haug, 1976) or the participation of b) carboxylate and c) sulphate groups (Lahaye & Axelos, 1993).

The gel behaviour of Ulvan is different from that of most polysaccharides which usually involve tight junction zones of ordered molecular structures like helices or flat buckled ribbons (Stephen, 1995). Ulvan gel results from the aggregation of bead-like structures interconnected by more hydrophilic polymeric fractions. This behaviour would be undoubtedly favoured by the necklace-type ultrastructure assumed by the polymer in solution, whose formation has been shown to be promoted by ionic interactions (Robic et al, 2009). To this view, the positive role of boric acid can also be related to its reactivity towards the neutrally charged hydroxyl moieties of Ulvan and subsequent substitution with charged borate ester groups, thus contributing to create additional charges on the beads surface of the polysaccharide and favouring their association.

The mechanical properties of these ionotropic hydrogels are usually poor due to their intrinsic weakness and tend to get worse when used in contact with body fluids due to the ion exchange phenomena that occurs between  $\text{Ca}^{2+}$  that stabilizes the network and the monovalent cations like  $\text{K}^+$  and  $\text{Na}^+$  present in the physiological liquids (LeRoux et al., 1999). These hydrogels found limited applications in tissue engineering due to their mechanical instability and uncontrolled dissolution in physiological conditions (Atala & Lanza, 2002).

### 3.2 Ulvan-based chemical hydrogels

In order to overcome the problems related to the mechanical instability of the physically gelled Ulvan and extend the range of their potential applications, the strategy of chemical crosslinking of Ulvan was undertaken (Morelli & Chiellini, 2010).

A smart and relatively innovative technique of obtaining chemically crosslinked hydrogels is represented by their photopolymerization in the presence of photoinitiators using visible or ultraviolet (UV) light.

Photopolymerization is used to convert a liquid monomer or macromer to a hydrogel by free radical polymerization in a fast and controllable manner under ambient or physiological conditions. The mechanism is triggered by visible or UV light that interact with light-sensitive compounds called photoinitiators to create free radicals that can initiate polymerization of species containing suitably reactive groups (typically double bonds).

Photopolymerization has several advantages over conventional polymerization and crosslinking techniques. These include spatial and temporal control over polymerization, fast curing rates at room or physiological temperatures and minimal heat production (Nguyen & West, 2002). Moreover photopolymerization does not require the use of many reactive species, initiator and catalysts usually involved in the conventional chemical crosslinking methods, thus representing a potentially safer technique.

The condition for UV photopolymerization is that polymeric materials need to be conjugated with radically polymerizable groups. In this context, methacryloyl or acryloyl groups, when grafted to the chain backbone via an oxygen or a nitrogen atom usually represent a good candidates for this function, as they work as degradable crosslinks sensitive to either hydrolysis (Benoit et al., 2006) or cell-mediated proteolysis (Mahoney & Anseth, 2006).

The introduction of vinyl or vinylidenic polymerizable groups on Ulvan has been conducted by using several different (meth)acryloyl precursors and conditions (Morelli & Chiellini, 2010) (Figure 5).

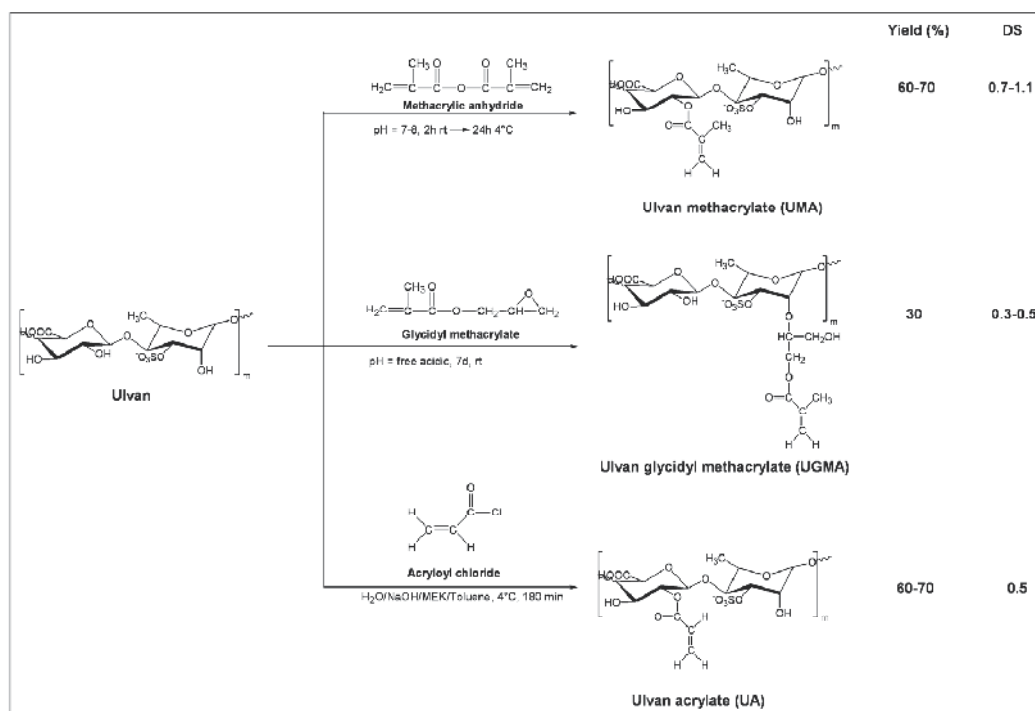


Fig. 5. Reaction of Ulvan with (Meth)acryloyl precursors and relative experimental conditions. Next to every macromer preparation are reported the mean values of the yield (%) of the final products and the degree of substitution (DS) expressed as the mean number of (meth)acryloyl group present in every repeating unit.

The reaction of Ulvan with organic chemical precursors is not straightforward because partially hampered by its insolubility in the common organic solvents. This compels its modification under heterogeneous and not favourable conditions as the ones reported in Figure 5. Also the aggregative behaviour of Ulvan in aqueous solutions limits its "reactive

surface" available for modifications and this may be the cause for the low degree of (meth)acryloyl substitution usually found on the final macromers.

The amount of UV polymerizable unsaturated groups introduced onto the polysaccharide would definitively affect the physical properties of the final hydrogels because it determines the number of "junction-zones" that crosslink the linear polymer chains. Both the substitution of the polar hydroxyl groups with the hydrophobic (meth)acryloyl moieties and the increase of the number of crosslinks inside the hydrogel structures would determine a minor absorption of water molecules with a consequent improvement in the mechanical properties of the hydrogels (Anseth et al., 1996). To this view the mean number of crosslinkable groups present in every repeating unit of Ulvan - expressed as substitution degree (SD) - represents a key parameter to be evaluated.

The calculation of the substitution degree (SD) of the macromers obtained by the different chemical routes reported in Figure 5, has been performed by  $^1\text{H}$ NMR analyses (Figure. 6).

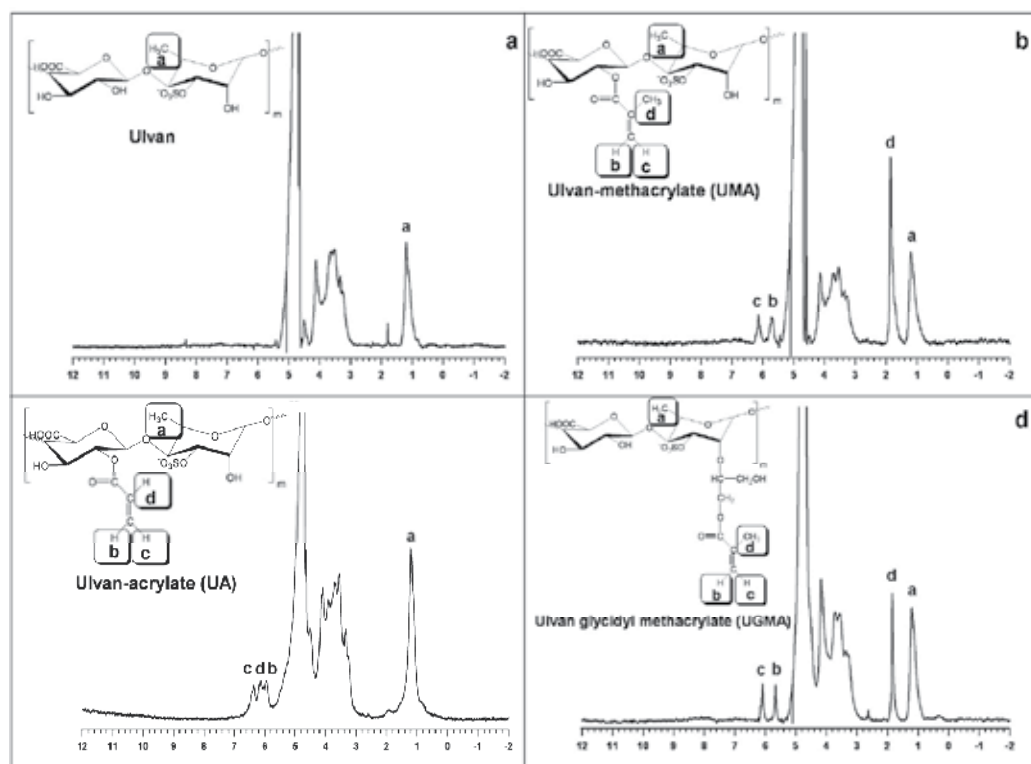


Fig. 6.  $^1\text{H}$ NMR spectra in  $\text{D}_2\text{O}$  of : a) Ulvan, b) Ulvan-methacrylate (UMA), c) Ulvan-acrylate (UA), d) Ulvan-glycidyl methacrylate (UGMA). Chemical structures of the main disaccharide repeating units of the polysaccharides are reported together with the relative peak assignment as highlighted in the small boxes.

The SD has been calculated by comparing the peak areas relative to the vinyl protons of the introduced (meth)acryloyl groups (Fig. 6b-d) with the peak area relative to the methyl group of the rhamnose present in the native Ulvan (Fig. 6a). The SD values reported in Figure 5 represent only a rough estimation of the actual values because the chemical structure of the

repeating unit of Ulvan used for the calculations (Fig. 6a) can not be considered univocal (Lahaye & Robic, 2007).

The most effective procedure for the preparation of macromers has been shown to utilize a large excess of methacrylic anhydride in slightly basic conditions for 24 hours at 4°C (Fig. 5). A fairly large amount of reactive is required because of the competitive hydrolysis that spoils the methacryloyl precursor during the reaction. The formation of the methacryloyl derivative of Ulvan was further confirmed by FT-IR analysis (Fig. 7).

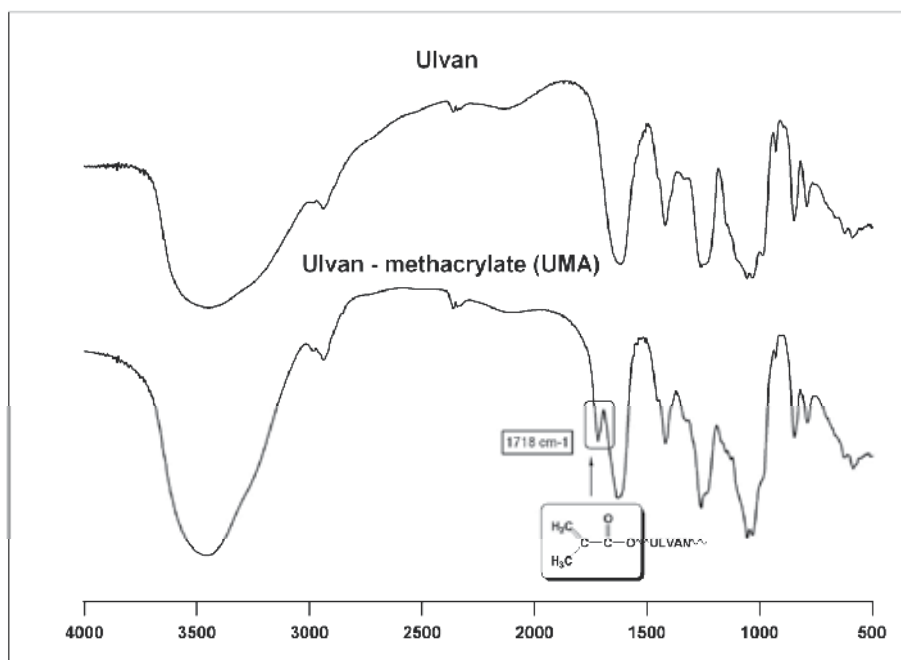


Fig. 7. FT-IR spectra of Ulvan and Ulvan methacrylate (UMA) macromer with the structure of the conjugated methacryloyl group and the relative absorption frequency reported in small boxes.

The spectra of the native Ulvan and the Ulvan methacrylate derivative are completely overlapping except for the peak at 1718  $\text{cm}^{-1}$  likely attributable to the presence of an  $\alpha,\beta$ -unsaturated carboxylic ester.

The preparation of hydrogels has been carried out by using a small amount of a cytocompatible photoinitiator – IRGACURE® 2959 – and exposing the polymeric solution to UV light – 365 nm – at short irradiation times. The mechanism of the covalent crosslinking between the polymeric chains involves the radical polymerization of the conjugated (meth)acryloyl groups and the formation of degradable carboxylic ester based “junction-zones” that act as crosslink moieties (Figure 8).

The crosslinking degree (CD) of Ulvan macromers have been evaluated by  $^1\text{H}$ NMR analyses of the solutions before and after definite times of irradiation by monitoring the peak areas of the reacting unsaturated protons (**b** and **c**, Figure 9). This technique has been applied to UMA because the preparation of this macromer proved to be the most effective in terms of yield and SD.

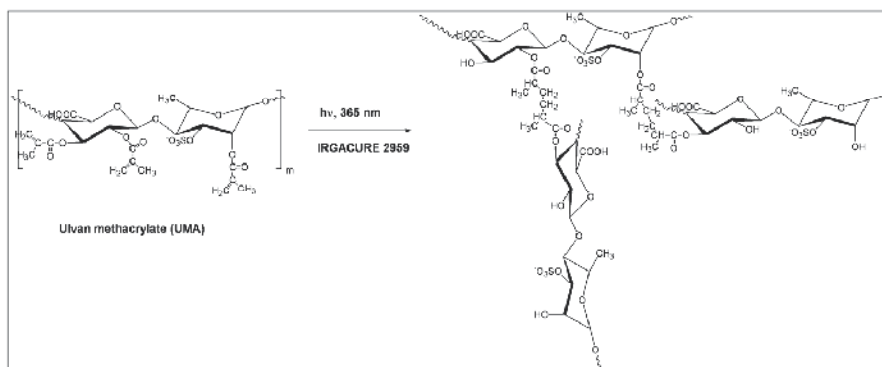


Fig. 8. Photopolymerization of Ulvan methacrylate under UV irradiation – 365 nm – in presence of a photoinitiator.

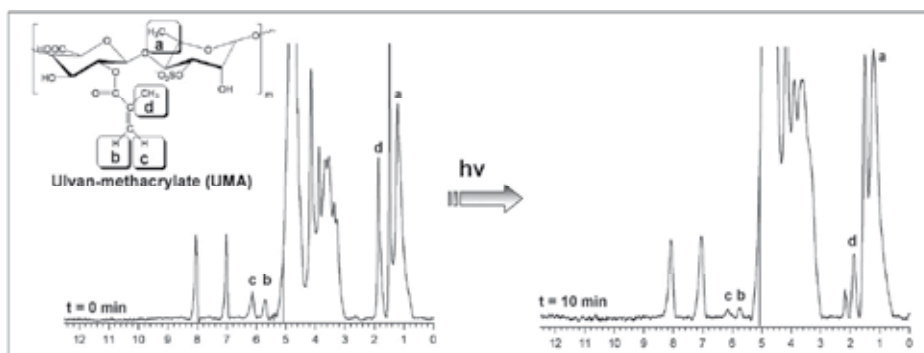


Fig. 9.  $^1\text{H}$ NMR spectra of Ulvan-methacrylate (UMA) before and after 10 min of UV irradiation in the presence of IRGACURE<sup>®</sup> 2959 as photoinitiator. Chemical structures of the main disaccharide repeating units of the macromer is reported together with the relative peak assignment as highlighted in the small box.

The exposure of Ulvan macromers to UV light Leads definitely to the formation of hydrogels but the photopolymerization is not complete even after 10 minutes of irradiation as demonstrated by the residual peak of the unreacted double bond protons **c** and **b** in the  $^1\text{H}$ NMR spectrum. The degree of crosslinking has been monitored at fixed irradiation times and showed that half (meth)acryloyl groups are polymerized after 5 minutes of UV curing (Table 1).

UV exposure time (min)	CD (%)
1	22.5
2	31.5
3	38.0
5	51.0
10	68.5

Table 1. Crosslinking degree (CD) for UMA having SD = 1 under UV irradiation (365 nm, 8 mW · cm<sup>-2</sup>) as a function of exposure time.

The incomplete crosslinking of Ulvan macromers under UV exposure could be ascribed to both the nature and the morphology assumed by this polysaccharide in solution. Indeed the antioxidant activity of Ulvan could reduce the rate of radical polymerization of the macromers by quenching the radicals formed during the UV irradiation. Moreover the aggregative behaviour of Ulvan in aqueous solution reduces the amount of (meth)acryloyl groups available for polymerization thus partially inhibiting the crosslinking.

The property of retaining water represents a key parameter for evaluating the quality of a hydrogel and its potential use for biomedical applications because it usually affects its permeability, biocompatibility and rate of degradation. The swelling ability of hydrogels could also provide information about their mechanical stability and chemical and physical properties, since the degree of water uptake is related both to the chemical nature and to the physical structure of the polymeric network (Qi et al., 2004). It is known, for example, that gels exhibiting a larger pore structure – likely due to a lower degree of crosslinking – have poor mechanical strength and higher swelling ratios (Anseth et al., 1996).

The swelling ability of hydrogels is usually quantified by measuring their Swelling Degree % (SD%) taken as the ratio (%) between the weight of the swollen hydrogel to that of the dried sample. The swelling degrees of the prepared Ulvan hydrogels have been carried out in phosphate buffer solutions (pH 7.4) and their behaviour was recorded during 7 days of immersion (Fig. 10).

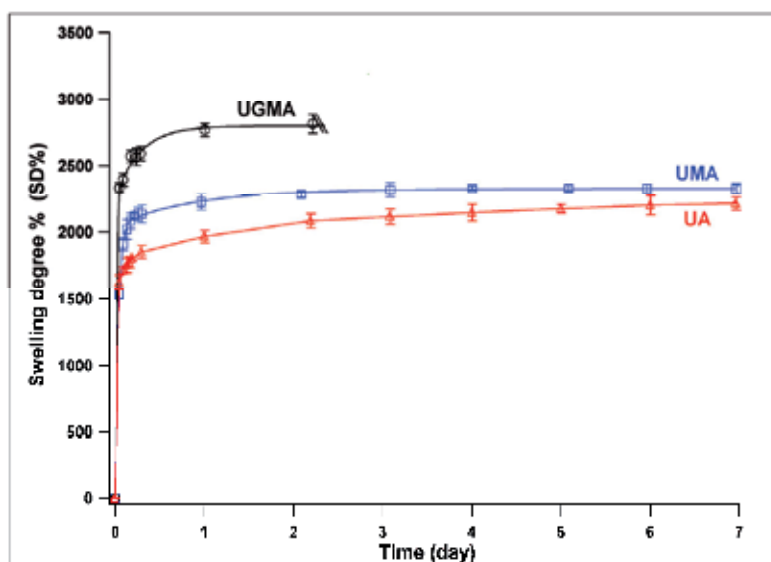


Fig. 10. SD% in PBS buffer solution (0.1 M, pH 7.4) of UV crosslinked (365 nm, approximately  $8 \text{ mW} \cdot \text{cm}^{-2}$ ) UMA and UGMA hydrogels as a function of time.

Pictures of the swollen scaffolds taken after 2 days of immersion in phosphate buffer saline (PBS) at pH 7.4, showed that the Ulvan methacrylate (UMA) hydrogels proved to be most stable in terms of texture and mechanical properties (Figure. 11).

The swelling degree experiments of UGMA-based samples were stopped after 2 days of immersion since the hydrogels were no longer coherent and hence not easy to handle. This



behaviour could be interpreted by considering the low degree of substitution typically obtained with this type of macromer (Figure 5) and subsequent low degree of crosslinking. The final hydrogels resulted more hydrophilic, as demonstrated by the highest swelling degree values (SD%) obtained, and less crosslinked thus leading to network with weak mechanical properties.

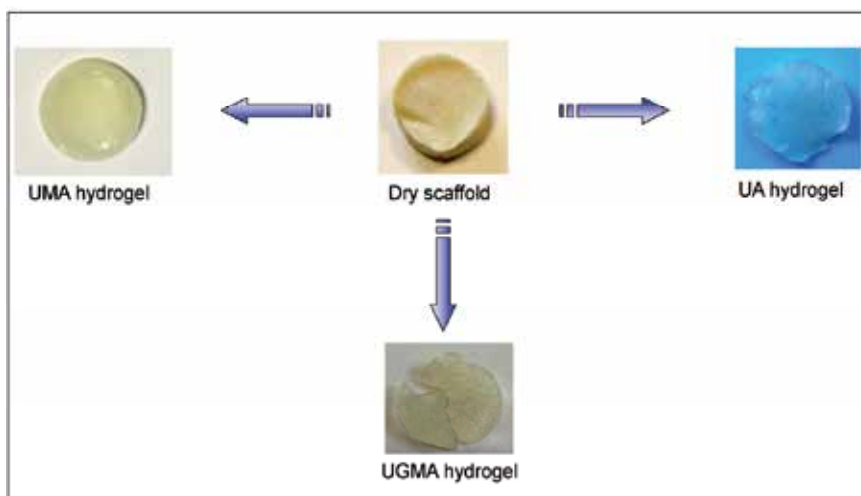


Fig. 11. Pictures of the swollen hydrogels obtained after 2 days of immersion in the swelling medium (phosphate buffer, 0.1M, pH 7.4).

The swelling degree values obtained with UMA- and UA-based macromers resulted to be similar thus indicating a similar density of crosslinking inside their structure. The interpretation of these data are not straightforward since UMA-based hydrogels were expected to be less hydrophilic and more crosslinked due to the higher amount of polymerizable group contained in their structure. Indeed the final texture of the UMA-based hydrogels indicated a better mechanical stability in respect to the other type of hydrogels. The unexpected lower SD (%) values obtained with UA-based hydrogels could be explained by the loss of material during the swelling experiments.

#### 4. Conclusion

Ulvan, a sulphated polysaccharide of algal origin, is worth of deeper attention for its potential use in technological and industrial-related applications. The exploitation of this abundant and renewable resource could represent an advantageous alternative approach to the use of fully synthetic materials based on fossil fuel feedstock.

In particular Ulvan represents an intriguing candidate material for biomedical applications due to its intrinsic beneficial biological activities and the possibility of easily modifying its structure according to the envisaged application. Its chemical structure similar to that of natural glycosaminoglycans such as chondroitin sulphate and hyaluronic acid make Ulvan an attractive candidate for their substitution or use in related applications.

In order to be employed in biomedical applications such as tissue engineering, regenerative medicine and drug delivery, Ulvan needs to be converted into an insoluble material under physiological conditions and to have mechanical properties suitable for the end application. The preparation of physically crosslinked Ulvan hydrogels has been reported since long times, but their weak mechanical properties and uncontrolled dissolution in presence of physiological fluids make them unsuitable for biomedical uses, where a scaffolding role is required

A novel method for covalent crosslinking of Ulvan through the UV mediated radical polymerization of activated macromers by double bond conjugated moieties, revealed to be promising in the preparation of chemically crosslinked Ulvan hydrogels. The conjugation of methacryloyl group to Ulvan through the reaction with methacrylic anhydride under slightly basic conditions gave the best results in terms of product yield and substitution degree. The hydrogels obtained after their exposure to UV light seemed to be very stable in physiological conditions.

The crosslinking of the Ulvan macromer precursors is usually not complete because is hampered both by its aggregative behaviour in solution that limits the availability of the (meth)acryloyl groups and very presumably by the radical quenching activity of the polysaccharide during the UV exposure thus negatively affecting the mechanical properties of the final hydrogels. Nevertheless the antioxidant activity of Ulvan could make this material a good candidate as a matrix for cell encapsulation due to the possible protection against the radicals produced during UV crosslinking (Fedorovich et al., 2009). The use of these materials as a base for cytocompatible scaffolds is also promoted by the softness related to partial crosslinking of these macromers, since it is known that cell spreading within hydrogels is influenced by matrix stiffness and soft matrices interestingly are expected to promote cell spreading (Liu & Chan-Park, 2009).

Moreover the possibility of preparing Ulvan based hydrogels by a straightforward technique such as UV crosslinking makes the use of Ulvan in biomedical fields even more attractive. Indeed UV photopolymerization allows the spatial and temporal control over the crosslinking and the fabrication of hydrogels in situ with the possibility of forming complex architectures that adhere and conform to tissue structure.

## 5. Acknowledgment

The present work was performed within the framework of NOE project Expertissues (NMP3-CT 2004-500328) and Expertissues Miniproject NATCOM.

## 6. References

- Alban, S., Schauerte, A., Franz, G. (2002). Anticoagulant sulphated polysaccharides: Part I. Synthesis and structure-activity relationships of new pullulan sulphates. *Carbohydrate Polymers*, Vol.47, No.3, (February 2002), pp. 267-276, ISSN 0144-8617.
- Alsberg, E., Anderson, K.W., Albeiruti, A., Franceschi, R.T., Mooney, D.J. (2001). Cell-interactive Alginate Hydrogels for Bone Tissue Engineering *Journal of Dental Research*, Vol.80, No.11, (November 2001), pp. 2025-2029, ISSN 1462-6446.

- Alves, A., Caridade, S.G., Mano, J.F., Sousa, R.A., Reis, R.L. (2010). Extraction and physico-chemical characterization of a versatile biodegradable polysaccharide obtained from green algae, *Carbohydrate Research*, Vol.345, No.15, (October 2010), pp. 2194-2200, ISSN 0008-6215.
- Anseth, K.S, Bowman, C.N., Peppas, L.B. (1996). Mechanical properties of hydrogels and their experimental determination *Biomaterials*, Vol.17, No.17, (January 1996), pp. 1647-1657, ISSN 0142-9612.
- Athukorala, Y., Ahn, G.N., Jee, Y.H., Kim, G.Y., Kim, S.H., Ha, J.H., (2008) Antiproliferative activity of sulphated polysaccharide isolated from an enzymatic digest of *Ecklonia cava* on the U-937 cell line, *Journal of Applied Phycology*, Vol.21, No. 3, (August 2008), pp. 307-314, ISSN 0273-2289.
- Atala, A., Lanza, R.P. (2002). *Methods of Tissue Engineering*, Academic Press, ISBN 978012436636, San Diego, CA.
- Barghini, A., Ilieva, V.I., Imam, S.H., Chiellini, E. (2010) PCL and PHB blends containing seaweed fibers: Morphology and Thermal-Mechanical Properties", *Journal of Polymer Science Part A: Polymer Chemistry*, Vol. 48, No. 23, (December 2010), pp. 5282-5288, ISSN 1520 - 5738.
- Benoit, D.S, Durney, A.R., Anseth, K.S. (2006). Manipulations in Hydrogel Degradation Behavior Enhance Osteoblast Function and Mineralized Tissue Formation, *Tissue Engineering*, Vol. 12, No. 6, (June 2006), pp. 1663-1673. ISSN 1076-3279.
- Bobin-Dudigeon, C., Lahaye, M., Guillon, F., Barry, J.L., Gallant, D. (1997). Factors limiting the biodegradation of *Ulva* sp cell-wall polysaccharides *Journal of the Science of Food and Agriculture*, Vol.75, No.3, (November 1997), pp. 341-351, ISSN 1097-0010.
- Bouhadir, K.H., Lee, K.Y, Alsberg, E., Damm, K.L., Anderson, K.W., Mooney, D.J. (2001). Degradation of Partially Oxidized Alginate and Its Potential Application for Tissue Engineering *Biotechnology Progress*, Vol.17, No.5, (September 2001), pp. 945-950, ISSN 1520-6033.
- Brand, X., Morand, P., (1997) Anaerobic digestion of *Ulva* sp. 1. Relationship between *Ulva* composition and methanisation, *Journal of Applied Phycology*, Vol.9, No. 6, (December 1997), pp. 511-524, ISSN 0273-2289.
- Brown, L., Rosner, B., Willet, W.W, Sachs, F.M. (1999). Cholesterol lowering effect of dietary fiber: a meta-analysis, *American Journal of Clinical Nutrition*, Vol. 69, No. 1, (January 1999), pp. 30-42 ISSN 0002-9165.
- Chiellini, E., Cinelli, P., Ilieva, V.I., Martera, M. (2008) Biodegradable Termoplastic Composites Based on Polyvinyl Alcohol and Algae, *Biomacromolecules*, Vol. 9, No. 3, (March 2008) pp. 1007 - 1013, ISSN 1525-1797.
- Chiellini, E., Cinelli, P., Ivanova Ilieva, V., Zimbardi, F., Kanellopoulos, N., de Wilde, B., Pipino, A., Anders, B., (2009) Hybrid Composites Based on Fibres of Marine Origin, *Int. J. Materials and Product Technology*, Vol. 36, No. 1-2-3-4, (January 2009), pp. 47-61 ISSN 0268-1900
- Christi, Y., (2007). Biodiesel from microalgae *Biotechnology Advances*, Vol.25, No.3, (February 2007), pp. 294-306, ISSN 0734-9750.

- Chung, T.W., Yang, J., Alkaike, T., Cho, K.Y., Nah, J.W., Kim, S.I., Cho, C.S. (2002). Preparation of alginate/galactosylated chitosan scaffold for hepatocyte attachment *Biomaterials*, Vol. 23, No.14, (July 2002), pp. 2827-2834, ISSN 0142-9612.
- Damonte, E.B., Matulewicz, M.C., Cerezo, A.S. (2004). Sulphated seaweed polysaccharides as antiviral agents *Current Medicinal Chemistry*, Vol.11, No.18, (September 2004), pp. 2399-2419, ISSN 0929-8673.
- Dar, A., Shachar, M., Leor, J., Cohen, S. (2002). Optimization of cardiac cell seeding and distribution in 3D porous alginate scaffolds *Biotechnology and Bioengineering*, Vol.80, No.3, (November 2002), pp. 305-312, ISSN 1097-0290.
- D'Ayala, G., Malinconico, M., Laurienzo, P., (2008). Biodiesel from microalgae *Molecules*, Vol.13, No.9, (September 2008), pp. 2069-2106, ISSN 1420-3049.
- Dobrynin, A.V. (2008). Theory and simulations of charged polymers: From solution properties to polymeric nanomaterials *Current Opinion in Colloid & Interface Sciences*, Vol.28, No.6, (December 2008), pp. 1859-1871, ISSN 0024-9297.
- Dobrynin, A.V., (1995). Scaling theory of polyelectrolyte solutions *Macromolecules*, Vol.13, No.6, (March 1995), pp. 376-388, ISSN 1359-0294.
- Demirbas, A., Demirbas, M.F. (2011). Importance of algae oil as a source of biodiesel *Energy Conversion and Management*, Vol.52, No.1, (January 2011), pp. 163-170, ISSN 0196-8904.
- Fedorovich, N.E., Oudshoorn, M.H., van Geemen, D., Hennink, W.E., Wouter, J.A., Dhert, J.A. (2009). The effect of photopolymerization on stem cells embedded in hydrogels, *Biomaterials*, Vol. 30, No. 3, (January 2009), 344-353, ISSN 0142-9612.
- Fletcher, R.L., (1996). *Marine Benthic Vegetation: Recent Changes and the Effect of Eutrophication*, Springer, ISBN 978-3-540-58106-2, Berlin, Germany.
- Guillon, F., Champ, M. (2000). Structural and physical properties of dietary fibres, and consequences of processing on human physiology. *Food Research International*, Vol. 33, No. 3-4, (April 2000), pp. 233-245, ISSN 0963-9969.
- Hamman, J.S. (2010). Chitosan Based Polyelectrolyte Complexes as Potential Carrier Materials in Drug Delivery Systems. *Marine Drugs*, Vol. 8, No. 4, (March 2010), pp. 1305-1322, ISSN 1660-3397.
- Hashimoto, T., Suzuki, Y., Yamamoto, E., Tanihara, M., Kakimaru, Y., Suzuki, K. (2004). Development of alginate wound dressings linked with hybrid peptides derived from laminin and elastin *Biomaterials*, Vol.25, No.7-8, (March 2004), pp. 1407-1414, ISSN 0142-9612.
- Hoffmann, A.S. (2002). Hydrogels for biomedical applications. *Advanced Drug Delivery Reviews*, Vol. 54, No. 1, (January 2002), pp. 3-12, ISSN 0169-409X.
- Haug, A. (1976) The influence of borate and calcium on the gel formation of a sulfated polysaccharide from *Ulva lactuca*, *Acta Chemica Scandinavica*, Vol. B30, No. 6 (January 1976), pp. 562-566, ISSN 0001-5393.
- John, R.P., Anisha, J.S., Madhavan Nampoothiri, K., Pandey, A. (2011). Micro and Macroalgal biomass: A renewable source for bioethanol *Bioresource Technology*, Vol.102, No.1, (January 2011), pp. 186-193, ISSN 0960-8524.
- Kaeffer, B., Benard, C., Lahaye, M., Blottiere, H.M., Cherbut, C., Biological properties of ulvan, a new source of green seaweed sulphated polysaccharides, on cultured

- normal and cancerous colonic epithelial cells, *Planta Medica*, Vol. 65, No. 6, (August 1999), pp. 527-531, ISSN 0032-0943.
- Lahaye, M. (1991). Marine algae as sources of fibres: Determination of soluble and insoluble dietary fibre contents in some 'sea vegetables, *Science of Food and Agriculture*, Vol. 54, No. 4, (January 1991), pp. 587-594, ISSN 0022-5142.
- Lahaye, M., Axelos, M.A.V. (1993). Gelling properties of water-soluble polysaccharides from proliferating marine green seaweeds (*Ulva* spp.), *Carbohydrate Polymers*, Vol.22, No. 4, (February 1993), pp. 261-265, ISSN 0144-8617.
- Lahaye, M., Brunel, M., Bonnin, M. (1997). Fine chemical structure analysis of oligosaccharides produced by an ulvan-lyase degradation of the water-soluble cell-wall polysaccharides from *Ulva* sp. (Ulvales, Chlorophyta) *Carbohydrate Polymers*, Vol.304, No.3-4, (November 1997), pp. 261-265, ISSN 0144-8617.
- Lahaye, M., Jegou, D., Buleon, A., (1994). Chemical characteristics of insoluble glucans from the cell wall of the marine green alga *Ulva lactuca* (L.) Thuret, *Carbohydrate Research*, Vol.262, No.1, (September 1994), pp. 115-125, ISSN 0008-6215
- Lahaye, M., Robic, A. (2007). Structure and functional properties of ulvan, a polysaccharide from green seaweeds, *Biomacromolecules*, Vol.8, No.6, (April 2007), pp. 1765-1774, ISSN 1525-7797.
- LaNasa, S.M., Hoffecker, I.T., Briant, S.J. (2010). Presence of pores and hydrogel composition influence tensile properties of scaffolds fabricated from well-defined sphere templates, *Journal of Biomedical Materials Research Part B: Applied Biomaterials*, Vol. 96B, No. 2, (July 2010), pp. 294-302, ISSN 1552-4981.
- Leiro, J.M., Castro, R., Arranz, J.A., Lamas, J. (2007). Immunomodulating activities of acidic sulphated polysaccharides obtained from the seaweed *Ulva rigida* C. Agardh, *International Immunopharmacology*, Vol.7, No.7, (July 2007), pp. 879-888, ISSN: 1567-5769.
- LeRoux, M.A., Guilak, F., Setton, L.A. (1999) Compressive and shear properties of alginate gels: Effect of sodium ions and alginate concentration, *Journal of Biomedical Materials Research*, Vol. 47, No. 1, (October 1999), pp. 46-52, ISSN 1552-4965
- Li, Q., Wang, D., Helisseeff, J.H. (2003). Heterogeneous-phase reaction of glycidyl methacrylate and chondroitin sulphate, *Macromolecules*, Vol. 36, No. 7, (April 2003), pp. 2556-2562, ISSN 0024-9297.
- Liu, Y., Chan-Park, M.B. (2009). Hydrogel based on interpenetrating polymer networks of dextran and gelatin for vascular tissue engineering, *Biomaterials*, Vol. 30, No. 2, (January 2009), 196 - 207, ISSN 0142-9612.
- Mahoney, M.J., Anseth, K.S. (2006). Three-dimensional growth and function of neural tissue in degradable polyethylene glycol hydrogels, *Biomaterials*, Vol. 27, No. 10, (April 2006), 2265-2274, ISSN 0142-9612.
- Mano, J.F., Silva, G.A., Azevedo, H.S., Malafaya, P.B., Sousa, R.A., Silva, S.S., Boesel, L.F., Oliveira, J.M., Santos, T.C., Marques, A.P., Neves, N.M., Reis, R.L. (2007). Natural origin biodegradable systems in tissue engineering and regenerative medicine: present status and some moving trends *Journal of the Royal Society Interface*, Vol. 22, No. 4, (December 2007), pp. 999-1030, ISSN 1742-5662.

- Matsumoto, M., Yochouchi, H., Suzuki, N., Ohata, H., Matsunaga, T. (2003). Saccharification of marine microalgae using marine bacteria for ethanol production *Journal of Applied Phycology*, Vol. 105, No.1-3, (February 2003), pp. 247-254, ISSN 0273-2289.
- Mazè, J., Morand, P., Potoky, P. (1993). Stabilisation of 'green tides' Ulva by a method of composting with a view to pollution limitation. *Journal of Applied Phycology*, Vol. 5, No. 2, (April 1993), pp. 183-190, ISSN 0273-2289.
- Melo, F.R., Pereira, M.S., Foguel, D., Mourao, P.A.S. (2004) Antithrombin-mediated anticoagulant activity of sulphated polysaccharides, *Journal of Biological Chemistry*, Vol. 279, No. 20 (May 2004), pp. 20824–20835, ISSN: 0021-9258.
- Morand, P., Briand, X. (1996). Excessive Growth of Macroalgae: A Symptom of Environmental Disturbance, *Botanica Marina*, Vol. 39, No. 1-6, (January 1996), pp. 491-516, ISSN 1437-4323.
- Morand, P., Briand, X., Charlier, R.H. (2006). Anaerobic digestion of Ulva sp. 3. Liquefaction juice extraction by pressing and a technico-economic budget *Journal of Applied Phycology*, Vol.18, No.6, (February 2006), pp. 741-755, ISSN 0921-8971.
- Morelli, A., Chiellini, F. (2010). Ulvan as a New Type of Biomaterial from Renewable Resources: Functionalization and Hydrogel Preparation, *Macromolecular Chemistry and Physics*, Vol. 211, No. 7, (April 2010), pp. 821-832, ISSN 1022-1352.
- Nguyen, K.T., West, J.L. (2002). Photopolymerizable hydrogels for tissue engineering applications, *Biomaterials*, Vol. 23, No. 22, (November 2002), 4307-4314, ISSN 0142-9612.
- Nacife, V.P., Soeiro, M.D., Gomes, R.N., D'Avila, H., Castro-Faria Neto, H.C., Meirelles, M.N.L. (2004) Morphological and biochemical characterization of macrophages activated by carrageenan and lipopolysaccharide in vivo. *Cell Structure and Function*, Vol. 29, No. 2 (September 2004), pp. 27–34, ISSN 0386-1796.
- Paradossi, G., Cavalieri, F., Chiessi, E. (2002). A conformational study on the algal polysaccharide ulvan *Macromolecules*, Vol.35, No.16, (July 2002), pp. 6404-6411, ISSN 0024-9297.
- Paradossi, G., Cavalieri, F., Pizzoferrato, L., Liquori, A.M., (1999). A physico-chemical study on the polysaccharide ulvan from hot water extraction of the macroalga Ulva, *International Journal of Biological Macromolecules*, Vol.25, No.4, (August 1999), pp. 309-315, ISSN 0141-8130.
- Patil, J.S., Kamalapur, M.V., Marapur, S.C., Kadam, D.V. (2010). Iontropic gelation and polyelectrolyte complexation: the novel technique to design hydrogel particulate sustained, modulated drug delivery system: a review. *Digest Journal of Nanomaterials and Biostructures*, Vol. 5, No. 1, (March 2010), pp. 241-248, ISSN 1842-3582.
- Pavlyuchenko, V.N., Ivanchev, S.S., (2009). Composite polymer Hydrogels, *Polymer Science Series A*, Vol. 51, No. 7, (July 2009), pp. 743-760, ISSN 0965-545X.
- Pereira, M.S., Melo, F.R., Mourao, P.A.S., (2002). Is there a correlation between structure and anticoagulant action of sulfated galactans and sulfated fucans?, *Glycobiology*, Vol. 12, No. 10, (October 2002), pp. 573-580, ISSN 0959-6658.

- Qi, H., Zhang, Q., Zhao, T., Chen, R., Zhang, H., Niu, X. Antioxidant activity of different sulphate content derivatives of polysaccharide extracted from *Ulva pertusa* (Chlorophyta) in vitro, (2005), *International Journal of Biological Macromolecules*, Vol.37, No.4, (December 2005), pp. 195-199, ISSN 0141-8130.
- Qi, H., Zhang, Q., Zhao, T., Hu, R., Zhang, K., Li, Z., In vitro antioxidant activity of acetylated and benzoylated derivatives of polysaccharide extracted from *Ulva pertusa* (Chlorophyta), (2006), *Bioorganic Medicinal Chemistry Letters*, Vol.16, No.9, (May 2006), pp. 2441-2445, ISSN 0960-894X.
- Qi, L., Williams, C.G., Sun, D.D.N., Wang, J., Leong, K., Elisseff, J.H. (2004) *Journal of Biomedical Material Research: Part A*, Vol. 68A, No. 1, (January 2004), pp. 28-33, ISSN 1552 -4965.
- Ricciardi, R., Auriemma, F., De Rosa, C. (2005). Structure and Properties of Poly(vinyl alcohol) Hydrogels Obtained by Freeze/Thaw Techniques *Macromolecular Symposia*, Vol.222, No.1, (March 2005), pp. 49-64, ISSN 1521-3900.
- Rioux, L.E., Turgeon, S.L., Beaulieu, M. (2007). Characterization of polysaccharides extracted from brown seaweeds *Carbohydrate Polymers*, Vol.69, No.3, (June 2007), pp. 530-537, ISSN 0144-8617.
- Robic, A., Gaillard, C., Sassi, J.F., Lerat, Y., Lahaye, M. (2009). Ultrastructure of Ulvan: A polysaccharide from green seaweeds *Biopolymers*, Vol.91, No.8, (August 2009), pp. 652-664, ISSN 0006-3525.
- Rocha de Souza, M.C., Marques, C.T., Dore, C.M.G., Ferreira da Silva, F.R., Rocha, H.A.O, Leite, E.L., (2007). Antioxidant activities of sulphated polysaccharides from brown and red seaweeds *Journal of Applied Phycology*, Vol.19, No.2, (April 2007), pp. 153-160, ISSN 0921-8971.
- Stephen, A.M., (1995). *Food Polysaccharides and their applications*, Marcel Dekker Inc., ISBN 0824793536, New York, USA.
- Stevens, M.M. (2008). Biomaterials for bone tissue engineering, *Materials Today*, Vol.11, No.5, (May 2008), pp. 18-25, ISSN 1369-7021
- Taboada, C., Millan, R., Miguez, I. (2010). Composition, nutritional aspects and effect on serum parameters of marine algae *Ulva rigida*, *Journal of the Science of Food and Agriculture*, Vol.90, No.3, (February 2010), pp. 445-449, ISSN 1097-0010.
- Tsai, C.S., (2007). *Biomacromolecules : introduction to structure, function, and informatics*, John Wiley & Sons, ISBN 0-471-71397-X, Hoboken, New Jersey, USA.
- Uhlen-Hansen, L., Wik, T., Kjellen, L., Berg, E., Forsdahl, F., Kolset, S.O. (1993) Proteoglycan metabolism in normal and inflammatory human macrophages. *Blood*, Vol. 82, No. 9, (November 1993), pp. 2880-2889, ISSN 0006-4971.
- Wijesekara, I., Pangestuti, R., Kim, S.H. (2011). Biological activity and potential health benefits of sulphated polysaccharides from marine algae *Carbohydrate Polymers*, Vol.84, No.1, (February 2011), pp. 14-21, ISSN 0144-8617
- Yu, P., Li, N., Liu, X., Zhou, G., Zhang, Q., Li, P. Antihyperlipidemic effects of different molecular weight sulphated polysaccharides from *Ulva pertusa* (Chlorophyta) (2003). *Pharmacological Research*, Vol.48, No. 6 (2003), pp. 543-549, ISSN: 1043-6618.

---

Zhang, H.J., Mao, W.J., Fang, F., Li, H.Y., Sun, H.H., Gehen, Y., Qi, X.H., Chemical characteristics and anticoagulant activities of a sulphated polysaccharide and its fragments from *Monostroma latissimum*, *Carbohydrate Polymers*, Vol.71, No.3, (February 2008), pp. 428-434, ISSN 0144-8617



# Silanization with APTES for Controlling the Interactions Between Stainless Steel and Biocomponents: Reality vs Expectation

Jessem Landoulsi<sup>1</sup>, Michel J. Genet<sup>2</sup>, Karim El Kirat<sup>3</sup>,  
Caroline Richard<sup>4</sup>, Sylviane Pulvin<sup>5</sup> and Paul G. Rouxhet<sup>2</sup>

<sup>1</sup>*Laboratoire de Réactivité de Surface,  
Université Pierre & Marie Curie -Paris VI,*

<sup>2</sup>*Institute of Condensed Matter and Nanosciences – Bio & Soft Matter,  
Université Catholique de Louvain,*

<sup>3</sup>*Laboratoire de Biomécanique et Bioingénierie,*

<sup>4</sup>*Laboratoire Roberval,*

<sup>5</sup>*Génie Enzymatique et Cellulaire,  
Université de Technologie de Compiègne,*

<sup>1,3,4,5</sup>*France*

<sup>2</sup>*Belgium*

## 1. Introduction

The surface of biomaterials is frequently chemically modified with the aim to modify the physicochemical properties (hydrophobicity, electrical charge, solvation) which control the interactions with biomolecules and consequently with cell surfaces, or to retain biochemical entities which are specifically recognized by the cells (Williams, 2010). Regarding inorganic materials, widespread procedures involve self-assembly of alkanethiols on gold, silver, copper or platinum (Wink et al., 1997). However, these substrates have limited interest in biomedical applications. Other procedures consist in grafting organosilanes on silica and other metal oxides (Weetall, 1993). The use of silane coupling agents has been reported in various biomaterials researches, such as surface modification of titanium (Nanci et al., 1998), natural fiber/polymer composites (Xie et al., 2010) or dental ceramics (Matinlinna et al., 2004; Matinlinna & Vallittu, 2007).

The silanization reaction at interfaces is complex and there is still considerable debate on the retention mechanisms and on the organization of the interface (Gooding & Ciampi, 2011; Haensch et al., 2010, Suzuki & Ishida, 1996). Depending on the nature of reactive moieties bound to Si in the silane (typically Cl or alkoxy group) and their number, and on the reaction conditions (particularly the presence of water), the relative importance of covalent binding to the surface, oligomerization, polymerization along the surface plane, three-dimensional polymerization may possibly vary. The efficiency of the surface modification is often demonstrated by its influence on biochemical or biological activity. However the nature of the interface produced is difficult to characterize, which limits the guidelines

available to improve the procedures. Moreover organic contaminants are always present on high energy solids. They are mainly of hydrocarbon nature and are readily adsorbed from surrounding air or in surface analysis spectrometers (Caillou et al., 2008; Landoulsi et al., 2008a). The possible influence of contaminants on the silanization process and product is usually not considered. In the case of silicon wafer silanized with 3-[methoxy(polyethyleneoxy)]propyl trimethoxysilane and trichlorosilane in organic solvents under a controlled atmosphere, the surface obtained was described as a 1 to 2 nm thick grafted silane layer covered by a thin layer of adventitious contaminants, suggesting that contamination was posterior to the silanization reaction. On the other hand, the silane layer was not stable in phosphate buffered saline at 37°C (Dekeyser et al., 2008).

Aminopropylalkoxysilanes are attractive for surface modification (Plueddemann, 1991), as their bifunctional nature is expected to offer the possibility of covalently attaching a biomolecule, either directly or through a linker. 3-Aminopropyl(triethoxysilane) (APTES) is one of the most frequently used organosilane agents for the preparation of amine-terminated films (Asenath Smith & Chen, 2008; Howarter & Youngblood, 2006; Kim et al., 2009a; Lapin & Chabal, 2009; Pasternack et al., 2008).

Table 1 presents a list of references in which APTES was used to hopefully graft biomolecules on different substrates. The survey is exhaustive for stainless steel substrates relevant for the field of biomaterials and illustrative for other substrates. Additional references are: El-Ghannam et al., 2004; Kim et al., 2010; Sasou et al., 2003; Sarath Babu et al., 2004; Quan et al., 2004; Subramanian et al., 1999; Jin et al., 2003; Cho & Ivanisevic, 2004; Katsikogianni & Missirlis, 2010; Sordel et al., 2007; Toworfe et al., 2006; Balasundaram et al., 2006; Doh & Irvine, 2006; Palestino et al., 2008; Son et al., 2011; Koh et al., 2006; Mosse et al., 2009; Weng et al., 2008; Charbonneau et al., 2011; Iucci et al., 2007; Chuang et al., 2006; Schuessele et al., 2009; Ma et al., 2007; Toworfe et al., 2009; Zile et al., 2011; Sargeant et al., 2008; Lapin & Chabal, 2009. Table 1 indicates the substrate and linker used, the main conditions of the APTES treatment and the evaluation of the surface treatment regarding biomolecule activity with the blank used for comparison. The table also presents the main data obtained by surface characterization. In some systems, no covalent grafting was aimed. In other systems, although it was aimed, there is no direct evidence for the formation of covalent bonds between the biomolecules and the substrate surface. On the other hand, the evaluation of the bio-efficacy was never based on comparisons involving a complete set of blanks: treatment with the biomolecule without silanization, without linker, without silanization and linker. In a study of surface modification with the aim to enhance mineralization, it has been demonstrated that APTES-coated glass retains a homopolymer with monoester phosphate groups, poly[(2-methacryloyloxy)ethyl phosphate], by proton transfer and electrostatic interaction, while the retention of a neutral homopolymer, poly[2-(acetoacetoxy)ethyl methacrylate], was attributed to covalent linkage by reductive amination between the keto groups of the polymer and the surface amine functions (Jasienak et al., 2009). The retention of the diblock copolymer seemed to occur via segments allowing covalent bonds to be formed. In Table 1, several systems show an improved behavior which may only be attributed to non covalent bonding between the biomolecule and the silanized substrate. In contradiction with frequent implicit considerations, the occurrence or improvement of bioactivity as a result of surface treatments does not demonstrate that the chemical schemes which motivated the treatments worked in reality. This question is crucial as many organic reactions that work well in solution are difficult to apply at solid surfaces (Kohli et al., 1998).

Stainless steels (SS) are extensively used in biomaterials researches and other applications involving contact with biologic compounds, owing to their adaptable mechanical properties, their manufacturability and their outstanding corrosion resistance. For instance, SS may be used in the manufacture of vascular stents, guide wires, or other orthopedic implants (Hanawa, 2002, Ratner, 2004). In these conditions, SS are subjected to the adsorption of biomolecules (proteins, polysaccharides, lipids) and biological materials (cellular debris). The surface modification of SS may thus be important to orient the host response as desired. The present work is dedicated to the surface composition of 316L SS surfaces at different stages of the procedure used to graft a protein via the use of APTES and of a bifunctional agent expected to link the NH<sub>2</sub>-terminated silane with NH<sub>2</sub> groups of the protein. Glucose oxidase was chosen as a model protein for reasons of convenience owing to previous works related to microbiologically influenced corrosion (Dupont et al., 1998, Landoulsi et al., 2009, Landoulsi et al., 2008b, Landoulsi et al., 2008c). A particular attention is given to (i) the real state of the interface (composition, depth distribution of constituents) at different stages and (ii) the mode of protein retention. Therefore, X-ray photoelectron spectroscopy is used in a way (angle resolved measurements, reasoned peak decomposition, validation by quantitative relationships between spectral data) to provide a speciation in terms of classes of compounds (silane, protein, contaminants), using guidelines established in previous works (Genet et al., 2008; Rouxhet & Genet, 2011). Water contact angle measurements are used to address the issue of the presence of contaminants and the perspectives of avoiding it.

Substrate	Linker	Biomolecule	Reference
<b>a. Substrate preparation</b> <b>b. APTES treatment</b> <b>c. Evaluation of efficiency regarding biomolecule activity. Substrate taken as blank</b> <b>d. Interface characterization</b>			
Stainless steel	EDC	Alginate	Yoshioka et al., 2003
a. Sonication in acetone, 5 min; heating 2 h at 500°C in air. b. In toluene, 1h; rinsing in toluene and ethanol; sonication in ethanol, 5 min; drying in air; curing 10 min at 105°C. c. Preventing adsorption of blood-clotting proteins. Blanks = native, silanized. d. XPS: elemental concentration, consistent evolution according to reaction steps; C 1s peak, demonstration of alginate retention, majority of carbon of C-(C,H) type at all stages.			
Stainless steel	GA	Lysozyme	Minier et al., 2005
a. Acid etching at 60 °C; rinsing in water; drying under N <sub>2</sub> gas flow. b. In ethanol/water, 3 min; curing 1 h at 100-150 °C in air; rinsing with water. c. Increase of the enzymatic activity in bacterial lysis. Blanks = native + enzyme, silanized + enzyme. d. IRRAS: Characteristic bands of APTES. XPS: elemental concentration, consistent evolution according to reaction steps; N/Si ratio vs photoelectron collection angle, consistent evolution.			
Stainless steel stent	none	Chitosan/heparin LbL film	Meng et al., 2009
a. Cleaning in ethanol/water (1/1, v/v); rinsing in water; drying under reduced pressure, 24 h at 30 °C. b. In ethanol, 4 h at 37 °C; rinsing in water, drying in air at 50 °C. c. Promoting re-endothelialization after stent implantation, improvement of			

<p>haemocompatibility (in vivo and in vitro tests). Blank = native stainless steel stent, native+chitosan.</p> <p>d. QCM on model substrate slide: in situ monitoring of the LbL film growth on APTES-coated silicon substrate.</p>			
Stainless steel screw	GA	Fibrinogen + bisphosphonate	North et al., 2004
<p>a. Sonication in acetone; acid etching; treatment in H<sub>2</sub>O<sub>2</sub>/NH<sub>4</sub>OH solution, 5 min at 80 °C.</p> <p>b. Vapor deposition, 10 min at 60 °C; curing 1 h at 150°C; sonication in xylene.</p> <p>c. Improvement of fixation of screws in rat tibia. Blank = test of bisphosphonate action.</p> <p>d. Ellipsometry on model substrate slide: consistent increase of the film thickness according to reaction steps.</p>			
Titanium	SMP	RGDC peptide	Xiao et al., 1997
<p>a. Acid etching; rinsing with different solvents; outgassing.</p> <p>b. In dry toluene, 120 °C, 3 h plus variants; sonication in various organic solvents and water.</p> <p>c. -</p> <p>d. Ellipsometry and radiolabeling: growth of silane surface layer upon repeating treatments. XPS peak shapes: semi-quantitatively consistent evolution according to reaction steps.</p>			
Titanium	GA	Chitosan	Martin et al., 2007
<p>a. Polishing; cleaning in different solvents followed by nitric acid passivation or piranha treatment.</p> <p>b. In toluene, 24 h; sonication in toluene, ethanol and water.</p> <p>c. -</p> <p>d. XPS: elemental concentration, consistent evolution according to reaction steps.</p>			
Titanium	none	Heparin/fibronectin	Li et al., 2011
<p>a. Polishing; sonication in different solvents, drying 2 h at 60 °C ; NaOH treatment, 2h at 80°C.</p> <p>b. In anhydrous ethanol, 10 h, sonication in ethanol; curing 6 h at 120 °C.</p> <p>c. Improvement of blood compatibility and promotion of endothelialization. Blanks = native, silanized.</p> <p>d. XPS : survey spectra consistent with treatments. AFM: small clumps after APTES step, and after APTES + protein step. Wet chemical analysis of proteins: consistent evolution according to reaction steps.</p>			
Ti-6Al-4V	SMP	Cyclic peptides	Porté-Durrieu et al., 2004
<p>a. Substrate oxidation; outgassing at 150 °C.</p> <p>b. In dry hexane under argon; rinsing with dry hexane; outgassing.</p> <p>c. Increase of osteoprogenitor cells attachment. Blanks = native, native + peptide.</p> <p>d. XPS: elemental concentration, consistent evolution according to reaction steps; N 1s peak, demonstration of peptide retention; C 1s peak, majority of carbon of C-(C,H) type at all stages.</p>			
Co-Cr-Mo; Ti-6Al-4V	GA	Trypsin	Puleo, 1997
<p>a. Cleaning in different solvent, acid passivation.</p> <p>b. In water 3 h or acetone 10 min; curing at 45 °C overnight.</p> <p>c. Decrease of the loss of enzymatic activity as a function of time for Co-Cr-Mo, no effect</p>			

for Ti-6Al-4V. Blank = native + enzyme, silanized + enzyme.			
d. Wet chemical analysis of amino groups on silanized substrate only.			
Magnesium	Ascorbic acid	BSA	Killian et al., 2010
a. Surface polishing; rinsing in water and ethanol.			
b. In toluene, 24 h at 70 °C; rinsing in different solvents; sonication in ethanol.			
c. -			
d. XPS: elemental concentration, consistent evolution according to reaction steps. ToF-SIMS: demonstration of silanization and protein retention.			
Tantalum coating	DS3; DSS; DSC; CDI	Collagen	Müller et al., 2005
a. Acid etching; rinsing with different solvents; drying in vacuum.			
b. In boiling toluene under argon; rinsing in chloroform, methanol, and in water.			
c. Increase of cell adhesion and proliferation (stem cell culture and subcutaneous implantation). Blanks = native, silanized.			
d. Wet chemical analysis: amino groups, collagen, consistent with expectation. AFM: typical structure of fibrillar collagen.			
SiO <sub>2</sub> , TiO <sub>2</sub> , Si <sub>3</sub> N <sub>4</sub>	GA	Antigen	Kim et al., 2009b
a. Plasma treatment.			
b. In ethanol/water (95/5, v/v), rinsing with ethanol ; curing 15 min at 120 °C.			
c. Antigen/antibody test. Influence of plasma exposure time.			
d. Water contact angle and XPS on cleaned substrate, influence of plasma exposure time.			
Silicon dioxide	SMP	RGD peptide	Davis et al., 2002
a. Oxidation and hydroxylation; rinsing with different solvents.			
b. In dry toluene, 120 °C, 3 h; sonication in various organic solvents and water.			
c. Increase of fibroblast proliferation. Blanks = no RGD.			
d. XPS: elemental concentration, consistent evolution according to reaction steps. AFM: small clumps after APTES step ; larger clumps after APTES+SMP step.			
Silicon dioxide	GA	Glucose oxidase	Libertino et al., 2008
a. Oxidation in a solution of ammonia and hydrogen peroxide.			
b. Vapor deposition; curing 40 min at 80 °C under vacuum.			
c. Slight decrease of the enzyme activity when the surface is not oxidized (a). No blank.			
d. AFM: consistent evolution of surface roughness according to reaction steps. XPS: elemental concentration, consistent evolution according to reaction steps.			
Silicon dioxide	LC-SPDP	Tagged Kcoil peptides	Boucher et al., 2009
a. Piranha treatment, 10 min at 100°C; rinsing in water; drying in air; storing in vacuum.			
b. In anhydrous toluene, 3 h; curing 1.5 h at 120°C; sonication in freshly distilled toluene.			
c. Improvement of binding efficiency (amount, affinity) of Ecoil-tagged EGF. Blank = silanized + LC-SPDP with blocked termination.			
d. Ellipsometry and water contact angle: consistent evolution according to reaction steps.			
Glass	none	Proteins from ECM, RGD peptide	Siperko et al., 2006
a. Cleaning in different solvent.			
b. In anhydrous ethanol + acetic acid, followed by addition of ultrapure water, 5 min; curing 15 min at 120°C.			
c. Improvement of osteoblast adhesion and growth. Blank = silanized.			

d. AFM: increase of surface roughness, presence of nanostructures presumably due to proteins or peptide.			
Poly(dimethylsiloxane)	SSMCC	DNA	Vaidya & Norton, 2004
a. Surface plasma oxidation.			
b. Vapor deposition, 30 min, 100 °C.			
c. Hybridization of attached DNA. No blank.			
d. XPS: elemental composition and peak shapes, demonstration of silane deposition.			
Polystyrene	BS <sup>3</sup> , GMBS	IgG	North et al., 2010
a. Plasma treatment.			
b. In ethanol+acetic acid; rinsing in methanol.			
c. -			
d. Fluorescence labeling: increase of amount of immobilized proteins by silanization + linker step.			
Cellulose	SMP	RGDC peptide	Bartouilh de Taillac et al., 2004
a. Drying, outgassing.			
b. In dry toluene under argon, 1.5 h; rinsing with dry toluene; outgassing.			
c. Increase of osteoprogenitor cells attachment and proliferation. Blank = native.			
d. XPS: qualitative consistency with expectations but probable Si contamination on final product.			

BSA = bovine serum albumin

BS<sup>3</sup> = bis(sulfosuccinimidyl) suberate

CDI = 1,1'-carbonyldimidazole

DSC = N,N'-disuccinimidyl-carbonate

DSS = N,N'-disuccinimidyl-suberate

DS3 = N,N'-disulphosuccinimidyl-suberate

EDC = 1-ethyl-3-(3-dimethylaminopropyl)carbodiimide.

ECM = extracellular matrix

EGF = epidermal growth factor

GA = glutaraldehyde

GMBS = 4-maleimidobutyric acid N-hydrosuccinimide ester

LbL = layer-by-layer

LC-SPDP = Succinimidyl 6-[30-(2-pyridylidithio)-propionamido]hexanoate

QCM = quartz crystal microbalance

RGDC = arginine - glycine - aspartic acid - cysteine

SMP = N-succinimidyl-3-maleimidopropionate

SSMCC = sulfosuccinimidyl-4-(N-maleimidomethyl)-cyclohexane-1-carboxylate

TNBS = 2,4,6-trinitrobenzenesulfonic acid

Table 1. Illustration of the use of APTES for retaining biomolecules on surfaces. The meaning of a, b, c, and d is given in the upper box.

## 2. Materials and methods

### 2.1 Materials

Disks of 316L SS (0.74 cm<sup>2</sup>, from Outokumpu Stainless AB, ARC) were used. The bulk chemical composition of 316L SS was given previously (Landoulsi et al., 2008a). All chemicals (NaCl, Na<sub>2</sub>SO<sub>4</sub>, NaNO<sub>3</sub>, NaHCO<sub>3</sub>, NaHPO<sub>4</sub>, Na<sub>2</sub>PO<sub>4</sub>) were provided by Prolabo (VWR, France) and ensured 99% minimum purity. 3-aminopropyl(triethoxysilane) (APTES, 99%), glucose oxidase (Gox, EC 1.1.3.4, 47200 U.g<sup>-1</sup>) from *Aspergillus Niger* and D-glucose

were purchased from Sigma-Aldrich (France). Bis(sulfosuccinimidyl) suberate (BS) was purchased from Pierce (Rockford, IL, USA).

## 2.2 Stainless steel surface preparation

The samples (both faces and perimeter) were polished with 1  $\mu\text{m}$  diamond suspension (Struers, Denmark), rinsed in binary mixture of milliQ water/ethanol (1/1, v/v) in a sonication bath (70W, 40 kHz, Branson, USA) and dried under nitrogen gas flow. The samples were then immediately immersed for 48 h in synthetic aqueous medium (NaCl 0.46 mmol.L<sup>-1</sup>, Na<sub>2</sub>SO<sub>4</sub> 0.26 mmol.L<sup>-1</sup>, NaNO<sub>3</sub> 0.2 mmol.L<sup>-1</sup>, NaHCO<sub>3</sub> 3.15 mmol.L<sup>-1</sup>, pH about 8), abundantly rinsed with milliQ water (Millipore, Molsheim, France) and dried under nitrogen gas flow. These samples are considered as native SS and designated as "nat".

## 2.3 Surface treatment procedure

The silanization of nat samples was performed in the gas phase with APTES. To this end, nat samples were placed, together with a small vial containing 100  $\mu\text{L}$  APTES, in a 7 dm<sup>3</sup> closed recipient under vacuum for 30 min at room temperature. The samples were cured for 1 h at 100°C under vacuum, rinsed and incubated for 6 h in milliQ water to eliminate the excess of non attached silanes. These are called "sil".

Both nat and sil samples were subjected to treatments with the coupling agent (BS) and/or the enzyme (Gox) as detailed below:

- i. "+BS" and "sil+BS" obtained after BS treatment (10 mM in milliQ water) for 30 min on nat and sil samples, respectively,
- ii. "+Gox" and "sil+Gox" obtained after Gox treatment (0.1 mg.mL<sup>-1</sup> in phosphate buffer pH~6.8) for 2 h, on nat and sil samples, respectively,
- iii. "+BS+Gox" and "sil+BS+Gox" obtained after both BS and Gox treatment (according to the procedure described above) on nat and sil samples, respectively.

After BS or Gox treatment, the samples were rinsed three times with milliQ water and dried under nitrogen gas flow.

In order to clarify the issue of surface contamination, nat samples were further cleaned by UV-ozone treatment (UVO Cleaner, Jelight Co, Irvine, Ca, USA) during 20 minutes. They were then placed in a Petri dish, left in the laboratory environment, and submitted to water contact angle measurements as a function of time.

## 2.4 X-ray photoelectron spectroscopy

XPS analyses were performed using a Kratos Axis Ultra spectrometer (Kratos Analytical, UK), equipped with a monochromatized aluminum X-ray source (powered at 10 mA and 15 kV) and an eight channeltrons detector. No charge stabilization device was used on these conductive samples. Analyses were performed in the hybrid lens mode with the slot aperture; the resulting analyzed area was 700  $\mu\text{m}$   $\times$  300  $\mu\text{m}$ . A pass energy of 40 eV was used for narrow scans. In these conditions, the full width at half maximum (FWHM) of the Ag 3d<sub>5/2</sub> peak of clean silver reference sample was about 0.9 eV. The samples were fixed on the support using a double-sided adhesive conducting tape. The pressure in the analysis chamber was around 10<sup>-6</sup> Pa. The photoelectron collection angle  $\theta$  between the normal to the sample surface and the electrostatic lens axis was 0° or 60°. The following sequence of spectra was recorded: survey spectrum, C 1s, O 1s, N 1s, P 2p, Cr 2p, Fe 2p, Ni 2p, Mo 3d, Na 1s, S 2p, Si 2p and C 1s again to check for charge stability as a function of time, and absence of sample degradation. The binding energy scale was set by fixing the C 1s

component due to carbon only bound to carbon and hydrogen at 284.8 eV. The data treatment was performed with the Casa XPS software (Casa Software Ltd., UK). The peaks were decomposed using a linear baseline, and a component shape defined by the product of a Gauss and Lorentz function, in the 70:30 ratio, respectively. Molar concentration ratios were calculated using peak areas normalized according to the acquisition parameters and the relative sensitivity factors and transmission functions provided by the manufacturer.

### 2.5 Atomic force microscopy (AFM)

The surface topography was examined using a commercial AFM (NanoScope III MultiMode AFM, Veeco Metrology LLC, Santa Barbara, CA) equipped with a  $125\ \mu\text{m} \times 125\ \mu\text{m} \times 5\ \mu\text{m}$  scanner (J-scanner). A quartz fluid cell was used without the O-ring. Topographic images were recorded in contact mode using oxide-sharpened microfabricated  $\text{Si}_3\text{N}_4$  cantilevers (Microlevers, Veeco Metrology LLC, Santa Barbara, CA) with a spring constant of  $0.01\ \text{N}\cdot\text{m}^{-1}$  (manufacturer specified), with a minimal applied force ( $<500\ \text{pN}$ ) and at a scan rate of 5-6 Hz. The curvature radius of silicon nitride tips was about 20 nm. Images were obtained at room temperature (21-24°C) in milliQ water. All images shown in this paper were flattened data using a third order polynomial. The surface roughness ( $R_{\text{rms}}$ ) was computed over an area of  $1\ \mu\text{m} \times 1\ \mu\text{m}$  using the Veeco software.

### 2.6 Water contact angle measurements

Water contact angles were measured at room temperature using the sessile drop method and image analysis of the drop profile. The instrument, using a CCD camera and an image analysis processor, was purchased from Electronisch Ontwerpbureau De Boer (The Netherlands). The water (milliQ) droplet volume was  $0.3\ \mu\text{L}$ , and the contact angle was measured 5 s after the drop was deposited on the sample. For each sample, the reported value is the average of the results obtained on 5 droplets.

## 3. Results

AFM images obtained in water on SS samples after different treatments are presented in Figure 1. The nat sample showed the presence of nanoparticles with different sizes (nat, Figure 1,  $R_{\text{rms}} = 3.2\ \text{nm}$ ), in agreement with previous results. The formation of nanoparticles, presumably made of ferric hydroxide, resulted from oxidation occurring during the 48 h of immersion subsequent to polishing (Landoulsi et al., 2008a). The surface of silanized SS exhibited particles with a bigger size (sil, Figure 1) and the roughness decreased slightly (sil, Figure 1,  $R_{\text{rms}} = 2.4\ \text{nm}$ ). The treatment with Gox, with or without previous treatment with BS, led to the formation of particles with a more uniform size and a higher density, in comparison with nat sample, and no appreciable change of surface roughness ( $R_{\text{rms}} = 1.7\ \text{nm}$  for sil+Gox and  $2.5\ \text{nm}$  for sil+BS+Gox, Figure 1).

XPS is a suitable method to obtain information regarding the different constituents at the surface (substrate, silane, other organic compounds). The elemental composition of the samples is given in Table 2. Representative C 1s and O 1s peaks recorded on SS surface prior to and after silanization, and after further treatments are given in Figure 2. After BS and/or Gox treatment of silanized SS, a relative increase of the component around 531.2 eV in the O 1s peak was observed (Figure 2). In the C 1s peak, an increase of the components at 286.3 and 288.7 eV was also clear, while the main component remained at 284.8 eV. The same



tendency regarding the C 1s and O 1s peaks was also observed after BS and/or Gox treatment of nat sample, but was less pronounced (data not shown). It may be attempted to

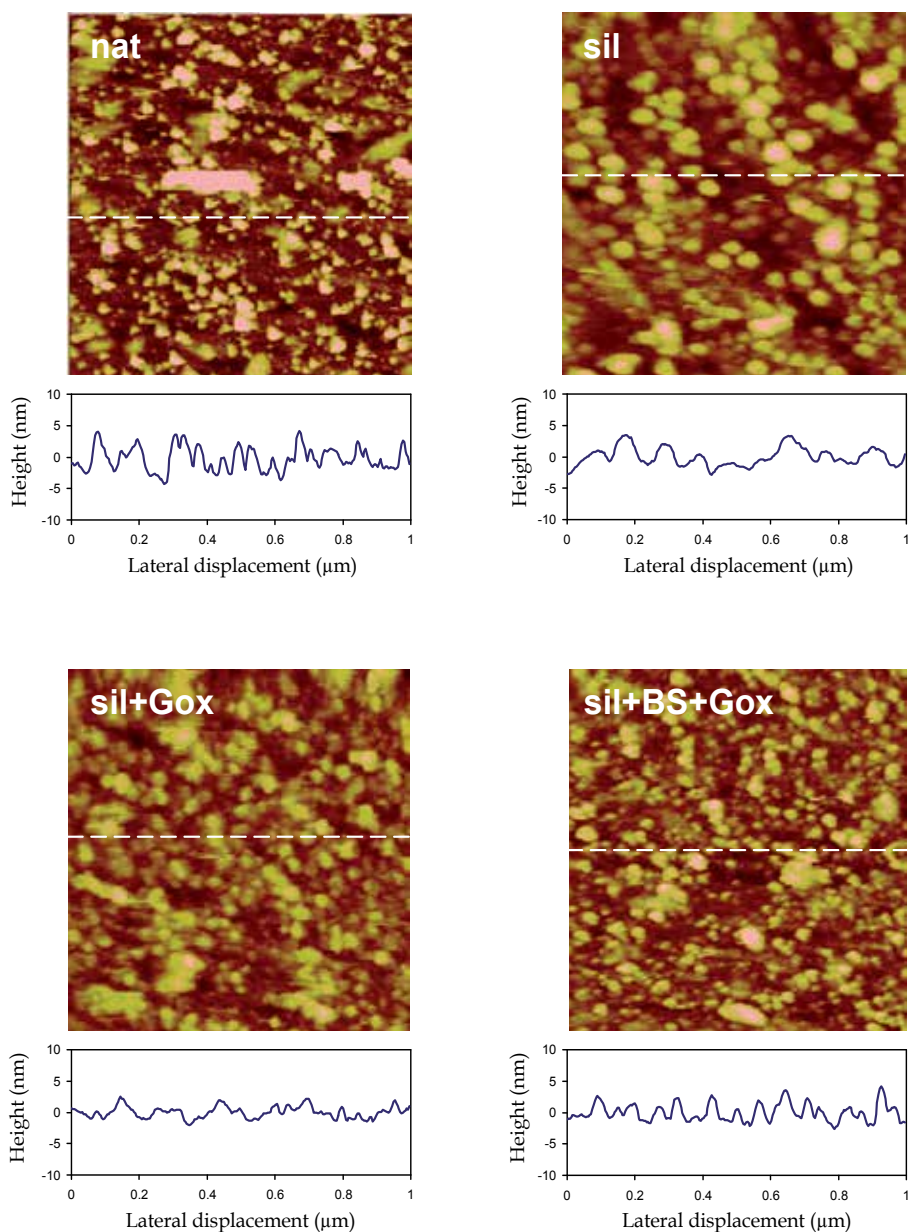


Fig. 1. AFM height images ( $1 \times 1 \mu\text{m}^2$ , contact mode, in water; z scale 10 nm) of native (nat), silanized stainless steel (sil), the same after adsorption of glucose oxidase (sil+Gox) and after treatment with glucose oxidase subsequent to treatment with the coupling agent (sil+BS+Gox). Cross sections were taken at the place indicated by the dashed lines.

extract chemical information by careful decomposition of the peaks. This requires to impose reasonable constraints (number of components, full width at half maximum FWHM) in order to insure reliable comparisons, and to check the chemical relevance of the results by examining correlations between spectral data of different natures (Genet et al., 2008; Rouxhet & Genet, 2011). In previous studies (Landoulsi et al., 2008a; Landoulsi et al., 2008b), we have demonstrated the usefulness of this approach, even when the evolution of the C 1s and O 1s peak shape is weak, in order to obtain information on the amount and the nature of organic and inorganic constituents on SS surfaces.

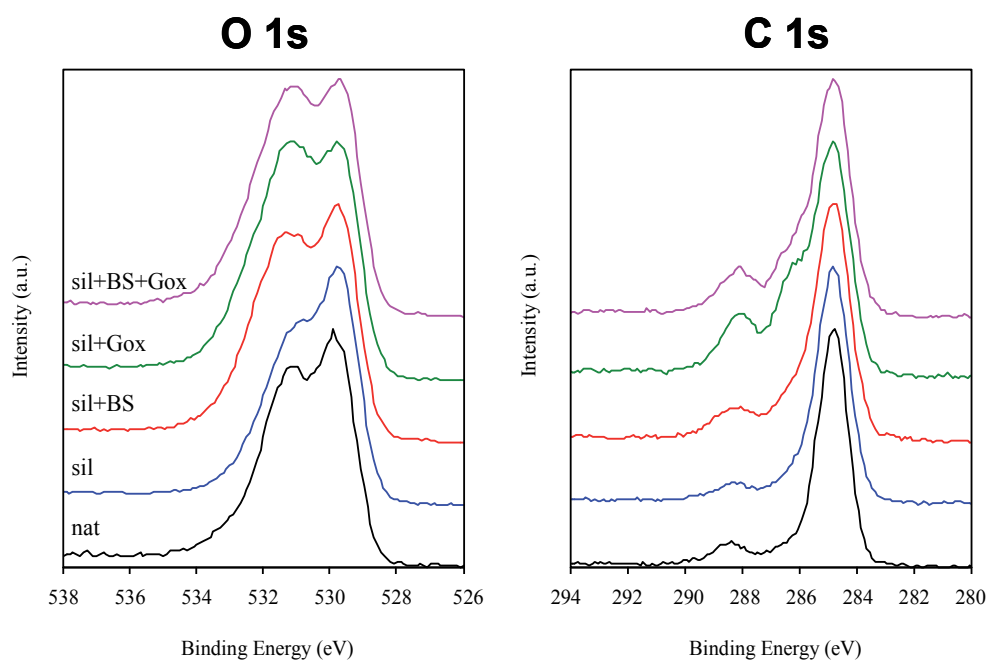


Fig. 2. O 1s and C 1s peaks of native (nat), of silanized stainless steel (sil), of the same after treatment with the coupling agent (sil+BS), after adsorption of glucose oxidase (sil+Gox) and after treatment with glucose oxidase subsequent to treatment with the coupling agent (sil+BS+Gox).

Figure 3 presents typical O 1s, N 1s and C 1s XPS peaks recorded on native SS (nat), silanized (sil) and the same after Gox treatment (sil+Gox). For the decomposition of these peaks, reasonable constraints were applied, based on our experience with the XPS analysis of biosurfaces (Genet et al., 2008, Rouxhet & Genet, 2011). The C 1s peak was decomposed in four components, the FWHM of which were imposed to be equal: (i) a component at 284.8 eV due to carbon only bound to carbon and/or hydrogen [C-(C,H)]; (ii) a component at about 286.3 eV due to carbon making a single bond with oxygen and/or nitrogen [C-(O,N)] in alcohol, amine, or amide; (iii) a component at 287.8 eV due to carbon making one double bond or two single bonds with oxygen (C=O, O-C-O) and (iv) a component at 288.7 eV attributed to carboxyl or ester functions [(C=O)-O-R].

The O 1s peak was decomposed in three components (Landoulsi et al., 2008a). The first one, at 529.7 eV, is due to inorganic oxygen in metal oxides (M-O) (NIST Database). The FWHM of the two other components were arbitrarily imposed to be equal. The component at about 531.2 eV may be due to oxygen making a double bond with carbon (C=O including amide and carboxyl group) and to oxygen of carboxylate. Contributions of metal hydroxides (M-O-H) as well as oxygen bound to silicon [Si-O] in silane are overlapping with this component (NIST Database; Genet et al., 2008). The last component, at 533.1 eV, is attributed to oxygen making single bonds with carbon (C-O-H of alcohol and carboxyl, C-O-C of ether and ester).

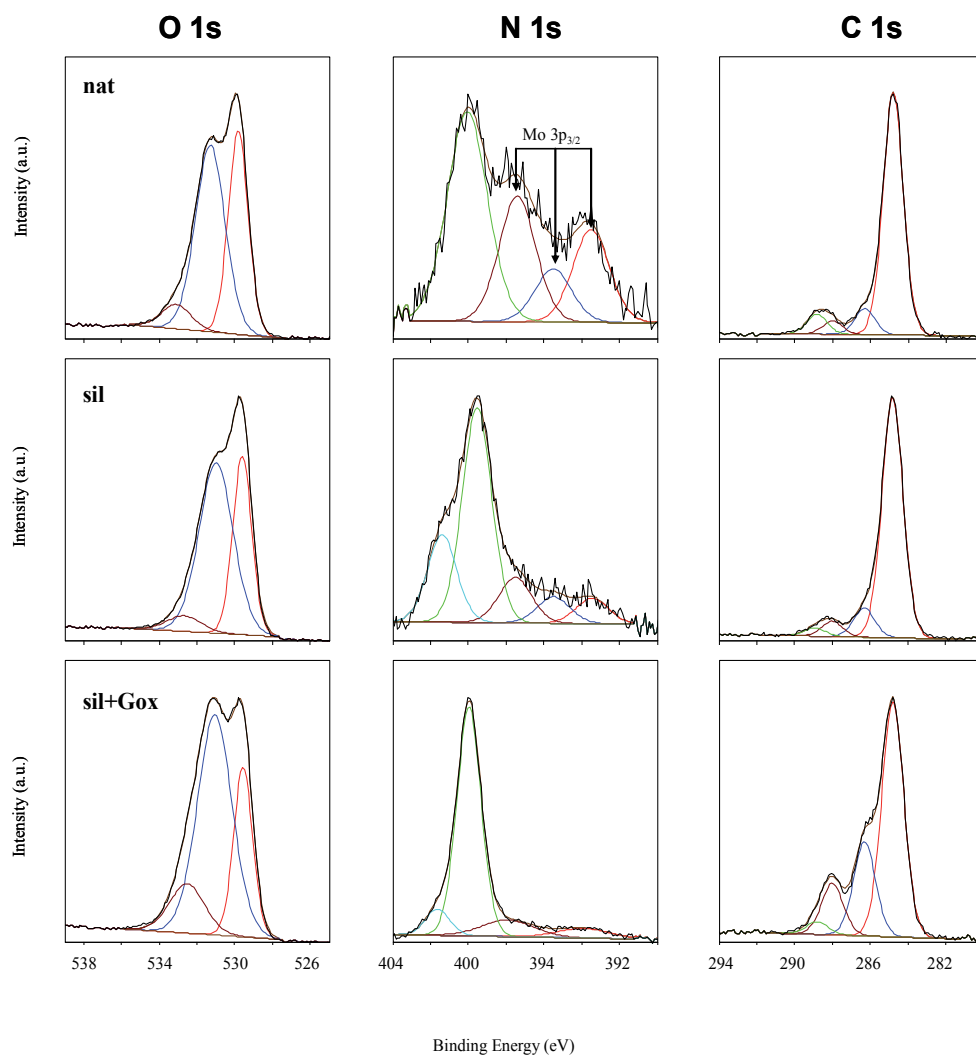


Fig. 3. Decomposition of O 1s, N 1s and C 1s peaks recorded on: native stainless steel (nat), silanized stainless steel (sil) and the same after adsorption of glucose oxidase (sil+Gox). The N 1s peak is overlapped with a Mo 3p<sub>3/2</sub> contribution.

The N 1s peak showed a main component at 400.0 eV attributed to amide or amine (N-C). An additional component appeared clearly near 401.6 eV in silanized SS samples (sil and sil+Gox, Figure 3), indicating the presence of protonated amines. The contributions at lower binding energies in the N 1s spectral window are due to Mo 3p<sub>3/2</sub> components (Olefjord & Wegrelius, 1996); the reliability of their quantification was checked by comparison with the Mo concentration deduced from the Mo 3p<sub>3/2</sub> and Mo 3d peaks (Landoulsi et al., 2008a). The N 1s contribution of sil shows a shape which is in agreement with spectra reported in the literature for APTES-modified surfaces (Suzuki et al., 2006; Xiao et al., 1997). It was not found justified to decompose it in three components attributed to amine, amide and protonated amine, respectively, as done in (Suzuki et al., 2006). The surface concentrations (mole fraction) associated with the components of C 1s, O 1s and N 1s peaks are given in Table 2.

	Ni <sup>ox</sup>	Ni <sup>met</sup>	Ni <sup>tot</sup>	Fe <sup>ox</sup>	Fe <sup>met</sup>	Fe <sup>tot</sup>	Cr <sup>ox</sup>	Cr <sup>met</sup>	Cr <sup>tot</sup>	Mo <sup>ox</sup>	Mo <sup>met</sup>	Mo <sup>tot</sup>	Si <sup>0</sup>
<b>nat</b>	1.23	0.73	<b>1.95</b>	7.59	1.57	<b>9.16</b>	4.69	0.33	<b>5.02</b>	0.34	0.12	<b>0.46</b>	<b>0.38</b>
<b>+BS</b>	0.81	0.54	<b>1.35</b>	8.32	1.89	<b>10.21</b>	5.96	0.40	<b>6.36</b>	0.46	0.12	<b>0.57</b>	<b>0.29</b>
<b>+Gox</b>	0.59	0.51	<b>1.10</b>	8.63	1.70	<b>10.33</b>	5.53	0.33	<b>5.86</b>	0.37	0.12	<b>0.49</b>	-
<b>+BS+Gox</b>	0.66	0.39	<b>1.05</b>	8.90	1.43	<b>10.33</b>	4.56	0.30	<b>4.87</b>	0.32	0.12	<b>0.44</b>	<b>0.36</b>
<b>sil</b>	0.47	0.33	<b>0.80</b>	7.89	1.22	<b>9.10</b>	4.59	0.27	<b>4.86</b>	0.31	0.10	<b>0.40</b>	<b>0.37</b>
<b>sil+BS</b>	0.47	0.43	<b>0.91</b>	6.91	1.45	<b>8.36</b>	5.24	0.33	<b>5.57</b>	0.35	0.11	<b>0.45</b>	<b>0.32</b>
<b>sil+Gox</b>	0.60	0.38	<b>0.98</b>	6.14	1.29	<b>7.42</b>	4.95	0.29	<b>5.23</b>	0.32	0.12	<b>0.44</b>	<b>0.26</b>
<b>sil+BS+Gox</b>	0.54	0.32	<b>0.86</b>	6.22	1.16	<b>7.39</b>	4.58	0.24	<b>4.82</b>	0.34	0.09	<b>0.42</b>	<b>0.30</b>

	C <sub>288.7</sub>	C <sub>287.8</sub>	C <sub>286.3</sub>	C <sub>284.8</sub>	C <sub>tot</sub>	O <sub>533.1</sub>	O <sub>531.2</sub>	O <sub>529.7</sub>	O <sub>tot</sub>	O <sub>org</sub>	N <sub>401.6</sub>	N <sub>400</sub>	N <sub>tot</sub>	Si <sub>org</sub>	Σ <sub>org</sub>
<b>nat</b>	2.45	2.29	3.92	39.62	<b>48.28</b>	2.36	19.02	12.60	<b>33.98</b>	<b>7.92</b>	0.00	0.73	<b>0.73</b>	<b>0.44</b>	<b>57.37</b>
<b>+BS</b>	2.89	2.08	3.88	34.87	<b>43.71</b>	2.48	18.96	13.86	<b>35.30</b>	<b>7.64</b>	0.00	1.21	<b>1.21</b>	<b>0.43</b>	<b>52.99</b>
<b>+Gox</b>	2.03	2.16	4.78	35.56	<b>44.53</b>	2.97	20.96	11.27	<b>35.20</b>	<b>7.50</b>	0.13	1.34	<b>1.48</b>	-	<b>53.50</b>
<b>+BS+Gox</b>	2.55	2.60	5.89	30.02	<b>41.06</b>	3.96	22.01	12.57	<b>38.54</b>	<b>9.46</b>	0.23	1.35	<b>1.58</b>	<b>0.89</b>	<b>52.99</b>
<b>sil</b>	1.15	2.37	4.57	36.13	<b>44.23</b>	1.95	21.22	12.28	<b>35.45</b>	<b>5.93</b>	0.63	1.54	<b>2.17</b>	<b>2.29</b>	<b>54.61</b>
<b>sil+BS</b>	2.03	3.30	6.48	32.72	<b>44.53</b>	1.07	23.16	9.71	<b>33.94</b>	<b>8.49</b>	0.66	2.65	<b>3.31</b>	<b>2.13</b>	<b>58.47</b>
<b>sil+Gox</b>	1.18	5.97	10.39	25.08	<b>42.62</b>	4.74	21.09	8.86	<b>34.70</b>	<b>11.78</b>	0.59	5.16	<b>5.75</b>	<b>1.74</b>	<b>61.90</b>
<b>sil+BS+Gox</b>	1.46	4.89	8.31	30.39	<b>45.05</b>	2.87	22.24	8.52	<b>33.63</b>	<b>9.86</b>	0.50	4.30	<b>4.80</b>	<b>2.01</b>	<b>61.72</b>

Table 2. Surface concentration (mole fraction (%)) computed over the sum of all elements except hydrogen) of elements determined by XPS ( $\theta = 0^\circ$ ) on stainless steel samples.

The Si 2p peak was decomposed in two components, at 99.3 and 101.8 eV, attributed to non oxidized silicon in SS (Si<sup>0</sup>) and to silicon of silane (Si<sub>org</sub>), respectively. It was not decomposed in Si 2p<sub>3/2</sub> and Si 2p<sub>1/2</sub> contributions because these are very close in energy. The decomposition procedure for Fe 2p<sub>3/2</sub>, Cr 2p, Ni 2p<sub>3/2</sub>, and Mo 3d peaks was described before (Landoulsi et al., 2008a). The Fe concentration may be underestimated due to the procedure used to treat the complex baseline of the Fe 2p peak. The distinction between contributions of oxidized (M<sup>ox</sup>) and nonoxidized (M<sup>met</sup>) metal elements was easily made. The concentrations obtained are also given in Table 2.

The concentration of oxygen present in organic compounds  $O_{org}$  may not directly be deduced from the O 1s peak owing to the overlap with inorganic hydroxide. However, for biological systems the sum of O and N concentrations may be evaluated by the

concentration of carbon in oxidized form,  $C_{ox}$ , in consistency with alcohol, primary amine, primary amide and ester functions. Accordingly,

$$O_{org} = C_{ox} - N = C_{286.3} + C_{287.8} + C_{288.7} - N_{tot} \quad (1)$$

where the name of an element in italic designates its concentration and the number in subscript designates the binding energy of the peak component. Errors would occur in case of a high concentration of polysaccharides ( $C_{ox}/O = 6/5$ ) or carboxyl ( $C_{ox}/O = 1/2$ ) (Genet et al., 2008 ; Landoulsi et al., 2008a).

The sum of the concentrations of the elements present in organic compounds is then given by:

$$\sum_{org} = C_{tot} + O_{org} + N_{tot} + Si_{org} = C_{tot} + C_{ox} + Si_{org} \quad (2)$$

For sake of uniformity, all spectral data involved in correlations below are ratioed to  $\sum_{org}$  (Table 2).

The concentration of the main elements or functions due to organic compounds, obtained at photoelectron collection angle  $\theta = 0^\circ$ , is plotted in Figure 4 as a function of the same quantity obtained at  $\theta = 60^\circ$ . A 1:1 relationship is obtained for all elements or functions and all samples, indicating no significant effect of the photoelectron collection angle  $\theta$  on the relative contribution of the constituents of the organic adlayer.

## 4. Discussion

### 4.1 Passive film composition

Table 2 shows that the apparent concentrations of metal elements varied only slightly according to the surface treatment. The main change concerned the decrease of the  $Fe^{ox}$  concentration for sil+BS, sil+Gox and sil+BS+Gox samples. However, no change in the shape of the Fe  $2p_{3/2}$  peak was observed (data not shown). For these samples, a significant decrease of the molar concentration of  $O_{529.7}$  was also noticed (Table 2). It appears that the oxide layer of SS passive film, after incubation in the aqueous medium for 48 h (nat sample), was mainly constituted with a mixture of Fe and Cr oxides/hydroxides and small amounts of partially oxidized Ni and Mo. This is in agreement with a previous study (Landoulsi et al., 2008a), however in the latter, the stoichiometry of the passive film was not computed.

The O 1s component at 529.7 eV is due to metal oxides. By considering that  $Mo^{ox}$  is in the form of  $MoO_3$  (Landoulsi et al., 2008a), the difference between the  $O_{529.7}$  concentration and three times the  $Mo^{ox}$  concentration should be due to Fe and Cr oxides. Figure 5 presents the relation between this difference and the sum of  $Fe^{ox}$  and  $Cr^{ox}$  concentrations. All data show reasonable linear regressions. The shift of the dots along the line when the photoelectron collection angle changes from  $0^\circ$  to  $60^\circ$  is due to the presence of the organic constituents on top of stainless steel. The average ratio between the  $y$  and  $x$  scales is 0.80 and 0.96 at  $\theta = 0$  and  $60^\circ$ , respectively; the slope of the regression lines is 1.03 (s.d. 0.23) and 1.42 (s.d. 0.12), respectively. Thus, the ratio oxide/metal ions in chromium and iron oxyhydroxides is of the order of 1 to 1.5.

The evaluation of the quantity of hydroxide associated to Fe and Cr is complex due to the multiple chemical functions overlapping in the  $O_{531.2}$  component.  $Ni^{ox}$  is in the form of  $Ni(OH)_2$  (component at  $\sim 855.6$  eV (Briggs & Seah, 1990, Zhou et al., 2006), spectra not shown). The amount of oxygen associated to silane depends on the products of APTES

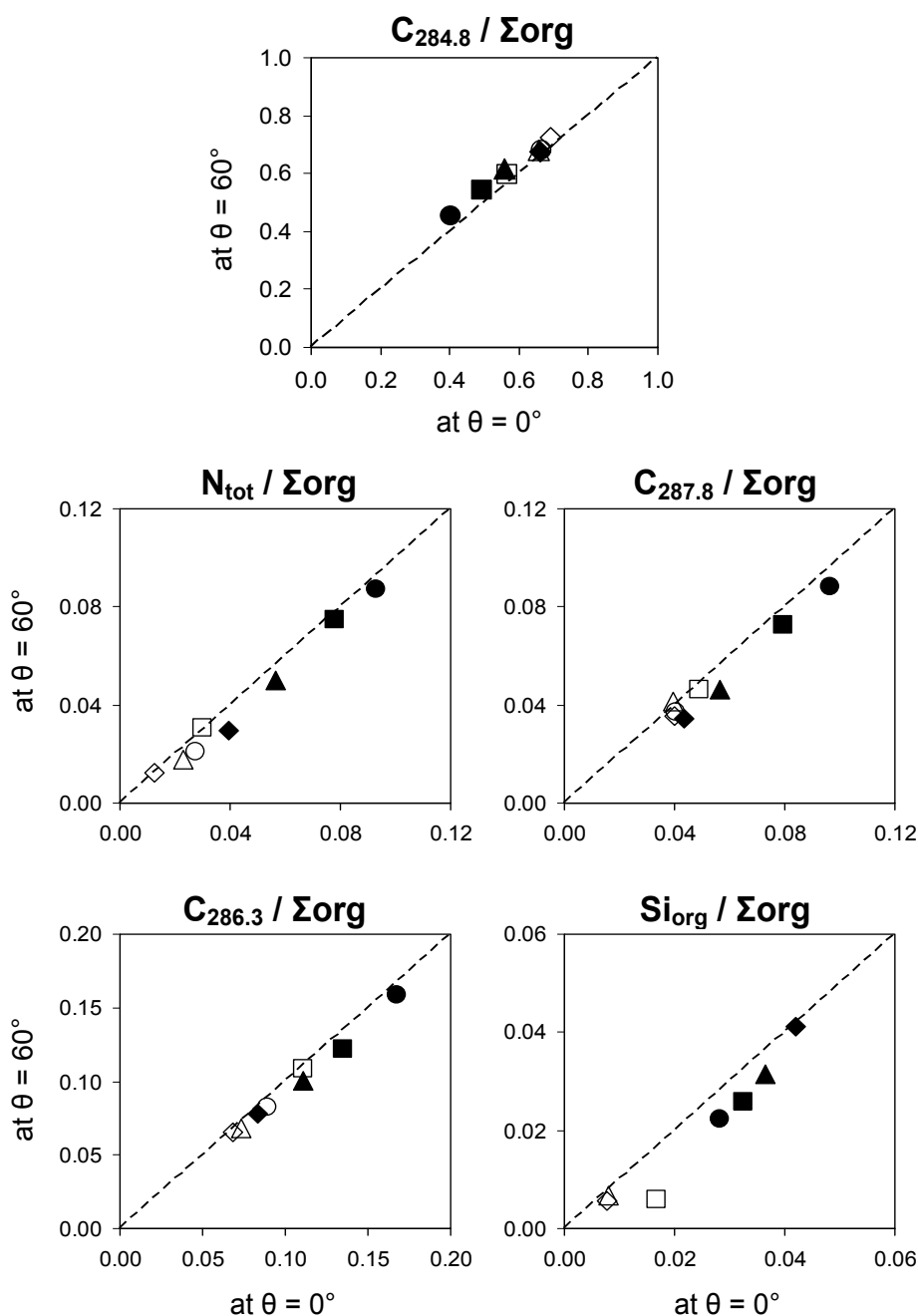


Fig. 4. Plots of molar concentrations ratioed to the sum of organic elements ( $\Sigma_{org}$ ) measured by XPS at  $\theta = 60^\circ$  vs  $\theta = 0^\circ$  on native (open symbols) or silanized stainless steel (closed symbols), as such (◆, ◇) or further treated with coupling agent BS (▲, △), glucose oxidase (●, ○) or coupling agent followed by glucose oxidase (■, □). The dashed lines represent a  $y/x$  ratio of 1:1.

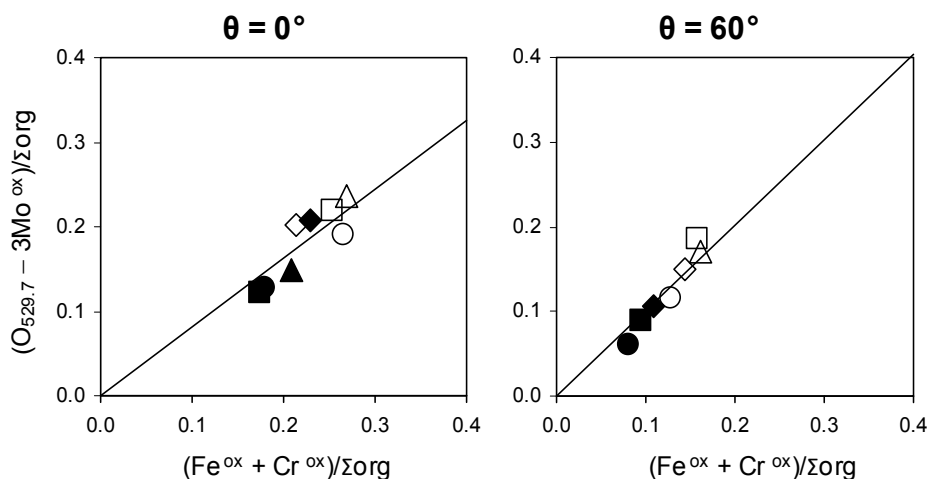


Fig. 5. Relations between molar concentrations ratioed to the sum of organic elements ( $\Sigma_{org}$ ) measured by XPS at  $\theta = 0^\circ$  (data from Table 2) and  $\theta = 60^\circ$  on native (open symbols) or silanized stainless steel (closed symbols), as such ( $\blacklozenge, \diamond$ ) or further treated with coupling agent BS ( $\blacktriangle, \triangle$ ), glucose oxidase ( $\bullet, \circ$ ) or coupling agent followed by glucose oxidase ( $\blacksquare, \square$ ).

reaction. The different possibilities, corresponding to the relative importance of grafting with respect to polymerization, are shown in Figure 6 and characterized by  $a$ , defined as the sum, over oxygen atoms which are not bound to a metal element, of the inverse of the number of bonds oxygen forms with silicon. Accordingly the concentration of inorganic hydroxide in the passive film may be given as follows:

$$OH_{inorg} = O_{tot} - O_{org} - O_{529.7} - a \times Si_{org} \quad (3)$$

where  $a$  can take the values of 0, 0.5, 1, 1.5 or 2 (Figure 6).

Figure 7 shows the plot of the concentration of hydroxide which should be associated with Fe and Cr, considering different values of  $a$ . Taking silicon into account ( $a \neq 0$ ) brings the silanized substrates better in line with the non-silanized substrates and the correlation improves as  $a$  increases, indicating that silane is polymerized and not just grafted. Depending on the value of  $a$ , the  $y : x$  ratio varies from 1.1 ( $a = 0$ ) to 0.8 ( $a = 2$ ).

These observations indicate that the stoichiometry of the Cr and Fe oxyhydroxide at the surface is close to (Fe,Cr)OOH. Many studies have reported a stratification in the passive film and the presence of Fe and Cr oxyhydroxides in the outermost layer (Le Bozec et al., 2001). In our case, no significant effect of the photoelectron collection angle appears in the  $OH_{inorg}/O_{529.7}$  ratio (Figure 8), whatever the value selected for  $a$  to evaluate  $OH_{inorg}$ . However it must be kept in mind that the surface roughness revealed by Figure 1, which is of the order of the inelastic mean free path of photoelectrons in oxides, may mask the effect of a stratification.

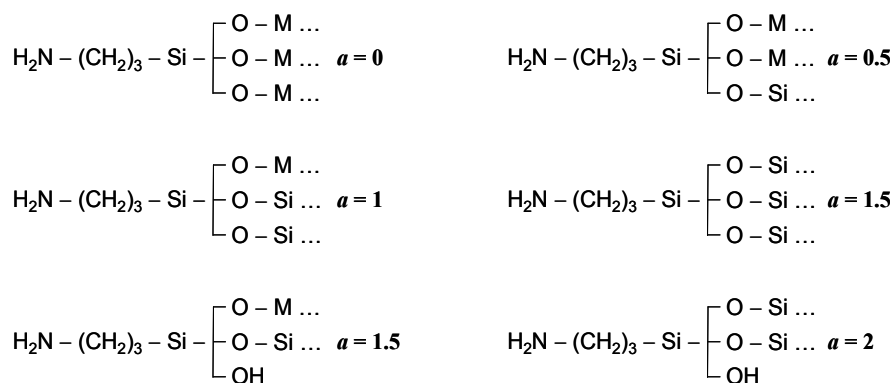


Fig. 6. Possible products of APTES reaction. "M" designates metal elements of stainless steel.

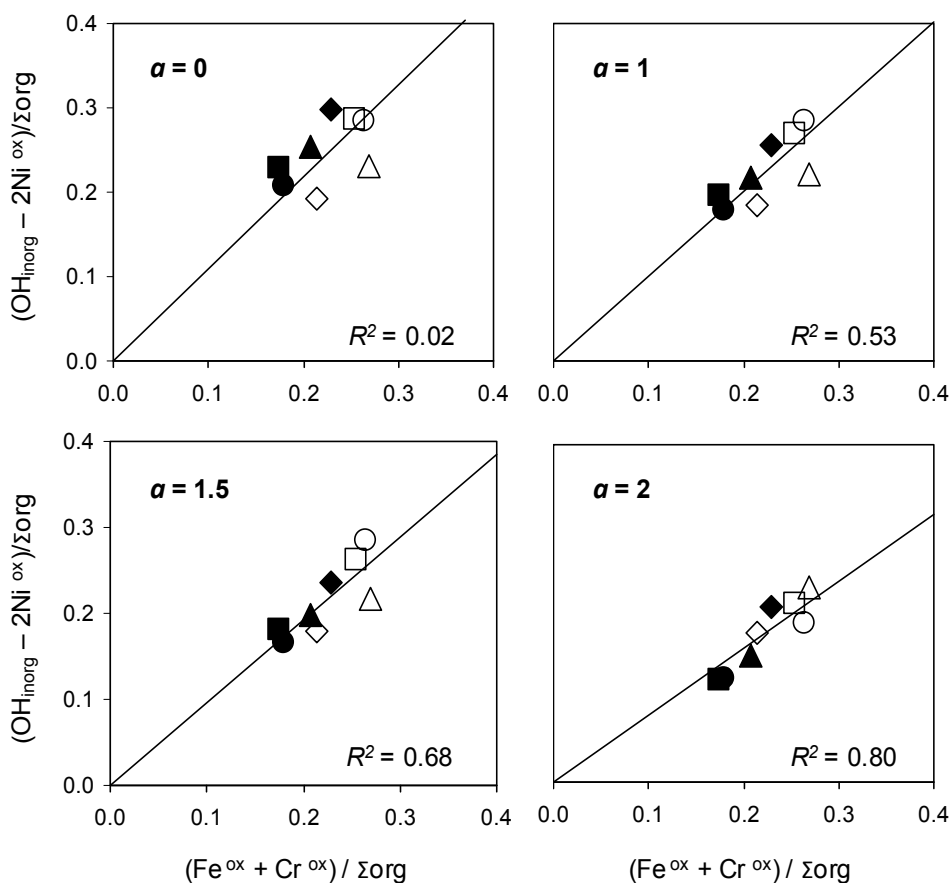


Fig. 7. Relations between molar concentrations ratioed to the sum of organic elements ( $\Sigma_{\text{org}}$ ) measured by XPS at  $\theta = 0^\circ$  (data from Table 2) on native (open symbols) or silanized stainless steel (closed symbols), as such (◆,◇) or further treated with coupling agent BS (▲,△), glucose oxidase (●,○) or coupling agent followed by glucose oxidase (■,□).



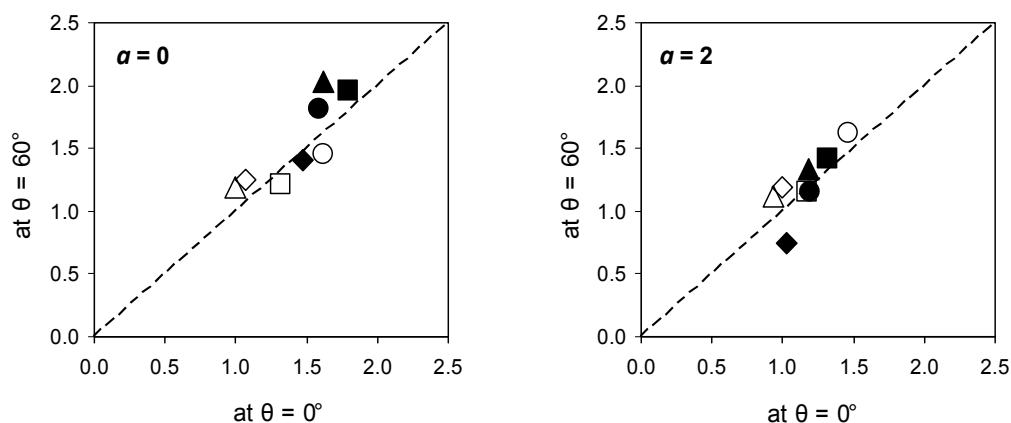


Fig. 8. Plots of  $\text{OH}_{\text{inorg}} / \text{O}_{529.7}$  ratio measured by XPS at  $\theta = 60^\circ$  vs  $\theta = 0^\circ$  on native (open symbols) or silanized stainless steel (closed symbols), as such ( $\blacklozenge, \blacklozenge$ ) or further treated with coupling agent BS ( $\blacktriangle, \blacktriangle$ ), glucose oxidase ( $\bullet, \circ$ ) or coupling agent followed by glucose oxidase ( $\blacksquare, \square$ ). The dashed lines represent a  $y/x$  ratio of 1:1.

#### 4.2 Chemical speciation of the organic adlayer

Table 2 reveals an increase of  $N_{\text{tot}}$  concentration as a result of surface treatments, and an increase of  $Si_{\text{org}}$  concentration for samples prepared with APTES treatment. However, the concentration of carbon is high and remains almost unchanged, suggesting that organic contaminants, mainly hydrocarbon-like compounds, are always dominating in the organic adlayer. If nitrogen was exclusively due to amide functions ( $\text{N}-\text{C}=\text{O}$ ) as in the peptide link of proteins, and if the C 1s component at 287.8 eV was exclusively due to amide, a 1:1 correlation would be found between the concentrations of  $C_{287.8}$  and  $N_{\text{tot}}$ . This is indeed observed (Figure 9a) for the set of samples involving the silanized substrate. As nitrogen is partly in the form of silane, relevant alternatives for the abscissa scale may be the concentration of  $N_{400}$  or the difference between the concentrations of  $N_{\text{tot}}$  and  $Si_{\text{org}}$ . If polysaccharides were present with protein, the  $C_{287.8}$  concentration should be corrected by subtracting the contribution of acetal and thus replaced by  $[C_{287.8} - (C_{286.3} - N_{400})/5]$  (Ahimou et al., 2007, Landoulsi et al., 2008a) or  $[C_{287.8} - (C_{286.3} - N_{\text{tot}} + Si_{\text{org}})/5]$ . A comparison between different plots in Figure 9 shows that the dots representative of samples prepared with non-silanized substrate remain clustered. The shift of the cluster along the ordinate scale according to the plot indicates that  $C_{287.8}$  concentration is higher than what can be attributed to amide. On the other hand, the samples prepared with silanized substrate preserve a unit slope whatever the plot, with much higher values of the coordinates for samples exposed to the enzyme, with or without the linker. This reveals an excellent agreement between the increases of concentrations of nitrogen and of carbon attributed to peptidic links ( $\text{N}-\text{C}=\text{O}$ ), which result from the Gox treatment. It also validates the C 1s peak decomposition and component attribution.

The meaning of the surface composition appears more clearly if it is summarized in terms of concentration of model molecular compounds. This approach was already used for microbial surfaces (Dufre ne & Rouxhet, 1996; Tesson et al., 2009), for food products (Rouxhet et al., 2008) and for stainless steel aged in different conditions (Landoulsi et al.,

2008b), considering proteins (Pr), polysaccharides (PS), and hydrocarbon-like compounds (HC) which represent mainly lipids in biological systems. The novelty here is to take silane (SI) into account in addition to the three classes of biochemical compounds; the chemical composition and density considered for these model compounds are listed in Table 3. Accordingly, the proportion of carbon atoms due to each model compound X ( $C_X/C_{tot}$ ) can be computed by solving the following system of equations:

$$(N_{tot} - Si_{org})/C_{tot} = 0.273 \times (C_{Pr}/C_{tot}) \quad (4)$$

$$O_{org}/C_{tot} = 0.312 \times (C_{Pr}/C_{tot}) + 0.833 \times (C_{PS}/C_{tot}) \quad (5)$$

$$Si_{org}/C_{tot} = 0.333 \times (C_{SI}/C_{tot}) \quad (6)$$

$$1 = (C_{Pr}/C_{tot}) + (C_{PS}/C_{tot}) + (C_{SI}/C_{tot}) + (C_{HC}/C_{tot}) \quad (7)$$

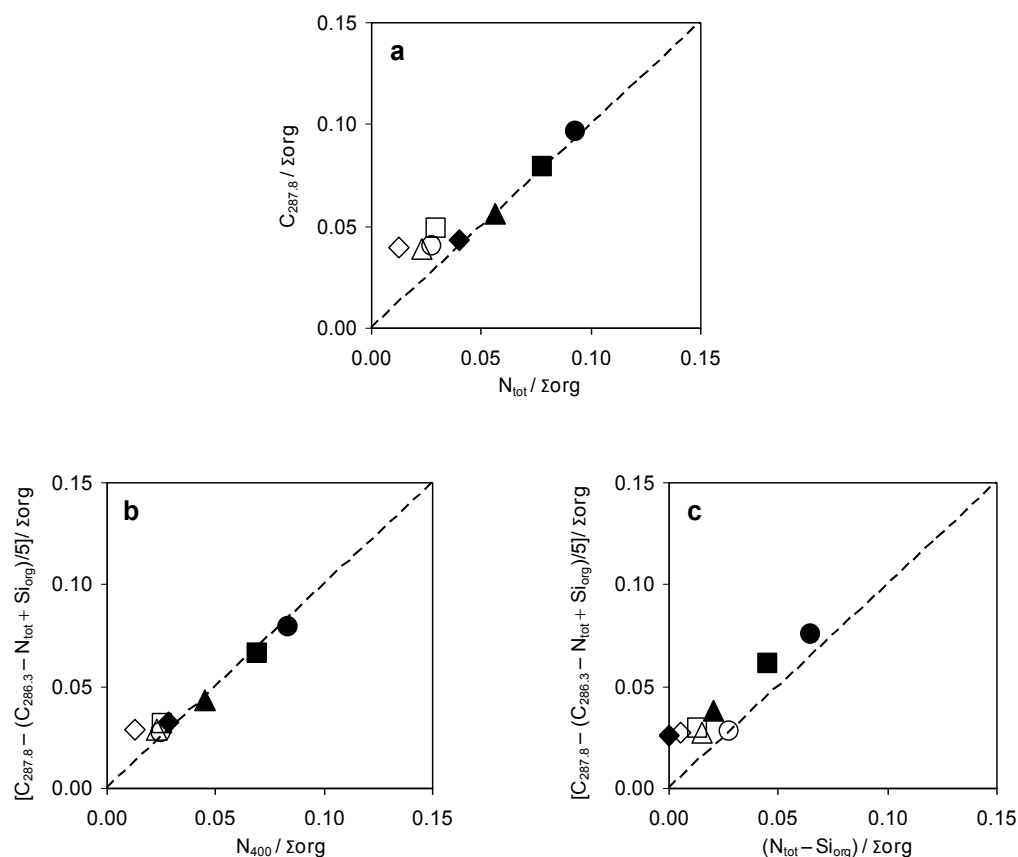


Fig. 9. Relations between molar concentrations ratioed to the sum of organic elements ( $\Sigma_{org}$ ) measured by XPS at  $\theta = 0^\circ$  (data from Table 2) on native (open symbols) or silanized stainless steel (closed symbols), as such (◆, ◇) or further treated with coupling agent BS (▲, △), glucose oxidase (●, ○) or coupling agent followed by glucose oxidase (■, □). The dashed lines represent a  $y/x$  ratio of 1:1.

The experimental concentration ratios ( $C_X/C_{tot}$ ) can be converted into weight percentages of model compounds (Genet et al., 2008, Rouxhet & Genet, 2011), using the carbon concentration specific to each compound (Table 3).

	O/C	N/C	Carbon concent. (mmol.g <sup>-1</sup> )	Density (g.cm <sup>-3</sup> )
<b>Proteins</b>	0.312*	0.273*	43.5	1.4
<b>Silane</b>	0.5	0.333	27.3	0.9
<b>Polysaccharides</b>	0.833	-	37.0	1.5
<b>Hydrocarbons</b>	-	-	71.4	0.9

\* Data computed from the amino acid sequence of glucose oxidase on the basis of ProtParam tool available on the ExPASy molecular biology server (<http://us.expasy.org>).

Table 3. Chemical composition of organic compounds (molar concentration ratio of elements and concentration of carbon) and their densities.

Results, presented in Table 4, show the often dominating presence of hydrocarbon-like compounds and polysaccharides, for all samples. Both compounds are due to adventitious contamination which may originate from adsorption from air, as always observed for high surface energy solids (Caillou et al., 2008; Mantel et al., 1995), but also from aqueous media (Landoulsi et al., 2008a). They may be taken as a global way to reflect the amount of compounds which contain hydrocarbon chains and oxygen, such as esters, but excluding proteins and silane. The concentration of silane deduced for non-silanized samples is non negligible but highly variable, and may also be attributed to contamination. A drastic increase of silane concentration is observed for all silanized samples (Table 4).

	(wt. %)				Thickness (nm)	
	Pr	SI	PS	HC	at $\theta = 0^\circ$	at $\theta = 60^\circ$
<b>nat</b>	2.9	5.8	29.5	61.7	3.6	2.2
<b>+BS</b>	(8.5)	6.1	28.3	57.1	3.2	2.1
<b>+Gox</b>	16.3	0.0	24.7	59.0	3.2	2.3
<b>+BS+Gox</b>	(7.3)	12.3	35.5	44.9	3.3	2.2
<b>sil</b>	0.0	29.0	22.2	48.8	3.8	2.7
<b>sil+BS</b>	(10.8)	25.5	25.2	38.5	3.9	2.8
<b>sil+Gox</b>	35.2	20.0	24.3	20.5	3.9	2.9
<b>sil+BS+Gox</b>	24.4	22.9	22.5	30.2	4.1	2.8

\* The data between brackets are protein equivalent of BS products and have no physical meaning.

Table 4. Chemical composition (weight %) of the organic adlayer present on stainless steel samples, as deduced from XPS data and expressed in terms of classes of molecular compounds\*. Thickness of the organic adlayer deduced from measurements at photoelectron collection angle  $\theta = 0^\circ$  and  $60^\circ$ .

The Gox treatment leads to a marked increase of the protein concentration on nat sample and a much stronger increase on sil sample. This may be attributed to physical adsorption

and to the fact that protonated amine of silane favors adsorption by electrostatic attraction (Jasienak et al., 2009). The pH of the Gox solution (6.8) is indeed higher than the isoelectric point of glucose oxidase (4.9).

In the above computation, the concentration of the BS coupling agent could not be evaluated. The reaction of BS with  $\text{NH}_2$  transforms an amine function into amide. If only one end of BS reacts with silane, the  $N_{400}$  concentration should be doubled, which is consistent with the increase found in Table 2. However, converting it into protein-equivalent gives a number with no physical meaning. When the second end of the coupling agent reacts with the protein, no additional nitrogen is incorporated, the evaluation of the protein concentration is correct but the suberate  $(\text{CH}_2)_6$  chain is counted in the HC concentration. This has no important impact owing to the high concentration of hydrocarbon-like compounds. Despite the limitations regarding the accuracy of the data in Table 4, it is clear that prior silanization increases markedly the concentration of glucose oxidase (sil+Gox and sil+BS+Gox compared to nat+Gox); however the treatment with the coupling agent does not increase the amount of immobilized enzyme (sil+BS+Gox compared to sil+Gox).

### 4.3 State of stainless steel surface

It appears in Table 4 that the SS surface prior to and after silanization or enzyme immobilization is bearing a high amount of organic contaminants. It may be argued that this is due to improper cleaning protocols, inappropriate sample manipulation or contamination in the XPS spectrometer. Actually, a clean stainless steel surface is getting quickly contaminated in contact with the surrounding atmosphere, as revealed by water contact angles, which can be measured quickly in the same environment. A nat sample showed a water contact angle of  $44^\circ$  which increased to about  $60^\circ$  within a delay of a few hours (Figure 10). When a nat sample was further treated with UV-ozone to oxidize organic compounds, the water contact angle was lowered down to  $12^\circ$ . However it increased rapidly in contact with the surrounding atmosphere (Figure 10) to reach values above  $40^\circ$  in a few hours. Similar results were obtained with 304L stainless steel. Wet cleaning essentially standardizes the surface contamination; further cleaning leaves a material with a high surface energy, which adsorbs quickly significant amounts of contaminants (Caillou et al., 2008).

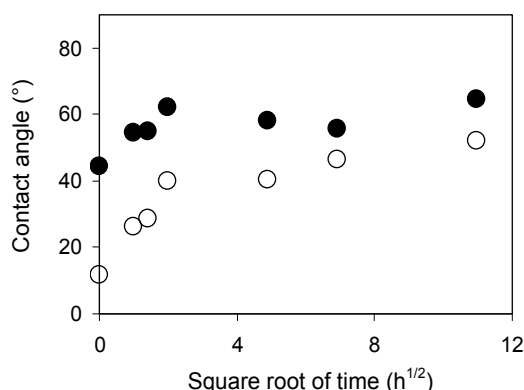


Fig. 10. Contact angle measurements as a function of incubation time in ambient atmosphere performed on (●) native stainless steel and (○) after UV-ozone treatment.

It must be emphasized that outgassing a material of high surface energy is not suitable to prevent adventitious contamination of the surface. Materials cleaned with UV-ozone treatment and showing a water contact angle below 5° reached an appreciable contact angle (20° for silica, 40° for stainless steel and gold) after a stay of 5 minutes in the vacuum of the spectrometer chamber. The high rate of contamination may be due to evacuation itself, owing to the increased proportion of organic compounds in the residual gas and to their increased rate of transfer (Caillou et al., 2008).

#### 4.4. Thickness of the organic adlayer

No variation of the relative concentrations of organic compounds was revealed by angle-resolved XPS analysis (Figure 4) but an effect of stratification may be masked by the surface roughness. The evaluation of the adlayer thickness may clarify whether the increase of the silane or protein concentration resulting from the respective treatments reflects an addition of or a substitution by new compounds in the adlayer.

If the surface is considered as atomically smooth and the organic layer is continuous with a constant thickness, the apparent concentration ratio  $[C]/[Cr]$  may be computed using the following equation:

$$\frac{[C]}{[Cr]} = \frac{i_{Cr} \sigma_c}{i_c \sigma_{Cr}} \frac{\lambda_c^{Org} C_c^{Org} \left[ 1 - \exp\left(\frac{-t}{\lambda_c^{Org} \cos\theta}\right) \right]}{\lambda_{Cr}^{Ox} C_{Cr}^{Ox} \exp\left(\frac{-t}{\lambda_{Cr}^{Ox} \cos\theta}\right)} \quad (8)$$

$i_c$  and  $i_{Cr}$  are the relative sensitivity factors of C and Cr, respectively, provided by the spectrometer manufacturer. The photoionization cross sections  $\sigma$  are 1 for C 1s and 11.7 for Cr 2p (Scofield, 1976). The superscripts Org and Ox designate the organic adlayer and the passive oxide layer, respectively. The concentration of Cr in the oxide layer ( $C_{Cr}^{Ox}$ ; between 0.015 and 0.020 mol.cm<sup>-3</sup>, depending on the sample), was determined on the basis of the above discussion indicating that the oxide layer is constituted with FeOOH, CrOOH, Ni(OH)<sub>2</sub> and MoO<sub>3</sub> (section 4.1). Note that this is in agreement with a concentration of inorganic oxygen close to ( $O_{tot} - O_{org}$ ), owing to the low concentration of silane. The concentration of carbon in the organic adlayer was determined on the basis of the surface composition modeled as detailed above, using the densities given in Table 3. The density of silane, was taken as the average between the densities of 3-aminopropyl(trimethylsilane) (0.8 g.cm<sup>-3</sup>) and 3-aminopropyl(trimethoxysilane) (1.0 g.cm<sup>-3</sup>). The electron inelastic mean free paths (IMFP) were calculated using the Quases program (<http://www.quases.com>) and the TPP2M formula (Tanuma et al., 1997), considering the matrix composition deduced above. For  $\lambda_{Cr}^{Ox}$ , values of 2.04 and 1.99 nm were computed for FeOOH and CrOOH, respectively (energy gap 2.3 and 1.6 eV, respectively). Considering an energy gap of 6 eV for the organic compounds, respective values of  $\lambda_c^{Org}$  and  $\lambda_{Cr}^{Org}$  were 3.79 and 3.04 nm in hydrocarbon-like compounds [(CH<sub>2</sub>)<sub>n</sub>], 3.59 nm and 2.89 nm in protein, 3.67 and 2.00 nm in polysaccharides [(C<sub>6</sub>(H<sub>2</sub>O)<sub>5</sub>)<sub>n</sub>], and 3.68 and 2.95 nm in silane [H<sub>2</sub>N(CH<sub>2</sub>)<sub>3</sub>SiO<sub>1.5</sub>].

The thickness of the organic adlayer deduced for photoelectron collection angles  $\theta = 0^\circ$  and  $60^\circ$  is given in Table 4. The difference between the values computed for the two

photoelectron collection angles is due to the approximation of a smooth surface while the analyzed surface is rough at the scale of the inelastic mean free paths. The real organic adlayer thickness should be between the values given in Table 4. Comparison between nat and sil samples suggests that silane just adds up to the contaminants. A 3.0 nm thick adlayer containing 25 wt.% silane corresponds to 4.5 molecules.nm<sup>-2</sup>. This value is consistent with a monolayer of silane, however the retained silane is mixed with a much larger amount of contaminants. The protein treatment of silanized substrates (compare sil+Gox and sil+BS+Gox to sil) led to a significant decrease of the amount of hydrocarbon-like compounds, while the adlayer thickness did not change appreciably. This suggests that the protein adsorption caused the displacement of part of contamination present on the silanized stainless steel surface in the form of hydrocarbon-like compounds.

## 5. Conclusion

The decomposition of the C 1s and O 1s peak provided a distinct evaluation of oxygen present in inorganic oxide, inorganic hydroxide and organic compounds. This led to a stoichiometry close to (Fe, Cr)OOH for iron and chromium species in the passive layer. The elemental composition of the organic adlayer was converted into concentration of model organic compounds: protein, silane and contaminants. For the latter, extreme poles of hydrocarbons and polysaccharides were taken as models.

Silanization increased markedly the retention of glucose oxidase, whether or not using a linker expected to couple the enzyme with the silane. Direct retention of the enzyme by the silane may be attributed to electrostatic attractions with the protonated amine groups (Jasienak et al., 2009). It is thus demonstrated, with the same biomolecule, that its retention by using an APTES-treated substrate and a linker does not infer covalent grafting through the linker. The occurrence of covalent binding might possibly be evaluated by examining the retention upon aging in electrolytes, keeping in mind that the silane layer itself may alter in these conditions (Dekeyser et al., 2008).

The thickness of the organic adlayer was of the order of 3 nm. In all cases, the concentration of contaminants exceeded the concentration of silane and protein. Angle-resolved measurements did not reveal any stratification in the organic adlayer, but this was not conclusive since the effect of a stratification may be masked owing to the roughness created by nanoparticles of inorganic oxyhydroxide present at the stainless steel surface. The presence of organic contaminants is unavoidable when high energy materials are exposed to air for a few hours or to vacuum for a very short time. However the influence of contaminants on the desired surface reactions is not known and is difficult to establish. The best to reduce contamination is to thoroughly clean the substrate by oxidation, to minimize the time of contact of substrates with air at any stage, and to strictly avoid outgassing. Water contact angle measurement is the best way to assess the cleanliness of the native substrate but the information will not be unambiguous after silanization and further treatments.

## 6. Acknowledgments

The authors thank Simon Degand for his help in statistics. They acknowledge the support of the "Conseil Régional de Picardie" (France) and the National Fondation for Scientific Research (F.N.R.S. - Belgium).

## 7. References

- Ahimou, F., Boonaert, C.J.P., Adriaensen, Y., Jacques, P., Thonart, P., Paquot, M. & Rouxhet, P.G. (2007) XPS analysis of chemical functions at the surface of *Bacillus subtilis*, *Journal of Colloid and Interface Science*, Vol. 309, No. 1, pp. 49-55.
- Asenath Smith, E. & Chen, W. (2008) How To Prevent the Loss of Surface Functionality Derived from Aminosilanes, *Langmuir*, Vol. 24, No. 21, pp. 12405-12409.
- Balasundaram, G., Sato, M. & Webster, T.J. (2006) Using hydroxyapatite nanoparticles and decreased crystallinity to promote osteoblast adhesion similar to functionalizing with RGD, *Biomaterials*, Vol. 27, No. 14, pp. 2798-2805.
- Bartouilh de Taillac, L., Porté-Durrieu, M.C., Labrugère, C., Bareille, R., Amédée, J. & Baquey, C. (2004) Grafting of RGD peptides to cellulose to enhance human osteoprogenitor cells adhesion and proliferation, *Composites Science and Technology*, Vol. 64, No. 6, pp. 827-837.
- Boucher, C., Liberelle, B.t., Jolicoeur, M., Durocher, Y. & De Crescenzo, G. (2009) Epidermal growth factor tethered through coiled-coil interactions induces cell surface receptor phosphorylation, *Bioconjugate Chemistry*, Vol. 20, No. 8, pp. 1569-1577.
- Briggs, D. & Seah, M.P. (1990) *Practical Surface Analysis, Auger and X-ray Photoelectron Spectroscopy* (Chichester, UK, Wiley).
- Caillou, S., Gerin, P.A., Nonckreman, C.J., Fleith, S., Dupont-Gillain, C.C., Landoulsi, J., Pancera, S.M., Genet, M.J. & Rouxhet, P.G. (2008) Enzymes at solid surfaces: Nature of the interfaces and physico-chemical processes, *Electrochimica Acta*, Vol. 54, No. 1, pp. 116-122.
- Charbonneau, C., Liberelle, B., Hébert, M.-J., De Crescenzo, G. & Lerouge, S. (2011) Stimulation of cell growth and resistance to apoptosis in vascular smooth muscle cells on a chondroitin sulfate/epidermal growth factor coating, *Biomaterials*, Vol. 32, No. 6, pp. 1591-1600.
- Cho, Y. & Ivanisevic, A. (2004) SiO<sub>x</sub> Surfaces with lithographic features composed of a TAT peptide, *The Journal of Physical Chemistry B*, Vol. 108, No. 39, pp. 15223-15228.
- Chuang, Y.-J., Huang, J.-W., Makamba, H., Tsai, M.-L., Li, C.-W. & Chen, S.-H. (2006) Electrophoretic mobility shift assay on poly(ethylene glycol)-modified glass microchips for the study of estrogen responsive element binding, *Electrophoresis*, Vol. 27, No. 21, pp. 4158-4165.
- Davis, D.H., Giannoulis, C.S., Johnson, R.W. & Desai, T.A. (2002) Immobilization of RGD to <1 1 1> silicon surfaces for enhanced cell adhesion and proliferation, *Biomaterials*, Vol. 23, No. 19, pp. 4019-4027.
- Dekeyser, C.M., Buron, C.C., Mc Evoy, K., Dupont-Gillain, C.C., Marchand-Brynaert, J., Jonas, A.M. & Rouxhet, P.G. (2008) Oligo(ethylene glycol) monolayers by silanization of silicon wafers: Real nature and stability, *Journal of Colloid and Interface Science*, Vol. 324, No. 1-2, pp. 118-126.
- Doh, J. & Irvine, D.J. (2006) Immunological synapse arrays: Patterned protein surfaces that modulate immunological synapse structure formation in T cells, *Proceedings of the National Academy of Sciences*, Vol. 103, No. 15, pp. 5700-5705.
- Dufrêne, Y.F. & Rouxhet, P.G. (1996) Surface composition, surface properties, and adhesiveness of *Azospirillum brasilense* - variation during growth, *Canadian Journal of Microbiology*, Vol. 42, pp. 548-556.

- Dupont, I., Féron, D. & Novel, G. (1998) Effect of glucose oxidase activity on corrosion potential of stainless steels in seawater, *International Biodeterioration & Biodegradation*, Vol. 41, No. 1, pp. 13-18.
- El-Ghannam, A.R., Ducheyne, P., Risbud, M., Adams, C.S., Shapiro, I.M., Castner, D., Gollidge, S. & Composto, R.J. (2004) Model surfaces engineered with nanoscale roughness and RGD tripeptides promote osteoblast activity, *Journal of Biomedical Materials Research Part A*, Vol. 68A, No. 4, pp. 615-627.
- Genet, M.J., Dupont-Gillain, C.C. & Rouxhet, P.G. (2008) XPS analysis of biosystems and biomaterials, in: M. E. (Ed) *Medical Applications of Colloids* (New York, Springer), pp. 177-307.
- Gooding, J.J. & Ciampi, S. (2011) The molecular level modification of surfaces: from self-assembled monolayers to complex molecular assemblies, *Chemical Society Reviews*, DOI: 10.1039/c0cs00139b.
- Haensch, C., Hoepfner, S. & Schubert, U.S. (2010) Chemical modification of self-assembled silane based monolayers by surface reactions, *Chemical Society Reviews*, Vol. 39, No. 6, pp. 2323-2334.
- Hanawa T. 2002. Metallic biomaterials. In: Ikada Y, editor. Recent research and developments in biomaterials, Research Signpost, p. 11-31.
- Howarter, J.A. & Youngblood, J.P. (2006) Optimization of silica silanization by 3-Aminopropyltriethoxysilane, *Langmuir*, Vol. 22, No. 26, pp. 11142-11147.
- Iucci, G., Dettin, M., Battocchio, C., Gambaretto, R., Bello, C.D. & Polzonetti, G. (2007) Novel immobilizations of an adhesion peptide on the TiO<sub>2</sub> surface: An XPS investigation, *Materials Science and Engineering: C*, Vol. 27, No. 5-8, pp. 1201-1206.
- Jasienak, M., Suzuki, S., Montero, M., Wentrup-Byrne, E., Griesser, H.J. & Grondahl, L. (2009) Time-of-flight secondary ion mass spectrometry study of the orientation of a bifunctional diblock copolymer attached to a solid substrate, *Langmuir*, Vol. 25, No. 2, pp. 1011-1019.
- Jin, L., Horgan, A. & Levicky, R. (2003) Preparation of end-tethered DNA monolayers on siliceous surfaces using heterobifunctional cross-linkers, *Langmuir*, Vol. 19, No. 17, pp. 6968-6975.
- Katsikogianni, M.G. & Missirlis, Y.F. (2010) Interactions of bacteria with specific biomaterial surface chemistries under flow conditions, *Acta Biomaterialia*, Vol. 6, No. 3, pp. 1107-1118.
- Killian, M.S., Wagener, V., Schmuki, P. & Virtanen, S. (2010) Functionalization of metallic magnesium with protein layers via linker molecules, *Langmuir*, Vol. 26, No. 14, pp. 12044-12048.
- Kim, J., Cho, J., Seidler, P.M., Kurland, N.E. & Yadavalli, V.K. (2010) Investigations of chemical modifications of amino-terminated organic films on silicon substrates and controlled protein immobilization, *Langmuir*, Vol. 26, No. 4, pp. 2599-2608.
- Kim, J., Seidler, P., Wan, L.S. & Fill, C. (2009a) Formation, structure, and reactivity of amino-terminated organic films on silicon substrates, *Journal of Colloid and Interface Science*, Vol. 329, No. 1, pp. 114-119.
- Kim, W.-J., Kim, S., Lee, B.S., Kim, A., Ah, C.S., Huh, C., Sung, G.Y. & Yun, W.S. (2009b) Enhanced protein immobilization efficiency on a TiO<sub>2</sub> surface modified with a hydroxyl functional group, *Langmuir*, Vol. 25, No. 19, pp. 11692-11697.



- Koh, I., Wang, X., Varughese, B., Isaacs, L., Ehrman, S.H. & English, D.S. (2006) Magnetic iron oxide nanoparticles for biorecognition: Evaluation of surface coverage and activity, *The Journal of Physical Chemistry B*, Vol. 110, No. 4, pp. 1553-1558.
- Kohli, P., Taylor, K.K., Harris, J.J. & Blanchard, G.J. (1998) Assembly of covalently-coupled disulfide multilayers on gold, *Journal of the American Chemical Society*, Vol. 120, No. 46, pp. 11962-11968.
- Landoulsi, J., Dagbert, C., Richard, C., Sabot, R., Jeannin, M., El Kirat, K. & Pulvin, S. (2009) Enzyme-induced ennoblement of AISI 316L stainless steel: Focus on pitting corrosion behavior, *Electrochimica Acta*, Vol. 54, No. 28, pp. 7401-7406.
- Landoulsi, J., Genet, M.J., Richard, C., El Kirat, K., Pulvin, S. & Rouxhet, P.G. (2008a) Evolution of the passive film and organic constituents at the surface of stainless steel immersed in fresh water, *Journal of Colloid and Interface Science*, Vol. 318, No. 2, pp. 278-289.
- Landoulsi, J., Genet, M.J., Richard, C., El Kirat, K., Rouxhet, P.G. & Pulvin, S. (2008b) Ennoblement of stainless steel in the presence of glucose oxidase: Nature and role of interfacial processes, *Journal of Colloid and Interface Science*, Vol. 320, No. 2, pp. 508-519.
- Landoulsi, J., Kirat, K.E., Richard, C., Féron, D. & Pulvin, S. (2008c) Enzymatic approach in microbial-influenced corrosion: A review based on Stainless Steels in Natural Waters, *Environmental Science & Technology*, Vol. 42, No. 7, pp. 2233-2242.
- Lapin, N.A. & Chabal, Y.J. (2009) Infrared characterization of biotinylated silicon oxide surfaces, surface stability, and specific attachment of streptavidin, *The Journal of Physical Chemistry B*, Vol. 113, No. 25, pp. 8776-8783.
- Le Bozec, N., Compère, C., L'Her, M., Laouenan, A., Costa, D. & Marcus, P. (2001) Influence of stainless steel surface treatment on the oxygen reduction reaction in seawater, *Corrosion Science*, Vol. 43, No. 4, pp. 765-786.
- Li, G., Yang, P., Qin, W., Maitz, M.F., Zhou, S. & Huang, N. (2011) The effect of coimmobilizing heparin and fibronectin on titanium on hemocompatibility and endothelialization, *Biomaterials*, Vol. 32, No. 21, pp. 4691-4703.
- Libertino, S., Giannazzo, F., Aiello, V., Scandurra, A., Sinatra, F., Renis, M. & Fichera, M. (2008) XPS and AFM characterization of the enzyme glucose oxidase immobilized on SiO<sub>2</sub> surfaces, *Langmuir*, Vol. 24, No. 5, pp. 1965-1972.
- Ma, L., Zhou, J., Gao, C. & Shen, J. (2007) Incorporation of basic fibroblast growth factor by a layer-by-layer assembly technique to produce bioactive substrates, *Journal of Biomedical Materials Research Part B: Applied Biomaterials*, Vol. 83B, No. 1, pp. 285-292.
- Mantel, M., Rabinovich, Y.I., Wightman, J.P. & Yoon, R.H. (1995) A Study of Hydrophobic Interactions between Stainless Steel and Silanated Glass Surface Using Atomic Force Microscopy, *Journal of Colloid and Interface Science*, Vol. 170, No. 1, pp. 203-214.
- Martin, H.J., Schulz, K.H., Bumgardner, J.D. & Walters, K.B. (2007) XPS Study on the Use of 3-Aminopropyltriethoxysilane to Bond Chitosan to a Titanium Surface, *Langmuir*, Vol. 23, No. 12, pp. 6645-6651.
- Matinlinna, J., P., Lassila, L., V. J., Özcan, M., Yli-Urpo, A. & Vallittu, P., K. (2004) An introduction to silanes and their clinical applications in dentistry, *International Journal of Prosthodontics*, Vol. 17, No. 211, pp. 155-164.

- Matinlinna, J.P. & Vallittu, P.K. (2007) Silane based concepts on bonding resin composite to metals, *The Journal of Contemporary Dental Practice*, Vol. 8, No. 2, pp. 1-8.
- Meng, S., Liu, Z., Shen, L., Guo, Z., Chou, L.L., Zhong, W., Du, Q. & Ge, J. (2009) The effect of a layer-by-layer chitosan-heparin coating on the endothelialization and coagulation properties of a coronary stent system, *Biomaterials*, Vol. 30, No. 12, pp. 2276-2283.
- Minier, M., Salmain, M.I., Yacoubi, N., Barbes, L., Méthivier, C., Zanna, S. & Pradier, C.-M. (2005) Covalent Immobilization of Lysozyme on Stainless Steel. Interface spectroscopic characterization and measurement of enzymatic activity, *Langmuir*, Vol. 21, No. 13, pp. 5957-5965.
- Mosse, W.K.J., Koppens, M.L., Gengenbach, T.R., Scanlon, D.B., Gras, S.L. & Ducker, W.A. (2009) Peptides grafted from solids for the control of interfacial properties, *Langmuir*, Vol. 25, No. 3, pp. 1488-1494.
- Müller, R., Abke, J., Schnell, E., Macionczyk, F., Gbureck, U., Mehrl, R., Ruszczak, Z., Kujat, R., Englert, C., Nerlich, M. & Angele, P. (2005) Surface engineering of stainless steel materials by covalent collagen immobilization to improve implant biocompatibility, *Biomaterials*, Vol. 26, No. 34, pp. 6962-6972.
- Nanci, A., Wuest, J.D., Peru, L., Brunet, P., Sharma, V., Zalzal, S. & McKee, M.D. (1998) Chemical modification of titanium surfaces for covalent attachment of biological molecules, *Journal of Biomedical Materials Research*, Vol. 40, No. 2, pp. 324-335.
- NIST X-ray Photoelectron Spectroscopy Database, NIST Standard Reference Database 20, Version 3.4 (Web Version), <http://srdata.nist.gov/xps/index.htm>.
- North, S.H., Lock, E.H., Cooper, C.J., Franek, J.B., Taitt, C.R. & Walton, S.G. (2004) Plasma-based surface modification of polystyrene microtiter plates for covalent immobilization of biomolecules, *ACS Applied Materials & Interfaces*, Vol. 2, No. 10, pp. 2884-2891.
- Olefjord, I. & Wegrelius, L. (1996) The influence of nitrogen on the passivation of stainless steels, *Corrosion Science*, Vol. 38, No. 7, pp. 1203-1220.
- Palestino, G., Agarwal, V., Aulombard, R., Peř rez, E.a. & Gergely, C. (2008) Biosensing and protein fluorescence enhancement by functionalized porous silicon devices, *Langmuir*, Vol. 24, No. 23, pp. 13765-13771.
- Pasternack, R.M., Rivillon Amy, S. & Chabal, Y.J. (2008) Attachment of 3-(Aminopropyl)triethoxysilane on silicon oxide surfaces: Dependence on solution temperature, *Langmuir*, Vol. 24, No. 22, pp. 12963-12971.
- Plueddemann, E.W. (1991) *Silane Coupling Agents* (New York, Plenum).
- Porté-Durrieu, M.C., Guillemot, F., Pallu, S., Labrugère, C., Brouillaud, B., Bareille, R., Amédée, J., Barthe, N., Dard, M. & Baquey, C. (2004) Cyclo-(DfKRG) peptide grafting onto Ti-6Al-4V: physical characterization and interest towards human osteoprogenitor cells adhesion, *Biomaterials*, Vol. 25, No. 19, pp. 4837-4846.
- Puleo, D.A. (1997) Retention of enzymatic activity immobilized on silanized Co-Cr-Mo and Ti-6Al-4V, *Journal of Biomedical Materials Research*, Vol. 37, pp. 222-228.
- Quan, D., Kim, Y. & Shin, W. (2004) Characterization of an amperometric laccase electrode covalently immobilized on platinum surface, *Journal of Electroanalytical Chemistry*, Vol. 561, pp. 181-189.
- Ratner B.D., Hoffman A.S., Schoen F.J. & Lemons J.E. (Eds) (2004) *Biomaterials Science: An Introduction to Materials in Medicine* (Academic Press, San Diego, U.S.A., 2d Ed.).

- Rouxhet, P.G. & Genet, M.J. (2011) XPS analysis of bio-organic systems, *Surface and Interface Analysis*. (In press).
- Rouxhet, P.G., Misselyn-Bauduin, A.M., Ahimou, F., Genet, M.J., Adriaensen, Y., Desille, T., Bodson, P. & Deroanne, C. (2008) XPS analysis of food products: toward chemical functions and molecular compounds, *Surface and Interface Analysis*, Vol. 40, No. 3-4, pp. 718-724.
- Sarath Babu, V.R., Kumar, M.A., Karanth, N.G. & Thakur, M.S. (2004) Stabilization of immobilized glucose oxidase against thermal inactivation by silanization for biosensor applications, *Biosensors and Bioelectronics*, Vol. 19, No. 10, pp. 1337-1341.
- Sargeant, T.D., Rao, M.S., Koh, C.-Y. & Stupp, S.I. (2008) Covalent functionalization of NiTi surfaces with bioactive peptide amphiphile nanofibers, *Biomaterials*, Vol. 29, No. 8, pp. 1085-1098.
- Sasou, M., Sugiyama, S., Yoshino, T. & Ohtani, T. (2003) Molecular flat mica surface silanized with methyltrimethoxysilane for fixing and straightening DNA, *Langmuir*, Vol. 19, No. 23, pp. 9845-9849.
- Schuessele, A., Mayr, H., Tessmar, J. & Goepferich, A. (2009) Enhanced bone morphogenetic protein-2 performance on hydroxyapatite ceramic surfaces, *Journal of Biomedical Materials Research Part A*, Vol. 90A, No. 4, pp. 959-971.
- Scofield, J.H. (1976) Hartree-Slater subshell photoionization cross-sections at 1254 and 1487 eV, *Journal of Electron Spectroscopy and Related Phenomena*, Vol. 8, No. 2, pp. 129-137.
- Siperko, L.M., Jacquet, R. & Landis, W.J. (2006) Modified aminosilane substrates to evaluate osteoblast attachment, growth, and gene expression in vitro, *Journal of Biomedical Materials Research Part A*, Vol. 78A, No. 4, pp. 808-822.
- Son, K.J., Ahn, S.H., Kim, J.H. & Koh, W.-G. (2011) Graft copolymer-templated mesoporous TiO<sub>2</sub> films micropatterned with Poly(ethylene glycol) hydrogel: Novel platform for highly sensitive protein microarrays, *ACS Applied Materials & Interfaces*, Vol. 3, No. 2, pp. 573-581.
- Sordel, T., Kermarec-Marcel, F., Garnier-Raveaud, S., Glade, N., Sauter-Starace, F., Pudda, C., Borella, M., Plissonnier, M., Chatelain, F., Bruckert, F. & Picollet-D'hahan, N. (2007) Influence of glass and polymer coatings on CHO cell morphology and adhesion, *Biomaterials*, Vol. 28, No. 8, pp. 1572-1584.
- Subramanian, A., Kennel, S.J., Oden, P.I., Jacobson, K.B., Woodward, J. & Doktycz, M.J. (1999) Comparison of techniques for enzyme immobilization on silicon supports, *Enzyme and Microbial Technology*, Vol. 24, No. 1-2, pp. 26-34.
- Suzuki, N. & Ishida, H. (1996) A review on the structure and characterization techniques of silane/matrix interphases, *Macromolecular Symposia*, Vol. 108, No. 1, pp. 19-53.
- Suzuki, S., Whittaker, M.R., Grøndahl, L., Monteiro, M.J. & Wentrup-Byrne, E. (2006) Synthesis of soluble phosphate polymers by RAFT and their in vitro mineralization, *Biomacromolecules*, Vol. 7, No. 11, pp. 3178-3187.
- Tanuma, S., Powell, C.J. & Penn, D.R. (1997) Calculations of electron inelastic mean free paths (IMFPs) VI. Analysis of the gries inelastic scattering model and predictive IMFP equation, *Surface and Interface Analysis*, Vol. 25, No. 1, pp. 25-35.
- Tesson, B., Genet, M.J., Fernandez, V., Degand, S., Rouxhet, P.G. & Martin-Jézéquel, V. (2009) Surface chemical composition of diatoms, *ChemBioChem*, Vol. 10, No. 12, pp. 2011-2024.

- Toworfe, G.K., Bhattacharyya, S., Composto, R.J., Adams, C.S., Shapiro, I.M. & Ducheyne, P. (2009) Effect of functional end groups of silane self-assembled monolayer surfaces on apatite formation, fibronectin adsorption and osteoblast cell function, *Journal of Tissue Engineering and Regenerative Medicine*, Vol. 3, No. 1, pp. 26-36.
- Toworfe, G.K., Composto, R.J., Shapiro, I.M. & Ducheyne, P. (2006) Nucleation and growth of calcium phosphate on amine-, carboxyl- and hydroxyl-silane self-assembled monolayers, *Biomaterials*, Vol. 27, No. 4, pp. 631-642.
- Vaidya, A.A. & Norton, M.L. (2004) DNA attachment chemistry at the flexible silicone elastomer surface: Toward disposable microarrays, *Langmuir*, Vol. 20, No. 25, pp. 11100-11107.
- Weetall, H.H. (1993) Preparation of immobilized proteins covalently coupled through silane coupling agents to inorganic supports. *Applied Biochemistry and Biotechnology*, Vol. 41, No. 157, pp. 157-188.
- Weng, Y.J., Hou, R.X., Li, G.C., Wang, J., Huang, N. & Liu, H.Q. (2008) Immobilization of bovine serum albumin on TiO<sub>2</sub> film via chemisorption of H<sub>3</sub>PO<sub>4</sub> interface and effects on platelets adhesion, *Applied Surface Science*, Vol. 254, No. 9, pp. 2712-2719.
- Williams, R. (2010) *Surface Modifications of Biomaterials: Methods Analysis and Applications* (Woodhead Publishing Ltd).
- Wink, T., van Zuilen, S.J., Bult, A. & van Bennekom, W.P. (1997) Self-assembled monolayers for biosensors. *Analyst*, Vol 122, pp. 43R-50R
- Xiao, S.J., Textor, M., Spencer, N.D., Wieland, M., Keller, B. & Sigrist, H. (1997) Immobilization of the cell-adhesive peptide Arg-Gly-Asp-Cys (RGDC) on titanium surfaces by covalent chemical attachment, *Journal of Materials Science: Materials in Medicine*, Vol. 8, No. 12, pp. 867-872.
- Xie, Y., Hill, C.A.S., Xiao, Z., Militz, H. & Mai, C. (2010) Silane coupling agents used for natural fiber/polymer composites: A review, *Composites Part A: Applied Science and Manufacturing*, Vol. 41, No. 7, pp. 806-819.
- Yoshioka, T., Tsuru, K., Hayakawa, S. & Osaka, A. (2003) Preparation of alginic acid layers on stainless-steel substrates for biomedical applications, *Biomaterials*, Vol. 24, No. 17, pp. 2889-2894.
- Zhou, G.-T., Yao, Q.-Z., Wang, X. & Yu, J.C. (2006) Preparation and characterization of nanoplatelets of nickel hydroxide and nickel oxide, *Materials Chemistry and Physics*, Vol. 98, No. 2-3, pp. 267-272.
- Zile, M.A., Puckett, S. & Webster, T.J. Nanostructured titanium promotes keratinocyte density, *Journal of Biomedical Materials Research Part A*, Vol. 97A, No. 1, pp. 59-65.

# Human Dentin as Novel Biomaterial for Bone Regeneration

Masaru Murata<sup>1</sup>, Toshiyuki Akazawa<sup>2</sup>, Masaharu Mitsugi<sup>3</sup>,  
In-Woong Um<sup>4</sup>, Kyung-Wook Kim<sup>5</sup> and Young-Kyun Kim<sup>6</sup>

<sup>1</sup>*Health Sciences University of Hokkaido,*

<sup>2</sup>*Hokkaido Organization,*

<sup>3</sup>*Takamatsu Oral and Maxillofacial Surgery*

<sup>4</sup>*Tooth Bank Co. Ltd,*

<sup>5</sup>*Dankook University,*

<sup>6</sup>*Seoul National University Bundang Hospital,*

<sup>1,2,3</sup>*Japan*

<sup>4,5,6</sup>*Korea*

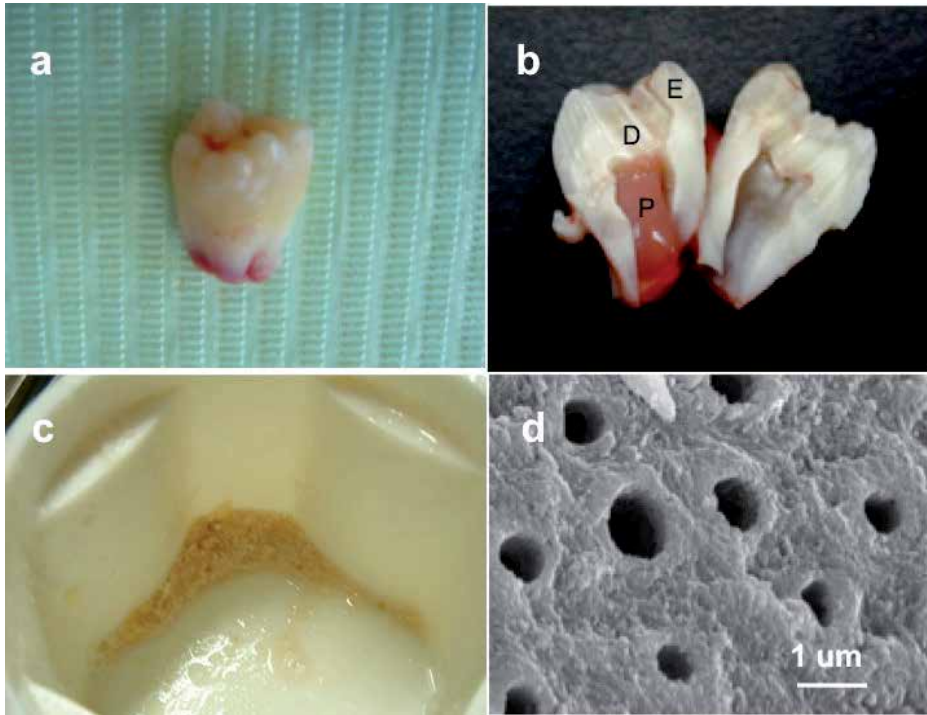
## 1. Introduction

Human dentin autograft was reported in 2003 as a first clinical case (Murata et al., 2003), while human bone autograft was done in 1820. There was a long-long time lag between the autografts of dentin and bone. In 2009, Korea Tooth Bank was established in Seoul for the processing of the tooth-derived materials in Seoul, and an innovative medical service has begun for bone regeneration. Recently, the tooth-derived materials have been becoming a realistic alternative to bone grafting.

The regeneration of lost-parts of the skeleton has been generally carried out with fresh, autogenous bone as a gold standard. To obviate the need for harvesting of grafts and thus, to avoid morbidity resulting from it, the researches for bone substitutes (Kuboki et al., 1995; Asahina et al., 1997; Takaoka et al., 1991; Artzi et al., 2004; Kim et al., 2010) or bone production via bio-engineering have begun (Wozney et al., 1988; Wang et al., 1990; Murata et al., 1999). In the regenerative field, there is a medical need for biomaterials that both allow for bone formation and also gradually absorb as to be replaced by bone. Non-absorbable materials are never replaced by bone and thus, reveal chronic inflammation in tissues as foreign bodies.

As bone and dentin consist of fluid (10%), collagen (20%) and hydroxyapatite (70%) in weight volume, our attention for biomaterials is collagenous and ceramic materials (Murata et al., 2000; Murata et al., 2002; Akazawa et al., 2006; Murata et al., 2007). Generally, extracted teeth have been discarded as infective medical dusts in the world. We have thought the non-functional teeth as native resource for self and family (Fig. 1). Therefore, we noticed on bone-inductive, absorbable properties of dentin, and have been studying a medical recycle of human teeth as a novel graft material for bone regeneration in Japan and Korea (Akazawa et al. 2007; Kim et al. 2010). Biomaterial science should support and develop the advanced regenerative therapy using enamel and dentin matrix for patients in the near future.

In this chapter, human dentin will be introduced as novel biomaterial and also as carrier matrix of the recombinant human bone morphogenetic protein-2 (BMP-2) delivery for bone engineering.



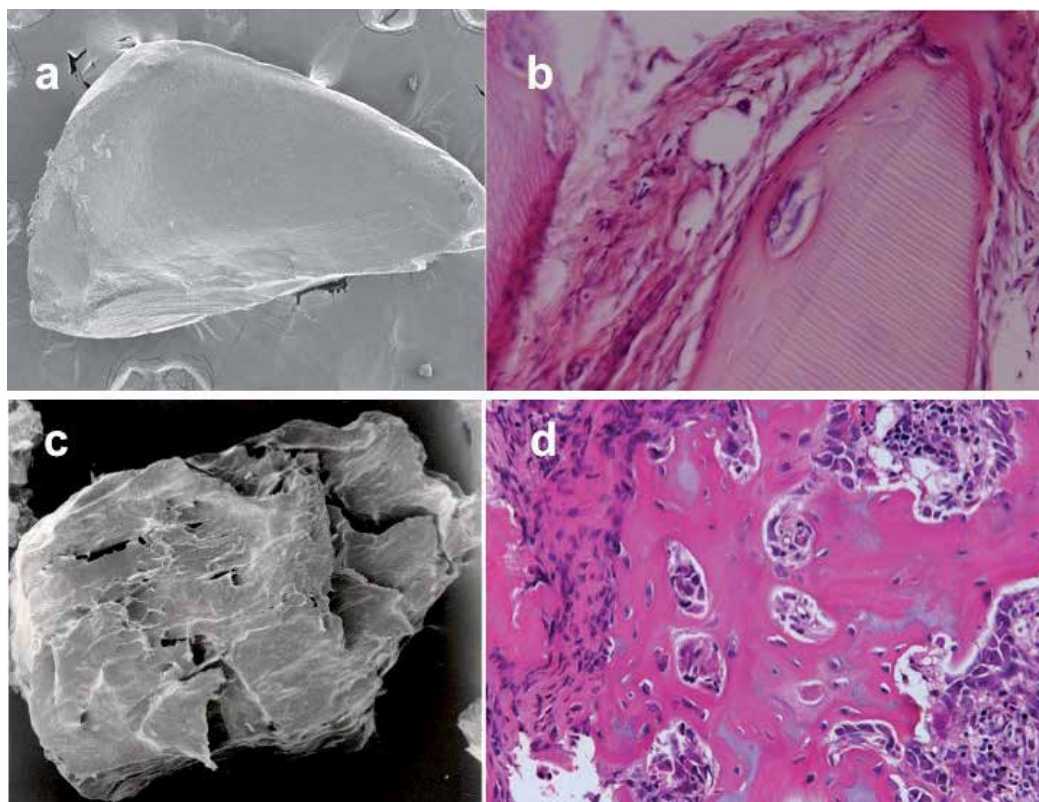
a: whole appearance of molar.  
 b: divided tooth (E; enamel, D; dentin, P; pulp).  
 c: crushed tooth granules.  
 d: SEM photograph of calcified dentin after crushing and washing. Note; dentinal tubes

Fig. 1. Human wisdom tooth

## 2. Bone induction of human dentin

In 1967, bone-inducing property in rabbit dentin was confirmed in the intramuscular pockets (Yeoman & Urist, 1967; Bang & Urist, 1967), after the discovery of bone induction by rabbit demineralized bone matrix (DBM) in 1965 (Urist, 1965). The rabbit studies reported that completely demineralized dentin matrix (DDM) induced bone at 4 weeks, while non-demineralized dentin (so-called, calcified dentin) induced bone at 8-12 weeks after implantation (Yeoman & Urist, 1967). In our study, human DDM including small patches of cementum derived from wisdom teeth, and human DBM derived from adult femur induced bone and cartilage independently in the subcutaneous tissues at 4 weeks (Murata et al., 2010a). The delayed inductive properties of the calcified dentin and bone may be related to the inhibition of BMP-release by the apatite crystals. Highly calcified tissues such as cortical bone and dentin are not earlier in osteoinduction and bone formation than spongy bone, decalcified bone (DBM), and decalcified dentin (DDM) (Huggins et al., 1970).

Dentin and bone are mineralized tissues and almost similar in chemical components. Both DDM and DBM are composed of predominantly type I collagen (95%) and the remaining as non-collagenous proteins including small amount of growth factors (Finkelman et al., 1990). In other words, DDM and DBM can be defined as acid-insoluble collagen binding bone morphogenetic proteins (BMPs), which are member of transforming growth factor-beta (TGF- $\beta$ ) super-family. BMPs were discovered from bone matrix (Urist, 1965; Sampath & Reddi., 1983), and had bone-inducing property in non-skeletal site (Murata et al., 1998). Animal dentin-derived BMPs were extracted with 4M guanidine HCl, and partially purified from rat, rabbit, and bovine (Butler et al., 1977; Urist & Mizutani, 1982; Kawai & Urist, 1989; Bessho et al, 1990). In addition, the concentration of TGF- $\beta$ , Insulin growth factor-I (IGF-I) and Insulin growth factor-II (IGF-II) were detected in human dentin (DDM). Briefly, the three growth factors were measured in the following concentration (ng/ $\mu$ g 4M guanidine hydrochloride-EDTA protein): TGF- $\beta$  (0.017), IGF-I (0.06) and IGF-II (0.52). All 3 growth factors were present in concentrations lower than that in human bone (Finkelman et al., 1990). Recently, both mature and immature types of BMP-2 were detected in human dentin and dental pulps (Ito et al., 2008).



a: SEM of DDM (granule size: 0.5mm), Note: smooth surface and no crack.

b: bone induction by DDM at 4 weeks.

c: SEM of DBM (granule size: 0.5mm), Note: micro-cracks and spaces of blood vessels.

d: bone induction by DBM at 4 weeks.

Fig. 2. Dematerialized dentin matrix (DDM) and dematerialized bone matrix (DBM)

Even after the demineralization of dentin, active types of BMPs bind collagen-rich matrices, similar to bone (Urist et al., 1973). The decalcified dentin (DDM) was known to be more active bone-inducing matrix than the calcified dentin (Yeoman & Urist, 1967), and roll type of decalcified dentin membrane revealed better activity of bone induction (Inoue et al., 1986).

Very interestingly, the demineralized treatment for bone and dentin increased their osteoinductivity and decreased their antigenicity (Reddi, 1974). These facts are scientifically very important for the processing procedures of hard tissue-derived graft materials (Kim et al., 2010; Murata et al., 2010a).

The acid-insoluble dentin matrix (DDM) after demineralization is an organic, absorbable material with original dentin structures. Human DDM, prepared from vital teeth-origin, were implanted into the subcutaneous tissue in 4 week-old nude mice, deficient in immunogenic reactions. The DDM induced bone and cartilage independently at 4 weeks after the subcutaneous implantation, similar to human DBM (Murata et al., 2010b). The independent differentiation of bone and cartilage was compatible to our previous study using ceramic and collagen combined with BMPs (Murata et al., 1998). The acid-insoluble collagen, DBM and DDM, possess the ability to coagulate platelet-free heparinized, citrated, and oxalated blood plasmas (Huggins & Reddi., 1973). Clotting constituents become denatured in contact with the insoluble coagulant proteins. The coagulation action of blood plasma by DBM and DDM should become advantageous for surgical operations. Collagenous materials has been commercially available as medical uses for more 30 years.

### **3. Clinical study of human dentin**

#### **3.1 Case 1: Bone augmentation, 48 year-old man**

First clinical study was reported at 81st IADR conference, Sweden in 2003 that DDM autograft had succeeded for bone augmentation (Murata et al., 2003).

The aim of this pioneering study is to observe new bone formation in the tissues obtained from the dental implant-placed region after the DDM graft for sinus lifting.

#### **Patient**

A 48-year-old male presented with missing teeth (#24-#26, #45-#47). Clinical examinations revealed an atrophied upper jaw in the region (Fig. 3,4). His medical history was unremarkable.

#### **Surgical procedure 1**

Four teeth (#17,#18,#25,#28) were extracted and 2 molars (#17,#18) were stocked at -80°C for DDM. His right occlusion was restored using dental implants as the first clinical step (Fig. 4b).

#### **Preparations of DDM**

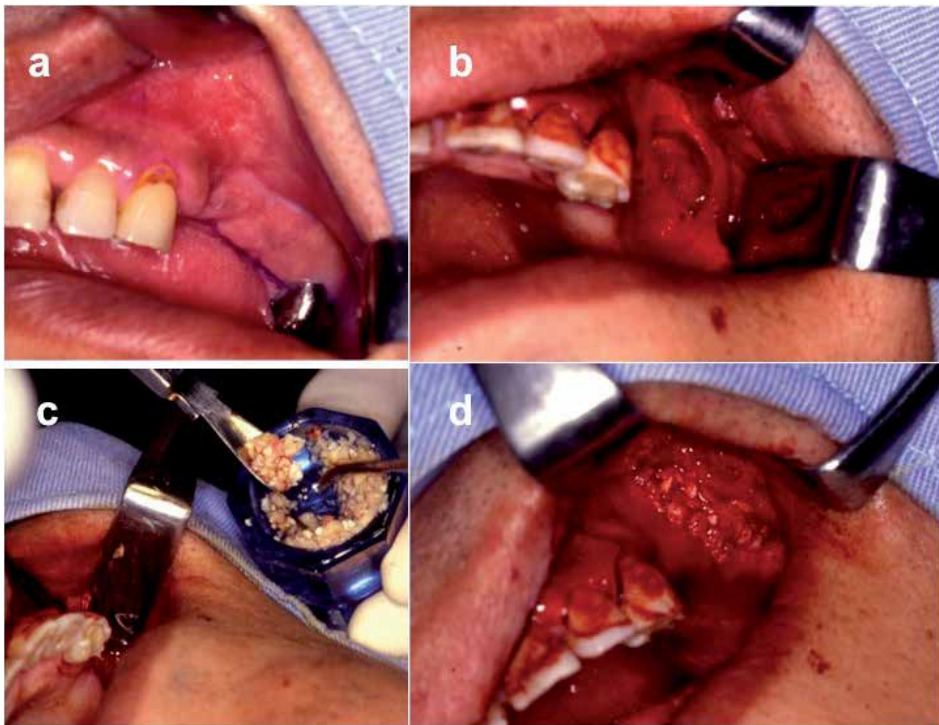
The autogenous DDM were obtained from non-functional vital teeth (#17, #18) (Fig. 4a). The molars were crushed by hand-made under the cooling with liquid nitrogen. The crushed tooth granules were decalcified completely in 0.6N HCl solution. The DDM granules including cementum were extensively rinsed in cold distilled water, and then freeze-dried (Murata et al., 2010a).

#### **Surgical procedure 2**

Sinus lifting procedure was done using autogenous dry DDM for bone augmentation (Fig. 3). At 5 months after the operation, 3 fixtures (FLIALIT-2®, FRIADENT) were implanted



into the augmented bone under local anesthesia (Fig. 4c). At the same time, bone biopsy was carried out for the tissue observation (Fig. 4d).



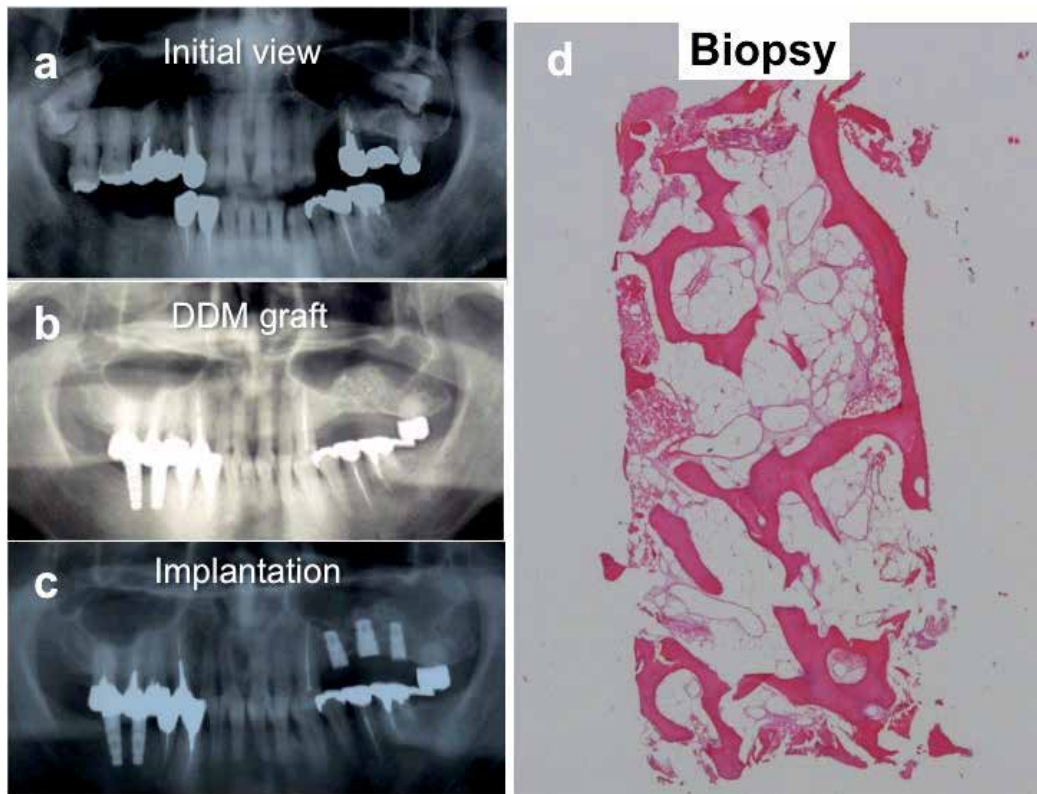
a: intraoral initial view (before operation), Note: 3 missing teeth and atrophied maxilla.

b: oval shaped window

c: autogenous DDM derived from 2 molars

d: view just after DDM autograft

Fig. 3. Case 1: DDM autograft for sinus lifting, 48 year-old man



a: initial view, b: 4 months after DDM graft, c: dental implant placement, d: mature bone with marrow

Fig. 4. X-ray photography and bone biopsy

### Results and discussion

The biopsy tissue showed that mature bone was interconnected with the remained DDM granules (Fig. 4d). We found that DDM facilitated its adaption of the grafted site and was slowly absorbed as new bone began to form.

### Conclusion

This patient was successfully restored with the dental implants after the DDM autograft. These results demonstrated that autogenous dentin could be recycled as an innovative biomaterial.

### 3.2 Case 2: Bone regeneration, 58 year-old woman

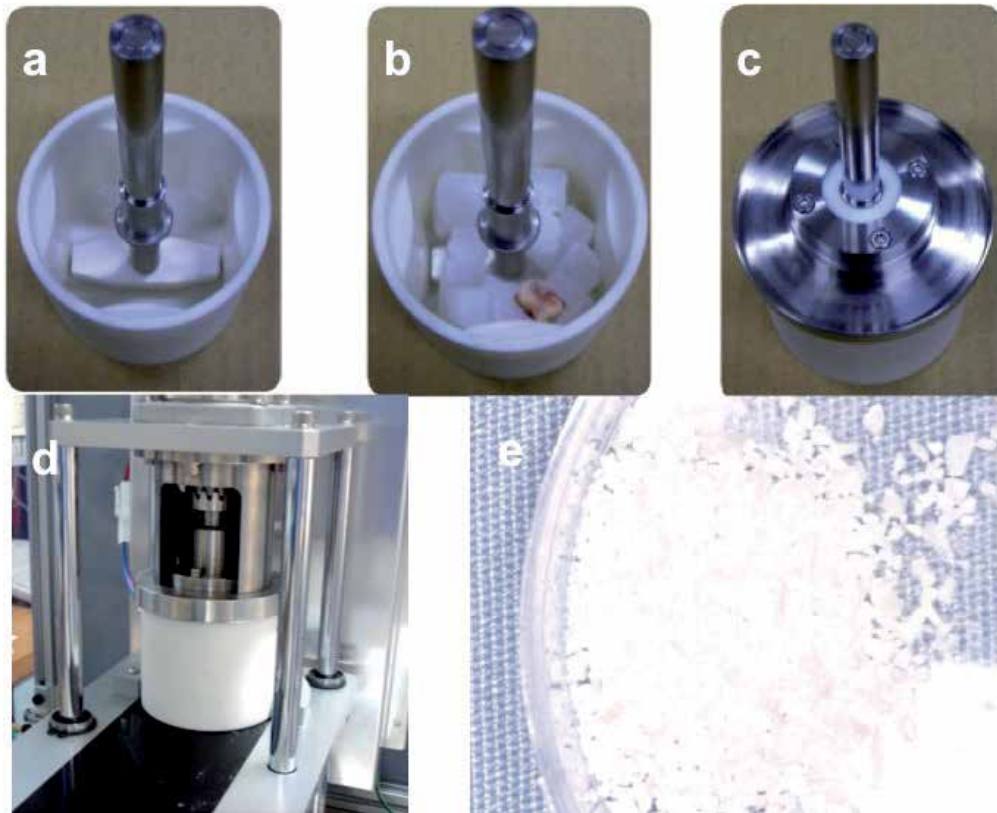
#### Patient

A 58-year-old female presented with missing teeth (#12-#22). A clinical examination revealed an atrophied upper jaw in the section. Her medical history was unremarkable.

#### Preparations of DDM

The autogenous DDM were obtained from a non-functional vital tooth (#17). The second molar was crushed with saline ice by our newly developed tooth-mill (DENTMILL®, Tokyo Iken Co., Ltd) at 12000rpm for 30 sec (Fig. 5). Briefly, vessel and blade were made in ZrO<sub>2</sub>,

which have gained the approval of Food and Drug Administration (FDA) for human use. The  $ZrO_2$  ceramics were fabricated by sintering at  $1400^\circ C$  for 2 h after the slip casting of the mixture of  $ZrO_2$  powder and distilled water (Fig. 5a). As the results of characteristics analyses of  $ZrO_2$  objects, the contraction rate, the relative density, and the bending strength were 21%, 99%, and 400MPa, respectively. The automatic mill could crush a tooth and/or a cortical bone block ( $1 \times 1 \times 1 cm^3$ ) under the condition of cooling using saline ice blocks ( $1 cm^3$ ) (Fig. 5b). The crushed tooth granules were decalcified completely in 0.026N  $HNO_3$  solution for 20 min. The DDM granules including cementum were extensively rinsed in cold distilled water (Fig. 5e), (Murata et al., 2009; Murata et al., 2010a).



a:  $ZrO_2$  vessel and blade, b: tooth with ice blocks, c: stainless cover, d: mill, e: DDM granules before clinical use.

Fig. 5. Preparation of DDM using automatic tooth mill (DENTMILL®, Tokyo Iken)

### Surgical procedure

Splitting osteotomy and cortical perforations were performed in the atrophied jaw and the autogenous DDM were transplanted to the treated bone in 2006 (Fig. 6a,b,c). At 4 months after the operation, 3 same fixtures (Synchro-stepped screw type: diameter; 3.4mm, length; 11mm, FLIALIT-2®, FRIADENT) were implanted into the augmented bone under local anesthesia (Fig. 6b). At the same time, bone biopsy was carried out for the tissue observation.

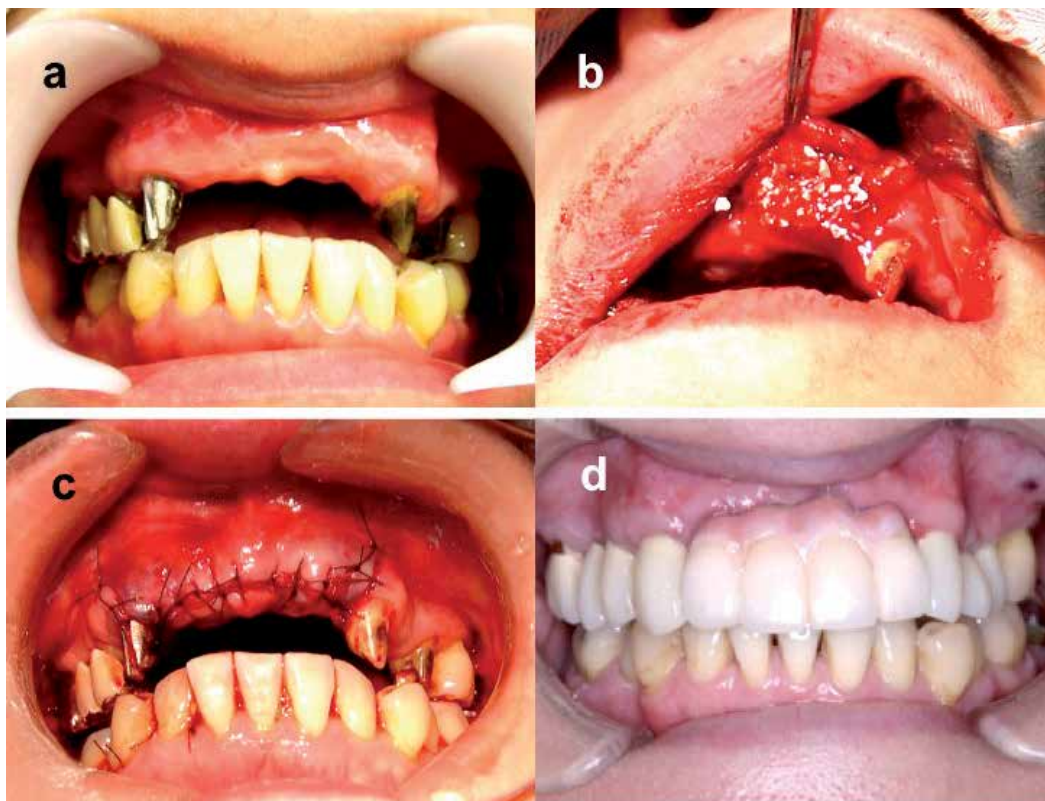
## Results and discussion

The biopsy tissue showed that DDM granules were received to host and the biological width (4-6mm) was acquired. The DDM residues were partially observed during the implant placement. Bone biopsy revealed the DDM were remodeled by bone at 4 months. This patient was successfully restored with the dental implants after the DDM autograft (Fig. 6d). Though animal-derived atelocollagens have been generally used as medical materials, autogenous decalcified dentin is a highly insoluble collagenous matrix and a safe biomaterial.

## Conclusion

Human DDM granules from vital teeth are collagenous matrices with osteoinductive potency, and the human dentin can be recycled as autogenous biomaterials for local bone engineering.

Case 1 and 2 were approved by the Ethical Committee in the Health Sciences University of Hokkaido. All subjects enrolled in this research have responded to an Informed Consent which has been approved by my Institutional Committee on Human Research and that this protocol has been found acceptable by them.



a: 4 missing teeth and atrophied upper maxilla b: DDM autograft before suture c: just after operation d: final view after prosthetic restoration using dental implantation

Fig. 6. Case 2: Bone regeneration, 58 year-old woman

## 4. Dentin scaffold for recombinant human BMP-2

### 4.1 Recombinant human BMP products

BMP-2, 4, and 7 are strong accelerating factors of bone induction. Currently, BMP-2 and BMP-7 have been shown in clinical studies to be beneficial in the therapy of a variety of bone-related conditions including delayed union and non-union. BMP-2 (Medtronic Co.Ltd.) and BMP-7 (Stryker Biotech Co.Ltd.) have received Food and Drug Administration (FDA) approval for human clinical uses (fractures of long bones, inter-vertebral disk regeneration), by delivery in purified collagen matrix or ceramics. Moreover, the BMP-2 product has been approved for certain dental applications. BMP-7 has also found use in the treatment of chronic kidney disease. In 2002, Curis licensed BMP-7 to Ortho Biotech Products, a subsidiary of Johnson & Johnson.

### 4.2 Acceleration of bone induction by BMP2 in human DDM scaffold

The aim of the following study was to estimate the increase of the bone-inductive potency by DDM combined with BMP-2 in rat subcutaneous tissues.

#### Composition of BMP-2 solution and DDM

One hundred micro-liter of recombinant human BMP-2 solution (0.0, 0.5, 1.0, 2.0, 5.0 $\mu$ g of BMP-2) was mixed with 70 mg of human DDM in a sterilized syringe. The composite was called as the BMP-2/DDM. The DDM alone with 100 $\mu$ l of PBS was also prepared as a BMP-free control.

#### Bioassay in rats

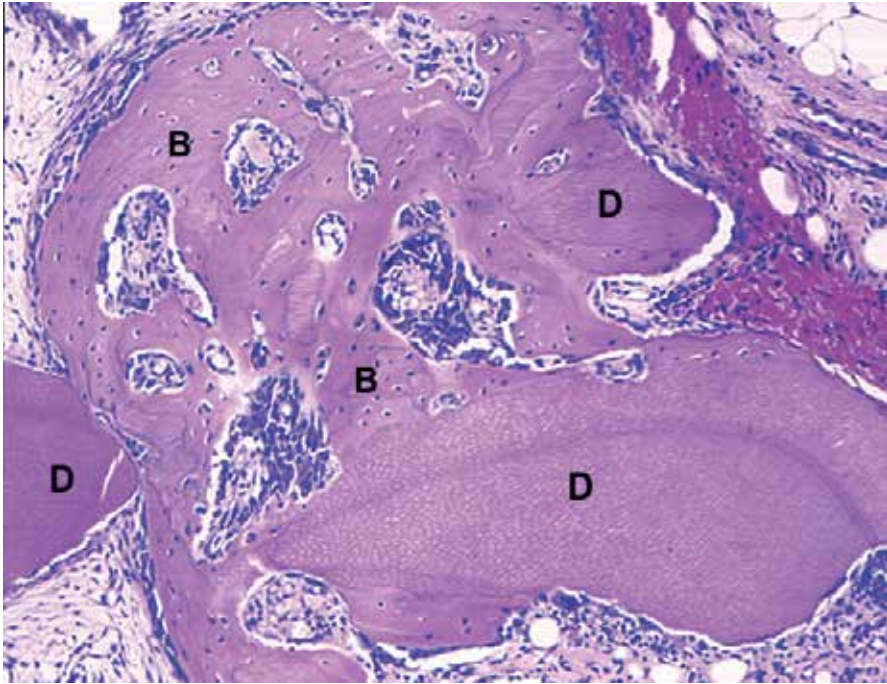
Wistar rats (male, 4 week-old) were subjected to intraperitoneal anesthesia and incisions were added to the back skin under the sterile conditions. Each animal received three BMP-containing composites (BMP-2/DDM) and one BMP-free control (DDM alone). The implanted materials were removed at 3 weeks after implantation, and prepared for histomorphological examinations. All procedures were followed the Guidelines in Health Sciences University of Hokkaido for Experiments on Animals.

#### Histological findings and Morphometric analysis at 3 weeks

In the BMP-2 (5.0 $\mu$ g)/DDM (70mg) group, bone with hematopoietic bone marrow developed extensively at 3 weeks. Chondrocytes were found only in the BMP-2 (0.5, 1.0 $\mu$ g)/DDM groups (Table 1). The BMP-2 (2.0, 5.0 $\mu$ g)/DDM groups accelerated bone induction predominantly (Fig. 7). In the DDM alone group, mesenchymal tissue was seen between DDM particles, and hard tissue induction was not observed at 3 weeks (Fig. 8). Morphometric analysis demonstrated that the volume of the induced bone and marrow increased at BMP-2 dose-dependent manner, while the DDM decreased at the dose-dependent (Table 1). Briefly, the volume of the bone and marrow in BMP-2 (1.0 $\mu$ g)/DDM and BMP-2 (5.0 $\mu$ g)/DDM showed 3.7% and 26.3%, respectively. BMP-2 (0.5 $\mu$ g)/DDM showed 0.0% and 4.0% in the volume of bone and cartilage, respectively.

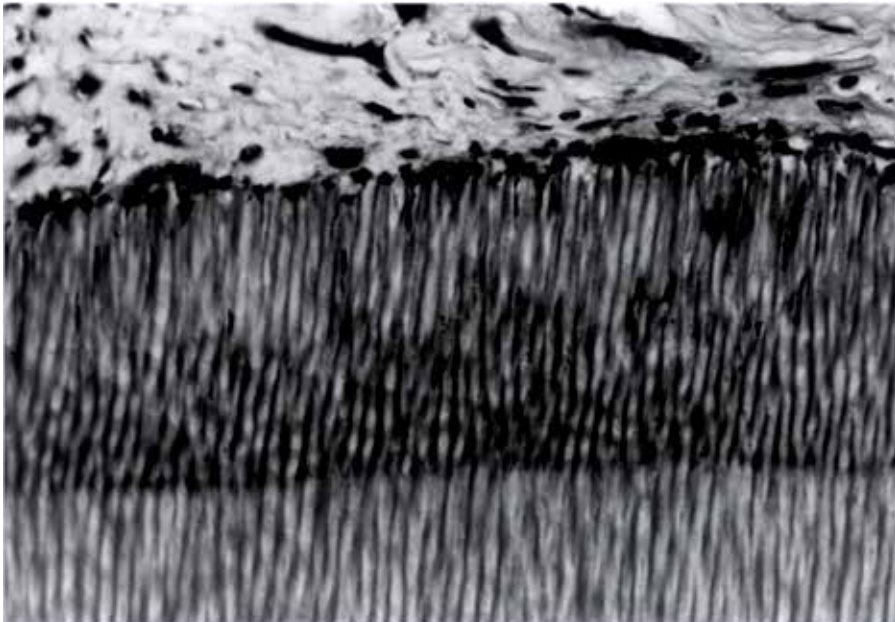
#### Conclusion

BMP-2 strongly accelerated bone formation in the DDM carrier system. DDM never inhibited BMP-2 activity and revealed better release profile of BMP-2. These results indicate that human recycled DDM are unique, absorbable matrix with osteoinductivity and the DDM should be an effective graft material as a carrier of BMP-2 delivering and a scaffold for bone-forming cells for bone engineering.



Induced bone (B) bridging between DDM (D) granules. Note: active osteoblast differentiation.

Fig. 7. Photograph in BMP-2 (5.0 $\mu$ g)/DDM (70mg) at 3 weeks



Fibroblasts on surface of DDM granule with original dentinal tubes.

Fig. 8. Photograph in DDM (70mg) alone at 3 weeks

	Dose of BMP-2 ( $\mu\text{g}$ )				
	0	0.5	1	2	5
bone	0	0	$3.7 \pm 1.41$	$7.4 \pm 0.94$	$20.3 \pm 4.64$
cartilage	0	$4.0 \pm 0.81$	$2.3 \pm 0.47$	0	0
bone marrow	0	0	0	0	$6.0 \pm 1.63$
DDM	$57.0 \pm 0.81$	$43.3 \pm 3.39$	$41.0 \pm 2.16$	$40.3 \pm 1.69$	$37.0 \pm 0.81$
mesenchymal tissue	$40.7 \pm 0.94$	$49.0 \pm 5.09$	$48.0 \pm 3.85$	$46.0 \pm 2.16$	$32.7 \pm 5.73$
connective tissue	$2.3 \pm 0.47$	$3.7 \pm 1.24$	$5.0 \pm 0.47$	$6.3 \pm 0.47$	$4.0 \pm 0.81$
All tissue: 100 % , values: mean $\pm$ SD , N: 9, Explanted time: 3 weeks					

The volume of bone and marrow showing a dose-dependent increase.

The volume of DDM showing a dose-dependent decrease.

Table 1. Morphometry of BMP-2 dose-dependent study.

## 5. Material science for patients in the near future

Biomaterials have had a major impact on the regenerative medicine and patient care for improving the quality of lives of human.

We have been challenging to be able to develop bioabsorbable materials, harmonized with living body, especially bone remodelling, using an innovative supersonic and acid-etching technology (Akazawa et al. 2010). Implanted biomaterials first contact to body fluid and cells. Human cells never live in dry condition. Generally, organ and tissue have interconnected porous structure for dynamic flow of body fluid. Material walls inhibit the body fluid permeation and the cell invasion. Therefore, we focused on the permeability of body fluid into the bulk of materials and the biomimetic structure for the living and working cells (Murata et al., 2007). Body fluid can permeate into collagenous materials such as DDM and DBM. Novel DDM material contains native growth factors, and adsorbs several proteins derived from body fluid. In addition, DDM with RGD sequences supports mesenchymal cell adhesion as anchorage matrix.

Most importantly, material scientists, engineers, and doctors must work together and cooperate as professionals for the development of functional materials and for the present and future of all patients.

## 6. References

- Akazawa, T., Murata, M., Sasaki, T., Tazaki, J., Kobayashi, M., Kanno, T., Matsushima, K., Itabashi, K., & Arisue, M. (2005). Bio-absorption and osteoinduction innovation of bone morphogenetic protein-supported functionally graded apatites originated from cattle bone. *J Am Ceram Soc*, 88.,12., 3545-3548.
- Akazawa, T., Murata, M., Sasaki, T., Tazaki, J., Kobayashi, M., Kanno, T., Matsushima, K., & Arisue, M. (2006). Biodegradation and bioabsorption innovation of the functionally graded cattle-bone-originated apatite with blood compatibility. *J Biomed Mater Res*, 76A., 1., 44-51.
- Akazawa, T., Murata, M., Hino, J., Nakamura, K., Tazaki, J., Kikuchi, M., & Arisue, M. (2007). Materials design and application of demineralized dentin/apatite composite granules derived from human teeth. *Archives of Bioceramics Research*, 7., 25-28.

- Akazawa, T., Murata, M., Takahata, M., Xianjun, D., Abe, Y., Nakamura, K., Hino, J., Tazaki, J., Ito, K., Ito, M., Iwasaki, N., Minami, A., Nakajima, T., & Sakamoto, M. (2010). Characterization of microstructure and bio-absorption of the hydroxyapatite ceramics modified by a partial dissolution-precipitation technique using supersonic treatment. *Journal of the Ceramic Society of Japan*, 118., 6., 535-540.
- Asahina, I., Watanabe, M., Sakurai, N., Mori, M., & Enomoto, S. (1997). Repair of bone defect in primate mandible using a bone morphogenetic protein (BMP)-hydroxyapatite-collagen composite. *J Med Dent Sci.*, 44., 3., 63-70.
- Artzi, Z., Weinreb, M., Givol, N., Rohrer, MD., Nemcovsky, CE., Prasad, HS., & Tal, H. (2004). Biomaterial resorption rate and healing site morphology of inorganic bovine bone and beta-tricalcium phosphate in the canine: a 24-month longitudinal histologic study and morphometric analysis. *Int J Oral Maxillofac Implants.*, 19., 3., 357-368.
- Bang, G. & Urist, MR. (1967). Bone induction in excavation chambers in matrix of decalcified dentin. *Arch Surg*, 94., 6., 781-789.
- Bessho, K., Tagawa, T., & Murata, M. (1990). Purification of rabbit bone morphogenetic protein derived from bone, dentin, and wound tissue after tooth extraction. *J Oral Maxillofac Surg*, 48., 162-169.
- Butler, WT., Mikulski, A., Urist, MR., Bridges, G., & Uyeno, S. (1977). Noncollagenous proteins of a rat dentin matrix possessing bone morphogenetic activity. *J Dent Res*, 56., 228-232.
- Finkelman, RD., Mohan, S., Jennings, JC., Taylor, AK., Jepsen, S., & Baylink, DJ. (1990). Quantitation of growth factors IGF-I, SGF/IGF-II, and TGF-beta in human dentin. *J Bone Miner Res.*, 5., 7., 717-23.
- Huggins, C., Wiseman, S., & Reddi, AH. (1970). Transformation of fibroblasts by allogeneic and xenogeneic transplants of demineralized tooth and bone. *J Exp Med*, 132., 1250-1258.
- Huggins, CB., & Reddi, AH. (1973). Coagulation of blood plasma of guinea pig by the bone matrix. *Proc Natl Acad Sci U S A.*, 70., 3., 929-33.
- Inoue, T., Deporter, DA., & Melcher, AH. (1986). Induction of chondrogenesis in muscle, skin, bone marrow, and periodontal ligament by demineralized dentin and bone matrix in vivo and in vitro. *J Dent Res*, 65., 12-22.
- Ito, K., Arakawa, T., Murata, M., Tazaki, J., Takuma, T., & Arisue, M. (2008). Analysis of bone morphogenetic protein in human dental pulp tissues. *Archives of Bioceramics Research*, 8., 166-169.
- Kawai, T., & Urist, MD. (1989). Bovine tooth-derived bone morphogenetic protein. *J Dent Res*, 68., 1069-1074.
- Kim, YK., Kim, SG., Byeon, JH., Lee, HJ., Um, IU., Lim, SC., & Kim, SY. (2010). Development of a novel bone grafting material using autogenous teeth. *Oral Surg Oral Med Oral Pathol Oral Radiol Endod.*, 109., 4., 496-503.
- Kuboki, Y., Saito, T., Murata, M., Takita, H., Mizuno, M., Inoue, M., Nagai, N. & Poole, R. (1995). Two distinctive BMP-carriers induce zonal chondrogenesis and membranous ossification, respectively; geometrical factors of matrices for cell-differentiation. *Connective Tissue Research*, 31., 1-8.



- Murata, M., Inoue, M., Arisue, M., Kuboki, Y., & Nagai, N. (1998). Carrier-dependency of cellular differentiation induced by bone morphogenetic protein (BMP) in ectopic sites. *Int J Oral Maxillofac Surg*, 27., 391-396.
- Murata, M., Huang, BZ., Shibata, T., Imai, S., Nagai, N., & Arisue, M. (1999). Bone augmentation by recombinant human BMP-2 and collagen on adult rat parietal bone. *Int J Oral Maxillofac Surg*, 28., 232-237.
- Murata, M., Maki, F., Sato, D., Shibata, T., & Arisue, M. (2000). Bone augmentation by onlay implant using recombinant human BMP-2 and collagen on adult rat skull without periosteum. *Clin Oral Impl Res*, 11., 289-295.
- Murata, M., Arisue, M., Sato, D., Sasaki, T., Shibata, T., & Kuboki, Y. (2002). Bone induction in subcutaneous tissue in rats by a newly developed DNA-coated atelocollagen and bone morphogenetic protein. *Br J Oral Maxillofac Surg*, 40., 131-135.
- Murata, M. (2003). Autogenous demineralized dentin matrix for maxillary sinus augmentation in human. The first clinical report. 81th International Association for Dental Research · Geteburg, Sweden, 2003, June.
- Murata, M., Akazawa, T., Tazaki, J., Ito, K., Sasaki, T., Yamamoto, M., Tabata, Y., & Arisue, M. (2007). Blood permeability of a novel ceramic scaffold for bone morphogenetic protein-2. *J Biomed Mater Res*, 81B., 2., 469-475.
- Murata, M., Akazawa, T., Tazaki, J., Ito, K., Hino, J., Kamiura, Y., Kumazawa, R., & Arisue, M. (2009). Human Dentin autograft for bone regeneration - Automatic pulverizing machine and biopsy -. *Bioceramics* 22, 22., 745-748.
- Murata, M., Kawai, T., Kawakami, T., Akazawa, T., Tazaki, J., Ito, K., Kusano, K., & Arisue, M. (2010a). Human acid-insoluble dentin with BMP-2 accelerates bone induction in subcutaneous and intramuscular tissues. *Journal of the Ceramic Society of Japan*, 118., 6., 438-441.
- Murata, M., Akazawa, T., Takahata, M., Ito, M., Tazaki, J., Hino, J., Nakamura, K., Iwasaki, N., Shibata, T., & Arisue, M. (2010b). Bone induction of human tooth and bone crushed by newly developed automatic mill. *Journal of the Ceramic Society of Japan*, 118., 6., 434-437.
- Reddi, AH. (1974). Bone matrix in the solid state:geometric influence on differentiation of fibroblasts. *Adv Biol Med Phys*, 15., 1-18.
- Sampath, TK., & Reddi, AH. (1983). Homology of bone-inductive proteins from human, monkey, bovine, and rat extracellular matrix. *Proc Natl Acad Sci USA*, 80., 6591-6595.
- Takaoka, K., Koezuka, M. & Nakahara, H. (1991). Telopeptide-depleted bovine skin collagen as a carrier for bone morphogenetic protein. *Journal of Orthopaedic Research*, 9., 902-907.
- Urist, MR. (1965). Bone: Formation by autoinduction. *Science*, 150., 893-899.
- Urist, MR., Iwata, H., Ceccotti, PL., Dorfman, RL., Boyd, SD., McDowell, RM., & Chien, C. (1973). Bone morphogenesis in implants of insoluble bone gelatin. *Proc Nat Acad Sci USA*, 70., 3511-3515.
- Urist, MR., Mizutani, H., Conover, MA., Lietze, A., & Finerman, GA. (1982) Dentin, bone, and osteosarcoma tissue bone morphogenetic proteins. *Prog Clin Biol Res*, 101., 61-81.
- Wang, EA., Rosen, V., D'alesandro, JS., Bauduy, M., Coredes, P., Harada, T., Israel, DI., Hewick, RM., Kerns, KM., La Pan, P., Luxenberg, DP., Mc Quaid, D., Moutsatsos,

- IK., Nove, J., & Wozney, JM. (1990). Recombinant human bone morphogenetic protein induces bone formation. *Proc Natl Acad Sci USA* 87., 2220-2224.
- Wozney, JM., Rosen, V., Celeste, AJ., Mitsock, LM., Whitters, MJ., Kriz, RW., Hewick, RM., & Wang, EA. (1988). Novel regulators of bone formation: molecular clones and activities. *Science*, 242., 1528-1534.
- Yeomans, JD. & Urist, MR. (1967). Bone induction by decalcified dentine implanted into oral, osseous and muscle tissues. *Arch Oral Biol*, 12., 999-1008.

# Comparative Metal Ion Binding to Native and Chemically Modified *Datura innoxia* Immobilized Biomaterials

Gary D. Rayson and Patrick A. Williams  
*Department of Chemistry and Biochemistry*  
*New Mexico State University, Las Cruces, NM*  
*USA*

## 1. Introduction

Removal of toxic heavy metal ions from contaminated water is required to provide safe drinking water. This can be effected either within the waste stream at contaminate source or at point of use. Incorporation of remediation technologies at either location requires the removal of pollutants at parts per million and parts per billion concentrations from water containing more benign metal ions (e.g.,  $\text{Ca}^{2+}$ ,  $\text{Mg}^{2+}$ , and  $\text{Na}^+$ ) at concentrations three to six orders of magnitude higher. Materials derived from plants or microorganisms (e.g., algae and fungi) have been shown to enable the reduction of trace concentrations of heavy metal ions to below regulatory limits (Davis, et al., 2003).

Such nonliving biomaterials have been reported to have exhibit high capacity, rapid binding, and selectivity towards heavy metals (Drake and Rayson, 1996). It is postulated that functional groups native to the lipids, carbohydrates, and proteins found in the cell walls of the biomaterial are responsible for uptake (biosorption) of metal ions (Gardea-Torresdey, et al., 1999; 2001; Drake and Rayson, 1996; Drake, et al., 1997; Kelley, et al., 1999). For biomaterials to become a commercially viable method of metal remediation and recovery these functional groups must be identified and their contribution to overall metal binding capacity quantified. Knowledge of such information would allow either simple chemical alteration to the biomaterial, allowing for targeting of specific metals, or an enhancement of biomaterial metal binding.

Significant progress has been made to identify the chemical functionalities involved in the biosorption of numerous metal ions by a variety of plant and algal tissues (Gardea-Torresdey, et al., 1999; 2001; Riddle, et al., 2002; Fourest and Volesky, 1996; Drake, et al., 1997; Jackson, et al., 1993). Several techniques have been reported to probe local chemical environments of biosorbed metal ions. These have included X-ray absorption (Gardea-Torresdey, et al., 1999; Riddle, et al., 2002), lanthanide luminescence (Drake, et al., 1997; Serna, et al., 2010), and metal NMR (Xia and Rayson, 1996; 2002; Kelley, et al., 1999; Majidi, et al., 1990) spectroscopy. Analysis of total metal ion binding isotherm data modeling (Volesky, 2000) has also been described. Efforts to address the chemical heterogeneity of those biosorbed materials have also employed regularized regression analysis of isotherm data (Lin, et al., 1996). Additionally, these chemical intensities have been studied through selective removal of binding moieties by their reactive modification (Drake, et al., 1996).

It has been shown that carboxyl groups present in the cell walls of nonliving biomaterials contribute to metal-ion binding (Gardea-Torresdey, et al., 1999; 2001; Riddle, et al., 1997; Kelley, et al., 1999). Our group has used a variety of methods (Lin, et al., 2002; Drake, et al., 1996; Xia and Rayson, 1995; Drake, et al., 1996; 1997) to characterize the binding groups present in the cell walls of *Datura innoxia*. This plant is a member of the *Solanaceae* plant family and native to Mexico and the southwestern United States. To minimize variability of cell types investigated, the cell-wall fragments used are cultured anther cells of the plant. This plant was selected for study because it is a heavy metal resistant perennial that is both tolerant of arid climates and resistant to herbivory (Drake et al., 1996).

Our group has concentrated primarily on nonviable biomaterials, specifically cell wall fragments from the cultured anther cells of *Datura innoxia*. The present study used frontal affinity chromatography with inductively coupled plasma optical emission spectroscopy (ICP-OES) detection for simultaneous monitoring both uptake and release of metal ions to both a chemically modified and native *D. innoxia* biomaterial (Williams and Rayson, 2003). The objective of the present study was to further investigate such sites through sequential exposure and subsequent stripping of three similar metal ions ( $\text{Cd}^{2+}$ ,  $\text{Ni}^{2+}$ , and  $\text{Zn}^{2+}$ ) to both a modified and the native biosorbents, thus to study the role of carboxylate surface functionalities on passive metal ion binding of this material.

It has been demonstrated (Drake, et al., 1996) that carboxylate-containing binding sites can be removed through the formation of the corresponding methyl esters by reaction with acidic methanol for 72 hours (Drake, et al., 1996). Undertaking a similar series of experiments with such a chemically modified sorbent enables the investigation of alternate binding sites.

## 2. Materials and methods

### 2.1 Esterification of biomaterial

The cultured anther cells from *D. innoxia* were washed and prepared as described elsewhere (Drake, et al., 1996; 1997). Only cell fragment aggregates with a mesh size greater than 200 ( $< 127 \mu\text{m}$ ) were used for esterification. Following a method described elsewhere (Drake, et al., 1996), 10.0 grams of the biomaterial were suspended in 0.1 M HCl in methanol. The slurry was continuously heated at  $60^\circ\text{C}$  and stirred for 72 hours. The biomaterial was then recovered through vacuum filtration, rinsed three times with  $16.0\text{-M}\Omega$  water (Barnstead, Millipore Ultrapure), freeze-dried, and set aside for later immobilization.

### 2.2 Immobilization of biomaterial

In their native state, biomaterials have poor mechanical strength, low density, and a small particle size that can cause column clogging (Stark and Rayson, 2000). These characteristics can yield poor candidates for column-based water treatment applications. For this study native and modified *D. innoxia* biomaterials were each immobilized in a polysilicate matrix. The 40-60-mesh size fraction of the ground, and sieved immobilized biosorbents was then packed into columns. The process for immobilization has been described in detail elsewhere (Stark and Rayson, 2000).

Briefly, a suspension of 20 grams of the 100-200 mesh fraction of the washed biomaterial was generated with 300 mL of 5% v/v sulfuric acid adjusted to pH 2.0 by addition of a 6% (w/v) solution of  $\text{Na}_2\text{SiO}_3 \cdot 5\text{H}_2\text{O}$ . This suspension was stirred for 1 hour and the pH of the solution

further raised to 7.0 by incremental addition of the Na<sub>2</sub>SiO<sub>3</sub> solution. A gelatinous polymer formed at pH 7.0. The solution was stirred an additional 30 minutes, covered and stored at 4°C overnight. The resulting aqueous layer was removed. Excess sulfate ions were removed from the gel by successive washings with distilled deionized water until the aqueous phase failed a sulfate test using a few drops of a 1.0% barium solution (as the nitrate salt). When no precipitate was visible, one final wash with the distilled deionized water was performed to ensure complete sulfate removal.

Remaining polymer was transferred to ceramic evaporating dishes and baked at approximately 100° C until completely dry. The immobilized *D. innoxia* biomaterial was then ground and sieved. The 40-60-mesh (423-635 µm) particle size fraction was collected. Percent compositions of cell wall biomaterial were determined gravimetrically to be 64.6% and 75.3% for the native and modified materials, respectively.

### 2.3 Biomaterial columns

The columns used have been described elsewhere (Williams and Rayson, 2003) and were constructed in-house from Plexiglas™ tubing (2.5 cm in length and 3 mm i.d.). Teflon™ tubing (0.8-mm i.d.) was used for all column connections. Interface of the column to the ICP-OES was accomplished by connecting the column outlet directly to the inlet of the cross-flow type nebulizer using the minimum length of Teflon™ tubing (15 cm). Column effluent was monitored for each of 27 different metals simultaneously. Table 1 list the elements observed and their respective emission wavelengths.

Element	Wavelength/nm	Element	Wavelength/nm	Element	Wavelength/nm
Na	589.00	Mg	279.00	Al	396.15
Ca	317.90	Cr	267.70	Mn	257.60
Fe	259.90	Ni	231.60	Cu	324.70
Zn	213.80	Cd	228.80	Ag	328.00
Sn	189.90	Pb	220.30	Ba	493.40
Sr	421.50	U	409.00	Y	371.00
V	242.40	Mo	202.00	Co	228.60
Si	251.60	As	193.60	Se	196.00
Tb	350.97	Eu	381.97	Th	283.73

Table 1. Elements and the corresponding emission wavelength used during monitoring of column effluents (elements of interests in this study indicated by boldface print).

Each column was packed with approximately 125 mg of the immobilized *D. innoxia* material and flow tested using distilled deionized water. Once packed and tested for leaks, each column was exposed to 20 mL of 1.0-M HCl using a peristaltic pump (Model Rabbit, Rainin) (1.0 mL/min for 20 min) and the effluent monitored for metals released from the biomaterial. Following the acid rinse, the columns were then exposed to 5 mL of distilled deionized water (1.0 mL/min for five minutes) to reestablish an ambient pH influent environment (~pH 6.2).

These studies involved, initially, the exposure of a small column (3.0 mm i.d., 10.0 mm in length) to an equimolar mixture of metal ions, specifically, Cd<sup>2+</sup>, Zn<sup>2+</sup>, and Ni<sup>2+</sup>, and exposure to solutions of each metal sequentially while continuously monitoring these (and other) metal species in the column effluent.

## 2.4 Frontal affinity chromatography with inductively coupled plasma atomic emission detection

This technique has been described in detail elsewhere (Williams and Rayson, 2003). Briefly, the biomass packed column, having been exposed to 20 mL of 1.0M HCl to remove any metals remaining on the biomaterial (effluent monitored by ICPAES), was exposed to 5 mL of 16 M $\Omega$ , distilled-deionized water. The influent was a metal-ion solution, 0.1mM-0.2mM, made from the nitrate salt of Cd<sup>2+</sup>, Ni<sup>2+</sup>, or Zn<sup>2+</sup>. Initially, the influent metal ion concentration increased as a step function.

Each influent was pumped through a column using a peristaltic pump (Rainin) at the rate of ~1.0 mL min<sup>-1</sup> to a cross-flow type nebulizer and Scott-type double-pass spray chamber of the ICP-OES spectrometer (Jarrell-Ash, AtomComp700). The biomaterial in each column was exposed to each metal solution for 50 minutes. The effluent was monitored and resulting break-through curves were recorded for each metal ion (Figures 1A-C). Following exposure to the column, bound metal ions were stripped from the column using each of two exposures to a 1.0 M HCl solution. The first 150-second (~2.5 mL) exposure removed approximately 98% of the metal ions on the column (Figure 1D). The second 20 minute (~20 mL) exposure removed the remaining 2%. This was followed by a 5 minute (~5 mL) rinse with distilled deionized water to return the pH to f the biomaterial to that of the natural water (~6.2). Influent pH was not buffered to a predetermined pH to more accurately emulate conditions of a natural water supply within a remediation application.

With a three metal system there are six combinations that the metals can be sequentially exposed to the biomaterial (CdZnNi, CdNiZn, NiCdZn, NiZnCd, ZnCdNi, and ZnNiCd) and all six were performed on each column. Specifically, the ZnNiCd sequence involved exposure of a column packed with a biosorbents to a 0.20 mM Zn<sup>2+</sup>solution for 50 minutes (Figure 1A). The influent was changed to a 0.20 mM Ni<sup>2+</sup> solution for another 50 minutes (Figure 1B). Similarly, a 0.20 mM Cd<sup>2+</sup> solution was pumped through the same column for an additional 50 minutes (Figure 1C). The column was then exposed to 1.0 M HCl for 2.5 and 20 minutes to remove all bound metal ions (Figure 1D).

Simultaneous exposure of the three metals at the same molar concentration was also undertaken for each column with both the native (Figure 2) and modified (not shown) biomaterials. All determinations were performed in triplicate with three separate columns packed with each individual biosorbent.

## 3. Results and discussion

### 3.1 Binding capacities of native and modified *d. innoxia*

Figure 1 illustrates a sequential 50-mL exposure of 0.1mM Zn<sup>2+</sup>, Ni<sup>2+</sup>, and Cd<sup>2+</sup> to the native *D. innoxia*. Figure 2 shows the sequential 50-mL exposures of 0.2mM Zn<sup>2+</sup>, Ni<sup>2+</sup>, and Cd<sup>2+</sup> to the modified biomaterial. Table 2 lists the observed binding capacities for the three metals to the modified *D. innoxia* reported in moles metal bound per gram of biomaterial for each replicate. The capacities reported are mass balance capacities, as the column effluent was monitored.

Simple statistical analysis using a t-test confirms the binding capacity of each metal to the biomaterial was decreased as expected. The position of the metal in the sequence was similarly indicated as affecting capacities in both the native and the modified biomaterial materials. Further statistical analysis indicated that not only the position in the sequence but

the history of exposure appears to impact apparent steady state binding metal ion capacities of the biomaterial.

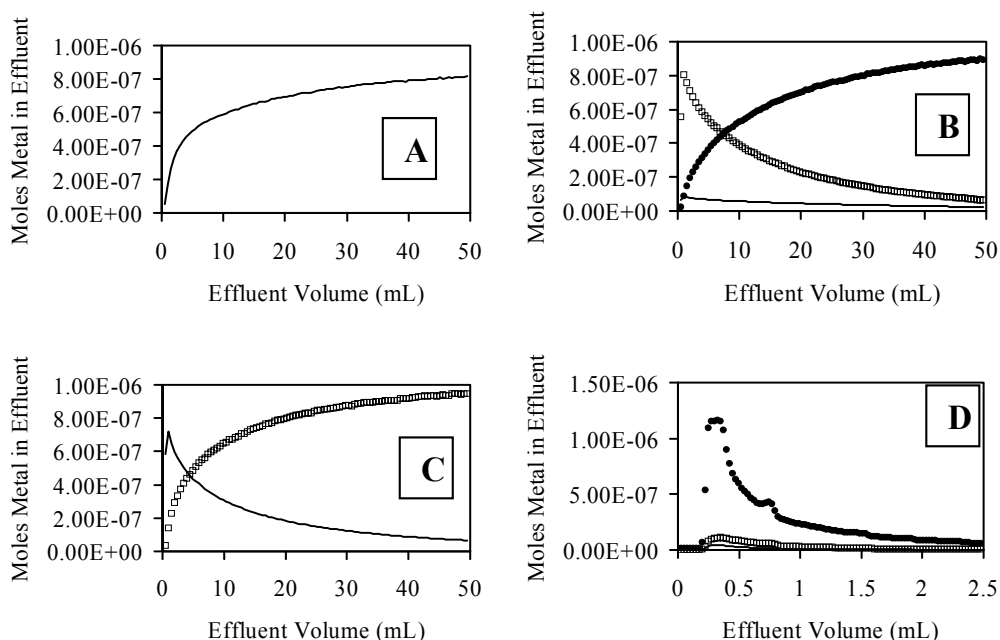


Fig. 1. Effluent profiles resulting from solutions of (A) 0.2mM Zn<sup>2+</sup> (—), (B) followed by 0.2 mM Ni<sup>2+</sup> (□), followed by 0.2mM Cd<sup>2+</sup> (●) pumped through a column packed with chemically modified *D. innoxia*. (D) Effluent profile of first 1.0M HCl wash of the metal-laden material.

### 3.2 Modified material three-metal sequential study

Total amounts of metal bound to the native and modified materials at each stage of the sequence are listed in Table 2. Although the average amount of the first metal ion bound was 24.5  $\mu\text{mol g}^{-1}$ , the average total metal ion bound after exposure to the second and third metals was 31.0  $\mu\text{mol g}^{-1}$ . This increase in the amount of metal captured by the biomass could be indicative of either the presence of metal ion-specific binding sites, or some degree of competitive metal ion binding.

Simultaneous exposure of the biosorbent material to an equimolar solution of all three metal-ions (0.2 mM) was undertaken. Figure 2A shows the resulting effluent concentration profile. Even with a total metal ion concentration of 0.6 mM, the effluent concentration maximized at only 94% of the influent concentration (i.e., 0.19 mM). The modified biomaterial average capacity with simultaneous exposure was 41.72  $\mu\text{mol g}^{-1}$  biomaterial. Specifically, total amounts of metal ion bound were 13.24, 14.17, and 14.31  $\mu\text{mol g}^{-1}$  for Ni<sup>2+</sup>, Zn<sup>2+</sup>, Cd<sup>2+</sup>, respectively. This suggests no significant binding preference of the *D. innoxia* cell material for these ions.

Figure 2B shows the effluent concentration profile of the subsequent 1.0 M HCl metal-ion recovery/strip step. Total metal ion recovered from the two acid washes was 27.48  $\mu\text{mol g}^{-1}$ .

This included 7.68, 10.21, and 9.59  $\mu\text{mol g}^{-1}$  for  $\text{Ni}^{2+}$ ,  $\text{Zn}^{2+}$ ,  $\text{Cd}^{2+}$ , respectively. Nickel recovery was lowest among the three ions (58.0%), while cadmium and zinc recovered 67.0% and 72.1%, respectively. This suggests the affinity of some of the  $\text{Ni}^{2+}$  binding sites were higher than those for each of the other two metal ions.

Sequence	Column a	Column b	Column c	Average	Std. Dev.	%RSD
Cd	28.26	22.63	25.49	25.46	2.56	10.05
Ni	23.57	20.79	23.35	22.57	1.84	8.16
Zn	24.56	24.88	26.76	25.40	1.57	6.16
Cd Ni	27.14	27.14	24.29	26.19	1.64	6.28
Cd Zn	30.33	24.57	24.51	26.47	3.34	12.62
Ni Cd	28.39	26.04	29.95	28.13	1.97	7.01
Ni Zn	29.72	25.95	25.57	27.08	2.29	8.47
Zn Cd	27.53	24.49	31.49	27.84	3.51	12.61
Zn Ni	25.99	26.09	27.66	26.58	0.94	3.52
Cd Ni Zn	30.83	27.00	30.06	29.30	2.02	6.91
Cd Zn Ni	27.89	24.21	27.54	26.55	2.03	7.64
Ni Cd Zn	32.89	26.00	25.42	28.10	4.15	14.78
Ni Zn Cd	21.63	24.57	27.69	24.63	3.03	12.29
Zn Cd Ni	27.45	27.45	40.95	31.95	7.80	24.40
Zn Ni Cd	26.27	23.75	23.62	24.55	1.49	6.09

Table 2. Influent metal bound at each stage of the sequential exposure study. Values presented are given in  $\mu\text{moles}$  metal per gram of modified biomaterial.

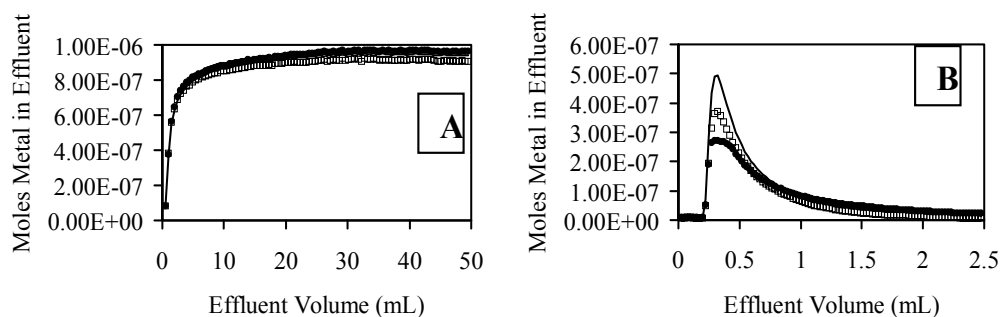


Fig. 2. Simultaneous exposure of 0.2mM  $\text{Ni}^{2+}$  ( $\square$ ),  $\text{Cd}^{2+}$  ( $\bullet$ ), and  $\text{Zn}^{2+}$  (—) to modified *D. innoxia* column (A) and its subsequent stripping using 1.0 M HCl (B).

### 3.3 Comparison of native and modified biomaterials

By examining the results from the native and modified *D. innoxia* studies together, a hypothesis regarding the carboxyl sites contribution to the metal-ion binding process can be formulated. It was proposed, in previous studies of *D. innoxia*, that esterification of carboxylate sites can decrease metal uptake by as much as 40% (Drake, et al., 1996), depending on the metal.



### 3.3.1 Influent and total metal bound comparison

By taking the ratio of metal bound for the modified and native biomaterials at each position in the sequence and averaging those ratios for both the influent metal bound and the total metal bound, the average effect of the esterification procedure on metal binding can be quantified. On average, the influent metal-ion bound decreased by 43% while the total metal bound decreased by 54%. Figure 3 illustrates a further breakdown these comparisons by metal-ion position within the sequence. For total metal bound to the biomaterial, metal ion position had only a small effect in the percentage decrease in binding capacity observed in the modified biomaterial. With the first metal ion capacity dropping 52%, the second decreased to 54% and the third decreased to 55%. However, the influent metal ion capacity seems to be more effected by its position in the sequence. The first metal ion exposed demonstrated a decrease in its capacity of 52%, while the second and third ions exposed decreased by only 42% and 40% respectively.

Figure 4 shows additional data regarding the influent metal bound by examining both position and specific metal ion exposed in the sequence. For nickel and zinc there was a steady decrease in the observed effect of the modification as their position in the sequence moved from first to third. Nickel was most pronounced, as the effect of the modification was decreased in capacity by 54% when nickel was the first ion exposed, 41% when it is the second, and 35% when the third. Zinc was similar as it drops from a 51% decreased in binding capacity when it was the first metal exposed, a 47% decrease when it was second, to a 41% decrease when it was third. Cadmium did not follow this pattern of decreasing effect based on position. When cadmium was the first metal exposed a decrease in binding capacity of 49% is observed, a decrease in capacity of 38% was observed when it was second, and a decrease of 44% when it metal on the column. The modified biomaterial total metal bound decreased between 49 – 57% depending on influent metal and position with no apparent pattern.

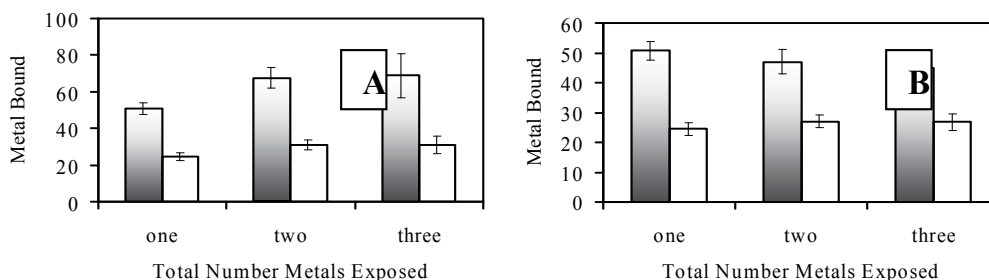


Fig. 3. Average total (A) and influent (B) metal-ion bound for native (shaded) and modified biomaterial based on number of metals exposed in series. Metal bound given in percentage metal bound.

Simultaneous exposure of the three metal-ions showed an overall decrease of 43.7% for total metal bound for the modified biomaterial. Zinc showed the largest decrease showing a 50.2% decrease in binding capacity. The modified biomaterial exhibited a loss of 43.5% for cadmium. Nickel showed the smallest effect from the modification losing 34.8% of its capacity. It should be noted that zinc, which lost the most, had the largest capacity ( $28.5 \mu\text{mol g}^{-1}$ ), while nickel, which demonstrated the smallest effect of modification, had the smallest capacity on the native biomaterial ( $20.3 \mu\text{mol g}^{-1}$ ).

### 3.3.2 Statistical analysis

Because of the numerous variables studied pertaining to the ability of this adsorbent to remove each of these metal ions from a flowing influent, it became imperative that statistical tools be employed to ascertain differences (and similarities) in metal binding. Variables that were tested include the esterification of carboxylate functionalities, the identity of the metal bond, the identity of the metal ion(s) displaced or removed, and the general history of a column of the biosorbent. The Student-t test was employed to test the hypothesis that the measured means of binding capacities between any two conditions were statistically the same. The criteria used for these test were a 95% confidence level with 2 - 5 degrees of freedom.

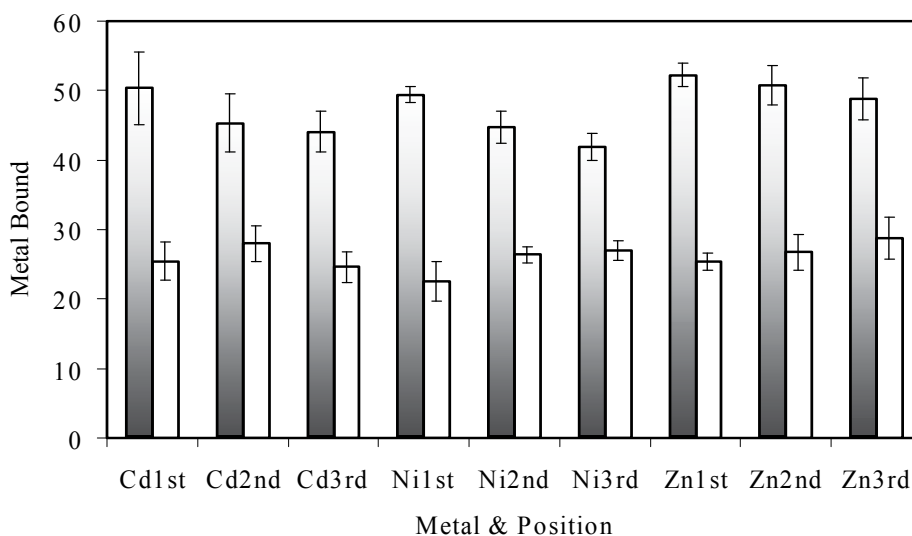


Fig. 4. Comparison of native (shaded) and modified *D. innoxia* columns influent-metal bound capacities. Metal bound is reported in micromoles per gram biomaterial.

To statistically treat the results presented above in the comparison of the native and esterified biomaterial, two methods of statistical analysis were used. The Student-t test was used to test the statistical difference between the amounts of metal bound to the biomaterial at each stage in the studies at each stage for the native and modified biomaterials. This would also reinforce the position that by undertaking a simple chemical modification, the binding properties of a biomaterial could be altered significantly. Also, the Student-t test was used to examine the impact of exposure order and history (e.g., whether the amount of cadmium bound to the biomaterial is statistically different for the series  $\text{Ni}^{2+} \Rightarrow \text{Zn}^{2+} \Rightarrow \text{Cd}^{2+}$  and  $\text{Zn}^{2+} \Rightarrow \text{Ni}^{2+} \Rightarrow \text{Cd}^{2+}$ ). Differences in the variances calculated for each stage were similarly evaluated using an F-test (again considering both the order of metal ion exposure and the exposure history of the material).

Table 3 summarizes the resulting statistical comparisons of the native and chemically modified *D. innoxia* materials using the software package 'Analysis ToolPak' within Microsoft® Excel™. Mass balance values of the influent metal bound were used in these

calculations. A confidence limit for each was 95% ( $\alpha = 0.05$ ). The t-values presented indicate the respective probabilities that the amounts of the influent metal bound at each position were the same for both the native and modified materials. The results indicated that modification of the biomaterial did significantly decrease the binding capacities of the *D. innoxia* for each metal at each position in the sequential exposure sequence.

The F-values listed in Table 3 indicated the respective probabilities that the variances of the mean values between the native and modified biomaterials were statistically different. There were two cases a clear (>95%) difference in the variances was indicated; 1) the conditions when cadmium was the first metal exposed to the column and 2) when nickel was the third metal introduced to the biosorbent material. In both cases, larger variances were observed for cadmium binding to the chemically modified material, with a percent relative standard deviation (%RSD) of 27.22% compared to 4.86% for the native material. The binding of nickel showed similar behavior with a 25.97% RSD for its binding to the modified material in comparison to an RSD of 4.50% for the native biosorbent. This suggested sites involved in the binding of  $\text{Cd}^{2+}$  initially exposed to the material and those pertaining to  $\text{Ni}^{2+}$  binding as the third exposure metal ion were the least homogeneously affected by the chemical modification (i.e., esterification) reaction.

	Cd position 1	Cd position 2	Cd position 3
$P T \leq t$ (two tail)	1.01E-04	3.72E-05	3.18E-07
$P F \leq f$ (one tail)	0.024	0.258	0.261
	Ni position 1	Ni position 2	Ni position 3
$P T \leq t$ (two tail)	1.58E-03	2.73E-03	2.86E-03
$P F \leq f$ (one tail)	0.119	0.419	0.006
	Zn position 1	Zn position 2	Zn position 3
$P T \leq t$ (two tail)	3.14E-07	1.66E-06	8.53E-07
$P F \leq f$ (one tail)	0.390	0.484	0.492

Table 3. Comparing influent metal bound at each position for the native and modified biomaterials. The  $P T \leq t$  value indicated the statistical probability that the mean values for the native and modified *D. innoxia* are the same. The  $P F \leq f$  value indicated the probability that the variances of the two means are the same.

One question that arose with regard to the sequential exposure of the sorbent to chemically similar metal ions is whether there is a statistically significant difference in the binding capacities as a function of the position of the metal in the exposure sequence (i.e., first, second, or third). This is related to the possible presence of cooperativity in the formation (or elimination) of binding sites for one metal because of the earlier binding of another metal ion to a (presumably) nearby site.

Table 4 summarizes a comparison of influent metal binding capacities within each of the studies based on metal position in the sequence using a Student t-test at 95% confidence. The t-values listed suggest there is no statistical difference in the amount of influent metal bound for either the native or modified biomaterials based on the position of each metal in the exposure sequence. Conversely, the F-values suggested statistical differences in the

variances based on position in the sequence for each of four cases: For nickel, binding to the native column comparing positions 1 and 3, and positions 2 and 3;. Also for cadmium exposed to the modified column comparing positions 1 and 3, and positions 2 and 3. These values again suggested greater inhomogeneity in the impact of the chemical modification procedure on the sites involved in the binding of these metal ions.

	1 vs. 2	1 vs. 3	2 vs. 3
T Cd native	0.739	0.671	0.985
T Ni native	0.196	0.462	0.338
T Zn native	0.380	0.707	0.596
T Cd modified	0.241	0.195	0.912
T Ni modified	0.699	0.686	0.955
T Zn modified	0.567	0.182	0.428
F Cd native	0.119	0.253	0.296
F Ni native	0.407	0.035	0.022
F Zn native	0.399	0.485	0.413
F Cd modified	0.400	0.025	0.041
F Ni modified	0.223	0.382	0.320
F Zn modified	0.476	0.397	0.421

Table 4. Comparing influent metal bound at each position. T values are statistical probability that the mean metal bound at each position in sequence are the same. F values are statistical probability that their variances are the same.

Tables 5a-c provide a closer look at metal position by considering the history of metal exposure as well as position of each metal ion in the sequence. The t-values for all three metals indicated no statistical difference as a result of metal exposure history to the influent metal bound for either the native or modified biomaterial. The F-values again suggest statistical differences in the variances in Ni<sup>2+</sup> binding based on exposure history. The modified biomaterial showed a difference in the variances for the comparison of the sequences CdZnNi with ZnCdNi, and CdNi with CdZnNi. Comparatively larger relative standard deviations (RSDs) were calculated for the sequences CdNi and ZnCdNi relative to that for the CdZnNi exposure sequence. A probable difference in variances for the comparison of CdNi with CdZnNi, and CdNi with ZnCdNi was also observed for the native material. Under these conditions, CdNi exhibited comparatively large standard deviation relative to those of the other two conditions.

### 3.3.3 Binding site matrix analysis

Traditional statistical analysis of the metal ion binding data suggested that the chemical modification of the *D. innoxia* material decreased the number of binding sites significantly, thus reducing metal binding capacities for the esterified biomaterial. Additionally, statistically significant changes in the Ni<sup>2+</sup> binding variability suggested non-uniform changes in metal-specific sites that resulted from the esterification reaction. In an effort to extract more information about the binding behavior of the biomaterial towards these three metals, a secondary method of data analysis was undertaken.

	2a vs. 2b	3a vs. 3b	2a vs. 3a	2a vs. 3b	3a vs. 2b	3b vs. 2b
T Native	0.955	0.471	0.607	0.710	0.830	0.784
F Native	0.105	0.384	0.345	0.247	0.183	0.264
T Modified	0.328	0.969	0.401	0.326	0.621	0.623
F Modified	0.268	0.196	0.416	0.148	0.207	0.060

Table 5a. Effect of column history on influent cadmium bound. T values are probability that the two compared means are statistically equivalent. F values are statistical probability that their variances are equivalent. 2a → NiCd, 2b → ZnCd, 3a → NiZnCd, 3b → ZnNiCd.

	2a vs. 2b	3a vs. 3b	2a vs. 3a	2a vs. 3b	3a vs. 2b	3b vs. 2b
T Native	0.483	0.104	0.326	0.557	0.345	0.665
F Native	0.093	0.454	0.036	0.043	0.267	0.304
T Modified	0.760	0.183	0.310	0.536	0.427	0.377
F Modified	0.459	0.034	0.047	0.413	0.055	0.374

Table 5b. Effect of column history on influent nickel bound. T values are probability that the two compared means are statistically equivalent. F values are statistical probability that their variances are equivalent. 2a → CdNi, 2b → ZnNi, 3a → CdZnNi, 3b → ZnCdNi.

	2a vs. 2b	3a vs. 3b	2a vs. 3a	2a vs. 3b	3a vs. 2b	3b vs. 2b
T Native	0.214	0.515	0.193	0.542	0.959	0.274
F Native	0.939	0.953	0.736	0.691	0.553	0.221
T Modified	0.412	0.327	0.383	0.440	0.470	0.354
F Modified	0.094	0.392	0.357	0.264	0.157	0.224

Table 5c. Effect of column history on influent zinc bound. T values are probability that the two compared means are statistically equivalent. F values are statistical probability that their variances are equivalent. 2a → CdZn, 2b → NiZn, 3a → CdNiZn, 3b → NiCdZn.

Three assumptions were made in pursuing this avenue of exploration. 1) There exist common binding sites shared between all three of the metal ions ( $\delta_0$ ). 2) For each metal ion, there exist ion-specific binding sites available only to that particular ion ( $\alpha, \beta, \gamma$ ). 3) For each stage in the influent solution exposure sequence, there may be enhancement or inhibition of binding due to the history of metal exposure, i.e., some level of cooperativity between sites. Making these assumptions allows for the construction of an overall binding equation for the three-metal system:

$$\begin{aligned}
 M_{\text{Bound}} = & [ \alpha_{\text{Cd}} X_{\text{Cd}} + \alpha_{\text{Ni}} X_{\text{Ni}} + \alpha_{\text{Zn}} X_{\text{Zn}} ] + \{ \beta_{\text{CdNi}} X_{\text{CdNi}} + \beta_{\text{CdZn}} X_{\text{CdZn}} \\
 & + \beta_{\text{NiCd}} X_{\text{NiCd}} + \beta_{\text{NiZn}} X_{\text{NiZn}} + \beta_{\text{ZnCd}} X_{\text{ZnCd}} + \beta_{\text{ZnNi}} X_{\text{ZnNi}} \} + ( \gamma_{\text{CdNiZn}} X_{\text{CdNiZn}} + \\
 & \gamma_{\text{CdZnNi}} X_{\text{CdZnNi}} + \gamma_{\text{NiCdZn}} X_{\text{NiCdZn}} + \gamma_{\text{NiZnCd}} X_{\text{NiZnCd}} + \gamma_{\text{ZnCdNi}} X_{\text{ZnCdNi}} + \gamma_{\text{ZnNiCd}} X_{\text{ZnNiCd}} ) \\
 & + \delta_0 X_{\text{common}}
 \end{aligned} \quad (1)$$

From the sequential experiments, the amount of total metal bound is known for each of the above situations except for metal binding to the common binding sites,  $X_{\text{Common}}$ . While the site-type  $X_{\text{Common}}$  is available for each condition, the degree to which it is available may be limited by the metal exposure history on the column and the comparative affinities of each metal for those sites. To account for this, a secondary set of data was incorporated into the

ensuing analysis. The total metal-bound data from the simultaneous exposure of all three metals to the biomaterial were indicative of situations in which all three unique metal binding sites ( $X_{Cd}$ ,  $X_{Ni}$ , and  $X_{Zn}$ ) are used along with only the common site,  $X_{Common}$ . This enabled the isolation of the common site from any binding enhancement or inhibition that could be attributed to metal history. By using the total amounts of each metal bound for each stage in the sequences and the amount of metal bound during the simultaneous exposure of the material to the three metals, 16 equations for metal binding can be written. The variables  $X_{Cd}$  through  $X_{common}$  can have values of either 1 (the site-type is involved) or 0 (the site-type is not involved). These can then be combined into a single, 16 by 16 matrix ( $X$  in Table 6) with the corresponding coefficients comprising the contents of 1 by 16 vector ( $c$ ). For each stage in the sequences the common site, the individual metal-ion sites, and the corresponding sequential site will make contributions to the total metal bound. For example, the total metal bound at the sequence stage  $Ni^{2+} \rightarrow Zn^{2+}$  can be represented by the equation:

$$M_{Total} = \alpha_{Ni} + \alpha_{Zn} + \beta_{NiZn} + \delta_0 \quad (2)$$

And the simultaneous exposure of all three metals can be represented by:

$$M_{Total} = \alpha_{Cd} + \alpha_{Ni} + \alpha_{Zn} + \delta_0 \quad (3)$$

Where  $M_{Total}$  is the total metal bound and the coefficients ( $\alpha$ ,  $\beta$ ,  $\gamma$ , and  $\delta$ ) indicate the contribution of each site-type to the total metal bound.

	$\alpha$ Cd	$\alpha$ Ni	$\alpha$ Zn	$\beta$ Cd Ni	$\beta$ Cd Ni	$\beta$ Cd Ni	$\beta$ Cd Ni	$\beta$ Cd Ni	$\beta$ Cd Ni	$\gamma$ Cd Ni Zn	$\gamma$ CdZn Ni	$\gamma$ NiCd Zn	$\gamma$ NiZn Cd	$\gamma$ ZnCd Ni	$\gamma$ ZnNi Cd	$\delta_0$
Cd	1	0	0	0	0	0	0	0	0	0	0	0	0	0	0	1
Ni	0	1	0	0	0	0	0	0	0	0	0	0	0	0	0	1
Zn	0	0	1	0	0	0	0	0	0	0	0	0	0	0	0	1
CdNi	1	1	0	1	0	0	0	0	0	0	0	0	0	0	0	1
CdZn	1	0	1	0	1	0	0	0	0	0	0	0	0	0	0	1
NiCd	1	1	0	0	0	1	0	0	0	0	0	0	0	0	0	1
NiZn	0	1	1	0	0	0	1	0	0	0	0	0	0	0	0	1
ZnCd	1	0	1	0	0	0	0	1	0	0	0	0	0	0	0	1
ZnNi	0	1	1	0	0	0	0	0	1	0	0	0	0	0	0	1
CdNiZn	1	1	1	0	0	0	0	0	0	1	0	0	0	0	0	1
CdZnNi	1	1	1	0	0	0	0	0	0	0	1	0	0	0	0	1
NiCdZn	1	1	1	0	0	0	0	0	0	0	0	1	0	0	0	1
NiZnCd	1	1	1	0	0	0	0	0	0	0	0	0	1	0	0	1
ZnCdNi	1	1	1	0	0	0	0	0	0	0	0	0	0	1	0	1
ZnNiCd	1	1	1	0	0	0	0	0	0	0	0	0	0	0	1	1
Simultaneous	1	1	1	0	0	0	0	0	0	0	0	0	0	0	0	1

Table 6. Matrix representing the contributions to total metal ion bound to the immobilized D. innoxia at each stage of influent metal ion exposure in the sequential experiments. A '1' indicates a contribution to total metal binding at the particular stage, a '0' indicates the site is not involved.

(A) Coefficient   Case	Exp. $\mu\text{mole/gram}$	1	2	3	4
Cd	25.53	29.58	62.68	187.30	-6.53
Ni	22.57	43.73	67.24	201.40	-1.94
Zn	25.40	53.4	65.29	211.10	0.36
CdNi	30.59	32.75	116.00	42.71	0.02
CdZn	31.03	47.59	112.80	57.55	1.28
NiCd	30.39	45.32	128.80	55.28	12.62
NiZn	29.94	47.78	113.60	57.74	-3.17
ZnCd	31.69	38.20	112.00	48.16	1.00
ZnNi	32.07	56.72	120.30	66.68	14.49
CdNiZn	31.27	31.87	167.60	-78.40	0.30
CdZnNi	28.80	32.57	162.60	-77.70	-0.96
NiCdZn	30.93	44.71	193.60	-65.50	13.17
NiZnCd	28.80	24.26	156.20	-86.00	-4.68
ZnCdNi	38.10	31.82	169.70	-78.40	2.56
ZnNiCd	28.69	30.96	167.30	-79.30	6.26
Simultaneous	41.72	36.41	191.70	410.20	-30.40

(B) Coefficient   Case	Exp. $\mu\text{mole/gram}$	1	2	3	4
Cd	50.35	45.60	756.48	334.45	-16.11
Ni	49.42	38.00	268.98	326.85	-11.68
Zn	52.27	46.14	-202.78	334.99	-7.64
CdNi	70.31	50.81	557.30	90.26	-8.63
CdZn	69.39	55.57	82.16	95.02	-3.49
NiCd	61.10	46.83	553.32	86.28	-8.19
NiZn	67.60	50.40	76.99	89.85	6.78
ZnCd	59.34	54.47	560.96	93.92	3.00
ZnNi	69.16	52.05	78.64	91.50	8.20
CdNiZn	74.07	39.35	-102.89	-128.61	-4.86
CdZnNi	73.12	40.19	-102.05	-127.77	0.24
NiCdZn	67.28	37.77	-104.47	-130.19	-2.02
NiZnCd	66.05	37.36	-104.88	-130.60	1.84
ZnCdNi	64.08	40.10	-102.14	-127.86	4.35
ZnNiCd	68.13	39.51	-102.73	-128.45	3.77
Simultaneous	72.87	40.68	-1505.70	673.19	-50.24

Table 7. Modified (A) and Native (B) columns experimental and calculated total metals bound, Case 1: All unique single metal bonds are included when appropriate in the sequential case and only all three unique sites along with the common site for the simultaneous case. Case 2: Same as case 1 except for the simultaneous all three, three metal binding site types are active along with the unique sites and common site. Case 3: The unique metal coefficients are not included in the simultaneous portion of the matrix calculation. Case 4: The unique metal coefficients are only included when they are the first metal on the column

The system can then be represented by the matrix equation:

$$[\mathbf{M}] = [\mathbf{c}] [\mathbf{X}] \quad (4)$$

with  $[\mathbf{A}]$  is a 1 by 16 vector containing the total amount of metal bound for each situation,  $[\mathbf{c}]$  is a 1 by 16 vector containing the contribution coefficients for each site type, and  $[\mathbf{X}]$  is the 16 by 16 matrix describing the types of binding that may be taking place. For example, the row in the matrix  $[\mathbf{X}]$  corresponding to the previous example ( $\text{Ni} \rightarrow \text{Zn}$ ) would be  $[0 \ 1 \ 1 \ 0 \ 0 \ 0 \ 1 \ 0 \ 0 \ 0 \ 0 \ 0 \ 0 \ 0 \ 1 \ ]$ . Both  $[\mathbf{M}]$  and  $[\mathbf{X}]$  are therefore known or determined experimentally. The contribution coefficient matrix,  $[\mathbf{c}]$ , can then be calculated by solving the multivariate equation.

$$[\mathbf{M}] [\mathbf{X}]^T ([\mathbf{X}] [\mathbf{X}]^T)^{-1} = [\mathbf{c}] \quad (5)$$

The superscripts T and -1 designate the corresponding transposed and inverted matrices, respectively.

Four matrices were examined using this methodology. The matrix presented in Table 6 includes all of the unique single metal bonds, where appropriate, in the sequential case, and only the three unique sites plus the common site for the simultaneous case. Tables 7a and b list the experimentally determined total amounts of metal bound with the predicted amounts from four separate theoretical calculations. Case 1 shows the results from the calculations using the matrix shown in Table 6. Case 2 is the same matrix as case 1 except for the simultaneous row, which now includes all three, three-metal binding sites (coefficients  $\gamma_{\text{NiZnCd}}$ ,  $\gamma_{\text{ZnCdNi}}$ , and  $\gamma_{\text{ZnNiCd}}$ ) along with the unique and common sites. Case 3 differs from case 2 by eliminating the unique sites from the simultaneous portion of the matrix. Case 4 is distinguished by only including the unique metal site type when the metal is the first metal introduced to the column.

Upon examining the results presented in Tables 7 a and b, it was evident that case 1 best approximated the experimental results. Figure 5 illustrates the values of the contribution coefficients for both the native and the modified (shaded) *D. innoxia* total metal bound studies.

The most striking and least surprising result of this analysis was the contribution the common site ( $\delta_0$ ) made to overall binding for both the native and the modified biomaterial. Also noteworthy, was the series of positive coefficients present in the two metal ion systems. For both the native and modified biomaterials, it appears that the presence of a metal ion enhanced the biomaterial's binding capacity. The lone exception to this was the impact of the NiZn sequence on the modified material.

The native biomaterial exhibited slight positive coefficients for the unique  $\text{Cd}^{2+}$  and  $\text{Zn}^{2+}$  sites and a moderate apparent inhibition for  $\text{Ni}^{2+}$ . All binary combinations of metal ions exposed to the native biomass resulted in moderate positive coefficient values. The tertiary combinations all yielded moderately negative values. This does not necessarily indicate an absolute inhibition of binding, but can be interpreted in terms of relative inhibition effects. Review of the experimental data listed in Table 7 b reveals single metal values as all near  $50 \mu\text{mol g}^{-1}$  (average 50.68). Comparatively, binary combinations ranged from  $60 - 70 \mu\text{mol g}^{-1}$  (average 66.15), an increase of 15 while tertiary combinations ranged from  $65 - 75 \mu\text{mol g}^{-1}$  (average 68.78), an increase which may not be statistically significant. This suggests some degree of cooperativity in metal-ion binding while the primary mechanism of metal ion binding is simple electrostatic (i.e., the dominance of the common sites).



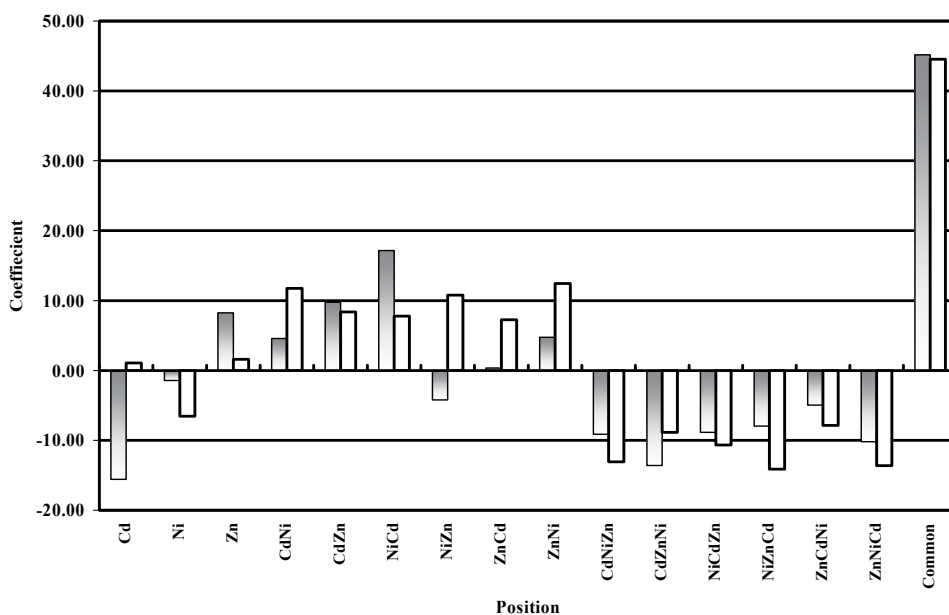


Fig. 5. Comparison of native and modified (shaded) *D. innoxia* matrix coefficients.

Binding Sites	Coefficient	Native Material	Modified Material
Cd	$\alpha_{Cd}$	1.07	-15.57
Ni	$\alpha_{Ni}$	-6.53	-1.42
Zn	$\alpha_{Zn}$	1.61	8.25
CdNi	$\beta_{CdNi}$	11.74	4.59
CdZn	$\beta_{CdNi}$	8.36	9.76
NiCd	$\beta_{CdNi}$	7.76	17.16
NiZn	$\beta_{CdNi}$	10.79	-4.20
ZnCd	$\beta_{CdNi}$	7.26	0.37
ZnNi	$\beta_{CdNi}$	12.44	4.74
CdNiZn	$\gamma_{CdNiZn}$	-13.07	-9.13
CdZnNi	$\gamma_{CdZnNi}$	-8.85	-13.60
NiCdZn	$\gamma_{NiCdZn}$	-10.67	-8.86
NiZnCd	$\gamma_{NiZnCd}$	-14.11	-7.95
ZnCdNi	$\gamma_{ZnCdNi}$	-7.84	-4.96
ZnNiCd	$\gamma_{CdNiZn}$	-13.61	-10.19
Common	$\delta_0$	44.53	45.15

Table 8. Coefficient values for both the native and modified *D. innoxia* metal ion binding sequences.

The modified biomaterial's coefficients behaved in a similar manner as the native. The single metal coefficients for  $Cd^{2+}$  and  $Ni^{2+}$  were both negative ( $Ni^{2+}$  slightly,  $Cd^{2+}$  moderately)

while  $Zn^{2+}$  was moderately positive. All of the binary combinations were moderately positive except for NiZn, which was moderately negative, and ZnCd, which was only slightly positive. The tertiary combinations were as on the native biomaterial, all moderately negative. Again, this only reflects relative inhibition of metal ion binding. The data listed in Table 7a reveals single metal bound values were all about  $25 \mu\text{mol g}^{-1}$  (average 24.5). These are compared to those for the binary combinations which ranged from  $30 - 32 \mu\text{mol g}^{-1}$  (average 31.0), an increase of 6. Similarly to the native material, the tertiary combinations ranged from  $29 - 39 \mu\text{mol g}^{-1}$  (average 31.1), a slight increase which may not be statistically significant. This again suggested that some degree of cooperativity in binding with the primary binding mechanism involving electrostatic attractions.

#### 4. Conclusions

Carboxylate groups are important functionalities for metal ion adsorption for the biomaterial *Datura innoxia*. Esterification of these functionalities was observed to reduce metal binding capacity 30-40%. Three metals of similar binding affinity to the biomaterial ( $Cd^{2+}$ ,  $Ni^{2+}$ , and  $Zn^{2+}$ ) were exposed sequentially to both the native esterified biomaterials immobilized within a polysilicate matrix. Removal of surface carboxylates significantly impacted the binding of each metal ion and the impact of each metal bound on the binding of the others. A model involving at least 16 binding sites for these metal ions revealed a majority of binding to involve species-independent or common sites and the presence of cooperativity for some metal-ion binding environments

#### 5. Acknowledgements

The authors wish to acknowledge the financial support of the Waste-management Education and Research Consortium funded by the US Department of Energy through New Mexico State University.

#### 6. References

- Davis, T.A.; Volesky, B.; Mucci, (2003) A. A Review of the Biochemistry of Heavy Metal Biosorption by Brown Algae. *Water Research* vol.37, No. 18 (November 2003) pp. 4311-4330 ISSN: 0043-1354.
- Drake, L.R.; Rayson, G. D. (1996) Plant Materials for Metal Selective Binding and Preconcentration *Analytical Chemistry*, vol. 68, no. 1 ( January 1996), pp. 22A-27A. ISSN 0003-2700
- Drake, L.R.; Lin, S.; Rayson, G.D. (1996) Chemical Modification and Metal Binding Studies of *Datura innoxia*. *Environmental Science and Technology*, vol. 30, no. 1 (January 1996) pp. 110-114. ISSN 0013 936X
- Drake, L.R.; Hensman, C.E.; Lin, S.; Rayson, G.D.; Jackson, P.J. (1997) Characterization of Metal Ion Binding Sites on *Datura innoxia* by Using Lanthanide Ion Probe Spectroscopy. *Applied Spectroscopy*, vol. 51, no. 10 (October 1997) pp. 1476-1483. ISSN 0003-7028

- Fourest, E.; Volesky, B. (1996) Contribution of Sulfonate Groups and Alginate to Heavy Metal Biosorption by Dry Biomass of *Sargassum fluitans* *Environmental Science and Technology* vol. 30, no. 1 (January 1996) pp. 277-282. ISSN 0013 936X
- Gardea-Torresdey, J.L.; Tiemann, K.J.; Gamez, G.; Dokken, K. (1999) Effects of Chemical Competition for Multi-metal Binding by *Medicago sativa* (alfalfa), *Journal of Hazardous Materials*, vol. 69, no. 1, (October 1999) pp. 41-51 ISSN: 0304-3894.
- Gardea-Torresdey, J.L.; Arteaga, S.; Tiemann, K.J.; Chinaelli, R.; Pingatore, N.; Mackay, W., (2001) Absorption of Copper(II) by Creosote Bush (*Larrea tridentata*): Use of Atomic and X-ray Absorption Spectroscopy, *Environmental Toxicology and Chemistry*, vol. 20, no. 11 (November 2001) pp. 2572-2579 ISSN: 0730-7268.
- Jackson, P.J.; Anderson, W.L.; DeWitt, J.G.; Ke, H.-Y.D.; Kuske, C.R.; Moncrief, R.M.; Rayson G.D., (1993) Accumulation of Toxic Metal Ions on Cell Walls of *Datura innoxia* Suspension Cell Cultures *In Vitro Cellular Developmental Biology-Plant*, vol. 29P, no. 4 October 1993) pp. 220-226 ISSN: 1054-5476.
- Kelley, C.; Mielke, R.E.; Dimaquibo, D.; Curtis, A.J.; DeWitt, J.G. (1999) Adsorption of Eu(III) onto Roots of Water Hyacinth. *Environmental Science and Technology*, vol. 33, no. 9 (May 1 1999) pp. 1430-1443. ISSN 0013 936X
- Lin, S.; Drake, L.; Rayson, G. D. (1996) Applications of Frontal Affinity Chromatography to the Study of Interactions Between Metal Ions and a Complex Biomaterial *Analytical Chemistry*, vol. 68, no. 23 (December 1 1996) pp. 4087-4093. ISSN 0003-2700
- Lin, S.; Drake, L. R.; Rayson, G. D. (2002) Affinity Distributions of Lead Ion Binding to an Immobilized Biomaterial Derived from Cultured Cells of *Datura innoxia* *Advances in Environmental Research* vol. 6, no. 4 (October 2002) pp. 523-532 ISSN: 1093-0191.
- Majidi, V.; Laude, D.A.; Holcombe, J.A. (1990) Investigation of the Metal Algae Binding-Site with Cd-113 Nuclear-Magnetic-Resonance. *Environmental Science and Technology*, vol. 24, no. 9 (September 1990) pp. 1309-1312. ISSN 0013 936X
- Riddle, S.G.; Ran, H.H.; DeWeitt, J.G.; Andrews, J.C. (2002) Field, Laboratory, and X-ray Absorption Spectroscopic Studies of Mercury Accumulation by Water Hyacinths. *Environmental Science and Technology*, vol. 36, no. 9 (May 1 2002) pp. 1965-1970. ISSN 0013 936X
- Serna, D.D.; Moore, J.L.; Rayson, G.D. (2010) Site-Specific Binding Isotherms to a *Datura innoxia* Biosorbent. *Journal of Hazardous Materials*, vol. 173, no. 1-3 (January 15 2010) pp.409-414 ISSN: 0304-3894.
- Stark P. C.; Rayson, G. D. (2000) Comparison of Metal Ion Binding to Immobilized Biogenic Materials in a Flowing System, *Advances in Environmental Research*, vol. 4, no. 2 (May 2000) pp. 113-122 ISSN: 1093-0191.
- Volesky, B. (2000) Biosorption of Heavy Metals: Methodology Example of Uranium Removal in *Biologische Abwasserreinigung*, vol. 14, no. , pp. 17-37.
- Williams, P.A.; Rayson, G. D. (2003) Simultaneous Multi-element Detection of Metal Ions Bound to a *Datura innoxia* Material, *Journal of Hazardous Materials* vol. B99, no. 3 (May 30 2003) pp. 277-285 ISSN: 0304-3894.
- Xia, H.; Rayson, G. D. (1998) Investigation of Al binding to a *Datura innoxia* material using <sup>27</sup>Al NMR *Environmental Science and Technology*, vol. 32, no. 18 (September 15 1998) pp. 2688-2692. ISSN 0013 936X

---

Xia, H.; Rayson, G.D., (2002)  $^{113}\text{Cd}$  NMR Spectrometry Of Cd Binding Sites On Algae And Higher Plant Tissues, *Advances in Environmental Research*, vol. 7, no. 1 (November 2001) pp. 157-167 ISSN: 1093-0191..

# Decellularization, Stabilization and Functionalization of Collagenous Tissues Used as Cardiovascular Biomaterials

Birzabith Mendoza-Novelo<sup>1</sup> and Juan Valerio Cauch-Rodríguez<sup>2</sup>

<sup>1</sup>*Universidad Politécnica de Juventino Rosas*

<sup>2</sup>*Centro de Investigación Científica de Yucatán  
México*

## 1. Introduction

Cardiovascular diseases are a worldwide problem being a significant cause of morbidity and mortality every year. Patients requiring heart valve replacements include those exhibiting degenerative valvular diseases and rheumatic fever. The pathological processes include stenosis, fibrosis, myxoid change and calcification. The fibrosis causes a reaction to normal haemodynamic while the myxoid change reduces tensile strength of the valve due to replacement of dense collagenous tissue by loose tissue rich in glycosaminoglycans. Moreover, these pathologies can be observed in normal valves or fibrotic valves (Lindop, 2007).

Fortunately, the development of cardiovascular prostheses, either synthetic or biological, has allowed to increase life expectancy and has improved the quality of life of patient requiring either heart valves (Flanagan & Pandit, 2003; Schoen & Levi, 1999; Vesely, 2005) or vascular grafts (Matsagas et al., 2006; Monn & West, 2008; Schmidt & Baier, 2000). The implant technology for cardiovascular systems made use of raw materials of different origins. For example, metallic materials and synthetic polymers have been widely used in mechanical valves for the replacement of diseased heart valves. However, some complications such as alterations in the hemodynamical function and thrombus formation have been found (Zilla et al., 2008).

Biological prostheses provide some answers to these complications, although the bioprosthesis do not fulfil their objectives satisfactorily, since they display others complications once implanted. The complications of tissue valves include calcification, remnant tissue immunogenicity, inflammatory degradation, mechanical damage and lack of repair (Zilla et al., 2008). Therefore, the need for safe, economic, physiologically acceptable and viable biomaterial has motivated the modification of collagen-rich tissues.

Collagenous tissues are alternative raw materials for the manufacture of medical devices due to their physical and biomechanical properties. These tissues promote cell interactions, exhibit good ion and macromolecular binding capacity in addition to their electrostatic, hemostatical and immunological properties (Li, 2007). Since 1960s, perichardial tissues and the porcine heart valves are two of the most widely used biological tissues in the construction of cardiovascular devices. The introduction of these biological biomaterials was

linked to the tissue crosslinking to increase durability. However, due to some complications in the stabilized tissue, several post-crosslinking protocols have been proposed to address these complications. More recently, biological scaffolds derived from acellular tissue has been used in tissue engineering and regenerative medicine.

Therefore, this chapter deals with the processing of collagenous tissue for the preparation of cardiovascular biomaterials. The processing techniques include the extraction of cellular and nuclear material by various decellularization methods, the preservation of tissue through of crosslinking reactions, hydrogen-bond interactions or interstitial space filling, and the functionalization or the blocking of free groups with various low molecular and macromolecular substances.

## 2. The biomaterial choice

The replacement of damaged organs or tissues is one of the objectives of the biomaterials science. For this, natural or synthetic materials can be used for example in the cardiovascular field in the manufacture of heart valves and vascular grafts. The success of a device depends not only on the type of biomaterials but also on a set of acceptable characteristics such as biocompatibility, biostability, haemocompatibility, anti-trombogenicity, resistance to degradation and calcification.

Among those biomaterials that can fulfil these requirements, natural tissues are good candidates and that is why they have been under investigation in the past fifty years.

### 2.1 Composition and sources of natural tissue

Natural tissue biomaterial can be obtained from either animal-derived tissue (xenograft) or human-derived tissue (homograft). However, due to the limited availability of autografts, animal-derived tissues are, in many cases, the first choice for cardiovascular biomaterials. Animal derived tissues widely used as biological biomaterials include perichardial tissue from various sources such as cows, calves and ostrich in addition to pig aortas.

Tissue-derived biomaterials are mainly comprised of collagen in addition to the tissue extracellular matrix (ECM) which is a complex mixture of structural and functional proteins such as collagen, proteoglycans, glycoproteins, elastin, metalloproteins, etc. Collagen, being the main structural protein, is a polypeptide that contain amino (-NH<sub>2</sub>), carboxylic acid (-COOH) and hydroxyl (-OH) functional groups as substituents, and together with the amide bonds in the polymer backbone form the reactive centers. The repetitive unit in the polymer backbone of collagen and the amino acid residues as side group are depicted in figure 1.

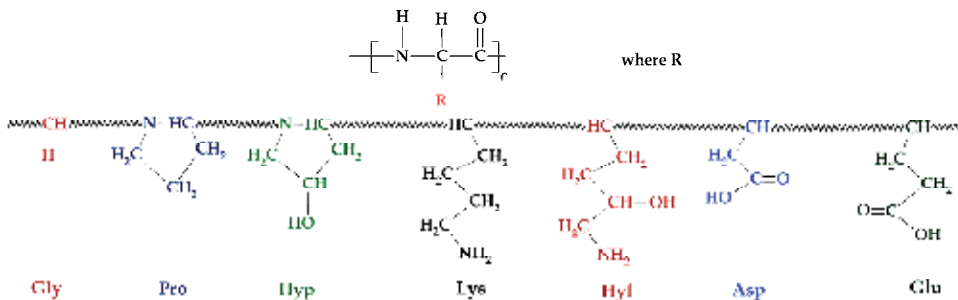


Fig. 1. Representation of the repetitive unit of collagen and some side group R of amino acid residue

The crystal lattice of collagen fibers are embedded in an amorphous matrix. The amorphous matrix is composed mainly by glycosaminoglycans as proteoglycans (sulphated glycosaminoglycans bound to proteins). In this matrix, in addition to the fibers, tissue cells and interstitial fluid (water or electrolytes) are embedded. The glycosaminoglycans are negatively charged polysaccharides of varying degrees of complexity. The glycosaminoglycan polymers consist of repeating disaccharide units, usually consisting of a hexosamine and an uronic acid (Yeung et al., 2001). The charged negatively units contribute to the elasticity and hydration of the tissues (Mavrilas et al., 2005), but may attract counter-ions, which could intervene in the processes of calcification of bioprostheses. The repetitive disaccharide unit of glycosaminoglycans mainly presents in native bovine perichardium is shown in figure 2.

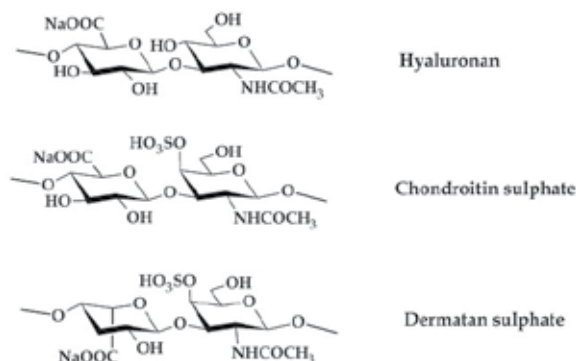


Fig. 2. Repetitive disaccharide units of common glycosaminoglycans in bovine perichardial tissue

The different soft tissues including cartilage, tendons, ligaments, skin and perichardium have the capacity of support mechanical load of variable magnitude. Therefore, the properties of the tissue depend on the number and the arrangement of collagen fibers, which can be parallel or perpendicular to the surface or randomly distributed in the matrix. The hierarchical nature of collagen confers to the tissue its structural complexity. The fibrous nature of bovine perichardial tissue is revealed in figure 3. In perichardial tissue, a multi-laminate structure is observed with difference in both serosa (Fig. 3b) and rugosa surface (Fig. 3a).

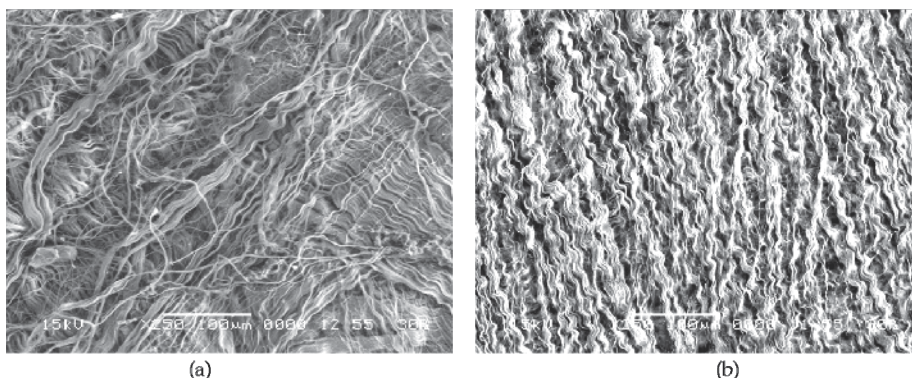


Fig. 3. SEM micrographs for the fibrosa (a) and the serosa surface (b) of native bovine perichardium

## 2.2 Properties of collagenous tissues

Collagen-rich tissues are composed of 75% of collagen, 20% of mucopolysaccharides and water, although elastin can be found in less than 5% (Cauch-Rodríguez, 2008). All these tissue components maintain the structural and functional integrity of the composite tissue. Some mechanical properties of collagenous tissues are shown in table 1.

Tissue	Property	Value	Reference
Bovine perichardium	Tensile strength	10.9 MPa	Lee at el., 1989
	Strain at rupture	33.0 %	
	Tissue modulus	58.2 MPa	
	Tensile strength	18.4 MPa	
Canine perichardium	Strain at rupture	21.4 %	Lee & Boughner, 1981; Wiegner & Bing, 1981
	Tissue modulus	198 MPa	
	Tensile strength	2.51 MPa	
	Strain at rupture	34.9 %	
Human perichardium	Tissue modulus	20.4 MPa	Lee & Boughner, 1985
	Tensile strength	6.25 MPa	
	Strain at rupture	30.8 %	
	Tissue modulus	54.6 MPa	
Porcine aortic valve leaflet	Tensile strength	6.25 MPa	Lee at el., 1984
	Strain at rupture	30.8 %	
	Tissue modulus	54.6 MPa	
	Tensile strength	6.25 MPa	

Table 1. Mechanical properties of some collagenous tissue

The thermal transitions experienced by materials with amorphous and/or crystalline regions are also observed in the collagenous tissue. When the biomaterial is heated, its specific volume increases, exhibiting the glass transition of amorphous regions and the fusion of crystalline collagen fibers to a temperature higher than the glass transition temperature (Li, 2007). The melting temperature of collagen fibers is an irreversible process and is often referred in the literature as the denaturation temperature ( $T_d$ ) or shrinkage temperature ( $T_s$ ). In fact, the denaturation temperature is widely used as an indicator of the tissue stabilization.

The collagenous tissues require chemical or physical treatments in order to be preserved or stabilized. In fact, the introduction of cardiovascular bioprostheses in 1960s was linked to the chemical fixation of porcine aortic valves or bovine perichardial tissue with glutaraldehyde. This process produces a non-living material without the capability of intrinsic repair as native tissue does after some structural injury (Flanagan & Pandit, 2003). The processed tissue tends to fail in modes related to the remnant immunogenicity,



inflammatory degradation, mechanical damage and pannus overgrowth (Zilla et al., 2008). In general, the stabilization of collagen-rich tissue is achieved by direct binding of functional groups to amino acid residues from collagen by coupling agents or by the linkage between the functional groups on collagen and various chemical agents. Both processes are referred in literature as the fixation or crosslinking processes. While the crosslinking agents make durable, stable and resistant tissues, the crosslinking density and the chemical process seems to have an effect on some of the major disadvantages of bioprostheses, such as calcification (Zilla et al., 2008). For this reason, a large number of crosslinking agents have been suggested with the aim of obtaining bioprosthesis that fulfill successfully its function. In addition to this treatment, there are reports on the post-crosslinking and pre-crosslinking treatments in order to reduce the calcification of biomaterial and in order to prepare porous biomaterials as scaffolds for tissue engineering.

### 3. Decellularization of tissues

The concept of decellularization is referred as the extraction of cellular components from natural tissues of human or animal origin. Different approaches have been reported as effective procedures to remove cells from xenogeneic and allogeneic collagenous tissue with the aim of removing cellular antigens and procalcifying remnants while the extracellular matrix (ECM) integrity is preserved as much as possible (Schmidt & Baier, 2000). The combination of chemical, physical and enzymatic methods destroys the cell membrane and removes nuclear and cellular material (Gilbert et al., 2006). The remaining acellular ECM will be a complex mixture of structural and functional proteins, glycoproteins and glycosaminoglycans arranged in a three-dimensional architecture. However, some mechanical and structural alterations on the ECM can be induced during the decellularization process.

#### 3.1 Effect of decellularization treatment on tissue properties

A biomaterial or scaffold for tissue engineering should provide not only mechanical support for the cell proliferation but also they must be versatile to give the required anatomical shape (Kidane et al., 2009). The decellularization of collagenous tissues has been explored as the ECM may serve as appropriate biological scaffold for cell attachment and proliferation. However, alterations both in the structural composition and in the mechanical properties of the remaining ECM can be induced during the decellularization protocols. The mechanical integrity can be affected and it may be associated either to the denaturation of the collagen triple helix or to the loss of macromolecular substances such as glycoproteins.

The efficiency of a given decellularization method and their effects on the properties of animal tissues must be studied in a specific manner due to compositional and structural differences (Gilbert et al., 2006). For example, the decellularization of porcine heart valve with sodium dodecyl sulphate, an anionic detergent, appeared to maintain the critical mechanical and structural properties of the valves leaflets (Liao et al., 2008) while decellularization of bovine perichardium with sodium dodecyl sulphate caused irreversible swelling, resulted in a reduction of the denaturation temperature (Courtman et al., 1994; García-Páez et al, 2000) and caused a reduction of almost 50% on tensile strength when compared to native tissue and tissue treated with Triton X100, a non-ionic detergent (Mendoza-Novelo & Cauich-Rodríguez, 2009).

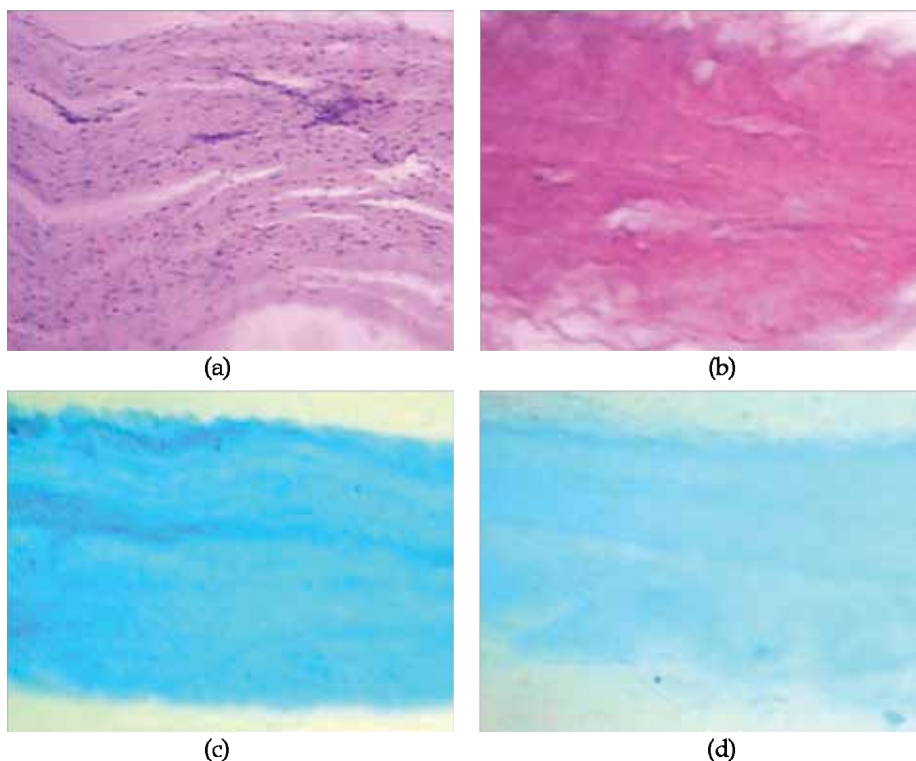


Fig. 4. Histological micrographs for native (a),(c) and decellurized (b),(d) perichardial tissue in H&E (top) and alcian blue (bottom) staining

It has been proposed that an anionic detergent binds to proteins, increases negative charges and results in tissue irreversible swelling (Courtman et al., 1994). In addition, a highly negative charged perichardial tissue has been associated to a higher tendency to tissue calcification (Jorge-Herrero et al., 2010). Due to these adverse effects, non-ionic detergents are preferred over ionic surfactants in the decellularization process of perichardial tissue. However, there are some issues related to the use of aromatic (phenolic) or non-aromatic (non-phenolic) non-ionic detergents used in the decellularization process. For example, the biodegradation products of derivatives of non-ionic detergents such as alkylphenol ethoxylates have been associated to toxicity (Argese et al., 1994) and estrogenic effects (Soto et al., 1991; Jobling & Sumpter et al., 1993). Figure 4 shows the histological results for bovine perichardial tissue decellularized with a non-aromatic non-ionic detergents. In this case, a reduction in the cell nuclei present in bovine perichardial tissue and a decrease in the glycosaminoglycan content after decellularization treatment were observed (Mendoza-Novelo et al., 2011).

In addition to tissue decellularization with nonionic surfactants, reversible swelling has also been studied. In this case, the reversible alkaline swelling did not change the three-dimensional architecture of native bovine perichardium. This means that the laminar structure and fibrous nature of the native perichardial tissue were maintained after decellularization although the opening of the interfibrillar spaces was observed. The reversible alkaline swelling cause a reversible change in the tissue thickness i.e. increased 45% after swelling step, but the tissue original thickness was regained after deswelling step.

However, the alkaline treatment altered the perichardial tissue stress relaxation behaviour (Mendoza-Novelo et al., 2011).

### 3.2 Pre-treatments (pre-crosslinking) methods to reduce tissue calcification

Bovine perichardium undergoes several treatments prior to crosslinking with the aim to improve its biocompatibility, to reduce immunogenicity, to decrease its tendency to calcification, to promote neo-vascularization and infiltration, and to increase cell adhesion and proliferation. Some of the pre-treatments proposed in the literature to reduce calcification of cardiovascular bioprostheses are showed in the table 2. It has been reported that with the treatment of bioprostheses with sodium dodecyl sulphate and Triton<sup>TM</sup>X-100 most of the acidic phospholipids are extracted resulting in the initial suppression of calcification in the cell membrane (Schmidt & Baier, 2000).

Pre-treatment	Anti-calcification action mode	Reference
Surfactants	Removal of acidic phospholipids	Schmidt & Baier, 2000; Chang et al., 2004
Alcohols	Removal of phospholipids and cholesterol Alteration in the collagen conformation Cellular death Removal of Cardiolipin	Vyavahare et al. 1997; Pfau et al. 2000; Pathak et al., 2002

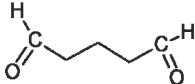
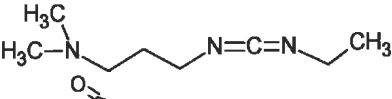
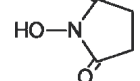
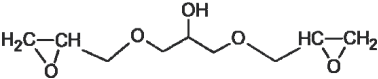
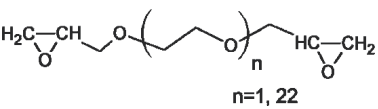
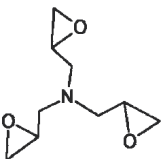
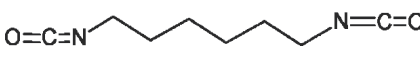
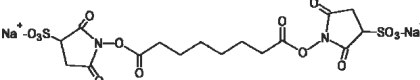
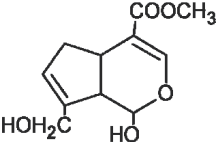
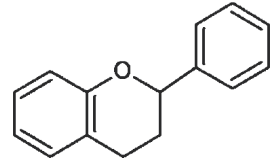
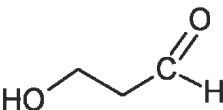
Table 2. Tissue pretreatment in order to reduce the bioprostheses calcification

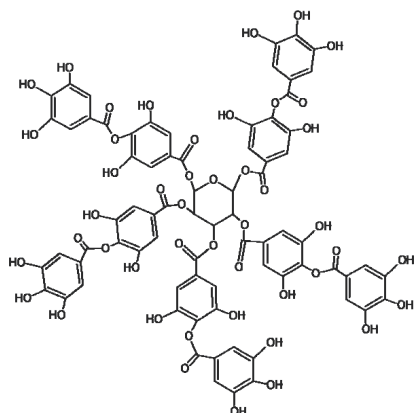
The pretreatment of collagen-rich biomaterials with different concentrations of ethanol may prevent calcification through the extraction of phospholipids and cholesterol but causes a permanent alteration in the collagen conformation (Schmidt & Baier, 2000). Additionally, this treatment affected the interaction of the tissue with water and lipids and increased the resistance of the tissue to the action of collagenase. Several high molecular weight alcohols have been used in order to remove cellular components that contain elements responsible for the calcification (Pathak et al., 2002). The pretreatment with 50% ethanol for 5 min reduces fibrosis of bovine perichardium implanted in the aorta of sheep as a result of cell death and cardiolipin removal more than the phospholipids extraction (Vyavahare et al., 1997). Mixtures of chloroform/methanol have also been effective in reducing tissue calcification (Jorge-Herrero et al., 1994).

## 4. Stabilization of tissues

The stability of tissues is increased by physical or chemical crosslinking. The fixation enhances tissue stability, inhibits autolysis, allows a prolonged shelf-life, and allows a surgeon to have medical devices of various sizes readily available for implantation (Schoen & Levy, 1999). The chemical treatments also mitigate immunogenicity while maintaining both thromboresistance and antimicrobial sterility but greatly influence their degradation and calcification. However, tissue calcification is multifactorial phenomenon where chemical crosslinking is considered just one of these factors. In fact, the alteration in the electrical charge that exists in the perichardial tissue surface has been associated to the

calcification (Jorge-Herrero et al., 2010). Several crosslinking techniques have been suggested as the ideal procedure to stabilize the collagen structure while maintaining their physical and natural shaping. The structure and name of some chemicals used as crosslinking agents for collagenous tissue are shown in table 3.

Structure of stabilization agents	Name	Reference
	Glutaraldehyde	Olde Damink et al., 1995; Duncan & Boughner, 1998; Langdon et al., 1999
	Ethyl-aminopropyl carbodiimide (EDAC)	Lee et al., 1996; Everaerts et al., 2004; Mendoza-Novelo & Cauich-Rodríguez, 2009
	hydroxysuccinimide (NHS)	
	Glycerol diglycidyl ether	Lee et al., 1994
	Ethylene glycol diglycidyl ether, n=1; Poly(ethylene oxide) diglycidyl ether, n=22	Tu et al., 1993; Sung et al., 1996; Zeeman et al., 2000
	Triglycidylamine	Conolly et al., 2005; Sack et al., 2007; Rapoport et al., 2007
	Hexamethylene diisocyanate	Naimark et al., 1995; Olde Damink et al., 1995; Nowatzki & Tirrel, 2004
	Disuccinimidyl suberate	Pathak et al., 2001
	Genipin	Sung et al. 1999; Sung et al., 2000
	Proanthocyanidin, Procyanidins	Han et al., 2003; Zhai et al., 2009
	Reuterin	Sung et al., 2002; Sung et al., 2003



Tannic acid

Isenburg et al., 2004;  
Isenburg et al., 2006

Table 3. Some chemical agents used for the stabilization and fixation of biological tissues

#### 4.1 Tissue crosslinking with glutaraldehyde

The procedure most studied and exploited in the manufacture of tissue valve includes the crosslinking with glutaraldehyde, which is also widely used as tanning agent in the leather industry. Glutaraldehyde is an important reagent in the biomedical field and has been used as crosslinking agent in the preparation of collagen-rich biomaterials or for the immobilization of enzymes or cell fixation.

Glutaraldehyde is an efficient agent for the crosslinking of collagen matrix because it reacts relatively quickly and because it is able to join separate protein molecules by means of the amino groups abundantly present in collagen. Glutaraldehyde is a cheap and water-soluble five-carbon bifunctional aldehyde that in aqueous solution consists of a mixture of free aldehyde, mono and dihydrated monomeric glutaraldehyde, monomeric and polymeric cyclic hemiacetals and various  $\alpha$ ,  $\beta$  unsaturated polymers (Whipple & Ruta, 1974). This means that glutaraldehyde itself forms a number of different reactive species and that these species may also react in different ways, rendering a highly crosslinked network. Glutaraldehyde crosslinking has been and is still applied to most of the experimental and clinical bioprostheses. This process consists in blocking the  $\epsilon$ -amino groups of lysine in the protein through imino bond formation. The contribution of glutaraldehyde as sterilization and crosslinking agent is partly due to its hydrophobicity and hydrophilicity, allowing it to penetrate both aqueous media and the cell membrane. However, in the manufacture of bioprostheses, the use of glutaraldehyde has led to many disadvantages associated with the residual free aldehyde groups. Table 4 shows some of the problems associated with glutaraldehyde tissue crosslinking and some solutions that have been suggested to solve them.

In aqueous solution, glutaraldehyde is presented as a mixture of free aldehyde, mono and dihydrate glutaraldehyde monomer, monomeric and polymeric cyclic hemiacetals, and several  $\alpha$  or  $\beta$  unsaturated polymers (Monsan et al., 1975). In turn, this heterogeneity of chemical species leads to a heterogeneous crosslinking. In addition, high concentration of glutaraldehyde promotes rapid surface crosslinking in the tissue (Olde-Damink et al., 1995), creating a barrier that impedes or prevents the diffusion of more glutaraldehyde within the biomaterial. In order to avoid this, the use of low concentrations has been suggested (Khor, 1997). It has also been proposed that glutaraldehyde protection as a monomer by the formation of di-acetals, between glutaraldehyde and alcohols in acidic medium (Giossis et al., 1998).

The fixation reaction was carried out by the exposure of the tissue balanced with glutaraldehyde acetals solutions to triethylamine vapours. This process allowed the diffusion of the non-reactive glutaraldehyde into the tissue, minimized the formation of polymeric glutaraldehyde and reduced the waterproofing (hydrophobicity) at the tissue surface (Yoshioka & Giossis, 2008).

The conditions of the crosslinking reaction (pressure for instance) have been varied with the aim of improving the biomechanical properties of bovine perichardium. The crosslinking of bovine perichardium with glutaraldehyde at a pressure of 4 mm Hg (low pressure) both statically and dynamically (1.2 Hz) has been reported. By comparing the properties of crosslinked bovine perichardium, the dynamically crosslinked tissue showed a very similar extensibility to native biomaterial (non-crosslinked) in contrast to statically crosslinked tissue, which showed a higher extensibility, while no differences were reported in other mechanical properties (Duncan & Boughner, 1998). The bovine perichardial fixation with glutaraldehyde under biaxial static pressures (~225 and ~1875 mmHg) has been proposed. The bovine perichardium treated at high pressure showed an increase in stiffness and almost isotropic behaviour, while low pressure-treated bovine perichardium preserved the anisotropy exhibited by the native tissue (Langdon, et al., 1999). Porcine valves have also been subjected to crosslinking at high pressure (80 mm Hg), low and zero pressure. In this case, it was reported an increase in the rigidity of the leaflets fixed under low pressure and the preservation of geometric corrugations and undulations of the native tissue when the leaflet were fixed without pressure (Lee et al., 1984).

Heat treatment during glutaraldehyde fixation has also been reported. The thermal treatment at 50°C showed an anti-calcifying effect which was attributed to structural changes in collagen or lipid extraction by heat treatment (Carpentier et al., 2001).

#### **4.1.1 Post-treatments after glutaraldehyde fixation**

The residual unbounded aldehyde groups that remain in the tissue after glutaraldehyde fixation process have been associated with degenerative phenomenon on different bioprosthesis. The grafting of different molecules on collagenous tissues treated with glutaraldehyde has been an answer to these disadvantages.

The grafted molecules are incorporated in order to block free aldehyde groups and thus to reduce or to neutralize both cytotoxicity and calcification. Some surface modification procedures of crosslinked collagenous tissues are described in table 5.

It is known that nitric oxide releasing compounds can improve the biocompatibility of blood-contacting medical devices (Frost et al., 2005; Masters et al., 2005). Two common nitric oxide generating substances immobilized on synthetic polymers are diazeniumdiolates and S-nitrosothiols (Frost et al., 2005). In the same line of thought, surface modification of polymeric materials, such as PET or PU, with thiol compounds is interesting as it might exchange nitric oxide with endogenous donors such as S-nitrosothiols that already circulate in blood (Gappa-Fahlenkamp et al., 2004; Gappa-Fahlenkamp & Lewis, 2005).

The thiol groups on the polymer allowed the exchange reaction with S-nitroso serum albumin and then, the release of nitric oxide to inhibit platelet adhesion on the polymeric surfaces (Duan & Lewis, 2002). This approach has been proposed in perichardial tissue biomaterial by using L-cysteine as thiol compound (Mendoza-Novelo & Cauch-Rodríguez, 2009). One additional advantage of L-cysteine grafting on glutaraldehyde-crosslinked perichardial tissue is that free aldehyde groups will be diminished or even eliminated on the tissue allowing its detoxification. A schematic representation of grafting of collagenous tissue with L-cysteine is described in the figure 5. Similar approaches with other amino

acids have been suggested in order to provide non-cytotoxic tissue biomaterial and biomaterial with reduced calcification, as it is shown in table 5. In this table, it is also included molecules of biological importance as well as peptide sequences used to improve cell adhesion after the fixation treatment.

Type of molecule		Effects on biomaterial	References
Macromolecules	Hyaluronic acid -	Reduce the calcification of glutaraldehyde-treated tissue	Ohri et al., 2004
	Heparin-	Reduce the calcium deposition and the cytotoxicity of glutaraldehyde-treated	Lee et al., 2000
	Poly(ethylene glycol)-	Inhibit the platelet surface attachment and spreading and decrease the calcification of glutaraldehyde-treated tissue	Vasudev & Chandy, 1999; Park et al., 1997
	RGD peptides-	Enhance the adhesion and proliferation of human mesenchymal stem cells on acellular tissue	Dong et al., 2009
Amino acids	L-arginine, L-glutamine, L-lysine, L-glutamic acid, L-cysteine -	Reduce the protein adsorption and platelet adhesion of glutaraldehyde treated tissue. However, BP treatment with amino acids does not effectively prevent calcification. Incorporation of thiol moieties to the tissue	Jorge-Herrero et al., 1996; Jee et al., 2003; Mendoza-Novelo & Cauch-Rodríguez, 2009
	Acids		
Acids	Homocysteic acid -	Reduce toxicity but does not affect the stability of glutaraldehyde-treated tissue	Stacchino et al., 1998
	Amino oleic acid -	Inhibit the calcification of glutaraldehyde-treated tissue	Chen et al., 1994

Table 5. Molecules grafted on crosslinked bovine perichardial tissue

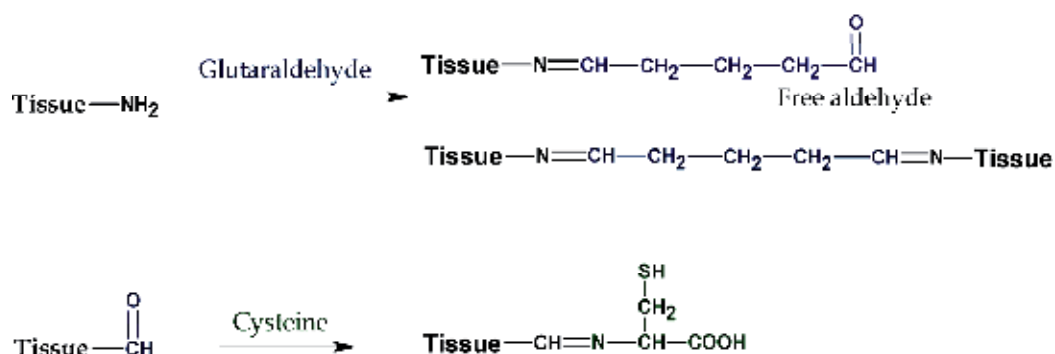


Fig. 5. Schematic representation of tissue crosslinking with glutaraldehyde and chemical coupling of L-cysteine

#### 4.2 Tissue crosslinking after carboxylic group activation

Due to the problems associated with the use of glutaraldehyde, various non-aldehyde alternative methods have been developed to stabilize and post-treat tissues. The crosslinking agents used in collagen-rich biomaterials can use both primary amino groups and acid groups of polypeptide chains. Historically, a water soluble carbodiimide (1-ethyl-3-(3-dimethyl amino propyl) carbodiimide / EDAC) was first used for the modification of carboxylic groups in proteins for peptide synthesis (Sheehan & Hlavka, 1956) and to promote crosslinking in gelatin (Sheehan & Hlavka, 1957).

The mechanism for the reaction between carboxylic groups and EDAC leading to amide bond formation is as follows: The addition of a carboxylic acid diimide produces an isourea ester, an O-acyl isourea. The intermediate O-acyl isourea is an activated carboxylic acid derivative with similar reactivity to an anhydride or acyl halide, and can be subjected to a subsequent nucleophilic substitution by an amine yielding a dialkyl amide and urea (Carraway & Khosland, 1972). Because carbodiimide is just a coupling agent, when used to crosslink collagen in the absence of agents with dual functionality, only promotes the formation of an amide bond between carboxylic acid and amino reactive groups present in the tissue, as depicted in figure 6.

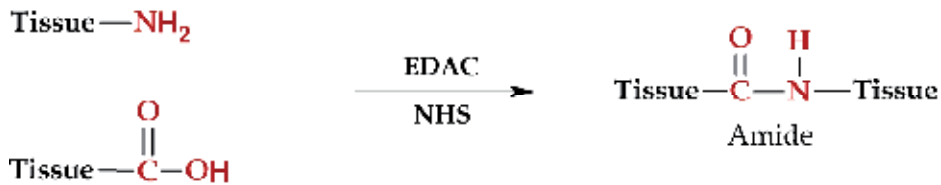


Fig. 6. Schematic representation of tissue crosslinking with EDAC and NHS



Fig. 7. Bovine perichardial tissue crosslinked with EDAC (rectangles) or glutaraldehyde (circles)

This requires that the activated carboxylic groups be close enough to the amino groups to achieve direct bonding (amide bond formation). The carbodiimides are hydrolyzed rapidly



in aqueous solution and the intermediate O-acyl isourea is extremely unstable producing a low crosslinking.

The crosslinking density and the shrinkage temperature of bovine perichardium treated with EDAC had values lower than a control of bovine perichardium fixed with glutaraldehyde (Mendoza-Novelo & Cauich-Rodríguez, 2009). However, the use of the N-hydroxysuccinimide (NHS) during crosslinking with EDAC improved the stabilization of tissue due to the formation of a stable intermediate compound after reaction of the NHS with carboxylic groups or isourea O-acyl intermediate (Lee et al., 1996). Such is the case reported for porcine aortic valves crosslinked by a two-step method. These steps included the blocking of the free primary amino groups of collagen with butanal and the crosslinking with Jeffamines™ of different molecular weights by activating the carboxylic acid groups with EDAC and NHS. This process led to a decrease in calcification (subcutaneous implantation in rats) of engineered tissue (Everaerts et al., 2004).

The appearance of bovine perichardial tissue crosslinked with glutaraldehyde and EDAC is shown in figure 7.

### 4.3 Tissue crosslinking with epoxy compounds

The chemistry of epoxy groups, cyclic ethers of three members, has also been explored and applied in the fixation of tissue. Polyepoxide compounds or epoxy bifunctional polyether react with amino groups from collagen opening the terminal epoxide ring (Tu et al., 1993; Lee et al., 1994; Khorn, 1997). This reaction is nucleophilic and can be carried out under acidic conditions (highly reactive protonated epoxy) or alkaline (amine at its most nucleophilic). In this case, the modification of swine tendons with ethylene glycol diglycidyl ether has been reported for the repair of cruciate ligaments (Sung et al., 1996). The 1,4-butanediol diglycidyl ether (BD) has been reported as a crosslinking agent in the preparation of bioprosthetic valves (Zeeman et al., 2000). However, the fixation of porcine valves with BD caused immune response, foreign body reaction (proliferation of lymphocytes and macrophages) and calcification of implanted tissue using rats as animal model to levels similar to glutaraldehyde-fixed tissue, although low levels of cytotoxicity were reported (van Wachem et al., 2000). The combined treatment of BD and EDAC-dicarboxylic acid or detergents led to a reduction in calcification (implantation in rats) but not at significant levels (van Wachem et al., 1994). Therefore, it was concluded that the treatment with BD did not represent an alternative to glutaraldehyde to reduce the calcification of bioprosthetic valves (van Wachem et al., 1994). However, in another report the crosslinking of bovine perichardium and porcine aortic valves with triglycidylamine, a molecule of high polarity and solubility in water, resulted in an improvement in biocompatibility (assessed using bovine aortic valve interstitial cells, human umbilical endothelial cells and rats artery smooth muscle cells) and resistance to calcification (subcutaneous implantation in rats) compared with glutaraldehyde-fixed tissues (Connolly et al., 2005). Furthermore, triglycidylamine-fixed tissues showed stable mechanical properties (Sacks et al., 2007) and optimal reduction of calcification when treatments included mercapto-aminobisphosphonate (Rapoport et al., 2007). It was hypothesized that the difference between these two results, which explored the chemistry of epoxy in the crosslinking of tissue, may be due to differences in water solubility, chemical heterogeneity and contamination with used epoxy residual reactants (Connolly et al., 2005).

#### 4.4 Tissue crosslinking with diisocyanate

Bifunctional molecules capable of crosslinking proteins by urea bond formation after reaction between terminal isocyanate groups and  $\epsilon$ -amino group of lysine residue have been explored. Such is the case of crosslinking of extracellular matrix proteins (elastin and fibronectin) with hexamethylene diisocyanate in dimethyl sulfoxide (Tirrell and Nowatzki, 2004). Similarly, the crosslinking of ovine skin collagen with hexamethylene diisocyanate has been reported. This crosslinking procedure was carried out in an aqueous medium including surfactants to increase solubility and promote the penetration of diisocyanate into the tissue (Olde Damink et al., 1995). Furthermore, the effects of the tissue crosslinking with hexamethylene diisocyanate and the effects of mixtures of water/isopropanol (50/50 and 0/100) as solvent on the thermal and biomechanical properties of bovine perichardium have been reported (Naimark et al., 1995). On the other hand, the stabilization of porcine perichardium has been achieved by the interaction of polyurethane oligomers containing isocyanate end groups (Loke et al., 1996). The interaction in organic media between perichardial tissue and polyurethane oligomers resulted in the increase of the denaturation temperature, a reduction in the content of lysine and a poor diffusion of polyurethane oligomers into the tissue (H&E staining). The crosslinking of bovine perichardium with polyurethane oligomers, EDAC and diphenyl phosphoric azide showed less cytotoxicity (assessed by a direct cytotoxicity test or Homsy test) than the tissue crosslinking with glutaraldehyde (Jorge-Herrero et al., 2005).

After these results, it is clear that diisocyanates are an alternative to glutaraldehyde in the preparation of bioprostheses. However, protein fixation with isocyanates has the disadvantage of using organic solvents. In addition, during the fixation in aqueous media, the crosslinking degree can be reduced due to competition of hydrolysis reactions. Therefore, the blocking reaction of isocyanate with bisulphite salts is an alternative in the preparation of water soluble isocyanates (Petersen, 1949). The protein crosslinking process with blocking isocyanates has the advantages of the use of aqueous media and reduced isocyanate toxicity (Mata-Mata et al., 2008). In this regard, the treatment of perichardial tissue with the carbamoylsulphonate blocked polyurethane prepolymers resulted in an increase of the *in vitro* tissue biostability (Mendoza-Novelo, 2011). The coating of collagen fiber network of perichardial tissue with polyurethane is shown in figure 8.

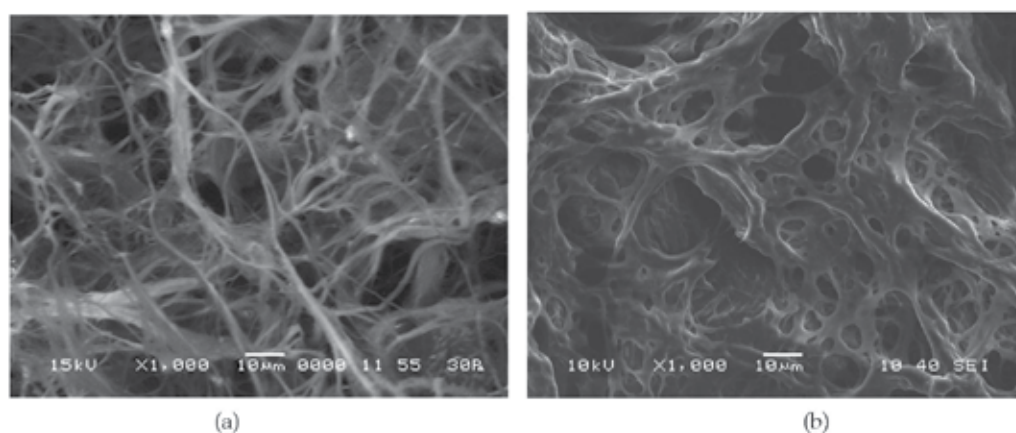


Fig. 8. SEM micrographs for bovine perichardium (a) native and treated with polyurethane prepolymers

#### 4.5 Tissue crosslinking with naturally-derived compounds

Crosslinking agents of natural origin have also been explored in the tissue crosslinking. Such is the case of genipin, an aglycone or an iridoid glycoside, which can be obtained by enzymatic hydrolysis of the glucoside previously isolated from gardenia fruit. The stabilization of porcine perichardium (Sung et al., 1999) and acellular bovine perichardium (Sung et al., 2000) with genipin probably was achieved through cyclic structures. The crosslinking density for genipin-fixed tissue was similar to glutaraldehyde and ethylene glycol diglycidyl ether -crosslinked tissues. Moreover, the genipin-crosslinked porcine perichardium was less cytotoxic (fibroblasts) than glutaraldehyde-crosslinked tissue, whereas exhibiting the same tensile strength and resistance to enzymatic degradation (Chang et al., 2002). Furthermore, acellular bovine perichardium fixed with genipin showed capacity of angiogenesis (microvessel infiltration) after implantation in rats (Liang et al., 2004). Moreover, cell extraction with solutions of Triton™X-100 and the crosslinking with different concentrations of genipin were used to establish a relationship between the crosslinking degree and the degradation rate or the model of acellular tissue regeneration (Chang et al., 2004).

Polyphenolic compounds have also been investigated as natural agents of tissue stabilization, such as the proanthocyanidins from the family known as condensed tannins, which are essentially oligomers of flavonoids available in several fruits and vegetables. The stabilization of collagen with proanthocyanidins may involve the formation of hydrogen bond type interactions between the phenolic hydroxyl and amide carbonyls of the polypeptide chains.

The proanthocyanidin has a high affinity for proline-rich proteins, because this amino acid is a good hydrogen bond acceptor (Zhai et al., 2006). The proanthocyanidins can be used to crosslink collagen sponges with similar density and efficiency to glutaraldehyde but with reduced calcification after 6 weeks implantation in rats and it was reported to be 120 times less toxic to fibroblasts direct contact (Han et al., 2003). The proanthocyanidin crosslinking procedure was repeated in decellularized porcine aortic valves resulting in low toxicity to bovine aortic valve interstitial cells and in the stimulation of cell proliferation to low concentrations of this stabilization agent in the culture media (Zhai et al., 2009).

The stabilization of elastin in porcine aortas has been achieved by treatment with polyphenolic tannins, which is composed of a central molecule of glucose (hydrophobic core) and one or more galloil residues (hydrophilic shell) (Isenburg et al., 2006). Polyphenolic compounds were acetylated tannic acid, pentagalol glucose, gallic acid and glucose. In this study, pentagalol glucose treatment was the least toxic to fibroblasts (Isenburg et al., 2004). Also, the study revealed that polyphenolic hydroxyl groups are essential for the interaction between the tannic acid and elastin. The combination of tannic acid and glutaraldehyde rendered a biostable tissue with high resistance toward elastase and collagenase and low tendency to calcify (Isenburg et al., 2006).

The reuterin ( $\beta$ -hydroxypropionic acid) produced by *Lactobacillus reuteri* has been used in the fixation of porcine perichardium (Sung et al., 2002). The reuterin is soluble in water, with antimicrobial and antifungal activity. The properties of reuterin-fixed tissue are comparable to glutaraldehyde-fixed tissue in terms of amino group content, denaturation temperature, tensile strength and collagenase digestion resistance (Sung et al., 2003).

Microbial (mTG; *Streptovorticillium mobaraense*) and tissue (TG2; tTG) transglutaminases (protein-glutamine  $\gamma$ -glutamyltransferase, EC 2.3.2.13) have been explored in the

crosslinking of collagen type I due to their ability to crosslink proteins through the  $\epsilon$ -amino group of lysine and  $\gamma$ -carboxamide group of glutamine residue (Chen et al., 2005; Chau et al., 2005). The results indicated the efficiency of this crosslinking agents in terms of denaturation temperature, mechanical strength, low toxicity to fibroblasts (Chen et al., 2005) and an increase in osteoblasts and fibroblasts adhesion and proliferation compared to native collagen (Chau et al., 2005).

#### 4.6 Other methods for the tissue stabilization

Others non-aldehydic crosslinking procedures have been proposed with the aims of prevent or mitigate tissue calcification. The disuccinimidyl glutarate (DSG) is another non-aldehyde alternative to tissue crosslinking. The process is carried out by the reaction between primary amino groups of tissue and NHS ester groups of DSG forming amide bonds with a length of five-carbon crosslinking and releasing NHS. The DSG crosslinked tissue was resistant to enzymatic degradation, exhibited low tendency to calcify and high temperature of denaturation. However, it was necessary to use dimethyl sulfoxide due to the insolubility of crosslinking agent in water (Pathak et al., 2000). In response to this drawback, a water soluble crosslinking agent has been used, i. e., the disuccinimidyl suberate. The presence of sulfonyl groups at the ends of the molecule conferred water solubility while retaining reactivity with amino groups by crosslinking chemistry similar to DSG, but with a length of 8 carbon intermediates. The tissue crosslinked under these conditions showed very low levels of calcium (0.2 mg/g of tissue) after 90 days of implantation in rats (Pathak et al., 2001). The crosslinking of collagen type I proposed for cartilage regeneration has also been achieved by the diimidoesters – dimethyl suberimidate (DMS). In this procedure, collagen amino groups react with DMS imidoester groups to form amidine groups and a length crosslinking of 8 carbons (Charulatha & Rajaram, 2003).

The stabilization of bioprosthetic tissue by filling the tissue interstitial spaces with polyacrylamide hydrogel resulted in the mitigation of tissue calcification in a rat study (Oosthuysen et al., 2006). Physical methods such as photo-oxidation (Khorn et al., 1997) or the use of ultraviolet radiation (Pfau et al., 2000) have also been proposed for the crosslinking of collagen-rich biomaterials. However, despite the increase in tissue shrinkage temperature, in some case the treated tissue did not show resistance to the proteins extraction (Moore et al., 1996).

#### 4.7 Masking reactions

At this point it is important to distinguish between the effective formation of crosslinking sites, i. e., two reactive sites in collagen linked by a same molecule of crosslinking agent, and the masking of crosslinking, i.e., the reaction between a single end of bifunctional crosslinking agent and one reactive site of collagen. Table 6 shows the possible reactions of crosslinking and masking between collagen and difunctional crosslinking agents.

#### 4.8 Glycosaminoglycans stabilization

Glycosaminoglycans present in both aortic valves and perichardium have been fixed to prevent the loss of these polysaccharides during the fixation of bioprosthetic valves. The sodium metaperiodate has been used for the stabilization of glycosaminoglycans in porcine aortic valves with the subsequent glutaraldehyde crosslinking (Vyavahare & Lovekamp, 2001). The stabilized porcine aortic valve showed compatibility and reduced calcification

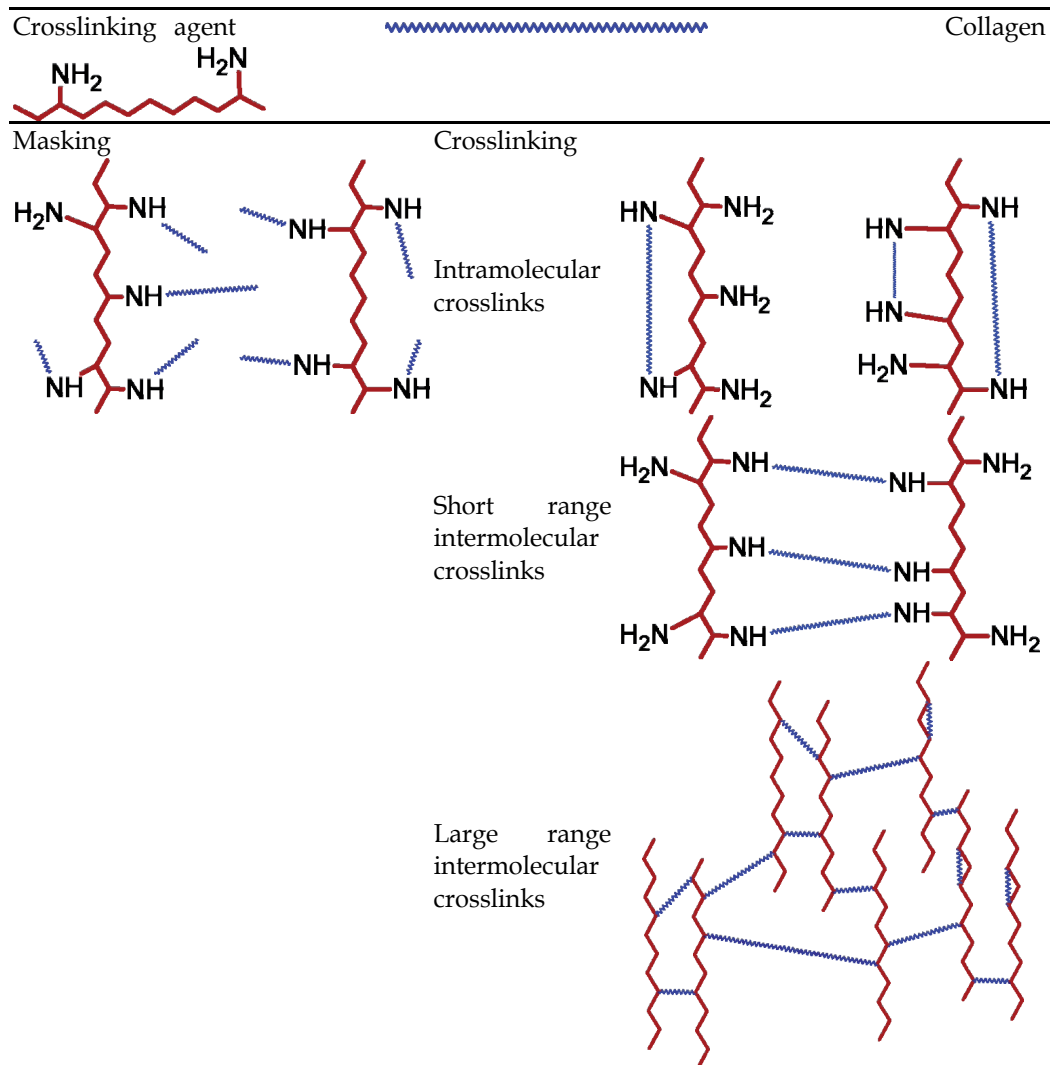


Table 6. Schematic representation of presumable masking and intra- or inter-molecular crosslinking structures

rates. Also it was reported the effectiveness of EDAC and neomycin (an inhibitor of the enzyme hyaluronidase) for the prevention of glycosaminoglycans loss (Ragharan et al., 2007; Shah & Vyavahare, 2008). The addition of exogenous glycosaminoglycans and the stabilization of endogenous glycosaminoglycans in ostrich perichardium reduced tissue calcification after implantation in rats, but slightly increased the presence of matrix-metalloproteinase at the implantation site (Arenaz et al., 2004).

## 5. Conclusions

Natural tissues from various sources can be used as biomaterials in the cardiovascular field after decellularization and fixation with various crosslinking agents. However, the current

approaches based on surfactants and difunctional crosslinking agents can affect the structure, GAG content, biocompatibility and calcification potential of these tissues. Because of this, different posttreatment methods have been suggested showing some improvements but until today, the vascular graft or heart valve obtained do not fulfill all the requirements for a long term use. In addition to this safety concerns, these treatments are not yet cost effective. Therefore, methods that preserve simultaneously the mechanical properties of collagen and the properties of the GAG matrix are desirable. Finally, those approaches that made use of enzymatic methods and low toxicity chemical such natural products and aminoacids as crosslinking agents seem promising alternatives.

## 6. References

- Arenaz, B.; Martín-Maestro, M.; Fernández, P.; Turnay, J.; Olmo, N.; Senén, J.; Gil-Mur, J.; Lizarbe, M.A. & Jorge-Herrero, E. (2004). Effects of periodate and chondroitin 4-sulfate on proteoglycan stabilization of ostrich perichardium. Inhibition of calcification in subcutaneous implants in rats. *Biomaterials*, Vol. 25, pp. 3359-3368
- Argese, E.; Marcomini, A.; Bettiol, C.; Perin, G. & Miana, P. (1994). Submitochondrial particle response to linear alkylbenzene sulfonates, nonylphenol polyethoxylates and their biodegradation derivatives. *Environmental Toxicology & Chemistry*, Vol. 13, pp. 737-742
- Carpentier, S.M., Shen, M., Chen, L., Cunanan, C.M., Martinet, B. & Carpentier, A. (2001). Biochemical properties of heat-treated valvular bioprostheses. *The Annals of Thoracic Surgery*, Vol. 71, pp. S410-S412
- Carraway, K.L. & Koshland, D.E. (1972). Carbodiimide modification of proteins. *Methods in Enzimology*, Vol. 25, pp. 616-623
- Cauich-Rodríguez, J.V. (2008). Materiales sustitativos del tejido blando, In: *Biomateriales*, Sastre, R., de Aza, S. & San Román, J., (Ed.), pp. 359- 368, Faenza Editrice Iberica, Faenza RA, Italia
- Chang, Y.; Liang, H.C.; Wei, H.J.; Chu, C.P. & Sung, H.W. (2004). Tissue regeneration patterns in a cellular bovine implanted in a canine model as a vascular path. *Journal of Biomedical Materials Research*, Vol. 69A, pp. 323-333
- Chang, Y.; Tsai, C.C.; Liang, H.C. & Sung, H. W. (2002). In vivo evaluation of cellular and acellular bovine pericardia fixed with a naturally occurring crosslinking agent (genipin). *Biomaterials*, Vol. 23, pp. 2447-2457
- Charulatha, V. & Rajaram, A. (2003). Influence of different crosslinking treatments on the physical properties of collagen membranes. *Biomaterials*, Vol. 24, pp. 759-767
- Chau, D.Y.S.; Collighan, R.J.; Verderio, E.A.M.; Addy, V.L. & Griffin, M. (2005). The cellular response to transglutaminase-cross-linked collagen. *Biomaterials*, Vol. 26, pp. 6518-6529
- Chen, R.N.; Ho, H.O. & Sheu, M.T. (2005). Characterization of collagen matrices crosslinked using microbial transglutaminase. *Biomaterials*, Vol. 26, pp. 4229-4235
- Chen, W.; Kim, J.D.; Schoen, F.J. & Levy, R.L. (1994). Effect of 2-amino oleic acid exposure conditions on the inhibition of calcification of glutaraldehyde crosslinked porcine aortic valve. *Journal of Biomedical Materials Research*, Vol. 28, pp. 1485-1495
- Connolly, J.M.; Alferiev, I.; Clark-Gruel, J.N.; Eidelman, N.; Sacks, M.; Palmatory, E.; Kronsteiner, A.; DeFelice, S.; Xu, J.; Ohri, R.; Narula, N.; Vyavahare, N. & Levy, R.J. (2005). Triglycidylamine Crosslinking of Porcine Aortic Valve Cusps or Bovine

- Perichardium Results in Improved Biocompatibility, Biomechanics, and Calcification Resistance: Chemical and Biological Mechanisms. *American Journal of Pathology*, Vol. 166, pp. 1-13.
- Courtman, D.W.; Pereira, C.A.; Kashef, V.; McComb, D.; Lee, J.M. & Wilson, G.J. (1994). Development of a perichardial acellular matrix biomaterial: Biochemical and mechanical effects of cell extraction. *Journal of Biomedical Materials Research*, Vol. 28, pp. 655-666
- Dong, X., Wei, X., Yi, W., Gu, C., Kang, X., Liu, Y., Li, Q. & Yi, D. (2009). RGD-modified acellular bovine perichardium as a bioprosthetic scaffold for tissue engineering. *Journal of Materials Science: Materials in Medicine*, Vol. 20, pp. 2327-2336
- Duan, X. & Lewis, R.S. (2002). Improved haemocompatibility of cysteine-modified polymers via endogenous nitric oxide. *Biomaterials*, Vol. 23, pp. 1197-1203
- Duncan, A.C. & Boughner, D. (1998). Effect of dynamic glutaraldehyde fixation on the viscoelastic properties of bovine perichardial tissue. *Biomaterials*, Vol. 19, pp. 777-783
- Everaerts, F.; Torrianni, M.; van Luyn, M.; van Wachem, P.; Feijen, J. & Hendricks, M. (2004). Reduced calcification of bioprostheses cross-linked via an improved carbodiimida based method. *Biomaterials*, Vol. 24, pp. 5523-5530
- Flanagan, T.C. & Pandit, A. (2003). Living artificial heart valve alternatives: a review. *European Cells & Materials*, Vol. 6, pp. 28-45
- Frost, M.C.; Reynolds, M.M. & Meyerhoff, M.E. (2005). Polymers incorporating nitric oxide releasing/generating substances for improved biocompatibility of blood-contacting medical devices. *Biomaterials*, Vol. 26, pp. 1685-1693
- Gappa-Fahlenkamp, H. & Lewis, R.S. (2005). Improved haemocompatibility of poly(ethylene terephthalate) modified with various thiol-containing groups. *Biomaterials*, Vol. 26, pp. 3479-3485
- Gappa-Fahlenkamp, H.; Duan X. & Lewis, R.S. (2004). Analysis of immobilized L-cysteine on polymers. *Journal of Biomedical Materials Research*, Vol. 71A, pp. 519-527
- García-Páez, J.M.; Jorge-Herrero, E.; Carrera-San Martín, A.; García-Sestafe, J.V.; Téllez, G.; Millán, I.; Salvador, J.; Cordon, A. & Castillo-Olivares, J.L. (2000). The influence of chemical treatment and suture on the elastic behavior of calf perichardium utilized in the construction of cardiac bioprostheses. *Journal of Materials Science: Materials in Medicine*, Vol. 11, pp. 273-2777
- Gilbert, T.W.; Sellaro, T.L. & Badylak, S.F. (2006). Decellularization of tissues and organs. *Biomaterials*, Vol. 27, pp. 3675-3683
- Giossis, G.; Yoshioka, S.A.; Braile, D.M. & Ramirez, V.D.A. (1998). The chemical protecting group concept applied in crosslinking of natural tissues with glutaraldehyde acetals. *Artificial Organs*, Vol. 22, pp. 210-214
- Isenburg, T.C.; Karamchandani, N.V.; Simionescu, D.T. & Vyavahare, N.R. (2006). Structural requirements for stabilization of vascular elastin by polyphenolic tannins. *Biomaterials*, Vol. 27, pp. 3645-3651
- Isenburg, T.C.; Simionescu, D. T. & Vyavahare, N. R. (2004). Elastin stabilization in cardiovascular implants: improved resistance to enzymatic degradation by treatment with tannic acid. *Biomaterials*, Vol. 25, pp. 3293-3302

- Isenburg, T.C.; Simionescu, D.T. & Vyavahare, N.R. (2006). Tannic acid treatment enhances biostability and reduces calcification of glutaraldehyde fixed aortic wall. *Biomaterials*, Vol. 27, 1237-1245
- Jee, K.S.; Kim, Y.S.; Park, K.D. & Kim, Y.H. (2003). A novel chemical modification of bioprosthetic tissues using L-arginine. *Biomaterials*, Vol. 24, pp. 3409-3416
- Jobling, S. & Sumpster, J.P. (1993). Detergent components in sewage effluent are weakly estrogenic to fish – An in vitro study using rainbow-trout. *Aquatic Toxicology*, Vol. 27, pp. 361-372
- Jorge-Herrero, E.; Fernández, P.; de la Tone, N.; Escudero, C.; García-Páez, J.M.; Buján, J. & Castillo-Olivares, J.L. (1994). Inhibition of the calcification of porcine valve tissue by selective lipid removal. *Biomaterials*, Vol. 15, pp. 815-820
- Jorge-Herrero, E.; Fernández, P.; Escudero, C.; García-Páez, J.M. & Castillo-Olivares, J.L. (1996). Calcification of perichardial tissue pretreated with different amino acids. *Biomaterials*, Vol. 17, pp. 571-575
- Jorge-Herrero, E.; Fonseca, C.; Barge, A.P.; Turnay, J.; Olmo, N.; Fernández, P.; Lizarbe, M.A. & García-Páez, J.M. (2010). Biocompatibility and calcification of bovine perichardium employed for the construction of cardiac bioprostheses treated with different chemical crosslink methods. *Artificial Organs*, Vol. 34, No. 5, pp. E168-E176
- Jorge-Herrero, E.; Olmo, N.; Turnay, J.; Martín-Maestro, M.; García-Páez, J.M. & Lizarbe, M.A. (2005). Biocompatibility of different chemical crosslinking in bovine perichardium employed for the construction of cardiac bioprostheses. Proceedings of 19th European Conference on Biomaterials, pp. P4, Sorrento, Italy, Sept 11-15
- Kidane, A.G.; Burriesci, G.; Cornejo, P.; Dooley, A.; Sarkar, S.; Bonhoeffer, P.; Edirisinghe, M. & Seifalian, A.M. (2009). Current developments and future prospects for heart valve replacement therapy. *Journal of Biomedical Materials Research Part B: Appl Biomater*, Vol. 88B, pp. 290-303
- Khor, E. (1997). Methods for the treatment of collagenous tissues for bioprostheses. *Biomaterials*, Vol. 18, pp. 95-105
- Langdon, S.E.; Chernecky, R.; Pereira, C.A.; Abdulla, D. & Lee, J.M. (1999). Biaxial mechanical/structural effects of equibiaxial strain during crosslinking of bovine perichardial xenograft materials. *Biomaterials*, Vol. 20, pp. 137-153
- Lee, J.M. & Boughner, D.R. (1981). Tissue mechanics of canine perichardium in different test environment. *Circulation Research*, Vol. 49, pp. 533-544
- Lee, J.M. & Boughner, D.R. (1985). Mechanical properties of human perichardium. Differences in viscoelastic response when compared with canine perichardium. *Circulation Research*, Vol. 55, pp. 475-481
- Lee, J.M.; Boughner, D.R. & Courtman, D.W. (1984). The glutaraldehyde-stabilized porcine aortic valve xenograft. II. Effect of fixation with or without pressure on the tensile viscoelastic properties of the leaflet material. *Journal of Biomedical Materials Research*, Vol. 18, pp.79-98
- Lee, J.M.; Edwards, H.H.L.; Pereira, C.A. & Samii, S.I. (1996). Crosslinking of tissue-derived biomaterials in 1-ethyl-3-(3-dimethylaminopropyl)-carbodiimide (EDC). *Journal of Materials Science: Materials in Medicine*, Vol. 7, pp. 531-541



- Lee, J.M.; Haberer, S.A. & Boughner, D.R. (1989). The bovine perichardial xenograft: I. Effect of fixation in aldehydes without constraint on the tensile viscoelastic properties of bovine perichardium. *Journal of Biomedical Materials Research*, Vol. 23, pp. 457-475.
- Lee, J.M.; Pereira, C.A. & Kan, L.W.K. (1994). Effect of molecular structure of poly(glycidyl ether) reagents on crosslinking and mechanical properties of bovine perichardial xenograft materials. *Journal of Biomedical Materials Research*, Vol. 28, pp. 981-992
- Lee, W.K.; Park, K.D.; Han D.K.; Suh, H.; Park, J.C. & Kim, Y.H. (2000). Heparinized bovine perichardium as a novel cardiovascular bioprosthesis. *Biomaterials*, Vol. 21, pp. 2323-2330
- Li, S.T. (2007). Biologic biomaterials: tissue-derived biomaterials (Collagen). In: *Biomaterials*, Wong, J. Y. & Bronzino, J.D., (Ed.), pp. 7-1 - 7-22, CRC Press, ISBN-13: 978-0-8493-7888-1, 3Boca Raton, FL, USA.
- Liang, H.C.; Chang, Y.; Hsu, C.K.; Lee, M.H. & Sung, H.W. (2004). Effects of crosslinking degree of an acellular biological tissue on its tissue regeneration pattern. *Biomaterials*, Vol. 25, pp. 3541-3552.
- Liao, J.; Joyce, E.M. & Sacks, M.S. (2008). Effects of decellularization on the mechanical and structural properties of the porcine aortic valve leaflet. *Biomaterials*, Vol. 29, pp. 1065-1074
- Lindop, G.B.M. (2007). Pathology of the Heart. *Surgery*, Vol. 25, pp. 187-197
- Lovekamp, J. & Vyavahare, N. Periodate-mediated glycosaminoglycan stabilization in bioprosthetic heart valves. (2001). *Journal of Biomedical Materials Research*, Vol. 56, pp. 478-486
- Loke, W.K.; Khor, E.; Wee, A.; Teoh, S.H. & Chian, K.S. (1996). Hybrid biomaterials based on the interaction of polyurethane oligomers with porcine perichardium. *Biomaterials*, Vol. 17, pp. 2163-2172
- Mata-Mata, J.L.; Mendoza, D.; Alvarado, D.I. & Amézquita, F.J. (2008). Dispersiones acuosas de poliuretano bloqueadas, una alternativa como agente curtiembre. *Polímeros: Ciência e Tecnologia*, Vol. 18, pp. 138-143.
- Matsagas, M.I.; Bali, C.; Arnaoutoglou, E.; Papakostas, J.C.; Nassis, C. & Papadopoulos, G. (2006). Carotid endarterectomy with bovine perichardium patch angioplasty: mid-term results. *Annals of Vascular Surgery*, Vol. 20, pp. 614-619
- Mavrilas, D.; Sinouris, E.A.; Vynios, D.H. & Papageorgakopoulou, N. (2005). Dynamic mechanical characteristics of intact and structurally modified bovine perichardial tissues. *Journal of Biomechanics*, Vol. 38, pp. 761-768
- Mendoza-Novelo, B. (2011). Caracterización fisicoquímica y biológica de un biomaterial cardiovascular basado en pericardio bovino y prepolímeros de poliuretano. Doctoral thesis. Universidad de Guanajuato, México, Marzo.
- Mendoza-Novelo, B. & Cauch-Rodríguez, J.V. (2009). The effect of surfactants, crosslinking agents and L-cysteine on the stabilization and mechanical properties of bovine perichardium. *Journal of Applied Biomaterials & Biomechanical*, Vol. 7, No. 2, pp. 123-131
- Mendoza-Novelo, B.; Ávila, E.E.; Cauch-Rodríguez, J.V.; Jorge-Herrero, E.; Rojo, F.J.; Guinea, G.V. & Mata-Mata, J.L. (2011). Decellularization of perichardial tissue and its impact on tensile viscoelasticity and glycosaminoglycans content. *Acta Biomaterialia*, Vol. 7, pp. 1241-1248

- Monsan, P.; Puzo, G. & Mazarguil, H. (1975). Mechanism of glutaraldehyde protein bond formation. *Biochimie*, Vol. 57, pp. 1281-1292
- Moore, M.A.; Chen, W.M.; Phillips, R.E.; Bohachevsky, I.K. & McIlroy, B.K. (1996). Shrinkage temperature versus protein extraction as a measure of stabilization of photooxidized tissue. *Journal of Biomedical Materials Research*, Vol. 32, pp. 209-214
- Naimark, W.A.; Pereira, C.A.; Tsang, K. & Lee, J.M. (1995). HMDC crosslinking of bovine perichardial tissue: a potential role of the solvent environment in the design of bioprosthetic materials. *Journal of Materials Science Materials in Medicine*, Vol. 6, pp. 235-241
- Nowatzki, P.J. & Tirrell, D.A. (2004). Physical properties of artificial extracellular matrix protein films prepared by isocyanate crosslinking. *Biomaterials*, Vol. 25, pp. 1261-1267
- Ohri, R.; Hahn, S.K.; Hoffman, A.S.; Stayton, P.S & Giachelli, C.M. (2004). Hyaluronic acid grafting mitigates calcification of glutaraldehyde-fixed bovine perichardium. *Journal of Biomedical Materials Research*, Vol. 70A, pp. 328-334
- Olde Damink, L. H. H., Dijkstra, P. J., van Luyn, M. J. A., van Wachem, P. B., Nieuwenhuis, P. & Feijen, J. (1995). Crosslinking of dermal sheep collagen using hexamethylene diisocyanate. *Journal of Materials Science Materials in Medicine*, Vol. 6, pp. 429-434
- Olde-Damink, L.H.H.; Dijkstra, P.J.; van Luyn, J.A.; van Wachem, P.B.; Nieuwenhuis, P. & Feijen J. (1995). Glutaraldehyde as a crosslinking agent for collagen-based biomaterials. *Journal of Material Science: Materials in Medicine*, Vol. 6, pp. 460-472
- Oosthuysen, A.; Zilla, P.P.; Human, P.A.; Schmidt, C.A.P. & Bezuidenhout, D. (2006). Bioprosthetic tissue preservation by filling with a poly(acrylamide) hydrogel. *Biomaterials*, Vol. 27, pp. 2123-2130
- Park, K.D.; Lee, W.K.; Yun, J.Y.; Han, D.K.; Kim, S.H.; Kim, Y.H.; Kim, H.M. & Kim, K.T. (1997). Novel anycalcification treatment of biological tissues by grafting of sulphonated poly(ethylene oxide). *Biomaterials*, Vo. 18, pp. 47-51
- Pathak, C.P.; Moore, M.A. & Phillips, R.E. (2002). Anticalcification treatments for fixed biomaterials. US patent, 6,479,079
- Pathak, C. P.; Phillips, R. E.; Akella, R. & Moore, M. A. (2000). Evaluation of disuccinimidyl glutarate as a crosslinking agent for tissues. *Sixth World Biomaterials Congress Transactions*, pp. 288, Hawaii, USA
- Pathak, C.P.; Phillips, R.E. & Moore, M.A. (2001). Water soluble tissue crosslinkers for bioprostheses. *Society for Biomaterials 27th Annual Meeting Transactions*, pp. 130, USA
- Petersen, S. (1949). Niedermolekulare Umserzungsprodukte aliphatischer Diisocyanate. 5. Mitteilung über Polyurethane. *Annalen der Chemie*, Vol. 562, pp. 205-229.
- Pfau, J.C.; McCall, B.R.; Card, G.L.; Cheung, D.T. & Duran, C.M.G. (2000). Lipid Analysis of Ethanol Extracts of Fresh Sheep Perichardial Tissue. *Sixth World Biomaterials Congress Transactions*, pp. 726, Hawaii, USA
- Pfau, J.C.; Umbriaco, J.; Duran, C.M.G. & Cheung, D.T. (2000). Cross-linking of collagen in various states of hydration using UV irradiation. *Sixth World Biomaterials Congress Transactions*, pp. 718, Hawaii, USA
- Raghavan, D.; Simionescu, D.T. & Vyavahare, N.R. (2007). Neomycin prevents enzyme-mediated glycosaminoglycan degradation in bioprosthetic heart valves. *Biomaterials*, Vol. 28, pp. 2861- 2868

- Rapoport, H.S.; Connolly, J.M.; Fulmer, J.; Dai, N.; Murti, B.H.; Gorman, R.C.; Gorman, J.H.; Alferiev, I. & Levy, R. J. (2007). Mechanisms of the in vivo inhibition of calcification of bioprosthetic porcine aortic valve cusps and aortic wall with triglycidylamine/mercapto bisphosphonate. *Biomaterials*, Vol. 28, pp. 690-699
- Sacks, M.S.; Hamamoto, H.; Connolly, J.M.; Gorman, R.C.; Gorman III, J.H. & Levy, R.J. (2007). In vivo biomechanical assessment of triglycidylamine crosslinked pericardium. *Biomaterials*, Vol. 28, pp. 5390-5398
- Schmidt, C.E. & Baier, J.M. (2000). Acellular vascular tissues: natural biomaterials for tissue repair and tissue engineering. *Biomaterials*, Vol. 21, pp. 2215-2231
- Schoen, F.J. & Levy, R.J. (1999). Tissue heart valves: current challenges and future research perspectives. *Journal of Biomedical Materials Research*, Vol. 47, pp. 439-75
- Shah, S.R. & Vyavahare N.R. (2008). The effect of glycosaminoglycan stabilization on tissue buckling in bioprosthetic heart valves. *Biomaterials*, Vol. 29, pp. 1645-1653
- Sheehan, J.C. & Hlavka, J.J. (1956). The use of water-soluble and basic carbodiimides in peptide synthesis. *Journal of Organic Chemistry*, Vol. 21, pp. 439-441
- Sheehan, J.C. & Hlavka, J.J. (1957). The cross-linking of gelatin using a water-soluble carbodiimide. *Journal of the American Chemical Society*, Vol. 79, pp. 4528-4529
- Soto, A.M.; Justicia, H.; Wray, J.M. & Sonnenschein, C. (1991). p-Nonylphenol, an estrogenic xenobiotic released from modified polystyrene. *Environ Health Persp*, Vol. 92, pp. 167-173.
- Stacchino, C.; Bona, G.; Bonetti, F.; Rinaldi, S.; Della Ciana, L. & Grignani, A. (1998). Detoxification process for glutaraldehyde-treated bovine pericardium: biological, chemical and mechanical characterization. *The Journal of Heart Valve Disease*, Vol. 7, pp. 190-194
- Sung, H.W.; Chang, Y.; Chang, W.H. & Chen, Y.C. (2000). Fixation of biological tissues with a naturally occurring crosslinking agent: fixation rate and effect of pH, temperature and initial fixative concentration. *Journal of Biomedical Materials Research*, Vol. 52A, pp. 77-87
- Sung, H.W.; Chang, Y.; Chiu, C.T.; Chen, C.N. & Liang, H.C. (1999). Crosslinking characteristics and mechanical properties of a bovine pericardium fixed with a naturally occurring crosslinking agent. *Journal of Biomedical Materials Research*, Vol. 47A, pp. 116-126
- Sung, H.W.; Chen, C.N.; Chang, Y. & Liang, H. F. (2002). Biocompatibility study of biological tissues fixed by a natural compound (reuterin) produced by *Lactobacillus reuteri*. *Biomaterials*, Vol. 23, pp. 3203-3214
- Sung, H.W.; Chen C.N.; Liang, H.F. & Hong, M.H. (2003). A natural compound (reuterin) produced by *Lactobacillus reuteri* for biological-tissue fixation. *Biomaterials*, Vol. 24, pp. 1335-1347
- Sung, H.W.; Shih, J.S. & Hsu, C. S. (1996). Crosslinking characteristics of porcine tendons: Effects of fixation with glutaraldehyde or epoxy. *Journal of Biomedical Materials Research*, Vol. 30, pp. 361-367
- Tu, R.; Lu, C.L.; Thyagarajan, K.; Wang, E.; Nguyen, H.; Shen, S.; Hata, C. & Quijano, R.C. (1993). Kinetic study of collagen fixation with polyepoxy fixatives. *Journal of Biomedical Materials Research*, Vol. 23, pp. 3-9
- van Wachem, T.P.B.; Brouwer, L.A.; Zeeman, R.; Dijkstra, P.J.; Feijen, J.; Hendriks, M.; Cahalan, P.T. & van Luyn, M.J.A. (2000). In vivo behavior of epoxy-crosslinked

- porcine heart valve cusps and walls. *Journal of Biomedical Materials Research Part B: Applied Biomaterials*, Vol. 53, pp. 18-27
- van Wachem, T.P.B.; van Luyn, M.J.A.; Olde Damink, L.H.H.; Dijkstra, P.J.; Feijen, J. & Nieuwenhuis, P. (1994). Biocompatibility and tissue regenerating capacity of crosslinked dermal sheep collagen. *Journal of Biomedical Materials Research*, Vol. 28, pp. 353-363
- Vasudev, S.C. & Chandy T. (1999). Polyethylene glycol-grafted bovine perichardium: a novel hybrid tissue resistant to calcification. *Journal of Materials Science: Materials in Medicine*, Vol. 10, pp. 121-128
- Vesely, I. (2005). Heart valve tissue engineering. *Circulation Research*, Vol. 97, pp.743-755
- Vyavahare, N.; Hirsch, D.; Lerner, E.; Baskin, J.Z.; Schoen, F.J.; Bianco, R.; Kruth, Hs.; Zand, R. & Levy, R.J. (1997). Prevention of bioprosthetic heart valve calcification by ethanol preincubation. *Circulation*, Vol. 95, pp. 479-488
- Yeung, B.K.S.; Chong, P.Y.C. & Petillo, P.A. (2001). Synthesis of glycosaminoglycans, In: *Glycochemistry*, Wang, P.C. & Bertozzi, C.R., (Ed.), pp. 425-492, Marcel Dekker, New York, U.S.A
- Yoshioka, S.A. & Giossis, G. (2008). Thermal and spectrophotometric studies of new crosslinking method for collagen matrix with glutaraldehyde acetals. *Journal of Material Science: Materials in Medicine*, Vol. 19, pp. 1225-1223
- Wei, H.J.; Liang, H.C.; Lee, M.H.; Huang, Y.C.; Chang, Y. & Sung, H.W. (2005). Construction of varying porous structures in acellular bovine pericardia as a tissue-engineering extracellular matrix. *Biomaterials*, Vol. 26, pp. 1905-1913
- Whipple, E.B. & Ruta, M. (1974). Structure of aqueous glutaraldehyde. *Journal of Organic Chemistry*, Vol. 39, pp.1666-1668
- Wiegner, A.W. & Bing, O.H.L. (1981). Mechanical and structural of canine perichardium. *Circulation Research*, Vol. 49, pp.807-814
- Zeeman, R.; Dijkstra, P.J.; van Wachem, T.P.B.; van Luyn, M.J.A.; Hendriks, M.; Cahalan, P.T. & Feijen, J. (2000). The kinetics of 1,4-butanediol diglycidyl ether crosslinking of dermal sheep collagen. *Journal of Biomedical Materials Research*, Vol. 51, pp. 541-548
- Zhai, W.; Chang, J.; Lin, K.; Wang, J.; Zhao, Q. & Sun, X. (2006). Crosslinking of decellularized porcine heart valve matrix by procyanidins. *Biomaterials*, Vol. 27, pp. 3684-3690
- Zhai, W.; Chang, J.; Lü, X. & Wang, Z. (2009). Procyanidins-crosslinked heart valve matrix: Anticalcification effect. *Journal of Biomedical Materials Research Part B: Applied Biomaterials*, Vol. 90B, pp. 913-219
- Zilla, P.; Brink, J.; Human, P. & Bezuidenhout D. (2008). Prosthetic heart valves: Catering for the few. *Biomaterials*, Vol. 29, pp. 385-406

# Research on Mg-Zn-Ca Alloy as Degradable Biomaterial

B.P. Zhang<sup>1,2</sup>, Y. Wang<sup>2</sup> and L. Geng<sup>2</sup>

<sup>1</sup>National Engineering Laboratory for Carbon Fiber Technology,  
Institute of Coal Chemistry, Chinese Academy of Sciences

<sup>2</sup>School of Materials Science and Engineering, Harbin Institute of Technology  
China

## 1. Introduction

Magnesium and magnesium alloys are light metals, which characterized a low density, high specific strength and strong specific stiffness. The fracture toughness of magnesium is greater than that of ceramic biomaterials such as hydroxyapatite. The Young's elastic modulus and compressive yield strength of magnesium are closer to those of cortical bone. Especially, Mg<sup>2+</sup> is present in large amount in the human body and involved in many metabolic reactions and biological mechanisms. The human body usually contains approximately 35g per 70kg body weight and the human body's daily demand for Mg is about 350 mg/day. Due to the excellent biomechanical properties and biocompatibility, magnesium alloys used to be introduced as implants into orthopedic and trauma surgery in recently years [1~3]. Various magnesium alloys have been investigated as biodegradable materials and some of them have been shown good biocompatibility. For example, AZ31, AZ91, WE43, LAE442, Mg-Ca and Mg-Zn have been investigated for bone implant application [4~8]. It has been shown that magnesium enhances osteogenesis response and increases newly formed bone. However, some magnesium alloys containing aluminum or heavy metal elements which have latent toxic effects on the human body. Thus, several problems such as inadequate strength, rapid corrosion and toxic ions must be solved before this unique metal is widely used in biomedical fields.

It is well known that pure magnesium has poor mechanical properties and the mechanical properties of magnesium can be effectively improved by the appropriate selection of alloying elements [1]. But, based on the aforementioned considerations, the range of alloying elements used in the degradable magnesium alloys is rather limited, Zn, Mn, Ca and perhaps a very small amount of low toxicity RE can be tolerated in the human body and can also be retard the biodegradation. Therefore, Mg-Ca binary alloys attract attention of researchers because Ca is an important element of human bones. The mechanical properties and biocompatibility of Mg-Ca binary alloy can be adjusted by controlling the Ca content and processing treatment. However, an inadequate mechanical properties as well as lower corrosion resistances of Mg-Ca binary alloys are the biggest drawback of these alloys [7][8]. Fortunately, in latest recent years, Mg-Zn system is paid more attention because Zn is one of abundant nutritional elements in human body [9] [10]. Additionally, it is a great potential

alloying element to improve the mechanical properties and corrosion resistance of Mg alloys [11][12]. And the addition of other alloying element can further improve the mechanical properties of Mg-Zn alloys [13] [14]. Zn/Mn-containing magnesium alloys, e.g. Mg<sub>2</sub>Zn<sub>0.2</sub>Mn [15] and Mg-1.2 Mn-1.0 Zn [16] ternary alloys are studied, the results indicate that Zn/Mn-containing magnesium alloys have satisfactory mechanical properties and can be potential biodegradable alloys. But, the degradation rates of Zn/Mn-containing magnesium alloys are so fast. After 9 weeks implantation, about 10~17% Mg-Mn-Zn magnesium implant has degraded. After 18 weeks implantation, about 54% Mg-Mn-Zn alloy has degraded [16]. The results studied by H.X. Wang et al [17] indicate that the Mg-Zn-Ca alloys coated with Ca-deficient hydroxyapatite have an excellent corrosion resistance in Kokubo's simulated body fluid (SBF), but the chemical composition of Mg-Zn-Ca alloys was not reported. L.Mao et al [18] studied the effects of Zn on microstructure and mechanical properties of biomedical Mg-Ca-Zn alloys. The results show that the microstructure is refined and the mechanical properties can be improved evidently with Zn content increasing. The mechanical properties of bending and compression can meet the requirements for hard tissue metal implants. However, the effect of Ca on microstructure and mechanical properties of biomedical Mg-Ca-Zn alloys, the corrosion resistance and cytotoxicity were not studied. Xuenan Gu et al[19] reported that the Mg<sub>66</sub>Zn<sub>30</sub>Ca<sub>4</sub> bulk metallic glasses sample presents a more uniform corrosion morphology than as-rolled pure Mg and Mg<sub>70</sub>Zn<sub>25</sub>Ca<sub>5</sub> samples. Both indirect cytotoxicity and direct cell culture experiments were carried out using L929 and MG63 cell lines. The results show higher cell viabilities for Mg-Zn-Ca extracts than that for as-rolled pure Mg. In addition, L929 and MG63 cells were found to adhere and proliferate on the surface of Mg<sub>66</sub>Zn<sub>30</sub>Ca<sub>4</sub> sample. Unfortunately, the cytotoxicity was tested by MTT, according to Janine Fischer et al[20] research, in the case of Mg materials, the use of MTT test kits leads to false positive or false negative results, because Mg is a very reactive element. It is conceivable that Mg in the highly alkaline environment may be able to open the ring form of the tetrazolium salt and bind to it, which could lead to a change in colors similar to the formation of formazan in the case of the MTT tests with cells.

It is reasonable to speculate that the Mg-Zn-Ca alloys with a proper Zn and Ca content can exhibit a superior combination of mechanical properties, corrosion resistance and biocompatibility. In this paper, Zn and Ca, which have no toxicity, are chosen as alloying elements to successfully improve the mechanical properties of magnesium. The effects of Zn and Ca content on mechanical properties, in-vitro corrodible property and cytotoxicity of Mg-Zn-Ca alloys have been systematically investigated to assess the feasibility of Mg-Zn-Ca alloys for use as bone implant materials.

## 2. Materials and methods

### 2.1 Materials

Mg-Zn-Ca alloys were prepared from high purity Mg (99.99 %), Purity Zn (99.8 %), and an Mg-26.9 wt. % Ca master alloy. Melting and alloying operations were carried out in a steel crucible under the protection of a mixed gas atmosphere of SF<sub>6</sub> (0.3 vol. %) and CO<sub>2</sub> (Bal.). Purity Zn and master alloy were added into the pure Mg melts at 720 °C. The melts were kept for 10min at 720°C to ensure that all the required alloying elements were dissolved in the melt alloy, and then the melts were cooled down to 700 °C and poured into a steel mold which had been pre-heated to 200 °C.

## 2.2 Composition and microstructure characterization

X-ray diffraction (XRD, Philips-X'Pert) using Cu K $\alpha$  radiation was employed for the identification of the constituent phases in the as-cast Mg-Zn-Ca alloy and their corrosion products after immersion. Microstructure observations of the alloys were conducted on Olympus optical microscope. The specimens for optical microscopy were etched with a solution of 8 vol. % acetic acid for 30 s, thoroughly flushed with water and alcohol, and then dried by hot air.

## 2.3 Mechanical properties

Tensile tests were carried out using an Instron-5569 universal testing machine at a constant crosshead speed of 1.0mm/min at room temperature. The tensile specimens with diameter of 6mm and gauge length of 30mm were cut by electric-discharge machining from the ingot. The Young's modulus was get from the tensile test. The fracture morphologies were examined by SEM (SEM, Hitachi-3000N).

## 2.4 In vitro degradation tests

Electro-chemical measurements and immersion tests were performed in a Hank's simulated body fluid to evaluate the in-vitro degradation properties. The chemical composite of Hank's simulated body was listed in table 2. The pH value of Hank's solution was adjusted with HCl and NaOH to 7.2~7.4, to avoid precipitation or formation of sediments in the solution. Its temperature was controlled around  $37 \pm 0.5$  °C, which is equal to the human body normal temperature. Pure Mg (>99.99%) was also tested as a contrast.

### 2.4.1 Electrochemical measurements

A typical three-electrode system consisting of graphite rod as counter electrode, saturated calomel electrode (SCE) as a reference electrode and specimen (1cm<sup>2</sup> exposed areas) as a working electrode was used. Potentiodynamic polarization experiments were carried out at a scan rate of 0.5 mV/s. The electrochemical measurements of specimens with thickness of 4 mm and a gauge diameter of 15mm were machined from the ingot and ground with 2000 grit SiC paper, and they were rinsed with distilled water and dried by hot air.

### 2.4.2 Immersion tests

The immersion tests were carried out in Hank's solution according to ASTM-G31-72 [21]. Samples were removed after 30 days of immersion, rinsed with distilled water, and were cleaned with chromic acid to remove the corrosion products. The degradation rates (in units of mm year<sup>-1</sup>) were obtained according to ASTM-G31-72. An average of five measurements was taken for each group. The pH value of the solution was also recorded in the immersion tests at absolute group for 144 hours.

## 2.5 Cytotoxicity assessments

L-929 cells were adopted to evaluate the cytotoxicity of Mg-Zn-Ca alloys. The cells were cultured in Dulbecco's modified Eagle's medium (DMEM), 10% fetal bovine serum (FBS), 100 Uml<sup>-1</sup>penicillin and 100 mg ml<sup>-1</sup> streptomycin at 37 °C in a humidified atmosphere of 5% CO<sub>2</sub>. The cytotoxicity tests were carried out by indirect contact. Extracts were prepared using DMEM serum free medium as the extraction medium with the surface area of extraction medium ratio 1.25 ml/cm<sup>2</sup> in a humidified atmosphere with 5% CO<sub>2</sub> at 37 °C for

72 h. The supernatant fluid was withdrawn and centrifuged to prepare the extraction medium, then refrigerated at 4 °C before the cytotoxicity test. The control groups involved the use of DMEM medium as negative controls. Cells were incubated in 96-well cell culture plates at  $5 \times 10^4$  cells/ml medium in each well and incubated for 24 h to allow attachment. The medium was then replaced with 100  $\mu$ l of extracts. After incubating the cells in a humidified atmosphere with 5% CO<sub>2</sub> at 37 °C for 2, 4 and 7 days, respectively, cell morphology was observed by optical microscopy (Nikon ELWD 0.3 inverted microscope). The neutral red viability assay was performed according to published procedures. A stock solution of neutral red (Beyotime, China) was prepared in water (1%). The stock solution was diluted to 50  $\mu$ g/ml in complete culture medium and 200  $\mu$ l of the staining solution were added to each well after removal of the exposure medium. The cells were incubated for 3 h at 37°C, The cells were then fixed with 200  $\mu$ l formaldehyde/CaCl<sub>2</sub>(3.7%/1%) and destained with 200  $\mu$ l methanol/glacial acetic acid (50%/1%), The plates were shaken for 60 min at room temperature using a plate shaker. Optical densities were measured at 540 nm in a multiwell spectrophotometer (Bio-RAD 680). The cell relative growth rate (RGR) was calculated according to the following formula:

$$\text{RGR} = \text{OD}_{\text{test}} / \text{OD}_{\text{negative}} \times 100\%$$

## 2.6 Animal test

### 2.6.1 Surgery

Animal tests were approved by the Ethics Committee of the First Affiliated Hospital of Harbin Medical University. The in-vivo degradation experiments were performed in the animal laboratory of the hospital. A total of 15 adult New Zealand rabbits (6 females), 2.0~2.5kg in weight, were used. In the experimental group, sodium pentobarbital (30mg kg<sup>-1</sup>) was administered to perform anesthesia by intravenous injection. The sterile Mg-Zn-Ca alloy rod sample was implanted into the femora of the rabbit.

After operation, all animals received a subcutaneous injection of penicillin to avoid a wound contamination and were allowed to move freely in their cages without external support. After operation, five rabbits were sacrificed randomly at 1, 2 and 3 months, respectively.

### 2.6.2 Degradation and histological analysis

The bone samples with magnesium implants were fixed in 2.5% glutaraldehyde solution and then embedded in epoxy resin for microstructure analysis. The samples were sliced by hard tissue slicer (ZJXL-ZY-200814-1). Samples were made perpendicular to the long axis of the implant to get a cross-section of the implant and surrounding bone tissue. The cross-section microstructure was observed by an optical microscope (Nikon ELWD 0.3 inverted microscope) and a scanning electronic microscope (Hitachi S-5500). The residual implant areas were measured on the cross-section images using analysis software. The ratio of the residual cross-section area of implants to the original cross-section area (residual area/implant area $\times$ 100%) was used to assess the in vivo degradation rate of magnesium alloys. The element distributions in the residual implants and the degradation layer after 3 months implantation were analyzed.

For histological analysis, the bone samples with magnesium implants were fixed in 4% formaldehyde solution, dehydrated, and then decalcified in ethylene diamine tetra acetate. Then, the specimens were embedded in paraffin and cut into films with 5  $\mu$ m in thickness.



The films were then stained with Hematoxylin and eosin. Histological images were observed on an optical microscope.

## 2.7 Statistical analysis

A t-test was used to determine whether any significant differences existed between the mean values of the cytotoxicity and animal tests of the experiment. The statistical significance was defined as  $P < 0.05$ .

## 3. Results and discussion

### 3.1 Phase compositions and microstructures evolution of the as-cast Mg-Zn-Ca alloys

#### 3.1.1 The effects of Zn content on phase compositions and microstructures of the as-cast alloys

In this study, in order to investigate the effects of Zn and Ca on the phase compositions and microstructures evolution of the as-cast Mg-Zn-Ca alloys, respectively, the initial content of Ca design as 0 wt. % and then changed the content of Zn to study the effects of Zn on phase compositions and microstructures. The chemical compositions of the Mg-xZn alloy obtained by ICP-AES were listed in Table 1. The impurity contents of the Mg-x Zn alloy were very low for better degradation properties and biocompatibility. X-ray diffraction (XRD) analyses were used to investigate the existing intermetallic phases in the Mg-x Zn Ca alloys (Fig. 1). As shown in Fig. 1, there was only  $\alpha$ -Mg diffraction peaks phase in the Mg-1.0Zn alloy. Diffraction peaks from the  $Mg_2Zn$  phase was not detected. With the Zn concentration increasing, MgZn phase's patterns were began to detect in Mg-5.0 Zn and Mg-6.0 Zn alloy.

Materials	Chemical composition (wt.%)					
	Al	Zn	Mn	Si	Fe	Mg
Mg-1.0Zn	0.023	0.976	0.058	0.031	0.004	Balance
Mg-2.0Zn	0.033	1.852	0.030	0.039	0.007	Balance
Mg-3.0Zn	0.029	2.732	0.022	0.036	0.007	Balance
Mg-4.0Zn	0.019	3.925	0.021	0.032	0.008	Balance
Mg-5.0Zn	0.027	5.223	0.031	0.034	0.009	Balance
Mg-6.0Zn	0.024	5.977	0.019	0.033	0.012	Balance

Table 1. Chemical compositions of the as-cast Mg-Zn alloy

The microstructures of the as-cast Mg-x Zn alloys were shown in Fig.2. Fig. 2(a) was taken from Mg-1.0 Zn alloy, in which the microstructure consists of the  $\alpha$ -Mg. The maximum solubility of Zn in the magnesium was about 2 wt. % at room temperature in the equilibrium state, when no more than 2 wt. % Zn was added, the Zn was solid solution in Mg matrix. When the contents of Zn was more than 4 wt. %, the microstructure obviously changed, there were more second phases precipitated and the morphogenesis of second phases were small particle. As shown in Fig.2 (f), with the increasing of Zn content, lamellar eutectic appears in the as-cast microstructure. The eutectic structures were very coarse and mostly distributed in the grain boundary and less in the areas of inter-dendrite,

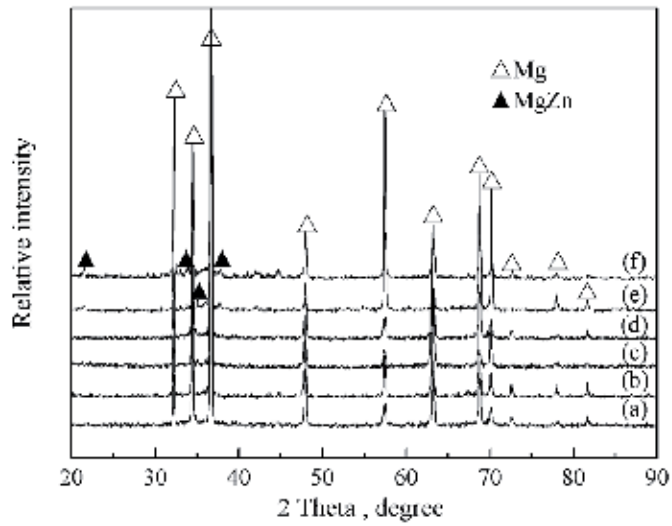
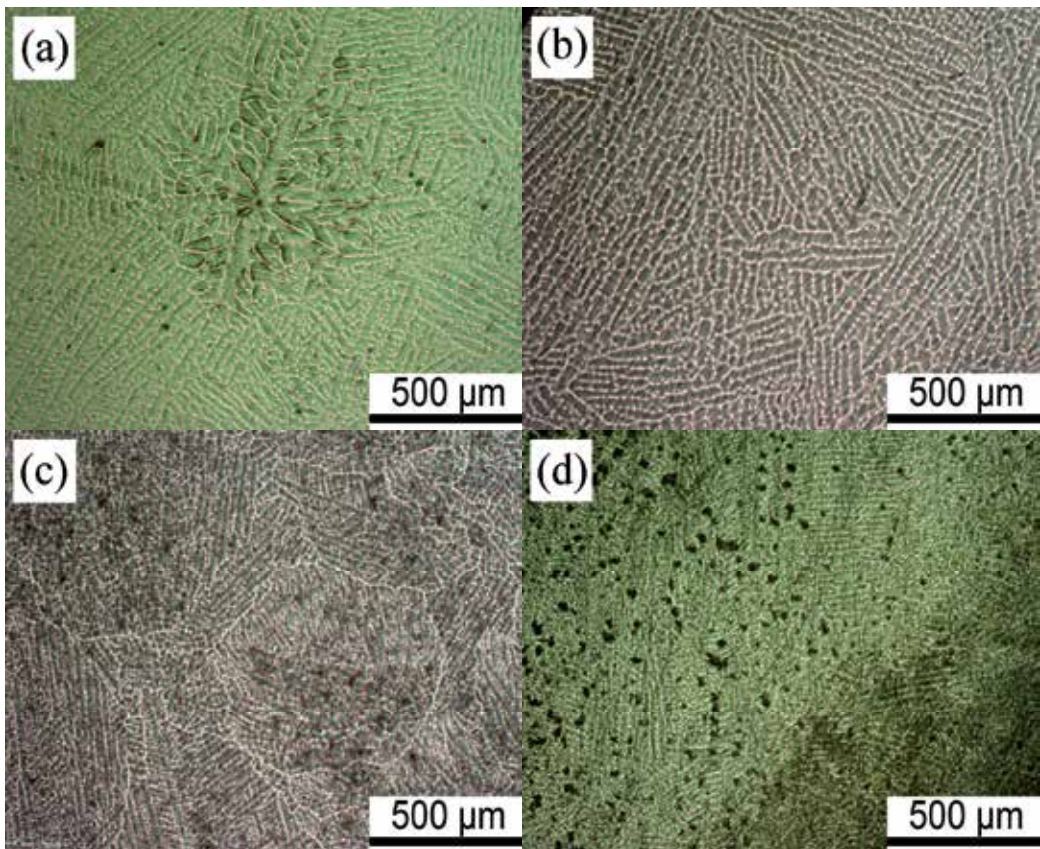


Fig. 1. XRD patterns of as-cast Mg-Zn alloys (a)Mg-1.0Zn; (b)Mg-2.0Zn; (c)Mg-3.0Zn; (d)Mg-4.0Zn; (e)Mg-5.0Zn; (f)Mg-6.0Zn



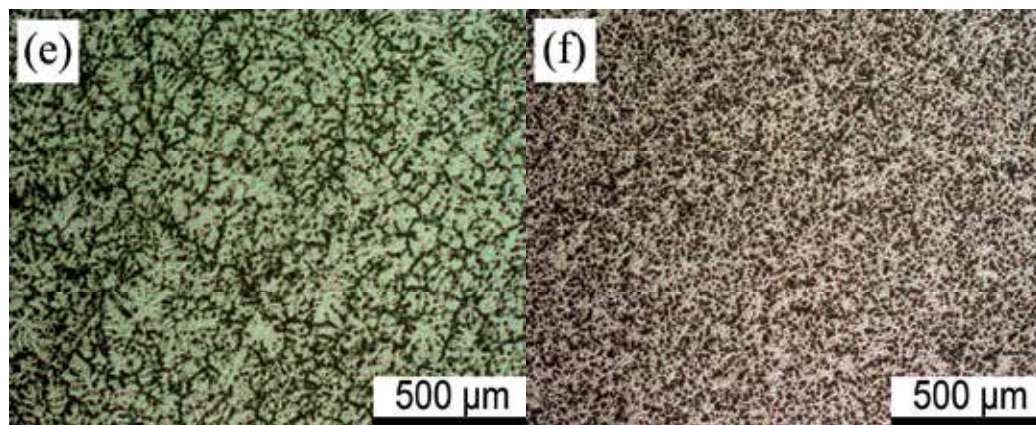


Fig. 2. Optical microstructure of as-cast Mg-Zn alloys (a) Mg-1.0Zn; (b) Mg-2.0Zn; (c) Mg-3.0Zn; (d) Mg-4.0Zn; (e) Mg-5.0Zn; (f) Mg-6.0Zn

### 3.1.2 The effects of Ca content on phase compositions and microstructures of the as-cast alloys

In present study, the mechanical properties show that when Zn content is 4wt. %, the Mg-xZn has good mechanical properties. Thus, the initial content of Zn designs as 4.0wt. % and then changed the content of Ca to study the effects on phase compositions and microstructures. The chemical compositions of the Mg-4.0 Zn-x Ca alloy obtained by ICP-AES were listed in Table 3. X-ray diffraction (XRD) analyses were used to investigate the existing phases in the Mg-4.0 Zn-xCa alloys, and the results were shown in Fig.3. The results showed that  $\alpha$ -Mg and MgZn phases were detected in the Mg-4.0 Zn alloy, and it also indicated that the diffraction peaks from the MgZn phase were very weak and that of the Mg were strong. There was no obvious change in diffraction peak when 0.2 wt. % Ca and 0.5wt. % Ca was added into the Mg-4.0 Zn alloy. With the Ca concentration increased to 1.5 wt. %,  $\text{Ca}_2\text{Mg}_6\text{Zn}_3$  phases began to be detected in Mg-4.0 Zn-xCa. When the Ca concentration increased to 2.0 wt. %,  $\text{Mg}_2\text{Ca}$ , and  $\text{Ca}_2\text{Mg}_5\text{Zn}_{13}$  phases began to be detected in the alloy.

Materials	Chemical composition (wt.%)						
	Al	Zn	Mn	Si	Fe	Ca	Mg
Mg-4.0Zn	0.023	3.926	0.058	0.031	0.004	0.007	Balance
Mg-4.0Zn-0.2Ca	0.033	1.852	0.030	0.039	0.007	0.180	Balance
Mg-4.0Zn-0.5Ca	0.029	2.732	0.022	0.036	0.007	0.452	Balance
Mg-4.0Zn-1.0Ca	0.019	3.925	0.021	0.032	0.008	0.915	Balance
Mg-4.0Zn-1.5Ca	0.027	5.223	0.031	0.034	0.009	1.635	Balance
Mg-4.0Zn-2.0Ca	0.024	5.977	0.019	0.033	0.012	2.158	Balance

Table 2. Chemical composition of the as-cast Mg-4.0Zn-xCa alloys

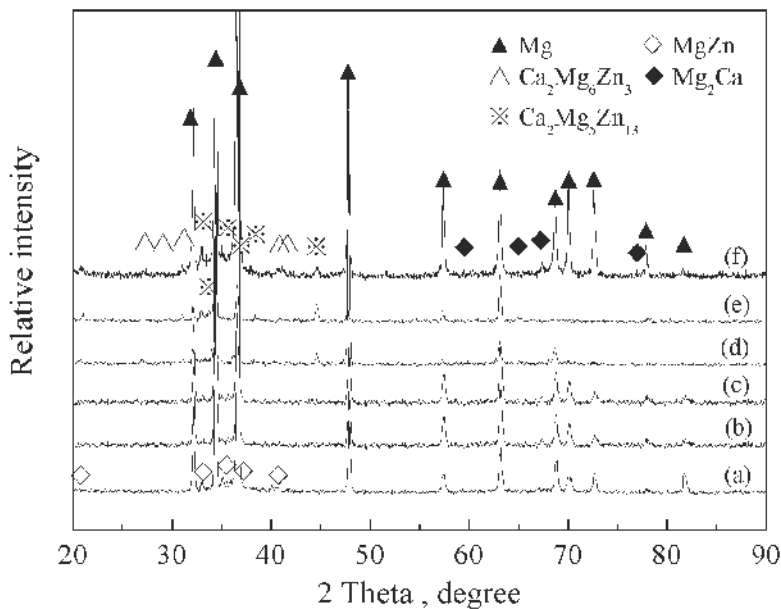


Fig. 3. XRD patterns of as-cast Mg-4.0Zn-xCa alloys (a) Mg-4.0Zn; (b) Mg-4.0Zn-0.2Ca; (c) Mg-4.0Zn-0.5Ca; (d) Mg-4.0Zn-1.0Ca; (e) Mg-4.0Zn-1.5Ca; (f) Mg-4.0Zn-2.0Ca

The microstructures of the as-cast Mg-4.0 Zn-x Ca alloys were shown in Fig.4. Fig. 4(a) was taken from the Mg-4.0 Zn alloy, which consisted of the dendrite  $\alpha$ -Mg matrix and some polygonal shaped second phases which distributed in the areas of inter-dendrite and grain boundary. The second phases were very coarse in the Mg-4.0 Zn. Fig. 4(b) was taken from the Mg-4.0 Zn-0.2 Ca alloy, which indicated that the microstructure had an evidently change compared with Mg-4.0 Zn alloy, and the second phase changed its shape and distributed in the areas of inter grain. With the increase of Ca concentration, however, lamellar eutectic appeared in the as-cast microstructure, eutectic structure was mostly distributed in the grain boundary and little in the areas of inter-dendrite, as shown in Fig. 3 (e) and (f) which were taken from Mg-4.0 Zn-1.5 Ca and Mg-4.0 Zn-2.0 Ca alloys, respectively. It's easy to find out that the morphogenesis of second phases have an obviously change by an increase in Ca content. At first the second phase was polygonal particles in Mg-4.0 Zn alloy, and then when less than 0.5 wt. % Ca was added in Mg-4.0 Zn alloy, the second phase changed its morphology, and it was small round particle. Finally when more than 0.5wt. % Ca was added, the second phase was lamellar structure.

In the initial stages of solidification, Zn and Ca were complete melts in the magnesium. Subsequently, as the solidification develops, the solute atoms are rejected by the growing  $\alpha$ -Mg and enriched in the residual liquid, which began to form clusters precipitation in the grain boundary and inter dendrite arm space. When the Ca concentration was increasing to 1.5 wt. %, it was apt to forming lamellar eutectic.

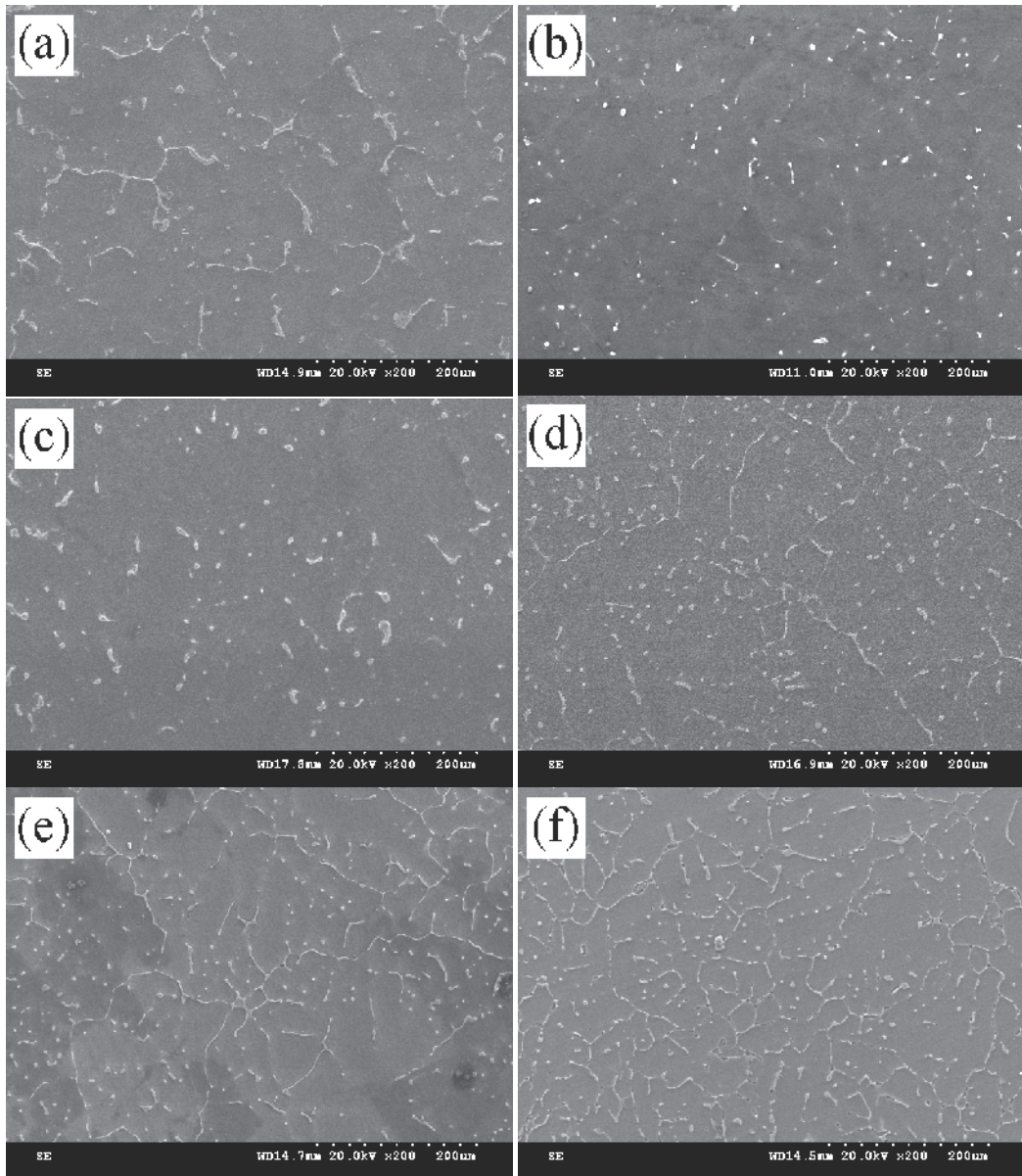


Fig. 4. Microstructure of as-cast Mg-4.0Zn-xCa alloys (a) Mg-4.0Zn; (b) Mg-4.0Zn-0.2Ca; (c) Mg-4.0Zn-0.5Ca; (d) Mg-4.0Zn-1.0Ca; (e) Mg-4.0Zn-1.5Ca; (f) Mg-4.0Zn-2.0Ca

### 3.2 Mechanical property evolution of the as-cast Mg- Zn-Ca alloys

#### 3.2.1 The effects of Zn content on mechanical property of as-cast alloys

The tensile tests were carried out at room temperature on the as-cast Mg-x Zn alloys. The tensile strength and elongation of present alloy were shown in Table 3. The typical stress-strain curves of Mg-x Zn alloys were depicted in Fig.5. As shown in Table 3 and Fig.5, after 1.0 wt.% Zn was added to the pure Mg, the mechanical properties of as-cast Mg-1.0Zn like

pure Mg was still weak, in which the yield strength was 21MPa, UTS was 101MPa and the elongation was 6.9%. With the increasing of Zn contents, the yield strength, UTS and the elongation was increased. When the Zn content was up to 4.0wt.%, the mechanical properties reach to the peak value, the yield strength was 58.1MPa, UTS was 216.85MPa and the elongation was 15.8%. The mechanical properties of Mg-Zn binary alloy when ulteriorly increasing of Zn contents was declined. Its UTS was 182 MPa, and its elongation was only 7.2 % for Mg-6.0 Zn alloy. Direct estimation of stacking fault energy by thermodynamic calculations showed that Zn reduces stacking fault energy of the Mg-Zn alloys. Stacking fault energy is an important physical properties of the material, which directly affects the mechanical properties, dislocation cross slip, phase stability and the dynamic recrystallization of metal materials. It has been confirmed that the stacking fault energy in magnesium alloy plays an important role in mechanical properties and the dynamic recrystallization[22]

Alloy	Yield strength(MPa)	UTS (MPa)	Elongation (%)
Mg-1.0Zn	20±2	101.5±3	6.96±0.5
Mg-2.0Zn	27±2	145.9±5	12.23±1.5
Mg-3.0Zn	47±1.5	167.8±10	13.7±1.0
Mg-4.0Zn	58±1.0	216.8±15	15.8±5.5
Mg-5.0Zn	68±1.5	185±5	9.2±0.5
Mg-6.0Zn	69±1.5	182±5	7.2±0.5

Table 3. Mechanical properties of Mg-xZn alloys at room temperature

### 3.2.2 The effects of Ca content on mechanical property of the as-cast alloys

The tensile strength and elongation of as-cast Mg-4.0 Zn-x Ca alloys were shown in table 4. The typical stress-strain curves of as-cast Mg-4.0 Zn-x Ca alloys were depicted in Fig.6. The ultimate tensile strength (UTS) and elongation of as-cast Mg-4.0 Zn alloy were 180MPa and 9.5%, respectively. After 0.2 wt. % Ca was added, the UTS and elongation of as-cast Mg-4.0 Zn-0.2 Ca alloy were improved to 215 MPa and 17.5%, respectively. When 0.5 wt. % Ca was added, the Mg-4.0 Zn-0.5 Ca alloy has similar mechanical property as the Mg-4.0 Zn-0.2 Ca alloy. However, the mechanical properties of as-cast Mg-4.0 Zn-1.0 Ca alloy began to decline. When the Ca concentration was up to 2.0 wt. %, the alloy showed worse mechanical property, its UTS was 142 MPa and elongation was only 1.7 %.

Fig.7 showed the typical fracture surfaces of as-cast Mg-4.0 Zn-x Ca alloys. As it was showed that the fracture type was ductile fracture when Ca concentration was lower than 0.5 wt. %. Big dimples and tearing edges can be evidently observed on the fracture surface of the as-cast Mg-4.0 Zn-0.2 Ca (Fig.8 (a)). When the Ca concentration was 1.0 wt. %, the Mg-4.0 Zn-1.0 Ca alloy showed mixture fracture morphology. When the Ca concentration was up to 2.0 wt. %, the fracture type of the alloy was brittle fracture. The pearl-shaped fracture can be easily observed on the fracture surface of the as-cast Mg-4.0 Zn-2.0 Ca alloy (Fig. 5 (c)).

Alloy	Yield strength (MPa)	UTS (MPa)	Elongation (%)
Mg-4.0Zn	58±1.0	216.8±15	15.8±5.5
Mg-4.0Zn-0.2Ca	58.1±1.0	225±5	17.5±1.0
Mg-4.0Zn-0.5Ca	70±3.0	180±5	12.3±1.5
Mg-4.0Zn-1.0Ca	83±2.0	175±10	8.7±1.0
Mg-4.0Zn-1.5Ca	83±3.0	167±5	7.1±2.5
Mg-4.0Zn-2.0Ca	90±4.0	143±5	2.1±0.5

Table 4. Mechanical properties of Mg-4.0wt.%Zn-xCa alloys at room temperature

The mechanical properties of magnesium were affected by each alloying constituent. Zinc was an effective alloying ingredient in magnesium. Because zinc had a relatively high solid solubility in magnesium at high temperature, a good mechanical properties were achieved by solid solution strengthen. Binary Mg-Zn alloys like Mg-Al alloys, also respond to age hardening, and contrary to Mg-Al alloys, coherent GP zone and semicoherent intermediate precipitate were formed to have an enhanced effect. However, in the Mg-Zn alloys, the maximum solubility of zinc in the magnesium drops to 1.6 wt. % (i.e. 0.6 at. %) at room temperature in the equilibrium state [23]. When the zinc content was more than 4.0 wt. %, in the solidification process, the melt zinc atoms would be rejected by the growing  $\alpha$ -Mg and enriched in the residual liquid, these rich areas were often prone to formation of microporosity.

In Mg-Zn alloys, the progressive addition of Ca had been found to substantially increase the temperature difference between liquid and solid phase lines, which was conducive to the grain refinement in the solidification process. At the same time, the introduction of Ca to Mg-Zn alloys result in precipitation of desolvating phase,  $\text{Ca}_2\text{Mg}_6\text{Zn}_3$  and  $\text{Ca}_2\text{Mg}_5\text{Zn}_{13}$ , which could enhance the strength and toughness of alloy [24][25][26]. The current work showed that an addition of small amount of Ca to Mg-4.0 Zn alloys had a marked increase in the tensile strength, but Ca content was excess of 0.5 wt. % make the tensile strength prone to decrease. The precipitates in the Mg-4.0 Zn-0.2 Ca and Mg-4.0 Zn-0.5 Ca alloys were  $\text{Ca}_2\text{Mg}_6\text{Zn}_3$  and  $\text{Ca}_2\text{Mg}_5\text{Zn}_{13}$  phases, which were small particles in the alloys. Thus, the tensile property of Mg-4.0 Zn-0.2 Ca and Mg-4.0 Zn-0.5 Ca alloys were improved. However, the maximum solubility of Ca in the magnesium was only 0.2 wt. % at room temperature and 1.2 wt. % at high temperature in the equilibrium state, when more than 1.0 wt. % Ca was added, the precipitates in the grain boundary began to continuously precipitated and the morphogenesis of the precipitates were changed to lamellar structure, made the tensile properties decline. When the Ca concentration was up to 2.0 wt. %, in the grain boundary tends to form eutectic structure which caused the tensile property deteriorate.

### 3.3 In-vitro degradation tests

#### 3.3.1 The effects of Zn content on in-vitro degradation of the as-cast alloys

The representative potentiodynamic polarization curves of Mg-xZn alloys in Hank's solution were shown in Fig.8, with pure Mg as contrast. As shown in Fig.8, the corrosion potential of the Mg-x Zn alloys was higher than that of pure Mg. The corrosion potential of

pure Mg was -1574mV. The corrosion potential was correlated with the Zn concentration. The corrosion potential of Mg-2.0Zn and Mg-3.0 Zn alloys were about -1561 and -1568 mV, respectively, which were nearly the same and about 10 mV high than that of pure Mg. The Mg-5.0 Zn and Mg-6.0 Zn alloy samples exhibit high corrosion potentials of about -1524 and -1547 mV, respectively, which were about 50 mV higher than that of pure Mg. It could be seen that the addition of Zn improved the corrosion potential of the as-cast Mg-x Zn alloys. But, the addition of elements Zn was also increased the current densities of the resulted as-cast Mg alloys in Hank's solution.

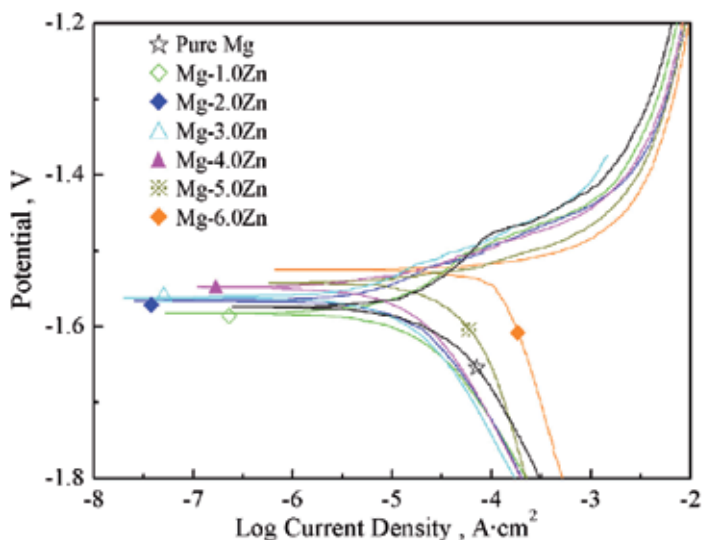


Fig. 8. Potentiodynamic polarization curves of Mg-Zn alloys in SBF solution

The reason for the increase corrosion potential of Mg-x Zn alloys was that the Zn element had a high electronegative. But, when the Zn concentration increased, the corrosion resistance was decreased. The reason for the reduced corrosion resistance of Mg-x Zn alloys was that the second phase precipitated during the solid solidification processes, which accelerated the corrosion rate due to the different electrochemical behaviors of  $\alpha$ -Mg and precipitates.

Generally, the cathodic polarization curves were assumed to represent the cathodic hydrogen evolution through water reduction, while the anodic polarization curves represented the dissolution of magnesium. It could be seen that the cathodic polarization current of hydrogen evolution reaction on Mg-1.0 Zn alloy sample was much lower than that of Mg-5.0 Zn and Mg-6.0 Zn Ca alloys sample, suggesting that over potential of the cathodic hydrogen evolution reaction was lower for Mg-1.0 Zn and Mg-2.0 Zn alloys sample. As a result, the cathodic reaction was kinetically more difficult on the Mg-1.0 Zn alloy and Mg-2.0 Zn alloy sample than that on the Mg-5.0 Zn Ca alloy samples. The degradation rates of Mg-1.0Zn degraded were slower thanMg-5.0Zn, Mg-6.0Zn, which was adherence to the electrochemical results.

### 3.3.2 The effects of Ca content on in-vitro degradation of the as-cast Mg-Zn-Ca alloys

The representative potentiodynamic polarization curves of the pure Mg and Mg-4.0 Zn-x Ca alloys in Hank's solution were shown in Fig.9. The mean corrosion potentials of Mg-4.0Zn-



xCa alloys are enhanced to  $-1574\text{mV}$ , which is increased by  $70\text{ mV}$  compared with  $-1646\text{ mV}$  of the pure Mg corrosion potential. However, it is confirmed that Mg-4.0 Zn-0.2 Ca alloy exhibits the best corrosion resistance among Mg-4.0Zn-xCa alloys, even higher than that of Mg-4.0 Zn alloy through further observation. This particular phenomenon can be explained as follows. Firstly, the addition of  $4.0\text{ wt. \%}$  Zn can cause the formation of coarse MgZn precipitate as shown in Fig.4 and 2(a), which reduces the corrosion resistance of Mg-4.0Zn alloy due to the different electrochemical behaviors between primary  $\alpha\text{-Mg}$  and precipitate. Then, the slight addition (less than  $0.5\text{ wt. \%}$ ) of Ca alloying element can cause MgZn precipitates to be effectively transform to fine ternary precipitates, which has been clearly documented in previous literature [27][28]. The refinement and homogenization of precipitate phase can improve the corrosion resistance of Mg-4.0Zn-0.2Ca alloy compared with that of Mg-4.0Zn alloy. Finally, increasing Ca content was over than  $0.5\text{wt. \%}$  cause the formation of another coarse  $\text{Mg}_2\text{Ca}$ ,  $\text{Ca}_2\text{Mg}_6\text{Zn}_3$  and  $\text{Ca}_2\text{Mg}_5\text{Zn}_{13}$  precipitates as shown in Fig.3 and 4. It is quite obvious that the precipitates increases with Ca content increasing, which decreases the corrosion resistance of as-cast Mg-4.0Zn-xCa alloys.

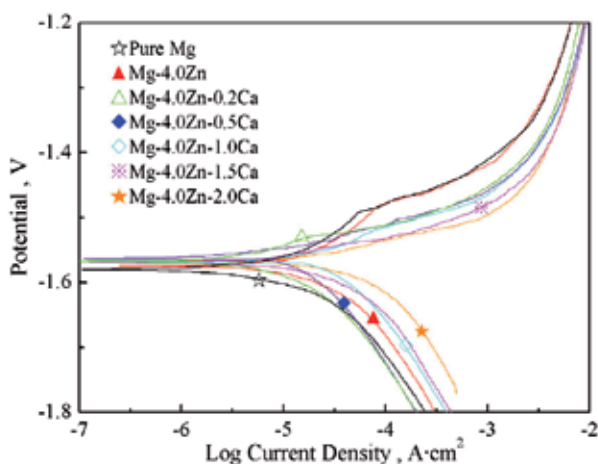


Fig. 9. The potentiodynamic polarization curves of as-cast Mg-4.0 Zn-x Ca alloys in Hank's solution.

It is well known that the cathodic polarization curves represent the cathodic hydrogen evolution through water reduction, while the anodic polarization curves do the dissolution of magnesium. That is to say, it is equivalent to that Mg-4.0 Zn-0.2 Ca alloy sample exhibits the lowest current of hydrogen evolution reaction and Mg-4.0 Zn-1.5 Ca and Mg-4.0Zn-2.0 Ca alloys samples does the highest ones, which indicates that over potential of the cathodic hydrogen evolution reaction of Mg-4.0 Zn-0.2 Ca alloy is much lower than those of Mg-4.0 Zn-1.5 Ca and Mg-4.0 Zn-2.0 Ca alloys. Therefore, the lowest cathodic hydrogen evolution reaction brings the highest corrosion resistance to the Mg-4.0 Zn-0.2 Ca alloy.

Fig.10 illustrates the pH variation of Hank's solution versus the immersion testing time for Mg-4.0Zn-xCa alloys. It could be observed that the pH variations of the alloys all obey the parabolic rate law. The pH variation rate decreases with the immersion time increasing. After 48 hrs immersion, all the pH values of the samples tend to be stable. In the early period of immersion, both pure Mg and the Mg-4.0Zn-xCa alloys acutely reacted with

Hank's solutions and rapidly generated bubbles. And these reactions of Mg and H<sub>2</sub>O in Hank's solution generated a large amount of OH<sup>-</sup> and led to the pH values of the solutions be obviously increased. Comparing the pH values of Mg-4.0Zn-xCa alloys, it can be found that the pH variations of pure Mg and Mg-4.0Zn-0.2Ca alloy are much lower than those of Mg-4.0Zn-1.5Ca and Mg-4.0Zn-2.0Ca alloys. The pH values of Mg-4.0Zn-1.5Ca and Mg-4.0Zn-2.0Ca alloys are remarkably increased to 8.2 from 7.4 after 12hrs immersion tests, which is even equal to those of pure Mg and Mg-4.0Zn-0.2Ca alloy after 96hrs immersion tests. At the end of the immersion tests, the pH values are increased to 8.22 and 8.32 for pure Mg and Mg-4.0 Zn-0.2 Ca alloy, respectively. In particular, the pH value is elevated to 11 from 7.4 for Mg-4.0Zn-2.0Ca alloy. This phenomenon can be explained as follows. The standard potential of coarse second phases of Mg-4.0Zn-1.5Ca and Mg-4.0Zn-2.0Ca alloys is higher than that of the pure Mg. Therefore, the selective attack occurred between  $\alpha$ -Mg and the second phase, and the reaction in Hank's solutions is acute. Thus, the pH values of Mg-4.0Zn-1.5Ca and Mg-4.0Zn-2.0Ca alloys are rapidly increased. However, the uniform microstructure and lower reaction rates of pure Mg, Mg-4.0Zn-0.2Ca and Mg-4.0Zn-0.5Ca alloys cause a slow increase of pH values. After 48hrs immersion, bubbles are quite decreased which corresponds a slow reaction rate and leads a slow increase of the pH values for the samples. In addition, the increasing corrosion films including HA and other phosphates formed by the reaction during the immersion test can further reduce the reaction rates or degradation of the alloys [29].

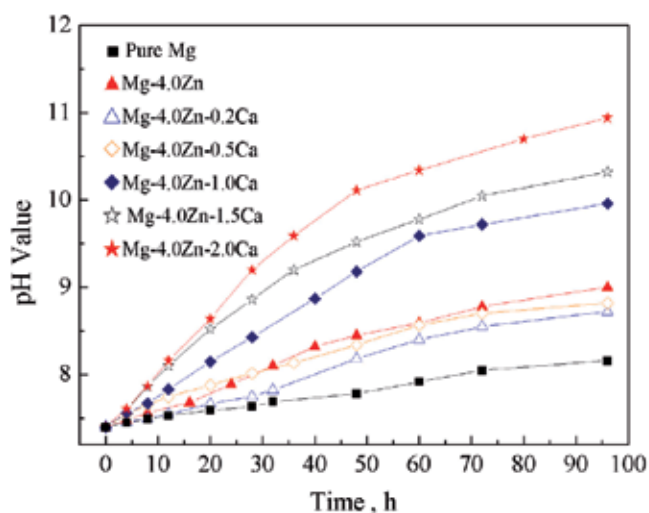


Fig. 10. pH variation of Hank's solution versus the immersion testing time for as-cast Mg-4.0Zn-xCa alloys.

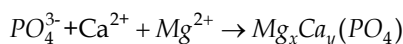
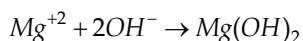
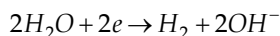
According to the above-mentioned search, we found that Mg-4.0Zn-0.2Ca alloy have an excellent corrosion resistance among the Mg-Zn and the Mg-Zn-Ca alloys. Thus, the immersion test was only performance on the Mg-4.0Zn-0.2Ca alloy. The degradation rates of the alloy after 30-day immersion were listed in Table 5. The degradation rates of Mg-4.0Zn-0.2Ca alloy degraded were slower than pure Mg, which was adherent to the electrochemical results.

Mg and the Mg-4.0Zn-0.2Ca alloy degraded quickly, during the early stage of immersion in SBF, accompanied by the rapid formation of an insoluble protective corrosion layer, which retarded degradation. The degradation process of Mg-4.0Zn-0.2Ca alloy could be roughly summarized as follows: just after immersion in SBF solution, magnesium alloy react with fluids on the surface and get dissolved in the surrounding fluids. With the increasing time of immersion, more  $Mg^{2+}$ ,  $Zn^{2+}$  and  $Ca^{2+}$  ions were dissolved into the solution, the local pH near the surface of the Mg could be  $>10$ [30]. As a result, a magnesium-containing calcium phosphate would precipitate from the SBF solution and deposited on the surface of the magnesium samples, per the following equation:

Anodic reaction:



Cathodic reaction:



Moreover, when  $Mg^{2+}$ ,  $Zn^{2+}$  and  $Ca^{2+}$  ions were dissolved into the solution, phosphate-containing Mg/Ca insoluble protective layer was formed and tightly attached to the matrix. Previous studies [31] have shown that this corrosion layer promotes the osteo-inductivity and osteo-conductivity, predicting good biocompatibility of magnesium and retarded degradation. Therefore, it is proposed that the  $Mg^{2+}$ ,  $Zn^{2+}$  and  $Ca^{2+}$  released during degradation are safe. Hence, we come to the conclusion that the degradation of the Mg-4.0Zn-0.2Ca alloy was harmless and has good biocompatibility.

	E(V)	Current(mA/cm <sup>2</sup> )	V(mm/year)
As-cast	-1.60	2.67	2.05
Extruded	-1.57	2.43	1.98

Table 5. Corrosion potential, corrosion current and corrosion rate of Mg-4.0Zn-0.2Ca alloys

### 3.3.3 Corrosion morphology and products

The samples after electrochemical measurements were observed by SEM. The typical Surface morphology of Mg-Zn-Ca alloys after electrochemical measurements was shown in Fig.11. Corrosion attack on a large area was observed. At the same time, the filiform corrosion and pitting corrosion were found on the Mg-Zn-Ca alloys sample's surface after electrochemical measurements. The former mainly distributed on the grain boundary, and the latter mostly occurred in second phase location.

XRD patterns of the corrosion products on the surface of Mg-Zn-Ca alloys immersed in Hank's solution were presented in Fig.12. The XRD results suggest that magnesium hydroxide [ $Mg(OH)_2$ ], other phosphates and hydroxyapatite (HA) were precipitated on the Mg-Zn-Ca alloys surface.

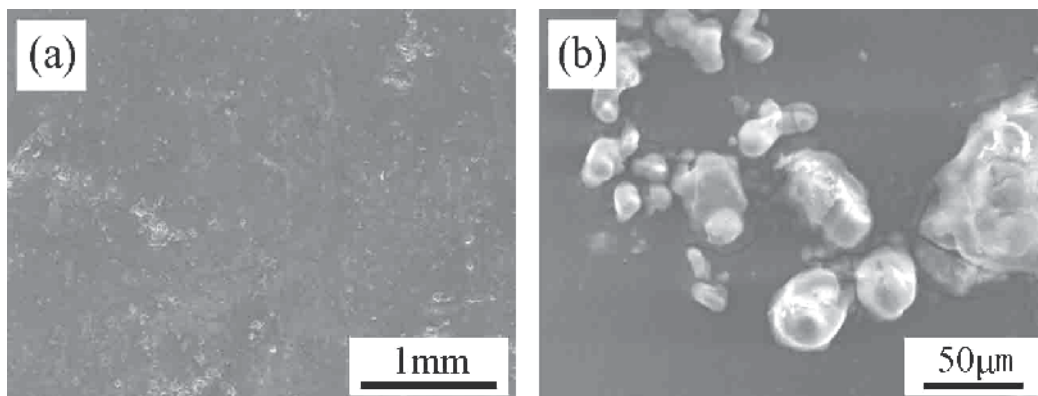


Fig. 11. The typical surface morphology of Mg-4.0 Zn-0.2 Ca alloy after electrochemical measurements: (a) macrostructure (b) microstructure

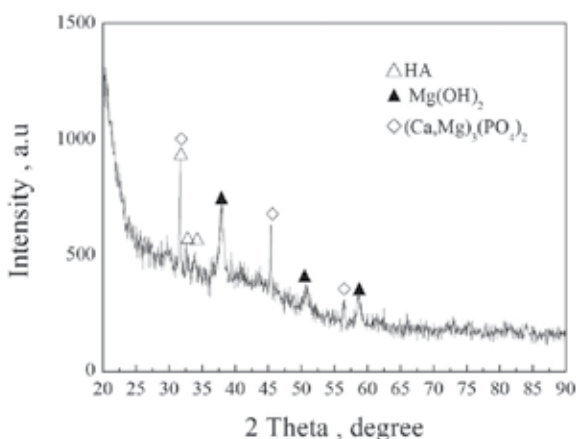


Fig. 12. XRD patterns of the corrosion products of Mg-4.0 Zn-0.2 Ca alloy immersed in Hank's solution.

### 3.4 Cytotoxicity assessments

The pH values of the extraction medium were measured, and only the values of Mg-1.0 Zn, Mg-2.0 Zn, Mg-3.0 Zn, Mg-4.0 Zn, Mg-4.0 Zn-0.2 Ca and Mg-4.0 Zn-0.5 Ca alloys were below than 8.0. That's mean all of these alloys have a potential probability used as the biomaterials. As the economic reason, only Mg-4.0 Zn-0.2 Ca was selected to evaluate the cytotoxicity through examining both the viability and morphology of L-929 cells in this study.

The morphologies of L-929 cells cultured in different extracts after 7 day incubation were shown in Fig.13. It could be seen that the cell morphologies in different extracts were normal and healthy, which was similar to that of the negative control. Fig.14 shows the RGR of L-929 cells after 2, 4 and 7 days of incubation. There was no significant difference between the RGR of cells in the extracts and those in the negative control. According to standard ISO 10993-5: 1999 [32], the cytotoxicity of these extracts was Grade 0-1. In other words, the Mg-4.0Zn-0.2Ca alloy has a level of biosafety suitable for in cellular applications.

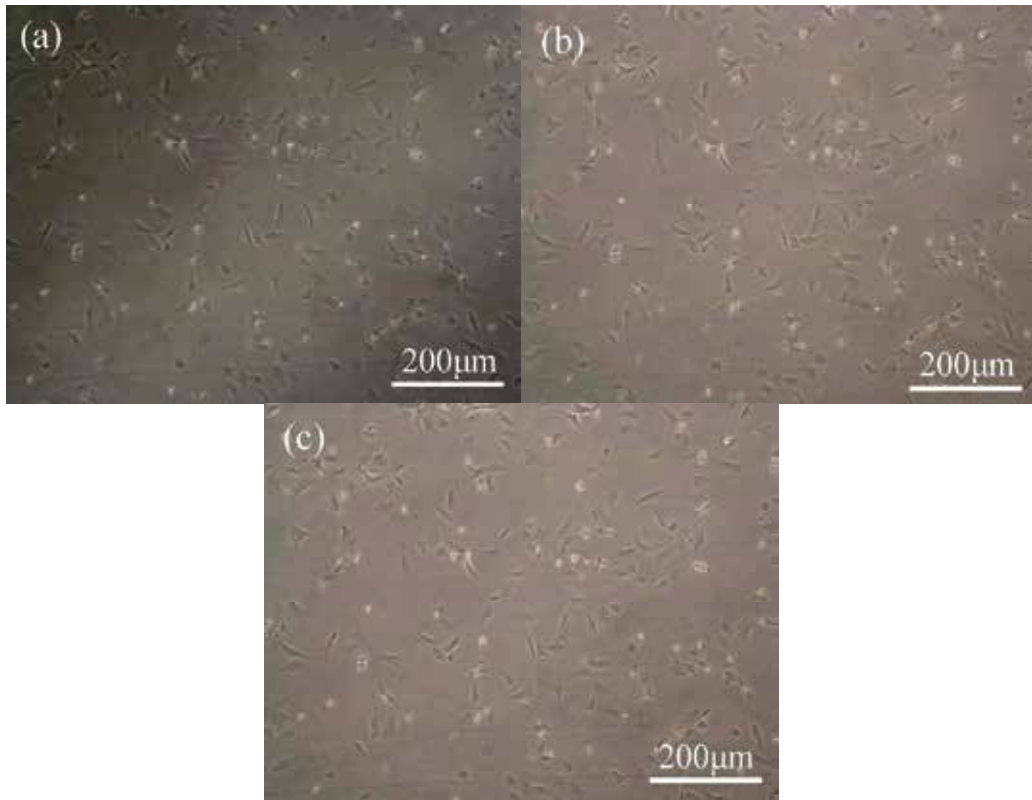


Fig. 13. Morphologies of L-929 cells cultured for 7 day in different extraction media:(a) Negative control, (b) as-cast, (c) extruded.

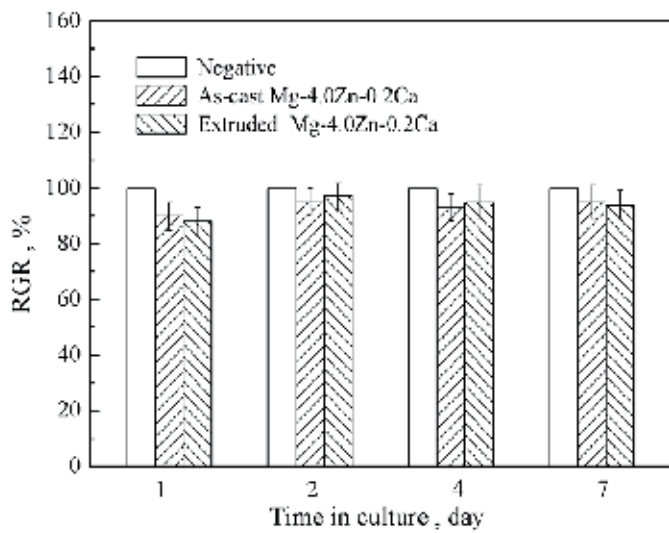


Fig. 14. Cell viability cultured in 100% extraction medium for 1, 2, 4 and 7 days.

The MTT tests were widely used cytotoxicity tests because they are easy, fast and cheap. But, in the case of Mg materials, the use of these test kits leads to false positive or false negative results. It is conceivable that Mg in the highly alkaline environment may be able to open the ring form of the tetrazolium salt and bind to it, which could lead to a change in colors similar to the formation of formazan in the case of the MTT tests with cells [20]. Thus the results of cytotoxicity tests conducted by MTT test will be higher than the true story. It is well known that the neutral red assay and the MTT assay exhibited almost identical reaction patterns for most test materials in L929 cells [33]. Thus, in this study, the neutral red kits were used to assay the cytotoxicity. Its measurement principle is based on the uptake of the vital dye neutral red into lysosomes of viable cells. Neutral red is accumulated because of the low intravesicular pH value. Lysosomes are, however, only one type of subcellular compartments which are acidified by ATP-driven proton pumps (V-type ATPase) and related low intravesicular pH value across vesicle membranes [34]. Accumulation of neutral red in acidic intracellular vesicles needs both ATP as a universal metabolic energy source for proton translocation against an electrochemical  $H^+$ -gradient and tightly sealed vesicle membrane to maintain potential differences. In an alkaline environment with  $Mg^{2+}$ , neutral red could lead to a change in color to yellow. But, the uptake of the vital dye neutral red into lysosomes was red color. The preliminary results of this test show that it seems not to be influenced by corroding Mg. Therefore, the neutral red assay may be regarded as a valid alternative method to determine cell viability, as it shows no interference with the corroding materials. The in-vitro cytotoxicity of Mg-4.0Zn-0.2Ca alloy was found to be Grade 0-1, indicating that the alloy was bio-safe.

### 3.5 In-vivo degradation

Furthermore, in order to further study the biocompatibility of Mg-4.0Zn-0.2Ca alloy, the in-vivo test was conducted on this new type magnesium alloy. Fig.15 showed the optical images of the cross-section of bone and magnesium implants after 3 months implantation. It could be seen that all the shapes of the magnesium implant had been changed from rod shape to irregular shape, indicating the implant was corroded by the body fluid, or the implant degraded in the body fluid. Meanwhile, a degradation layer or a reaction layer could be clearly found on the surface of the alloy implant, as indicated by D in Fig.15. In addition, newly formed bone was observed between the degradation layer and bone tissue around the magnesium alloy implants, as shown by N in Fig.15. The degradation rate was calculated according to the ratios of the cross section area of the residual implant to the original implant. After 3 months implantation, about 35-38% Mg-4.0Zn-0.2Ca alloy implant was degraded. Significant difference ( $p < 0.05$ ) in the in-vivo degradation rates was observed.



Fig. 15. Optical images of the cross-sections of Mg-Zn-Ca implants and bones after 3 months post implantation (M, metal; D, degradation layer; N, new bone; B, bone).

Fig.16 showed a high magnification microstructure of the bone implant interface after 3 months implantation by SEM. It could be clearly seen that the degradation layer was not dense, and many cracks were found. In order to reveal the chemical composition of the degradation layer, EDS was used to analyze the chemical composition of interface. The results were shown in Fig.16 (b). From the analysis results, it could be figured out that the degradation layer was mainly composed of carbon, oxygen, magnesium, calcium and phosphorous. However, the chemical composition was not homogeneous through the whole layer. At the position close to the Mg implant side, higher calcium content and higher Ca/P ratio were found. At the position close to the bone side, the calcium content was still high, but the Ca/P ratio became much smaller compared with at the position close to the Mg implant side. However, there was a sharp change in Mg content at the interface.

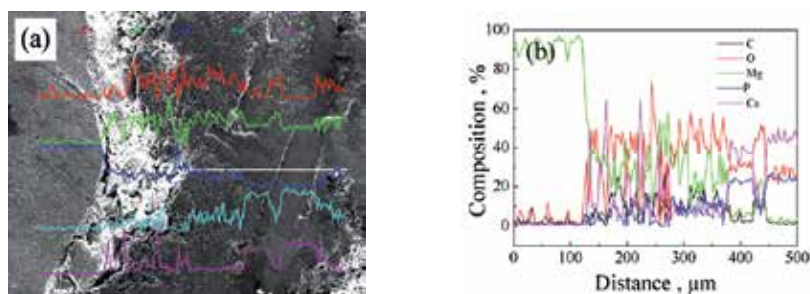


Fig. 16. (a) SEM microstructure of the interface between magnesium implant and bone interface after 3 months post implantation, (b) EDS analysis patterns of implant and bone interface after 3 months post implantation.

### 3.6 Histological analysis

Fig.17 showed the tissue response to the Mg-4.0Zn-0.2Ca alloy pins implantation at 1, 2 and 3 months. It could be clearly seen that some lymphocytes were identified in histological tissue in 1 month after operation, but there was no visible evidence of multinucleated giant cells. After 2 months implantation, there was an active bone formation, which was evident by large number of new disorganized trabeculae. After 3 months implantation, new bone tissue was formed around the magnesium implant. In comparison with the histological microstructure obtained at the cortical bone near the implantation site, as shown in Fig.17, no difference could be found in the histological microstructure between the new bone and the cortical bone.

Magnesium alloys have attracted much attention as potential biodegradable bone implant materials due to their biodegradability in the bioenvironmental as well as their excellent mechanical properties such as high strength and an elastic modulus close to that of bone. In this paper, the in-vitro cytotoxicity and in-vivo biocompatibility of new kind of Mg-4.0Zn-0.2Ca alloy was studied. The cytotoxicity test indicated that the Mg-4.0Zn-0.2Ca alloy had no cytotoxicity. Rabbit implantation indicated that the Mg-4.0Zn-0.2Ca alloy did not cause any inflammation reaction. One month after operation, all magnesium implants were fixed tightly. There was no gap between the bone and the residual implant. Optical images from Fig.15 and SEM microstructure from Fig.16 showed clearly that there was a degradation layer formed on the surface of the magnesium implants. Histological images showed that new bone tissue was in contact with the magnesium implant through this degradation layer.

Line scanning in Fig.17 proved that large amount of Ca and P was found around the magnesium implant. In the present study, the histological analyses revealed that this magnesium-containing calcium phosphate degradation layer could promote or accelerate the new bone formation.

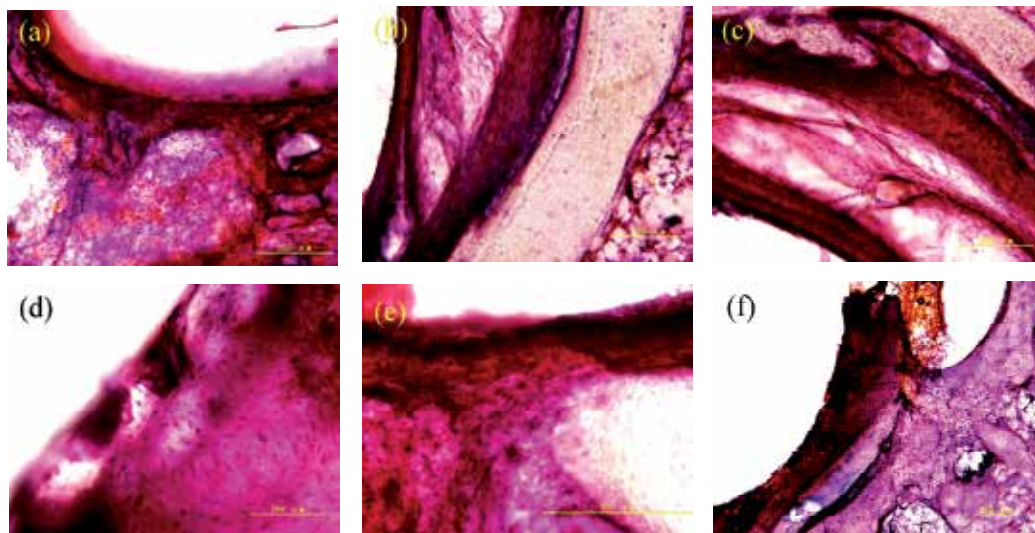


Fig. 17. Tissue response of the Mg-Zn-Ca alloy implantation at 1, 2 and 3 months (a) Mg-4.0Zn-0.2Ca 1 month, (b) Mg-4.0Zn-0.2Ca 2 month, (c) Mg-4.0Zn-0.2Ca 3 month, (d) cortical bone.

In-vivo degradation was a very complex process, so it was difficult to accurately assess the degradation rate of an implant material. F. Witte et al [35] found that the corrosion of a magnesium rod in the medullary cavity was not homogeneous in all cross-sections by used micro-computed tomography. In our study, the cross-section area of the residual implant was calculated to describe the degradation rate of the Mg implant. Due to the inhomogeneous corrosion of a magnesium rod in the medullary cavity, the calculated degradation rate based on the images was similar to the real in-vivo degradation rate of magnesium implants.

In-vivo degradation, compare with other metal implants, is an ultimate merit of magnesium alloy. After implantation in the rabbit, Mg-4.0Zn-0.2Ca alloy would be reacted with body fluid on the surface and get dissolved in the surrounding body fluid. At first, the released  $Mg^{2+}$ ,  $Zn^{2+}$  and  $Ca^{2+}$  could be absorbed by the surrounding tissues and excreted through the gastrointestinal route and the kidney. However, with the increasing time of implantation, more  $Mg^{2+}$ ,  $Zn^{2+}$  and  $Ca^{2+}$  ions are dissolved into the solution, the local pH near the surface of the Mg implants could be  $>10$ [36]. As a result, an insoluble magnesium-containing calcium phosphate would be precipitated from the body fluid on the surface of the magnesium implant and tightly attached to the matrix, which retarded degradation. In addition, the corrosion layer on the Mg-4.0Zn-0.2Ca alloy contained Mg, Ca and P, which could promote osteoinductivity and osteoconductivity, predicting good biocompatibility of magnesium. Therefore, it is proposed that the  $Mg^{2+}$ ,  $Zn^{2+}$  and  $Ca^{2+}$  released during degradation should be safe.



#### 4. Conclusion

In this paper, we developed ternary Mg-Zn-Ca alloys as biodegradable materials. The following conclusions can be drawn.

The mechanical properties of the as-cast Mg-Zn-Ca alloys can be tailored by the Zn and Ca content. The tensile strength can be increased from 105MPa to 225Mpa, and the elongation can be increased from 4.2% to 17%.

The in-vitro degradation of Mg-Zn-Ca alloys revealed that Zn and Ca not only elevated the corrosion potential of the magnesium alloys, but also influence their corrosion current. A protective layer of Mg(OH)<sub>2</sub> and other Mg/Ca phosphates was formed on the surface of Mg-Zn-Ca alloys when immersed in SBF solution, which declined the degradation rate.

In vitro cytotoxicity assessments indicated that Mg-4.0 Zn-0.2Ca alloy did not induce toxicity in L-929 cells and are suitable for biomedical applications.

Implanted in rabbits, the alloy did not induce inflammation reactions or affect the new bone formation. We could draw a conclusion that the Mg-4.0Zn-0.2Ca alloy had good biocompatibility.

#### 5. References

- [1] M.M.Avedesian, H.Baker. editors. ASM Specialty Handbook, Magnesium and Magnesium Alloys, ASM International Materials Park, USA, Ohio, 1999, p. 14.
- [2] F. Witte, V. Kaese, H. Haferkamp, E. Switzer, A. Meyer-Lindenberg, C.J. Wirth. *Biomaterials* 26 (2005) 3557.
- [3] P.S. Mark, M.k. Alexis, H. Jerawala, D. George. *Biomaterials*.27 (2006) 1728.
- [4] L.P. Xu, G.N. Yu, E.L. Zhang, F. Pan, K.Yang. *J. Biome. Mater. Res.* .83A(2007)703.
- [5] R.Zeng, W. Dietzel, F. Witte, N. Hort, C. Blawert. *Adv. Biomater.*10 (2008)B3.
- [6] X.N. Gu, Y.F. Zheng, Y.Cheng, S.P. Zhong, T.F. Xi. *Biomaterials*.30 (2009) 484..
- [7] Z.J. Li, X.N. Gu, S.Q. Lou, Y.F. Zheng. *Biomaterials*.29 (2008)1329.
- [8] Y.Wan, G. Xiong, H.Luo, F. He, Y. Huang, X. Zhou. *Mater. Design* 29 (2008)2034.
- [9] H.Tapiero, K.D.Tew. *Biomed Pharmacother.* 57 (2003) 399.
- [10] S.X. Zhang, X.N. Zhang, C.L. Zhao, J.N. Li, Y. Song, C.Y. Xie. *Acta Biomater.*6(2010)626.
- [11] P.M. Jardim, G. Solórzano, J.B. Vander Sande. *Mater Scie Eng A.* 381 (2004) 196.
- [12] G. Ben-Hamu, D. Eliezer, K.S. Shin. *Mater Sci Eng A.*447 (2007) 35.
- [13] H.Tapiero, K.D.Tew. *Biomed Pharmacother.* 57 (2003) 399.
- [14] Y. Ortega, M.A. Monge, R.Pareja. *J Alloys Compd.* 463 (2008) 62
- [15] E. Zhang, D.S.Yin, L.P.Xu, L.Yang, K.Yang. *Mater.Sci.Eng.C.* 29(2009) 987.
- [16] L.P. Xu, G.N. Yu, E. Zhang, F. Pan, K.Yang. *J. Biomed. Mater. Res. A.* 83A(2007)703.
- [17] H.X.Wang, S.K.Guan, X. Wang, C.X.Ren, L.G.Wang. *Acta Biomater.*6(2010)1743.
- [18] L.Mao, Y.Wang, Y.Wan, F. He, Y.Huang. *Heat Treat. Metal.* 34(2009)19.
- [19] X.N.Gu, Y.F. Zheng, S.P. Zhong, T.F. Xi, J.Q Wang, W.H. Wang. *Biomaterials* 31 (2010) 1093.
- [20] J.Fischer, M.H.Prosenc, M.Wolff, N.Hort, R.Willumeit, F.Feyerabend. *Acta Biomater.* 6(2010) 1813.
- [21] American Society for Testing and Materials. ASTM-G31-72: standard practice for laboratory immersion corrosion testing of metals. In: Annual Book of ASTM Standards. Philadelphia, PA: American Society for Testing and Materials; 2004.
- [22] A. Datta, U.V. Waghmare, U. Ramamurty, *Acta Mater.* 56 (2008) 2531.

- [23] H. Okamoto. *J. Phase Equilibria*. Diffus.15 (1994) 129.
- [24] X.Gao, S.M.Zhu, B.C.Muddle, J.F.Nie, *Scripta Mater.* 53 (2005) 1326.
- [25] J.C. Oh, T. Ohkubo, T. Mukai, K. Hono, *Scripta Mater.* 53 (2005) 675.
- [26] L.Geng, B.P. Zhang, A.B. Li, C.C. Dong, *Mater. Lett.* 63 (2009) 557.
- [27] Y.C. Xin , C.L.Liu , K.F.Huo, G.Y. Tang, X.B.Tian, P.K.Chu. *Surf. Coat.Tech.* 203 (2009) 2554.
- [28] Y. C. Xin, K. F. Huo, T. Hu, G. Y. Tang, P. K. Chu. *Acta Biomate.* 4 (2008) 2008.
- [29] Y. C. Xin, K. F. Huo, T. Hu, G. Y. Tang, P. K. Chu. *J. Mater. Res.* 24 (2009) 2711.
- [30] Y. C. Xin, T. Hu, P. K. Chu. *J. Electrochem.Soc.*157(2010)C238.
- [31] F. Witte, F.Feyerabend, P.Maier, J.Fischer, M. Störmer, C.Blawert, et al. *Biomaterials.* 28(2007)2163.
- [32] ANSI/AAMI. ISO 10993-5: 1999. Biological evaluation of medical devices. Part 5. Tests for cytotoxicity: in vitro methods. Arlington, VA: ANSI/AAMI.
- [33] H. Schweikl, G .Schmalz. *Eur. J. Oral. Sci.*104(1996) 292.
- [34] N. Nelson. *J Exp Biol* 172(1992) 19.
- [35] F.Witte, J. Fischer, J.Nellesen, H.A. Crostack, V. Kaese, A. Pisch, F. Beckmann, H. Windhagen. *Biomaterials.* 27(2006)1013.
- [36] A. Simaranov, I. Sokolova, A. Marshakov, Y. Mikhailovskii. *Prot. Metal.* 27(3) (1991) 329.

## **Part 2**

### **Biomechanical and Physical Studies**



# Biomechanical Properties of Synovial Fluid in/Between Peripheral Zones of Articular Cartilage

Miroslav Petrtyl, Jaroslav Lisal and Jana Danesova

*Laboratory of Biomechanics and Biomaterial Engineering, Faculty of Civ. Engineering,  
Czech Technical University in Prague  
Czech Republic*

## 1. Introduction

The properties and behaviour of articular cartilage (AC) have been studied from numerous aspects. A number of biomechanical models of the properties and behaviour of AC are available today. The traditional model presents cartilage as homogeneous, isotropic and biphasic material (Armstrong et al., 1984). There also exist models of transversally isotropic biphasic cartilage material (Cohen et al., 1992; Cohen et al., 1993), non-linear poroelastic cartilage material (Li et al., 1999), models of poroviscoelastic (Wilson et al., 2005) and hyperelastic cartilage material (Garcia & Cortes, 2006), models of triphasic cartilage material (Lai et al., 1991; Ateshian et al., 2004), and other models (Wilson et al., 2004; Jurvelin et al., 1990). The published models differ, more or less, by the angle of their authors' view of the properties and behaviour of articular cartilage during its loading.

The authors base their theories on various assumptions concerning the mutual links between the structural components of the cartilage matrix and their interactions on the molecular level.

The system behaviour of AC very depend on nonlinear properties of synovial fluid (SF). Certain volumes of SF are moveable components during the mechanical loading in the peripheral zone of AC. Biomechanical properties of peripheral zone of AC are significantly influenced by change of SF viscosity due to mechanical loading.

The hydrodynamic lubrication systems and influences of residual strains on the initial presupplementation of articular plateaus by synovial fluid were not sufficiently analyzed up to now.

Our research has been focused on analyses of residual strains arising in AC at cyclic loading and on the viscous properties of SF. Residual strains in articular cartilage contribute the preaccumulation of articular surfaces by synovial fluid.

SF reacts very sensitively to the magnitude of shear stress and to the velocity of the rotation of the femoral and tibial part of the knee joint round their relative centre of rotation when the limb shifts from flexion to extension and vice versa. Shear stresses decrease aggregations of macromolecules of hyaluronic acid in SF.

Articular cartilage (AC) is a viscohyperelastic composite biomaterial whose biomechanical functions consist

1. in transferring physiological loads into the subchondral bone and further to the spongy bone,
2. in ensuring the lubrication of articular plateaus of joints and
3. in protecting the structural components of cartilage from higher physiological forces.

The macromolecular structure of AC in the peripheral zone (Fig. 1.) has two fundamental biomechanical safety functions, i.e. to regulate the lubrication of articular surfaces and to protect the chondrocytes and extracellular matrix from high loading.

The rheological properties of SF play the key role in the achievement of the optimum hyaluronan concentration.

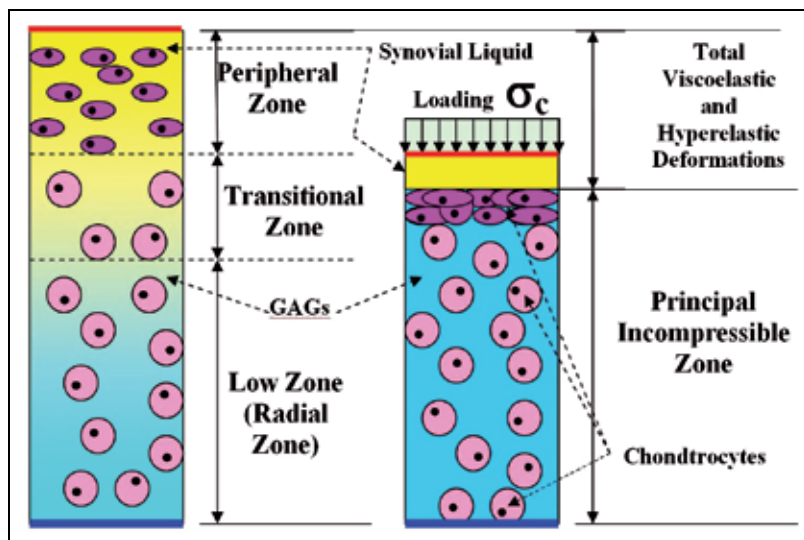


Fig. 1. Complex structural system of articular cartilage (collagen fibres of 2<sup>nd</sup> type are not drawn)

The properties of SF in the gap between the opposite surfaces of articulate cartilage are not homogeneous during loading. The properties of SF change not only during biomechanical loading, but also during each individual's life time. The viscous properties of this fluid undergo changes (in time) due to mechanical loading. As a consequence of its very specific rheological characteristics, SF very efficiently adapts to external biomechanical effects. Exact knowledge of the rheological properties of synovial fluid is a key tool for the preservation and treatment of AC. The significance of the specific role of SF viscosity and viscosity deviations from predetermined physiological values were first pointed out as early as the 1950s to 1990s (Johnson et al., 1955; Bloch et al., 1963; Ferguson et al., 1968; Anadere et al., 1979; Schurz & Ribitsch, 1987; Safari et al., 1990 etc.). The defects of concentrations of the dispersion rate components were noticed by Mori (Mori et al., 2002). In this respect, it cannot be overlooked that mechanical properties of SF very strongly depend on the molecular weight of the dispersion rate (Sundblad et al., 1953; Scott & Heatley, 1999; Yanaki et al., 1990; Lapcik et al., 1998) and also on changes in the aggregations of macromolecular complexes in SF during mechanical effects (Myers et al., 1966; Ferguson et al., 1968; Nuki & Ferguson, 1971; Anadere et al., 1979 and Schurz & Ribitsch, 1987).

Synovial fluid is a viscous liquid characterized by the apparent viscosity  $\eta$ . This viscosity depends on stress and the time during which the stress acts. SF is found in the pores of the

peripheral zone of AC and on its surface (in the gap between the opposite AC surfaces). The viscosity of synovial fluid is caused by the forces of attraction among its molecules being fully manifested during its flow. In other words, viscosity is a measure of its internal resistance during the SF flow. In the space between the opposite AC surfaces, its flow behaves like a non-Newtonian fluid.

As was pointed out above, biomechanical effects play a non-negligible and frequently a primary role in regulating rheological properties.

The principal components of synovial fluid are water, hyaluronic acid **HA**, roughly 3-4 mg/ml, D-glucuronic acid and D-N-acetylglucosamine (Saari et al., 1993 and others). By its structure, hyaluronic acid is a long polymer, which very substantially predetermines the viscous properties of synovial fluid. Its molecular structure is evident from Fig. 2. *Synovial fluid* also contains an essential growth hormone *prolactin* (PRL) and *glycoprotein lubricin*.

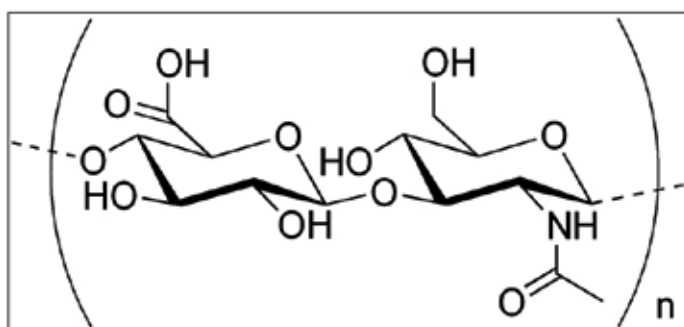


Fig. 2. Molecular complex of hyaluronic acid (HA)

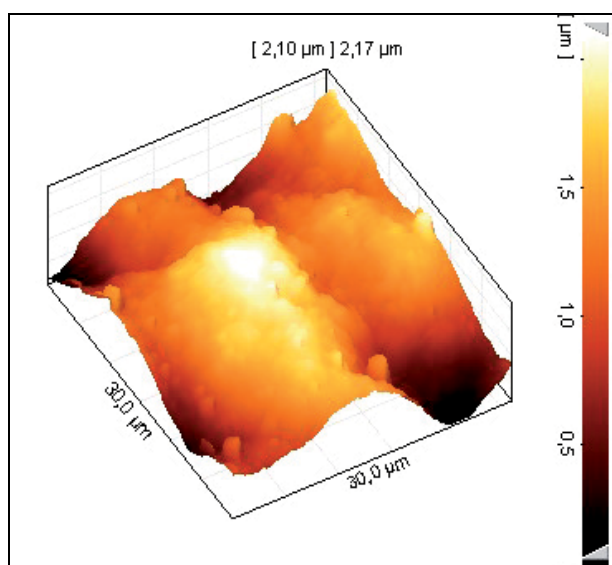


Fig. 3. Topography of the surface of articular cartilage verified by means of FAM (Force Atomic Microscope). The height differences of surface points range up to ca 200 nm - 2,4 μm. In unloaded condition, they are flooded by synovial fluid

Prolactin induces the synthesis of proteoglycans and, in combination with glucocorticoids, it contributes to the configuration of chondrocytes inside AC and to the syntheses of type II collagen. The average molecular weight of human SF is 3 – 4 MDa.

Important components of SF are lubricin and some proteins from blood plasma ( $\gamma$ -globulin and albumin), which enhance the lubricating properties of SF (Oates, 2006). The importance of HA and proteins for the lubricating properties of SF was also described (Swann et al., 1985; Rinaudo et al., 2009).

In the gap between AC surfaces, synovial fluid forms a micro-layer with a thickness of ca 50  $\mu\text{m}$ . It fills up all surface micro-depressions (Fig. 3. and 4., Petrtýl et al., 2010) and in accessible places its molecules are in contact with the macromolecules of residual SF localized in the pores of the femoral and tibial peripheral zone of AC.

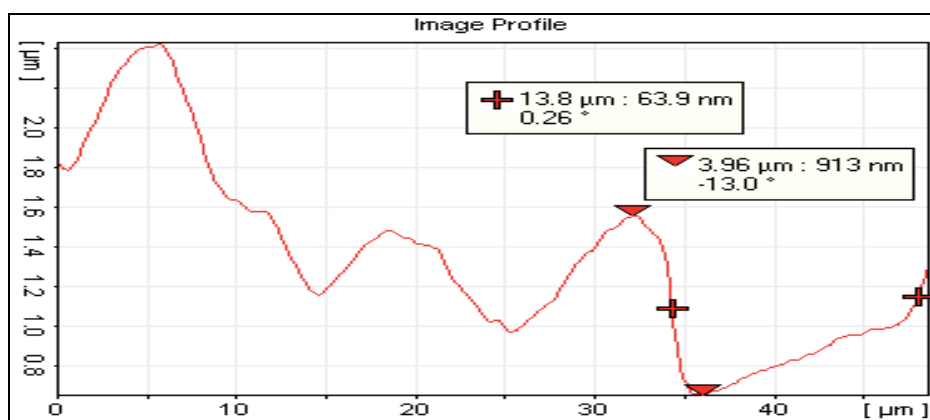


Fig. 4. Topography of the articular cartilage surface of a man (58 years of age). The AC surface oscillates to relative heights of 2.5  $\mu\text{m}$ . During fast shifts of the AC surface (due to the effect of dynamic shifting forces/dynamic bending moments or shear stresses), the AC surface is filled up with generated synovial gel (with less associated NaHA macromolecules) with *low viscosity*

SF is a rheological material whose properties change in time (Scott, 1999 and others). As a consequence of loading, associations of polymer chains of HA (and some proteins) arise and rheopexic properties of SF are manifested (Oates et al., 2006). Due to its specific rheological properties, SF ensures the lubrication of AC surfaces. The key component contributing to lubrication is HA/NaHA. In healthy young individuals, the endogenous production of hyaluronic acid (HA) reaches the peak values during adolescence. It declines with age. It also decreases during arthritis and rheumatic arthritis (Bloch et al., 1963; Anadere et al., 1979; Davies & Palfrey, 1968; Schurz & Ribitsch, 1987 and numerous other authors). Some AC diseases originate from the disturbance of SF lubrication mechanisms and from the defects of genetically predetermined SF properties. Therefore, the lubrication mechanisms of AC surfaces must be characterized with respect to the rheological properties of SF.

## 2. Contents

The objectives of our research has been aimed on the definition of the biomechanical properties of SF which contribute to the lubrication of the opposite surfaces of articular



cartilage, on the analysis of the effects of shear stresses on changes in SF viscosity and on the analysis of the residual strains arising in AC at cyclic loading.

## 2.1 Rheological properties of synovial fluid

With respect to the project objectives, the focus of interest was on the confirmation of the rheological properties of hyaluronic acid with sodium anions (sodium hyaluronan, NaHA) in an amount of  $3.5 \text{ mg ml}^{-1}$  in distilled water without any other additives. The use of only NaHA was based on the verification of the association of HA macromolecules and on the manifestation of highly specific rheological properties of SF, which regulate its lubrication function. The rheological properties were verified using the rotation viscometer Rheolab QC (Anton Paar, Austria). Viscosity values were measured continuously within 8 minutes.

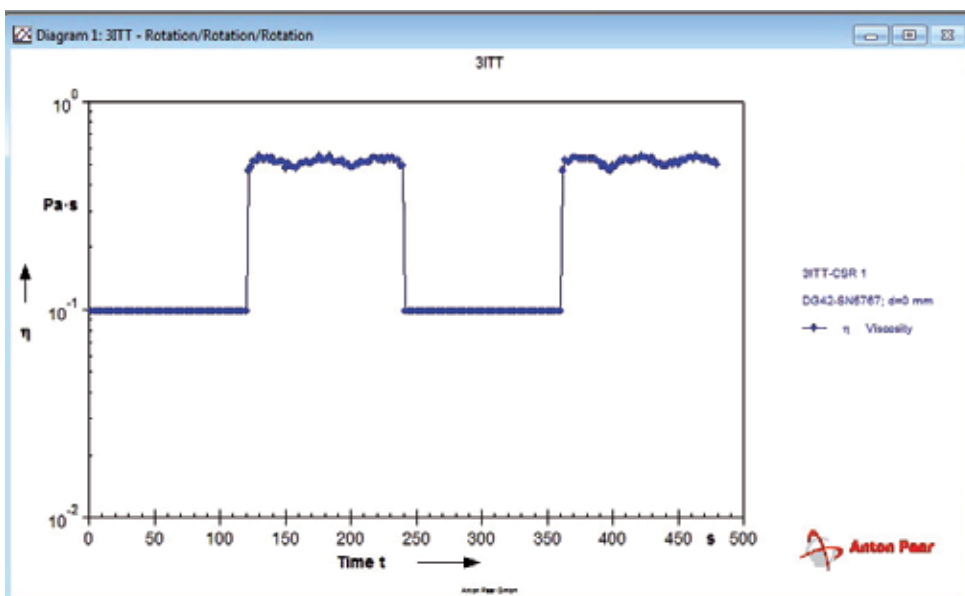


Fig. 5. SF apparent viscosity as related to time (velocity gradient  $100\text{s}^{-1}$ )

Samples were subjected to the effect of constant velocity gradient ( $100\text{s}^{-1}$  –  $500\text{s}^{-1}$  –  $1000\text{s}^{-1}$  –  $2000\text{s}^{-1}$ ) in time 0 – 120s and 240 – 360s. Samples were subjected in the tranquility state in time 120 – 240s and 360 – 480s. The measurements were performed at the temperature of human body ( $37^\circ\text{C}$ ).

Fig. 5. clearly shows that at the constant SF flow velocity gradient  $100\text{s}^{-1}$  there is a distinct time-related constant values in viscosity. The verified synthetic synovial fluid possesses *pseudoplastic properties*. It is evident that the *macromolecules of hyaluronic acid (NaHA/HA) in a water dispersion environment principally contribute to the pseudoplastic behaviour of the fluid. This property is of key importance for controlling the quality of the AC surface protection.*

Fig. 6. also shows that at the constant SF flow velocity gradient  $2000\text{s}^{-1}$  there is a distinct time-related constant values in viscosity. The viscosity of SF after unloading always returns to the same values (ca  $0.8 \text{ Pa s}$ ).

Fig. 7. shows that viscosity values of SF with increasing rate of flow velocity gradient 0 –  $2000 \text{ s}^{-1}$  (in time 0 – 60s) decrease. Viscosity values of SF are constant with constant rate of velocity gradient  $2000 \text{ s}^{-1}$  (in time 60 – 180s).

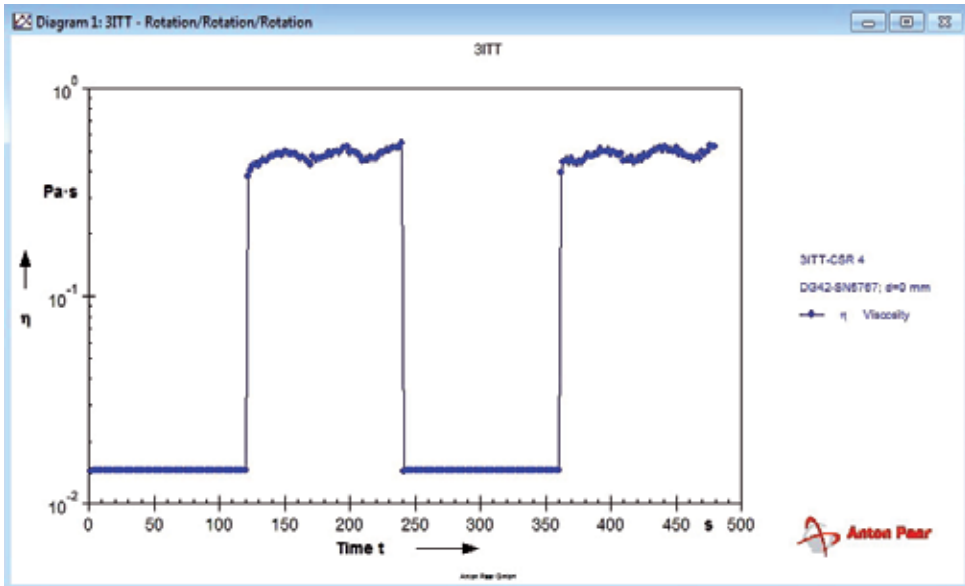


Fig. 6. SF apparent viscosity as related to time (velocity gradient  $2000\text{s}^{-1}$ )

Due to the fact that the lubrication abilities of SF strongly depend on the magnitude of viscosity, and SF viscosity depends on the SF flow velocities, the effects of the magnitudes and directions of shifting forces or shear stresses respectively on the distributions of the magnitudes and directions of SF flow velocity vectors in the space between the opposite AC surfaces had to be analyzed.

The kinematics of the limb motion (within one cycle) shows that during a step the leg continuously passes through the phases of flexion – extension – flexion (Fig. 8). The effect of shifting forces (or shear stresses respectively) is predominantly manifested in the phases of flexion, while normal forces representing the effects of the gravity (weight) of each individual mostly apply in the phases of extension, Fig. 8. The distributions of the magnitudes of SF flow velocity vectors depend on the shifts of the tibial and femoral part of the knee joint, Fig. 9., reaching their peaks in places on the interface of SF with the upper and lower AC surface, Fig. 10. The velocities of SF flows very substantially affect the SF behavior contributing to the lubrication of AC surfaces and their protection.

At rest the bonds are created among the macromolecules of hyaluronic acid (HA) leading to the creation of associates. *By associating molecular chains of HA (at rest) into a continuous structure, a spatial macromolecular grid is created in SF which contributes to the growth in viscosity and also to the growth in elastic properties.*

The associations of HA molecules are the manifestation of cohesive forces among HA macromolecular chains. SF represents a dispersion system (White, 1963) in which the dispersion rate is dominantly formed by snakelike HA macromolecules. The dispersion environment is formed by water. Cohesive forces among NaHA polymer chains in SF are of physical nature. The density (number) of bonds among HA macromolecules is dominantly controlled by mechanical effects. Fig. 9. In relation to the magnitudes of velocity gradients, NaHA macromolecules are able to form “thick” synovial gel which possesses elastic properties characteristic of solid elastic materials, even though the dispersion environment of synovial gel is liquid.

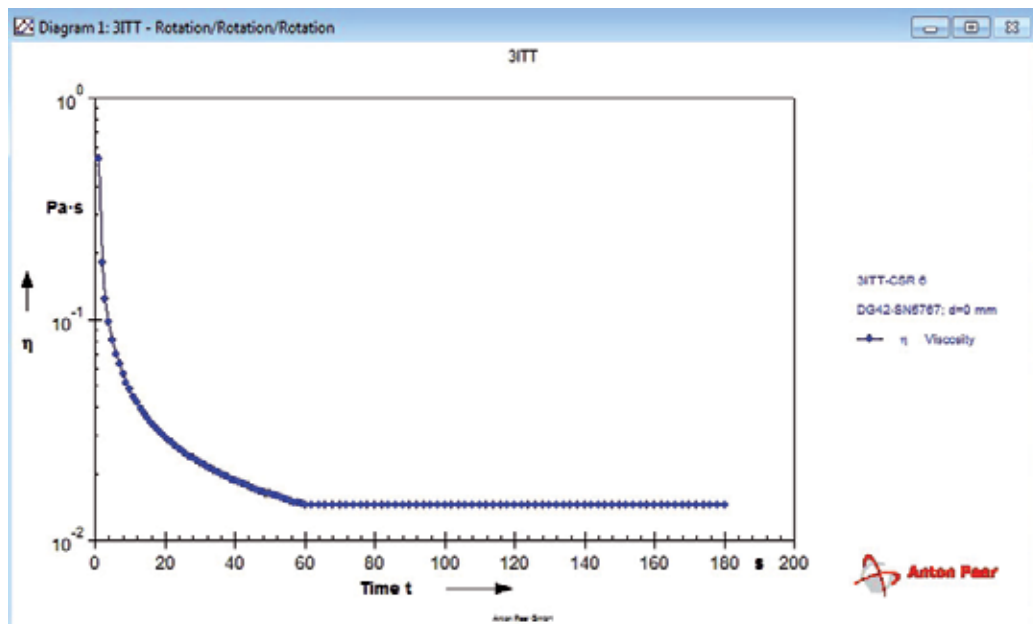


Fig. 7. Viscosity values of SF with increasing rate of flow velocity gradient 0 – 2000  $s^{-1}$  (in time 0 – 60s) decrease. Viscosity values of SF are constant with constant rate of velocity gradient 2000  $s^{-1}$  (in time 60 – 180s)

SF represents a mobile dispersion system in which *synovial gel is generated due to non-Newtonian properties of SF*. Within this system, the macromolecules of hyaluronic acid can be intertwined into a three-dimensional grid, which continuously penetrates through the dispersion environment formed by water. The pseudoplastic properties of SF are manifested through mechanical effects (for example while walking or running), Fig. 8., Fig. 9. *Physical netting occurs, which is characterized by the interconnection of sections of polymer chains into knots or knot areas*. Generally speaking, the association of individual molecules of hyaluronic acid (HA/NaHA) occurs in cases of reduced affinity of its macromolecular chains to the solvent. In other words, the *macromolecules of hyaluronic acid (HA) form a spatial grid structure in a water solution* (Fig. 9.).

Mutually inverse shifts and inverse rotations of the opposite AC surfaces cause inverse flows of SF on its interface with the AC surface (Fig. 10.).

The greatest magnitudes of SF velocity vectors due to the effect of shear stresses  $\tau_{xy}$ , (or the effects of shifting forces respectively) are found near the upper and lower AC surface. They are, however, mutually inversely oriented. Fig. 10. displays the right-oriented velocity vector direction near the upper surface, and the left-oriented one near the lower AC surface. The magnitudes of velocity vectors decrease in the direction towards the central SF zone. In this thin neutral zone, the velocity vector is theoretically zero in value. A very thin layer (zone) of SF in the vicinity of the central zone, with very small to zero velocities, can be appointed **neutral SF zone**.

At very small velocities of SF flows, the *viscosity of the neutral central zone is higher than the viscosity in the vicinity of AC surfaces*. Under the conditions of very low viscosity, the SF material in the vicinity of AC surfaces is characterized by a low friction coefficient. Friction reaches values of ca 0.024 – 0.047 (Radin et al., 1971).

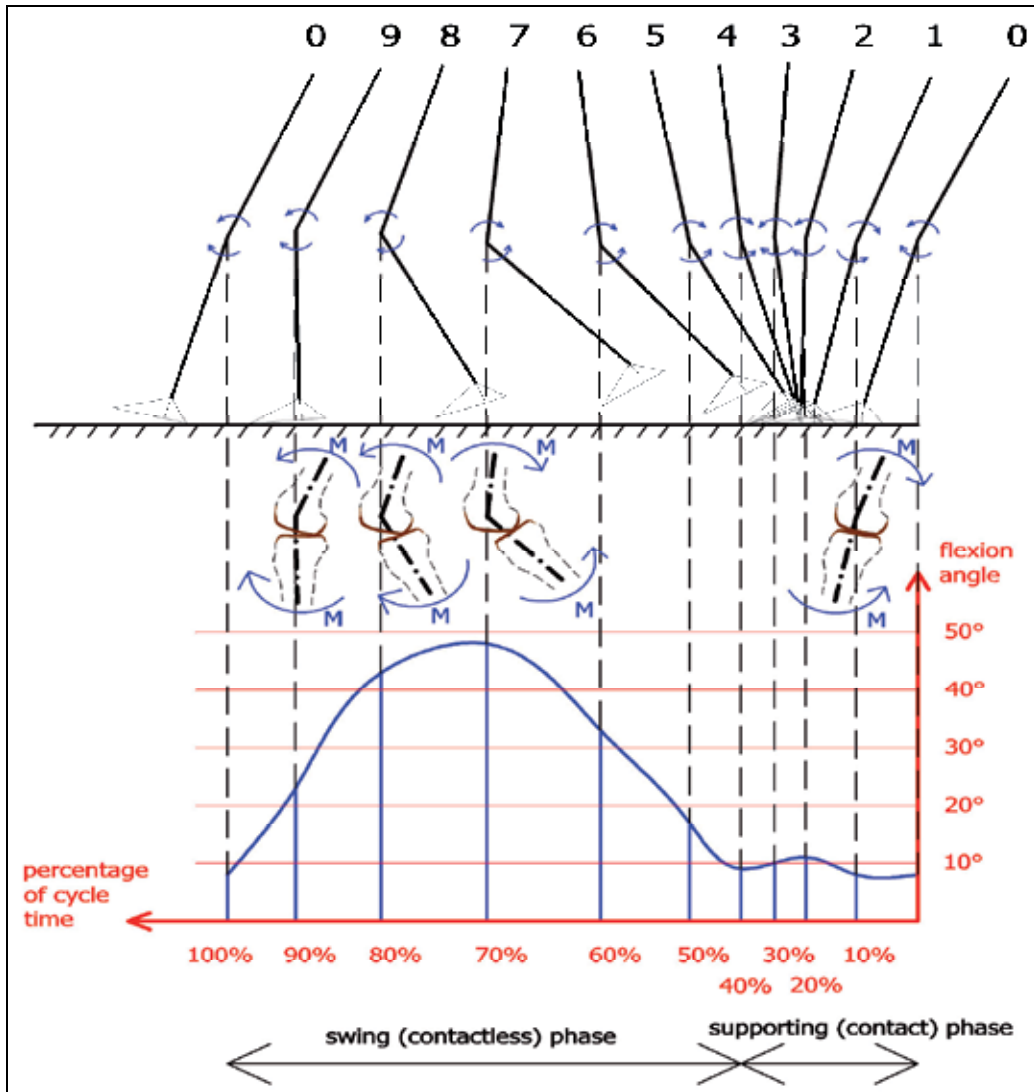


Fig. 8. Orientation diagram of the magnitudes of angles between the axes of the femoral and tibial diaphysis during the “flexion - extension - flexion” cycle of the lower limb in relation to the time percentage of the cycle

The total *thickness of the gap* between the opposite AC surfaces is only ca 50  $\mu\text{m}$ , including height roughness of the surfaces near both peripheral layers  $2 \times 2.5 \mu\text{m}$ , Fig. 4., Fig. 9. (Petrýl et al., 2010). In quiescent state, the AC surfaces are flooded with SF (synovial gel) while during the leg motion (from flexion to extension and vice versa) synovial sol with the relatively low viscosity is generated in SF in peripheral zones of AC. In other words, *due to the effect of shear stresses*  $\tau_{xy}$  the viscosity  $\eta$  of SF decreases and synovial sol is generated. Aggregations of macromolecules of hyaluronic acid decrease. *The most intense aggregations* are in places of the smallest SF velocities, i.e. in neutral (central) zone of SF between the AC surfaces.

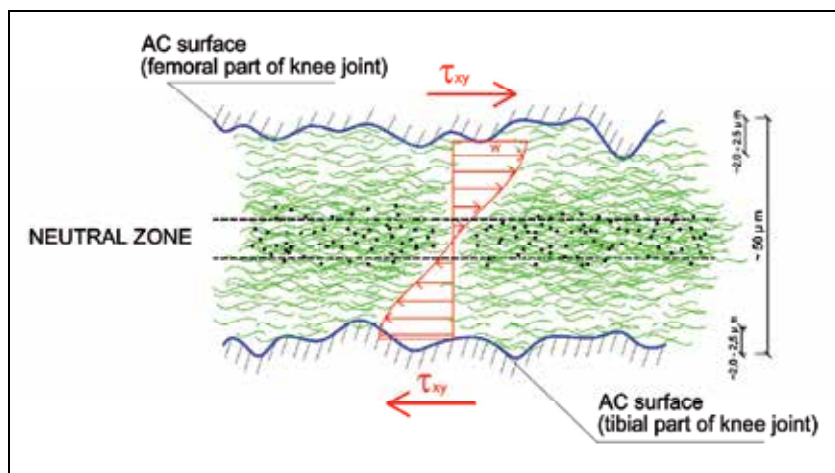


Fig. 9. Diagram of the distribution of magnitudes and directions of SF flow velocity vectors in the gap between AC surfaces. Associations of NaHA/HA macromolecules decline in places with the greatest SF flow velocity gradient, i.e. in zones adjoining each AC surface. The SF flow velocity gradient decreases in the direction towards the neutral zone

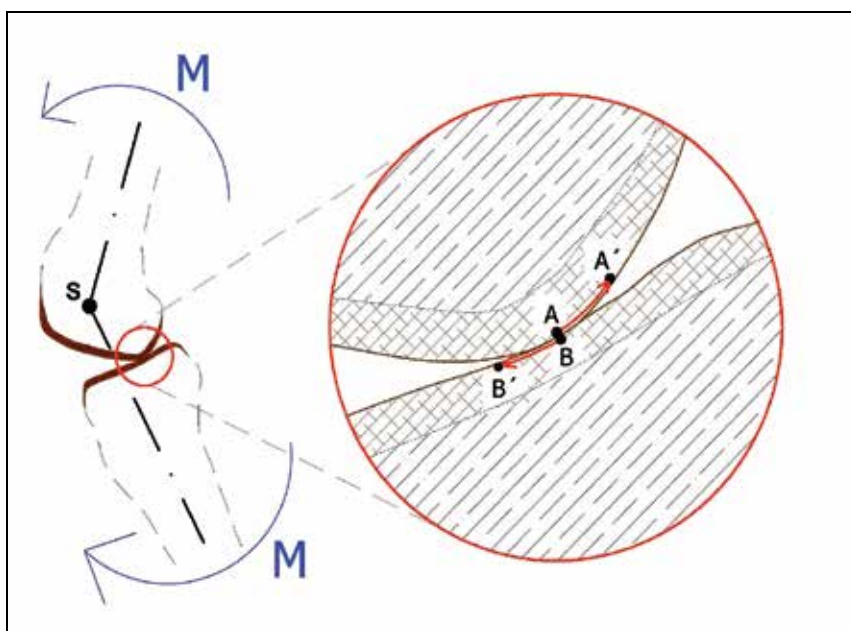


Fig. 10. Rotation of the tibial and femoral part of the knee joint during the transition from flexion to extension. During the rotation of the femoral part of the knee joint (due to the effect of the left-hand rotation moment  $M$ ) round the current (relative) centre of rotation (which is the intersection of longitudinal axes of the femur and tibia), point  $A$  moves to position  $A'$ . During a simultaneous rotation of the tibial part of the knee joint (due to the effect of the right-hand rotation moment  $M$ ) round the same current (relative) centre of rotation, point  $B$  moves to position  $B'$

Due to pseudoplastic properties of SF in the space between the opposite AC surfaces (Fig. 9.), non-physiological *abrasive wear* of the surfaces of AC peripheral zones is efficiently prevented.

The SF solution process in the gap between the AC surfaces is not an isolated phenomenon. It is interconnected (during walking, running etc.) with residual SF in the pores of the intercellular matrix in peripheral zones of the tibial and femoral part of AC. Under high loads, an *integrated unit* is generated which, after the *formation of an incompressible "cushion"*, is able to transfer extreme loads thus protecting the peripheral and internal AC structures from their destructions.

## 2.2 Residual strains during the cyclic loading in the articular cartilage

In agreement with our analyses, the properties and behaviors of articular cartilage in the biomechanical perspective may be described by means of a complex viscohyperelastic model (Fig. 11.). The biomechanical compartment is composed of the Kelvin Voigt viscoelastic model (in the peripheral and partially in the transitional zone of AC) and of the hyperelastic model (in the middle transitional zone and the low zone of AC). The peripheral zone is histologically limited by oval (disk shaped) chondrocytes. The viscohyperelastic properties of AC are predetermined by the specific molecular structures.

The mechanical/biomechanical properties of articular cartilage are topographically non homogeneous. The material variability and non homogeneity depends on the type and the size of physiological loading effects (Akizuki et al., 1986; Petryl et al., 2008).

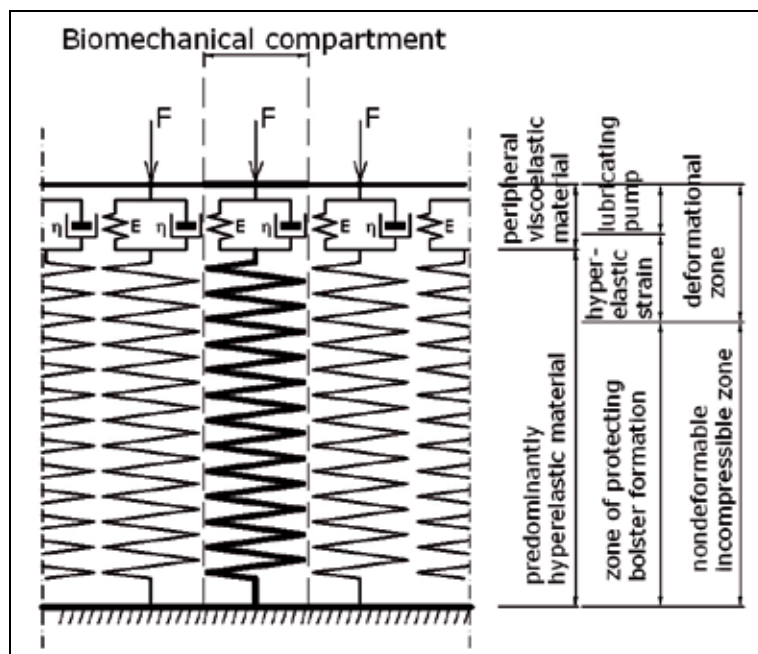


Fig. 11. Mechanical diagram of the complex viscohyperelastic model of articular cartilage. The mechanical compartment is composed of the Kelvin Voigt viscoelastic model (in the peripheral and transitional zone of AC) and of the hyperelastic model (in the middle transitional zone and the low zone of AC)

AC is composed of cells (chondrocytes), of extracellular composite material representing a reinforcing component - collagen 2<sup>nd</sup> type (Benninghoff, 1925) and of a non reinforcing, molecularly complex matrix (Bjelle, 1975). A matrix is dominantly composed of glycoprotein molecules and firmly bonded water. In the peripheral zone, there is synovial fluid unbound by ions.

The principal construction components of the matrix are glycoproteins. They possess a saccharide component (80-90 %) and a protein component (ca 20 - 10 %). Polysaccharides are composed of molecules of chondroitin-4-sulphate, chondroitin-6-sulphate and keratansulphate. They are bonded onto the bearing protein, which is further bonded onto the hyaluronic acid macromolecule by means of two binding proteins. Keratansulphates and chondroitinsulphates are proteoglycans which, through bearing and binding proteins and together with the supporting macromolecule of hyaluronic acid, constitute the proteoglycan (or glycosaminoglycan) aggregate. As the saccharide part contains spatial polyanion fields, the presence of a large number of sulphate, carboxyl and hydroxyl groups results in the creation of *extensive fields of ionic bonds with water molecules*.

The proteoglycan aggregate, together with *bonded water*, creates an amorphous extracellular material (matrix) of cartilage, which is bonded onto the reinforcing component - collagen 2<sup>nd</sup> type. Glycosaminoglycans are connected onto the supporting fibres of collagen type II by means of electrostatic bonds. In articular cartilage, nature took special efforts in safeguarding the biomechanical protection of chondrocytes in the peripheral zone. In the biomechanical perspective, chondrocytes are protected by glycocalix (i.e. a spherical saccharide envelope with firmly bonded water). Glycocalix is composed of a saccharide envelope bonded onto chondrocytes via transmembrane proteoglycans, transmembrane glycoproteins and adsorbed glycoproteins. *The glycocalix envelopes create gradually the incompressible continuous layer during the loading in peripheral zone of AC (Fig. 12.)*.

Our research has been focussed on analyses of viscoelastic strains of the upper peripheral cartilage zone, on the residual strains arising at cyclic loading, on the analyses of strain rate and on the creation of a peripheral incompressible cartilage cushion.

The peripheral cartilage zone consists of chondrocytes packaged in proteoglycans (GAGs) with firmly bonded molecules of water. In the intercellular space, there is unbound synovial fluid which contains water, hyaluronic acid, lubricin, proteinases and collagenases. Synovial fluid exhibits non-Newtonian flow characteristics. As was pointed out above, under a load the synovial fluid is relocated on the surfaces of AC.

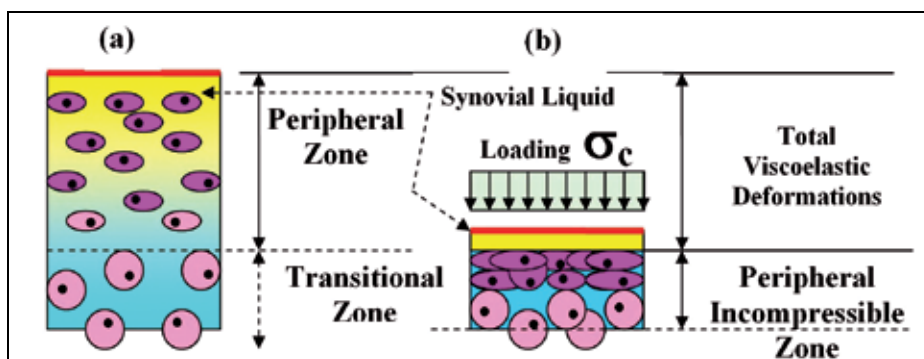


Fig. 12. Peripheral zone of articular cartilage without (a)/ with (b) loads. The peripheral incompressible zone is integrated with the incompressible zone in the middle (transitional) zone and low (radial) zone

During loading, the chondrocytes with GAGs encapsulation (in the peripheral zone) create a continuous incompressible mezzo layer with protected chondrocytes. Simultaneously, an incompressible peripheral zone arises in the middle of the transitional zone and in the low (radial) zone of AC. There are dominantly hyperelastic properties in the transitional and the low radial zone (Fig. 11.). Stress states can be simulated by the modified Cauchy stress tensor for incompressible hyperelastic material.

Viscous properties in the peripheral zone of articular cartilage result from the interaction between the molecules of the extracellular matrix and the molecules of free (unbound) synovial fluid. The transport of SF molecules through the extracellular space and the lack of bonding of these molecules onto glycosaminoglycans create the basic condition for the viscous behaviors of cartilage. High dynamic forces are dominantly undertaken by the AC matrix with firmly bonded water in its low and middle zone with a simultaneous creation of an incompressible tissue, a cushion (Fig. 1.).

The articular cartilage matrix with viscoelastic properties functions dominantly as a *protective pump* and a regulator of the amount of SF permanently maintained (during cyclic loading) between articular plateaus. The importance of the *protective pump* is evident from the function of retention of AC strains during cyclic loading. Due to slow down viscoelastic strain, part of accumulated (i.e. previously discharged) SF from the preceding loading cycle is *retained in articular cartilage* (Fig. 13.).

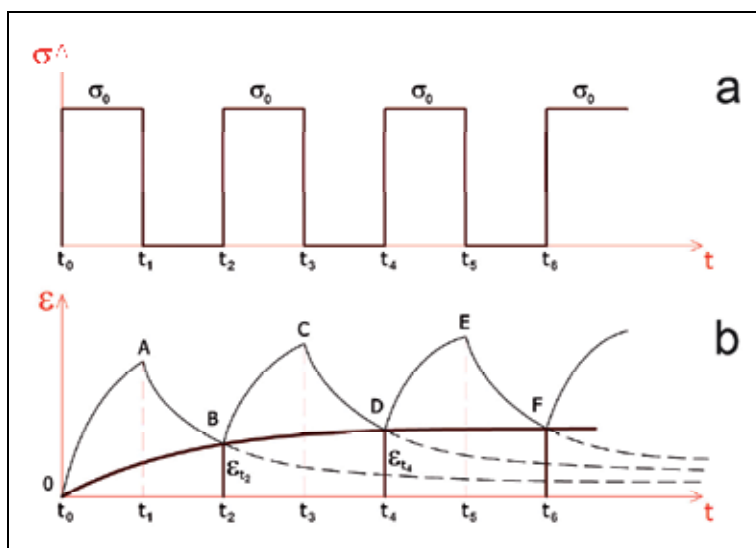


Fig. 13. Application of Kelvin Voigt viscoelastic model for the expression of step by step increments of strains  $\varepsilon_{ti}$  in the peripheral zone of AC during cyclic loading (e.g. while walking or running)

Fig. 13. in its upper part (a) shows the loading cycles e.g. during walking, while in the lower part (b) strains during the strain time growth and during strain relaxation are visible. The strain time growth occurs during the first loading (see the first concave curve OA of the strain growth). At the time  $t_1$  after unloading strain relaxation occurs (see the convex shape of the second curve AB). At the time  $t_2$  the successive (second) loading cycle starts. The strain time growth during the successive loading cycle, however, does not start at a zero



value (as was the case during the initial, first loading cycle), but at point B, or at the value of the residual strain  $\epsilon_{t2}$ . *The first residual strain provides the initial presupplementation of articular plateaus with synovial fluid.* Fig. 13. manifests that the envelope curve OBDF slightly grows during cyclic loading to stabilize after a certain time at a steady value characterizing long-term strain (during the time of cyclic loading) and long-term presupplementation of articular space with synovial fluid. After cyclic loading stops (i.e. after AC unloading) during the last loading cycle, as seen in Fig. 1., the strain relaxation follows the convex curve, and strains asymptotically approach to the time axis  $t$  (or zero). After the termination of the last loading cycle, SF (in the form of synovial sol) is sucked back into the peripheral layer of AC. The mechanism of viscous strain time growth and viscous strain relaxation creates a highly efficient *protective pump* functioning not only to discharge and suck back synovial fluid, but also to pump (accumulate) it into the articular space. Stresses in the peripheral zone may be expressed for the Kelvin Voigt model by the constitutive equation:

$$\sigma(t) = \eta \frac{d\epsilon(t)}{dt} + E\epsilon(t) \tag{1}$$

where  $\eta$  is the coefficient of viscosity,  $E$  is the modulus of elasticity,  $\epsilon(t)$  is the strain of AC and  $\frac{d\epsilon(t)}{dt}$  is the strain rate of cartilage tissue in the peripheral zone.

Equation (1) is a first order linear differential equation for an unknown function  $\epsilon(t)$ . The solution to the non-homogeneous equation (1) under the given initial conditions determines the time related strain of articular cartilage. In our case, it is in the form:

$$\epsilon(t) = e^{-\frac{1}{\eta}Et} \left[ \frac{1}{\eta} \int_{t_0}^t \sigma(\tau) e^{\frac{1}{\eta}E\tau} d\tau \right] \tag{2}$$

Let us further consider the case where articular cartilage is loaded by a constant load  $\sigma(\tau) = \sigma_c = const$  (Fig. 13.):

$$\epsilon(t) = \frac{\sigma_c}{E} \left[ 1 - e^{-\frac{1}{\eta}E(t-t_0)} \right] \tag{3}$$

Equation (3) implies that the strain of AC is a function of time depending on the magnitude of the constant stress  $\sigma_c$  also (for example by shifting an individual’s weight onto one foot). The presence of residual strain (marked by a thick line in Fig. 13.) ensures the accumulation of synovial fluid between articular plateaus. It means that during each step (during cyclic loading) articular plateaus are presupplemented with the lubrication medium – synovial fluid. The magnitudes of residual strains of AC play a key role in the presupplementation of AC surface plateaus with synovial fluid. The magnitudes of residual strains may be determined from the functions expressing strain during the strain time growth and from the functions expressing strain during the strain relaxation of AC, this may be performed separately for each loading cycle of cartilage (Fig. 13.).

For the 1<sup>st</sup> phase of the first loading cycle, for  $t \in < t_0; t_1 >$ , (Fig. 13.) the concave curve is defined by function (3) for the articular cartilage strain.

Discrete strain at the time  $t_0$  is  $\varepsilon_{t_0} = 0$ , at the time  $t_1$  discrete strain is:

$$\varepsilon_{t_1} = \frac{\sigma_c}{E} \left[ 1 - e^{\frac{-1}{\eta} E(t_1 - t_0)} \right] \quad (4)$$

For the 2<sup>nd</sup> phase of the first loading cycle (for  $t \in \langle t_1; t_2 \rangle$ ) (Fig. 13.), the convex curve AB is defined by the function for articular cartilage strain:

$$\varepsilon(t) = \varepsilon_{t_1} e^{\frac{-1}{\eta} E(t - t_1)} \quad (5)$$

Discrete strain at the time  $t_0$  is  $\varepsilon_{t_0} = 0$ , at the time  $t_1$  discrete strain is:

$$\varepsilon_{t_2} = \varepsilon_{t_1} e^{\frac{-1}{\eta} E(t_2 - t_1)} \quad (6)$$

The magnitudes of strains during cyclic loading at the starting points of loading and unloading of articular cartilage may be expressed by recurrent relations. For the time  $t_i$  with an odd index, the strain at the respective nodal points is:

$$\varepsilon_{t_{(2k+1)}} = \frac{\sigma_c}{E} \left[ 1 - e^{\frac{-E}{\eta(k+1)l}} \right]_{k=0,1,2,\dots} \quad (7)$$

where  $l$  is the length of the time interval  $\langle t_i; t_{i+1} \rangle$ . For the time  $t_i$  with an even index, the strain is:

$$\varepsilon_{t_{2k}} = \frac{\sigma_c}{E} \left[ e^{\frac{-E_i}{\eta}} - e^{\frac{-E}{\eta(k+1)l}} \right]_{k=0,1,2,\dots} \quad (8)$$

where  $l$  is the length of the time interval  $\langle t_i; t_{i+1} \rangle$ ,  $i = 0, 1, 2, \dots$ . During long-term cyclic loading and unloading, for  $k \rightarrow \infty$  the strain  $\varepsilon_{t(2k+1)}$  asymptotically approaches the steady state  $\sigma_c/E$ ; for  $k \rightarrow \infty$  the strain  $\varepsilon_{t_{2k}}$  asymptotically approaches the steady state  $\frac{\sigma_c}{E} e^{\frac{-E_i}{\eta}}$ . It is evident that for  $k \rightarrow \infty$  it holds true that:

$$\varepsilon_{t_{(2k+1)}} = \frac{\sigma_c}{E} > \varepsilon_{t_{2k}} = \frac{\sigma_c}{E} e^{\frac{-E_i}{\eta}} \quad (9)$$

### 2.2.1 The strain rate of articular cartilage in peripheral zone during the strain time growth

Strain  $\varepsilon(t)$  of AC during the strain time growth in the interval of  $t \in \langle t_0; t_1 \rangle$  is given by equation (3). Because  $\frac{d\varepsilon(t)}{dt} = \dot{\varepsilon}(t) > 0$  (in the indicated interval) the function  $\varepsilon(t)$  is increasing. The strain rate of AC during the strain-time growth in interval of  $t \in \langle t_0; t_1 \rangle$  is given by equation (10):

$$\frac{d\varepsilon(t)}{dt} = \frac{\sigma_c}{\eta} e^{\frac{-1}{\eta}E(t-t_0)} \tag{10}$$

From equation (10) is evident, that the strain rate of articular cartilage in interval of  $t \in \langle t_0; t_1 \rangle$  decelerates. The strain rate shortly after the load is the highest.

**2.2.2 The strain rate of articular cartilage in peripheral zone during the strain relaxation**

The strain of peripheral zone in time  $t_1$  during unloading is given by equation (11):

$$\varepsilon(t) = \varepsilon_{t_1} e^{\frac{-1}{\eta}E(t-t_1)} \tag{11}$$

The strain rate  $\frac{d\varepsilon(t)}{dt} = \dot{\varepsilon}(t) < 0$ . It means that the strain function  $\varepsilon(t)$  in interval of  $t \in \langle t_1; t_2 \rangle$  is decreasing. The strain rate in the same interval of  $\langle t_1; t_2 \rangle$  is decreasing also. Strain rate during the strain relaxation in interval of  $\langle t_1; t_2 \rangle$  is given by equation (12):

$$\frac{d\varepsilon(t)}{dt} = \varepsilon_{t_1} e^{\frac{-1}{\eta}E(t-t_1)} \left[ -\frac{E}{\eta} \right] \tag{12}$$

The strain rate of articular cartilage shortly after the unloading (during the strain relaxation) is distinctly higher than to the end of interval of  $\langle t_1; t_2 \rangle$ . Strain rate  $\left| \frac{d\varepsilon(t)}{dt} \right|$  with increasing time in interval of  $t \in \langle t_1; t_2 \rangle$  is decreasing.

**3. Conclusions**

The above described analyses lead to the formulation of the following key conclusions: Synovial fluid is a viscous pseudoplastic non-Newtonian fluid. Apparent viscosity of SF decreases with increasing rate of flow velocity gradient. SF does not display a decrease in viscosity *over time at a constant flow velocity gradient* (as it is typical for thixotropic material). The rheological properties of synovial fluid essentially affect the biomechanical behaviour of SF between the opposite AC surfaces and in the peripheral AC zone also. During the shifts of the femoral and tibial part of AC in opposite directions the velocities of SF flows decrease in the direction towards the neutral central zone of the gap between the AC surfaces. **Non-linear abatement in viscosity** in the direction from the *neutral ("quiescent") layer* of SF towards the opposite AC surfaces contributes to the lubrication quality and very efficiently protect the uneven micro-surfaces of AC.

The viscoelastic properties of the peripheral zone of AC and its molecular structure ensure the regulation of the transport and accumulation of SF between articular plateaus. The hydrodynamic lubrication biomechanism adapts with high sensitivity to biomechanical stresses. The viscoelastic properties of AC in the peripheral zone ensure that during cyclic loading some amount of SF is always retained accumulated between articular plateaus, which were presupplemented with it in the previous loading cycle. During long-term harmonic cyclic loading and unloading, the strains stabilize at limit values.

The limit strain value of AC during loading is always greater than its limit strain value after unloading. Shortly after loading, the strain rate is always greater than before unloading. In

this way, the hydrodynamic biomechanism quickly presupplements the surface localities with lubrication material. Shortly after unloading, the strain rate is high. During strain relaxation, it slows down. This is the way how the articular cartilage tissue attempts to retain the lubrication material between the articular plateaus of synovial joints as long as possible during cyclic loading.

Analogically to the low and the middle zone of AC where an incompressible zone arises under high loads whose dominant function is to bear high loads and protect chondrocytes with the intercellular matrix from destruction, in the peripheral zone as well a partial incompressible zone arises whose function is to bear high loads and protect the peripheral tissue from mechanical failure. The appearance of the incompressible tissue in all zones is synchronized aiming at the creation of a single (integrated) *incompressible cushion*. The existence of an incompressible zone secures the protection of chondrocytes and extracellular material from potential destruction.

### 3.1 Significance of results for clinical practice

Metabolic processes during the HA synthesis are very dynamic. The chondrocytes in AC actively synthesize and catabolise HA so that its optimal “usability” is achieved (in a relatively short time). The HA synthesis is usually in equilibrium with catabolic processes. These processes result in the achievement of the optimum HA concentration. The studies of metabolic processes (Schurz et al., 1987) implied that the half-life of the functional existence of HA molecules are mere 2-3 weeks. The solved project makes it evident that the “short lifecycle” of HA is dominantly caused by dynamic (biomechanical) effects. During leg movements, long snakelike NaHA/HA macromolecules are exposed to fast changes in shape accompanied by permanently arising and vanishing physical (non-covalent) bonds. To avoid the shortage of HA/NaHA, old polymer chains are replaced with new chains. The disturbance of HA new formation processes may lead to initiations of pathological processes. Mechanical effects during movements continuously initiate new groupings of HA macromolecules and newly arising (and vanishing) bonds among them. Frequent variations of kinetic energy transfers into HA molecular structures contribute to HA fragmentations in the biophysical perspective. These fragmentations may also be biochemically accelerated by hyaluronisades (Saari et al., 1993). HA fragments may initiate the formation of macrophages and extensive inflammations of AC.

The above examples of the interrelated nature of the causes of some AC defects show the key role of the rheological properties of non-Newtonian synovial fluid.

## 4. Acknowledgment

The contents presented in this chapter was supported by the Research Grant from MSMT No.6840770012.

## 5. References

- Akizuki, S.; Mow, V.C.; Muller, F.; Pita, J.C; Howell, D.S. & Manicourt, D.H. (1986). Tensile properties of human knee joint cartilage: I. Influence of ionic conditions, weight bearing, and fibrillation on the tensile modulus, *J. of orthopaedic research*, Vol. 4, No. 4, pp. 379-392

- Anadere, I.; Chmiel, H. & Laschner, W. (1979). Viscoelasticity of "normal" and pathological synovial fluid. *Biorheology*, Vol. 16, No. 3, pp. 179-184
- Armstrong, C.G.; Lai, W.M. & Mow, V.C. (1984). An analysis of the unconfined compression of articular cartilage. *J. Biomech. Eng.*, Vol. 106, No. 2, (May 1984), pp. 165-173, ISSN 0148-0731
- Ateshian, G.A.; Chahine, N.O.; Basalo, I.M. & Hung, C.T. (2004). The correspondence between equilibrium biphasic and triphasic material properties in mixture models of articular cartilage. *J. of Biomechanics*, Vol. 37, No. 3, (March 2004), pp. 391-400, ISSN 0021-9290
- Benninghoff, A. (1925). Form und Bau der Gelenkknorpel in ihren Beziehungen zur Funktion, *Zeitschrift für Zellforschung und Mikroskopische Anatomie*, Vol. 2, No. 5, pp. 783-862
- Bjelle, A. (1975). Content and Composition of Glycosaminoglycans in Human Knee Joint Cartilage: Variation with Site and Age in Adults. *Connective tissue research*, Vol. 3, No. 2-3, (January 1975), pp. 141-147, ISSN 0300-8207
- Bloch, B. & Dintenfass, L. (1963). Rheological study of human synovial fluid. *Australian and New Zealand Journal of Surgery*, Vol. 33, No. 2, (November 1963), pp. 108-113
- Cohen, B.; Gardner, T.R. & Ateshian, G.A. (1993). The influence of transverse isotropy on cartilage indentation behavior - A study of the human humeral head. In: *Transactions Orthopaedic Research Society*, Orthopaedic Research Society, pp. 185, Chicago, IL
- Cohen, B.; Lai, W.M.; Chorney, G.S.; Dick, H.M.; Mow, V.C. (1992). Unconfined compression of transversely-isotropic biphasic tissue, In: *Advances in Bioengineering*, American Society of Mechanical Engineers, pp. 187-190, ISBN 0791811166
- Davies, D.V. & Palfey, A.J. (1968). Some of the physical properties of normal and pathological synovial fluids. *J. of Biomechanics*, Vol. 1, No. 2, (July 1968), pp. 79-88, ISSN 0021-9290
- Ferguson, J.; Boyle, J.A.; McSween, R.N.; Jasani, M.K. (1968). Observations on the flow properties of the synovial fluid from patients with rheumatoid arthritis. *Biorheology*, Vol. 5, No. 2, (July 1968), pp. 119-131
- Garcia, J.J.; Cortes, D.H. (2006). A nonlinear biphasic viscohyperelastic model for articular cartilage, *J. of Biomechanics*, Vol. 39, No. 16, pp. 2991-2998, ISSN 0021-9290
- Johnson, J.P. (1955). The viscosity of normal and pathological human synovial fluids. *J. Biochem*, Vol. 59, No. 3, (April 1955), pp. 633-637
- Jurveli, J.; Kiviranta, I.; Saamanen, A.M.; Tammi, M. & Helminen, H.J. (1990). Indentation stiffness of young canine knee articular cartilage—Influence of strenuous joint loading. *J. of Biomechanics*, Vol. 23, No. 12, pp. 1239-1246, ISSN 0021-9290
- Lai, W.M.; Hou, J.S. & Mow, V.C. (1991). A Triphasic Theory for the Swelling and Deformation Behaviors of Articular Cartilage. *J. Biomech. Eng.*, Vol. 113, No. 3, (August 1991), pp. 245-351, ISSN 0148-0731
- Lapcik, L. Jr.; Lapcik, L.; De Smedt, S.; Demeester, J. & Chabreck, P. (1998). Hyaluronan: Preparation, Structure, Properties, and Applications. *Chemical reviews*, Vol. 98, No. 8, (December 1998), pp. 2663-2684, ISSN 0009-2665
- Li, L.P.; Soulhat, J.; Buschmann, M.D.; Shirazi-Adl, A. (1999). Nonlinear analysis of cartilage in unconfined ramp compression using a fibril reinforced poroelastic model. *Clinical Biomechanics*, Vol. 14, No. 9, (November 1999), pp. 673-682, ISSN 0268-0033
- Mori, S.; Naito, M. & Moriyama, S. (2002). Highly viscous sodium hyaluronate and joint lubrication. *International Orthopaedics*, Vol. 26, No. 2, (April 2002), pp. 116-121, ISSN 0341-2695
- Myers, R.R.; Negami, S. & White, R.K. (1966). Dynamic mechanical properties of synovial fluid. *Biorheology*, Vol. 3, pp. 197-209

- Nuki, G. & Ferguson, J. (1971). Studies on the nature and significance of macromolecular complexes in the rheology of synovial fluid from normal and diseased human joints. *Rheologica acta*, Vol. 10, No. 1, pp. 8-14
- Oates, K.M.N.; Krause, W.E.; Jones, R.L. & Colby, R.H. (2006). Rheopexy of synovial fluid and protein aggregation. *J. R. Soc. Interface*, Vol. 3, No. 6, (February 2006), pp. 167-174, ISSN 1742-5689
- Petrtyl, M.; Bastl, Z.; Krulis, Z.; Hulejova, H.; Polanska, M.; Lisal, J.; Danesova, J. & Cerny, P. (2010). Cycloolefin-Copolymer/Polyethylene (COC/PE) Blend Assists with the Creation of New Articular Cartilage. *Macromolecular Symposia Special Issue: Layered Nanostructures – Polymers with Improved Properties*, Vol. 294, No. 1, (August 2010), pp. 120-132
- Petrtyl, M.; Lisal, J. & Danesova, J. (2008). The states of compressibility and incompressibility of articular cartilage during the physiological loading (in czech), *Locomotor Systems, Advances in Research, Diagnostics and Therapy*, Vol. 15, No. 3-4, (October 2008), pp. 173-183, ISSN 1212-4575
- Radin, E.L.; Paul, I.L.; Swann, D.A. & Schottstaedt, E.S. (1971). Lubrication of synovial membrane. *Ann. Rheum. Dis.*, Vol. 30, No. 3, (May 1963), pp. 322-352, ISSN 0003-4967
- Rinaudo, M.; Rozand, Y.; Mathieu, P. & Conrozier, T. (2009). Role of different pre-treatments on composition and rheology of synovial fluids. *Polymers*, Vol. 1, No. 1, pp. 16-34, ISSN 2073-4360
- Saari, H.; Konttinen, Y.T.; Friman, C. & Sorsa, T. (1993). Differential effects of reactive oxygen species on native synovial fluid and purified human umbilical cord hyaluronate. *Inflammation*, Vol. 17, No. 4, (August 1993), pp.403-415, ISSN 0360-3997
- Safari, M.; Bjelle, A.; Gudmundsson, M.; Högfors, C. & Granhed, H. (1990). Clinical assessment of rheumatic diseases using viscoelastic parameters for synovial fluid. *Biorheology*, Vol. 27, No. 5, pp. 659-674
- Schurz, J. & Ribitsch, V. (1987). Rheology of synovial fluid. *Biorheology*, Vol. 24, No. 4, pp. 385-399
- Scott, J.E. & Heatly, F. (1999). Hyaluronan forms specific stable tertiary structures in aqueous solution: a <sup>13</sup>C NMR study., *Proc. Natl. Acad. Sci. USA*, Vol. 96, No. 9, (April 1999), pp. 4850-4855, ISSN 0027-8424
- Sundblad, L. (1953). Studies on hyaluronic acid in synovial fluids. *Acta Soc. Med. Ups.*, Vol. 58, No. 3-4, (April 1953), pp. 113-238
- Swann, D.A.; Silver, F.H.; Slyater, H.S., Stafford, W. & Shore, E. (1985). The molecular structure and lubricating activity of lubricin isolated from bovine and human synovial fluids. *The Biochemical Journal*, Vol. 225, No. 1, (January 1985), pp. 195-201
- White, R.K. (1963). The rheology of synovial fluid. *The journal of bone and joint surgery*, Vol. 45, No. 5, (July 1963), pp. 1084-1090, ISSN 1535-1386
- Wilson, W.; van Donkelaar, C.C.; van Rietbergen, B.; Ito, K. & Huijkes, R. (2005). Erratum to “Stresses in the local collagen network of articular cartilage: a poroviscoelastic fibril-reinforced finite element study” [Journal of Biomechanics 37 (2004) 357-366] and “A fibril-reinforced poroviscoelastic swelling model for articular cartilage” [Journal of Biomechanics 38 (2005) 1195-1204]. *J. of Biomechanics*, Vol. 38, No. 10, (October 2005), pp. 2138-2140, ISSN 0021-9290
- Wilson, W.; van Donkelaar, C.C.; van Rietbergen, B.; Ito, K. & Huijkes, R. (2004). Stresses in the local collagen network of articular cartilage: a poroviscoelastic fibril-reinforced finite element study. *J. of Biomechanics*, Vol. 37, No. 3, (March 2004), pp. 357-366, ISSN 0021-9290
- Yanaki, T. & Yamaguchi, T. (1990). Temporary network formation of hyaluronate under a physiological condition. 1. Molecular-weight dependence. *Biopolymers*, Vol. 30, No. 3-4, pp. 415-425, ISSN 0006-3525

# Charge Transport and Electrical Switching in Composite Biopolymers

Gabriel Katana<sup>1</sup> and Wycliffe Kipnusu<sup>2</sup>

<sup>1</sup>*Physics Department, Pwani University College, P.O. Box 195 Kilifi,*

<sup>2</sup>*Institute of Experimental Physics I, University of Leipzig, 04103 Leipzig,*

<sup>1</sup>*Kenya*

<sup>2</sup>*Germany*

## 1. Introduction

Polymers are long chain macromolecules made up of many repeating units called monomers. They are found in nature and can also be made synthetically. Natural/bio polymers are considered to be environmental benign materials as opposed to synthetic polymers. Research geared toward producing innocuous products from biopolymers has intensified. Improved understanding of properties of biopolymers allows for the design of new eco-friendly materials that have enhanced physical properties and that make more efficient use of resources. Biopolymers also have the advantage of being biodegradable and biocompatible. They are therefore of interest for application in advanced biomedical materials, for instance tissue engineering, artificial bones or gene therapy (Eduardo et al., 2005). Other possible fields of applications are related to electrical properties, making this class of materials attractive for potential uses in electronic switches, gates, storage devices, biosensors and biological transistors (Finkenstadt & Willett 2004). Plant biopolymers constitute the largest pool of living organic matter most of which can be attributed to four distinct classes of organic compounds; lignin, cellulose, hemicellulose and cuticles. Cuticles are mainly made up of polymethylenic biopolymers which include cutin and suberin. Cutin-containing layers are found on the surfaces of all primary parts of aerial plants, such as stems, petioles, leaves, flower parts, fruits and some seed coats. In addition, cutin may be found on some internal parts of plants such as the juice-sacs of citrus fruits (Heredia, 2003). Composition, structure and biophysical data of plant cuticles have recently been reviewed (Jeffrey, 2003; Pollard et al. 2008; and Domínguez et al., 2011) and will only be mentioned briefly. The main constituents of cutin are esterified fatty acids hydroxylated and epoxy hydroxylated with chain lengths mostly of 16 and 18 carbon atoms. It also contains some fraction of phenolic and flavanoid compounds.

## 2. Charge transfer mechanism in biopolymers

Several biopolymers have well documented properties as organic semiconductors (Eley et al., 1977; Leszek et al., 2002; Radha & Rosen, 2003; Mallick & Sakar, 2000; Lewis & Bowen, 2007; Ashutosh & Singh 2008). DNA-based biopolymer material possesses unique optical and electromagnetic properties, including low and tunable electrical resistivity, ultralow

optical and microwave low loss, organic field effect transistors, organic light emitting diodes (LED) ( Hagen et al., 2006). Nonlinear optical polymer electro-optic modulators fabricated from biopolymers have demonstrated better performance compared to those made from other materials (Piel et al., 2006). Naturally occurring Guar gum biopolymer chemically modified with polyaniline exhibits electrical conductivity in the range of  $1.6 \times 10^{-2}$  S/cm at room temperature (Ashutosh & Singh 2008). Mallick & Sakar (2000) investigated electrical conductivity of gum arabica found in different species of Acacia babul [*Acacia Arabica*] (Boutelje, 1980) and found that its electrical properties are similar to that of synthetic conducting polymer doped with inorganic salt and are proton conducting in nature.

Charge transport in biomolecular materials takes place mainly through two processes: Super exchange transport and hopping transport. Super exchange is a chain mediated tunneling transport. In this process electrons or holes are indirectly transferred from a donor to acceptor group through an energetically well- isolated bridge, where the bridge orbitals are only utilized as coupling media. In the hopping mechanism, the electron temporarily resides on the bridge for a short time during its passing from one redox center to the other, but in the super-exchange, the conjugated bridge only serves as a medium to pass the electron between the donor and acceptor (Tao et al., 2005). Tunnelling is a process process that decays exponentially with the length of the molecule. A simple tunneling model assumes a finite potential barrier at the metal-insulator interface. It describes free electron flow for a short distance into the sample from the metal contact. At low voltages the charge transfer is described by Simmons relations (DiBenedetto et al., 2009) but at higher applied voltages the tunneling is determined by Fowler-Nordheim process. Superexchange process can either be coherent or non-coherent. Coherent tunneling process is whereby a charge carrier moves from a donor to acceptor fast enough such that there is no dephasing by nuclear motions of the bridge (Weiss et al., 2007). Consequently, charges do not exchange energy with the molecules. However this process does not take place at significantly long distances. Incoherent superexchange on the other hand is a multi-step process in which a localized charge carrier interacts with phonons generated by thermal motion of the molecules (Singh et al., 2010)

As opposed to superexchange, hopping transport in biopolymers is a weakly distance dependent incoherent process. Generally superexchange is a short range transfer of charges in a spatial scale of a few Å while hopping transport takes place over a longer distance greater than 1nm. The exact mechanism of tunneling and hopping is not fully understood but it is known to be influenced by several factors. First, type of charge carriers in biopolymers which can either be holes, electrons or even polarons influences charge transport. Hole transfer is initiated by photo-oxidation of the donor groups attached to the terminus of the molecule whereas electron transfer occurs by chemical reduction of the acceptor group. A direct reduction of the molecule in contact with the metal electrode occurs when the voltage is applied. The interplay between donor acceptor and coupling fluctuation in biological electron transfer has also been observed (Skourtis et al., 2010). Secondly, band structure and hopping sites also influence charge transport. Although there are no band structures in biomolecules, energy gaps exist due to different hybridized electronic states. These energy gaps provide hopping sites through which charges propagate. Finally, conformation and spatial changes for the conducting state may overlap and hence create hopping sites as described by variable range hopping (Shinwari et al., 2010). Variable range hopping mainly describes transport mechanism in solid-state materials, but has also been observed in biopolymers (Mei Li et al., 2010). Similar to superexchange, electron hopping in



biopolymers is a multi-step process. According to this mechanism, the overall distance between primary electron donor and final electron acceptor is split into a series of short electron transfer steps. The essential difference is the existence of bridge units (oxidized or reduced species) that function as relays system and the fact the hopping process has a weak distance dependence (Cordes & Giese, 2009). Both of the two processes can take place at the same time and have been observed by several experimental groups. Treadway et al. (2002) noted that DNA assemblies of different lengths, sequence, and conformation may allow tunneling, hopping, or some mixture of the two mechanisms to actually dominate.

From measurements that probed changes in oxidized guanine damage yield with response to base perturbations, Armitage et al. (2004) noted that charge transfer through base-base of DNA molecules takes place through hopping via the  $\pi$ - $\pi$  bond overlap. Tao et al. (2005) reported electron hopping and bridge-assisted superexchange charge transfer between donor and an acceptor groups in peptide systems. The charge and dipole of the peptide play an important role in the electron transfer (Amit et al., 2008). Galoppini & Fox (1996) demonstrated the effect of electric field generated by the helix dipole on electron transfer in Aib-rich  $\alpha$  helical peptides and found out that other than the effect from secondary structure ( $\alpha$  helix and  $\beta$  sheet), dipole and hydrogen bonding, the solvent also has a marked influence on the study of the electron transfer. Due to complexity of peptides, the importance of individual amino acids in controlling electron transfer is not yet understood in detail.

Similar studies in proteins have concluded that electron transfer can occur across hydrogen bonds and that the rate of such transfer is greatly increased when the electron motions are strongly coupled with those of the protons (Ronald et al., 1981). While studying energy transport in biopolymers, Radha & Rossen (2003) suggested, based on the experimental results, that a soliton in biopolymers is an energy packet (similar to the "conformon" which is the packet of conformational strain on mitochondria) associated with a conformational strain localized in region much shorter than the length of a molecule. It was also noted by the same group that as the soliton (localized curvature) moves on the polymer, it could trap an electron and drag it along. This mechanism may be important in understanding charge transport in biological molecules, where curvatures abound. Studies on charge transport in ethyl cellulose- chloranil systems have also been done, (Khare et al., 2000) where the space charge limited current (SCLC) was found to be the dominant mode of electrical conduction at high field in these systems.

Mechanisms leading to charge conduction in metal-polymer-metal configuration have been the subject of intensive study in the past two decades. Much of these studies have focused on doped and undoped synthetic polymers where the commonly discussed high-field electronic conduction mechanism for various films are Fowler-Nordheim tunneling, Poole-Frenkel (P-F), Richardson-Schottky (R-S) thermionic emissions, space charge limited conduction and variable range hopping. Based on the same sample geometry it is reasoned that the mechanism mentioned above could also contribute to detectable current flow in biopolymers sandwiched between metal electrodes. These mechanisms are discussed hereunder and in section 5, experimental results based on cutin biopolymer are presented and discussed in reference to the charge transport mechanism mentioned above.

## 2.1 Fowler-Nordheim tunneling

In Fowler-Nordheim tunneling the basic idea is that quantum mechanical tunneling from the adjacent conductor into the insulator limits the current through the structure. Once the carriers have tunneled into the insulator they are free to move within the material.

Determination of the current is based on the Wentzel, Kramers and Brillouin (WKB) approximation from which Eq. (1) is obtained.

$$J_{FN} = \chi_{FN} E^2 \exp \left[ -\frac{4 \sqrt{2m^*} (q\phi_B)^{3/2}}{3 q\hbar E} \right] \quad (1)$$

where  $J_{FN}$  is the current density according to Fowler -Nordheim,  $\chi_{FN}$  is the Fowler Nordheim constant,  $E$  is the electric field,  $m^*$  is the effective mass of the tunneling charge,  $\hbar$  is a reduced plancks constant,  $q$  is the electron charge and  $\phi_B$  is the potential barrier height at the conductor/insulator interface. To check for this current mechanism, experimental  $I$ - $V$  characteristics are typically plotted as  $\ln(J/E^2)$  vs  $1/E$ , a so-called Fowler-Nordheim plot. Provided the effective mass of the insulator is known, one can fit the experimental data to a straight line yielding a value for the barrier height.

## 2.2 Field emission process

Whereas Fowler-Nordheim tunneling implies that carriers are free to move through the insulator, it cannot be the case where defects or traps are present in an insulator. The traps restrict the current flow because of a capture and emission process. The two field emission charge transport process that occur when insulators are sandwiched between metal electrodes are Poole-Frenkel and Schottky emission process. Thermionic (schottky) emission assumes that an electron from the contact can be injected into the dielectric once it has acquired sufficient thermal energy to cross into the maximum potential (resulting from the superposition of the external and the image-charge potential). If the sample has structural defects, the defects act as trapping sites for the electrons. Thermally trapped charges will contribute to current density according to Poole-Frenkel emission. They are generally observed in both organic and inorganic semiconducting materials. Poole-Frenkel effect is due to thermal excitation of trapped charges via field assisted lowering of trap depth while Schottky effect is a field lowering of interfacial barrier at the blocking electrode. Expression for Poole-Frenkel and Schottky effects are given in Eq. (2) and (3) respectively.

$$J_{PF} = J_{PFO} \exp[(\beta_{PF} E^{1/2}) / kT] \quad (2)$$

$$J_S = J_{SO} \exp[(\beta_S E^{1/2}) / kT] \quad (3)$$

$J_{SO}$  and  $J_{PFO}$  are pre-exponential factors,  $\beta_S$  is the Schottky coefficient,  $\beta_{PF}$  is the Poole-Frenkel coefficient, and  $E$  is the electric field. The theoretical values of Schottky and Poole-Frenkel coefficient are related by Eq.(4):

$$\beta_S = \left( e^3 / 4\pi\epsilon\epsilon_0 \right) = \beta_{PF} / 2 \quad (4)$$

where  $q$  is electron charge,  $\epsilon$  is relative permittivity,  $\epsilon_0$  permitibility in free space

## 2.3 Space charge limited current

For structures where carriers can easily enter the insulator and freely move through the insulator, the resulting charge flow densities are much higher than predicted by Fowler-Nordheim tunneling and Poole-Frenkel mechanism. The high density of these charged

carriers causes a field gradient, which limits the current density and the mechanism is then referred to as space charge limited current. Starting from the basic Gauss's law in one-dimension, assuming that the insulator contains no free carriers if no current flows the expression for the space charge limited current can be obtained as shown in Eq. (5)

$$J = \frac{9\varepsilon\mu V^2}{8d^3} \quad (5)$$

where  $J$  is current density,  $\varepsilon$  is relative permittivity,  $\mu$  is charge mobility,  $V$  is applied voltage and  $d$  is electrode spacing. Space charge limited current results from the fact that when the injected carrier concentration exceeds the thermal carrier concentration, the electric field in the sample becomes very non-uniform, and the current no longer follows Ohm's law.

#### 2.4 Variable-range hopping mechanism

Charge conduction in semiconducting polymers is thought to take place by hopping of charge carriers in an energetically disordered landscape of hopping sites (Meisel et al., 2006). The variable-range hopping (VRH) conduction mechanism originally proposed by Mott for amorphous semiconductors (Mott & Davis, 1979) assuming a phonon-assisted hopping process has also been observed in conducting polymers and their composites at low temperature (Ghosh et al., 2001; Luthra et al., 2003; Singh et al., 2003). Bulk conductivity of conducting polymers depends upon several factors, such as the structure, number and nature of charge carriers, and their transport along and between the polymer chains and across the morphological barriers (Long et al., 2003). When the phonon energy is insufficient (low temperature), carriers will tend to hop larger distances in order to locate in sites which are energetically closer than their nearest neighbours. Eq. (6) gives the DC conductivity based on the VRH conduction model.

$$\sigma = \frac{\sigma_0}{\sqrt{T}} \exp\left[-\left(\frac{T_d}{T}\right)^{1/4}\right] \quad (6)$$

where the pre-exponential factor  $\sigma_0$  is given by Eq.(7)

$$\sigma_0 = \frac{q^2 v_{ph}}{2(8\pi k)^{1/2}} \left[ \frac{N_{(EF)}}{\gamma} \right]^{1/2} \quad (7)$$

and  $q$  is the electron charge,  $k$  is the Boltzmann's constant,  $v_{ph}$  is the typical phonon frequency obtained from the Debye temperature ( $\approx 10^{13}$  Hz),  $\gamma$  is the decay length of the localized wave function near the Fermi level and  $N_{(EF)}$  is the density of states at the Fermi level. The characteristic Mott temperature  $T_d$ , as shown in Eq.(8) corresponds to the hopping barrier for charge carriers (also known as the pseudo-activation energy) and measures the degree of disorder present in the system.

$$T_d = 18.11 \frac{\gamma^3}{kN_{(EF)}} \quad (8)$$

Two other Mott parameters, the variable range hopping distance ( $R_{VRH}$ ) and hopping activation energy ( $W$ ) are given by Eq. (9) and (10) respectively

$$R_{VRH} = \left[ \frac{9}{8\pi\gamma kTN_{(EF)}} \right]^{1/4} \quad (9)$$

$$W = \frac{3}{4\pi R^3 N_{(EF)}} \quad (10)$$

### 3. Electrical switching mechanism in biopolymers

Biomolecules often have sensitive bio-active sites that can change under external stimuli such as temperature, light, electrical signals, PH and chemical/biochemical reactions of their environs. Such switchable biomolecules are of tremendous usefulness in diverse areas including biological, medical and bio-electronic technology. Most research groups in this field are interested in investigating new class of switchable biological systems albeit the field is still at its infancy stage. Chu et al. (2010) reported electro-switchable oligopeptides as a function of surface potential. Oligolysine peptides exhibit protonated amino side chain at PH-7 providing the basis of switching "ON" and "OFF" of the biological activity on the surface upon application of negative potential. Switching initiated by PH changes has been observed in other biomolecules and biopolymers (Zimmermann et al., 2006). Biomolecular motors of actomyosin experience rapid and reversible on-off switching by thermal activation (Mihajlovi et al., 2004). The most optimistic approach of integrating photo switchable biomolecules into opto-electronic devices is provided by highly photo sensitive bacteriorhodopsin. This molecule has shown remarkable photo sensitive switching of its electrical properties that mimic conventional Gate transistors (Roy et al., 2010; Pandey, 2006; Qun et al., 2004). Bottom-up approach toward building optical nano-electronic devices is also feasible with the discoveries of switchable photoconductivity in even the smallest structures such as quantum dots of cross-linked ligands (Lilly et al., 2011).

Electrical switching in biomolecules has wider applications in electronic industry. However, a lucid understanding of microscopic switching mechanism in these biological systems is still an outstanding challenge. In most investigations probing electrical switching in organic molecules, an external electrical signal is applied to the sample sandwiched between metal electrodes. Many materials have been reported to show hysteretic impedance switching where a system in its high impedance state (OFF) is switched by a threshold voltage into a low impedance state (ON) and remains in the ON state even with the reversal of applied voltage. This phenomenon is also known as resistive switching. Switching mechanism depend on whether the contribution comes from thermal, electronic, or ionic effects (Waser et al., 2007). Resistive switching is generally dependent on number of mobile charges, their mobility and the average electric field. In the case where the current is highly localized within a small sample area, filamental conduction take place (Scott et al., 2007). This simply involves formation of metallic bridge connecting the two electrodes. Filamental conduction accounts for negative differential resistance (NDR) model which is the basis of many molecular switching processes (Ren et al., 2010). Although this model was originally applied to inorganic materials, it can also explain resistive switching in organic samples (Tseng et al., 2006). The model assumes a trap- controlled channel where tunnelling take place in between chains of metallic islands. Similarly a decrease in electron transport channels and weak coupling between electrodes and the contact molecule causes NDR switching behaviour. Electric field induced switching mechanism is common in literature (Waser et al., 2007). In

general terms, built up of space charges trapped within the sample due to presence of defects create a field which is large enough to cause flow of mobile charge carriers. This phenomenon is sometimes called coulomb blockade (Tang et al., 2005). At high electric fields, charges are injected by Fowler-Nordheim tunnelling and subsequently trapped. As a result, electrostatic barrier character of the structure is modified and so is its resistance.

The most insightful switching mechanism in biomolecules is the redox process and the formation of charge transfer complex through donor-acceptor coupling. Aviram et al. (1988) suggested that electron- proton motion within hemiquinones molecules that comprised of catechol and o-quinone, molecules between two contacts switch the molecules to low impedance (ON) state due to the formation of semiquinones free radicals. When an electron is injected into the molecules from the metal contact, it is gained by an electron acceptor molecule. An electron donor molecule then transfers the electron to the opposite contact thus allowing flow of charge.

The present chapter discusses structural characteristics (by use of Fourier Transform Infra-Red spectroscopy and Atomic Force Microscopy). Electrical conduction in cuticular membranes of Nandi flame (*Spathodea campanulata*, P. Beav) seeds hereafter referred just as cuticles. Fig. 1 shows the cuticle also presented still attached to the seed. The cuticles are thin (about 2  $\mu\text{m}$ ), translucent and very light. They are adapted to wind dispersion of the seeds.

## 4. Structural characterization

### 4.1 Fourier transform infra Red (FTIR) spectroscopy

Fig.2 shows the Fourier Transform Infra Red (FTIR) spectroscopy of the pristine cuticle. The samples were first annealed at 350K for 12 hrs before measurement. The wide band at 3348  $\text{cm}^{-1}$  which has been observed in many other cuticular membranes (Bykov, 2008) is assigned to O-H stretching vibration. It is caused by presence of alcoholic and phenolic hydroxyl groups involved in hydrogen bonds. Methylene is the most repeated structural unit in the cutin biopolyester (Jose, et al., 2004) and these shows up in the spectra band around 2300  $\text{cm}^{-1}$ . The band at 2916  $\text{cm}^{-1}$  is assigned to C-H asymmetric and symmetric stretching vibrations of methoxyl groups. Absorption around 1604  $\text{cm}^{-1}$  and 1427  $\text{cm}^{-1}$  are assigned to the stretching of C=C bonds and the stretching of benzenoid rings. Absorption bands in the range 1300-1150  $\text{cm}^{-1}$  are related to asymmetric vibration of C-O-C linkages in ester to esters or phenolic groups. Fig. 3 show the infra red (IR) spectra of cuticle compared with the spectra of other biopolymers.



Fig. 1. Thin and translucent cuticle attached to the Nandi flame seed

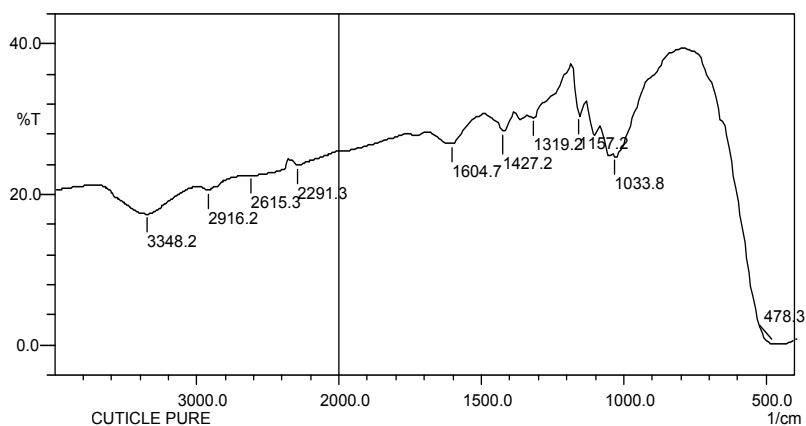


Fig. 2. FT-IR spectrum of pristine cuticle

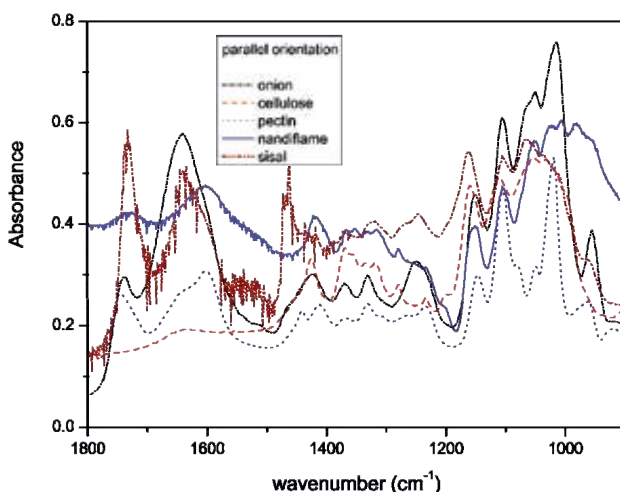


Fig. 3. Comparison of IR spectrum of Nandi flame cuticle with those of other biopolymers

#### 4.2 Atomic force microscopy (AFM)

The AFM scans (Fig. 4) shows that NFSC has a highly oriented surface topography. The AFM permits measurement of the distance variations in the surface of the sample by use of two pairs of cursors. The cursors can be made to scale the surface in nanometer (nm) or micrometer ( $\mu\text{m}$ ).

The interstitial region between the ridges represented in the dark area in Fig. 4 represents cavities in the membrane with a diameter of about 0.5nm. It is important to note that molecular basal spacing (cavities) in the range of 0.4-0.5nm has also been observed from molecular dynamic simulations of a cutin oligomer (Dominguez et al., 2011) and is attributed to the distance between the methylene groups of oligomeric chain. The presence of such cavities is a typical property of amorphous cross-linked polymers and may be important in explaining the interaction between cutin and endogenous low-molecular weight compounds such as phenolics and flavonoids.

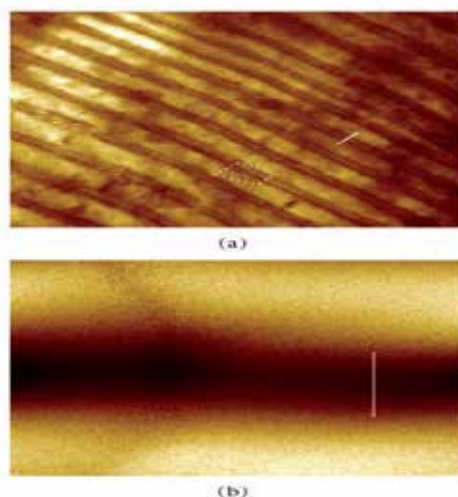


Fig. 4. AFM topographic scans showing surface structure of the cuticle; (a) is a map from the scan on a larger area of about  $3 \times 10^5$  square pixels (b) is a scan on a single pixel of about  $2.5 \times 10^6$  nm<sup>2</sup>. Dotted lines on (a) represents the region shown by (b). Scale bars  $\sim 0.5$ nm. Taken from (Kipnusu et al., 2009).

## 5. Electrical characterization and charge transport mechanism

This section discusses electrical characteristics of the cuticle samples. Current-voltage (I-V) data measured as a function of annealing temperature, irradiation and pooling temperature was used in analyzing the electrical characteristics. Samples were separately annealed and irradiated before electrode coating was done. When annealing, cuticles were placed inside a temperature-controlled furnace, which was fitted inside an electrical shielded cage of a Lindberg/Blue Tube Furnace of model TF55035C. Samples were annealed at various temperatures of 320K, 350K and 400K for a constant period of 12hrs each. Irradiation of the sample was done with He-Ne laser beam of wavelength 632.8nm in a dark room each for a different period of 10minutes, 30minutes, and 60minutes. Electrode coating on the film of pristine, pre-annealed and pre-irradiated samples was done by using quick drying and highly conducting Flash-Dry silver paint obtained from SPI Supplies (USA). A mask of a circular aperture of 0.56 cm diameter was used while coating to ensure uniformity in size of coated surface. Circular aluminum foil of the same diameter was placed on freshly coated surface such that the sample was sandwiched between two aluminum electrodes. These metal-sample-metal sandwiches were left to dry at room temperature for a period of 24hrs to ensure that there was good ohmic contacts between aluminum electrode and the sample. The same Flash-Dry Silver paint was used to connect thin wires onto the aluminum electrodes. When measuring I-V at different temperatures, a sample sandwiched between aluminium electrodes was placed inside the Lindberg/Blue Tube Furnace and temperature varied in steps of 5K between 350K and 500K at constant electric fields of 0.75V/cm, 1.50V/cm, 2.25V/cm, 3.00V/cm, and 3.75V/cm.

Fig. 5(a) shows the I-V characteristics of pristine and annealed samples. These indicate clearly that there was electrical switching and memory effect in the cuticle samples. At

certain threshold voltage,  $V_{th}$  current rises rapidly by an order of 2. There are two distinct regions for the increasing voltage. At low voltages the  $\log I$  versus  $\log V$  plots are approximately linear with a slope of 1; while at higher voltages, above a well-defined threshold voltage  $V_{th}$ , the plots are again approximately linear with a slope of  $2.04 \pm 0.07$ . These plots therefore show that at low voltages, OFF-state, current follows ohms law but after switching to ON-state at higher voltages, current follows a power law dependence given by  $I \propto V^n$  where  $n = 2.04 \pm 0.07$  obtained from linear regression fitting parameters where the standard deviation was shown as 0.03 and coefficient of correlation as 0.0001. This shows that the ON-state region is governed by Space charge limited current (SCLC) controlled by single trapping level, the injecting carrier concentration dominating the thermally generated carriers. During the switching process the current increases appreciably leading to a local increase in temperature (Collins et al., 1993). The current does not follow the same path on decreasing applied electric field hence indicating that the samples exhibit memory switching that is not erased by annealing. The threshold voltage  $V_{th}$  for pristine samples is  $5.0 \pm 0.5$  volts. The width of  $V_{th}$  or transition voltage during switching from OFF to ON states is about 1.0 V. Inset of Fig 5 (a) shows non-uniform increase of  $V_{th}$  with the increase in annealing temperature and tends to attain a plateau at higher annealing temperature. Decrease in magnitude of the negative dielectric anisotropy during annealing is a major reason for the increase in  $V_{th}$  for the annealed samples (Katana & Muysoki, 2007). Annealing polymeric films at different temperatures causes structural changes which affects electrical conductivity. Annealing temperature increases grain size in the polymer films causing many changes in the electrical and other properties (Leszek et al., 2002). Threshold voltage  $V_{th}$  for pristine cuticles is higher than  $V_{th}$  reported for some synthetic polymers; PMMA (1.6V), PS (4.5V), Phthalocyanine (0.3V), 2,6-(2,2-bicyanovinyl) pyride (5.01V), Langmuir-Blodgett (1.0V) (Katana & Muysoki, 2007; Otternbacher et al., 1991; Xue et al., 1996; Sakai et al., 1988).

Fig. 5(b) shows I-V curves for cuticle samples that were pre-irradiated with laser light of wavelength 632.8nm for different duration of time. Just as noted for the annealed samples, I-V curves for irradiated samples shows electrical switching and memory effect with  $V_{th}$  that increases with the increase in irradiation time (see inset Fig. 5b). Increasing time of irradiation increases electrical conductivity. The increase in conductivity for irradiated samples can be attributed to dissociation of primary valence bonds into radicals. Dissociation of C-C and C-H bonds leads to degradation and cross linking which improves electrical conductivity (Ashour et al., 2006). Exposure of polymers to ionizing radiation produces charge carriers in terms of electron and holes which may be trapped in the polymer matrix at low temperatures (Feinheils et al., 1971). If the original conductivity is small, then the presence of these carriers produces an observable increase in conductivity of the polymer. Irradiation of polymers results in excitations of its molecules and creation of free electrons and ions that migrate through the polymer network till they are trapped. The electronic and ionic configurations created, cause changes in the electric conductivity. In the study of effect of gamma irradiation on the bovine Achilles tendon (BAT) collagen, Leszek et al. (2002) reported changes in electrical conductivity that is dose dependent. Higher concentration of free radicals generated by irradiation of collagen created charge carriers that increased electrical conductivity.



Fig.5(c) shows I-V curves of the cuticles obtained at different poling/measurement. These curves show that electrical current increases as measurement temperature increase. This is due to thermal excitation of the trapped charges across the potential barrier. The curves also show that forward bias characteristics have two regions which are typical examples of ohmic conduction for voltages below  $V_{th}$  (OFF-state) and a space charge limited current (SCLC) for voltages above  $V_{th}$  (ON-state). Increase in temperature facilitates diffusion of ions in the space charge polarization. Thermal energy may also aid in overcoming the activation barrier for orientation of polar molecules in the direction of the field. Charge carrier generation and transport in mitochondrial lipoprotein system has been investigated by electrical conductivity and the results show that increase in temperature causes a transition in conductivity where steady state conduction is correlated with chain segmental reorientations of phospholipid moiety below the transition and with an interfacial polarization process above it (Eley et al., 1977).

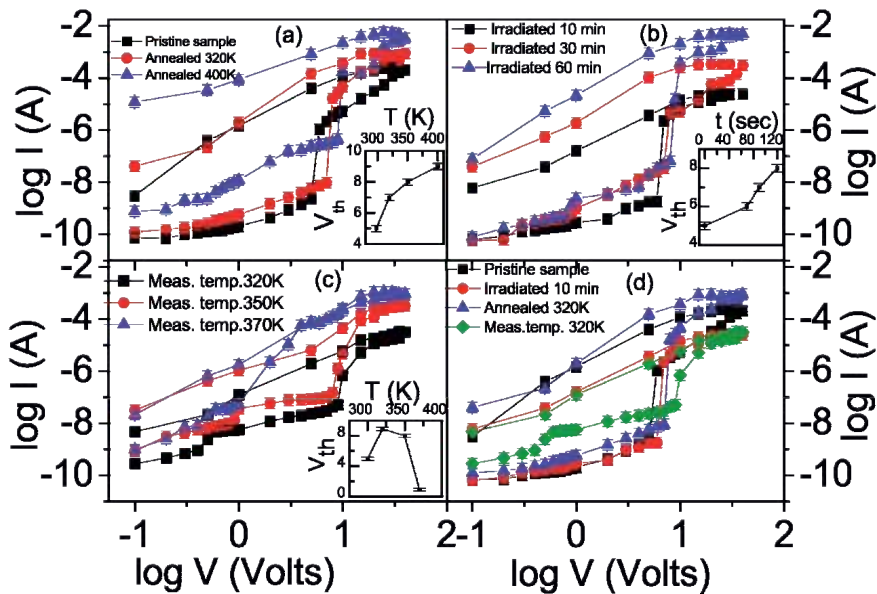


Fig. 5. I-V curves of the pristine cuticles and cuticles treated at different conditions. (a) pristine & samples pre-annealed at 320K and 400K for 12hrs each. (b) pristine & samples pre-irradiated with laser light of wavelength 632.8nm for the duration shown in the legends. (c) pristine samples measured at different temperatures. The insets in (a), (b) and (c) show variation of threshold voltage as a function of the annealing temperature, irradiation time, and measurement temperature respectively. (d) shows combined curves with the conditions shown in the legends.

$V_{th}$  rapidly decreases with the increase in measurement temperature and that switching and memory effect almost disappears at higher temperatures (370K). This is due to the fact that the  $V_{th}$  decreases and that the gap between current in the forward bias and reverse bias in the ON-state region almost closed up such that the forward bias current nearly follows the same path as the reverse bias current which indicates a loss of memory.

It is difficult to draw unambiguous conclusion from Fig.5 (d) because all the three imposed conditions affect conductivity in unique ways and also depends on duration of annealing, irradiation and the measurement temperature. However it is worthy mentioning that at measurement temperature of 320K conductivity is higher than conductivity of presitne samples at low electric field (OFF state). This observation is however reversed at higher electric fields where conductivity of pristine samples is higher.

Switching and memory behavior can be attributed to the fact that external electric field triggers embedded molecules with redox centers hence creating some traps. Switching mechanism in these systems is by quantum interference of different propagation parts within the molecules which involve permutation of Lowest Unoccupied Molecular Orbitals (LUMO<sub>+1</sub>) and Highest Occupied Molecular Orbitals (HOMO<sub>-1</sub>)-the frontier orbitals. To get electric field induced switching effect, the relative energies of HOMO (localized on the donor group) and LUMO (localized on the acceptor group) must be permuted (Aviram et al., 1988). This switching model supposes that both the permuting orbitals are initially doubly degenerate resulting to what is referred to as frontier orbitals. In the absence of electric field HOMO<sub>-1</sub> is localized on the acceptor group and LUMO<sub>+1</sub> on the donor group. When the external field is applied, electron orbitals are "pulled" towards the acceptor group reducing the HOMO-LUMO gap of frontier orbitals and the switching and hybridization between HOMO<sub>-1</sub> and LUMO<sub>+1</sub> takes place. While the strength of the field increases, the HOMO-LUMO gap in the molecular spectrum becomes smaller and the HOMO, HOMO<sub>-1</sub> and LUMO orbital split into the HOMO-LUMO gap and hence become delocalized. Electrical switching can also in part be explained by formation of quinoid and semiquinone structures from phenolic compounds accompanied by redox reactions. The quinoid form is planar, and is highly conjugated compared to phenyl groups. Changes in bond length and rotation of benzene ring during formation of quinoid structure results in activation barriers which are considered to be the origin of the temperature dependence conductance. Details of this explanation is found in Kipnusu et al. (2009b)

Fowler-Nordheim emission current is given in equation (1). To check for this current mechanism, experimental *I-V* data for annealed samples of NFSC were analyzed by plotting  $\ln(J/E^2)$  versus  $1/E$ . Four plots were made to represent different regime with different levels of measured current (Fig.6). Fowler-Nordheim tunneling mechanism is confirmed by straight lines with negative slopes given by;  $4(2m^*)^{1/2} / 3q\hbar(q\phi_B)^{3/2}$  where  $m^*$  is the effective mass of the tunneling charge,  $q$  is the electron charge,  $\hbar$  is a reduced planck constant, and  $\phi_B$  is the barrier height expressed in eV units. Fig.6 shows that Fowler-Nordheim curves for low and high fields forward bias and low field reverse bias were quite non-linear or had positive slopes therefore ruling out possibility of Fowler-Nordheim mechanism in these regimes. However in Fig.6 (d) the curves are relatively linear with negative slopes. This is the high fields' regime of the reverse bias where the current increased with decreasing voltage (see Fig.5). Making an assumption that  $m^*$  equals the electron rest mass (0.511MeV), and using the slope obtained from linear fits of Fig. 6 (d), the potential barrier height at the Al/cuticle junction is found to be 11.28 eV and 1.13 eV for pure samples and samples annealed at 400K respectively. Vestweber et al. (1994) noted that if the barrier height exceeds 0.3 eV tunnel process prevail with the consequence that high anodic fields are required in order to attain high current densities. It can therefore be concluded that Fowler-Nordheim quantum mechanical tunneling was responsible for the

surge of current with decreasing field since the model assumes that once the carriers have tunneled into the insulator they are free to move within the material.

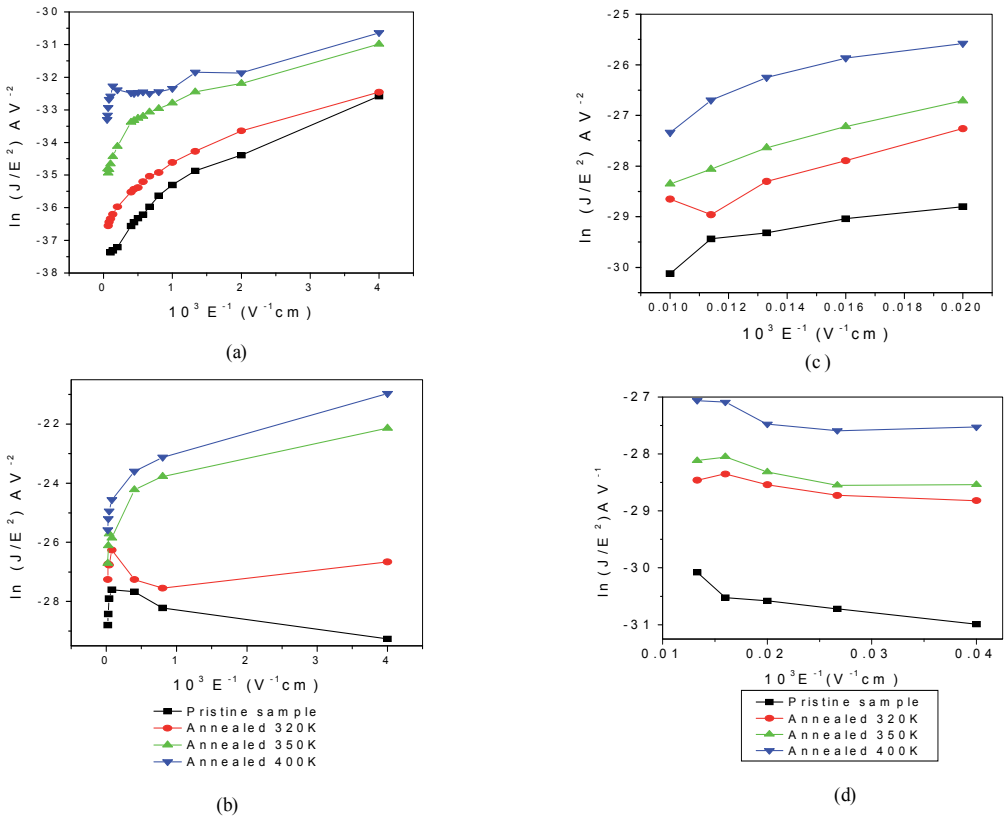


Fig. 6. Fowler-Nordheim curves: (a) Forward bias at low electric field (b) Reverse bias at low electric field (c) forward bias at high electric field and (d) reverse bias at high electric field.

Fig. 7. shows curves of current density versus square root of electric ( $\ln J$  versus  $E^{1/2}$ ) in the low field for forward bias regime. These curves neither support conduction mechanism by Poole-Frenkel nor Schottky emissions which predict linear graphs of  $\ln J$  versus  $E^{1/2}$  with positive slopes. Fig.8 shows linear fittings of  $\ln J$  versus  $E^{1/2}$  for forward and reverse bias at high fields ( $10^4$  - $10^5$  V/cm). The current levels in the reverse bias are higher than forward bias. This behaviour may be interpreted either in terms of Poole-Frenkel effect which is due to thermal excitation of trapped charges via field assisted lowering of trap depth or by Schottky effect which is a field lowering of interfacial barrier at the blocking electrode (Deshmukh et al. 2007). The expressions for these processes are given in Eq.(2) and (3) respectively. Schottky coefficient ( $\beta_S$ ) and Poole-Frenkel coefficient ( $\beta_{PF}$ ) are related as shown in Eq. (4). Using the value of static dielectric permittivity ( $\epsilon$ ) of 3.0, (determined from dielectric spectroscopy) theoretical values of  $\beta_S$  and  $\beta_{PF}$  obtained from Eq. (4) are  $3.51 \times 10^{-24}$  J V $^{1/2}$  m $^{1/2}$  and  $7.01 \times 10^{-24}$  J V $^{1/2}$  m $^{1/2}$  respectively. Experimental values of  $\beta$  obtained from the slopes of plots of  $\ln J$  versus  $E^{1/2}$  (Fig.8) at different temperatures are listed in Table 1. The standard deviation and coefficient of linear correlation were obtained as 0.34 and 0.005

respectively. The large discrepancy in experimental values of  $\beta$  listed in Table 1 and theoretical values of  $\beta_S$  and  $\beta_{PF}$  leads to a conclusion that current transport mechanism in our samples governing the high field at a temperature range of 320K-370K cannot be explained in terms of Shottky or Poole-Frenkel emission.

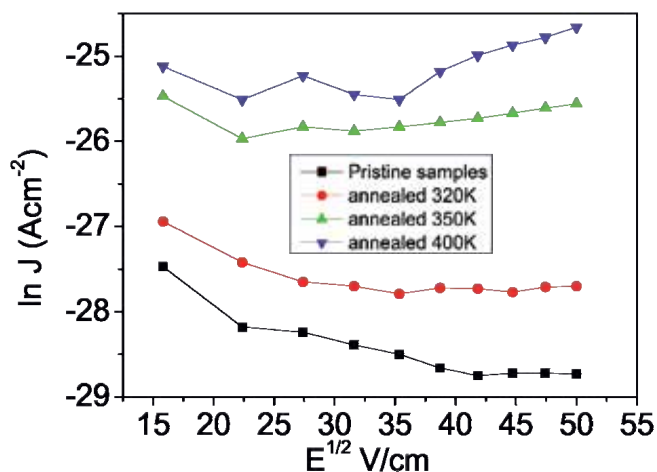


Fig. 7. Semi logarithmic plots of  $\ln J$  versus  $E^{1/2}$  for the low field of 225-2500 V/cm at a temperature range of 320K-400K

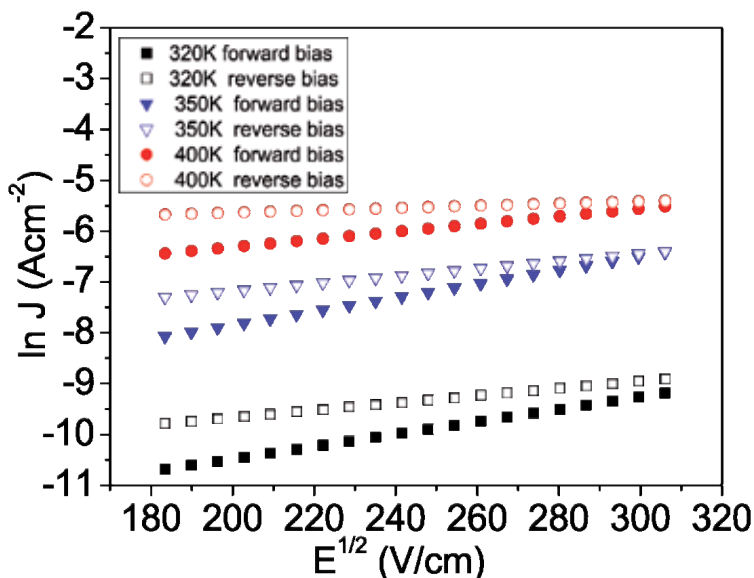


Fig. 8. Semi logarithmic plots of  $\ln J$  versus  $E^{1/2}$  for the high field of  $3.2 \times 10^4$ -  $9.8 \times 10^5$  V/cm in forward and reverse biases at temperature range of 320K-400K

To analyze the effect of temperature on conductivity of the samples, Arrhenius curves ( $\log \sigma$  vs  $10^3/T$ ) for different polarizing fields (0.75kV/cm, 1.50kV/cm, 2.25kV/cm, 3.00kV/cm, and 3.75kV/cm) were plotted (Fig. 9) using the Arrhenius Eq. (11);

$$\sigma = \sigma_0 \exp\left(\frac{-E_a}{kT}\right) \quad (11)$$

where  $\sigma$  is conductivity,  $\sigma_0$  the pre-exponential factor,  $E_a$  the activation energy,  $k$  is Boltzmann's constant, and  $T$  is temperature in Kelvin. Conductivity was obtained from the Eq. (12);

$$\sigma = \frac{I}{V} \frac{d}{A} \quad (12)$$

where  $I$  is measured current,  $V$  is measured Voltage,  $d$  is the thickness of the samples ( $\approx 4.0 \times 10^{-4}$  cm), and  $A$  is the electrode active area (circular electrode of diameter 0.56cm was used). Initial increase in conductivity at low temperature is due to the injection of charge carriers directly from the electrodes. The increase in conductivity at selectively low field is due to the increase in the magnitude of the mean free path of the photon (Sangawar et al., 2006). At high temperatures, the increase in conductivity may be attributed to softening of the polymer which causes the injected charge carrier to move more easily into the volume of the polymer giving rise to a large current. Increased conductivity at higher temperatures could also be due to thermionic emission across the barrier potential.

Temperature (K)	Experimental $\beta \times 10^{-23}$ ( $\text{Jm}^{1/2} \text{V}^{1/2}$ ) values	
	Forward bias	Reverse bias
320	$5.65 \pm 0.12$	$3.17 \pm 0.12$
350	$6.31 \pm 0.14$	$3.56 \pm 0.12$
370	$3.44 \pm 0.04$	$0.93 \pm 0.02$

Table 1. Values of  $\beta$  obtained from experimental data

Variable range hopping mechanism predicts linear dependence of  $\ln(\sigma T^{1/2})$  versus  $T^{-1/4}$  with negative slope (Fig.9, inset b). The Mott parameters-  $T_d$ ,  $\gamma$  and  $N(E_F)$ - are determined from equations 6 to 10 using the slope and intercept values of the plots in inset (b) of Fig. 9 and assuming a phonon frequency ( $\nu_{ph}$ ) of  $10^{13} \text{ s}^{-1}$ . Other Mott parameters, the hopping distance  $R$  and average hopping energy  $W$  are determined from Eq. (9) and Eq. (10) respectively. Mott parameters from this calculation are listed in Table 2. Table 3 shows the variations of the Mott parameters with temperature in our samples. It is evident from Table 3 that  $\gamma R > 1$  and  $W > kT$ , which agrees with Mott's condition for variable range hopping. It can therefore be concluded that the main conduction mechanism in NFSC is the variable range hopping.

Mott parameters	Value
T0 (K)	$4.58 \times 10^{10}$
N(EF) ( $\text{eV}^{-1}\text{cm}^{-3}$ )	$9.04 \times 10^{19}$
$\alpha$ ( $\text{cm}^{-1}$ )	$3.0 \times 10^8$
R (cm)	$1.44 \times 10^{-7}$
W (eV)	0.89

Table 2. Mott parameters at temperature range of (320-440K)

T (K)	R ( $\text{cm}^{-1}$ )	W (eV)	kT (eV)	$\gamma R$
300	$1.54 \times 10^{-7}$	0.72	0.026	41.6
350	$1.49 \times 10^{-7}$	0.81	0.030	40.1
400	$1.44 \times 10^{-7}$	0.89	0.034	38.7
450	$1.39 \times 10^{-7}$	0.98	0.039	37.6

Table 3. Variation of Mott parameters at temperature range of 300-450K

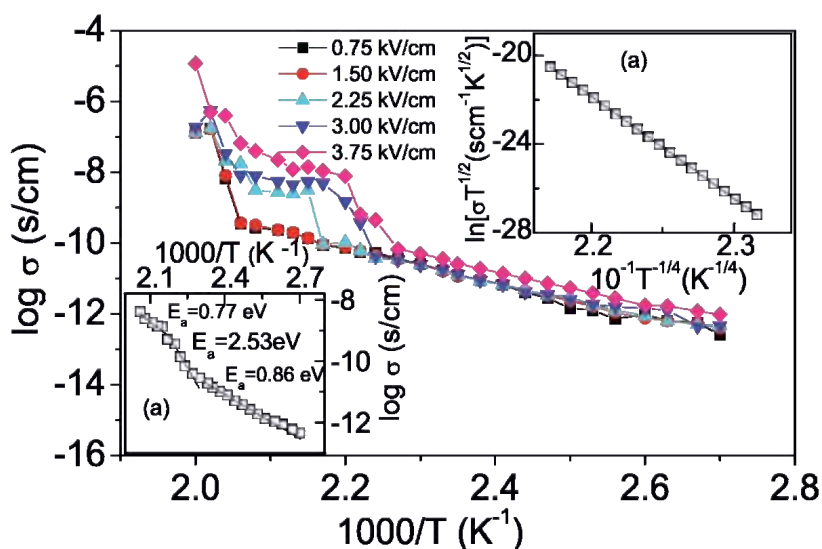


Fig. 9. Arrhenius plots showing variation of  $\sigma$  vs  $1/T$  at different electric fields. Inset (a) average Arrhenius plot showing activation energy at low and intermediate temperature ranges. Inset (b) plot of  $\ln(\sigma T^{1/2})$  versus  $(T^{-1/4})$  within a temperature of 350K-440K and average electric field of 2.25Kv/cm.

Degree of localization of the carriers in the trap states is indicated by  $\gamma R > 1$  which shows that the charges are highly localized. Table 3 also shows that when the temperature decreases, the average hopping energy  $W$  decreases and the average hopping distance  $R$  increases, supporting the fact that when the phonon energy is insufficient (low temperature), carriers will tend to hop larger distances in order to locate in sites which are energetically closer than their nearest neighbours.

## 6. Conclusion

Current-Voltage characteristics of the cuticles, as a function of irradiation, annealing, and temperature, show electrical switching with memory effect. The threshold voltage increases with irradiation time and annealing temperature but it decreases with increase in measurement temperature. The threshold voltage of the annealed and irradiated samples ranges between 6-8 volts. Electrical conduction in the OFF state follows Ohms' law but changes to space charge limited current after switching to ON state. A combination of Fowler-Nordheim field emission process and redox processes are responsible for electrical switching of the samples. Conduction at low temperatures takes place by variable range hopping mechanism. Since this biomaterial is biodegradable and is also considered to be biocompatible and immunologically inert, it has high potential in biomedical applications. It can be used in making contact eye lenses, scaffolds in tissue engineering, and in controlled release of drugs. Most notably, due to its switching properties, its use in the design of biosensors utilizing ion channels is very feasible.

## 7. References

- Amit, P.; Watson, R; Lund, P; Xing, Y.; Burke, K.; Yufan H.; Borguet, E.; Achim, C; & Waldeck D. (2008). Charge Transfer through Single-Stranded Peptide Nucleic Acid Composed of Thymine Nucleotides. *J.Phys. Chem.*, Vol. 112, pp. 7233-7240
- Armitage N., Briman M., & Gruner M. (2004). charge transfer and charge transport on the double helix. *Phys.stat. sol.(b)* Vol.241(1), pp. 69-75
- Ashour, H., Saad, M., & Ibrahim, M. (2006). Electrical Conductivity for Irradiated, Grafted Polyethylene and Grafted Polyethylene with Metal Complex. *Egypt. J. Solids*, Vol. 29( 2), pp. 351-362.
- Ashutosh, T., & Singh, S. (2008). Synthesis and characterization of biopolymer-based electrical conducting graft copolymers. *J. Appl. Polym. Sci*, Vol.108(2), pp.1169-1177.
- Aviram A., Joachim C. & Pomerantz M. (1988). Evidence of Switching and Rectification by a Single Molecule Effected with a Scanning Tunneling Microscope. *Chem. Phys. Lett.*, Vol.146(6), pp. 490-495
- Boutelje, J. (1980). *Encyclopedia of world timbers, names and technical literature.* (Enc wTimber).p234
- Bykov, I. (2008). *Characterization of Natural and Technical Lignins using FTIR Spectroscopy.* Master thesis, Lulea University of Technology, Lulea
- Chun L.; Parvez, Y. Iqbal, Y.; Marzena A.; Lashkor, M.; Preece, J. & Mendes, P. (2010). Tuning Specific Biomolecular Interactions Using Electro-Switchable Oligopeptide Surfaces. *Adv. Funct. Mater.*, Vol.20, pp.2657-2663

- Collins, R. & Abass, A. (1993). Electrical switching in Au-PbPc-Au thin film sandwich devices. *Thin Solid Films*, Vol.235, pp.22-24
- Cordes, M. & Giese B. (2009). Electron transfer in peptide and proteins. *Chemical society review*, Vol. 38, pp. 892-901
- Deshmukh, S., Burghate, D., Akhare, V., Deogaonkar, V., & Deshmukh, P. (2007). Electrical conductivity of polyaniline doped PPV-PMMA polymer blends. *Bull.Matter. Sci.* Vol. 30(1), pp.51-56
- DiBenedetto, S.; Facchetti, A.; Rather, M.; & Marks, T. (2009). Molecular self-assembly monolayers and multilayers for organic and unconventional inorganic thin films transistor applications. *Advanced materials*, Vol.21, pp. 1407-1433
- Domínguez, E.; Alejandro, J.; Guerrero, H. & Heredia, A. (2011). The biophysical design of plant cuticles: an overview. *New Phytologist*, vol. 189, pp. 938-949
- Eduardo, R., Margarita, D., & Pilar, A. (2005). Functional biopolymer nanocomposites based on layered solids. *J. Mater. Chem.* 15: 3650-3662 DOI: 10.1039/ b505640n
- Eley, D., Lockhart, N., & Richardson, C. (1977). Electrical properties and structural transitions in the mitochondrion. *Journal of Bioenergetics and Biomembranes*, Vol.9(5), pp.289-301
- Feinleib J., DeNeufville J., Moss S., and Ovshinsky S. (1971). Rapid reversible light-induced crystallization of amorphous semiconductors. *Applied Physics Letters*, Vol.18, pp. 254-257
- Finkenstadt, V. & Willett, J. (2007). Preparation and characterization of electroactive biopolymers. *Macromolecular symposia* ISSN 0258-0322.
- Galoppini, E, and Fox M. (1996). Role of dipoles in peptide electron transfer. *J.Am. Chem. Soc.* Vol.118, pp. 2299-2300.
- Ghosh, M., & Meikap, A., Chattopadhyay ,S. and Chatterjee, S. (2001) Low temperature transport properties of Cl-doped conducting polyaniline. *J. Phys. Chem. Solids*, Vol.62, pp. 475-84
- Gmati, F., Arbi, F., Nadra, B., Wadia, D. and Abdellatif, B. (2007). Comparative studies of the structure, morphology and electrical conductivity of polyaniline weakly doped with chlorocarboxylic acids. *J. Phys.: Condens. Matter*, Vol. 19, pp.326203
- Hagen, J.; Li, W.; & Steckl, J. (2006). Enhanced emission efficiency in organic light-emitting diodes using deoxyribonucleic acid complex as an electron blocking layer. *Applied Physics Letters*, Vol. 88, pp. 171109(1-3)
- Heredia, A. (2003). Biophysical and biochemical characteristics of cutin, a plant barrier biopolymer, *Biochimica et Biophysica Acta* Vol. 1620 pp. 1 - 7
- Jose J. B., Matas, A. J., & Heredia, A. (2004). Molecular characterization of the plant biopolyester cutin by AFM and spectroscopic techniques. *Journal of Structural Biology*. Vol. 147, pp.179-184
- Katana, G. & Musyoki, A. (2007). Fabrication and performance testing of gas sensors based on organic thin films. *J. Polym. Mater.* Vol.24 (4), pp.387-394
- Khare, P., Pandey, R., and Jain P. (2000) .Electrical transport in ethyl cellulose -chloranil system. *Bull.Mater. Sci.* Vol.23 (4), pp.325-330
- Kipnusu, W.; Katana, G.; Migwi, M.; Rathore, I.; & Sangoro J.(2009). Charge Transport Mechanism in Thin Cuticles Holding Nandi Flame Seeds, *International Journal of Biomaterials*, doi:10.1155/2009/548406



- Kipnusu, W.; Katana, G.; Migwi, M.; Rathore, I.; & Sangoro J. (2009). Electrical Switching in Thin Films of Nandi Flame Seed Cuticles. *International Journal of Polymer Science*, doi:10.1155/2009/830270
- Leszek, K., Ewa, M., & Feliks, J. (2002). Changes in the Electrical Conductivity of the - irradiated BAT collagen. *Polish J Med Phys & Eng.* Vol.8(3), pp.157-164
- Lewis, T. & Bowen, P. (2007). Electronic Processes in Biopolymer Systems. *Electrical Insulation*, IEEE Transactions, EI- Vol.19 (3), pp. 254-256
- Lilly, G.; Whalley, A.; Grunder, S.; Valente, C.; Frederick, M.; Stoddart, J & Weiss, E. (2011). Switchable photoconductivity of quantum dot films using cross-linking ligands with light-sensitive structures. *Journal of Materials Chemistry*, in press match 2011 DOI: 10.1039/c0jm04397d
- Long, Y., Chen, Z., Wang, N., Zhang, Z., & Wan, M. (2003). Resistivity study of polyaniline doped with protonic acids, *Physica B* Vol.325, pp.208-213
- Luthra, V., Singh, R., Gupta, S., & Mansingh, A. (2003). Mechanism of dc conduction in polyaniline doped with sulfuric acid *Curr. Appl. Phys.* Vol.3, 219-222.
- Mallick, H., & Sakar, A. (2000). An experimental Investigation of electrical conductivity in biopolymers. *Bull.mater.sci.* Vol.23.4, pp. 319-324
- Mei Li, Z.; Turyanska, L.; Makarovsky, O.; Amalia Patan, A.; Wenjian Wu, W.; & S Mann, S. (2010). Self-Assembly of Electrically Conducting Biopolymer Thin Films by Cellulose Regeneration in Gold Nanoparticle Aqueous Dispersions. *Chem. Mater.* ,Vol. 22, pp. 2675-2680
- Meisel, D., Pasveer, W., Cottaar, I., Tanase, I., Coehoorn, R., Bobbert, P., Blomp, W., De Leeuw D., & Michels, M. (2006). Charge-carrier mobilities in disordered semiconducting polymers: effects of carrier density and electric field. *phys. stat. sol.* (c) Vol.3, (2), pp. 267- 270.
- Mihajlović, G.; Brunet, N.; Trbović, J.; Xiong, P.; Molnár, S.; & Chase, P. (2004). All-electrical switching and control mechanism for actomyosin-powered nanoactuators, *Appl. Phys. Lett.*, Vol. 85, (6), pp. 1060-1062
- Mott, N. & Davis, E. (1979). *Electronic Processes in Non-Crystalline Materials* (Oxford: Clarendon) p 157-60
- Ottenbacher, D., Schierbaum, K., & Gopel, W. (1991). Switching effect in metal/ Phthalocyanine/metal sandwich structures. *Journal of molecular electronics* Vol.7(7), pp.9-84
- Pandey, P.C. (2006). Bacteriorhodopsin—Novel biomolecule for nano devices. *Analytica Chimica Acta*, Vol. 568, pp. 47-56
- Priel, A.; Ramos, A.; Tuszynski, J.; & Horacio F.; Cantiello, H. (2006). A Biopolymer Transistor: Electrical Amplification by Microtubules. *Biophysical Journal* Vol. 90 , pp. 4639-4643
- Pollard, M.; Beisson, F.; Li, Y.; & Ohlrogge, J. (2008). Building lipid barriers: biosynthesis of cutin and suberin. *Trends in Plant Science*, vol. 13, (5), pp. 236-246
- Qun, L., Stuart, J.; Birge, R.; Xub, J.; Andrew Stickrath, A.; & Bhattacharya, P. (2004). Photoelectric response of polarization sensitive bacteriorhodopsin films. *Biosensors and Bioelectronics* ,Vol.19, pp.869-874
- Radha, B., & Rossen, D. (2003). Nonlinear elastodynamics and energy transport in biopolymers. ArXiv:nlin.PS/ 0304060 v1

- Ren, Y.; Chen, K.; He, J.; Tang, L.; Pan, A.; Zou, B.; & Zhang, Y. (2010). Mechanically and electrically controlled molecular switch behavior in a compound molecular device. *Applied Physics Letters*, Vol 97, pp. 103506 (1-3)
- Ronald, P., Peter, R., and Albert S. (1981). Water structure-dependence charge transport in proteins. *Proc. Natl. Acad. Sci USA*. Vol. 78 (1), pp. 261-265
- Roy, S.; Prasad, M.; Topolancik, J.; & Vollmer, F. (2010). All-optical switching with bacteriorhodopsin protein coated microcavities and its application to low power computing circuits. *Journal of Applied Physics*, Vol. 107, pp. 053115(1-9)
- Sakai, K., Matsuda H., Kawada H., Eguchi K., & Nakagiri T. (1998). Switching and memory phenomena in Langmuir-Blodgett films. *Appl. Phys. Lett.* Vol. 53(14), pp. 1274-1276
- Sangawar, V., Chikhalikar P., Dhokne R., Ubale A., & Meshram S. (2006). Thermally stimulated discharge conductivity in polymer composite thin films. *Bull. Mater. Sci.* 29: 413-416
- Singh, M.; Graeme, B.; Allmang, M.; (2010). Polaron hopping in nano-scale poly(dA)-poly(dT) DNA. *Nanoscale Res. Lett.* Vol. 5, pp. 501-504
- Singh, R., Kaur A., Yadav K., and Bhattacharya D. (2003). Mechanism of dc conduction in ferric chloride doped poly(3-methyl thiophene) *Curr. Appl. Phys.* 3: 235-238
- Shinwari, M.; Deen, M.; Starikov, E and Gianarelio, C. (2010). Electrical conductance in biological molecules. *Advance functional materials*, Vol. 20. Pp. 1865-1883
- Skourtis, S.; Waldeek, D. & Beratan, D. (2010). Fluctuation in biological and bioinspired electron transfer reaction. *Annual Review Phys. Chem.* March 2010, Vol. 61, pp. 461-485
- Tang, W., Shi, H., Xu, G., Ong, B., Popovic, Z., Deng, J., Zhao, J. & Rao, G. (2005), Memory Effect and Negative Differential Resistance by Electrode- Induced Two-Dimensional Single- Electron Tunneling in Molecular and Organic Electronic Devices. *Advanced Materials*, 17: 2307-2311
- Tao, L., Erfan, A., & Heinz-Bernhard, K. (2005). Peptide electron transfer. *Chem. Eur. J.*, Vol. 11, pp. 5186-5194.
- Treadway, C.; Hill, M.G. & Barton, J.K. (2002). Charge transport through a molecular  $\pi$ -stack: double helical DNA. *Chemical Physics*, Vol. 281, pp. 409-428
- Tseng, R.; Ouyang, J.; Chu, C.; Huang, J.; & Yanga, Y. (2006). Nanoparticle-induced negative differential resistance and memory effect in polymer bistable light-emitting device. *Applied Physics Letters*, Vol. 88, pp. 123506 (1-3)
- Waser, R. & Aono, M. (2007). Nanoionics-based resistive switching memories, *Nature materials*, Vol. 6, pp. 833-840
- Weiss E.; Kriebel, J.; Maria-Anita Rampi, M.; & Whitesides, G. (2007). The study of charge transport through organic thin films: mechanism, tools and applications. *Philosophical Transaction of the Royal Society A*. Vol. 365 pp. 1509-1537
- Xue, Z., Ouyang, M., Wang, K., Zhang, H., and Huang, C. (1996). Electrical switching and memory phenomena in the Ag-BDCP thin film. *Thin Solid Films*, Vol. 288, pp. 296-299
- Zimmermann, R.; Osaki, T.; Jiler, T.; Gauglitz, G.; Dukhin, S. & Werner, C. (2006). Electrostatic Switching of Biopolymer Layers. Insights from Combined Electrokinetics and Reflectometric Interference. *Anal. Chem.*, Vol. 78, pp. 5851-5857

# Biomimetic Materials as Potential Medical Adhesives – Composition and Adhesive Properties of the Material Coating the Cuvierian Tubules Expelled by *Holothuria dofleinii*

Yong Y. Peng<sup>1</sup>, Veronica Glattauer<sup>1</sup>, Timothy D. Skewes<sup>2</sup>,  
Jacinta F. White<sup>1</sup>, Kate M. Nairn<sup>1</sup>, Andrew N. McDevitt<sup>3</sup>,  
Christopher M. Elvin<sup>3</sup>, Jerome A. Werkmeister<sup>1</sup>,  
Lloyd D. Graham<sup>4</sup> and John A.M. Ramshaw<sup>1</sup>

## 1. Introduction

Novel, distinct adhesive systems have been described for a wide range of marine species (Kamino, 2008). These highly effective, natural materials provide a link between biological science and material science, and can serve as models on which new, bioinspired synthetic materials could be based. These various adhesive systems have developed independently, on many occasions, and provide a wide range of opportunities for the development of new, biologically-inspired adhesives. The natural adhesives include, for example, the marine mussel (*Mytilus sp.*) (Lin et al., 2007), barnacle (Nakano et al., 2007) and stickleback (Jones et al., 2001) adhesives, which are protein-based, as well as sponge, certain algal and marine bacterial adhesives (Mancuso-Nichols et al., 2009) that are polysaccharide-based.

In the present paper, we examine the adhesive system found associated with the Cuvierian tubules of a holothurian species (sea cucumber), *Holothuria dofleinii*. This is an example of the particularly rapid marine adhesive that is found on the surface of Cuvierian tubules when they are expelled (DeMoor et al., 2003; Müller et al., 1972; VandenSpiegel & Jangoux, 1987). The unique nature of this natural adhesive system, especially its rapid action under water, has suggested that if the mechanism can be understood, then it may prove to be possible to mimic the adhesive through biotechnology and/or synthetic chemistry. An adhesive that functions readily in an aqueous environment would be particularly valuable, especially in medical applications, as the majority of existing adhesives bind to dry surfaces more strongly than the same surfaces when wet.

Cuvierian tubules provide a host defence mechanism for certain species of holothurians (Lawrence, 2001; VandenSpiegel & Jangoux, 1987). It has long been known that, on expulsion, the Cuvierian tubules fill with liquid and lengthen, become sticky and rapidly

---

<sup>1</sup>CSIRO Materials Science and Engineering, Bayview Avenue, Clayton, VIC 3169, Australia

<sup>2</sup>CSIRO Marine and Atmospheric Research, Middle Street, Cleveland, QLD 4163, Australia

<sup>3</sup>CSIRO Livestock Industries, Carmody Road, St Lucia, QLD 4067, Australia

<sup>4</sup>CSIRO Food and Nutritional Sciences, Julius Ave, North Ryde, NSW 2113, Australia

immobilise most organisms with which they come into contact (VandenSpiegel & Jangoux, 1987). The tubules, once expelled, are immediately adhesive on contact with a solid surface (VandenSpiegel & Jangoux, 1987), such as the exoskeleton or skin of a predator. Crabs, molluscs and sea stars can stimulate tubule expulsion, and the tubules stick to these species. This adhesion happens entirely under water, and does not need the mixed environment of the intertidal zone where many of the other potential adhesives are sourced.

Sticky tubules are found only within the family Holothuridae within the order Aspidochirotrida, and mostly in the genus *Bohadschia* and the genus *Holothuria*. Various authors have described the ultrastructure of the tubules, especially for *H. forskåli* (Lawrence, 2001; VandenSpiegel & Jangoux, 1987; VandenSpiegel et al., 2000), as well as their expulsion and release (Flammang et al., 2002) and the timeframe of regeneration (Flammang et al., 2002; VandenSpiegel et al., 2000).

Flammang and Jangoux (2004) suggested, from the differences in the surface (adhesive) protein types and compositions in *H. forskåli* and *H. maculosa*, that the adhesion proteins and mechanism may differ between species. Other studies showed that adhesive strengths varied between species, with the adhesion in *H. leucospilota* being several times greater than for six other species (Flammang et al., 2002). A limited number of studies have probed the mechanism of adhesion, focusing on *H. forskåli* and *H. leucospilota* (De Moor et al., 2003; Müller et al., 1972; Zahn et al., 1973). These studies have shown that best adhesion is found at temperatures, salinity and pH similar to those found in the marine environment in which the organism flourishes, and is most effective with hydrophilic surfaces (Flammang et al., 2002; Müller et al., 1972; Zahn et al., 1973). Increasing concentrations of urea led to a loss of adhesion, suggesting that native protein structure(s) or interactions(s) may be required for effective bonding (Müller et al., 1972). Later biochemical studies have also suggested that the adhesive mechanism involves protein components (DeMoor et al., 2003).

In the present study, we have extended the information on Cuvierian tubule adhesion. In this study we examined the tubules of a different species, *H. dofleinii* Augustin, 1908. We have examined the distribution of the adhesive substance on the surface of expelled tubules, along with the molecular weights and amino acid compositions of its main protein components. We have estimated the strength of adhesion of *H. dofleinii* tubules to different substrata, and examined the effects of salinity, pH, ionic strength and denaturants on the adhesive properties.

## 2. Materials and methods

### 2.1 Collection of materials

Individual *H. dofleinii* were obtained from shallow subtidal seagrass banks in Moreton Bay, Queensland, at a depth of about 1-2 metres at low tide, close to the western side of Stradbroke Island (153° 26.4' E 27° 25.13' S to 27° 25.68' S), and were held for up to 5 days prior to use in filtered, recirculating seawater tanks at 21.5 – 22 °C. The identification of the animals was based on morphology, spicule shape and size and 18S-RNA sequencing (Peng & Skewes, unpublished data).

### 2.2 Sample preparation

To collect expelled Cuvierian tubules, *H. dofleinii* individuals were held and gently stimulated underwater until tubules were expelled. Immediately after expulsion, a tubule was individually collected using polytetrafluoroethylene-tipped forceps, and was allowed

to drain briefly (<20 sec), but not by squeezing as had been proposed by others (Zahn et al., 1973). Intact tubules prior to expulsion were obtained by dissection of animals that had been euthanised by freezing at minus 20 °C.

### 2.3 Microscopy

To look for the presence of glycoprotein on the surface of expelled tubules, samples were treated with fluorescently-labelled lectins; fluorescein isothiocyanate (FITC)-labelled concanavilin A (ConA), FITC-labelled *Datura stramonium* agglutinin (DSA), and FITC-labelled *Lycopersicon esculentum* agglutinin (LEA) (all from Sigma, St Louis). All FITC-labelled lectins were applied as 20 µg/mL solutions in Tris-buffered saline (TBS) for 60 min, followed by 3 × 5 min washes in TBS. Samples were examined using appropriate narrow pass filters on an Olympus BX61 fluorescence microscope.

To examine the distribution of adhesiveness on tubules, individual freshly expelled tubules after draining (see above) were transferred to a wash solution in a plastic trough which contained a suspension of 0.5% w/v Bio-Gel P2 (45-90 µm particle size) in 3.5% w/v NaCl, 10 mM sodium phosphate, pH 7.6. After 5 sec immersion, the tubules were washed 3 times in 3.5% NaCl, 10 mM sodium phosphate, pH 7.6 and were then drained and placed onto glass slides. After air drying, the tubules were examined by microscopy.

For scanning electron microscopy (SEM) expelled tubules were examined using a Philips XL30 FESEM microscope at an accelerating voltage of 2 kV.

### 2.4 Gel electrophoresis analysis

Freshly expelled and drained tubules were allowed to adhere to a glass plate and were air dried. The tubules on glass plates were removed by peeling, leaving the layer of adhesive, and potentially other components of the tubule wall as a print on the glass (DeMoor et al., 2003). This material was collected by removal with a sharp razor blade and was then extracted in electrophoresis sample buffer, containing 2-mercaptoethanol. SDS-polyacrylamide gel electrophoresis (SDS-PAGE) was based on the method of Laemmli (1970) using Invitrogen NuPAGE Novex 4-14% Bis-Tris Gel with MES running gel buffer, at 180V for 60 min. Molecular weights were determined by comparison to globular protein standards (BioRad) using BioRad Quantity One v.4.4.0 software. For protein identification, gels were stained by Coomassie Blue R-250. Samples that had not been dried completely, but only sufficient to remove excess liquid, appeared to give samples that contained less insoluble material, although the yield of adhesive proteins was less.

### 2.5 Amino acid analysis

Protein extracts were separated by SDS-PAGE, followed by transfer of the protein bands to PVDF membrane using Invitrogen NuPAGE Transfer buffer (NP0006-1). Amino acid analysis of PVDF membrane pieces used vapour-phase hydrolysis (5.8 M HCl at 108 °C for 18 h), followed by precolumn derivatisation with 6-aminoquinolyl-*N*-hydroxysuccinimidyl carbamate (Cohen & DeAntonis, 1994). Derivatives were separated and quantified by reversed phase (C18 Waters AccQTag) HPLC at 37 °C (Cohen, 2001) (Australian Proteome Analysis Facility), using a Waters Alliance 2695 Separation Module, a Waters 474 Fluorescence Detector and a Waters 2487 Dual λ Absorbance Detector in series.

## 2.6 Adhesion properties

Adhesion properties were measured using a 90 Degree Adhesive Peel Strength Test (Dimas et al., 2000), adapted to the rapid evaluation of tubules from a single animal under different experimental conditions. Individual expelled tubules, as above, were transferred to a wash solution in a plastic trough containing a wash solution determined by the particular test (see below). The numbers of samples tested in a given experiment are given in the results Tables; in each case, tubules from a minimum of 3 separate animals were used. After  $60 \pm 2$  sec, the tubule was removed from the wash solution and allowed to drain for 5 sec. It was then laid across the width of a 25 mm wide strip of substratum, selected for the particular test. The tubule was allowed to adhere to the test substratum under its own weight for  $60 \pm 2$  sec. This differs from previous studies where a load was applied during adhesion (Flammang et al., 2002). During the adhesion period the tubule was trimmed to leave <10 mm overhanging one side of the substratum and about 50 mm on the other side. The flat width of the tubule was measured and also recorded photographically, with a ruler placed adjacent, for subsequent verification. At the end of the 60 sec adhesion period, each tubule-substratum assembly was then transferred to a frame that allowed the substratum to be held horizontally with the adhered tubule on the underside, i.e. with the free c. 50 mm length of tubule hanging below. The load was then increased stepwise (2.5 g/5 sec) to the overhang of the tubule until the tubule-substratum adhesion failed by peeling. The total load at failure was recorded. The maximum force tested was 0.2 N (approximately 20 g load) which equated to about 0.05 N/mm for an average tubule, because higher loads typically took too long to add and the tubule could have begun to desiccate at that stage, potentially changing the adhesive strength. A minimum of six determinations was made for each test condition. Data are presented as the total force at failure (N) divided by tubule width (mm). Although we did not test values above 0.05 N/mm, our conservative approach did not hinder examination of conditions that led to reduction of adhesive strength.

Experiments to test adhesion to different substrata used a wash solution of simulated seawater comprising 3.5% NaCl, 10 mM sodium phosphate buffer, pH 7.6. Various substrata were tested, including clean glass (microscope slide), aluminium, polyvinyl chloride, chitin (from crab), polycarbonate, poly(methyl methacrylate) (PMMA) and polytetrafluoroethylene (PTFE), all cut to a similar size. As the chitin substratum lacked stiffness, the samples were first glued with cyanoacrylate onto a glass microscope slide. The chitin sample also had an irregular surface and was not uniform like the other materials.

The effects on tubule-glass adhesion of various chloride or sodium salts (50 mM) were examined by supplementing the 3.5% NaCl, 10 mM sodium phosphate buffer, pH 7.6, before washing the tubules. The effect of NaCl concentration on tubule-glass adhesion was examined using different NaCl concentrations in 10 mM sodium phosphate buffer, at final pH 7.6. The effect of pH on tubule-glass adhesion was examined using solutions prepared using three salts: Tris/chloride, sodium citrate and sodium acetate, each at 50 mM in 3.5% NaCl, 10 mM sodium phosphate. Similarly, the effect of urea on tubule-glass adhesion was examined using different urea concentrations in 3.5% NaCl, 10 mM sodium phosphate at a final pH of 7.6. Glass was used as the standard substratum as it was readily available in uniform quality, and had previously been shown to be an excellent material for adhesion of *H. forskåli* tubules (Flammang et al., 2002).

### 3. Results and discussion

#### 3.1 Tubule structure and microscopy

Dissection of euthanised *H. dofleinii* showed that the body cavity contained a large number, several dozen, Cuvierian tubules in their compressed form (Figure 1A). In their compressed form the tubules were not sticky, but they rapidly became sticky on mechanical extension, even from the dead animals. The compressed, individual tubules showed a corrugated and folded surface (Figure 1B), which would allow extension when required, like a concertina bellows. In cross-section (Figure 1C) a three-lobed channel could be seen that would allow fluid insertion for expansion of the tubules. When expelled and fully extended *in vivo*, these tubules became instantly sticky and changed from the 25-35 mm compressed length up to around 350-400 mm. The fully extended tubules (Figure 1D) were typically about 4mm flat width when fully inflated, and still showed some patterning from the folding that was present in the compressed state. Individual animals contained several dozen non-inflated tubules, but when the animals were stimulated only a small number were expelled, normally around 8-12.

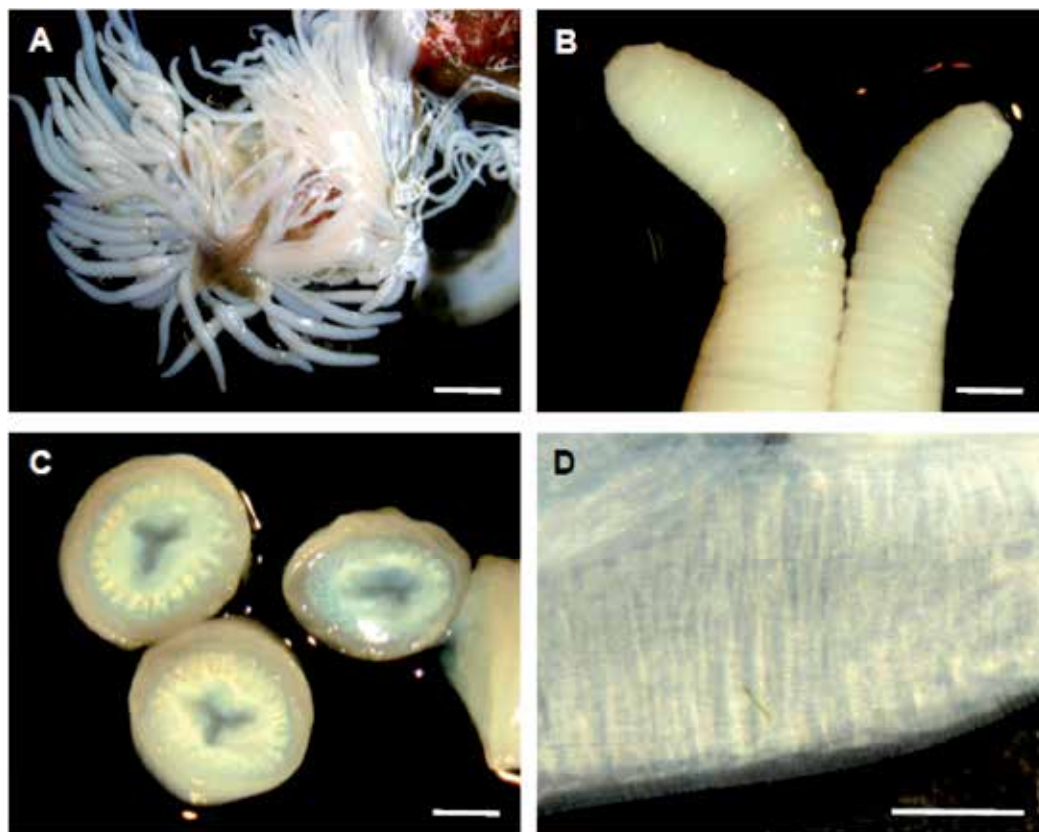


Fig. 1. Cuvierian tubules for *H. dofleinii*. (A, B, C) After dissection of a euthanised animal, showing, (A) the total mass of tubules, (B) the tips of compressed tubules, and (C) the cross-section of compressed tubules. (D) The surface of an *in vivo* expelled tubule. Bar (A) = 10 mm, Bars (B, C, D) = 1 mm.

The surfaces of naturally extended tubules showed strong binding of FITC-DSA (Figure 2A) and FITC-LEA lectins to the tubule surface, with a series of bands that resemble the original folding of the un-extended tubule. FITC-ConA lectin binding was weak, suggesting that the DSA and LEA binding was specific for carbohydrate or glycosylated protein on the surface, rather than non-specific binding. These 2 lectins recognise very similar carbohydrate entities; (N-acetyl glucosamine)<sub>2</sub> by DSA and (N-acetyl glucosamine)<sub>3</sub> by LEA, which are distinct from the  $\alpha$ -mannose or  $\alpha$ -glucose recognised by ConA. SEM of the surface of expelled tubules (Figure 2B) showed that the surface had fibrous-like structures, suggesting aggregates of the adhesive material overlaying a further fibrous, collagenous layer of the wall of the tubule.

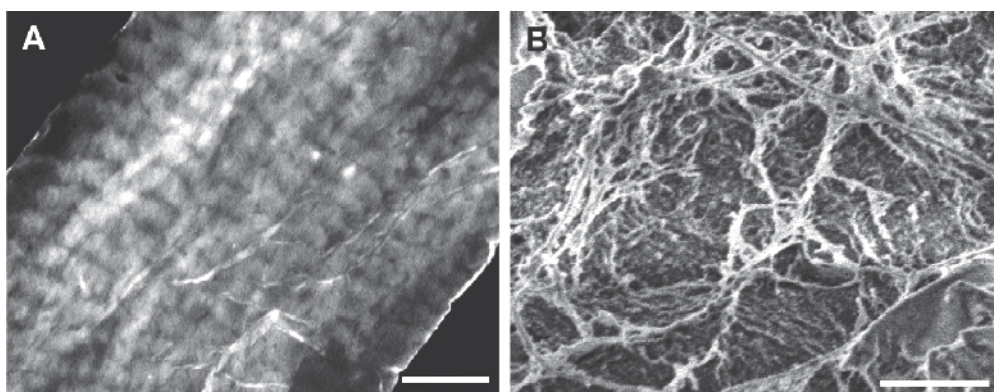


Fig. 2. Cuvierian tubules from *H. dofleinii*. (A) Fluorescence microscopy of FITC-labelled DSA bound to expelled Cuvierian tubules. Bar = 0.5 mm. (B) SEM of expelled Cuvierian tubules. Bar = 2.5  $\mu$ m

When freshly expelled tubules were briefly immersed in 3.5% NaCl containing Bio-Gel P2 particles, and then washed in 3.5% NaCl, particles bound to the tubule (Figure 3). These data showed that the surface of the tubule was generally adhesive, and there was no specific localisation of the particles, for example to the fibrous-like patches seen by SEM.

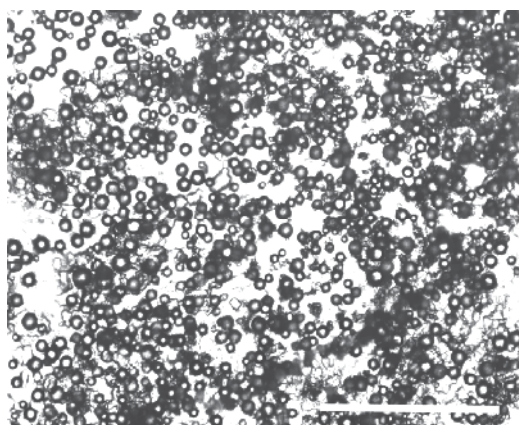


Fig. 3. Cuvierian tubules from *H. dofleinii*. Adhesion of Bio-Gel P2 beads to freshly expelled Cuvierian tubules from *H. dofleinii*. Bar = 0.5 mm



### 3.2 Gel electrophoresis analysis

The adhesion print isolated from glass showed a range of proteins of well-defined molecular weights when analysed under reducing conditions by SDS-PAGE (Figure 4). A similar pattern, except as noted below, was observed from >10 separate samples from different animals. Seven bands, H2 at 89 kDa, H3 at 70 kDa, H4 at 61 kDa, H6 at 44 kDa, H7 at 37 kDa, H8 26 kDa and H9 at 17 kDa, were consistently present in all tubule samples that were examined (n > 12). Band H4 has been examined as a single entity, but in some gels (Figure 4) it appeared that it may comprise 2 components. For all other bands, although each appeared to be a single component, it is also possible that more than one component could be present, migrating similarly. In many samples, but not all, an additional band, H5 at 53 kDa, was present. As it was not consistently present it was assumed that it may not be a key component of the adhesive system and hence was not examined further. In a few samples, an additional band H1 was observed at 150-170 kDa. This band seemed to be more prevalent in samples where tubule fragments were present in the adhesion print, and could possibly be related to the collagen that is the main structural component of the tubule (Watson and Silvester, 1959). The collected material sometimes contained a proportion of material that remained insoluble in the sample buffer. Examination of the adhesive prints under a microscope suggested that the samples that subsequently contained more insoluble material also contained more fibrous material that could be from the collagenous wall of the tubule. Samples with little wall material typically had little, if any insoluble material.

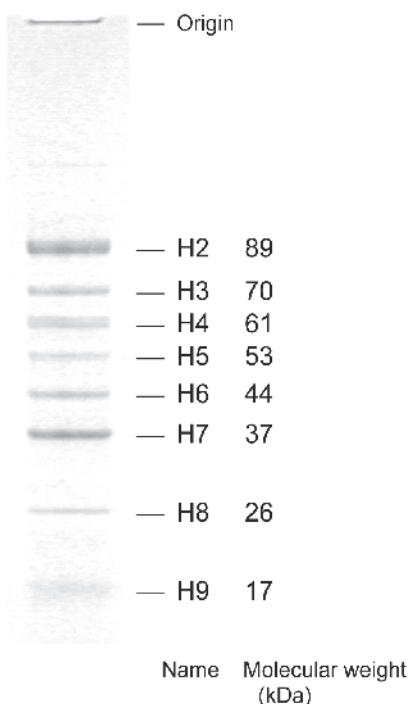


Fig. 4. SDS-PAGE of the reduced proteins from the surface of a freshly expelled Cuvierian tubule from *H. dofleinii*. The gel was stained with Coomassie Blue R-250. Key bands are labelled and their estimated molecular weights, interpolated from a standard curve using globular protein standards (BioRad), are given.

Previously, Flammang and colleagues (DeMoor et al., 2003) have shown a gel electrophoresis pattern for the tubule print from *H. forskali* samples. In this case, a high background staining was present, and the bands were generally less well defined and more poorly resolved. In some cases the apparent *H. forskali* bands had comparable molecular weights to those observed in the present study. Thus the sharp bands at 95 kDa and 45 kDa may be similar to the H2 (89 kDa) and H6 (44 kDa) bands, while the diffuse bands at 63 kDa and 33 kDa may be similar to the H4 (63 kDa) and the H7 (37 kDa) bands, respectively.

### 3.3 Amino acid analysis

The amino acid compositions determined from amino acid analyses of the 6 principal bands are given in Table 1. No data were collected for Band H4 as it appeared to be a doublet (Figure 3). Deamidation during acid hydrolysis means that Asn cannot be distinguished from Asp, nor can Gln be distinguished from Glu; the two pairs are given as Asx and Glx respectively. This prevents an estimation of pI for each of these proteins. Hydroxyproline was not observed in any of the 6 principal bands.

Comparison of the analyses for the various bands did not show signature features for any particular band, and the compositions were broadly similar for all bands. All of the bands had high contents of Gly (7.8-16.8 mol%) and Glx (11.6-16.2 mol%) relative to the average for eukaryotic proteins (6.9 and 9.7 mol%, respectively) (Doolittle, 1986); similarly, DeMoor et al. (2003) observed high Gly contents (16-22 mol%) for the proteins extracted from *H. forskali*. As noted above, the SDS-PAGE molecular weight data suggests that it is possible that some bands could be related between the species - H2 and 95 kDa, H6 and 45 kDa and H7 and 33 kDa. Comparison of the amino acid composition data, however, did not show strong similarities. However, it has been suggested (Flammang and Jangoux, 2004), that the protein components present in the adhesives differ between species.

	H2	H3	H6	H7	H8	H9
Asx	9.7	8.7	12.1	13.1	9.7	15.0
Ser	9.8	11.6	7.0	6.5	10.2	8.0
Glx	16.2	13.3	13.2	12.7	15.0	11.6
Gly	16.1	16.8	7.8	8.1	13.6	10.5
His	1.1	1.0	1.3	ND	0.7	1.3
Arg	3.6	5.2	4.9	4.1	5.5	4.4
Thr	3.9	5.2	5.1	5.0	4.9	4.6
Ala	7.8	7.0	9.2	9.4	6.8	8.0
Pro	3.2	4.9	3.9	3.2	6.3	3.1
Tyr	1.8	2.5	2.4	1.9	3.0	2.4
Val	4.6	5.5	6.4	6.4	5.5	5.7
Met	ND	0.4	3.2	3.8	0.4	5.0
Lys	8.8	4.9	8.3	9.4	5.0	7.0
Ile	4.1	3.8	5.6	5.3	3.5	4.8
Leu	7.0	7.0	7.3	8.3	7.5	5.8
Phe	2.4	2.4	2.5	3.0	2.5	2.6

Table 1. Amino acid analysis of individual protein bands after separation by SDS-PAGE. Results are given as Mol %. ND = Not detected. Trp was not determined.

### 3.4 Adhesion characteristics

In the present study, a 90 Degree Peel Test was used to evaluate the adhesion of freshly expelled Cuvierian tubules. This method was chosen as we had encountered problems when tensile testing the *H. dofleinii* tubules following the approach used by Flammang and colleagues (Flammang et al., 2002). Specifically, when *H. dofleinii* tubules were sandwiched between two materials to which there was good adhesion, e.g. glass or metals, testing could lead to strength values which reflected the structural failure of the Cuvierian tubule rather than the failure of the adhesive, especially if some drying had occurred (data not shown). This method would only allow the determination of a minimum value for the adhesive strength as the latter exceeded the break strength of the tubule material itself.

The present test was suitable for rapidly examining numerous, freshly expelled samples, thus allowing ready comparison between the effects of various treatment solutions. The various treatments (i.e., incubations of tubules in the appropriate wash solutions) prior to adhesive testing were rapid (1 min) as it appeared that the adhesion could decline if tubules were left soaking for lengthy periods (data not shown). With *H. forskåli*, a lag period of about 60 min at 16 °C was recorded before adhesion started to decline, decreasing to about 15 min at 26 °C (Müller et al., 1972). In another study (Flammang et al., 2002) a longer lag phase was observed, and an initial increase in adhesive strength was reported. Yet others have reported adhesive strength to fall after 20 min (Zahn et al., 1973). The present approach, therefore, used short incubations in order to minimise time-based variations and to mimic the timescale over which tubules would be required to act in the natural environment.

Previous studies (Flammang et al., 2002) have shown that a compressive force of 2–10 N during adhesion led to a 6- to 8-fold increase in the resulting bond strength. In the present case, no compressive load was added so as to better simulate the natural process of ensnaring a predator.

Tubule widths showed little variation between individual samples, the average size being 4.0 mm. Tubules that were not fully expelled, and which therefore had a lesser diameter, were discarded. The observed width is larger than that found for *H. forskåli* (Flammang et al., 2002; Zahn et al., 1973) and *H. leucospilota* (Flammang et al., 2002), the species previously studied in detail, and also larger than for *H. impatiens* and *H. maculosa*; these other species generally have tubule diameters of 1–2 mm (Flammang et al., 2002). Although there are many potential tubules within the body cavity (Figure 1A) *H. dofleinii* expels only a few, typically 8–12 for organisms stimulated in the holding tanks compared with the more numerous thin tubules expelled by *H. leucospilota* or *H. forskali* (Flammang et al., 2002).

Adhesive strength was also found to vary when different substrata were examined, all after washing the tubules in 3.5% NaCl 10 mM Na/PO<sub>4</sub>, pH 7.6. There was a trend for strongest adhesion to be observed with hydrophilic substrata, glass and aluminium (Table 2). Adhesion to polycarbonate, PMMA, and PTFE was very poor; indeed, for PMMA and PTFE, the load required for peel was barely more than the weight of the 50 mm of tubule overhang. Intermediate adhesion values were observed with polyvinyl chloride and crab chitin surfaces (Table 2). The chitin samples were unusual in having a textured surface rather than a smooth one. Previously, Zahn, Flammang and colleagues had shown strong adhesion to hydrophilic surfaces such as glass and stainless steel, and poor adhesion to hydrophobic ones such as paraffin wax, polystyrene and polyethylene (Zhan et al., 1973; Flammang et al, 2002). In general our results are consistent with this trend: the best adhesion was observed with glass whilst the poorest was observed with PTFE.

Solution	Force/width	S.D.	n
----------	-------------	------	---

	(N/mm)		
Glass	> 0.050	-	10
Aluminium	> 0.050	-	6
Polyvinyl chloride	0.024	0.006	11
Chitin	0.021	0.005	8
Polycarbonate	0.010	0.002	8
PMMA	0.009	0.003	7
PTFE	0.008	0.002	6

Table 2. Force required to peel Cuvierian tubules off various substrata to determine adhesive strength.

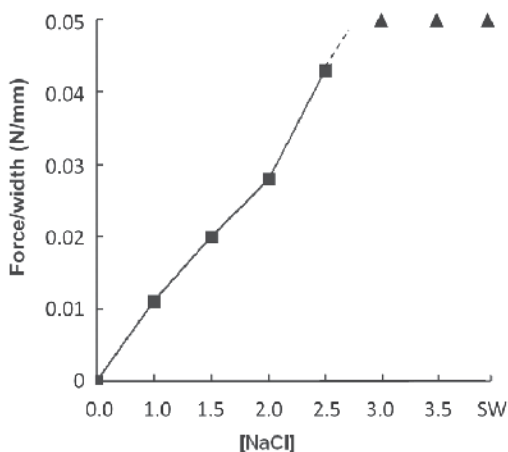


Fig. 5. The effect of different washing solutions on the adhesiveness of *H. dofleinii* Cuvierian tubules for glass. The effect of NaCl concentration; where ▲ indicates conditions where the force per unit width exceeded 0.05 N/mm. SW is natural sea water.

Adhesive strength decreased with decreasing NaCl concentration (Figure 5). At  $\geq 3\%$  NaCl the adhesion exceeded 0.05 N/mm. Reducing the NaCl concentration incrementally from 2.5% to 1.0% NaCl led to a steady decline in adhesive strength (Figure 5). The adhesive strength at 1% NaCl, which is comparable in concentration to physiological saline, was significantly weaker than in 3.5% NaCl simulated seawater. This is consistent with the previous observations on *H. forskåli* tubules (Flammang et al., 2002). It suggests that hydrophobic interactions may be important in the adhesive mechanism.

The effects on tubule-glass adhesion of other chloride or sodium salts (50 mM) (Table 3) showed that in all cases there was a loss of adhesive strength. For chloride salts, the loss was smaller when Tris rather than ammonium was the cation (Table 3). The other salts examined were all sodium salts of carboxylic acids, for whose action no simple mechanism could be proposed. Thus while formate (a monocarboxylate) and oxalate (a dicarboxylate) both showed similar adhesion, that observed with acetate (another monocarboxylate) was  $\sim 35\%$  below the value observed for formate. However, the values presented in Table 3 show only a trend as the errors in measurement are such that the different systems are not necessarily distinguishable. Supplementation with EDTA (a tetracarboxylate) was the most effective at disrupting bond strength, and essentially led to complete loss of adhesion (Table 3). It is not

clear whether this is due to the multiple carboxyl groups of this salt, to its strong metal ion chelating capability, or to some other property. However, certain other marine adhesives, such as that from *Mytilus*, do require metal activity (Hwang et al., 2010). A previous study which tested 15 different amino acids at 0.5% w/v solutions on adhesion by *H. forskåli* tubules (Müller et al., 1972) showed that most had little, if any, effect. The exceptions were the hydrophobic amino acids leucine (20% loss) and phenylalanine (57% loss). For phenylalanine, the loss was slow to develop (taking several minutes) and could not be reversed by washing (Zahn et al., 1973).

Solution	Force/width (N/mm)	S.D.	n
3.5% NaCl	> 0.050		>8
Tris/chloride	0.050	0.008	6
Sodium formate	0.047	0.012	6
Sodium oxalate	0.046	0.011	8
Ammonium chloride	0.036	0.008	8
Sodium citrate	0.035	0.009	7
Sodium acetate	0.030	0.006	8
Sodium EDTA	<0.003		8

Table 3. Comparison of the effects of different salt solutions on adhesion of Cuvierian tubules onto glass. All salts were 50mM in 3.5% NaCl, 10 mM sodium phosphate, pH 7.6

The effect of pH on the adhesive strength of the *H. dofleinii* adhesive showed that for Tris/chloride buffer, the best observed strength of those tested was at pH 7.6, and that the observed strength decreased at both lower and higher pH values (Figure 6). For citrate and acetate buffers, adhesive strength declined progressively as the pH was lowered from pH 7.6, with little adhesion remaining at pH 5.0 (Figure 6). A loss of adhesive strength at acidic pH values was also observed by Müller et al. (1972), who used paraffin wax as a (poor) substratum for tubule adhesion.

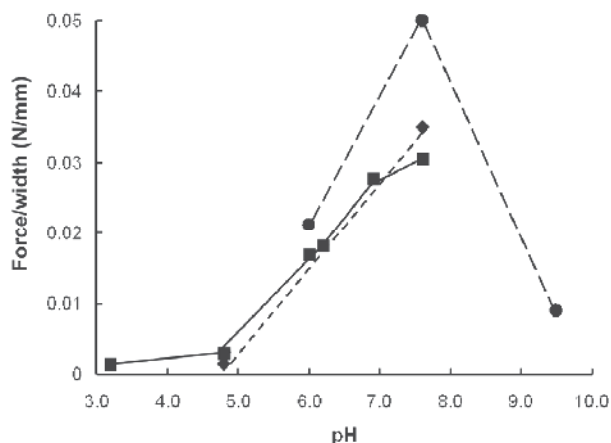


Fig. 6. The effect of different washing solutions on the adhesiveness of *H. dofleinii* Cuvierian tubules for glass. The effect of changes in pH, where ■ indicates acetate buffers, ◆ indicates citrate buffers and ● indicates Tris/Chloride buffers.

Some reports suggest that proteins may play an important role in the adhesion of Cuvierian tubules from *H. forskåli* (DeMoor et al., 2003; Flammang & Jangoux, 2004; Müller et al., 1972). For example, the adhesive residue left when tubules are peeled from a surface consists mainly of protein (DeMoor et al., 2003), and the treatment of tubules with proteases causes loss of adhesion (Müller et al., 1972). However, it has been reported that the proteins most likely differ between species (Flammang & Jangoux, 2004), making further comparative biochemical surveys important for elucidating the mechanism.

The effect of urea on tubule-glass adhesion showed that bond strength decreased progressively with increasing urea concentration until it was completely lost at 2 M urea (Figure 7). However, if tubules that had been incubated for about 60 sec in 2 M urea were then rinsed for about 60 sec in simulated sea water, some adhesion was restored, although the extent was rather variable. Urea disrupts hydrogen bonding, and its effect on adhesion may reflect some partially reversible protein unfolding (Zahn et al., 1972). The rapidity and partial reversibility of the effect indicates that there is not a complete urea-mediated release of proteins from the tubule surface.

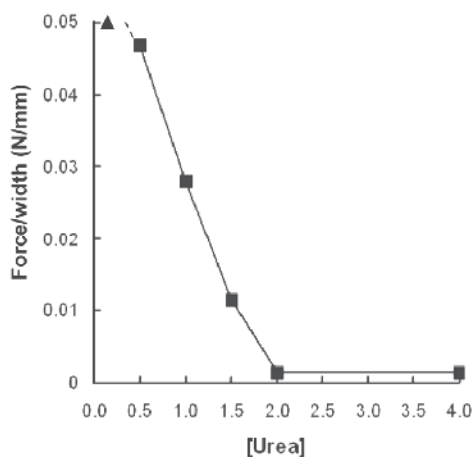


Fig. 7. The effect of different washing solutions on the adhesiveness of *H. dofleinii* Cuvierian tubules for glass. (C) The effect of urea concentration, where ▲ indicates conditions where the force per unit width exceeded 0.05 N/mm.

#### 4. Conclusion

The distinct features of the Cuvierian tubule adhesion mechanism, especially its rapid action under water, are unique. If the mechanism can be understood, then it may be possible to design a synthetic system with analogous properties. An adhesive that provided instant grip in an aqueous environment would be very valuable, especially in medical applications, as the majority of existing adhesives bind well only to dry surfaces.

It appears that although the tubules of *H. dofleinii* are distinct from those of other species, especially in their size and the number expelled, the adhesive properties of these Cuvierian tubules (including preferences for hydrophilic surfaces, pH optima, etc.) are similar to those found in other species, even if mechanistic details may differ between species as has been proposed previously (Flammang and Jangoux, 2004). It is thought that during expulsion and tubule elongation, granular cells that are internal in the pre-release tubule become located

on the tubule surface and release their contents on contact with a surface (VandenSpiegel and Jangoux, 1987) leading (in whole or in part) to the observed adhesion. Histology has shown that these granules contain protein and lipid, but lack polysaccharide (VandenSpiegel and Jangoux, 1987). Biochemical studies have indicated that the granules contain a protein of around 10 kDa, and it has been suggested that polymers of this protein account for the higher molecular weight proteins that are seen in the adhesive prints (Flammang and Jangoux, 2004), but this seems highly unlikely in *H. dofleinii* as the protein bands are very well resolved by gel electrophoresis and the calculated molecular weights of these bands do not conform to such a regular series of increases.

Our present study emphasises that the adhesives of natural systems are optimised for the specific environments in which they have evolved, such as the present marine environment. An analogue intended for medical use would need to be optimised to yield maximum adhesion in the physiological conditions that prevail in mammalian tissues. In the present case, the adhesion works better at higher NaCl concentrations that found in medical applications so understanding more about the mechanism and the protein structures and properties will be needed in order to adapt this system for applications where lower NaCl concentrations are present.

## 5. Acknowledgments

We wish to thank Nicole Murphy for assistance with Holothurian collection and Dr Anita Hill for helpful discussions. This study was facilitated by access to the Australian Proteome Analysis Facility supported under the Australian Government's National Collaborative Research Infrastructure Strategy (NCRIS). The project received support from the CSIRO Wealth from Oceans National Research Flagship.

## 6. References

- Cohen, S.A. (2001). Amino acid analysis using precolumn derivatisation with 6-aminoquinolyl-*N*-hydroxysuccinimidyl carbamate. *Methods in Molecular Biology*, Vol.159, pp. 39-47, ISSN 1064-3745
- Cohen, S.A. & DeAntonis, K.M. (1994). Applications of amino acid analysis derivatisation with 6-aminoquinolyl-*N*-hydroxysuccinimidyl carbamate: Analysis of feed grains, intravenous solutions and glycoproteins. *Journal of Chromatography*, Vol.661, No.1-2, (February), pp. 25-34, ISSN 0021-9673
- DeMoor, S.; Waite, J.H.; Jangoux, M. & Flammang, P. (2003). Characterization of the adhesive from cuvierian tubules of the sea cucumber *Holothuria forskali* (Echinodermata, Holothuroidea). *Marine Biotechnology*, Vol.5, No.1, (January), pp. 45-57, ISSN 1436-2228
- Dimas, D.A.; Dallas, P.P.; Rekkas, D.D. & Choulis, N.H. (2000) Effect of several factors on the mechanical properties of pressure-sensitive adhesives used in transdermal therapeutic systems. *AAPS PharmSciTech*, Vol.1, No.2, (June), pp. 80-87, ISSN 1530-9932
- Doolittle, R.F. (1986). *Of URFs and ORFs: a primer on how to analyse derived amino acid sequences*, University Science Books, ISBN 0-935702-54-7, Mill Valley, CA, USA
- Flammang, P. & Jangoux, M. (2004). *Final Report ONR Grant N00014-99-1-0853*

- Flammang, P.; Ribesse, J. & Jangoux, M. (2002) Biomechanics of adhesion in sea cucumber Cuvierian tubules (Echinodermata, Holothuroidea). *Integrative and Comparative Biology*, Vol.42, No.6, (December), pp. 1107-1115, ISSN 1540-7063
- Hamel, J.-F. & Mercier, A. (2000). Cuvierian tubules in tropical holothurians; usefulness and efficiency as a defence mechanism. *Marine and Freshwater Behaviour and Physiology*, Vol.33, pp. 115-139, ISSN 1023-6244
- Hwang, D.S.; Zeng, H.; Masic, A.; Harrington, M.J.; Israelachvili, J.N. & Waite, J.H. (2010). Protein- and metal-dependent interactions of a prominent protein in mussel adhesive plaques. *Journal of Biological Chemistry*, Vol.285, No.33, (August), pp. 25850-25858, ISSN 0021-9258
- Jones, I.; Lindberg, C.; Jakobsson, S.; Hellqvist, A.; Hellman, U.; Borg, B. & Olsson, P.E. (2001). Molecular cloning and characterization of spiggin. *Journal of Biological Chemistry*, Vol.276, No.21, (May), pp. 17857-17863, ISSN 0021-9258
- Kamino, K. (2008). Underwater adhesive of marine organisms as the vital link between biological science and material science. *Marine Biotechnology*, Vol.10. No.2, (March), pp. 111-121, ISSN 1436-2228
- Laemmli, U.K. (1970). Cleavage of structural proteins during the assembly of the head of bacteriophage T4. *Nature*, Vol.227, No.5259, (August), pp. 680-685, ISSN 0028-0836
- Lawrence, J.M. (2001). Function of eponymous structures in echinoderms; a review. *Canadian Journal of Zoology*, Vol.79, No.7, (July), pp. 1251-1264, ISSN 0008-4301
- Lin, Q.; Gourdon, D.; Sun, C.; Holten-Andersen, N.; Anderson, T.H.; Waite, J.H. & Israelachvili, J.N. (2007). Adhesion mechanisms of the mussel foot proteins mfp-1 and mfp-3. *Proceeding of the National Academy of Sciences of the United States of America*, Vol.104, No.10, (March), pp. 3782-3786, ISSN 0027-8424
- Mancuso-Nichols, C.A.; Nairn, K.M.; Glattauer, V.; Blackburn, S.I.; Ramshaw, J.A.M. & Graham, L.D. (2009) Screening microalgal cultures in search of microbial exopolysaccharides with potential as adhesives *Journal of Adhesion*, Vol.85, No.2-3, pp. 97-125, ISSN 0021-8464
- Müller, W.E.G.; Zahn, R.K. & Schmid, K. (1972). The adhesive behaviour in Cuvierian tubules of *Holothuria forskali*. Biochemical and biophysical investigations. *Cytobiology*, Vol.5, No.3, pp. 335-351, ISSN 0070-2463
- Nakano, M.; Shen, J.R. & Kamino, K. (2007). Self-assembling peptide inspired by a barnacle underwater adhesive protein. *Biomacromolecules*, Vol.8, No.6, (June), pp. 1830-1835, ISSN 1525-7797
- VandenSpiegel, D. & Jangoux, M. (1987). Cuvierian tubules of the holothuroid *Holothuria forskali* (Echinodermata): a morphofunctional study. *Marine Biology*, Vol.96, No.2, pp. 263-275, ISSN 0025-3162
- VandenSpiegel, D.; Jangoux, M. & Flammang, P. (2000). Maintaining the line of defence: regeneration of Cuvierian tubules in the sea cucumber *Holothuria forskali* (Echinodermata, Holothuroidea). *Biological Bulletin*, Vol.198, No.1, (February), pp. 34-49, ISSN 0006-3185
- Watson, M.R. & Silvester, N.R. (1959). Studies of invertebrate collagen preparations. *Biochemical Journal*, Vol.71, No.3, (March), pp. 578-584, ISSN 0264-6021
- Zahn, R.K.; Müller, W.E.G. & Michaelis, M. (1973). Sticking mechanisms in adhesive organs from a *Holothuria*. *Research in Molecular Biology*, Vol.2, pp. 47-88, ISSN 0340-5400



# Mechanical and Biological Properties of Bio-Inspired Nano-Fibrous Elastic Materials from Collagen

Nobuhiro Nagai<sup>1,2</sup>, Ryosuke Kubota<sup>2</sup>,

Ryohei Okahashi<sup>2</sup> and Masanobu Munekata<sup>2</sup>

<sup>1</sup>*Division of Clinical Cell Therapy, Center for Advanced Medical Research and Development, ART, Tohoku University, Graduate School of Medicine*

<sup>2</sup>*Division of Biotechnology and Macromolecular Chemistry, Graduate School of Engineering, Hokkaido University  
Japan*

## 1. Introduction

Collagen-based biomaterials have been widely used in medical applications, because of its many advantages, including low antigenicity, abundant availability, biodegradability, and biocompatibility [1]. Collagen represents the major structural protein, accounting for nearly 30% of all vertebrate body protein. The collagen molecule comprises three polypeptide chains ( $\alpha$ -chains) which form a unique triple-helical structure (Fig. 1) [2]. Each of the three chains has the repeating structure glycine-X-Y, where X and Y are frequently the imino acids proline and hydroxyproline (Fig. 1b). The collagen molecules self-aggregate through fibrillogenesis into microfibrils forming extracellular matrix (ECM) in the body [3-5]. The fibrils provide the major biomechanical matrix for cell growth (Fig. 1a), allowing the shape of tissues to be defined and maintained. The main application of collagen for biomaterials is as a scaffold for tissue engineering and a carrier for drug delivery [2, 6-9]. Many different forms of collagen biomaterials, such as film [10, 11], gel [12-17], sponge [18-20], micro-/nano-particle [21, 22], and fiber [23], have been fabricated and used in practice. However, most collagen biomaterials become brittle and fail under quite low strains, which limit their application to biomedical engineering fields that need larger mechanical properties, especially elasticity [16].

Recently, we reported a novel crosslinking method of improving the mechanical properties and thermal stability of collagen [24]. The method mimics actual biological events to form collagen matrix in the body; monomeric collagens extruded from cells into extracellular environment initially form microfibrillar aggregates, then lysyl oxidase crosslinking during their assembly to form fibrils (Fig. 1). The *in vitro* crosslinking during collagen fibrillogenesis, namely “bio-inspired crosslinking”, creates a crosslinked collagen fibrillar gel with high mechanical properties at certain crosslinking agent concentrations [25, 26]. Fibril formation involves the aggregation and alignment of collagen molecules, and helps increase the collagen’s thermal stability. The introduction of crosslinking during fibril formation further increases the thermal stability of collagen. The synergistic effects of crosslinking and fibril formation are found to enable an increase in the thermal stability of

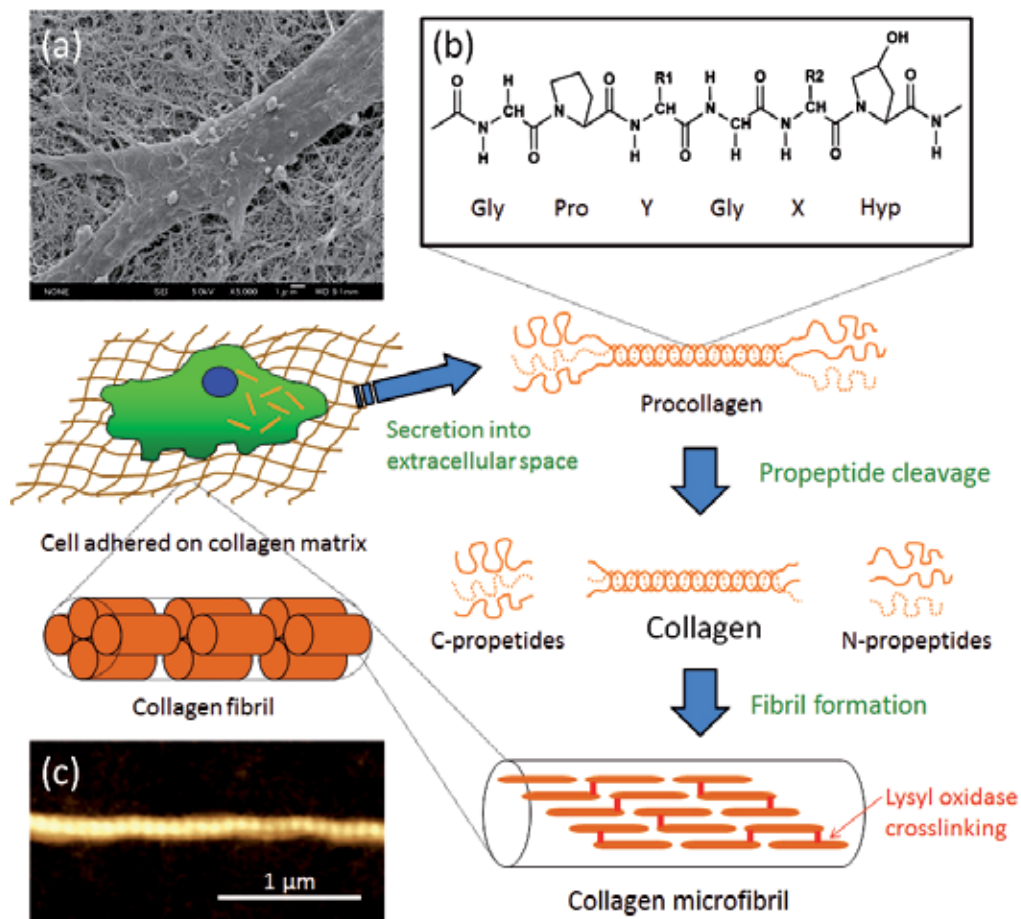


Fig. 1. Schematic representation of collagen synthesis process. Procollagen consists of a 300 nm long triple helical domain (comprised of three alpha-chains each of approximately 1000 residues) flanked by a trimeric globular C-propeptide domain and a trimeric N-propeptide domain. Procollagen is secreted from cells and is converted into collagen by the removal of the N- and C-propeptides by proteases. The collagen spontaneously self-assembles into cross-striated fibrils that occur in the extracellular matrix of connective tissues. The fibrils are stabilized by covalent crosslinking, which is initiated by oxidative deamination of specific lysine and hydroxylysine residues in collagen by lysyl oxidase. (a) Scanning electron microscopy image of a human fibroblast adhered on reconstituted salmon collagen fibrillar matrix [17]. (b) Chemical structure of a collagen alpha-chain. (c) Atomic force microscopy image of reconstituted salmon collagen fibril [17]. The repeating broad dark and light zones (where  $D=67$  nm, the characteristic axial periodicity of collagen) can be seen in the fibril.

salmon-derived collagen (SC) [24]. Additionally, heat denaturation of the bio-inspired crosslinked SC gel provides elastic materials, which has the elongation of over 200% at break point [24]. So far, the elasticity of the collagens that had been crosslinked “after” fibrillogenesis is not as high as that crosslinked “during” fibrillogenesis (bio-inspired crosslinking) [25]. This may indicate that the bio-inspired crosslinking confer intrafibrillar

crosslinking as well as interfibrillar one, allowing for homogenous crosslinking sites and larger mechanical properties. Therefore, the bio-inspired crosslinking may provide more wide range of applications of collagen biomaterials. However, the bio-inspired crosslinking has not yet been applied to bovine collagen (BC), which is widely used for medical applications for past decades, because the bio-inspired crosslinking has been developed for thermal stabilization of "fish collagens" with low-denaturation temperature to develop marine-derived collagen biomaterials [13-17, 24-26]. In this study, we studied the crosslinking condition to create bio-inspired crosslinked BC gel and prepared the elastic material from the BC gel (e-BC gel) by heat treatment. The mechanical properties (tensile strength and elongation rate) and biological properties (biodegradability, cell culture, and blood compatibility) of the e-BC gel were evaluated. Herein, we report the fabrication of the bio-inspired elastic material from BC and demonstrate its applicability for biomaterials, especially in vascular tissue engineering.

## 2. The bio-inspired crosslinking conditions for BC

Acid-soluble collagen molecules self-assemble and form fibrils under physiological conditions. The pH, NaCl concentration, and temperature are important factors to provide a successful reconstituted collagen fibrillar gel. First, we evaluated the effect of NaCl concentrations on fibril formation of BC at constant pH of 7.4 and temperature of 37°C. The fibril formation of BC was monitored by a turbidity change observed at 310 nm [26, 27]. Figure 2 shows that a rapid rise in turbidity was observed in the mixture of BC solution and 30 mM Na-phosphate buffer at NaCl concentration from 50mM to 100 mM. Then, the rise in turbidity increase was gradually decreased at over 140 mM NaCl. The fibril formation rate of collagen is known to be reduced by addition of salts [4], which appears to reduce electrostatic interaction among collagen molecules. The bio-inspired crosslinking needs active fibrillogenesis during crosslinking (see below) [17, 26]. Therefore, the optimum range of NaCl concentration for BC fibril formation was determined to be 50-100 mM.

Cross-linking generally reinforces the biomaterials composed of collagen fibrils for further improvement of mechanical properties. Various techniques for stabilizing collagen have been developed and reported. These techniques are divided into chemical treatments and physical treatments. Glutaraldehyde is one of the most widely used chemical agents [28, 29]; it is known, however, that there are side effects to its use in cross-linking [30], for example, cytotoxicity, enhancement of calcification, and a mild inflammatory response compared with using other reagents. The water soluble condensing agent 1-ethyl-3-(3-dimethylaminopropyl) carbodiimide hydrochloride (EDC) has been reported to be significantly less cytotoxic than glutaraldehyde because EDC reagents do not remain in the linkage and are simply washed away during the cross-linking process [28, 29]. On the other hand, physical cross-linking methods such as UV irradiation [31, 32] and dehydrothermal treatment [33, 34] do not introduce any additional chemical units. These methods may therefore be more biocompatible than chemical treatments. However, the mechanical properties of materials cross-linked by physical treatments are lower than those cross-linked by chemical treatments. Therefore, EDC was used for a crosslinking agent in this study.

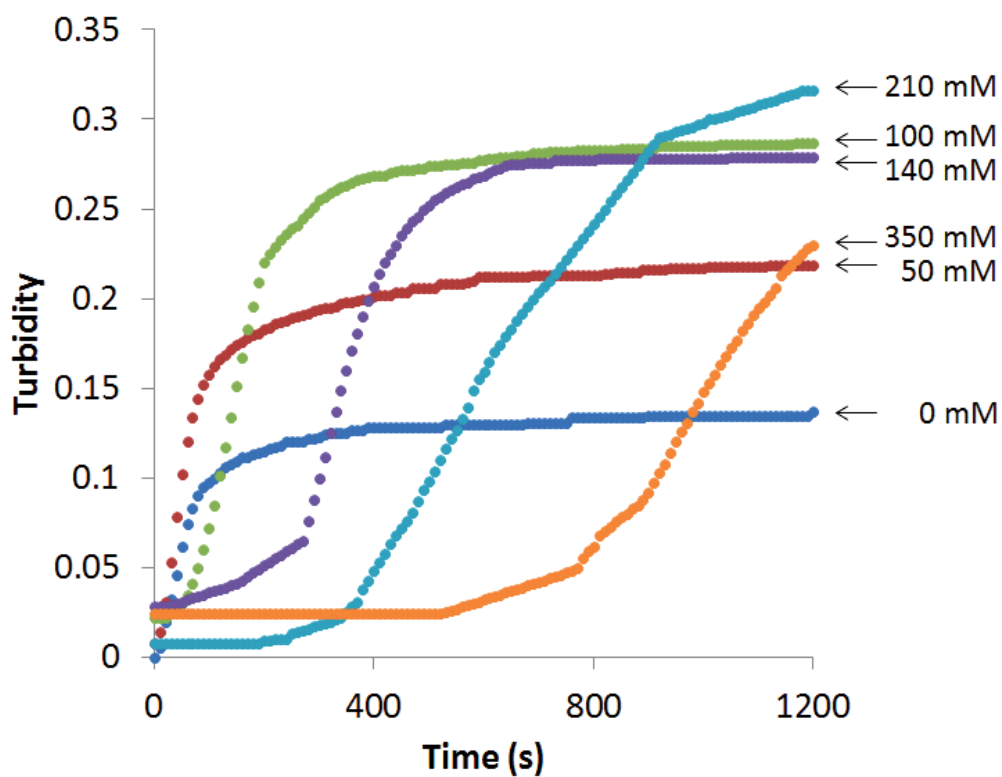


Fig. 2. Effect of NaCl concentration on fibril formation curve. The values in the graphs indicate the final NaCl concentrations in the gels.

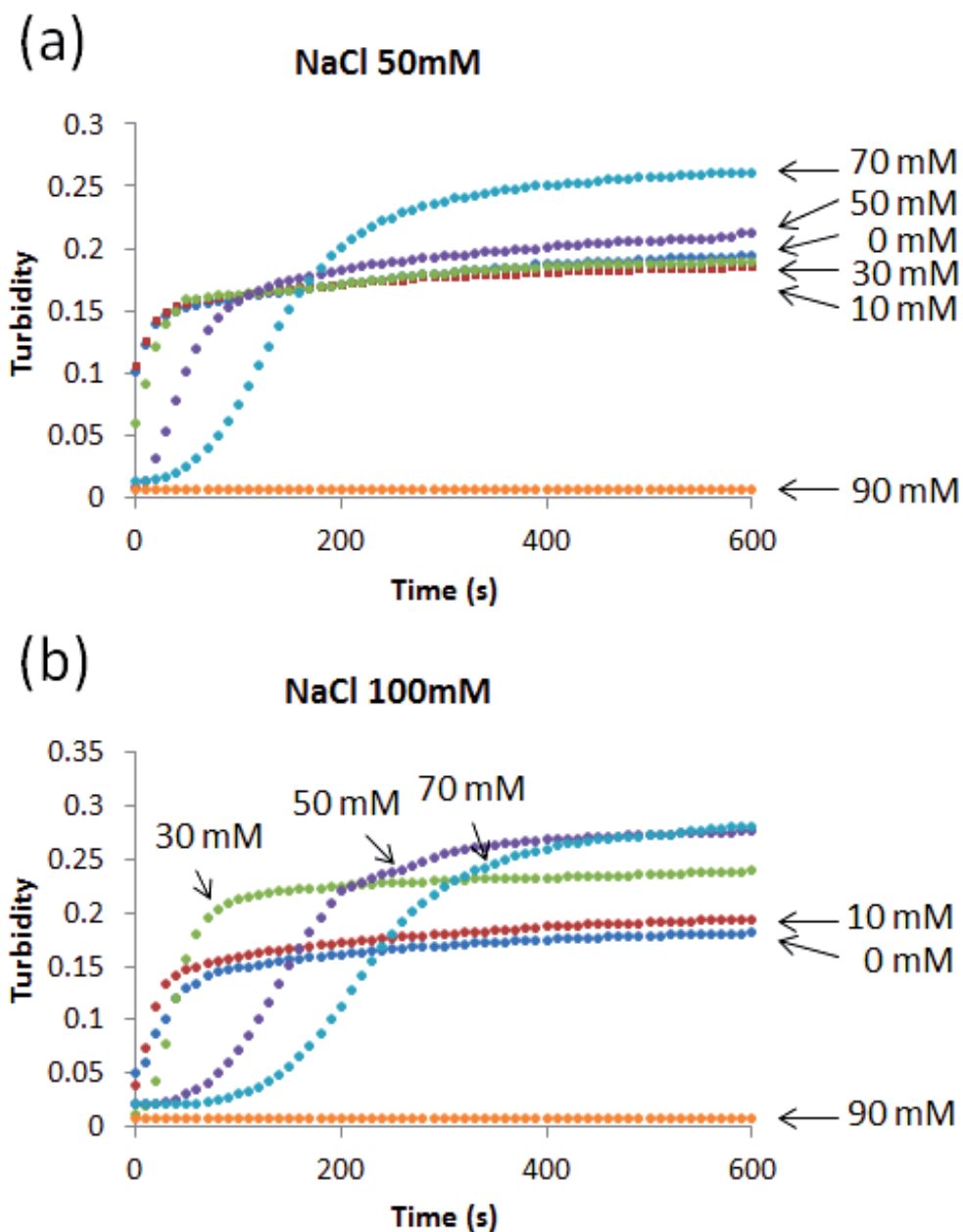


Fig. 3. Effect of EDC concentrations on fibril formation curve in the presence of 50 mM NaCl (a) and 100 mM NaCl (b). The values in the graphs indicate the final EDC concentrations in the gels.

The turbidity changes in BC solution mixed with Na-phosphate buffer including various EDC concentration at 50 mM or 100 mM NaCl were monitored using a spectrophotometer

(Fig. 3a, b). The rate of fibril formation decreased with increasing EDC concentration, which indicates EDC exhibited an inhibitory effect on collagen fibril formation. These inhibitory effects were probably the results of the rapid reaction of EDC to monomeric collagens upon mixing of the EDC containing buffer and acidic collagen solution, by which the ability to form fibrils was reduced or lost through random and nonfibrous aggregation of monomeric collagens. Further increased EDC concentration above 90 mM completely suppressed fibril formation irrespective of NaCl concentrations. Based on these results, it appeared that a buffer that would enable a faster fibril formation rate would be desirable. According to a previous report, EDC is sufficiently stable and active under such conditions [35].

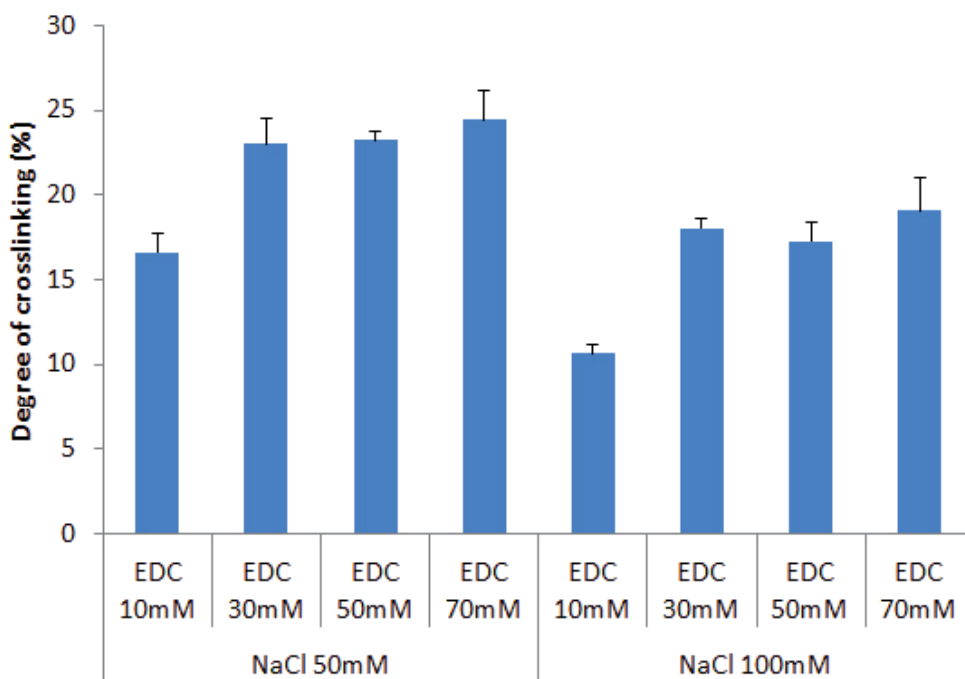


Fig. 4. Degree of crosslinking in the collagen. Values are mean  $\pm$  SD (n=4).

The degree of crosslinking was determined as the decrease in the free amino group content of the collagen molecules [19, 26]. The free amino group content was measured spectrophotometrically after the reaction of the free amino groups with 2,4,6-trinitrobenzenesulfonic acid and was expressed as the decrease in the ratio of the free amino group content of the crosslinked sample to that of the uncrosslinked sample. An increase in the degree of crosslinking with increase in the EDC concentration was observed (Fig. 4). The degree of crosslinking was slight lower at NaCl concentration of 100 mM compared to the NaCl concentration of 50 mM. This may be attributed to lower ability of fibril formation observed at NaCl concentration of 50 mM. Fig 2 shows that the plateau level in turbidity at 50 mM NaCl was lower than that at 100 mM NaCl. Lower fibril formation may result in an increase of nonfibrous aggregates, which can lead to high degree of crosslinking due to increased sites of crosslinking in monomeric collagens. The synergistic effects of crosslinking and fibril formation were thought to be complete at EDC and NaCl concentrations of 70 mM and 100 mM, respectively.

### 3. Fibril formation of BC

To produce an elastic material from bio-inspired crosslinked BC gel (e-BC gel), heat denaturation process is needed. By heat treatment, the cross-linked collagen fibrils shrink, maintaining the cross-linkage among the collagen molecules and fibrils through the denaturation of triple-helical collagen molecules to the random-coil form [24]. At the same time, uncross-linked collagen molecules and fibrils may be lost through dissolution to water. In fact, the original BC gels crosslinked with the EDC concentrations of 30-70 mM showed drastic shrinkage (Fig. 5) and rubber-like elasticity after heat treatment at 60°C for 5 min. The BC gels crosslinked with EDC concentrations of 0-10 mM dissolved away after heat treatment due to incomplete crosslinking.

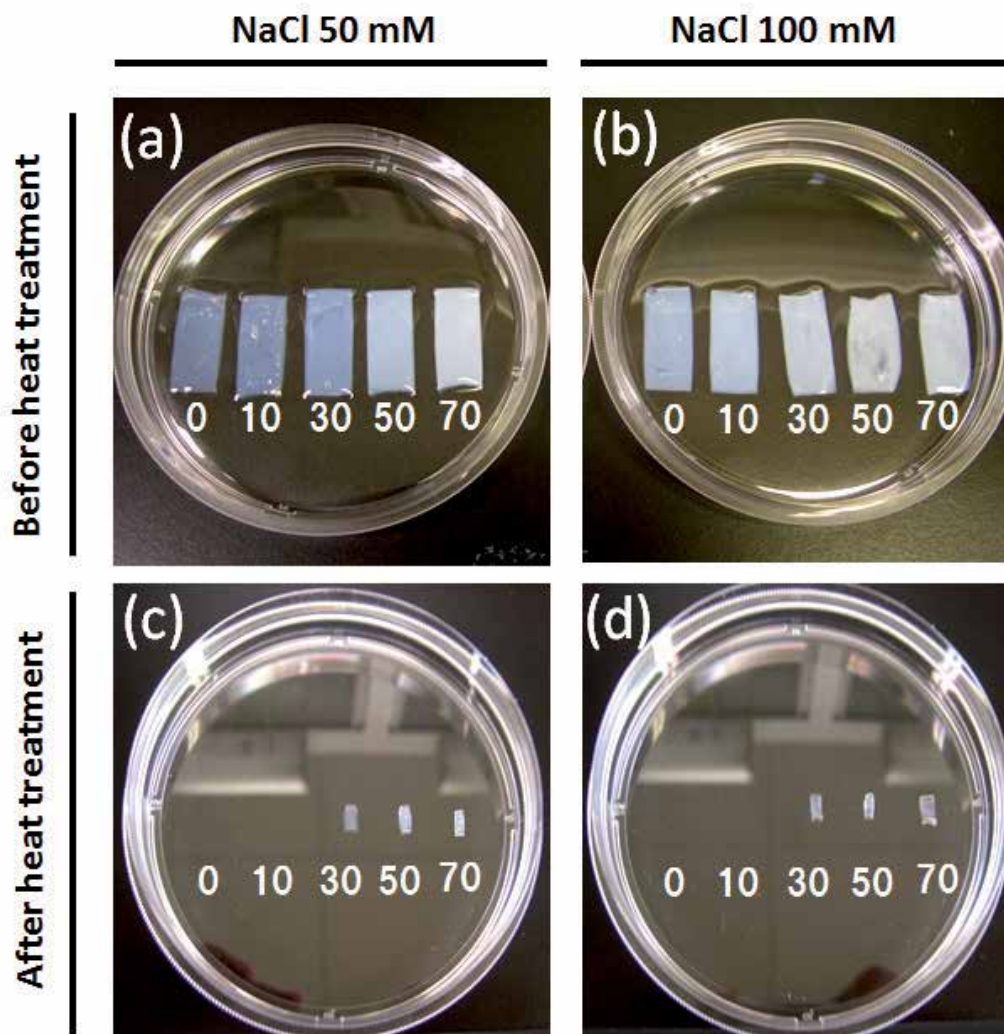


Fig. 5. Appearances of BC gels (a, b) and e-BC gels (c, d). The values in the graphs indicate the final EDC concentrations (mM) in the gels.

The collagen fibrils were observed by high-resolution scanning electron microscopy (SEM). The preparation of the specimen was performed according to a previous report [16, 24]. Figure 6 shows the well-developed networks of nano-fibrils on the BC gel and e-BC gel. The width of the fibrils on the BC-gel was in the range of 50–100 nm (Fig. 6a). However, a wider (width; >200 nm) and winding fibril-like structure was observed on the e-BC gel (Fig. 6b), indicating that the fibril structure of collagen was deformed through the heat treatment. The wide and winding fibril-like structure of the e-BC gel should be directly derived from the collagen nano-fibrils of the original BC gel through swelling of the fibrils by comparison of both surface structures.

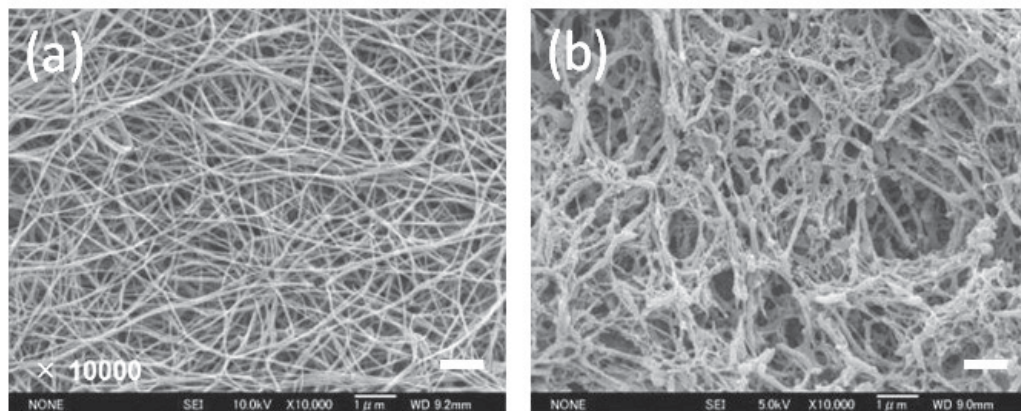


Fig. 6. SEM images of BC gels (a) and e-BC gels (c). Bars: 1  $\mu\text{m}$ .

#### 4. Mechanical properties of e-BC gel

The mechanical properties of the e-BC gel were evaluated by tensile tests. The original BC gel rarely had elasticity and stretchability similar to the usual collagen materials. However, the e-BC gel showed rubberlike elasticity and high stretchability. Figure 7 shows the stress-strain curves to the breaking point obtained in the strain rate of 0.1 mm/s ( $n = 5$ ). Salmon-derived elastic collagen gels (e-SC gel) were used as controls [24]. The mean values  $\pm$  standard deviation (SD) of elongation at the break of the e-BC gel and e-SC gel were  $201 \pm 47\%$  and  $260 \pm 59\%$ , respectively (Fig. 7c). At the early stage of loading, stress was almost linearly increased depending on the strain. Above a strain of ca. 100%, an increase in strain hardening was observed. There was no significant difference in elongation between the two e-gels. According to the report by Koide and Daito [31], collagen films reinforced by traditional cross-linking reagents, glutaraldehyde and tannic acid, showed only small elongation at the breaking point (6.6% and 12.4%, respectively). Weadock et al. showed small ultimate strains (approximately 40% and 30%) of collagen fibers cross-linked by UV irradiation and dehydrothermal treatment, respectively [36]. Even a purified skin with an intact fibrous collagen network gives elongation at a breaking point of 125% [36]. Recently, it was reported that a chemically cross-linked collagen-elastin-glycosaminoglycan scaffold, which are the contents analogous to the actual tissue/organs, demonstrated good stretchability (150% strain) [37]. To the best of our knowledge, this is the first report of a material from bovine collagen with elongation at a breaking point over 200%. Although the mechanism of the high stretchability was not well understood, the denaturation of the



collagen molecules probably plays an important role in the elongation, i.e., the bend structure of denatured collagen fibrils observed in Fig. 6b is considered to provide its rubber-like stretchability.

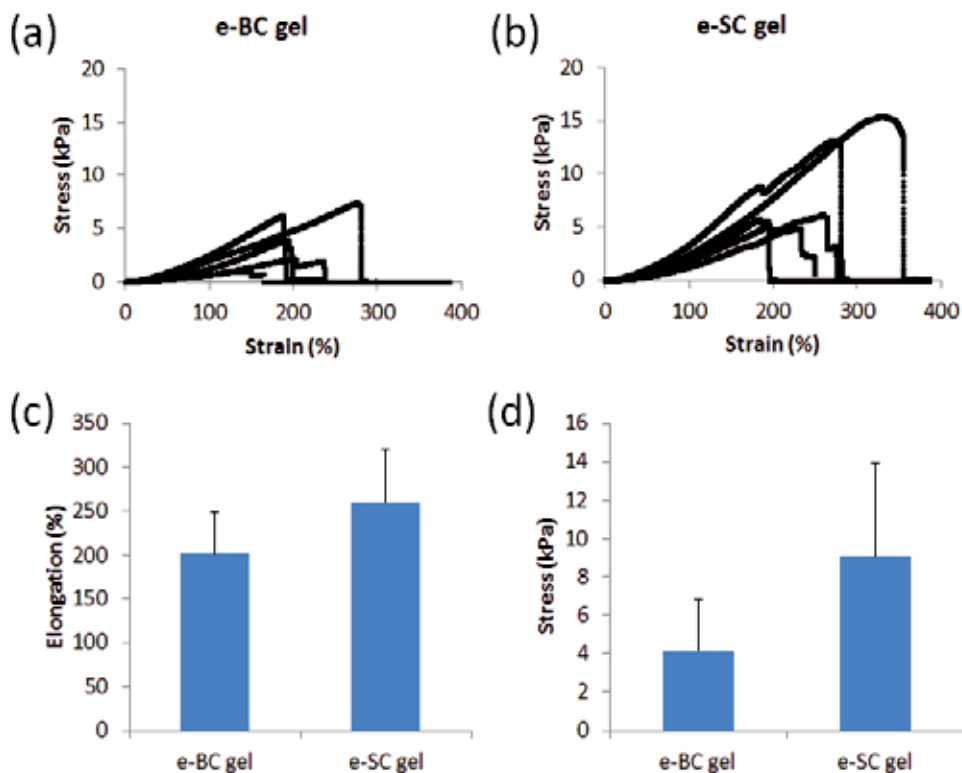


Fig. 7. Stress-strain curves generated from tensile testing of e-BC gels (a) and e-SC gels (b). The specimen ( $5 \times 3 \times 12$  mm) was gripped to achieve a gauge length of 8 mm and stretched in the strain rate of 1.25%/s. (c) Elongation at the break of the e-BC gel and e-SC gel. (d) Ultimate strength at the break of the e-BC gel and e-SC gel. Values are mean  $\pm$  SD ( $n=5$ ).

The mean values  $\pm$  SD of ultimate strength at the break of the e-BC gel and e-SC gel were  $4.1 \pm 2.6$  kPa and  $9.0 \pm 4.8$  kPa, respectively (Fig. 7d). The strength of the e-BC gels was lower than that of e-SC gels, although there was no significant difference between the two. Collagen exhibits a limited mechanical resistance so that collagen requires an additional skeletal material such as inorganic materials [38]. Bio-inspired crosslinking can provide a collagen scaffold with high mechanical strength as well as stretchability. It is useful without the addition of any other material. Because a collagen solution is a precursor for fabrication of various collagen forms, bio-inspired crosslinking would be a useful fabrication process of widely various collagen biomaterials.

## 5. Biological properties of e-BC gel

To investigate the potential of the e-BC gel for use as a cell culture scaffold, we measured the growth rates of human umbilical vein endothelial cells (HUVECs) cultured on the e-BC gel.

The cell number was evaluated by the 3-[4,5-dimethylthiazol-2-yl]-2,5-diphenyl tetrazolium bromide (MTT) test [13]. The MTT test is an established method to determine viable cell number by measuring the metabolic activity of cellular enzymes. Figure 8 shows steady increases in cell number with culture time on both the e-BC gel and tissue culture plate (TCP). There was a lag time before steady increase in cell number on the e-BC gel. Semler et al. reported that cells shows high growth rate on matrices with high mechanical compliance such as TCP, whereas the cells aggregate three-dimensionally on matrices with low mechanical compliance such as collagen gel [39]. Therefore, the difference in the mechanical properties of the surface of the culture substrate might affect the initial rate of cell growth.

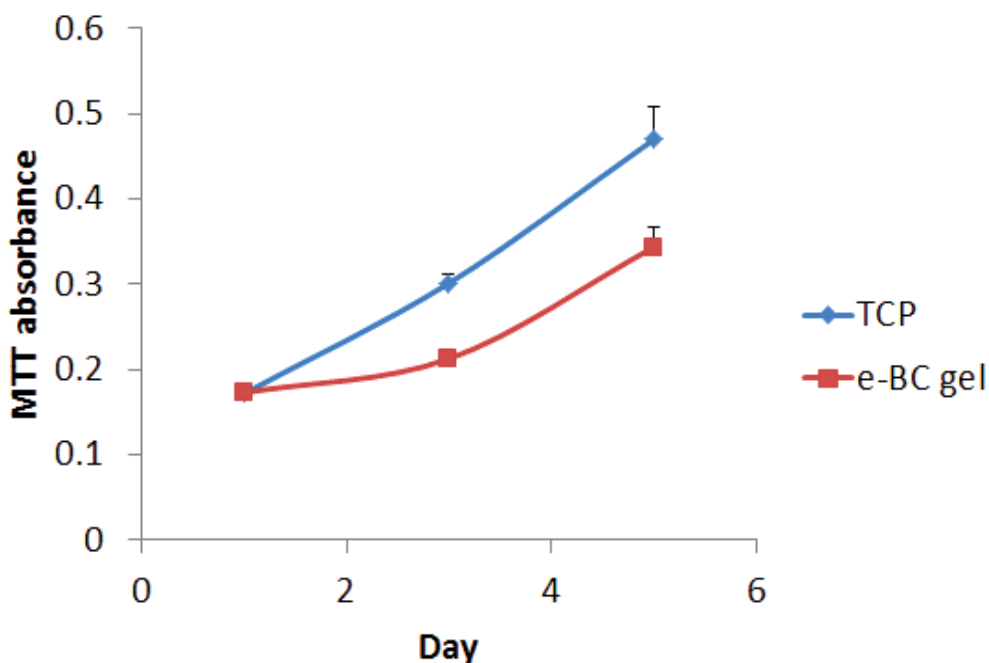


Fig. 8. Growth curves of HUVECs cultured on e-BC gels and plastic tissue culture plate. Values are mean  $\pm$  SD ( $n=4$ ).

The SEM images show the distribution and spreading morphology of the HUVECs cultured on the e-BC gel at day 1 and day 5 after cultivation (Fig. 9). Apparently, the cells at 5d cultivation were confluent and showed cobblestone-like morphologies (Fig 9b). HUVECs also grow better on the e-SC gel and shows confluent at day 6 after cultivation [13]. Therefore, the e-BC gel could be used as a cell culture scaffold as well as the e-SC gel. EDC cross-links collagen molecules by the formation of isopeptides without being incorporated itself, thus precluding depolymerization and the possible release of potentially cytotoxic reagents. Furthermore, the by-product of the cross-linking reaction and un-reacted EDC in the e-BC gel should be completely removed by the drastic shrinkage in hot water. It is expected that the e-BC gel has good biocompatibility and no cytotoxicity.

To assess the degradability of the e-BC gel in collagenase solution (50 U/ml), protein content measurement was performed using a bicinchoninic acid protein assay kit as

previously described [40]. Figure 10 shows that e-BC gel was completely digested for 24 h as well as the e-SC gel. The e-BC gel degraded slightly later than the e-SC gel. This may be due to the low denaturation temperature of SC (19°C). The physiological concentration range of collagenase is approximately 1 U/ml [41], therefore, the e-BC gels might show the slow degradation profile *in vivo* than the *in vitro* results. Additionally, e-SC gel gradually degrades 1 month after implantation in rat subcutaneous pouches [16], e-BC gel, therefore, would show the same or later biodegradation profile *in vivo*.

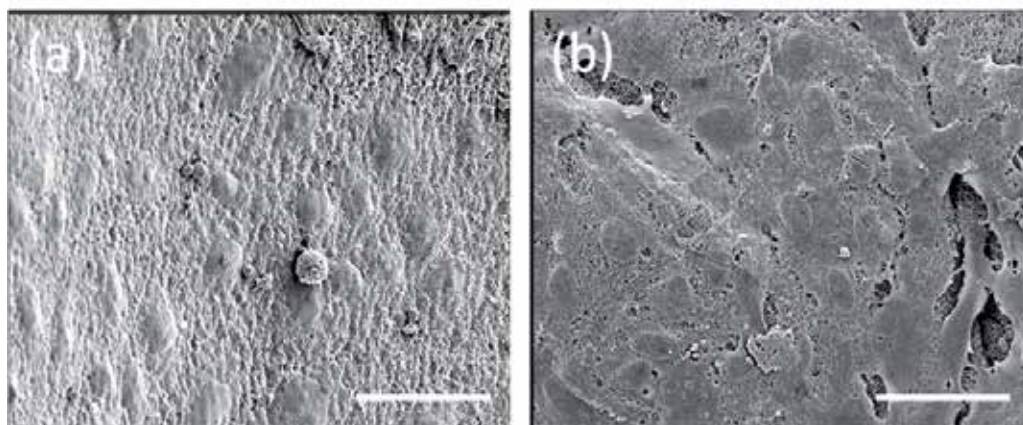


Fig. 9. SEM images of HUVECs cultured on e-BC gel for 1d (a) and 5d (b). Bars: 50 μm.

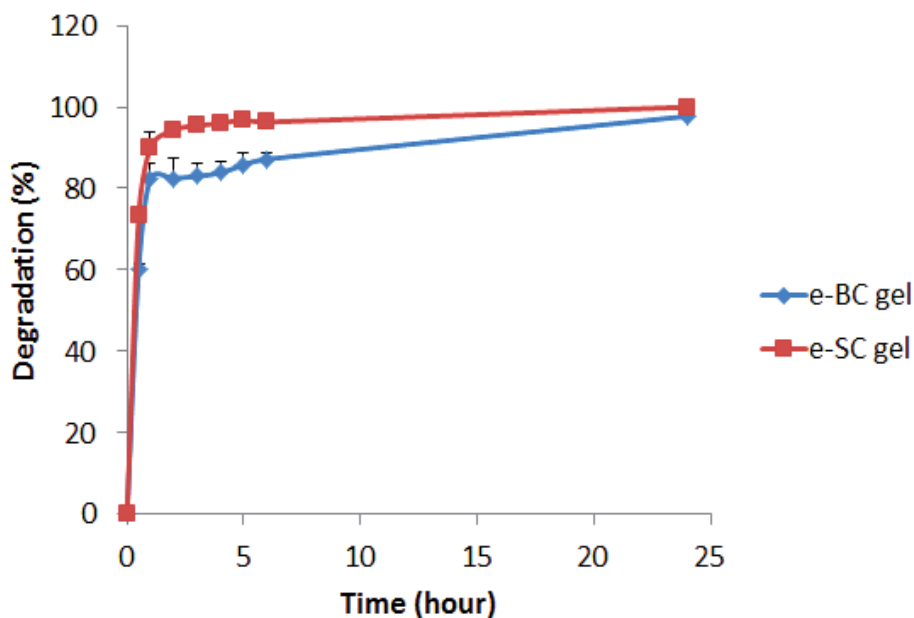


Fig. 10. In vitro degradation rate of e-BC gel and e-SC gel in collagenase solution. Values are mean  $\pm$  SD (n=4).

Owing to the mechanical, biological, and biodegradable properties of the e-BC gel, it could potentially be used to engineer blood vessels *in vivo*. Synthetic materials such as polyethylene terephthalate (Dacron) and expanded polytetrafluoroethylene (ePTFE) have been clinically applied as vascular grafts for a long time to replace or bypass large-diameter blood vessels. However, when used in small-diameter blood vessels (inner diameter < 6 mm), the patency rates are poor compared to autologous vein grafts. These failures are due to early thrombosis and gradual neointimal hyperplasia, and the pathological changes occurred due to the lack of blood or mechanical compatibility of the synthetic grafts [42]. To address this problem, tissue engineering approach is promising. A variety of biodegradable polymers and scaffolds have been evaluated to develop a tissue-engineered vascular graft [43-46]. These approaches depend on either the *in vitro* or *in vivo* cellular remodeling of a polymeric scaffold. For successful *in vivo* cellular remodeling, the biocompatibility, biodegradability, and mechanical properties of the scaffold must be suitable to the dynamic environment of the blood vessel. Therefore, the ideal scaffold should employ a biocompatible and biodegradable polymer with elastic properties that interact favorably with cells and blood. Therefore, the interaction of the e-BC gel with rat whole blood and plasma was investigated to assess their blood compatibility for use in vascular-tissue engineering.

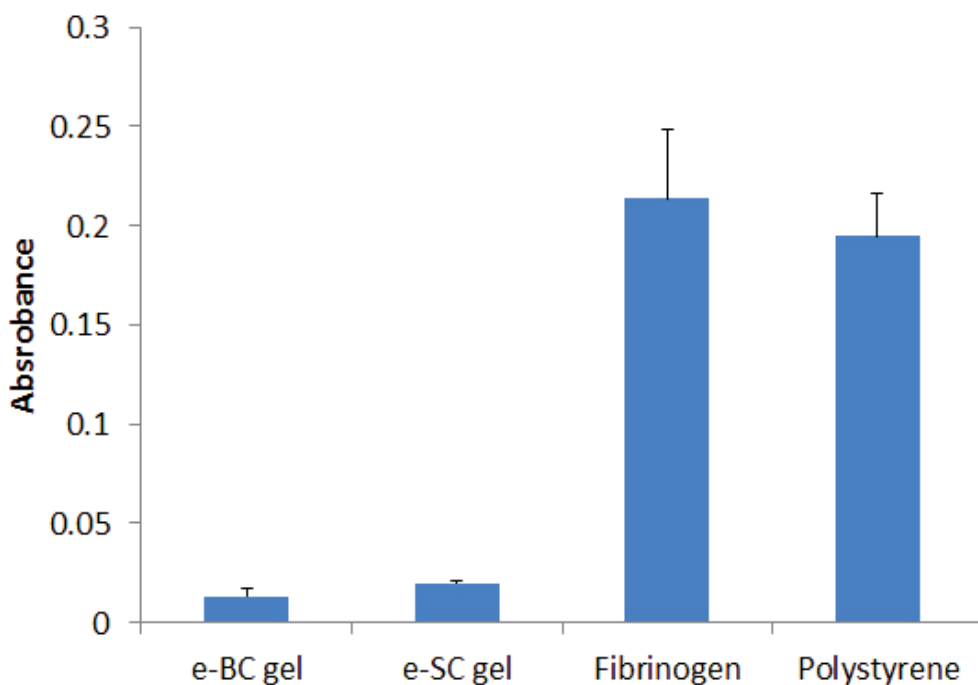


Fig. 11. Platelet adhesion rates on the e-BC gel, e-SC gel, and the control samples. Values are mean  $\pm$  SD (n=4).

After incubation of the e-BC gel with platelet-rich plasma (PRP) collected from rat blood, the colored *p*-nitrophenol produced by the acid-phosphatase reaction of the platelets was measured with a microplate reader at an absorbance of 405 nm. The percentage of adherent

platelets was calculated according to the methods reported previously [14]. Figure 11 shows the number of platelets that adhered to the samples. The platelet number was estimated from the acid phosphatase reaction [47]. There was a linear relationship between the PRP concentration and the absorbance values at 405 nm, indicating that the acid phosphatase reaction of the platelets may be considered a reliable indicator of platelet number (data not shown). The results demonstrate that the platelet adhesion rates were markedly low on the e-BC gel when compared to the fibrinogen-coated or polystyrene surfaces. The e-SC gel also showed an adhesion rate as low as the e-BC gel. We are separately studying the fabrication of a vascular graft using the e-SC gel [16]. Consequently, the e-BC gel can potentially be used for the fabrication of tissue-engineered vascular graft.

Considering that the platelets adhered better to the collagen-coated than to the gelatin-coated surface [14], the anticoagulant ability of the e-BC gel may have been due to heat denaturation. The e-BC gel was prepared by heat treatment at 60°C resulting in collagen denaturation (gelatinization). Polanowska-Grabowska and coworkers reported that the platelet adhesion rate on a gelatin-coated surface was lower than on collagen-coated or fibrinogen-coated surfaces [48]. However, blood coagulation is known to depend on material properties, such as surface-free energy, surface charge, and wettability; these properties govern protein adsorption involving platelet adhesion [49, 50]. Experiments using human whole blood are needed to test the clinical applications of the gels. Further examinations are necessary to ensure the blood compatibility of the e-BC gel.

## 6. Conclusion

In conclusion, we successfully fabricated an elastic collagen material from EDC cross-linked BC fibrillar gel by heat treatment. "Bio-inspired crosslinking" used in this study involves collagen fibril formation in the presence of EDC as a crosslinking reagent, which was developed in an attempt to mimic the *in vivo* simultaneous occurrence of fibril formation and crosslinking. We successfully prepared the bio-inspired crosslinked BC gels by adjusting the NaCl and EDC concentrations during collagen fibril formation. An advantage of bio-inspired crosslinking is the achievement of homogenous intrafibrillar crosslinking as well as interfibrillar one, providing higher mechanical properties compared to the traditional sequential crosslinking in which monomeric collagen initially forms fibril, then subsequently crosslinked using chemical or physical methods. Another advantage is the elastic properties of bio-inspired crosslinked BC gels after heat treatment. Although common collagen materials dissolved in water at a temperature above their denaturation temperature, we found that the bio-inspired cross-linked BC gel drastically shrank at a high temperature without remarkable dissolution. The collagen gel obtained interestingly showed rubber-like elasticity and high stretchability. The human cells showed good attachment and proliferation on this elastic material, suggesting its potential to be utilized in biomaterials for tissue engineering. Additionally, the elastic material demonstrated excellent blood compatibility. Our future work will focus on fabrication of small-caliber tubes (inner diameter < 6 mm) for small-caliber vascular grafts and preclinical animal studies to further assess the safety and effectiveness of the collagen-based vascular grafts.

## 7. Acknowledgment

This study was supported by Grants-in-Aid for Young Scientists (B) (20700393) from the Ministry of Education, Science, and Culture, Japan.

## 8. References

- [1] Lee CH, Singla A, Lee Y. Biomedical applications of collagen. *Int J Pharm.* 2001;221:1-22.
- [2] Friess W. Collagen--biomaterial for drug delivery. *Eur J Pharm Biopharm.* 1998;45:113-36.
- [3] Na GC, Phillips LJ, Freire EI. In vitro collagen fibril assembly: thermodynamic studies. *Biochemistry-U.S.* 1989;28:7153-61.
- [4] Williams BR, Gelman RA, Poppke DC, Piez KA. Collagen fibril formation. Optimal in vitro conditions and preliminary kinetic results. *J Biol Chem.* 1978;253:6578-85.
- [5] Kadler KE, Holmes DF, Trotter JA, Chapman JA. Collagen fibril formation. *Biochem J.* 1996;316 ( Pt 1):1-11.
- [6] Cen L, Liu W, Cui L, Zhang W, Cao Y. Collagen tissue engineering: development of novel biomaterials and applications. *Pediatr Res.* 2008;63:492-6.
- [7] Glowacki J, Mizuno S. Collagen scaffolds for tissue engineering. *Biopolymers.* 2008;89:338-44.
- [8] Sano A, Maeda M, Nagahara S, Ochiya T, Honma K, Itoh H, et al. Atelocollagen for protein and gene delivery. *Adv Drug Deliv Rev.* 2003;55:1651-77.
- [9] Ramshaw JA, Peng YY, Glattauer V, Werkmeister JA. Collagens as biomaterials. *J Mater Sci Mater Med.* 2009;20 Suppl 1:S3-8.
- [10] Schlegel AK, Mohler H, Busch F, Mehl A. Preclinical and clinical studies of a collagen membrane (Bio-Gide). *Biomaterials.* 1997;18:535-8.
- [11] Tiller JC, Bonner G, Pan LC, Klibanov AM. Improving biomaterial properties of collagen films by chemical modification. *Biotechnol Bioeng.* 2001;73:246-52.
- [12] Hao W, Hu YY, Wei YY, Pang L, Lv R, Bai JP, et al. Collagen I gel can facilitate homogenous bone formation of adipose-derived stem cells in PLGA-beta-TCP scaffold. *Cells Tissues Organs.* 2008;187:89-102.
- [13] Kanayama T, Nagai N, Mori K, Munekata M. Application of elastic salmon collagen gel to uniaxial stretching culture of human umbilical vein endothelial cells. *J Biosci Bioeng.* 2008;105:554-7.
- [14] Nagai N, Kubota R, Okahashi R, Munekata M. Blood compatibility evaluation of elastic gelatin gel from salmon collagen. *J Biosci Bioeng.* 2008;106:412-5.
- [15] Nagai N, Mori K, Munekata M. Biological properties of crosslinked salmon collagen fibrillar gel as a scaffold for human umbilical vein endothelial cells. *J Biomater Appl.* 2008;23:275-87.
- [16] Nagai N, Nakayama Y, Zhou YM, Takamizawa K, Mori K, Munekata M. Development of salmon collagen vascular graft: mechanical and biological properties and preliminary implantation study. *J Biomed Mater Res B Appl Biomater.* 2008;87:432-9.
- [17] Nagai N, Mori K, Satoh Y, Takahashi N, Yunoki S, Tajima K, et al. In vitro growth and differentiated activities of human periodontal ligament fibroblasts cultured on salmon collagen gel. *J Biomed Mater Res A.* 2007;82:395-402.
- [18] Hosseinkhani H, Hosseinkhani M, Tian F, Kobayashi H, Tabata Y. Bone regeneration on a collagen sponge self-assembled peptide-amphiphile nanofiber hybrid scaffold. *Tissue Eng.* 2007;13:11-9.
- [19] Nagai N, Yunoki S, Suzuki T, Sakata M, Tajima K, Munekata M. Application of cross-linked salmon atelocollagen to the scaffold of human periodontal ligament cells. *J Biosci Bioeng.* 2004;97:389-94.

- [20] Shen X, Nagai N, Murata M, Nishimura D, Sugi M, Munekata M. Development of salmon milt DNA/salmon collagen composite for wound dressing. *J Mater Sci Mater Med.* 2008;19:3473-9.
- [21] Nagai N, Kumasaka N, Kawashima T, Kaji H, Nishizawa M, Abe T. Preparation and characterization of collagen microspheres for sustained release of VEGF. *J Mater Sci Mater Med.* 2010;21:1891-8.
- [22] Glattauer V, White JF, Tsai WB, Tsai CC, Tebb TA, Danon SJ, et al. Preparation of resorbable collagen-based beads for direct use in tissue engineering and cell therapy applications. *J Biomed Mater Res A.* 2010;92:1301-9.
- [23] Srinivasan A, Sehgal PK. Characterization of biocompatible collagen fibers--a promising candidate for cardiac patch. *Tissue Eng Part C Methods.* 2010;16:895-903.
- [24] Yunoki S, Mori K, Suzuki T, Nagai N, Munekata M. Novel elastic material from collagen for tissue engineering. *J Mater Sci Mater Med.* 2007;18:1369-75.
- [25] Yunoki S, Matsuda T. Simultaneous processing of fibril formation and cross-linking improves mechanical properties of collagen. *Biomacromolecules.* 2008;9:879-85.
- [26] Yunoki S, Nagai N, Suzuki T, Munekata M. Novel biomaterial from reinforced salmon collagen gel prepared by fibril formation and cross-linking. *J Biosci Bioeng.* 2004;98:40-7.
- [27] Nagai N, Kobayashi H, Katayama S, Munekata M. Preparation and characterization of collagen from soft-shelled turtle (*Pelodiscus sinensis*) skin for biomaterial applications. *J Biomater Sci Polym Ed.* 2009;20:567-76.
- [28] Lee CR, Grodzinsky AJ, Spector M. The effects of cross-linking of collagen-glycosaminoglycan scaffolds on compressive stiffness, chondrocyte-mediated contraction, proliferation and biosynthesis. *Biomaterials.* 2001;22:3145-54.
- [29] Olde Damink LH, Dijkstra PJ, van Luyn MJ, van Wachem PB, Nieuwenhuis P, Feijen J. In vitro degradation of dermal sheep collagen cross-linked using a water-soluble carbodiimide. *Biomaterials.* 1996;17:679-84.
- [30] Goissis G, Marcantonio E, Jr., Marcantonio RA, Lia RC, Cancian DC, de Carvalho WM. Biocompatibility studies of anionic collagen membranes with different degree of glutaraldehyde cross-linking. *Biomaterials.* 1999;20:27-34.
- [31] Koide T, Daito M. Effects of various collagen crosslinking techniques on mechanical properties of collagen film. *Dent Mater J.* 1997;16:1-9.
- [32] Suh H, Lee WK, Park JC, Cho BK. Evaluation of the degree of cross-linking in UV irradiated porcine valves. *Yonsei Med J.* 1999;40:159-65.
- [33] Weadock KS, Miller EJ, Bellincampi LD, Zawadsky JP, Dunn MG. Physical crosslinking of collagen fibers: comparison of ultraviolet irradiation and dehydrothermal treatment. *J Biomed Mater Res.* 1995;29:1373-9.
- [34] Toba T, Nakamura T, Matsumoto K, Fukuda S, Yoshitani M, Ueda H, et al. Influence of dehydrothermal crosslinking on the growth of PC-12 cells cultured on laminin coated collagen. *ASAIO J.* 2002;48:17-20.
- [35] Nakajima N, Ikada Y. Mechanism of amide formation by carbodiimide for bioconjugation in aqueous media. *Bioconjug Chem.* 1995;6:123-30.
- [36] Olde Damink LH, Dijkstra PJ, Van Luyn MJ, Van Wachem PB, Nieuwenhuis P, Feijen J. Changes in the mechanical properties of dermal sheep collagen during in vitro degradation. *J Biomed Mater Res.* 1995;29:139-47.

- [37] Daamen WF, van Moerkerk HT, Hafmans T, Buttafoco L, Poot AA, Veerkamp JH, et al. Preparation and evaluation of molecularly-defined collagen-elastin-glycosaminoglycan scaffolds for tissue engineering. *Biomaterials*. 2003;24:4001-9.
- [38] Wahl DA, Czernuszka JT. Collagen-hydroxyapatite composites for hard tissue repair. *Eur Cell Mater*. 2006;11:43-56.
- [39] Semler EJ, Ranucci CS, Moghe PV. Mechanochemical manipulation of hepatocyte aggregation can selectively induce or repress liver-specific function. *Biotechnol Bioeng*. 2000;69:359-69.
- [40] Nagai N, Yunoki S, Satoh Y, Tajima K, Munekata M. A method of cell-sheet preparation using collagenase digestion of salmon atelocollagen fibrillar gel. *J Biosci Bioeng*. 2004;98:493-6.
- [41] Yao C, Roderfeld M, Rath T, Roeb E, Bernhagen J, Steffens G. The impact of proteinase-induced matrix degradation on the release of VEGF from heparinized collagen matrices. *Biomaterials*. 2006;27:1608-16.
- [42] Isenberg BC, Williams C, Tranquillo RT. Small-diameter artificial arteries engineered in vitro. *Circ Res*. 2006;98:25-35.
- [43] Iwai S, Sawa Y, Ichikawa H, Taketani S, Uchimura E, Chen G, et al. Biodegradable polymer with collagen micro sponge serves as a new bioengineered cardiovascular prosthesis. *J Thorac Cardiovasc Surg*. 2004;128:472-9.
- [44] Lepidi S, Grego F, Vindigni V, Zavan B, Tonello C, Deriu GP, et al. Hyaluronan biodegradable scaffold for small-caliber artery grafting: preliminary results in an animal model. *Eur J Vasc Endovasc Surg*. 2006;32:411-7.
- [45] Shum-Tim D, Stock U, Hrkach J, Shinoka T, Lien J, Moses MA, et al. Tissue engineering of autologous aorta using a new biodegradable polymer. *Ann Thorac Surg*. 1999;68:2298-304; discussion 305.
- [46] Wildevuur CR, van der Lei B, Schakenraad JM. Basic aspects of the regeneration of small-calibre neoarteries in biodegradable vascular grafts in rats. *Biomaterials*. 1987;8:418-22.
- [47] Eriksson AC, Whiss PA. Measurement of adhesion of human platelets in plasma to protein surfaces in microplates. *J Pharmacol Toxicol Methods*. 2005;52:356-65.
- [48] Polanowska-Grabowska R, Simon CG, Jr., Gear AR. Platelet adhesion to collagen type I, collagen type IV, von Willebrand factor, fibronectin, laminin and fibrinogen: rapid kinetics under shear. *Thromb Haemost*. 1999;81:118-23.
- [49] Kulik E, Ikada Y. In vitro platelet adhesion to nonionic and ionic hydrogels with different water contents. *J Biomed Mater Res*. 1996;30:295-304.
- [50] Lee JH, Khang G, Lee JW, Lee HB. Platelet adhesion onto chargeable functional group gradient surfaces. *J Biomed Mater Res*. 1998;40:180-6.



# ***In Silico* Study of Hydroxyapatite and Bioglass®: How Computational Science Sheds Light on Biomaterials**

Marta Corno, Fabio Chiatti, Alfonso Pedone and Piero Ugliengo  
*Dipartimento di Chimica I.F.M. and NIS, Università di Torino, Torino*  
*Dipartimento di Chimica, Università di Modena & Reggio Emilia, Modena*  
*Italy*

## **1. Introduction**

Hydroxyapatite and Bioglass® are two well-known biomaterials, belonging to the vast class of ceramic supplies, both highly biocompatible and widely applied in the biomedical field. In spite of a huge research regarding engineering applications of both inorganic materials, still many aspects of their tissue integration mechanism have not been completely cleared at a molecular level. Thus, *in silico* studies play a fundamental role in the prediction and analysis of the main interactions occurring at the surface of these biomaterials in contact with the biological fluid when incorporated in the living tissue (prevalently bones or teeth). Hydroxyapatite [HA,  $\text{Ca}_{10}(\text{PO}_4)_6(\text{OH})_2$ ] owes its relevance and use as a biomaterial since it constitutes the majority of the mineral phase of bones and tooth enamel in mammals (Young & Brown, 1982). For sake of completeness, we mention that hydroxyapatite is also studied as an environmental adsorbent of metals and a catalyst (Matsumura & Moffat, 1996; Toulhat et al., 1996). One of the first applications of HA in biomedicine dates back to 1969, when Levitt *et al.* hot-pressed it in powders for biological experimentations (Levitt et al., 1969). From then on, several commercial forms of HA have appeared on the market. The material has also been utilized for preparing apatitic bioceramic, due to its bioresorbability which can be modulated changing the degree of crystallinity. There are so many examples of applications, from  $\text{Mg}^{2+}$ -substituted hydroxyapatite (Roveri & Palazzo, 2006) to the synthesis of porous hydroxyapatite materials by colloidal processing (Tadic et al., 2004), starch consolidation (Rodriguez-Lorenzo et al., 2002), gel casting (Padilla et al., 2002) and more. Furthermore, recent applications follow a biologically inspired criterion to combine HA to a collagen matrix aiming at the improvement of mechanical properties and bioactivity (Wahl et al., 2007). However, a complete review of all the practical as well as hypothetical uses of HA in the biomaterial area is outside the scope of this Chapter.

Inside the bone, a highly hierarchical collagen-mineral composite, hydroxyapatite is in the form of nano-sized mineral platelets (Currey, 1998; Fratzl et al., 2004; Weiner & Wagner, 1998) and contains carbonate ions for the 4-8 weight % (Roveri & Palazzo, 2006). In section 2.1 of this Chapter, two aspects of defects which can be encountered in a synthetic or natural HA sample will be presented. The first aspect deals with non-stoichiometric surfaces and

their adsorptive behavior towards simple molecules (water and carbon monoxide). The second concerns the inclusion of carbonate ions in the pure HA bulk structure to simulate the apatite bone tissue. These examples of applying sophisticated computational techniques to the investigation of defects in HA represent a very recent progress achieved in our laboratory inside this biomedical research area, which has been carried out since 2003. For the interested reader, a summary of the last years work on simulation of HA in our research group has been recently published (Corno et al., 2010).

As for bioactive glasses, the first synthesis was performed in 1969-71 by Larry Hench in Florida (Hench et al., 1971). He had synthesised a silicate-based material containing calcium and phosphate and had implanted this composition in rats' femurs (Hench, 2006). The result was a complete integration of the inorganic material with the damaged bone. This very first composition was called Bioglass® 45S5 ( $45\text{SiO}_2 - 24.5\text{Na}_2\text{O} - 24.5\text{CaO} - 6\text{P}_2\text{O}_5$  in wt. % or 46.1  $\text{SiO}_2$ , 24.4  $\text{Na}_2\text{O}$ , 26.9  $\text{CaO}$  and 2.6  $\text{P}_2\text{O}_5$  in mol %) and has been introduced in clinical use since 1985. The interest has been then to investigate the steps of the bioactivity mechanism leading to the formation of a strong bond between the material and the biological tissue. The most renowned hypothesis is the so-called Hench mechanism and its crucial step resides in the growth of a thin amorphous layer of hydroxy-carbonated apatite (HCA) (Hench, 1998; Hench & Andersson, 1993; Hench et al., 1971). Indeed, on that layer biological growth factors are adsorbed and desorbed to promote the process of stem cells differentiation. Moreover, before the growth of HCA, several other chemical reactions occur, dealing particularly with the exchange of sodium and calcium ions present in the Bioglass® with protons derived from the biological fluid. The influence of the chemical components of the inorganic material on its bioactivity has recently been object of scientific research and discussion. For instance, additives such as fluorine (Christie et al., 2011; Lusvardi et al., 2008a), boron, magnesium (A. Pedone et al., 2008) and zinc (Aina et al., 2011) were considered in a number of systematic studies. In section 2.2 of this Chapter, the role of phosphate concentration inside models with the 45S5 composition will be highlighted, since these changes in content can affect the crucial mechanism of gene activation and modify the local environment of the silicon framework and of Na and Ca sites, as well as the dissolution rate of silica (O'Donnell et al., 2009).

The joint use of experimental and theoretical techniques nowadays has reached a very large diffusion due to the completeness of the derived information. Particularly, in the biological or biochemical field, computational methods are essential to the investigation of interfacial mechanisms at a molecular level. Moreover, very often the interplay between experimental and calculated data allows researchers to improve both methodologies. A huge amount of examples could be reported, but for sake of brevity here we limit to our own experience of collaboration with a number of experimentalists. Indeed, in our research papers, dealing either with HA or with bioactive glasses, there is always a detailed comparison with measured data, for instance by means of NMR (Pedone et al., 2010), IR and Raman spectroscopy and of adsorption microcalorimetry (Corno et al., 2009; Corno et al., 2008). In our computational studies, we refer to quantum-mechanical techniques, which are very accurate but also quite heavy as for the need of resources. Usually, high parallel computing systems are required to run the simulations and we have successfully used the supercomputers of several HPC centers, such as the Barcelona Supercomputing Centre (Spain) or the CINECA Supercomputing Center (Italy).

The most used theoretical framework in the last decade's literature is the Density Functional Theory, which grants a good compromise in terms of accuracy of the representation and

computational time. Our calculations are performed either with the pure GGA PBE functional (Perdew et al., 1996) or with the hybrid B3LYP (Becke, 1993), both well-known functionals. Two *ab initio* approaches are possible within DFT and they differ for the type of basis set functions. Indeed, a localized Gaussian basis set can be considered, as in the present case, or a plane waves one, also extremely diffuse. An *excursus* of advantages and disadvantages of these approaches is not useful in this context and will be omitted, by focusing exclusively on Gaussian type functions.

## 2. Hydroxyapatite and Bioglass® as computational case study

All the calculations mentioned in this Chapter have been performed using the CRYSTAL code in its latest release (Dovesi et al., 2005a; Dovesi et al., 2005b; Dovesi et al., 2009). This periodic quantum-mechanical software has been developed by the Theoretical Chemistry group of the University of Turin (Italy) together with the Daresbury Laboratory (UK) since 1988. CRYSTAL is capable of computing systems with every dimensionality, from molecules to real infinite crystals and it supports massive parallel calculations. This code uses local Gaussian basis sets and can deal with many electronic structure methods, from Hartree-Fock to Kohn-Sham Hamiltonians. Structural, electrostatic and vibrational properties of the studied materials have been characterized with the program. Another crucial aspect in modeling is the graphical visualization and representation of structures. For all the images displayed in this Chapter, MOLDRAW (Ugliengo et al., 1993), J-ICE (Canepa et al., 2011b) and VMD (Humphrey et al., 1996) programs were used. Further more precise computational details can be read in a number of our recent papers on both HA (Corno et al., 2009; Corno et al., 2006; Corno et al., 2007; Corno et al., 2010) and bioactive glasses (Corno & Pedone, 2009; Corno et al., 2008).

### 2.1 Defects in hydroxyapatite bulk and surfaces

Hydroxyapatite (HA) is a mineral which occurs in nature in two polymorphs, a monoclinic form, thermodynamically stable at low temperatures, and an hexagonal form, which can be easily stabilized by substitution of the OH<sup>-</sup> ions (Suda et al., 1995). These ions are aligned along the *c* axis (the [001] direction), as highlighted in Fig. 1. The single crystal structure of the hexagonal form of HA is characterized by the  $P6_3/m$  space group. The mirror plane, perpendicular to the [001] direction, is compatible with the column of OH<sup>-</sup> ions because of an intrinsic static disorder of these ions, which can point, with no preference, in one of the two opposite directions ([001] or [00-1]). The result is a fractional occupation of the sites in the solved crystallographic structure (50% probability for each direction). As *ab initio* simulation cannot take into account the structural disorder, we reduced the symmetry to  $P6_3$ , removing the mirror plane and fixing the directions of the OH<sup>-</sup> ions. In the most stable configuration found, both the OH<sup>-</sup> ions point in the same direction, as reported in Fig. 1. The oxygen atom of the OH<sup>-</sup> ion is close to three Ca ions, which form an equilateral triangle in the *ab* plane. Moreover, there are six phosphate ions inside the crystallographic cell, all symmetry equivalent.

The bulk structure of crystalline HA, fully characterized in the literature (Corno et al., 2006), has been considered as a starting point to model the surfaces which are experimentally found to be the most important: (001) in terms of reactivity, and (010) in terms of exposure in the crystal habit (Wierzbicki & Cheung, 2000). Those surfaces have already been fully characterized at an *ab initio* level, and all the structural, geometrical and electronic properties

have been predicted and compared with the experimental values (Corno et al., 2007). More recently, these modeled surfaces were also employed to study the adsorption of different typologies of molecules that span from water (Corno et al., 2009) to organic acids (Canepa et al., 2011a), amino-acids (Rimola et al., 2008) and small peptides (Corno et al., 2010; Rimola et al., 2009), providing results comparable with the experimental heats of adsorption, when available.

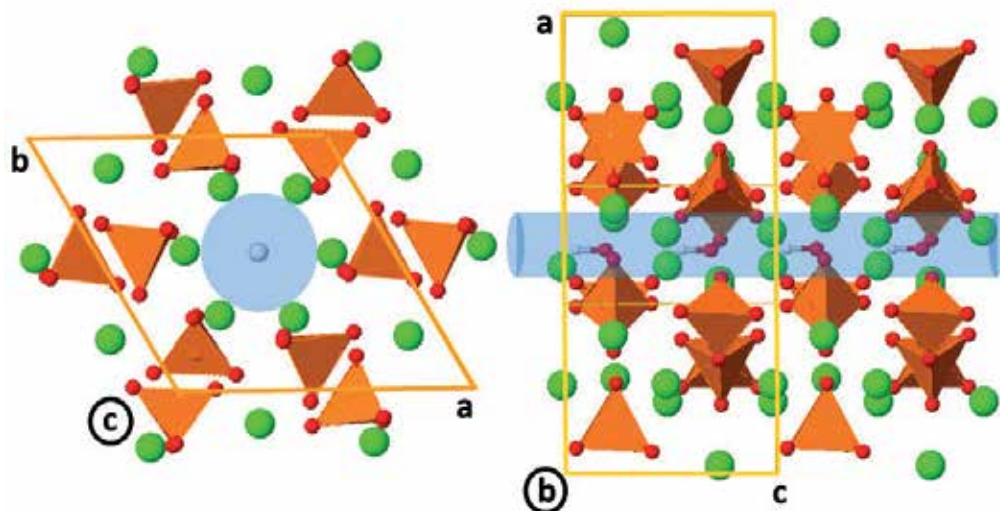


Fig. 1. Two views of the unit cell of the HA bulk structure: calcium in light green, oxygen red, hydrogen light grey and phosphate ions as orange tetrahedra. In the blue cylinders, the column of OH<sup>-</sup> ions can be observed. Unit cell borders are drawn in light orange.

Nonetheless, the study of the possible terminations along the [010] direction is not yet complete, because two new kinds of (010) surfaces have been discovered experimentally. These surfaces are non-stoichiometric, because their composition is different from the bulk.

### 2.1.1 The (010) non-stoichiometric surfaces

In 2002, a HRTEM study highlighted three possible terminations for the (010) surface. As a matter of fact, HA shows an alternation of two layers, Ca<sub>3</sub>(PO<sub>4</sub>)<sub>2</sub> (A-type) and Ca<sub>4</sub>(PO<sub>4</sub>)<sub>2</sub>(OH)<sub>2</sub> (B-type), which can be interrupted in three different ways (Sato et al., 2002). As the sequence is ...-A-A-B-A-A-B-A-A-B-..., the periodicity can be truncated by exposing as last layers ...-A-B-A or ...-A-A-B or ...-B-A-A, as shown in Fig. 2. As already done in previous work with other surfaces, we investigated these three possible structures with a slab approach. From the bulk, we extracted a piece of matter along the desired direction, in this case the [010], generating two faces which are exposed to vacuum. These faces ought to be the same to remove any possible dipole moment across the slab, due to geometrical dissimilarities. This necessity may bring the loss of stoichiometricity, in terms of the possibility of obtaining the bulk by replicating the slab along the non-periodic direction: neither B-A-A-B-A-A-B nor A-A-B-A-A-B-A-A can be replicated to regenerate the bulk. Only the stoichiometric surface, characterized by a Ca/P ratio of 1.67, maintains the bulk sequence A-B-A-A-B-A. The slab structure terminating in -A-A-B is called *Ca-rich* (010)

surface as its Ca/P ratio increases to 1.71. The last one is called *P-rich* (010) surface, with a Ca/P ratio of 1.62.

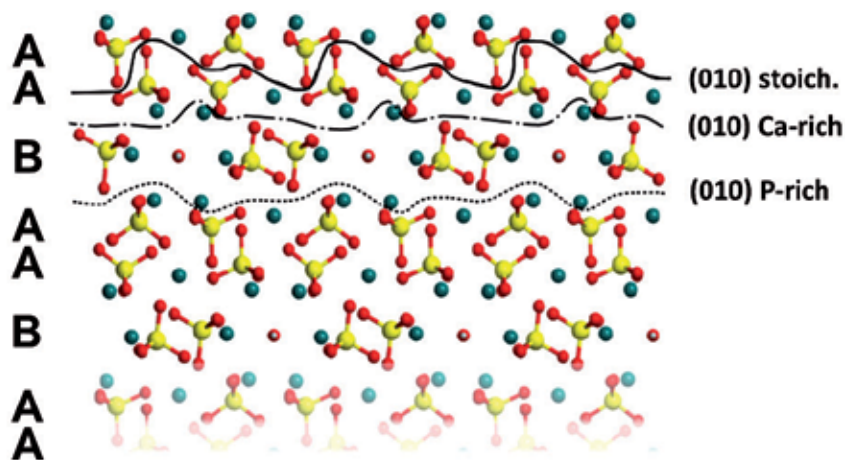


Fig. 2. The three possible terminations along the [010] direction of HA. Colour coding: calcium cyan, oxygen red, hydrogen grey and phosphorous yellow.

Clearly, due to the non-stoichiometric nature of these new surfaces,  $E_{\text{surf}}$  cannot be defined using the classical formula:

$$E_{\text{surf}} = (E_{\text{slab}} - n \cdot E_{\text{bulk}}) / (2 \cdot A) \quad (1)$$

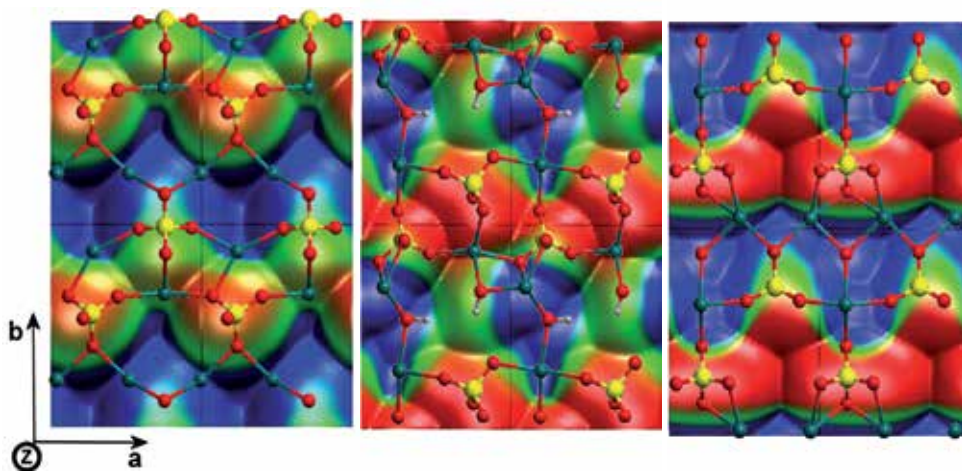


Fig. 3. Upper views of the three (010) surfaces: on the left side, the stoichiometric surface, in the middle, the Ca-rich surface and, on the right side, the P-rich surface. Each structure is superimposed on an isodensity surface color-coded with the electrostatic potential (blue is most positive, red is most negative). The maps have been generated with the VMD program (Humphrey, Dalke & Schulten, et al., 1996). Calcium represented in cyan, oxygen in red, hydrogen in grey and phosphorous in yellow.

where  $A$  is the surface area (doubled, because two faces are generated),  $E_{\text{bulk}}$  and  $E_{\text{slab}}$  are the calculated energies of the related models and  $n$  is an integer number, required to match the chemical potentials of the two systems. Astala and Stott adopted a clever and rather involved scheme to evaluate the phase existence conditions for the two non-stoichiometric surfaces, showing that the region of their stability is outside the stability window defined by bulk HA,  $\text{Ca}(\text{OH})_2$  and  $\beta\text{-Ca}_3(\text{PO}_4)_2$  (Astala & Stott, 2008).

The typology of the exposed layers differentiates the (010) stoichiometric surface from the non-stoichiometric ones. Indeed, the (010) Ca-rich surface exposes the OH<sup>-</sup> ions belonging to the B layer, while both the stoichiometric and the P-rich surfaces contain the OH ions in an inner layer (see the structures displayed in Fig. 3 for details).

	Stoichiometric	Ca-rich	P-rich
$a$ (Å)	6.98	6.93	7.00
$b$ (Å)	9.28	9.27	9.33
$\gamma$ (°)	89.87	90.01	90.02
Area (Å <sup>2</sup> )	64.83	64.24	65.24
* Thickness (Å)	13.28	20.05	20.23
<Ca-O> (Å)	2.41	2.39	2.40
<P-O> (Å)	1.55	1.55	1.55
<O-H> (Å)	0.97	0.97	0.97
<OPO> (°)	109.5	109.4	109.4
Band Gap (eV)	6.21	6.80	6.65
Dipole (Debye)	$3.5 \cdot 10^{-3}$	$4.0 \cdot 10^{-3}$	$1.4 \cdot 10^{-2}$

\* The slab thickness is the perpendicular distance between the most exposed Ca ions on the upper and lower faces of the slab.

Table 1. Most important geometrical parameters of the HA (010) surfaces. The values in <...> correspond to the arithmetical averages of the considered feature.

In Fig. 3, the most exposed layers of the three terminations are reported, superimposed on the isodensity surface colorcoded with the electrostatic potential. The isodensity value is fixed to  $10^{-6}$  electrons and the electrostatic potential spans from -0.02 a.u. (red) to +0.02 a.u. (blue). Positive values of the potential are visible in correspondence of the Ca ions while negative potential zones are mostly located upon superficial phosphate ions.

In Table 1, a geometrical analysis of the three surfaces is reported. The cell parameters are slightly different between the three cases, but the rectangular shape is mostly maintained. The slab thickness is not comparable, because of a different number of layers for each surface model. The interatomic distances and angles are, however, very similar.

Two important intensive parameters can classify the stability of a slab structure, the electronic band gap and the total dipole moment across the slab: each surface has a dipole moment close to zero and a band gap typical of electrical insulators. The three surfaces are, then, stable and can be adopted as a substrate to study the adsorption of molecules.

### 2.1.2 Adsorption of H<sub>2</sub>O and CO upon the most exposed Ca ions of the (010) surfaces

The chemical reactivity of the most exposed cations of a surface is experimentally studied with the IR technique by monitoring the perturbation of the vibrational frequency of the probe molecule, which is compared to the value for the free molecule. Of the possible probe

molecules, those commonly used are carbon monoxide and water, because of their selectivity towards cations, the ease of interpretation of their spectra, and the high sensitivity of IR instrumentation in the region where their vibrational frequencies fall (medium IR). The (010) stoichiometric surface has already been fully characterized by Corno *et al.* in relation to the adsorption of these molecules (Corno *et al.*, 2009), whereas the non-stoichiometric surfaces are the subject of this work. Calculations provide binding energies and vibrational frequencies of the probe molecules which can be used as a future reference to be compared with experimental measurements. In Fig. 4, the optimized structures of the adducts are reported for water and CO.

The adsorptions of water upon the most exposed cations of the non-stoichiometric surfaces are characterized by BE values of 131 and 125 kJ/mol (BSSE  $\approx$  35 %), for the Ca-rich and P-rich surfaces, respectively. These values also take into account the formation of two hydrogen bonds between the water molecule and exposed anions, either phosphate only, or also hydroxyl anions in the case of the (010) Ca-rich surface. If the thermal and vibrational contributions are taken into account, these values decrease to 117 and 110 kJ/mol, respectively, allowing a consistent comparison with the experimental differential heat of adsorption of water of 110 kJ/mol (Corno *et al.*, 2009). The latter value has been obtained from experimental micro-calorimetric studies of water adsorption on microcrystalline HA, for a loading of water comparable with our models.

The adsorption of CO upon the most exposed Ca ions gives results highly representative of the strength of the cationic site as no hydrogen bond can be formed: the BE values upon the Ca-rich and P-rich surfaces are, respectively, 38 and 40 kJ/mol (BSSE  $\approx$  20 %), showing an almost equivalence for the two Ca ions for the two surfaces.

When the vibrational features are considered, a crucial point is the comparison between the frequencies of the free and the adsorbate molecule. While the stretching mode of CO is easily identified in both cases, the modes of the adsorbed water molecule are no longer easily referable to those of the free molecule. The free water molecule is characterized by two stretching modes (the symmetric and, at higher frequencies, the anti-symmetric) and one bending mode. When the molecule interacts with the surface, these two kinds of stretching modes are no longer classifiable on a symmetry ground. The hydrogen bonds which are formed with the most exposed anions of the surface cause the loss of the  $C_{2v}$  symmetry of the molecule: each OH bond oscillates independently. As in previous work, we decided to compare the lower OH stretching frequency of the adsorbed molecule to the symmetric mode and *vice versa* (Corno *et al.*, 2009).

With these remarks, the calculated symmetric stretching shifts are -761 and -329  $\text{cm}^{-1}$  for the (010) Ca-rich and (010) P-rich surfaces, respectively, while the anti-symmetric shifts are -310 and -328  $\text{cm}^{-1}$ . The shifts of the bending frequencies are 113 and 88  $\text{cm}^{-1}$ . When a hydrogen bond pattern occurs, the stretching mode shifts are negative due to the electronic density transfer and the resulting decrease of the bond strength. Instead, the bending frequencies increase because of the restraint caused by the hydrogen bond itself. The larger shift of the symmetric stretching of the  $\text{H}_2\text{O}$  adsorbed on the (010) Ca-rich surface, in combination with a larger bending shift, indicates the formation of a very strong hydrogen bond with an exposed anion of the (010) Ca-rich surface. Experimentally, the shift of the stretching is -400  $\text{cm}^{-1}$  while the bending shift is 40  $\text{cm}^{-1}$ . The calculated values are, then, in agreement with the experimental ones as long as the signs and the trends are considered (Bertinetti *et al.*, 2007).

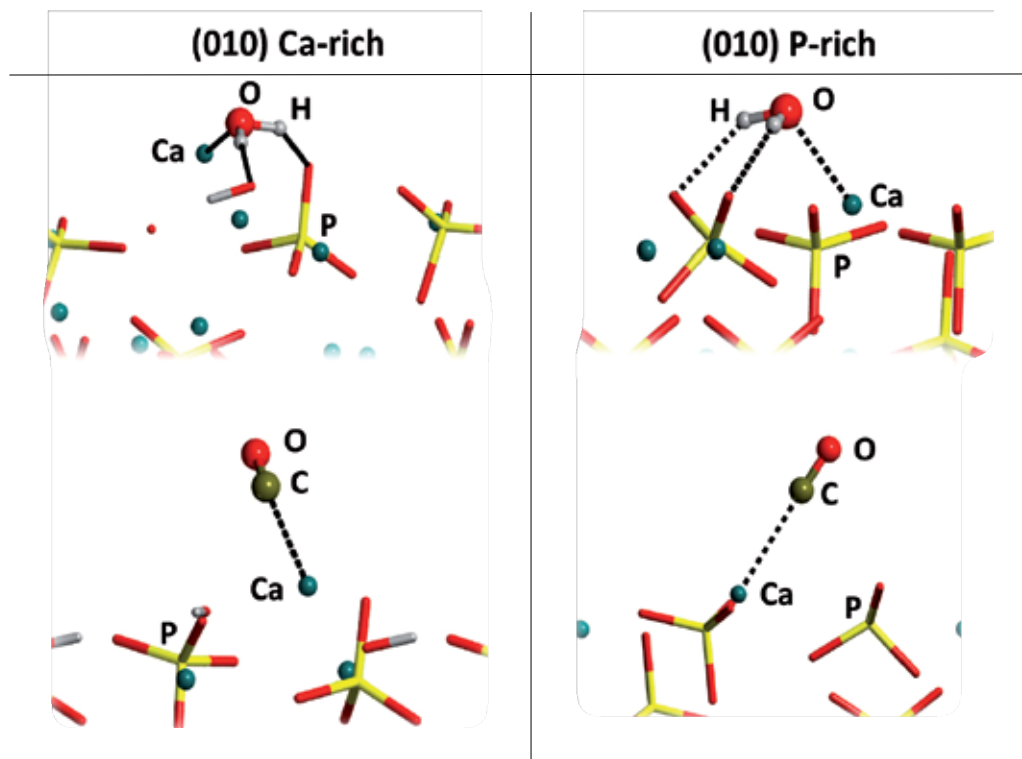


Fig. 4. Best views of the interactions between the most exposed ions of the (010) Ca-rich and (010) P-rich surfaces and the two probe molecules, water and carbon monoxide. The interactions with Ca ions and the hydrogen bonds are represented with dotted lines.

The stretching frequency shifts of the CO molecule are  $40\text{ cm}^{-1}$  for the (010) Ca-rich surface and  $41\text{ cm}^{-1}$  for the (010) P-rich surface. These BE and frequency shifts values indicate that the Ca ion can reasonably be considered as the major cause of the activity of HA towards polar molecules free from H-bond interactions.

A comparison with the experimental IR spectrum of CO adsorbed on HA reveals two main components, characterized by an upward shift of the stretching frequency of the adsorbed molecule of about  $+27$  and  $+41\text{ cm}^{-1}$ , respectively. The highest shift is attributed to a tiny fraction of the most exposed calcium ions, which are those modeled in our studies, so proving a good agreement. On the other hand, the majority of calcium sites contribute to the lowest shift (Bertinetti et al., 2007; Sakhno et al., 2010).

### 2.1.3 Hydroxyapatite and carbonate ion defects

HA is the main component of the inorganic phase of bones and teeth, but, as many studies have demonstrated, the mineral present in those tissues is neither crystalline nor without defects (Fleet & Liu, 2003; Fleet & Liu, 2004; Fleet & Liu, 2007; Rabone & de Leeuw, 2005; Astala & Stott, 2005; Astala et al., 2006; Rabone & de Leeuw, 2007; de Leeuw et al., 2007). Indeed, it incorporates many other elements, ions or compounds, such as Mg or other alkaline earth metals instead of Ca, and, above all, the carbonate anion. Many studies, both theoretical and experimental, have already been conducted on the role of the carbonate ion



on the hydroxyapatite structure, in order to comprehend where and how this ion is located. The results of these studies assert that the  $\text{CO}_3^{2-}$  can substitute an  $\text{OH}^-$  ion of the structure, a *type A* defect, or a  $\text{PO}_4^{3-}$ , a *type B* defect. This hypothesis has been confirmed by IR spectra in which the vibrational mode frequencies of the carbonate are different for each type of substitution.

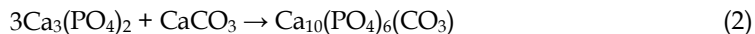
As the net charge of the carbonate is different from those of the substitutional anions, charge compensation is required.

In the case of the type A defect, the charge excess can be compensated by creation of an ionic vacancy removing another OH ion, also because of the larger steric encumbrance of the carbonate ion with respect to the hydroxyl ion (Peroos et al., 2006).

In the case of the type B defect, the electro-neutrality can be maintained in five different ways (Astala & Stott, 2005):

1. Removal of one OH ion and creation of one Ca vacancy (B1 complex);
2. Removal of one Ca ion for every two carbonate ions (B2 complex);
3. Substitution of one Ca with one hydrogen (B3 complex);
4. Substitution of one Ca with one alkaline ion;
5. OH ion incorporation close to the carbonate ion.

When considering the type A defect, it is first necessary to notice that, in the hydroxyapatite unit cell, only two OH ions are present (Fig. 1). If they are both removed at once but only one carbonate ion is included, the resulting structure is no longer a hydroxyapatite, as it had lost all the hydroxyl ions, and has to be considered a carbonated apatite. In Fig. 5, this stable structure is reported. The similarity between carbonate apatite and calcite structures is clear: the averaged distance  $\langle \text{Ca-OC} \rangle$  is 2.35 Å in the carbonate apatite and 2.34 Å in the calcite. From the *ab initio* calculation, it is also possible to predict the enthalpy of formation of the carbonate apatite from the calcium phosphate and the calcite structures, considering the reaction (2):



The B3LYP enthalpy of formation is -35 kJ/mol, directly comparable with the value of -32 kJ/mol obtained with the VASP code and the PW91 functional (Rabone & de Leeuw, 2007).

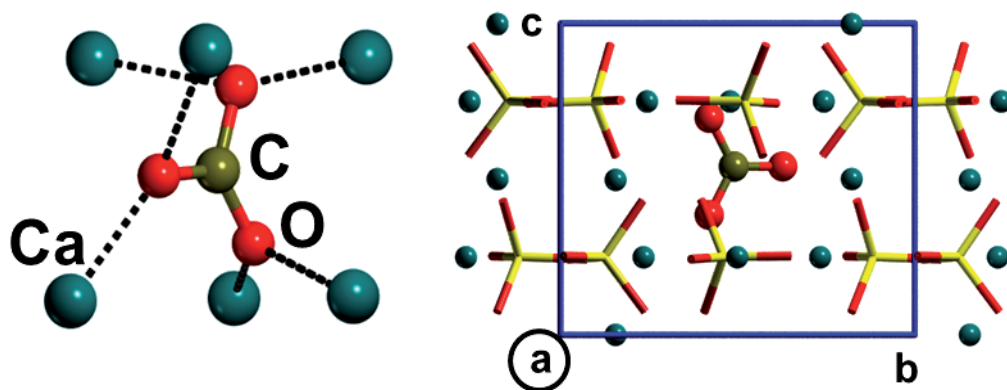
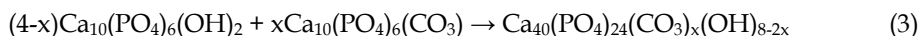


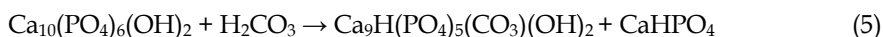
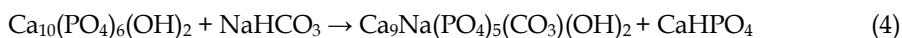
Fig. 5. Carbonated apatite. On the left side, a view of the carbonate ion is reported, highlighting its distances to the closest Ca ions. On the right side, the cell, where both OH are removed and one carbonate is substituted, is reported after full relaxation of the atoms.

As the main interest in the type A defect is the stability of the OH-CO<sub>3</sub><sup>2-</sup> substitution as a function of CO<sub>3</sub><sup>2-</sup> content, we modeled three cases using a 2x2 supercell:



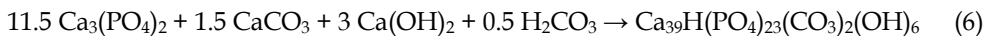
The most stable case occurs (see Fig. 6A) when three out of four pairs of OH ions ( $x=3$ ) were substituted with carbonate ions ( $\Delta E_r = -24$  kJ/mol). It is notable that the percentage of carbonate related to this minimum energy structure (4.4%) is close to that found in dentine tissue (5.6%) and in tooth enamel (3.5%) (Dorozhkin, 2009).

Among the five typologies of B type defect, we investigated only the substitution of Ca with Na or H. As all the phosphate ions are equivalent by symmetry, the substitution with carbonate is easy. On the contrary, in the cationic substitution to restore the neutrality, there is a choice among ten Ca ions. These are not equivalent, as the symmetry is broken by the carbonate substitution. We selected only four Ca ions, those nearest to the carbonate, because from the experiment it is known that the two defective substituents are close to each other. Indeed, in the four selected cases, the most stable structures are those in which the distance between the substituents is minimum. The different stabilities were obtained by calculating the energy variation ( $\Delta E_r$ ) for the following reactions:



The  $\Delta E_r$  is 108 kJ/mol for reaction (4) and -94 kJ/mol for reaction (5), indicating that the inclusion of H is much more preferable than Na. The reason relies upon the formation of bulk water between the H and the OH ion of the column. This water molecule stabilizes the structure and its removal requires 136 kJ/mol, because of the occurrence of rather strong H-bonds. The two structures are reported in Fig. 6 (B/Na and B/H).

We also calculated some bulk structures in which both typologies (A and B) of substitutions were present at the same time, in order to better mimic the bone features. Among all the simulated structures, the most favorable situation is the one reported in Fig. 6 (A+B/H): a carbonate ion substitutes a pair of OH ions while another carbonate replaces a phosphate with formation of a water molecule. The hydrogen bonds formed by the water molecule are stronger than those of the B defect model, highlighting that the two defects interact and influence each other. The energy of formation of the mixed A+B/H structure is -752 kJ/mol for the reaction 6.



## 2.2 Bioglass: the effect of varying phosphorous content

As already described in the Introduction of this Chapter, bioactive glasses are extensively studied as prostheses for bone and tooth replacement and regeneration. In particular, the 45S5 composition has continuously been investigated, not only in its compact form, whose applications are limited to low load-bearing, but also as particulates and powders for bone filler use. Hence, the computational investigations of the variation in composition for the different glass components still represent a very interesting and stimulating task.

In the computational area, the most natural method to simulate glassy materials is usually classical molecular dynamics via the melt-and-quench procedure. Recently, much

theoretical research work has been carried out on bioglasses using *ab initio* molecular dynamics, though the transferability of empirical potentials remains a challenging goal, typical of classical techniques (Tilocca, 2010).

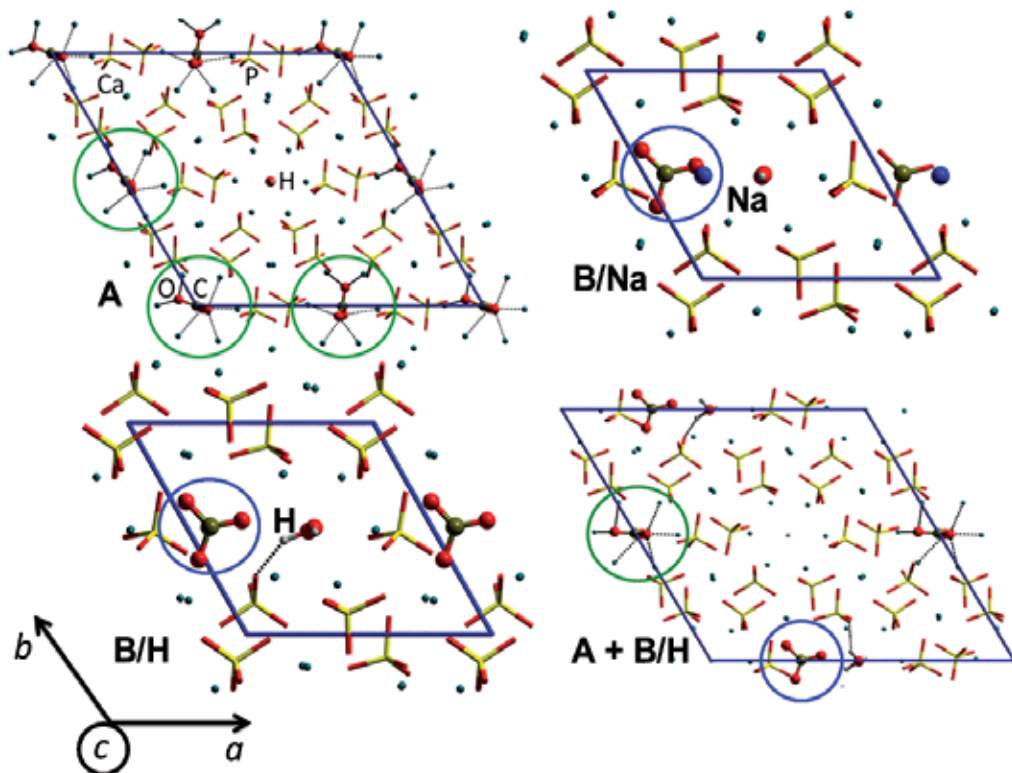


Fig. 6. Top views of the most stable carbonated hydroxyapatite structures. The carbonate can substitute a pair of hydroxyl ions (green circles) or a phosphate ion (blue circles). Top left, type A defect with three out of four pairs of OH ions substituted; top right, type B defect with Na as charge compensator; bottom left, type B with H as charge compensator; bottom right, type A and B, with H as charge compensator of the B type.

### 2.2.1 Multi-scale strategy for the modelling of 45S5 Bioglass®

The *ab initio* modelling of an amorphous material as the 45S5 Bioglass® has straightway caused a number of challenges. As the internal coordinates are not available from classical structural analysis, we have developed a multi-scale strategy to obtain a feasible amorphous bioglass model similar in composition to the 45S5. This approach has been largely illustrated in previous papers (Corno & Pedone, 2009; Corno et al., 2008; A. Pedone et al., 2008) so that here we only summarize the most important steps.

Firstly, we adopted classical molecular dynamics simulations to model a glassy bulk structure which could be close to the 45S5 composition keeping the size of the unit cell small enough for *ab initio* calculations, *i.e.* 78 atoms. In order to reproduce the correct ratio between SiO<sub>2</sub>, P<sub>2</sub>O<sub>5</sub>, Na<sub>2</sub>O and CaO components, the experimental density of 2.72 g/cm<sup>3</sup> has been maintained fixed in a cubic box of 10.10 Å per side. After randomly generating atomic

positions, a melt-and-quench procedure was simulated: heating at 6000 K and then equilibrating for 100 ps. Next, continuously cooling from 6000 to 300 K in 1140 ps with a nominal cooling rate of 5 K/ps was performed. The temperature was decreased by 0.01 K every time step using Nose-Hoover thermostat with the time constant parameter for the frictional coefficient set to 0.1 ps (Hoover, 1985). Simulations were carried out in the constant volume NVT ensemble and 100 ps of equilibration at constant volume and 50 ps of data production were run at 300 K. On the derived structures, static energy minimizations were carried out at constant pressure and volume and the most representative model was chosen for *ab initio* calculations.

The final candidate structure was minimized both in terms of internal coordinates and lattice parameters, performing full relaxation runs. In Figure 7a the quantum-mechanical optimized structure of the selected Bioglass model is displayed. In the unit cell, which has become triclinic due to the lattice parameter deformation, two phosphate groups are present: one isolated (orthophosphate) and the other linked to one silicon atom. The structural analysis was followed by the simulation of the IR spectrum. Figure 7b reports the comparison between experimental (Lusvardi et al., 2008b) and computed spectra, which shows a very good agreement between the two spectra. The punctual assignment of each peak in the simulated case has been published in a previous paper (Corno et al., 2008), where the 45S5 model has been compared with an amorphous silica structure, to investigate the role of network modifier cations and phosphate groups in structural and vibrational properties of a pure SiO<sub>2</sub> framework. Hence, the reliability of the chosen multi-scale strategy has been proved.

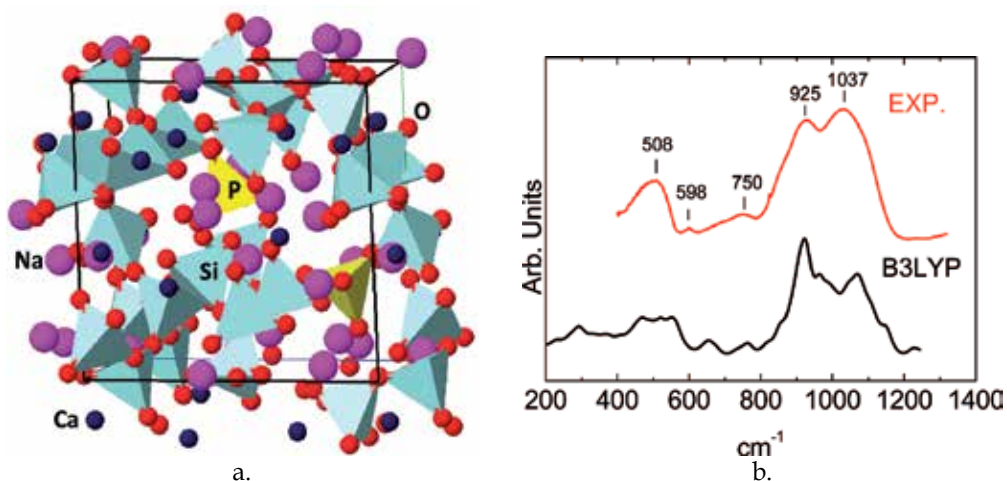


Fig. 7. 45S5 Bioglass model: a. best view of the optimized structure ( $\text{Na}_{12}\text{Ca}_7\text{P}_2\text{Si}_{13}\text{O}_{44}$  composition), colour coding: silicon light blue, oxygen red, sodium pink, calcium dark blue and phosphorous yellow; cell parameters drawn in red for  $a$ , in green for  $b$  and in blue for  $c$ , while cell borders are in black; b. experimental (red line) and B3LYP (black line) IR spectra. (Corno et al., 2008; Lusvardi et al., 2008b)

### 2.2.2 Simulation of bioactive glasses with different P<sub>2</sub>O<sub>5</sub> content

More recently, the influence of P<sub>2</sub>O<sub>5</sub> content on the structure of bioactive glass compositions has been object of investigation (O'Donnell et al., 2009; O'Donnell et al., 2008a; O'Donnell et

al., 2008b). Indeed, it is well known that structural and compositional features of bioactive glasses are strongly connected to their bioactivity (Clayden et al., 2005; Lin et al., 2005). In particular, it has been demonstrated (Tilocca, 2010) that in compositions less bioactive than the 45S5 the majority of phosphate groups are linked to one or two silicon atoms. Conversely, in bioactive glasses as the 45S5, almost all the phosphate groups are isolated and mobile (Tilocca & Cormack, 2007).

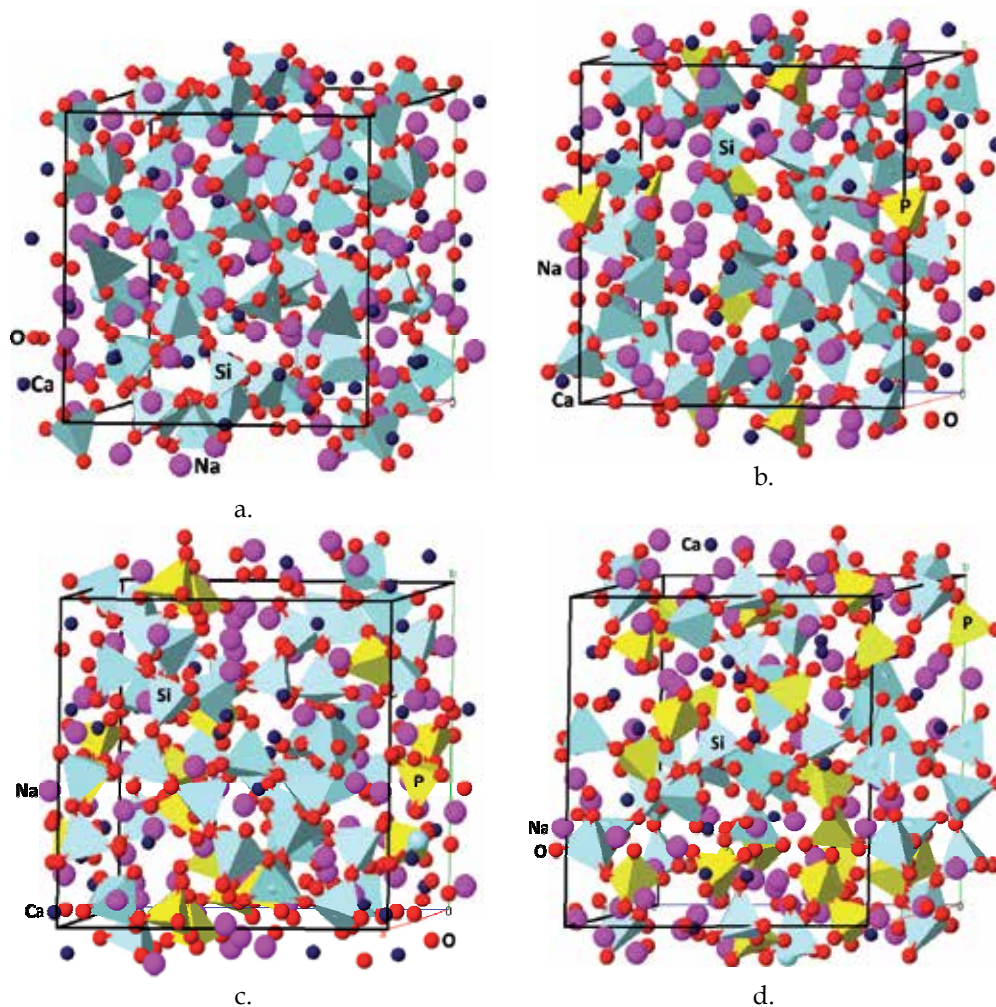


Fig. 8. Best views of the optimized structures of the four studied glass models: a. no phosphorous (P0); b. 2.5% phosphorous (P2.5); c. 5.5% phosphorous (P5.5) and d. 9.5% phosphorous (P9.5). Colour coding: silicon light blue, oxygen red, sodium pink, calcium dark blue and phosphorous yellow. Cell parameters drawn in red for *a*, in green for *b* and in blue for *c*, while cell borders are in black (their values listed in Table 5).

In our research work, we have aimed to correlate the change in phosphorous content with the change in structural and vibrational properties, these latter as a tool to detect the local

coordination of the  $\text{PO}_4$  group. To this extent, four models of phosphate soda-lime glasses were studied by applying the same melt-and-quench procedure used for the 45S5 Bioglass®. The unit cell size has also been increased from the former 78 atoms to new models containing an average of 250 atoms. The larger size has allowed us to derive models which could be more representative of the amorphous long-range disorder typical of glassy materials.

The main structural features of the four modelled structures, whose correspondent images are displayed in Figure 8., are listed in Table 2, together with their molar composition. The “P0” structure refers to a phosphorous-free soda-lime glass.

Model	SiO <sub>2</sub>	CaO	Na <sub>2</sub> O	P <sub>2</sub> O <sub>5</sub>	<i>a</i>	<i>b</i>	<i>c</i>	$\alpha$	$\beta$	$\gamma$	Volume
P0	45	24	22	-	14.97	14.23	14.77	91.3	90.7	89.2	3144
P2.5	41	23	20.5	2.5	14.47	14.72	14.69	90.0	91.5	90.9	3128
P5.5	35	23	20.5	5.5	14.68	14.47	15.08	91.4	90.0	87.9	3199
P9.5	27	21	19.5	9.5	14.71	14.78	14.50	92.2	90.2	90.1	3150

Table 2. Molar per cent composition of the four studied models of glasses together with the unit cell parameter values of the optimized structures illustrated in Fig. 6. Lattice parameters expressed in Å, angles in degrees and volumes in Å<sup>3</sup>.

A direct comparison of volume values for the four models is not reasonable, since there are a number of tiny differences in molar composition in order to maintain the desired ratios between components as well as the total electroneutrality. Indeed, no linear relationship exists between the increase in %P<sub>2</sub>O<sub>5</sub> and volume.

A comparison between the structural and vibrational features of the two models mostly similar in composition to the 45S5 Bioglass® has been carried out, *i.e.* the unit cell with 78 against that with 248 atoms (P2.5 of Figure 8b). In the smaller structure, as already described and illustrated in Figure 7, two phosphate groups are present: one isolated and the other connected to the silicon framework. In the larger model, five phosphate groups are located inside the unit cell, three of which are isolated, while the others linked to the siliceous network. In terms of Q<sup>n</sup> species (a Q<sup>n</sup> species is a network-forming ion, like Si or P, bonded to *n* bridging oxygens), the 60% of the total number of PO<sub>4</sub> groups is represented by Q<sup>0</sup> (orthophosphates), while the remaining 40% is equally divided among Q<sup>1</sup> and Q<sup>2</sup> (see Figure 9b, blue curve). If we analyse the total radial distribution function *g*(*r*) for the P2.5 model plotted in Figure 9a., it clearly appears by the two peaks that the bond length of the P-NBO bond (NBO stands for non-bridging oxygen) is slightly shorter than that for the P-BO bonds (1.552 compared to 1.616 Å, respectively). Moreover, the P-BO bonds are numerically much less, as visible from the part b. of the same Figure 9.

Considering the Q<sup>n</sup> distribution for the other two phosphorous-containing models, namely P5.5 and P9.5, it results: for P5.5 the 73% of the total 11 phosphate groups are isolated while the rest are Q<sub>1</sub> and for the total 19 phosphate groups of the P9.5 model, 37% are isolated, 58% are Q<sub>1</sub> and the 5% Q<sub>2</sub>, in other words 7 Q<sub>0</sub>, 11 Q<sub>1</sub> and a Q<sub>2</sub>. The graph in Figure 9a. schematizes the different distribution for the larger models.

The P-O bond distances, both for bridging and non-bridging oxygens, vary according to the different Q<sup>n</sup> species, as reported in Table 3.

As a general comment, P-NBO distances follow the trend: Q<sup>0</sup> > Q<sup>1</sup> > Q<sup>2</sup> while for P-BO values in case of Q<sup>1</sup> and Q<sup>2</sup> species there is no definite trend, probably due to the limited number of sites in the considered structures.

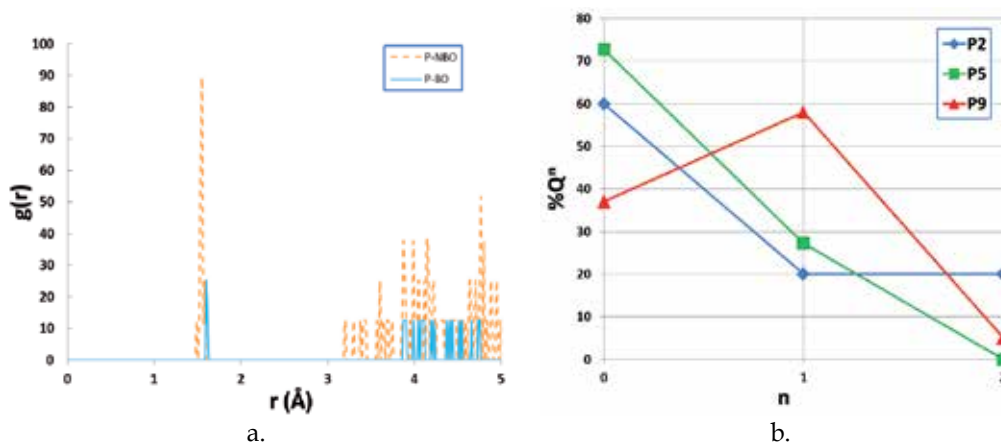


Fig. 9. a. Radial distribution function of the total P-O bonds, distinguishing between non-bridging oxygen (NBO, orange dotted line) and bridging oxygen (BO, blue line); b. percentage distribution of the phosphate groups in terms of Q<sup>n</sup> species for the three large models P2.5 (blue), P5.5 (green) and P9.5 (red).

Model	<P-NBO> Q <sup>0</sup>	<P-NBO> Q <sup>1</sup>	<P-NBO> Q <sup>2</sup>	<P-BO> Q <sup>1</sup>	<P-BO> Q <sup>2</sup>
P2.5	1.556	1.539	1.508	1.597	1.602
P5.5	1.559	1.523	-	1.660	-
P9.5	1.557	1.531	1.515	1.631	1.588

Table 3. Average P-O bond lengths for both bridging and non-bridging oxygen of the three P2.5, P5.5 and P9.5 models are reported in Å.

### 2.2.3 Effect of P<sub>2</sub>O<sub>5</sub> content on the simulated IR spectra

A complete vibrational analysis was outside our computational facilities, due to the size of the simulated bioglass models (250 atoms inside the unit cell, no symmetry). An alternative approach, here adopted, is the so-called “fragment” calculation of frequency. It consists on the selection of the interesting atoms – in this case phosphate groups – to be considered for the calculation of vibrational normal modes. Obviously this approach is an approximation and needs to be first tested. Our test case was the 45S5 structure of Figure 7a, for which the full IR spectrum was available. In particular for the phosphate groups containing Q<sup>1</sup> and Q<sup>2</sup> species, the question was to decide whether to include or not the linked silicon atom with or without its connected oxygen atoms.

Figure 10 reports three simulated IR spectra of the 45S5 model: the full spectrum (black line), the full spectrum including only modes involving phosphate groups (red line) and the partial spectrum where the fragment contains only phosphate groups and silicon atoms linked to the Q<sup>1</sup> species.

In order to dissect the contribution to the full IR spectrum (black spectrum, Fig. 10) of modes involving the displacements of P atoms we rely on the Potential Energy Distribution (PED). All modes involving the P atom in the PED of the full spectrum are included whereas the remaining ones are removed from the spectrum (red spectrum, Fig. 10). The comparison with the spectrum (blue spectrum, Fig. 10) computed by including as a fragment the PO<sub>4</sub> (for fully isolated groups) and PO<sub>4</sub>(SiO<sub>4</sub>)<sub>1,2</sub> (for the other cases) shows a good agreement

with the black spectrum, so that this methodology has been adopted to compute the spectra for the larger structures with variable P content. In other words, the differences in peaks between the red and the blue spectra of Figure 10 are due to the presence (blue line) or absence (red line) of the extra  $\text{SiO}_4$  group.

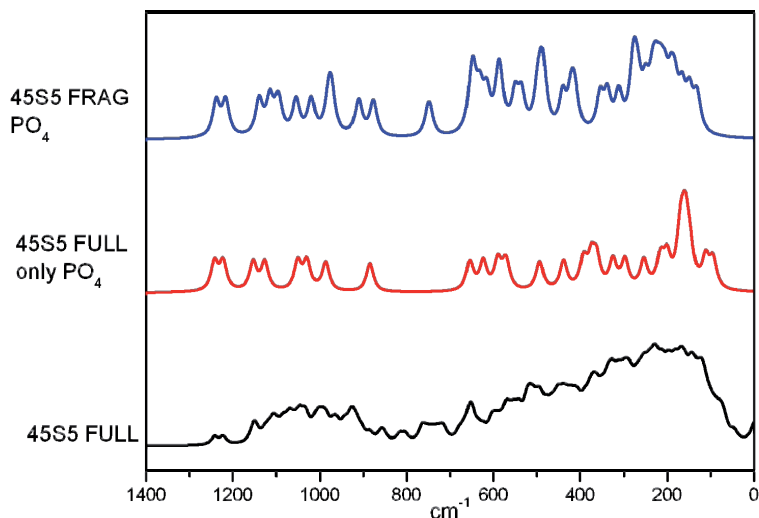


Fig. 10. Simulated IR spectra of the similar 45S5 Bioglass® model in the following sequence from bottom to top: full frequency calculation (black line), full frequency calculation including only  $\text{PO}_4$ -involved modes (red line) and fragment calculation considering in the fragment  $\text{PO}_4$  and  $\text{SiO}_4$  which is directly bonded to  $\text{PO}_4$ . No IR intensities are reported and the chosen band width is of  $20 \text{ cm}^{-1}$ .

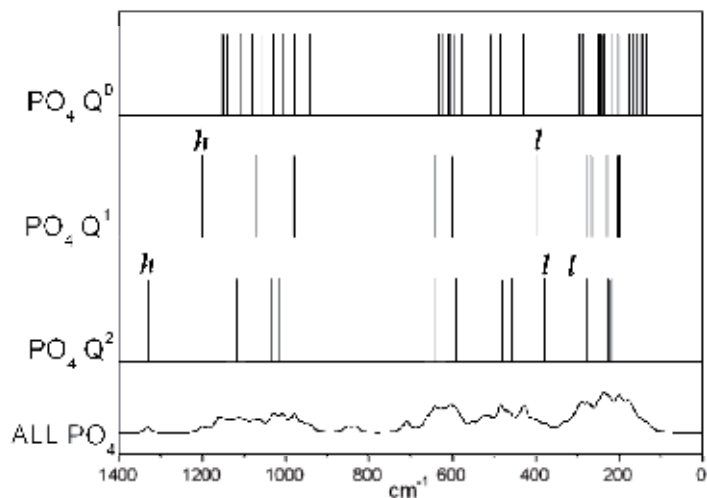


Fig. 11. IR peaks assignment for phosphate groups of the P2.5 model based on the different  $Q^n$  species. Label *h* and *l* refer to the peculiar bands at high and low frequencies, respectively, that allow us to distinguish the  $Q^0$  species from the  $Q^1$  and  $Q^2$ . In case of  $Q_2$ , see Fig. 12 for the schematic representation of the associated normal modes.



Figure 11 illustrates a specific example of how to detect the various phosphate groups in terms of  $Q^n$  (isolated or connected phosphates) by IR spectroscopy. We reported at the bottom of the graph the P2.5 IR spectrum of the phosphates computed applying the aforementioned procedure (fragment mode). The three bar charts refer each one to the  $Q^n$  species present inside the structure and show only the frequencies involving that specific class of phosphate groups (isolated or connected to the network). It is interesting to note the shift of the highest and lowest bands comparing  $Q^1$  and  $Q^2$  cases: the highest frequency – indicated with the label  $h$  – corresponds to the stretching of the P=O bond and is shifted to higher values in case of  $Q^2$ , with respect to  $Q^1$  and  $Q^0$ . On the contrary, in the region of low frequencies, modes involving the  $Q^2$  species are shifted to lower values compared to the  $Q^1$  ones. The OPO bending region (600-700  $\text{cm}^{-1}$ ) remains almost unaffected.

Figure 12 illustrates the graphical representation of the normal modes displacement for the five stretching and bending modes of the  $Q^2$  species present in the P2.5 glass.

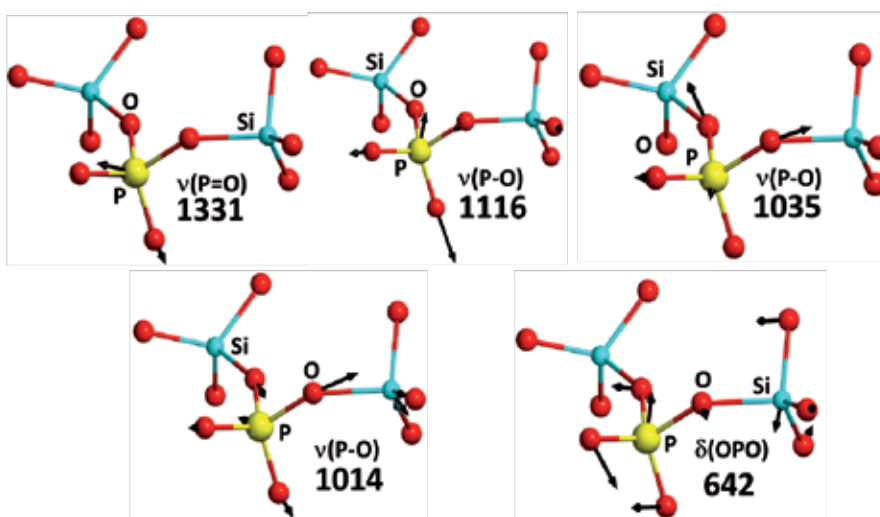


Fig. 12. Schematic representation of the normal mode displacement assigned to the  $Q^2$  species for the P2.5 model ( $\text{PO}_4$  structural unit connected to 2  $\text{SiO}_4$  groups). Colour coding: Si light blue, oxygen red, phosphorous yellow; frequencies expressed in  $\text{cm}^{-1}$ .

The simulated IR spectra for the phosphate groups of the three phosphorous-containing models have been then compared one to each other and to the phosphorous-free structure P0, as displayed in Figure 13.

The first evident difference between phosphorous-free P0 and the other models is the absence of bands in the spectral region at high frequencies (1200-1400  $\text{cm}^{-1}$ ). As we have discussed above, that is the typical region of the P=O stretching mode of phosphate groups. This mode is shifted to lower frequencies and the band is broadened when passing from P2.5 to P9.5. Another clear indication of the presence of phosphate groups is the band at about 600-700  $\text{cm}^{-1}$ , which corresponds to the O-P-O bending region. The 1100-800  $\text{cm}^{-1}$  spectral range, on the contrary, is not easily assigned to phosphate groups inside the bioglass since also Si-O stretching are located in that zone. However, the effect of increasing the  $\text{P}_2\text{O}_5$  content inside the unit cell is reflected in a general broadening of the P-O stretching and O-P-O bending modes.

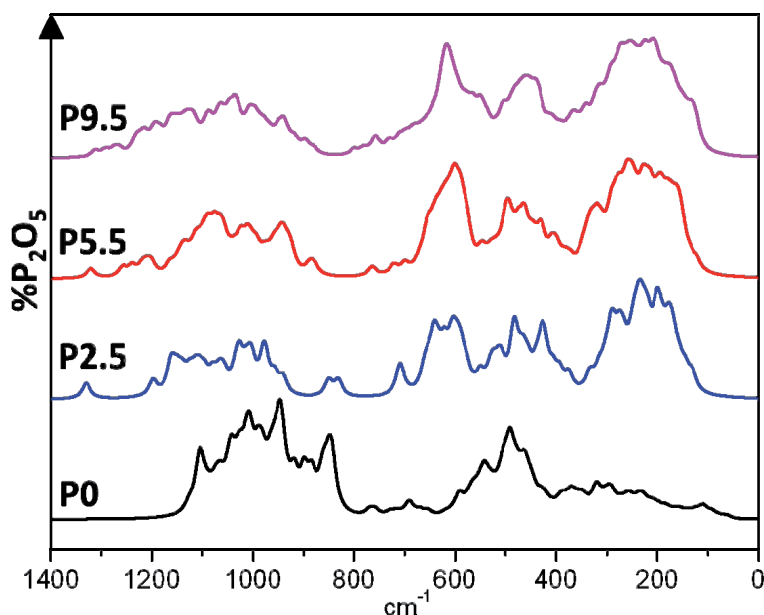


Fig. 13. Simulated IR spectra of the four models of glasses at increasing %P<sub>2</sub>O<sub>5</sub> content.

#### 2.2.4 Future perspectives: Surface modelling

The natural subsequent step in bioactive glass simulation deals with the modeling of surfaces. Indeed, each process of the Hench mechanism that leads to the implant integration typically occurs at the interface between the inorganic material and the biological fluid. Thus, the knowledge of surface properties, such as electrostatic potential and adsorptive behavior towards simple molecules as water, becomes essential in the investigation of bioglasses (Tilocca & Cormack, 2009).

Modeling surfaces is generally not a trivial task, particularly when the bulk material is amorphous. For an amorphous material the identification of a particular face by crystallographic indexes is rather arbitrary as the atomic density is statistically distributed in space in a rather uniform way. A second difficulty is the need of breaking both ionic and covalent bonds during the slab definition which may render the system non-neutral.

In Figure 14, the model of one of the many possible bioglass surfaces extracted from the P2.5 bulk of Figure 8b is presented. The surface was cut out from the bulk as a real 2D slab (infinite in the two dimensions), dangling bonds were saturated with hydrogen atoms and a full optimization run was performed. The resulting surface is very interesting per se, but much more considering its behaviour when hydrated, since water molecules are ubiquitously present in the biological fluids where the material is immersed. In particular, a key issue is to see whether H<sub>2</sub>O will chemisorb by dissociating on the exposed Na<sup>+</sup> and Ca<sup>2+</sup> cations, a step essential in the Hench mechanism.

In our laboratory a systematic study of the several possible surfaces of the structure with the 45S5 composition is on-going. The application of different methodologies, such as *ab initio* molecular dynamics, already used in the literature (Tilocca, 2010), will be considered to fully characterize the adsorption processes of water and even collagen occurring at the interface between bioactive material and the biological tissue.

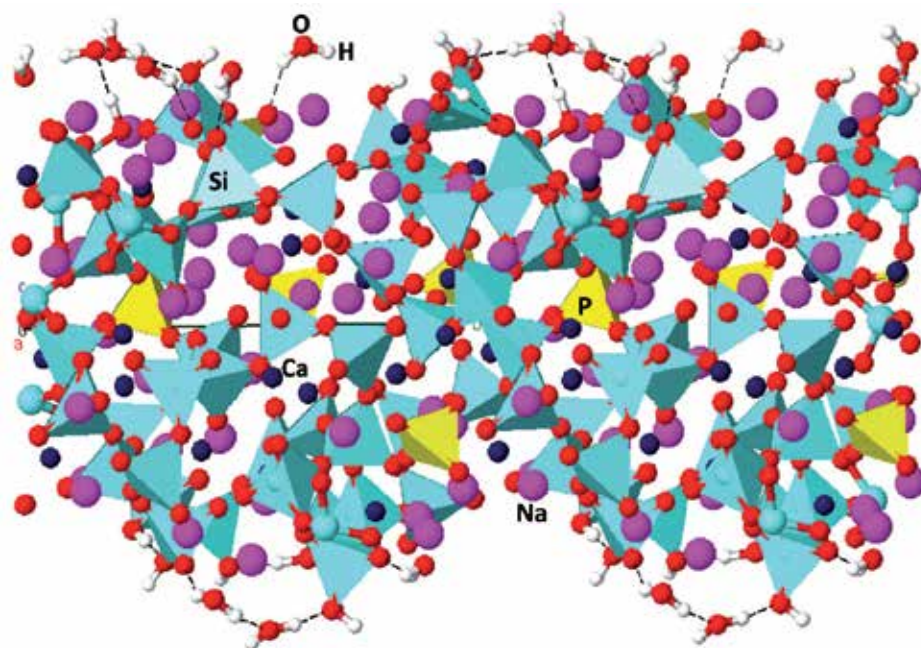


Fig. 14. Surface model of the P2.5 bioglass with adsorbed water molecules at both top and bottom faces. Colour coding: silicon light blue, oxygen red, sodium pink, calcium dark blue, phosphorous yellow, hydrogen bonds black dotted line.

### 3. Conclusion

In the present Chapter it has been explained how crucial the computational techniques are when applied together with experimentalist measurements in the understanding of biological complex systems and mechanisms dealing with biomaterials for a large number of reasons. Indeed, computational methods are extremely powerfully applied to predict structure formation and crystal growth as well as to describe at a molecular level the real interactions responsible of the attachment of the inorganic biomaterial to the organic tissue. In the investigation of phenomena related to a complex system such as the human body, many approximations are required, so a reductionist approach is employed also in the computational analysis.

In this Chapter, the approach has been explained for two typical biomaterials: hydroxyapatite and Bioglass® 45S5. In particular, for the first material, the aim was to describe the study of its (010) non-stoichiometric surfaces in interaction with water and carbon monoxide. For the latter, the adopted strategy has been analyzed and then a specific example has been reported, dealing with the spectroscopic characterization of computed vibrational features with the increasing amount of phosphorous in a sufficiently large unit cell starting from the well-know 45S5 Bioglass® composition.

The general knowledge gained in recent years through the use of computational techniques such as those described in this chapter is great, but not enough to fully understand the peculiar characteristics of the materials that make up the musculo-skeletal system and to provide appropriate care for important illnesses such as osteoporosis or degenerative and metabolic diseases, benign and malignant tumors and trauma.

To achieve this goal it is fundamental to understand the structure and properties of natural bone at a molecular level and to investigate the chemical-physical interaction between collagen and mineral phase comprising the bone composite.

This can only be achieved through the development and use of multiscale computational methods that combine quantum, classical and continuum approaches enabling to study chemical-physical-biological phenomena on large-scales both in space and time.

Regarding the study of the human bone, we believe that the key issues to be addressed by computational science researchers in the coming years will be the study of the structure and assembly of the collagen protein, the interaction at the molecular level of collagen with the mineral apatite, and finally the structure and mechanical properties of collagen-apatite composite.

As for the study of bioactive glasses, an important line of research that is developing in different research groups located in different nations involves the characterization of the chemical and physical properties and reactivity of the 45S5 Bioglass® surface. However, it will be wise not to neglect the study of the effect of composition on the structure and bioactivity of different systems and the study of the thermodynamics and crystallization kinetics of crystalline phases that are well-known to affect the bioactivity of the glass. Finally, the design of new bioactive glasses will also rely on a deep understanding of their fracture mechanism and the prediction of important properties such as brittleness and toughness, which determine the final use of glass.

#### 4. Acknowledgment

The authors would like to thank the Distributed European Infrastructure for Supercomputing Applications (DEISA) for allowing of computational resources under the Extreme Computing Initiative (BIOGLASS Project). CINECA computing centre is also kindly acknowledged.

Colleagues V. Bolis (Dip. DiSCAFF, University of Eastern Piedmont) and G. Martra (Dip. Chimica IFM, University of Torino) are acknowledged for fruitful discussion and for providing the HA samples, synthesized and kindly supplied by ISTECCNR (Faenza, Italy). R. Dovesi, B. Civalleri and the CRYSTAL team (Dip. Chimica IFM, University of Torino) are thanked for discussion and continuous support with the use of the code.

Part of the results on carbonated HA has been obtained by G. Ulian during his Master Degree Thesis, entitled "DFT study of carbonated defect in hydroxyapatite", 2010, University of Torino.

#### 5. References

- Aina, V., Bonino, F., Morterra, C., Miola, M., Bianchi, C. L., Malavasi, G., Marchetti, M. & Bolis, V. (2011) Influence of the Chemical Composition on Nature and Activity of the Surface Layer of Zn-Substituted Sol-Gel (Bioactive) Glasses. *The Journal of Physical Chemistry C*, Vol.115, No.5, pp.2196-2210, ISSN 1932-7447.
- Astala, R. & Stott, M. J. (2005) First Principles Investigation of Mineral Component of Bone: CO<sub>3</sub> Substitutions in Hydroxyapatite. *Chemistry of Materials*, Vol.17, No.16, pp.4125-4133, ISSN 1520-5002.
- Astala, R. & Stott, M. J. (2008) First-principles study of hydroxyapatite surfaces and water adsorption. *Physical Review B*, Vol.78, No.7, pp.075427, ISSN 1550-235X.

- Astala, R., Stott, M. J. & Calderin, L. (2006) Ab Initio Simulation of Si-Doped Hydroxyapatite. *Chemistry of Materials*, Vol.18, No.2, pp.413-422, ISSN 1520-5002.
- Becke, A. D. (1993) Density-functional thermochemistry. III. The role of exact exchange. *The Journal of Chemical Physics*, Vol.98, No.7, pp.5648-5652, ISSN 0021-9606.
- Bertinetti, L., Tampieri, A., Landi, E., Ducati, C., Midgley, P. A., Coluccia, S. & Martra, G. (2007) Surface Structure, Hydration, and Cationic Sites of Nanohydroxyapatite: UHR-TEM, IR and Microgravimetric Studies. *The Journal of Physical Chemistry C*, Vol.111, No.10, pp.4027-4035, ISSN 1932-7447.
- Canepa, P., Chiatti, F., Corno, M., Sakhno, Y., Martra, G. & Ugliengo, P. (2011a) Affinity of hydroxyapatite (001) and (010) surfaces to formic and alendronic acids: a quantum-mechanical and infrared study. *Physical Chemistry Chemical Physics*, Vol.13, No.3, pp.1099-1111, ISSN 1463-9084.
- Canepa, P., Hanson, R. M., Ugliengo, P. & Alfredsson, M. (2011b) J-ICE: a new Jmol interface for handling and visualizing crystallographic and electronic properties. *Journal of Applied Crystallography*, Vol.44, No.1, pp.225-229, ISSN 0021-8898.
- Christie, J. K., Pedone, A., Menziani, M. C. & Tilocca, A. (2011) Fluorine Environment in Bioactive Glasses: Ab Initio Molecular Dynamics Simulations. *The Journal of Physical Chemistry B*, Vol.115, No.9, pp.2038-2045, ISSN 1520-6106.
- Clayden, N. J., Pernice, P. & Aronne, A. (2005) Multinuclear NMR study of phosphosilicate gels derived from  $\text{POCl}_3$  and  $\text{Si}(\text{OC}_2\text{H}_5)_4$ . *Journal of Non-Crystalline Solids*, Vol.351, No.3, pp.195-202, ISSN 0022-3093.
- Corno, M., Busco, C., Bolis, V., Tosoni, S. & Ugliengo, P. (2009) Water Adsorption on the Stoichiometric (001) and (010) Surfaces of Hydroxyapatite: A Periodic B3LYP Study. *Langmuir*, Vol.25, No.4, pp.2188-2198, ISSN 1520-5827.
- Corno, M., Busco, C., Civalleri, B. & Ugliengo, P. (2006) Periodic *ab initio* study of structural and vibrational features of hexagonal hydroxyapatite  $\text{Ca}_{10}(\text{PO}_4)_6(\text{OH})_2$ . *Physical Chemistry Chemical Physics*, Vol.8, No.21, pp.2464-2472, ISSN 1463-9084.
- Corno, M., Orlando, R., Civalleri, B. & Ugliengo, P. (2007) Periodic B3LYP study of hydroxyapatite (001) surface modelled by thin layer slab. *European Journal of Mineralogy*, Vol.19, No.5, pp.757-767, ISSN 0935-1221.
- Corno, M. & Pedone, A. (2009) Vibrational features of phospho-silicate glasses: Periodic B3LYP simulations. *Chemical Physics Letters*, Vol.476, No.4-6, pp.218-222, ISSN 0009-2614.
- Corno, M., Pedone, A., Dovesi, R. & Ugliengo, P. (2008) B3LYP Simulation of the Full Vibrational Spectrum of 45S5 Bioactive Silicate Glass Compared to v-Silica. *Chemistry of Materials*, Vol.20, No.17, pp.5610-5621, ISSN 1520-5002.
- Corno, M., Rimola, A., Bolis, V. & Ugliengo, P. (2010) Hydroxyapatite as a key biomaterial: quantum-mechanical simulation of its surfaces in interaction with biomolecules. *Physical Chemistry Chemical Physics*, Vol.12, No.24, pp.6309-6329, ISSN 1463-9084.
- Currey, J. D. (1998) Mechanical properties of vertebrate hard tissues. *Proceedings of the Institution of Mechanical Engineers, Part H: Journal of Engineering in Medicine*, Vol.212, No.6, pp.399-411, ISSN 2041-3033
- de Leeuw, N. H., Bowe, J. R. & Rabone, J. A. L. (2007) A computational investigation of stoichiometric and calcium-deficient oxy- and hydroxy-apatites. *Faraday Discussions*, Vol.134, 195-214, ISSN 1364-5498.
- Dorozhkin, S. V. (2009) Calcium Orthophosphates in Nature, Biology and Medicine. *Materials*, Vol.2, No.2, pp.399-498, ISSN 1996-1944.
- Dovesi, R., Civalleri, B., Orlando, R., Roetti, C. & Saunders, V. R. (2005a). Ab Initio Quantum Simulation in Solid State Chemistry. In *Review in Computational Chemistry*, Vol. 21,

- K.B. Lipkowitz, R. Larter & T.R. Cundari (Ed.), pp. 1-127, John Wiley & Sons Inc., ISBN 9780471682394, New York
- Dovesi, R., Orlando, R., Civalleri, B., Roetti, C., Saunders, V. R. & Zicovich-Wilson, C. M. (2005b) CRYSTAL: a computational tool for the ab initio study of the electronic properties of crystals. *Zeitschrift fur Kristallographie*, Vol.220, No.5-6, pp.571-573, ISSN 0044-2968.
- Dovesi, R., Saunders, V. R., Roetti, C., Orlando, R., Zicovich-Wilson, C. M., Pascale, F., Civalleri, B., Doll, K., Harrison, N. M., Bush, I. J., D'Arco, P. & Llunell, M., CRYSTAL2009 User's Manual, Available from: <<http://www.crystal.unito.it>>
- Fleet, M. E. & Liu, X. (2003) Carbonate apatite type A synthesized at high pressure: new space group (*P*-3) and orientation of channel carbonate ion. *Journal of Solid State Chemistry*, Vol.174, No.2, pp.412-417, ISSN 1095-726X.
- Fleet, M. E. & Liu, X. (2004) Location of type B carbonate ion in type A-B carbonate apatite synthesized at high pressure. *Journal of Solid State Chemistry*, Vol.177, No.9, pp.3174-3182, ISSN 1095-726X.
- Fleet, M. E. & Liu, X. (2007) Coupled substitution of type A and B carbonate in sodium-bearing apatite. *Biomaterials*, Vol.28, No.6, pp.916-926, ISSN 0142-9612.
- Fratzl, P., Gupta, H. S., Paschalis, E. P. & Roschger, P. (2004) Structure and mechanical quality of the collagen-mineral nano-composite in bone. *Journal of Materials Chemistry*, Vol.14, No.14, pp.2115-2123, ISSN 0959-9428.
- Hench, L. (2006) The story of Bioglass®. *Journal of Materials Science: Materials in Medicine*, Vol.17, No.11, pp.967-978, ISSN 0957-4530.
- Hench, L. L. (1998) Biomaterials: a forecast for the future. *Biomaterials*, Vol.19, No.16, pp.1419-1423, ISSN 0142-9612.
- Hench, L. L. & Andersson, O. H. (1993). Bioactive glasses. In *An introduction to bioceramics*. In *An introduction to bioceramics*, L.L. Hench & W. J. (Ed.), pp. 42-62, World Scientific, ISBN 978-981-02-1400-5 Singapore.
- Hench, L. L., Splinter, R. J., Allen, W. C. & Greenlee, T. K. (1971) Bonding Mechanism at the Interface of Ceramic Prosthetic Materials. *Journal of Biomedical Materials Research A*, Vol.5, No.6, pp.117-141, ISSN 1552-4965.
- Hoover, W. G. (1985) Canonical dynamics: Equilibrium phase-space distribution. *Physical Review A*, Vol.31, No.3, pp.1695-1697, ISSN 1094-1622.
- Humphrey, W., Dalke, A. & Schulten, K. (1996) VMD: Visual Molecular Dynamics. *Journal of Molecular Graphics*, Vol.14, No.1, pp.33-38, ISSN 1093-3263.
- Levitt, S. R., Crayton, P. H., Monroe, E. A. & Condrate, R. A. (1969) Forming methods for apatite prostheses. *Journal of Biomedical Materials Research A*, Vol.3, 683-684, ISSN 1097-4636.
- Lin, C. C., Huang, L. C. & Shen, P. (2005) Na<sub>2</sub>CaSi<sub>2</sub>O<sub>6</sub>-P<sub>2</sub>O<sub>5</sub> based bioactive glasses. Part 1: Elasticity and structure. *Journal of Non-Crystalline Solids*, Vol.351, No.40-42, pp.3195-3203, ISSN 0022-3093.
- Lusvardi, G., Malavasi, G., Cortada, M., Menabue, L., Menziani, M. C., Pedone, A. & Segre, U. (2008a) Elucidation of the Structural Role of Fluorine in Potentially Bioactive Glasses by Experimental and Computational Investigation. *The Journal of Physical Chemistry B*, Vol.112, No.40, pp.12730-12739, ISSN 1520-6106.
- Lusvardi, G., Malavasi, G., Menabue, L., Menziani, M. C., Pedone, A., Segre, U., Aina, V., Perardi, A., Morterra, C., Boccafoschi, F., Gatti, S., Bosetti, M. & Cannas, M. (2008b) Properties of Zinc Releasing Surfaces for Clinical Applications. *Journal of Biomaterials Applications*, Vol.22, 505-526, ISSN 1530-8022.

- Matsumura, Y. & Moffat, J. B. (1996) Methanol adsorption and dehydrogenation over stoichiometric and non-stoichiometric hydroxyapatite catalysts. *Journal of the Chemical Society, Faraday Transactions*, Vol.92, No.11, pp.1981-1984, ISSN 0965-5000.
- O'Donnell, M. D., Watts, S. J., Law, R. V. & Hill, R. G. (2008a) Effect of P2O5 content in two series of soda lime phosphosilicate glasses on structure and properties - Part I: NMR. *Journal of Non-Crystalline Solids*, Vol.354, No.30, pp.3554-3560, ISSN 0022-3093.
- O'Donnell, M. D., Watts, S. J., Law, R. V. & Hill, R. G. (2008b) Effect of P2O5 content in two series of soda lime phosphosilicate glasses on structure and properties - Part II: Physical properties. *Journal of Non-Crystalline Solids*, Vol.354, No.30, pp.3561-3566, ISSN 0022-3093.
- O'Donnell, M., Watts, S., Hill, R. & Law, R. (2009) The effect of phosphate content on the bioactivity of soda-lime-phosphosilicate glasses. *Journal of Materials Science: Materials in Medicine*, Vol.20, No.8, pp.1611-1618, ISSN 1573-4838.
- Padilla, S., Roman, J. & Vallet-Regi, M. (2002) Synthesis of porous hydroxyapatite by combination of gelcasting and foams burn out methods. *Journal of Materials Science: Materials in Medicine*, Vol.13, No.12, pp.1193-1197, ISSN 1573-4838.
- Pedone, A., Charpentier, T., Malavasi, G. & Menziani, M. C. (2010) New Insights into the Atomic Structure of 45S5 Bioglass by Means of Solid-State NMR Spectroscopy and Accurate First-Principles Simulations. *Chemistry of Materials*, Vol.22, No.19, pp.5644-5652, ISSN 1520-5002.
- Pedone, A., Malavasi, G., Cormack, A. N., Segre, U. & Menziani, M. C. (2008) Elastic and dynamical properties of alkali-silicate glasses from computer simulations techniques. *Theoretical Chemistry Accounts: Theory, Computation, and Modeling (Theoretica Chimica Acta)*, Vol.120, No.4-6, pp.557-564, ISSN 1432-2234.
- Pedone, A., Malavasi, G., Menziani, M. C., Segre, U. & Cormack, A. N. (2008) Role of Magnesium in soda-lime glasses: insight into structure, transport and mechanical properties through computer simulations. *The Journal of Physical Chemistry C*, Vol.112, No.29, pp.11034-11041, ISSN 1932-7447.
- Perdew, J. P., Burke, B. & Ernzerhof, M. (1996) Generalized Gradient Approximation Made Simple. *Physical Review Letters*, Vol.77, No.18, pp.3865-3868, ISSN 1079-7114.
- Peroos, S., Du, Z. M. & de Leeuw, N. H. (2006) A computer modelling study of the uptake, structure and distribution of carbonate defects in hydroxy-apatite. *Biomaterials*, Vol.27, No.9, pp.2150-2161, ISSN 0142-9612.
- Rabone, J. A. L. & de Leeuw, N. H. (2005) Interatomic Potential Models for Natural Apatite Crystals: Incorporating Strontium and the Lanthanides. *Journal of Computational Chemistry*, Vol.27, No.2, pp.253-266, ISSN 1096-987X.
- Rabone, J. A. L. & de Leeuw, N. H. (2007) Potential routes to carbon inclusion in apatite minerals: a DFT study. *Physics and Chemistry of Minerals*, Vol.34, No.7, pp.495-506, ISSN 1432-2021.
- Rimola, A., Corno, M., Zicovich-Wilson, C. M. & Ugliengo, P. (2008) *Ab Initio* Modeling of Protein/Biomaterial Interactions: Glycine Adsorption at Hydroxyapatite Surfaces. *Journal of the American Chemical Society*, Vol.130, No.48, pp.16181-16183, ISSN 0002-7863.
- Rimola, A., Corno, M., Zicovich-Wilson, C. M. & Ugliengo, P. (2009) *Ab initio* modeling of protein/biomaterial interactions: competitive adsorption between glycine and water onto hydroxyapatite surfaces. *Physical Chemistry Chemical Physics*, Vol.11, No.40, pp.9005 - 9007, ISSN 1463-9084.

- Rodriguez-Lorenzo, L. M., Vallet-Regi, M., Ferreira, J. M. F., Ginebra, M. P., Aparicio, C. & Planell, J. A. (2002) Hydroxyapatite ceramic bodies with tailored mechanical properties for different applications. *Journal of Biomedical Materials Research A*, Vol.60, 159-166, ISSN 1097-4636.
- Roveri, N. & Palazzo, B. (2006). Hydroxyapatite Nanocrystals as Bone Tissue Substitute. In *Tissue, Cell and Organ Engineering*, C.S.S.R. Kumar (Ed.), pp. 283-307, Wiley-VCH, ISBN 978-3-527-31389-1, Weinheim.
- Sakhno, Y., Bertinetti, L., Iafisco, M., Tampieri, A., Roveri, N. & Martra, G. (2010) Surface Hydration and Cationic Sites of Nanohydroxyapatites with Amorphous or Crystalline Surfaces: A Comparative Study. *The Journal of Physical Chemistry C*, Vol.114, No.39, pp.16640-16648, ISSN 1932-7447.
- Sato, K., Kogure, T., Iwai, H. & Tanaka, J. (2002) Atomic-Scale {101-0} Interfacial Structure in Hydroxyapatite Determined by High-Resolution Transmission Electron Microscopy. *Journal of the American Ceramic Society*, Vol.85, No.12, pp.3054-3058, ISSN 1551-2916.
- Suda, H., Yashima, M., Kakihana, M. & Yoshimura, M. (1995) Monoclinic <--> Hexagonal Phase Transition in Hydroxyapatite Studied by X-ray Powder Diffraction and Differential Scanning Calorimeter Techniques. *The Journal of Physical Chemistry*, Vol.99, No.17, pp.6752-6754, ISSN 0022-3654.
- Tadic, D., Beckmann, F., Schwarz, K. & Epple, M. (2004) A novel method to produce hydroxyapatite objects with interconnecting porosity that avoids sintering. *Biomaterials*, Vol.25, No.16, pp.3335-3340, ISSN 0142-9612.
- Tilocca, A. (2010) Models of structure, dynamics and reactivity of bioglasses: a review. *Journal of Materials Chemistry*, Vol.20, No.33, pp.6848-6858, ISSN 0959-9428.
- Tilocca, A. & Cormack, A. N. (2007) Structural effects of Phosphorus Inclusion in Bioactive Silicate Glasses. *The Journal of Physical Chemistry B*, Vol.111, No.51, pp.14256-14264, ISSN 1520-6106.
- Tilocca, A. & Cormack, A. N. (2009) Surface Signatures of Bioactivity: MD Simulations of 45S and 65S Silicate Glasses. *Langmuir*, Vol.26, No.1, pp.545-551, ISSN 0743-7463.
- Toulhat, N., Potocek, V., Neskovic, M., Fedoroff, M., Jeanjean, J. & Vincent, V. (1996) Perspectives for the study of the diffusion of radionuclides into minerals using the nuclear microprobe techniques. *Radiochimica Acta*, Vol.74, No.1, pp.257-262, ISSN 0033-8230.
- Ugliengo, P., Viterbo, D. & Chiari, G. (1993) MOLDRAW: Molecular Graphics on a Personal Computer. *Zeitschrift fur Kristallographie*, Vol.207, No.1, pp.9-23, ISSN 0044-2968.
- Wahl, D. A., Sachlos, E., Liu, C. & Czernuszka, J. T. (2007) Controlling the processing of collagen-hydroxyapatite scaffolds for bone tissue engineering. *Journal of Materials Science: Materials in Medicine*, Vol.18, 201-209, ISSN 1573-4838.
- Weiner, S. & Wagner, H. D. (1998) The material bone: structure-mechanical function relations. *Annual Review of Materials Science*, Vol.28, No.1, pp.271-298, ISSN 0084-6600.
- Wierzbicki, A. & Cheung, H. S. (2000) Molecular modeling of inhibition of hydroxyapatite by phosphocitrate. *Journal of Molecular Structure: THEOCHEM*, Vol.529, No.1-3, pp.73-82, ISSN 0166-1280.
- Young, R. A. & Brown, W. E. (1982). Structures of Biological Minerals. In *Biological Mineralization and Demineralization*, G.H. Nancollas (Ed.), pp. 101-141, Springer-Verlag, ISBN 978-0387115214, Berlin, Heidelberg, New York.



# The Use of Vibration Principles to Characterize the Mechanical Properties of Biomaterials

Oswaldo H. Campanella<sup>1</sup>, Hartono Sumali<sup>2</sup>,  
Behic Mert<sup>3</sup> and Bhavesh Patel<sup>1</sup>

<sup>1</sup>*Agricultural and Biological Engineering Department and  
Whistler Carbohydrate Research Center, Purdue University, West Lafayette, IN*

<sup>2</sup>*Sandia National Laboratories, Albuquerque, NM*

<sup>3</sup>*Department of Food Engineering, Middle East Technical University, Ankara*

<sup>1,2</sup>USA

<sup>3</sup>Turkey

## 1. Introduction

Mechanical properties are a primary quality factor in many materials ranging from liquids to solids including foods, cosmetics, certain pharmaceuticals, paints, inks, polymer solutions, to name a few. The mechanical properties of these products are important because they could be related to either a quality attribute or a functional requirement. Thus, there is always a need for the development of testing methods capable to meet various material characterization requirements from both the industry and basic research.

There is a wide range of mechanical tests in the market with a wide price range. However, there is an increasing interest in finding new methods for mechanical characterization of materials specifically capable to be adapted to in-line instruments. Acoustic/vibration methods have gained considerable attention and several instruments designed and built in government labs (e.g. Pacific Northwest National Laboratory and Argon National Laboratory) have been made commercially available.

To measure mechanical properties of material a number of conventional techniques are available, which in some cases may alter or change the sample during testing (destructive testing). In other tests the strains/deformations applied are so small that the test can be considered non-destructive. Both types of test are based on the application of a controlled strain and the measurement of the resulting stress, or viceversa. Different types of deformations, e.g. compression, shear, torsion are used to test these materials.

Depending on the type of material, different conventional techniques utilized to measure its mechanical properties can be grouped as viscosity measurement tests (liquid properties), viscoelasticity measurement tests (semiliquid/semisolid properties), and elastic measurement tests (solid properties).

Acoustics based techniques can be used for all types of material and the following sections discuss in detail how these techniques have been adapted and used to measure materials whose properties range from liquids to solids. Some of the applications discussed in this chapter are based on the basic impedance tube technique. Applications of this technique for

material characterization in air have been around for almost a century. The technique is described in basic acoustics text books such as Kinsler et al., (2000) and Temkin (1981). Impedance tube methods based on standing waves and the transfer function method have been accepted as standard methods by the American Society for Testing and Materials (ASTM 1990 and 1995), thus they will not be discussed in this chapter. Instead the chapter will focus on liquids, semiliquid and semisolid materials, many of them exhibiting viscoelastic properties, i.e. those properties that are more representative of biomaterials behavior.

## **2. Vibration fundamentals and analysis**

The theoretical background that supports mechanical characterization of materials using vibration/acoustic based methods is mainly based on the characterization of acoustic waves propagating through the material. In that sense the analysis can be classified on the type of material being tested, i.e. liquid, viscoelastic semifluid, and viscoelastic semisolid.

### **2.1 Liquid materials**

The analysis of liquid samples can be further classified based on the type of container used to confine the testing liquid. One of more important aspects to consider in this classification is the rigidity of the container walls. Two cases are considered: containers with rigid walls and containers with deformable/flexible walls.

#### **2.1.1 Rigid wall containers**

Since acoustic waves reveal useful information on the characteristic of the material through which they travel, measurement of acoustical properties such as velocity, attenuation, and phase changes resulting mainly from wave reflections in the transfer media are often used as a tool for mechanical characterization of materials. Specifically, ultrasound has found a wide range of applications in the measurement of the viscosity of liquids. Mason et al. (1949) first introduced an ultrasonic technique to measure the viscosity of liquids. They used the reflection of a shear wave in the interface between a quartz crystal and the sample liquid. Since then many other ultrasonics related techniques have been developed to measure viscosity of liquids [Roth and Rich (1953), Hertz et al. (1990), and Sheen et al., (1996)]. However, acoustical techniques that use sonic frequency have been rather limited. The main reason for this has been the lack of practical approaches that can employ frequencies in the sonic range to study the rheology of liquids. Tabakayashi and Raichel (1998) tried to use sonic frequency waves for rheological characterization of liquids. They affixed a hydrophone and a speaker to both ends of a cylindrical tube and analyzed the effect of the liquid non-Newtonian behavior on the propagation of the sound waves. The approach used by these authors is similar to the well known impedance tube method commonly applied to gases contained in cylindrical tubes, known as waveguides, but their analysis did not include the effect of the tube boundaries on sound propagation which can be of importance. In that sense, the application of the impedance tube techniques to test liquids has been limited because the loss of wall rigidity, i.e. the tube boundary, which normally it does not occur in tubes filled with air or air waveguides. Thus, when the tube is filled with a liquid, the tube may become an elastic waveguide and the rigid wall approximation loses its validity. The key assumption of having rigid walls is related to the shape of the acoustic

wave moving through the liquid. In order to have manageable equations to estimate the viscosity of the liquid from acoustic measurements using these systems it is important to generate planar standing waves from which acoustic parameters can be readily obtained. Mert et al. (2004) described a model and the experimental conditions under which the assumption of standing planar waves stands.

If a tube with rigid walls is considered the propagation of unidirectional plane sound waves though the liquid contained in the rigid tube can be described by the following equation (Kinsler et al., 2000):

$$\frac{\partial^2 p}{\partial t^2} - C_1^2 \frac{\partial^2 p}{\partial x^2} \quad (1)$$

where  $p$  is the acoustic pressure,  $t$  is time,  $x$  distance and  $C_1$  the speed of the sound in the testing liquid. The solution of Equation (1) can be expressed in terms of two harmonic waves travelling in opposite directions and whose composition gives place to the formation of standing waves (Kinsler et al., 2000):

$$p(x, t) = p^+ e^{[i\omega t + \hat{k}(L-x)]} + p^- e^{[i\omega t - \hat{k}(L-x)]} \quad (2)$$

$p^+$  is the amplitude of the wave traveling in the direction  $+x$  whereas  $p^-$  is the amplitude of the wave traveling in the direction  $-x$  and  $i$  is the imaginary number equal to  $\sqrt{-1}$ . The complex wave number  $\hat{k} = \omega / C_1 - i\alpha$  includes the attenuation  $\alpha$  due to the viscosity of the liquid,  $\omega$  is the frequency of the wave. The corresponding wave velocity can be obtained from integration of the pressure derivative respect to the distance  $x$ , an equation that is known as the Euler equation (Temkin, 1981) and calculated as  $v(x, t) = -\frac{1}{\rho_0} \int \frac{\partial p}{\partial x} dt$ , which yields:

$$v(x, t) = P^+ e^{[i\omega t + \hat{k}(L-x)]} - P^- e^{[i\omega t - \hat{k}(L-x)]} \quad (3)$$

By applying the boundary conditions such that at  $x = 0$  the fluid velocity is equal to the velocity of the piston that creates the wave, which is  $v(0, t) = v_0 e^{i\omega t}$ . The other boundary condition is derived from the practical situation of using an air space on the other end of the tube, which mathematical provides a pressure release condition at  $x = L$ , written as  $p(L, t) = 0$ . With these boundary conditions the coefficients  $P^+$  and  $P^-$  in Equation 3 can be calculated as:

$$P^+ = \frac{\rho_0 C_1 v_0}{2 \cos \hat{k} L} \quad \text{and} \quad P^- = -\frac{\rho_0 C_1 v_0}{2 \cos \hat{k} L} \quad (4)$$

where  $\rho_0$  is the density of the liquid, in repose, and  $v_0$  the amplitude of the imposed wave. An analysis made by Temkin (1981) showed that two absorption mechanisms produce the attenuation of the sound energy. One is due to the attenuation effects produced by the dilatational motion of the liquid during the acoustic wave passage. The other term arises from the grazing/friction motion of the liquid on the wall of the tube. It can be shown that the attenuation due to wall effects is significantly larger than the attenuation due to the

dilatational motion of the liquid (Herzfeld and Litovitz, 1959). Thus, a simplified form can be used to obtain the complex wave number ( $\hat{k}$ ) and ultimately the attenuation ( $\alpha$ ) from which the fluid viscosity can be extracted. The complex wave number is given by the following equation:

$$\hat{k} = k_1 - i\alpha \quad (5)$$

where the real number  $k_1$  is calculated as  $k_1 = \frac{\omega}{C_1}$  and  $\alpha$  is the attenuation of the wave due

to the viscosity of the testing liquid.

For measurement purposes it is convenient to estimate the acoustic impedance as  $p/v$ , which from Equations (2) and (3) after application of the Fourier transform to the pressure and velocity variables yields:

$$Z_{a0} = \frac{\tilde{p}}{\tilde{v}} = \frac{i\rho_0\omega}{\hat{k}} \tan \hat{k}L = \frac{i\rho_0\omega \sin \hat{k}L}{\hat{k} \cos \hat{k}L} \quad (6)$$

Where  $\tilde{p}$  and  $\tilde{v}$  are the Fourier transformed pressure and velocity respectively. The acoustic impedance is a complex number, as well as its inverse, which is known as mobility. Thus, the magnitude or absolute value of the mobility  $Abs(1/Z_{a0})$  can be calculated. From values of the acoustic impedance or mobility the complex wave number  $\hat{k}$  can be obtained as well as its real and imaginary components, from which the viscosity of the liquid and the intrinsic sound velocity in the liquid of interest can be estimated from the following equation (Temkin, 1981):

$$\hat{k} = k_1 - \frac{i}{RC_1} \left\{ \left( \frac{\omega\mu}{2\rho} \right)^{0.5} + \left( \frac{\omega^2}{2C_1^2} \right) \left[ \left( \frac{\mu}{\rho} \right)^{0.5} + \left( \frac{\mu}{3\rho} \right)^{0.5} \right] + \frac{\omega^2}{4C_1^2} \left( \frac{\mu}{\rho} \right)^{0.5} \right\} \quad (7)$$

Viscosities of the liquids can be also estimated from the Kirchhoff's equation, which has been derived for waveguides containing a gas and are given by the following equation (Kinsler et al., 2000):

$$\alpha = \frac{1}{RC_1} \sqrt{\frac{\mu\omega}{2\rho_0}} \quad (8)$$

The parameter  $R$  in Equations 7 and 8 is obtained from to the magnitude of the mechanical impedance at the resonance frequency (see Figure 2).

From Equation (6) can be observed that plots of the acoustic impedance becomes a maximum when  $\cos(\hat{k}L)$  is a minimum, i.e. when the frequencies are given by the relationship  $f = \frac{C_1}{2L} \left( n + \frac{1}{2} \right)$ , where  $n = 0,1,2,3,\dots$ , which is in terms of the length of liquid  $L$  and the velocity of sound in the liquid  $C_1$ , can provide a location of those maxima. Those theoretical observations were experimentally validated by Mert et al. (2004) using an experimental setup as that described in Figure 1.

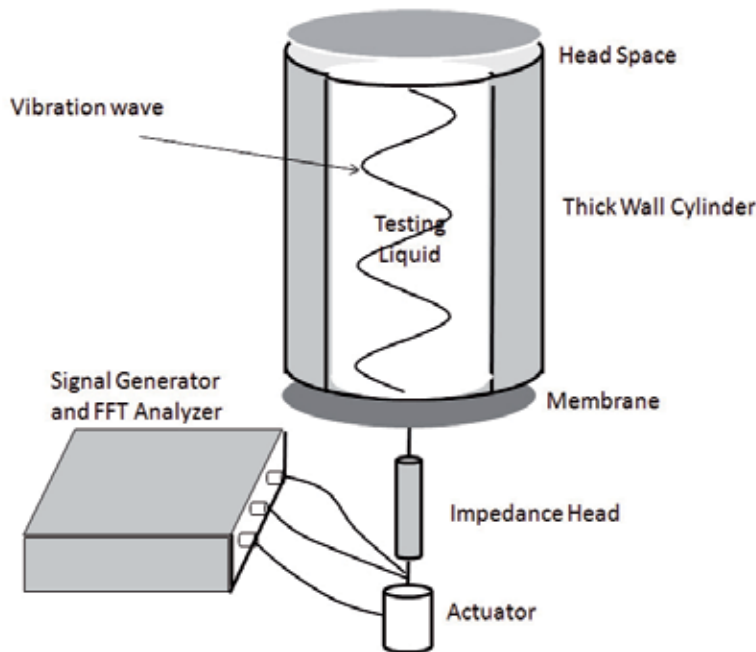


Fig. 1. Schematic of the apparatus to measure viscosity of liquids inside a thick wall rigid tube.

Further details of this experimental setting can be found elsewhere in Mert et al. (2004).

It has been hypothesized that plots of absolute mobility as a function of frequency should exhibit peaks and valleys corresponding to the resonance and anti-resonance frequencies of the standing waves from which the rheological properties of the liquid, notably its viscosity, can be obtained. To validate the theory described above, liquids with known physical properties including viscosity, density and sound velocity though them (the latter measured by a pulse-echo ultrasound method) were tested. Table 1 list viscosity of the liquids (liquids 1 to 4) used for this test along with their relevant physical properties.

Liquid	Viscosity <i>mPa . s</i>	Density <i>kg/m<sup>3</sup></i>	Intrinsic sound velocity <i>m/s</i>
1	17	800	1246
2	96	971	1010
3	990	969	967
4	4900	963	943
5	10,050	980	-

Table 1. Physical properties of the liquids used to validate theory; properties are at 25°C.

Figure 2 illustrates measured magnitude of the mechanical impedances  $Abs(1/Z_{a0})$  liquids 2, 3, and 4 (see Table 1). It is clearly shown in the figure the effect of the liquid viscosity on the measured impedance, in general the higher is the viscosity of the liquid the lower is the value of the magnitude of the mechanical impedance at the peak/resonance frequency. The resonance frequency (frequency where peaks in impedance are obtained) is also affected by the viscosity of the liquid and tend to decrease when the viscosity of the liquid increases, which would be indicating a decrease in the sound velocity though the liquid. The latter in

fully agreement with the ultrasonic pulse-echo measurements used to estimate the sound velocities in the different liquids, which are reported in Table 1.

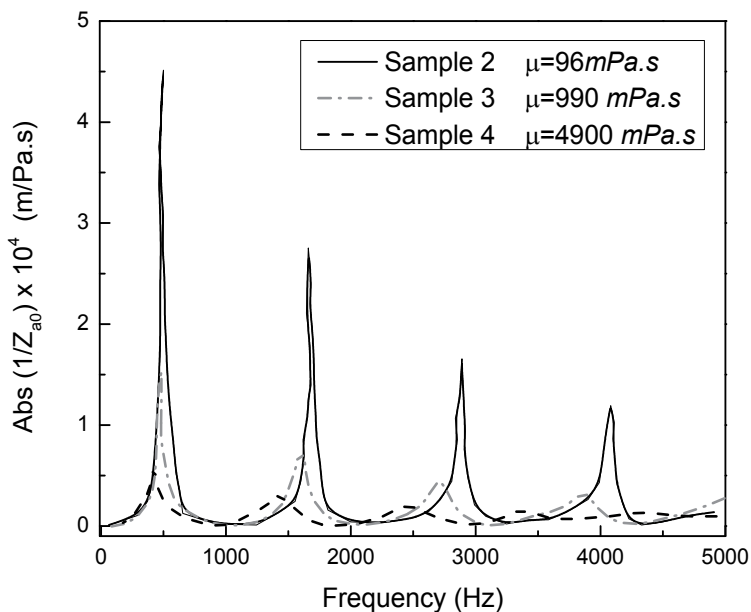


Fig. 2. Effect of viscosity on the magnitude of acoustical impedances measured in a setup as illustrated in Figure 1 at the driver position  $x = 0$ . Liquids 2, 3 and 4 were tested and properties and given in Table 1.

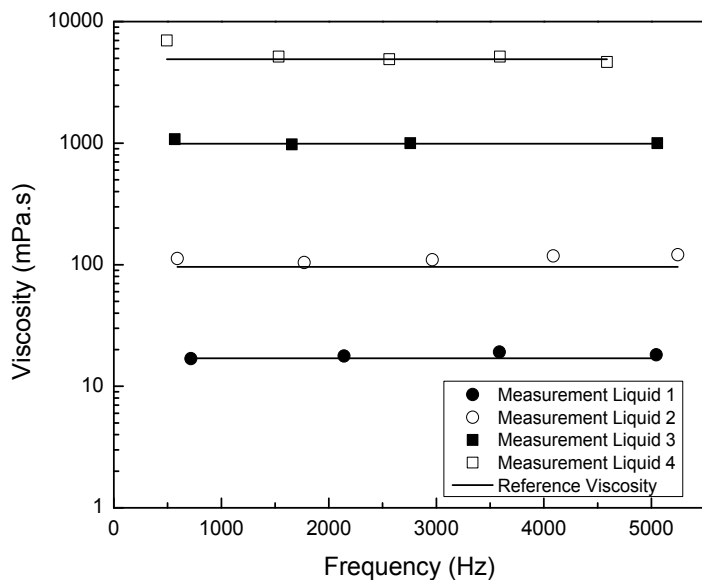


Fig. 3. Viscosities obtained from the different resonance frequencies for 4 different liquids obtained from the measured mechanical impedance and from Equation (7).

Extracted viscosities from impedance measurements along reported values of the liquid viscosities are illustrated in Figure 3.

Liquid viscosities were estimated from Equations 7 and 8 but better accuracy was obtained with Equation 7 that was derived for waveguides containing liquids (Mert et al., 2004). Results of the calculated viscosities are illustrated in Figure 3.

### 2.1.2 Flexible wall containers

When the walls of the waveguides are not rigid, during propagation of the waves the walls of the container expand and the overall liquid bulk modulus decreases leading to reduced sound velocity in the liquids. In addition, the fluid velocity cannot be assumed to be 0 at the can wall due to the expansion of the wall. These conditions make the governing equations used to estimate the wave attenuation and other relevant acoustic parameters very elusive, thus it is not possible estimate the liquid viscosity directly. One can overcome this problem by an empirical approach, which is by defining the quality factor  $Q$ , which is determined from the following equation:

$$Q = \frac{\omega_0}{\omega_2 - \omega_1} \quad (9)$$

$\omega_1$  and  $\omega_2$  are the frequencies at which the amplitude of mechanical impedance response is equal to half the actual value at resonance and  $\omega_0$  is the resonance frequency (Kinsler et al., 2000). If the quality  $Q$  is known in a given container-liquid system it would be possible to have an estimation of the viscosity of the liquids contained in the container, which would serve for quality control purposes. To prove that concept Mert and Campanella (2007) performed a study where a shaker applied vibrations to a cylindrical can containing a liquid using a system, schematically shown in Figure 1. The vibration was able to move the can containing the liquid, and a wave was generated through the liquid, which reflected back in the interface between the liquid and the headspace to form standing waves resulting from composition of the forward and reflected wave. Properties of the standing waves were measured in the frequency domain, and in particular the resonance frequency and the amplitude of the wave at that resonant frequency were obtained and using a calibration curve approach related empirically to the rheological properties of the liquid. It is important to note that these measurements do not provide the true viscosity of the testing liquid because the walls of the can are not rigid and deform significantly due to the vibration. Despite of that the properties of the standing waves, measured by the quality  $Q$ , were highly correlated with the rheology of the liquid, which was tested offline in a rheometer (Mert and Campanella, 2007). Results shown in Figure 4 are a frequency spectra for the liquids reported in Table 1.

Quality factors  $Q$  for the testing liquids can be estimated from the two peaks observed in Figure 4 and potted as a function of the liquid viscosity as illustrated in Figure 5. However, as shown in Figure 4, the first resonances peaks do not seem to provide sufficient resolution and the second resonance peaks, at higher frequency, are used to find a relationship with the liquid viscosity.

Although interesting from an academic standpoint correlations like the one shown in the Figure 5 are not of practical applicability. However, if the can/cylinder contains a product

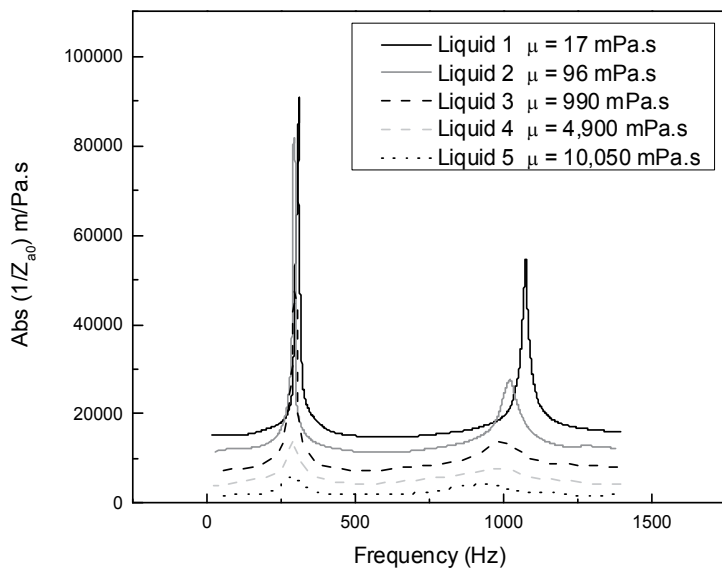


Fig. 4. Amplitudes at resonance frequencies for standard liquids given in Table 1. Curves were shifted up for clarity.

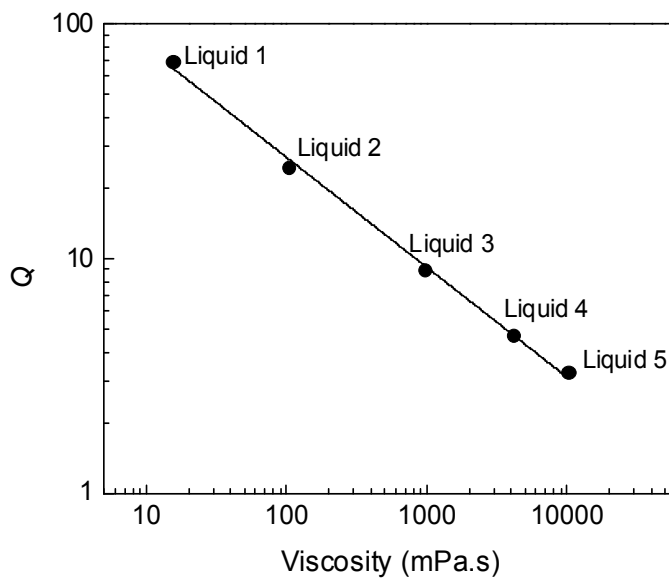


Fig. 5. Quality factor  $Q$  versus viscosity of liquid standards



whose viscosity is an important quality parameter, the present method would be of great applicability because the viscosity of the liquid could be assessed quickly without the necessity of opening the can (i.e. non-destructive method). One example of such application is testing cans of tomato products, which are widely produced and consumed in most part of the world and the viscosity of these products is a key parameter associated to their quality in terms of sensory evaluation and processing applications. Viscosity of tomato products is evaluated using a number of rheological techniques that range from empirical to more fundamental methods. One standard method is the use of the Brookfield<sup>TR</sup> viscometer. This viscometer is based on the rotation of a particular element (spindle) inside a can containing the product. The viscosity of the product is obtained basically from the resistance offered by the product to the rotation of the spindle provided shear rates and shear stresses can be accurately calculated. Since the geometries of the spindles often are not regular it is difficult to estimate the rheological parameters, i.e. shear stress and shear rate, which enable the calculation of the liquid viscosity. Tomato paste is a very viscous product that exhibits an important structure that can be destroyed during testing. One approach to overcome this problem is the use of a helical-path spindle, which through a helical movement continuously is touching a fresh sample. Given the complicated rheology, results of this test are considered empirical. The other approach is to use technically advanced rheological equipment, which though the use of geometries such as parallel plates the sample can be minimally disturbed. For these cases the true viscosity of these tomato purees can be obtained. These materials are known as non-Newtonian to indicate that their viscosities are a function of the shear rate. Most of the non-Newtonian liquids can be described by a rheological model known as the power-law model which can be expressed by the following equation:

$$\eta = k\dot{\gamma}^{n-1} \quad (10)$$

where  $\eta$  is the apparent viscosity of the material, which is a function of the applied shear rate  $\dot{\gamma}$  and  $k$  and  $n$  are rheological parameter known as the consistency index and the flow behavior, respectively. The value of  $k$  is an indication of the product viscosity whereas  $n$  gives a relation between the dependence of the viscosity with the applied shear rates. For tomato products  $n < 1$ , and the smaller is the value of  $n$  the largest is the effect of the shear rate on the viscosity of the liquid. To test the feasibility of vibration methods, cans of tomato puree and dilutions ranging from 23% to 3.5% solids were tested in an apparatus similar to the one shown in Figure 1. Results of the tests can be observed in Figure 6, where frequency spectra resulting from some the tests are shown. Figure 7 shows possible correlations between the quality  $Q$  measured from the frequency spectra data and the parameter  $k$  determined using a standard rheological technique and a parallel plate geometry.

As indicated in Figure 6 the frequency spectra peaks shift to lower frequencies when the solid content of the concentrates increases. In the range of frequency tested the two peaks are visible for concentrates with low solid content whereas the second peak at higher frequencies disappears for concentrates with higher higher solid contents (23 Brix). The amplitude of the Absolute value of the mobility is considerably decreased when the solid content and the viscosity of the concentrate increase (Figure 6). Given the existence of two peaks quality values can be extracted from the two peaks and relate them with the measured rheological properties, in this case the value of the consistency index (Figure 7). It

can be seen in the figure that correlations of the liquid rheological properties with its acoustic properties measured by the quality factor  $Q$  are strong and that the quality evaluated at the first peak provides a better representation of the liquid viscosity. This is also enhanced due to the presence of two peaks for low and moderate solid contents (measured as Brix), which provides more experimental points to establish the correlation (see Figure 7 – and compare first peak and second peak data).

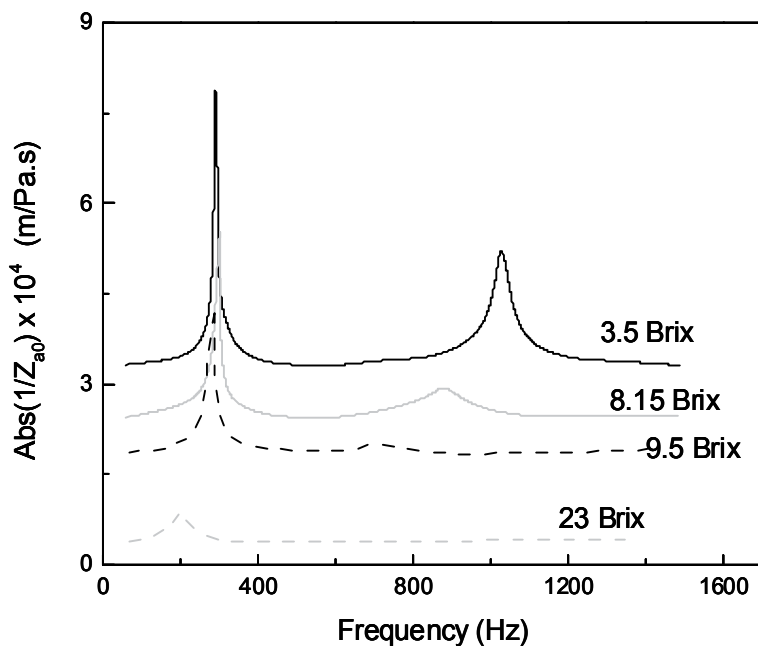


Fig. 6. Frequency response spectra of tomato concentrates at different soluble solids concentrations, measured as Brix. Curves were shifted up for clarity.

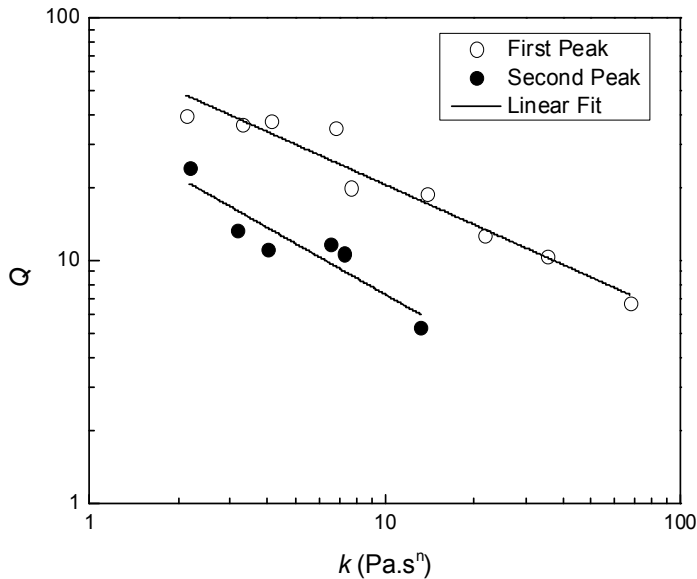


Fig. 7. Quality factor versus the consistency index  $k$  value for tomato puree and its dilutions

## 2.2 Viscoelastic materials

### 2.2.1 Semifluid materials

Squeezing flow is a well-known technique that has been applied to characterize the properties of various biomaterials ranging from liquids to semisolids. The traditional method involves measuring the force required to squeeze a sample between two cylindrical disks either at a constant velocity or by applying a constant force or stress (Campanella and Peleg 2002).

The oscillatory squeezing flow method (OSF) uses the same geometry as the standard squeezing flow method but it involves the application of small amplitude oscillations at random frequencies up to 20 kHz (Mert and Campanella, 2008). The method allows one to calculate both the viscous and elastic components of the sample viscoelasticity by measuring the response of the material in terms of force and acceleration to those oscillations. Transformation of the measured force and acceleration to the frequency domain yields a frequency spectrum for the sample and, ultimately, its resonance frequency. From analysis of this frequency response, two important viscoelastic properties of the samples, the loss modulus  $G''$  (viscous) and the storage modulus  $G'$  (elastic), can be obtained.

The application of acoustic principles to the squeezing flow method is a novel technique, which convert the squeezing flow method into OSF method can measure the rheological properties of materials that range from pure liquids to solids. Advantages of this method include it being non-invasive, little to no sample preparation, and its ability to monitor rapid changes during dynamic processes.

A schematic of the OSF testing apparatus is illustrated in Figure 8. The design uses a piezoelectric crystal stack attached to an impedance head. Upon the application of voltage, the upper plate oscillates, and the force and acceleration at the oscillating plate are measured

through the impedance head and transformed into the frequency domain using a Fast Fourier Transformation (FFT) routine. This transformation is very useful because from the inspection of the frequency response of the measurement it is possible to identify a characteristic resonance frequency for the sample.

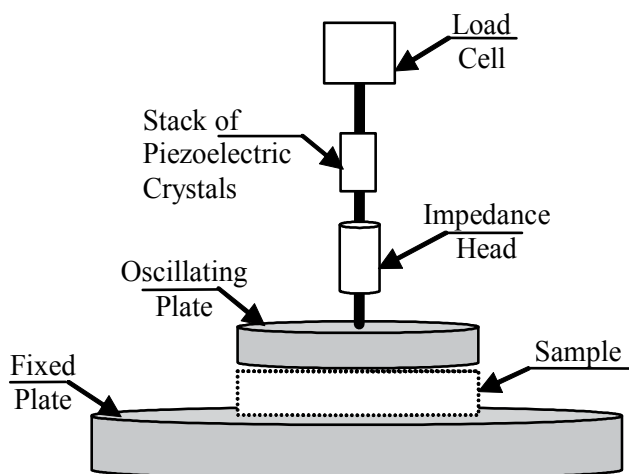


Fig. 8. Schematic of the OSF testing apparatus

Since the samples are considered viscoelastic they can be represented by a combination of elastic component, with a stiffness  $S$ , and viscous components with a damping  $R$ . A schematic of the elastic-viscous system used for analysis of the measurements is illustrated in Figure 9. For the testing, the sample is placed between the oscillating plate and a fixed plate. The oscillating plate is then brought down to touch the sample and the gap between

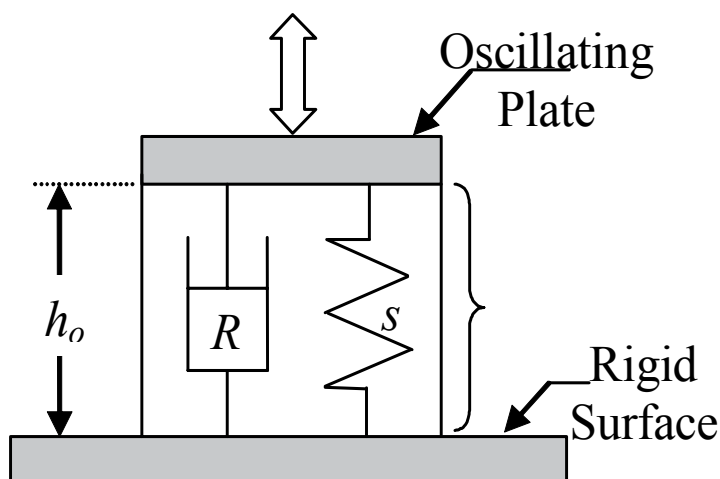


Fig. 9. Schematic of the spring-dashpot system, used for the analysis of the data.  $h_o$ ,  $R$ , and  $S$  are the height, the viscous resistance (damping), and the stiffness of the sample respectively.

the plate ( $h_0$ ) is noted. A load cell is attached above the oscillating plate to control the squeezing force applied to the sample prior the application of the oscillation. The squeezing force is simply applied to make sure that a good contact is established between the oscillating plate and the sample. It will be shown below, however, that the results are independent of that squeezing force.

The frequency response data is obtained using software that interfaces the results obtained with the signal generator device (see also details in Figure 1). The transformed mechanical

impedance  $\hat{Z} = \frac{\hat{F}}{\hat{u}}$  is then calculated from the force and velocity measured on the oscillating

plate with the impedance head.  $\hat{F}$  and  $\hat{u}$  are the Fourier transformed variables and since they have been transformed into the frequency domain, they, as well as the mechanical impedance, are complex variables. The measured complex mechanical impedance at the driving point can be defined as:

$$\hat{Z}_{meas} = \hat{Z}_{instrument} + \hat{Z}_{sample} \quad (11)$$

where  $\hat{Z}_{meas}$  is the measured impedance,  $\hat{Z}_{instrument}$  is the instrument impedance that can be calculated simply as  $\hat{Z}_{instrument} = im_{plate}\omega$  because the instrument does not have any spring mechanism or internal damping. From Equation (11) the sample impedance  $\hat{Z}_{sample}$  can be obtained by subtracting the instrument impedance from the measured impedance.

The rheological behavior of the sample can be described in terms of the viscous component ( $R$ ), which provides the damping of the oscillation and the elastic component ( $S$ ), which provides the sample elasticity (Figure 9). The relationship between the mechanical impedance and the damping (viscous component) and stiffness (elastic component) of the sample can be described by Equation (12) below:

$$\hat{Z}_{sample} = R_{sample} + i \cdot \left( \omega \cdot m - \frac{S_{sample}}{\omega} \right) \quad (12)$$

where  $\omega$  is the angular frequency of the oscillation,  $m$  is the mass of the system, and  $i$  is  $\sqrt{-1}$ .

The mobility of the sample, can be plotted as a function of frequency to provide the resonance spectrum of the sample. The resonance frequency,  $f_{res}$  of the sample, which is obtained as the frequency at which the mobility is a maximum is directly related to the stiffness and the mass of the system by Equation (13):

$$f_{res} = \sqrt{\frac{S_{sample}}{m}} \quad (13)$$

A typical plot of Mobility versus frequency for different concentrations of xanthan gum, a biopolymer that produces viscoelastic suspensions, is illustrated in Figure 10.

The higher is the concentration of xanthan gum the higher is its elasticity, which is clearly illustrated in the Figure 10 by a shifting to the right of the resonance frequency. That shifting of the frequency is a clear indication on increase in the stiffness of elasticity of the sample with concentration (see Equation 13).

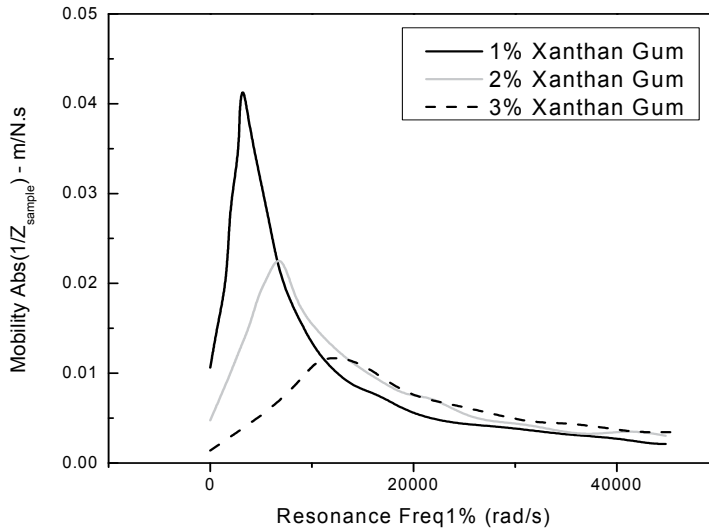


Fig. 10. Mobility plots obtained with the OSF method for xanthan gum dispersions of different concentrations

Although the mobility and the elastic and viscous components of a viscoelastic sample are often useful as quality and processing parameters (Gonzalez et al., 2010), for modeling purposes it is necessary to get quantitative and fundamental rheological information of a sample in terms of elastic and viscous modulus. Phan-Thien (1980) demonstrated that for viscoelastic materials subjected to squeezing flow under an oscillating plate, the squeezing flow force can be calculated as:

$$F_o \cos(\omega t) = \frac{3\pi a^4}{2h_o^3} \eta^* u_o \cos(\omega t) \quad (14)$$

where  $a$  is the radius of the top plate,  $h_o$  is the distance between plates and  $\eta^* = \eta' - i\eta''$  is the complex dynamic viscosity of the sample.  $\eta' = \frac{G''}{\omega}$  and  $\eta'' = \frac{G'}{\omega}$  are the viscous and elastic components of the sample, respectively. Application of FFT to Equation (15) yields:

$$\hat{Z}_{sample} = \frac{3\pi a^4}{2h_o^3} \eta^* \quad (15)$$

Expressions can be rearranged and using the definition of the complex viscosity  $\eta^*$ , expressions for the viscoelastic moduli, i.e. the storage and loss modulus,  $G'$  and  $G''$ , can be obtained as:

$$G' = \left[ \text{Im}(\hat{Z}_{sample}) + \frac{3m_{effective} \omega a^2}{20h_o^2} \right] \cdot \frac{2h_o^3 \omega}{3\pi a^4} \quad (16)$$

$$G'' = \operatorname{Re}(\hat{Z}_{\text{sample}}) \cdot \frac{2h_0^3 \omega}{3\pi a^4} \quad (17)$$

$\operatorname{Im}(\hat{Z}_{\text{sample}})$  and  $\operatorname{Re}(\hat{Z}_{\text{sample}})$  are the imaginary and real part, respectively, of the sample complex mechanical impedance  $\hat{Z}_{\text{sample}}$ . It is important to note that for the calculation of the storage modulus  $G'$  by Equation (16) is required to know the mass of the system, which consist of an effective mass that includes the mass of the sample and the squeezing force imposed to achieve good contact between the oscillating plate and the sample. If Equation (12) is rewritten in terms of those masses we can obtain an equation for the measured complex mechanical impedance:

$$\hat{Z}_{\text{meas}} = R_{\text{sample}} + i(\omega m_{\text{plate}} + \omega m_{\text{effective}} - S_{\text{sample}} / \omega) \quad (18)$$

The inertia produced by the plate instrument can be easily estimated as  $\hat{Z}_{\text{instrument}} = i\omega m_{\text{plate}}$ . However, to estimate the inertia produced by the effective mass  $m_{\text{effective}}$  some additional calculations are required. If the imaginary part of the sample impedance is divided by the frequency, the following equation is obtained:

$$\frac{\operatorname{Im}(\hat{Z}_{\text{sample}})}{\omega} = (m_{\text{effective}} - S_{\text{sample}} / \omega^2) \quad (19)$$

The term  $S_{\text{sample}} / \omega^2$  in Equation (19) approaches to zero as the frequency is very high, which results in  $\operatorname{Im}(\hat{Z}_{\text{sample}}) / \omega \approx m_{\text{effective}}$ . Results of this calculation show that the parameter  $\operatorname{Im}(\hat{Z}_{\text{sample}}) / \omega$  reaches an asymptotic value, which is independent of the squeezing force applied to the sample,  $S$  equals to  $m_{\text{effective}}$ . That value can then be used to calculate the storage modulus by Equation (16). Results for a xanthan gum suspension of concentration 2%, and whose mobility versus frequency data is shown in Figure 10, are shown in Figure 11 in terms of the viscoelastic storage and loss moduli defined by Equations (16) and (17). As shown in the figure the data compares well with those obtained with a conventional rheometer at comparable frequencies. It must be also noted that the range of frequencies of the OSF method is significantly higher than those applied by conventional rheological methods where inertia may play an important role.

### 2.2.2 Semisolid materials

Physical properties of solid viscoelastic foods and other biological products are very important in food production, storage, handling, and processing. The importance of the knowledge of the physical properties of biomaterials is demonstrated in the case of fruits. One of the most important quality parameter of fruits is its texture. Texture is the first judgment a purchaser makes about the quality of a fruit, before sweetness, sourness, or flavor. Since fruit texture is such an important attribute, one would expect the changes in texture during maturation and cool-storage to be well understood, however this is not the case. One of the main limitations to the study of fruit texture is the accurate and precise measurement of texture as perceived by a consumer.

Traditionally, the texture of fruits is measured by a Magness Taylor pressure tester (Magness and Taylor, 1925). This simple device measures the force required to insert a metal

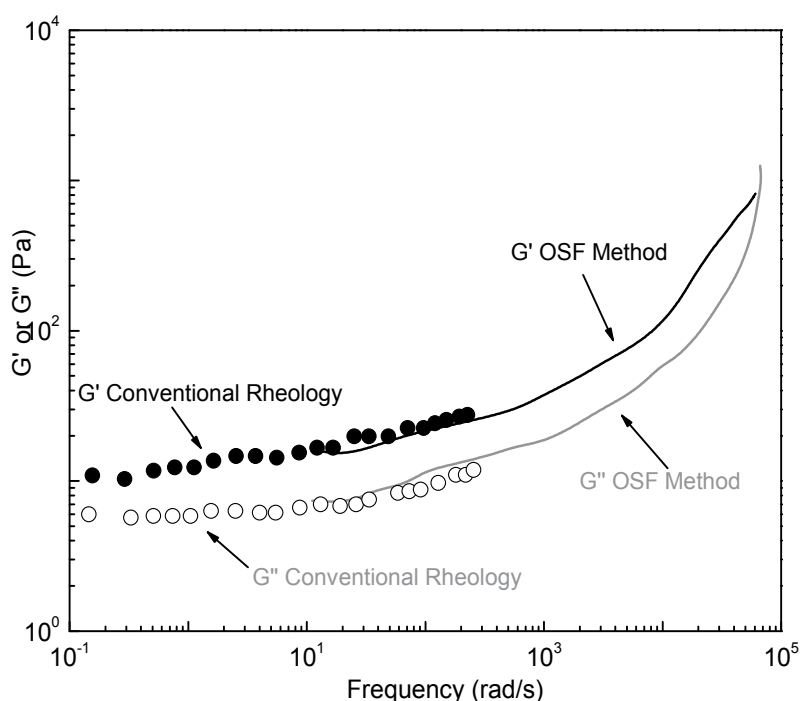


Fig. 11. Storage and loss modulus of a xanthan gum suspension of 2% concentration obtained with the OSF and conventional rheological methods

cylindrical plunger for a given distance into the fruit flesh. Although this device is cheap, quick, and easy to use, it has some disadvantages. Firstly, it is a destructive test, and it is not possible to have repeated measurements on a single fruit. Due to extremely high fruit-to-fruit variability, repeated measures on the same fruit would be highly desirable, especially from a research perspective. Secondly, there is high variability between operators, depending on the speed and force that the plunger is inserted into the fruit. However the greatest limitation of the Magness Taylor fruit pressure tester is that it measures the compression or crushing force that the cells of the fruit cortex are able to withstand. This force is very different from the force that is exerted on a fruit by the teeth of a consumer or the pressure that the consumer can exert with the fingers to assess the fruit texture. Biting an apple, for instance, involves cleaving cells apart, the exact opposite of the force measured by pressure testers. Universal Testing Machines (UTM), like for example the Instron™ instrument, are devices that can measure cleaving force, but they are slow, expensive, and again the method used with these machines is a destructive test.

Throughout the literature, there is abundant evidence that the ripeness or softness of intact fruits is related to their vibration properties. A device that uses vibrations to characterize intact fruits was patented in 1942 (Clark et al., 1942). Vibration properties of some fruits are correlated with firmness and ripeness. Finney (1970) explored methodologies for measuring and characterizing the vibration response of many fruits, and concluded that Young's modulus and shear modulus of apple flesh were correlated with the product between the resonance frequency squared and the mass of the whole fruit. It was also found that the



stiffness coefficient measured by vibration was closely associated with sensory panel subjective evaluations of Red Delicious apples (Finney, 1970, 1971). Garrett (1970) argued that the stiffness factor should be proportional to the frequency squared times mass to the two-thirds power. Cooke (1972) confirmed Garrett's theory using elastic theory relating the stiffness factor to the shear modulus of the fruit flesh. Both Finney's and Garrett's stiffness factors have been shown to correlate well with the fruit modulus (Clark and Shackelford, 1973; Yamamoto et al., 1980; and De Bardemaeker (1989); Abbott, 1994; Abbott and Liljedahl, 1994). Differences in shear moduli between green and ripe fruits can be detected non-destructively, and relatively easily, by vibration testing.

Through a few decades of development, a vibration-based characterization method called Experimental Modal Analysis (EMA) has advanced to become a very efficient tool for obtaining the dynamic properties such as natural frequency, damping and mode shapes in aerospace and mechanical engineering. For fruits, natural frequency is related to the shear modulus of the tissue (Cooke, 1972), which in turn determines the firmness of the fruit. For instance, in apples, high damping prevents them from giving a nice crisp ringing sound when tapped (De Baerdemaeker and Wouters, 1987). Mode shapes are an important indicator of the whole fruit's conditions such as ripeness, bruises, or defects (Cherng, 2000). It is obvious that there is abundant information on the texture and quality of fruits that could be associated with their acoustic parameters. This section of the chapter is meant to give an idea of the direction that researchers have taken in the last decade or so. To give specific examples, a few details are given on the measurement of Young's modulus, finite element modeling, and experimental modal analysis.

### 2.2.2.1 Measuring modulus of elasticity

An instrument that measures force as a function of displacement, such as a UTM, can be used to obtain force-displacement curves of the samples. For a melon, the flesh and the rind should be tested differently. Melons have a rind that is significantly stiffer than the flesh. The cylindrical samples of the flesh can be tested with a compression test. The rind samples can be tested using a three point jig, and treated as a simply supported beam for analysis.

For modeling vibrations, where only small displacements are of interest, the tests should be limited to small displacements and changes in the cross-section and in the length can be ignored in the data processing. Also, the mechanical properties of biological materials in general are not constant. Because of the structures at the micro scale, the Young's modulus is a function of strain. The following method can be used to facilitate the computation of the Young's modulus at zero deformation. The stress-strain curve can be fit to a cubic function

$$\sigma = a_3\varepsilon^3 + a_2\varepsilon^2 + a_1\varepsilon + a_0 \quad (20)$$

The coefficients  $a_0$  through  $a_3$  can be obtained by cubic regression analysis. The Young's modulus is the derivative of the stress with respect to strain

$$E = \frac{d\sigma}{d\varepsilon} = 3a_3\varepsilon^2 + 2a_2\varepsilon + a_1 \quad (21)$$

For vibration analysis and modeling, the most important value of the Young's modulus is at zero strain, which is simply  $a_1$ . Therefore, the constitutive relation for vibration models is

$$\sigma = E\varepsilon \quad (22)$$

where  $E = a_1$  from the test above.

In the bending test where the rind is treated as a simply supported beam, the equation for the young's modulus can be derived accordingly. If the force is applied in the middle of the span, then the deflection at that point is

$$x = \frac{FL^3}{48EI} \quad (23)$$

If the material is linear, the constant Young's modulus is

$$E = \frac{L^3}{48I} \frac{F}{x} \quad (24)$$

Where  $L$  is the span, and  $I$  is the moment of inertia of the rind sample, which is given by

$$I = \frac{\text{base} \cdot \text{height}^3}{3} \quad (25)$$

For nonlinear materials,  $E$  can be obtained by taking the derivative of the force with respect to  $x$ . In particular, the Young's modulus at zero strain is

$$E(x) = \frac{L^3}{48I} \left. \frac{dF}{dx} \right|_{x=0} \quad (26)$$

The modulus of elasticity of a melon was measured statically using an UTM machine, which can record the force as a function of deflection. For the flesh, cylindrical core samples were cut out of the melon; whereas for the rind, beam-like samples were cut out (Ehle, 2002). The force-displacement curve for the cylindrical core compression test was transformed into a stress-strain curve for small deflections by dividing the force by the cross-section area and dividing the deflection by the length. The small changes in cross-section area and the length were neglected because the displacement was small. Cubic regression of the stress-strain curve obtained the coefficients in Equation 20. Then Equation 21 was used to calculate the slope, which was the Young's modulus. The value at zero strain is the value used for modeling the vibration properties of the melon. Figure 12 shows that a cubic function fits the data very well, and that the slope at zero strain can be obtained accurately. In the above compression test of the flesh samples, the Young's modulus could also be obtained from the load-displacement curve without transforming into the stress-strain curve numerically. A little algebra gives:

$$E(x) = \frac{L}{A} \left. \frac{df}{dx} \right|_{x=0} \quad (27)$$

For the bending test, the force-displacement data were processed according to Eq. 24 to obtain the Young's modulus of the rind. The result shows characteristics similar to those illustrated in Figure 12.

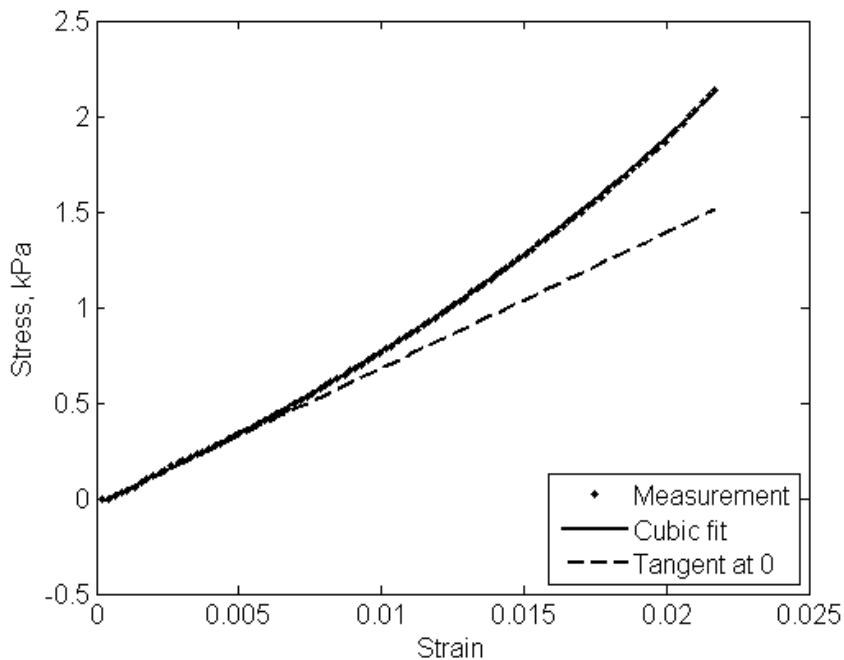


Fig. 12. Stress-strain curve of a core sample from compression test.

### 2.2.2.2 Numerical modal analysis with finite element modeling (FEM)

The application of stresses and strains in biological materials not only has a component associated to consumer evaluation but also it is related to quality control. Many of the stresses and strains are applied locally either during processing or consumption of the fruits. But they are distributed over the entire surface, thus it is necessary to use methods that can estimate the distribution of stresses over the product. Finite Element Modeling (FEM) is a well developed and proven mathematical and simulation tool to apply to the study of quality of fruits during consumption, storage and processing.

Cherng (2000) stated that the lowest natural frequency for hollow fruit like melons corresponded to the elongation along the major axis. Cooke (1972) concluded that the most important mode was the first twisting mode because it corresponds to the shear modulus of the flesh, which in turn corresponds to the fruit ripeness. Finite element models published in Cherng (2000) did not model the rind separately but assumed that the rind has the same properties as the flesh. Nourain et al (2004) compared a finite element model to experimental modal analysis results.

As an illustration, a finite element mesh used for a melon fruit is shown in Figure 13, with an octant removed to show the inside. The idealized melon-like geometry is a prolate ellipsoid with the major axis in the vertical direction. The major radius of the flesh is 77.5mm. The minor radius is 75mm. The hollow radii are 52.5mm (major) and 50mm (minor). The rind thickness is 2.5mm. For simulation purposes assumptions for the rind Young's modulus was 4.0 MPa whereas values used for the flesh Young's modulus were 1.0MPa, 1.5MPa, 2MPa, and 3MPa. The modal frequencies will be given in the order corresponding to those Young's moduli. The Young's moduli selected above are somewhat arbitrary and do not represent the values shown in Figure 12 from the test applied to a

melon. The purpose of this model is to give insight into how the vibration modes change with the stiffness of the flesh.

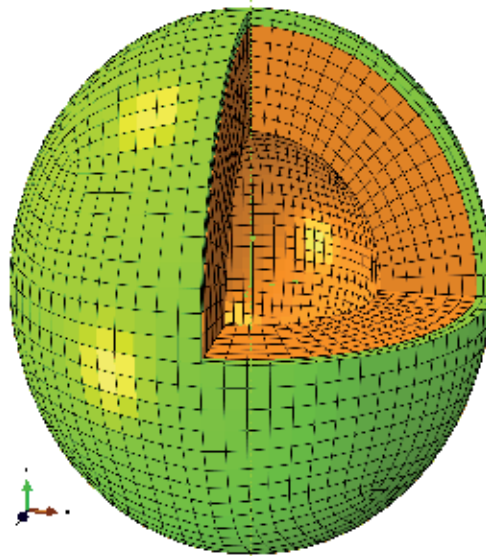


Fig. 13. A finite element mesh of a melon model

Figure 14 shows the elastic mode with the lowest natural frequency, which is elongation in the minor axis direction. Figure 15 shows the second mode, which is elongation in the major axis direction. Figure 16 shows the twisting mode. When the Young's modulus is 1.5MPa or lower, this mode changes shapes into the shape shown in Figure 17

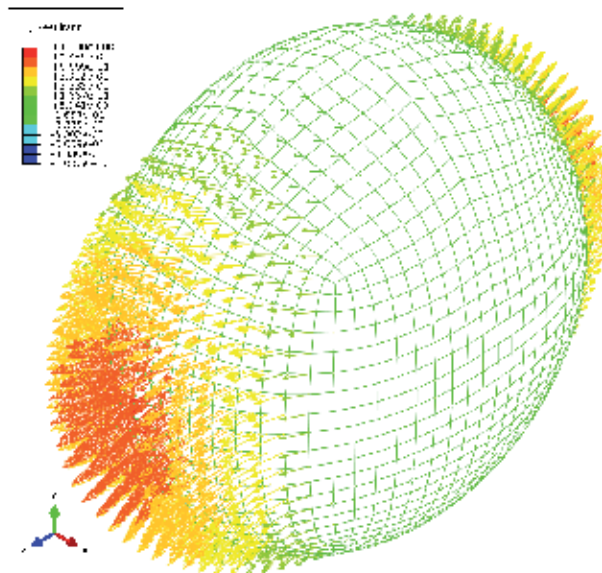


Fig. 14. Mode 1, "sideways elongation", 75.2Hz, 90.4Hz, 97.4Hz, 115.0Hz

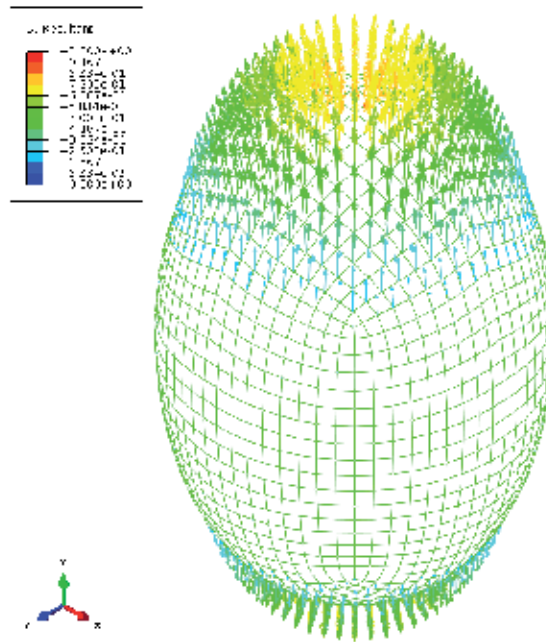


Fig. 15. Mode 2, elongation along the major axis, 79.4Hz, 91.5Hz, 102.0Hz, 120Hz

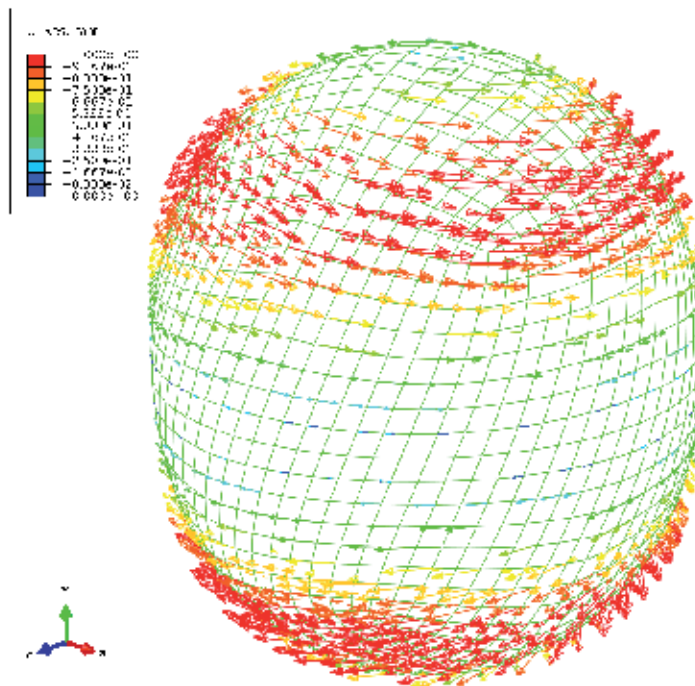


Fig. 16. Twisting about vertical axis, 101.4Hz, 125.1Hz, 135.0Hz, 152.3Hz

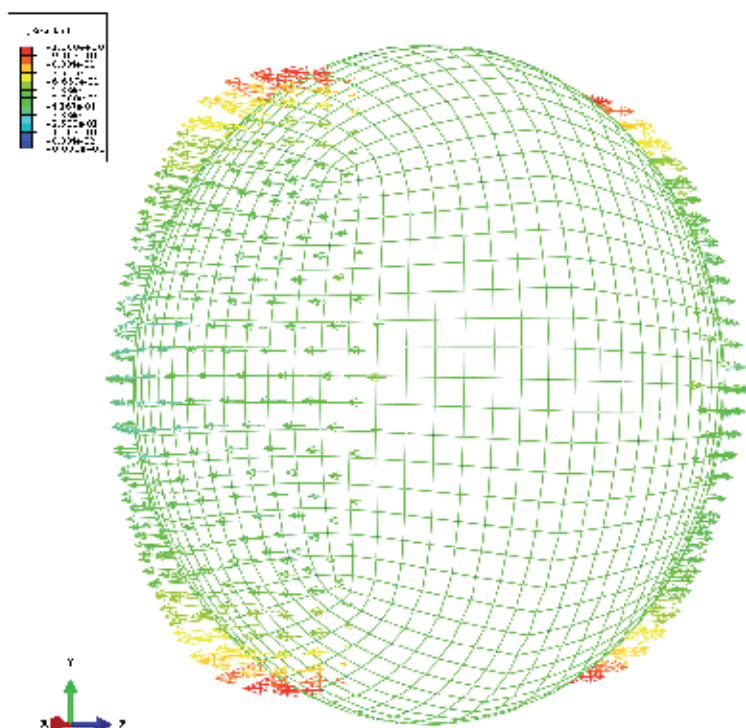


Fig. 17. Mode replacing the twisting mode when flesh Young's modulus is 1.5MPa

### 2.2.3 Experimental modal analysis of the fruit

Experimental modal analysis is a technique to obtain natural frequency, mode shapes and damping ratios of an elastic structure by application of a vibrational stimulus to the sample and sensing the resulting vibration at various locations on the sample surface. This section illustrates an experimental modal analysis on a melon fruit (Ehle, 2002). The excitation was a pulse force delivered by an impact hammer. A force transducer at the tip of the hammer measured the force. An accelerometer was used to measure the acceleration response at several points all over the surface of the melon. The measurement points were designed to follow a grid pattern where the distances between adjacent points were almost uniform throughout the surface of the fruit. The melon most closely resembled a sphere. Table 2 and Fig. 18 show the measurement points. A tri-axial accelerometer must be used to sense the important torsional mode (Fig. 8) as well as radial motions.

Layer	1	2	3	4	5	6	7	8	9
Points	1	2-7	8-19	20-37	38-55	56-73	74-85	86-91	92
Longitudinal Angle (deg)	90	67.5	45	22.5	0	-22.5	-45	-67.5	-90
Latitudinal Angle (deg)	N/A	60	30	15	15	15	30	60	N/A

Table 2. Locations of the points where acceleration was measured on the melon.

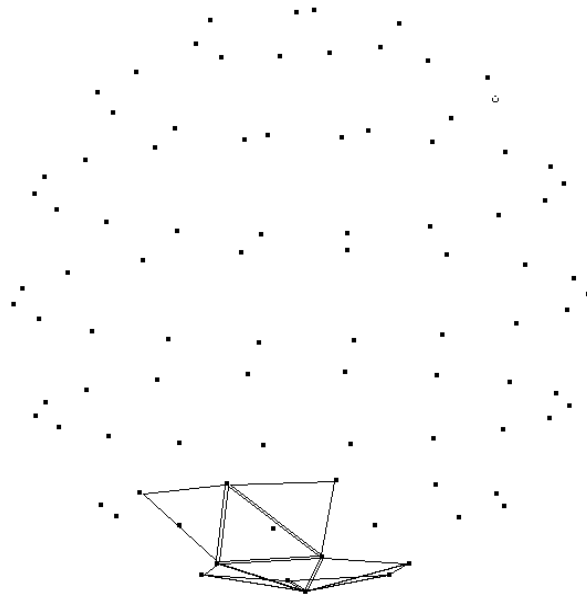


Fig. 18. Measurement points for the above described testing

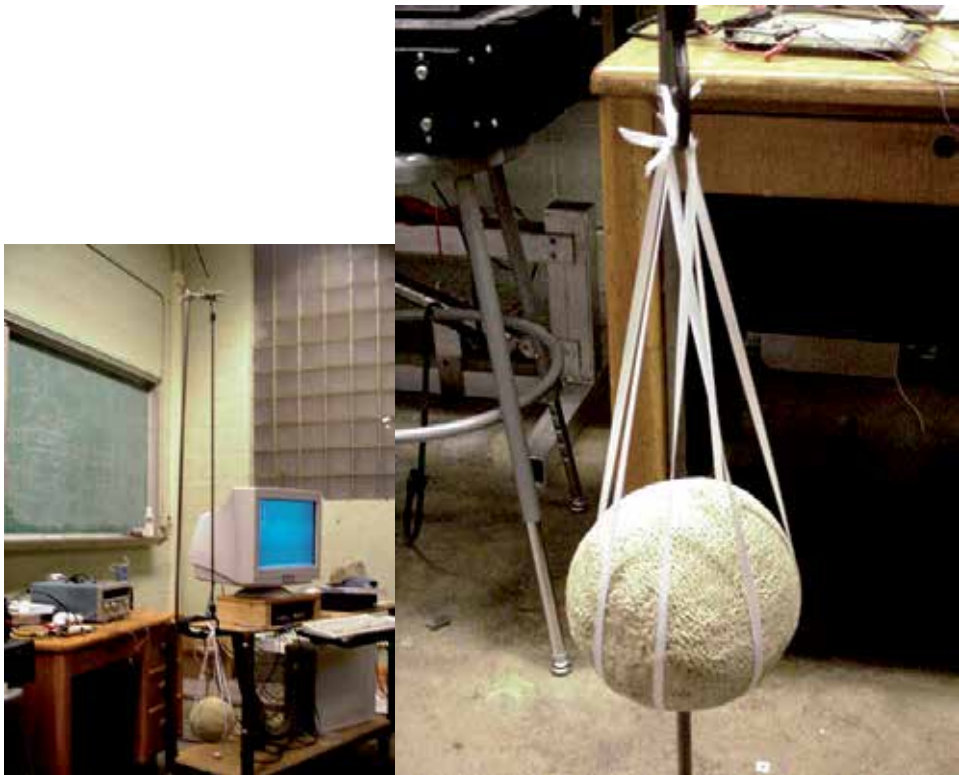


Fig. 19. A long elastic cord and rubber bands supporting the melon.

Any method used to hold the melon is a boundary condition which will alter the vibration modes. However, the free-free boundary condition has been proven to not alter the vibration modes. This boundary condition can be approximated by suspending the melon from a rigid structure with elastic cords. Soft elastic cords are used in the suspension so that the rigid-body vibration of the melon and its suspension has very low natural frequency and does not alter the elastic modes. Figure 19 shows the suspension the setup used for the holding of the sample.

The porous surface of the melon made it difficult to affix the accelerometer to the surface of the melon using conventional methods. To make sure the accelerometer was affixed snugly to the surface of the melon, wax was applied to the bottom of the accelerometer. This allowed for the mating of the accelerometer to the surface of the melon, which would result in better vibration transmission. Also the accelerometer was held in place by a “cradle” made from rubber bands (Figure 20). The width of the rubber bands was approximately 6 mm, just wide enough to cover the top surface of the accelerometer. The rubber band was positioned in such a way as to apply sufficient pressure so that the surface of the accelerometer was always held normal to the surface of the melon. This configuration allowed for an effective and easy-to-move attachment method to install the accelerometer.



Fig. 20. Accelerometer attachment

To excite the fruit a modal hammer with a force transducer was used. A plastic tip was used as opposed to the metal tip. The plastic tip allowed for the force from the hammer to stay within the crucial 20dB range past the cut off frequency of 500 Hz. The accelerometer then measured the resulting accelerations of the surface of the melon. An FFT analyzer transformed the acceleration and force into the frequency domain, and obtained the ratio of acceleration to force, which was the Frequency Response Function (FRF) at each sense point.



To reduce random noise, the average of data from ten impacts was used to compute each FRF. The *coherence* is a function in the frequency domain that indicates the quality of the FRF. A perfect coherence is 1.0. A coherence less than that at a given frequency means that the vibration sensed by the accelerometer at that particular frequency is not a linear response to the excitation from the impact hammer. A low coherence in general indicates excessive noise, nonlinearity, or other causes of bad measurement.



Fig. 21. Frequency response function obtained by hitting the melon rind directly

Figure 11 shows a typical FRF (top curve) and coherence (bottom curve) from the measurement. Each measurement point in Table 1 resulted in one FRF. A peak at a certain frequency means large vibration at that frequency, which indicates a mode at that frequency. If the FRF at a particular point shows a valley or low response at a modal frequency, it is indicating that the point is a node (point of no motion) of the corresponding mode shape. Using those rules, the mode shapes at any resonant frequency could be visually determined. A modal analysis program uses mathematical algorithms to compute the natural frequency, damping and mode shapes from the FRFs. It was used to analyze data from this test, but may not be necessary if the tester can figure out the modes by careful visual examination of the FRFs.

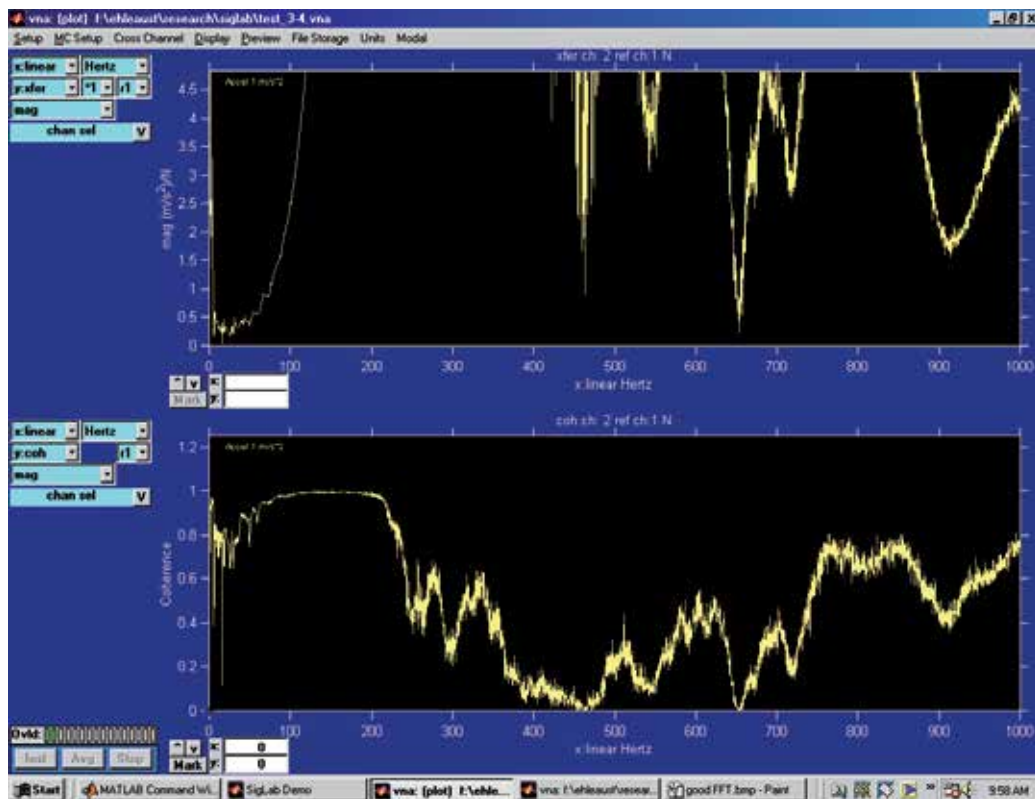


Fig. 22. An FRF (top) and coherence (bottom) obtained without a local stiffener on the surface of the melon.



Fig. 23. A stiffening metal disk on the melon rind.

It is important that the excitation force contain energy at all the frequencies of interest. That means that the force imparted by the hammer on the fruit must be a sharp enough pulse in the time domain. Experimental modal analysis is most commonly done on hard structures such as vehicles, buildings or metal structures. The surface of the fruit is much softer than most other structures for which the hammer tip was designed. Hitting the fruit with a hammer would result in a broad pulse in time domain, which translates into a narrow-band excitation in the frequency domain. As a result, the impulse spectrum of the excitation force would not have enough energy to excite vibration modes higher than 200 Hz without its intensity dropping more than 20 dB from its DC magnitude. When that condition is violated, the coherence of the data is very poor as seen in figure 22. To overcome this narrow-band excitation problem, a small metal disk (Figure 23) was attached to the fruit at the point of impact. This resulted in a significantly broader-band force excitation.

### 3. Concluding remarks

This chapter has presented a few examples of research that has been done to take advantage of the advancement in vibration analysis along with applications to characterize the rheological properties of biomaterials. The literature shows that the rheological properties of biomaterials are associated to quality indicators, specifically for foods to their texture and their sensory evaluation, thus many of the applications described in this chapter deal with food materials. In particular, this chapter has shown examples of application of basic vibration theories to measure the rheology of liquids as well as viscoelastic semi fluids and semi solid materials. The static measurement of modulus, finite element computation of the vibration natural frequencies and mode shapes, and an experimental modal analysis of a melon fruit are also described.

The authors believe that research on testing of biomaterials using vibration methods may help achieve:

- Higher quality foods due to better selection, testing, handling, grading and processing
- Lower prices due to quick nondestructive tests in harvesting, selection and grading of raw materials as well as testing finished products like for example during canning operations
- Increase in food safety due to, for example, the ability to detect dangerous salmonella in eggs from the change in physical properties detected by quick and accurate vibration based methods (Sinha et al., 1992) or infestation in fruits.
- Better design of food packaging, handling and transportation.
- Better tools to monitor the rheological properties of raw materials, e.g. during cooking and drying of cereal (Gonzalez et al., 2010)
- More interdisciplinary research combining engineering and food and biological sciences.

#### 4. References

- Abbott, J.A., (1994). Firmness measurement of freshly harvested delicious apples by sensory methods, sonic transmission, magness-taylor, and compression. *Journal of American Society of Horticultural Science*, 119(3), 510-515.
- Abbott, J.A., Liljedahl, L.A., (1994). Relationship of sonic resonant frequency to compression test and magness-taylor firmness of apples during refrigerated storage. *Transactions of the ASAE*, 37(4), 1211-1215.
- American Society for Testing and Materials, (1995). Standard test method for impedance and absorption of acoustical materials by the impedance tube method. ASTM Designation: C, 384-95.
- American Society for Testing and Materials, (1990). Standard test method for impedance and absorption of acoustical materials using a tube, two microphones, and a digital frequency analysis system, ASTM Designation: E, 1050-90.
- Campanella, O.H., Peleg, M., (2002). Squeezing flow viscometry for nonelastic semiliquid-foods theory and applications. *Critical Reviews in Food Science and Nutrition*, 42(3), 241-264.
- Chen, H., De Baerdemaeker, J., (1993). Modal analysis of the dynamic behavior of pineapples and its relation to fruit firmness. *Transactions of the ASAE*, 36(5), 1439-1444.
- Cherng, P.A., (2000). Vibration modes of ellipsoidal shape melons. *Transactions of the ASAE*, 43(5), 1185-1193.
- Clark, H.L., Lake, B., Mikelson, W., (1942). Fruit ripeness tester, U.S. Patent 2277037.
- Clark, R.L., Shackelford, P.S., (1973). Resonant and Optical Properties of Peaches as Related to Flesh Firmness. *Transactions of the ASAE*, 16(6), 1140-1142.
- Cooke, J.R., (1972). An interpretation of the resonant behavior of intact fruits and vegetables. *Transactions of the ASAE*, 15(4), 1075-1080.
- De Baerdemaeker, J., Wouters, A., (1987). Mechanical properties of apples: II. Dynamic measurement methods and their use in fruit quality evaluation, In: Jowitt R.

- (Eds). Physical properties of foods 2, Elsevier Applied Science, Pp.417-428, London, U.K.,
- Ehle, A., (2002). Measuring modulus of elasticity and vibration modes of a melon. Undergraduate Research Report, (unpublished), Purdue University, West Lafayette, IN, USA.
- Finney, E., (1970). Mechanical resonance within red delicious apples and its relation to fruit texture. *Transactions of the ASAE*, 13(2), 177-180.
- Finney, E., (1971). Dynamic elastic properties and sensory quality of apple fruit. *Journal of Texture Studies*, 2, 62-74.
- Garrett, R.E., (1970). Velocity of Propagation of Mechanical Disturbance in Apples, PhD Thesis, Cornell University, Ithaca, New York.
- D.C. Gonzalez, D.C, Khalef, N., Wright, K, Okos,M.R., Hamaker, B.R and Campanella, O.H. (2010). Physical aging of processed fragmented biopolymers. *Journal of Food Engineering*, 100(2), 187-193.
- Hertz, T.G., Dymling, S.O., Lindstrom, K., Persson, H.W., (1990). Review of Scientific Instruments, 62, 457.
- Herzfeld, F.K., Litovitz, T.A, (1959). Absorption and Dispersion of Ultrasonic Waves. Academic Press, New York.
- Kinsler, L.E., Frey, A.R., Coppens, A.B. and Sanders, J.V., (2000). Fundamentals of Acoustics (4th edn). John Wiley and Sons, Inc, New York.
- Magness, J.R., Taylor, G.F., (1925). An improved type of pressure tester for the determination of fruit maturity. USDA Agri. Circular , 350, Pp.8. Washington, D.C., USDA.
- Mason, W.P., Baker, W.O., McSkimin, H.J., Heiss, J.H., (1949). Measurement of shear elasticity and viscosity of liquids at ultrasonic frequencies. *Phys. Rev.* 75, 936.
- Mert, B., Campanella, O.H., (2007). Monitoring the rheological properties and solid content of selected food materials contained in cylindrical cans using audio frequency sound waves. *Journal of Food Engineering*, 79 (2), 546-552.
- Mert, B., Campanella, O.H., (2008). The study of the mechanical impedance of foods and biomaterials to characterize their linear viscoelastic behavior at high frequencies. *Rheologica Acta*, 47, 727-737.
- Mert, B., Sumali, H., Campanella, O.H., (2004). A new method to measure viscosity and intrinsic sound velocity of liquids using impedance tube principles at sonic frequencies. *Review of Scientific Instruments*, 75(8), 2613–2619.
- Nourain, J., Ying, Y.B., Wang, J., Rao, X., (2004). Determination of acoustic vibration in watermelon by finite element modelling. *Proceeding of SPIE*, 5587, 213, doi:10.1117/12.576953
- Phan-Thien, N.,(1980). Small strain oscillatory squeeze film flow of simple fluids. *Journal of the Australian Mathematical Society (Ser. B)*, 32, 22–27.
- Roth,W., Rich, S.R., (1953). A new method for continuous viscosity measurement. General theory of the ultra-viscoson. *Journal of Applied Physics*, 24, 940-950
- Sheen, S.H., Chein, H.T., Rapis, A.C., (1996). Measurement of shear impedances of viscoelastic fluids, *IEEE Ultrasonic Symposium Proceedings*, IEEE, New York.1, pp. 453.

- Sinha, D.N. Johnston, R.G. Grace, W.K., Lemanski, C.L., (1992). Acoustic resonances in chicken eggs. *Biotechnology Progress*, 8, 240-243.
- Takabayashi, K., Raichel, D.R., (1998). Discernment of non-Newtonian behavior in liquids by acoustic means, *Rheol. Acta*, 37, 593-600.
- Temkin, S., (1981). *Elements of Acoustics*. John Wiley and Sons, New York.
- Yamamoto, H.M., Iwamoto, M., Haginuma, H., (1980). Acoustic Impulse Response Method for Measuring Natural Frequency of Intact Fruits and Preliminary Applications to Internal Evaluation of Apples And Watermelons. *Journal of Texture Studies*, 11, 117-136.

# The Effects of Endurance Running Training on Young Adult Bone: Densitometry vs. Biomaterial Properties

Tsang-Hai Huang<sup>1</sup>, Ming-Yao Chang<sup>2</sup>, Kung-Tung Chen<sup>3</sup>,  
Sandy S. Hsieh<sup>4</sup> and Rong-Sen Yang<sup>5</sup>

<sup>1</sup>*Institute of Physical Education, Health and Leisure Studies,  
National Cheng Kung University, Tainan,*

<sup>2</sup>*Department of Biomedical Engineering, National Cheng Kung University, Tainan*

<sup>3</sup>*College of Humanities, Social and Natural Sciences,  
Minghsin University of Science and Technology, Hsinchu*

<sup>4</sup>*Graduate Institute of Exercise and Sport Science,  
National Taiwan Normal University, Taipei*

<sup>5</sup>*Department of Orthopaedics, National Taiwan University & Hospital, Taipei,  
Taiwan*

## 1. Introduction

Densitometric measurement of bone mineral parameters has been developed in recent decades. Since bone strength is associated with bone mineral density (BMD) and/or bone mineral content (BMC), densitometric measurement is widely accepted and used as one golden standard in clinical settings to determine bone health. Based on this concept, some human studies have suggested that endurance training, such as long distance running, provides no benefit and may even be harmful to bone health or bone mineral accretion during development, since long distance runners often have low BMD and/or BMC and may even exhibit conditions associated with bone loss or osteopenia.<sup>1, 2</sup> Conversely, serum bone marker assays in healthy distance runners show normal or positive bone metabolism status.<sup>3, 4</sup> Therefore, the definite role of endurance running training (ERT) on bone health remains a controversial issue. It would be valuable to further clarify whether ERT benefits bone health through a pathway other than absolutely increasing BMD or BMC.

Clinical observations of human subjects require further basic studies to investigate possible mechanisms. Animal studies can provide unique ways not feasible in studies using human subjects of assessing the effects of endurance running on bone. Generally, previous animal studies further verified benefits of ERT to bone health. However, the limitations of animal studies must be clarified before applying their findings to human beings.

The present article reviews the phenomena shown in bone of adolescent or young adult distance runners. Moreover, previous animal studies which adopted growing and young adult rats as subjects are reviewed, and the applicability of the findings to humans is also discussed.

## 2. The effects of endurance training on human bone: results and limitations

Conventionally, the extrinsic parameters of bone, such as BMD, BMC, and size-related measurements (*e.g.*, bone dimension, bone geometry), have been widely accepted as indicators of bone strength as well as predictors of fracture risk. Unfortunately, endurance running is usually considered an exercise mode that confers no benefit in terms of bone mineral accretion.<sup>1, 2</sup> Moreover, distance runners reportedly have low BMD and are often candidates for osteoporosis or stress fracture.<sup>1, 2, 5-8</sup> This section reviews studies on the effects of distance running training on both BMD and bone metabolism.

### 2.1 Results of human studies

#### 2.1.1 BMD and BMC in distance runners

For references to human studies, the NIH website (<http://www.ncbi.nlm.nih.gov/sites/entrez/>) was searched by subject (adolescent, young adult runners) and research type (cross-sectional studies). Additionally, the major purpose of this article is to describe the long-term effects of ERT on bone in runners without concomitant health problems. Hence, reports describing energy deficiencies and/or serious menstrual cycle disorders in runners were excluded. The summary of previous cross-sectional studies in Table 1 indicates that distance runners usually reveal lower BMD and BMC values than those who engage in higher impact sports.<sup>9</sup> According to Frost's theory,<sup>10</sup> the slenderer body dimensions (Body Mass Index = 20 ~ 22) of runners who have a relatively lower body weight (BW) might partially contribute to a lower BMD and BMC. However, when compared to body-size matched control groups or another non-weight bearing exercise group, runners still do not seem to have much advantage on whole body, lumbar spine or regional cortical bone BMD.<sup>11-18</sup> Although oligomenorrhea or amenorrhea has been considered the cause of low BMD in female runners, even healthy female runners with normal menstrual cycles had lower BMD when compared to their size-matched control subjects.<sup>12-14</sup> Thus, ERT is usually concluded to be profitless for bone mineral accretion and bone health as well. However, if the analysis is limited to weight-bearing sites, runners do reveal higher site-specific regional BMD and/or BMC (*e.g.*, femoral neck, distal tibia, calcaneus) than do controls.<sup>15, 19-21</sup> Therefore, ERT is not entirely non-beneficial for bone mineral accretion when considering BMD and/or BMC as the major predictors of bone health.

Table 1 shows the findings of several studies indicating that distance runners have absolutely higher BMD values than do control groups.<sup>3, 22-24</sup> In the research publicized by Brahm and associates,<sup>3</sup> the runners showed only a slightly higher total-body BMD (3.6% higher,  $p=0.03$ ), and no significant difference from the control group in total-body BMC was revealed. Interestingly, this study found that runners had distinctly higher BMD values in the legs and in the proximal femora. Regarding subject specificity, the training level of subjects or the normality of control subjects would be a major concern. Compared to elite distance runners, high school or club level runners may be trained at a more moderate intensity. Thus, these subjects did not really have typical body dimensions (*e.g.* slender body shape, low BMI) of elite distance runners.<sup>22, 24</sup> On the other hand, the BMI of 20.7 in the control group recruited in Kemmler *et al.* may have been too low for a normal control group.<sup>23</sup>



Authors	Subjects (gender, age, BMI, training status)	Results	Vs. control group
Grimston et al. <sup>12</sup>	♀, age (C:32.9, NR:32.2, LR:30.3), BMI (C: 20.6, NR:20.5, LR: 21.7), Training (NR:55.6km/wk for 7.7yr, LR: 53.0km/wk, 9.2yr) <sup>a</sup>	Most subjects reveal normal menstrual cycle (11-13 cycle/yr), LR group showed lower BMD in L2-L4, femoral neck, and tibia than C group	↓
Robinson et al. <sup>13</sup>	♀, collegiate gymnasts (n = 21, age 16.2±1.7 years) runners (n = 20, 14.4±1.7 years), and nonathletic college women (n = 19, 13.0±1.2 years), No BMI data.	Lumbar spine BMD was lower in runners compared with both gymnasts and controls. Whole body BMD was lower in runners compared with gymnasts and controls.	↓
Taaffe et al. <sup>14</sup>	♀, 19.7±1.2yr, 19.5, 4-5d/wk, college level runners	Runners showed significantly lower BMD in femoral neck, lumbar spine but not in whole body BMD.	↓
Mudd et al. (2007) <sup>9</sup>	♀, 20.2±1.3yr, 21.0±1.6, college level athletes	Runners had lowest lumbar spine and pelvis BMD when compared to other athletes	↓
Emslander et al. <sup>17</sup>	♀, 20.3±0.6 yr, 21.9, 40mile/wk for 3yr	No significant difference was shown in total body, spine and proximal femoral BMD among runners, swimmers and control groups.	=
Duncan et al. <sup>18</sup>	♀, 17.8±1.4 yr, 21.3±1.6, 8.4±1.2 h/wk for 6.2±1.7 yr, high school level athletes	Areal BMD estimation was performed on mid-third femur. Runners had higher BMD only than cyclist. No difference was shown among groups of runners, swimmers, triathlete and controls.	=
Moen et al. <sup>25</sup>	♀, 15.1-18.8 yr, No BMI data, 58.1km/wk for >1.5yrs	There is no significant difference among amenorrheic runners, eumenorrheic runners, and controls in lumbar BMD.	=
Greene et al. <sup>16</sup>	♂, 16.8±0.6yr, 20.68±1.6, 6hr/wk for 2yr	After adjusting for lean tissue mass per kg of body weight, no difference in BMC was detected.	=
Jüriimäe et al. <sup>11</sup>	♀, 22.6±4.3 yr, 20.6±1.6, 6h/wk for > 5yr	Endurance trained group showed no difference with normal-weight control group in BMD, but was lower than over-weight control group.	=
MacDougall et al. <sup>15</sup>	♂, 22-45yr, runners were divided into five groups per their training mile/wk <sup>b</sup>	Runners with running mileage 15-20mile/wk showed the highest BMD values in legs but not in total body and spine. Runners with higher	SS ↑

		training mileage did not show difference in BMD as compared to control group.	
Greene et al. <sup>20</sup>	♀, 16±1.7, 18.7±1.5, 6hr/wk for >2yr	Runner showed higher BMD and BMC in distal tibia, densitometric measurement performed only in distal tibia.	SS ↑
Egan et al. <sup>19</sup>	♀, 21.5±2.6 yr, 20.23, 8.4±3.4h/wk for 6.0±2.1yr	All sports groups had higher BMD values than did the controls. Runners showed a higher BMD only in legs and proximal femur, but lower than rugby athletes.	SS ↑
Fredericson et al. <sup>21</sup>	♂, 24.2±3.2 yr, 20.3±1.3, 70mile/wk for at least 1yr	Soccer player was higher in BMD of the skeleton at all sites measured. Runners only showed higher BMD in calcaneus than control group.	SS ↑
Brahm et al. <sup>3</sup>	♀&♂, 32yr, 22, 7h/wk for 12yr	Runners were significantly higher in total body, legs, femoral neck, trochanter wards triangle and calcaneus BMD than control group.	↑
Stewart & Hannan <sup>24</sup>	♂, 27.6±6.1yr, 21.9±1.3, 8.7±2.7h/week, club level runners	Runners showed higher total body and legs BMD.	↑
Duncan et al. <sup>22</sup>	♀, 17.6±1.4 yr, 21.3±1.6, 8.4±1.2 h/wk for 6.2±1.7 yr, high school level athlete	Runner were significantly higher in total body, lumbar spine, femoral neck and leg BMD as compared to BMI-matched control group	↑
Kemmler et al. <sup>23</sup>	♂, 26.6±5.5yr, 20.9, 9.25±2h/wk for 8.9 yr	Runners were higher in total body BMD, legs, pelvis, femoral neck, calcaneus BMD as compared to the BMI (20.7) matched control group	↑

Note: <sup>a</sup>, subjects were divided into three groups (NR, runners with normal BMD; LR, runners with low BMD, C, control group); <sup>b</sup>, runners were divided into five groups according to their training mileage per week, BMI value was not matched among groups that control group showed the highest value; ↓, runners were comprehensively lower than control group in total body and local bone; =, no significant difference was shown between runners and control group; SS ↑, runners showed site-specific increment in BMD; ↑, runners showed higher BMD in total body as well as in local bone.

Table 1. Summary of cross-sectional studies of BMD in adolescent or young adult distance runners

### 2.1.2 Results of human studies: Bone metabolism status in distance runners

As mentioned above, ERT conferred no clear benefits to bone health. An important inquiry is whether endurance running influences the physiology (*e.g.* exercise-induced acidosis) or causes related abnormalities in hormonal homeostasis (*e.g.* menstrual disorders in females or lower testosterone in males) that negatively affect the bone.

It's well known that patients with pathological acidosis suffer negative bone turn-over, which causes a net bone mineral loss.<sup>26</sup> Endurance exercise may induce acidosis, which negatively affects bone metabolism. However, transient acidosis caused by exercise is buffered by  $\text{HCO}_3^-$  and disappears within hours after exercise.<sup>27</sup> In addition, it has been suggested that acid buffer capacity is enhanced after a period of exercise training.<sup>28</sup> At the cellular level, a single bout of intense exercise induces transient increases in serum and urine calcium levels without showing cellular osteoclastical activities.<sup>29,30</sup>

With respect to the impact from abnormalities of hormone regulation, oligomenorrhea and amenorrhea related to bone loss are often reported in female runners undergoing intensive training. However, recent investigations suggest that endurance running does not directly cause menstrual disorders and the subsequent bone loss.<sup>31-33</sup> Menstrual disorders in endurance runners are more likely due to either energy or nutrition deficiencies. Therefore, dietary adjustment is usually more effective than hormone replacement therapy for restoring menstrual cycles and bone metabolism.<sup>34</sup> In males, ERT is known to lower testosterone, but lower testosterone does not necessarily correlate with lower BMD.<sup>35</sup> In addition, runners with different training mileage (from 5 to 75 mile/week) do not significantly differ in serum testosterone levels.<sup>15</sup>

Regarding studies of bone metabolism status, healthy distance runners at rest usually exhibit normal bone metabolism, and some studies even show a positive bone metabolism status, as revealed by serum bone markers.<sup>3,4</sup> Brahm *et al.*, in a study of bone metabolism in runners using various serum markers, found that runners had lower bone formation as well as lower bone resorption activities.<sup>3</sup> Moreover, triathletes reveal no difference in bone metabolism during the intense competitive season as compared to their non-training period.<sup>4</sup>

## 2.2 Limitation of human studies

To summarize the above, distance runners do not seem to acquire much benefit from their training when densitometric measurements are used to determine the bone health. However, as shown by serum bone marker assays, distance runners did not reveal an inadequate bone metabolism status. Actually, over the past decades, an increasing number of reports suggest that BMD does not accurately predict bone health or bone strength. Patients with fractures also show normal BMD values.<sup>36</sup> The BMD and BMC measures apparently correlate strongly with body mass and body size.<sup>11, 37-39</sup>

Today, "bone quality" is used as a new term to represent bone health, which is composed of various parameters, including tissue architecture, turnover, microfracture and mineralization, of a healthy bone.<sup>40</sup> Further, the organization of the bone matrix may also play an important role in bone strength.<sup>41</sup> Unfortunately, many of the bone quality measurements are too invasive to be feasible in human subjects. Thus, animal studies have been frequently used for further clarifying related issues.

## 3. Comprehensive results of animal studies: BMD and BMC

In biomedical science, animal experiments are performed to establish models that mimic human physiological phenomena. Either estimation methods or experimental designs, which may not be feasible in humans, can then be performed to further investigate possible mechanisms. Rodent models of treadmill activity are commonly used to investigate the effects and mechanisms of exercise on bone metabolism. This section reviews the findings of

previous animal studies. Briefly, the results of animal studies using rodents as subjects showed gender differences, which might affect their further applicability in human subjects. As mentioned above, intensity-trained runners usually have a lower body mass and often have equal or even lower bone mass than non-athletes. Therefore, an animal model of ERT would be expected to reveal the same phenomena. Animal studies reviewed in the present article were selected according to training type (typically endurance treadmill training) and the age of animals (growing or young adult rats).

### **3.1 Rodents adapted to endurance exercise showed gender differences**

#### **3.1.1 Male rodent studies**

Table 2 summarizes the outcomes of studies using male rats as subjects. The studies were reviewed and classified into two categories. The first category includes those using diet control or adjustment to achieve equivalent BW gains between exercise and control groups.<sup>42-47</sup> These studies demonstrated that trained animals have a higher BMD.<sup>43-45</sup> Tissue mechanical properties were not available in every study, and only one of them shows a higher load-withstanding capacity in the femoral diaphysis.<sup>43</sup> However, it must be mentioned that diet prohibition for the purpose of equalizing body weights among groups might cause an additional negative effect on tissue mechanical properties. Diet prohibition impairs the tissue levels (intrinsic) and mechanical properties of bone, suggesting that dietary manipulation of a control group might not be appropriate.<sup>48, 49</sup>

The second category of studies included animals fed *ad libitum*. In these studies, the exercise groups revealed significantly less BW gain after a programmed ERT.<sup>50-55</sup> With lower BW, exercise trained animals showed no difference or lower BMD values as compared to the sedentary control group. As in human subjects, male rats undergoing intense ERT exhibit lower BW gain and no benefits to bone health when considering BMD or BMC as a predictor. However, the higher load-withstanding and energy-absorption capacity of the bones in training rats introduced new research into how endurance exercise benefits bone quality (see section 4).

#### **3.1.2 Female rodent studies**

Compared with the treadmill training results for male rats, those for female rats are inconsistent with human subjects, and the data are somewhat controversial. Table 3 summarizes the results of ERT in growing or young adult female rats. Most studies indicate that female growing or young adult rats exhibit no change in BW after a period of ERT.<sup>56-64</sup> One study even reported increased BW in female rats after training.<sup>58</sup> Of the studies performing BMD analysis in female rats, many report positive effects from endurance running not only in site-specific increments but also in whole bone. Although densitometric measurements demonstrate this advantage, female rats rarely show improved biomechanical properties and may even reveal adverse effects after an intense training program (see Table 3). Therefore, female rats acclimate to ERT differently than do male rats. In human beings, distance runners are also expected to exhibit gender differences in physiological response to similar ERT. However, it seems inappropriate to use the gender difference found in rats to explain the one found in humans, since a period of programmed ERT would commonly reduce BW either in women or men. Thus, the phenomena observed in female rats may not be applicable to female humans. Based on the idea that animal models should mimic the phenomena shown in human subjects, studies using female rats may not be applicable to female humans, since female rats and women have been shown to respond differently to ERT. Possible reasons are discussed in the next section.

Author	strain, age	Protocol	BW control	BW or BW gain (g)	BMD or BMC	Biomechanical testing
Nordsletten et al. <sup>53</sup>	Wistar, 11 wk	27m/min, 60min/d, 10% inclination, 5d/wk, 4 wk	—	EXE<CO N*	N/A	Ultimate bending moment (N·m×10 <sup>-2</sup> ) EXE > CON
Brourrin et al. <sup>50</sup>	Wistar, 10wk	30m/min, 1.5h/d, 5d/wk, 5wk	—	EXE<CO N*	N/A	No data
Horcajada-Molteni et al. <sup>51</sup>	Wistar, 8wk	20m/min to 30m/min, 60min/d, 6d/wk, 90d	—	EXE<CO N*	Femoral BMD: NS	Femoral failure load (N): EXE > CON*
Huang et al. <sup>54</sup>	Wistar, 5wk	24m/min, 60min/d, 5 d/wk, 10wk	—	EXE<CO N*	Tibiae BMD (g/cm <sup>2</sup> ) :NS	No data
Huang et al. <sup>52</sup>	Wistar, 7 wk	22m/min, 60min/d, 5d/wk, 8wk	—	EXE < CON*	Tibia and femur BMD: NS	Three-point bending load (N), energy (mJ), stress (MPa), toughness (mJ/mm <sup>3</sup> ): EXE > CON*
Huang et al. <sup>55</sup>	Wistar, 7wk	Two groups: 22m/min, 60min/day vs. 30m/min, 5d/wk, 8wk	—	EXE < CON*	EXE < CON* in total femur (p=0.04)	Femoral midshaft bending energy and toughness (mJ & mJ/mm <sup>3</sup> ): EXE > CON
Joo et al. <sup>43</sup>	Wistar, 4 wk	30 m/min, 60 min/d, 5 d/wk, 10wk	+	NS	Femurs BMD (g/cm <sup>2</sup> ) EXE > CON	Femoral mid-diaphysis Bending stress (N/mm <sup>2</sup> ): NS Maximum load (N): EXE > CON
Kiuchi, et al. <sup>44</sup>	Wistar, 4 wk	35m/min, 5° inclination, 60min/d, 5d/wk, 10 wks	+	NS	BMC: EXE > CON*	No data
Notomi et al. <sup>46</sup>	S.D., 4 wk	24m/min, 60min/d, every other d, 4 wk	+	NS	NS	Vertebra and femoral maximal load (N): NS
Sakamoto & Grunewald <sup>47</sup>	Wistar, 4 wk	24m/min, 75min/d, 5d/wk, 8 wk	+	NS	N/A	Tibia breaking strength (kg): NS

Newhall et al. <sup>45</sup>	S.D., 47 d	10.2km/d, for 6 wks (voluntary running)	+	EXE > CON	Femur BMD & BMC: EXE > CON*	N/A
Ferreira et al. <sup>42</sup>	Wistar, 10 wk	12m/min, 1h/d, 10 wks.	+	NS	NS	N/A

Note: Protocol, training protocols were presented serially by the final training intensity (m or cm per minute), training time per day (minute or hour per day), training frequency (times per week), and training periods (day or week); d, day; wk, week; min, minute; NS, none significant difference; N/A, none available.

Table 2. Studies of endurance running training vs. growing or young adult male rats

Author	Strain and age	Protocol	BW control	BW or BW gain and tissue measurement	BMD or BMC	Biomechanical testing
Iwamoto et al. <sup>56</sup>	S.D., 4wk	24m/min, 60min/d, 5 d/wk, 8wk or 12wk	–	BW: NS Muscle weight & Femoral length (12wk): EXE > CON*	Femoral and L6 vertebral BMD (mg/ $\mu$ L): NS Femoral and L6 vertebral bone volume ( $\mu$ L), wet weight (mg): EXE > CON*	N/A
Iwamoto et al. <sup>57</sup>	Wistar, 4wk	24m/min, 60min/d, 5 d/wk, 7wk or 11wk	–	BW: NS Femoral length: EXE > CON*	Tibial BMC (g): EXE > CON* Tibial BMD (g/cm <sup>2</sup> ): NS	N/A
Hagihara et al. <sup>58</sup>	Wistar rats, 8wk	A group: control group B-E group: 4~7d/wk, running at 15m/min, 30min/d, 8wk	–	BW gain: B > A*	Tibial trabecular BMD (mg/cm <sup>3</sup> ): B, C, D, E > A group*. But, NS in tibial cortical BMD.	N/A
Wheeler et al. <sup>59</sup>	S.D., 120 d	55%, 65%, 75% $\dot{V}O_{2max}$ , 30min/d, 60min/d, 90min/d, 4d/wk, 10wk	–	BW: NS	Tibial BMD (g/cm <sup>2</sup> ): EXE > CON	Group trained at 75% $\dot{V}O_{2max}$ and 90min/d showed higher stiffness but lower energy to

						withstand torsion test.
Raab et al. <sup>60</sup>	Fischer 344, 2.5 month	36m/min, grade15%, 60min/day, 5days/wk for 10wk		BW: NS	N/A	Femur ultimate force (kg/mm): NS
Hou et al. <sup>61</sup>	S.D., 8 wk	49cm/s, 12% grade, 60min/d, 5d/wk, 10 wk (~75-80% of maximum oxygen capacity)	—	BW: NS	N/A	Femoral neck maximum load (N): NS Energy to maximum load (mJ): NS
Shimamura et al. <sup>62</sup>	Wistar, 6 wk	25m/min, 60min/d, 5d/wk, for 7 or 11 wk	—	BW: NS	BMC in Total tibia (mg): EXE > CON*	N/A
van der Wiel et al. <sup>63</sup>	Wistar, 5 month	20m/min,30 min/d, 5° inclination, 5d/wk, 17wk	—	BW: NS	Total body BMC (g): NS CON : 9.3±1. 1 EXE : 9.9±1.0	Femoral neck maximal load (N): NS Femoral shaft maximal load (N): NS
Salem et al. <sup>64</sup>	S.D., 8 wk	45 cm/s, 5% grade, 60 min/d, 3d/wk, 10wk	—	BW: NS	N/A	Femoral neck maximal load (N):NS

Note: Protocol, training protocols were presented serially by the final training intensity (m or cm per minute), training time per day (minute or hour per day), training frequency (times per week), and training periods (day or week); d, day; wk, week; min, minute; NS, none significant difference; N/A, none available.

### 3.1.3 Gender differences revealed by animal studies

Table 3. Studies of endurance running training vs. growing or young adult female rats

As mentioned above, male and female rats adapt differently to endurance treadmill training, especially in densitometric measurements. The reasons for this gender difference in rodents have been comprehensively investigated elsewhere. According to the theory of Frost,<sup>10</sup> this difference may partially contribute to different adaptations in BW gain. Female rats usually exhibit a similar or sometimes higher body mass after training; they therefore may acquire a greater advantage from local mechanical loading than male rats with lower BW gain after forced endurance treadmill training or voluntary running.<sup>65-68</sup> The mechanisms of this gender difference in BW gain associated with ERT are unknown. A possible explanation is the involvement of gonadal hormones in BW regulation. Endurance exercise reportedly lowers plasma testosterone levels in male rats.<sup>69</sup> The down regulation of this anabolic

hormone in growing male rats may account for the significantly lower protein mass gain and BW gain. In female rats, however, estrogens would suppress body mass, food consumption and fat deposition.<sup>70, 71</sup> Progesterone, on the other hand, has been verified to increase body fat and body mass.<sup>72, 73</sup> Moreover, a previous study suggests that regular treadmill training results in extended periods of progesterone secretion, which was associated with significant weight gain.<sup>74</sup> Women may respond to ERT with similar regulation in progesterone. However, the up-regulation of progesterone may be more pronounced in rats than in women, since female rats reveal no decrease in BW even under vigorous ERT.<sup>60</sup>

### 3.2 Studies of male rats mimic human practice

An analysis of gender differences observed in the above animal studies reveals that ERT increases BMD and BMC in female rats but not in male rats. However, the physiological response (e.g. BW gain) of female rats to ERT differs from that in female humans. Given that animal studies are intended to clarify the mechanisms of biological phenomena in humans, female rats may not be a suitable model for investigating the effects of ERT on developing or young adult bone. On the other hand, the changes in BW and densitometric parameters associated with ERT in male rats were similar to those in humans, indicating that male rats are a suitable model for investigating the effects of endurance running.

## 4. Effects of endurance training on bone biomaterial properties

Aside from BMD and BMC, biomaterial related analysis will provide more valuable information to predict the capacity that bone tissue can withstand extra mechanical loading generated by daily physical activity or accidents (e.g. fall), and thus, prevent bone from loading-induced damage.

Generally, biomaterial properties of bone tissue can be analyzed at a structural level and a tissue level. Structure biomaterial properties are size-dependent, that is, tissues bigger in size tend to be stronger than smaller ones. Conversely, tissue-level properties are analyzed under size-independent conditions using mathematic methods (e.g. normalized tissue size by cross-sectional moment of inertia) or mechanical methods (e.g. a specimen with consistent size is sectioned from a whole tissue).<sup>75</sup>

### 4.1 Effects on structural (whole bone) properties

Structural properties are calculated from original biomechanical testing raw data without any normalization. Related parameters are load (Nt), displacement (mm), energy (mini joule, mJ) and stiffness (Nt/mm) etc. As shown in previous studies, results of rodents' whole tissue biomechanical properties after a period of endurance running training were controversial. Some studies show that exercise groups were higher in load-withstanding capacity,<sup>51-53</sup> while others revealed a higher energy absorption capacity.<sup>55</sup> One possible explanation for these discrepancies may be differences in training protocol. Animals trained at a higher intensity tended to show higher bone strength (e.g. higher bending load or moment),<sup>51, 53</sup> suggesting that higher mechanical loading generated by intensively running may benefit to bone strength. Moreover, the specific testing conditions would also affect testing results; for instance, Nordsletten and colleagues measured bone strength *in vivo*, at which time bone strength may be affected by muscle strength gains achieved through training.<sup>53</sup>



However, in considering the applicability of exercise, a training program with moderate exercise intensity would be expected to show a higher compliance and therefore be more appropriate for the general population. As shown in Table 2, animals trained at a relatively moderate intensity (20-24m/min), which corresponds to 70%  $\dot{V}O_2$  max,<sup>76</sup> also had lower body masses and slightly lower (~5% lower) total BMD ( $p = 0.04$ ), but were not found to have enhanced structural bone strength.<sup>55</sup> The authors' previous study used body mass as a covariate to equalize raw data, which then revealed a comprehensively stronger bone tissue either in structural or tissue-level biomaterial properties.<sup>52</sup> With lower body mass, the data of the exercise group would be adjusted to a higher level, and the effects of ERT seemed to become "good" for animal bones. However, it would be a more relevant and natural study if animals were fed ad libitum and data were not adjusted.

In aspects of biological efficiency, an athlete at her/his optimal physiological status will not necessarily be absolutely higher in every physiological parameter. Therefore, a smaller muscle mass or skeleton size seems to be a benefit, rather than a weakness, for a distance runner or an endurance athlete. With such a smaller bone size, moderate ERT rats did not show absolutely enhanced structural bending load values but, interestingly, they showed better energy absorption capacity in long bone tissue that ERT rats were found to have a four-fold increase in energy absorption after long bone tissue reached the yield-point (post-yield energy).<sup>55</sup> As mentioned in previous studies,<sup>41</sup> post-yield behaviors are highly correlated to tissue-level changes (e.g. collagen fiber orientation).

## 5. Effects on tissue-level (material) properties

In our previous studies, we used mathematical methods to estimate tissue-level biomaterial properties. Through calculating long bone's cross-sectional moment of inertia, we normalized load-displacement data to stress and strain. Under such conditions, ERT rats' worse structural material properties disappeared. Additionally, exercise and control groups showed no differences in yield stress, yield toughness or elastic modulus (Young's modulus),<sup>55</sup> suggesting that endurance training is not harmful for bone material properties. ERT's benefits on the post-yield biomaterial behaviors seemed to be more size-independent and associated with tissue-level (e.g. bone matrix, collagen) changes. Because measuring post-yield mechanical properties using beam bending theory is only valid in the pre-yield regime,<sup>75</sup> reporting post-yield stress, strain or toughness is inappropriate. Therefore, we discussed this tissue-level adaptation base on the post-yield parameters measured from load-displacement data. As shown in our two recent studies, either moderate ERT or endurance swimming training benefits bone tissue more in terms of energy absorption capacity,<sup>55,77</sup> especially in post-yield energy. Similar results of enhanced post-yield behavior were provided by another ERT animal study, which showed a short-term treadmill running (21 days) enhanced tibia post-yield deformation in mice.<sup>78</sup> Moreover, such effects on post-yield behavior changes seem to apply not only to endurance training. After a short-term (5 days) freefall landing exercise, Wistar rats revealed an increased post-yield energy absorption in ulnae.<sup>79</sup> Such an enhanced absorption capability is more likely due to tissue-level (e.g. bone matrix, collagen orientation etc) changes rather than structural adaptation. As mentioned in previous studies, tissue-level properties can be divided into the inorganic mineral phase (e.g., hydroxyapatite), which determines tissue stiffness and strength,<sup>80, 81</sup> and the organic bone matrix, which plays a key role in energy absorption,<sup>82, 83</sup> It has been suggested that the networks of collagen, one of the major components of bone matrix, could affect the energy dissipation between the yield point and fracture point in bone tissue.<sup>84-86</sup>

Collagen fiber orientation (CFO) has been measured by circularly polarized light microscopes as one parameter to represent the collagen network and to predict post-yield energy of bone tissue.<sup>84</sup> Hence, the post-yield behavior revealed by ERT rats' bone tissue could partially stem from a highly organized collagen fiber network. Though the information regarding collagen orientation in the present study is not available in our previous rodent studies,<sup>55,77</sup> it has been reported that dogs after one-year of intensive endurance running (40km/day) revealed a higher organization of collagen fibers in bone tissues.<sup>87</sup> Such highly organized collagen fibers seemed to be able to compensate for the 10% BMD decrease in running dogs. Thus, a highly organized CFO would be expected in rodent studies. As mentioned above, rats subjected to short-term freefall landing exercise (5 days, 10 or 30 times per day) from a height of 40cm also showed enhanced post-yield energy of ulnae.<sup>79</sup> In that study, authors tried to measure the CFO of cross-sectional ulnae. Unfortunately, no difference in CFO between exercise and control groups was found. One major reason for this lack of significant results could be species difference. That is, CFO analysis might not be sensitive enough to detect biomaterial differences in rodents. To date, CFO-related analysis in bone tissue specimens have all been obtained from big mammals,<sup>88, 89</sup> which have more mature Haversian's systems and visible osteons. However, in smaller mammals (e.g. young adult rodents), it is not possible to find Haversian's systems or complete osteon.<sup>90, 91</sup> Per our observation, the organization of collagen fiber tends to be relatively irregular in rats and, thus, CFO analysis might not be sensitive enough to predict post-yield material properties.

On the other hand, cross-links within collagen networks might be another contributor to changes in tissue post-yield behaviors.<sup>92</sup> In an exercise-related study, Kohn and colleagues verified that cortical toughness enhanced by a 21-day ERT could be correlated with the overall maturity of collagen cross-links.<sup>93</sup>

In addition to individually measure CFO or cross-links, the biomaterial properties (e.g. tissue strength or tissue post-yield behaviors) might benefit from better integration between collagen and its crosslinks. Related measurement methods are awaited and are worthy of further study.

Finally, microdamage is another factor influencing tissue's post-yield behavior. Accumulation of microdamages (or microcracks) would lead to a fragile bone with lower capability in post-yield energy dissipation.<sup>84, 94</sup> However, such accumulated microdamages seemed to be more related to aging. Also, as in CFO-related studies, microdamage studies have been more frequently done in big mammals. Whether microdamage measurement can be performed on exercise-related rodent study needs further verification.

## 6. Summary

Endurance running is a popular aerobic activity and typical training type. However, related human studies reveal no significant benefits to bone health based on densitometric measurement of bone mineral. On the other hand, animal studies apparently indicate that ERT enhances biomaterial of bone tissue in a size-independent way. The effects of endurance running on the organic bone matrix or other parameters, as well as their relationship to mechanical properties of bone tissues, are worthy of further study.

## 7. Acknowledgments

This study was supported by a grant from the National Science Council: NSC 99-2410-H-006 -114 -MY2. Miss Jae Cody is appreciated for her editorial assistance.

## 8. References

- [1] Burrows M, Bird S. The physiology of the highly trained female endurance runner. *Sports medicine (Auckland, NZ)* 2000;30:281-300.
- [2] Burrows M, Nevill AM, Bird S, Simpson D. Physiological factors associated with low bone mineral density in female endurance runners. *British journal of sports medicine* 2003;37:67-71.
- [3] Brahm H, Strom H, Piehl-Aulin K, Mallmin H, Ljunghall S. Bone metabolism in endurance trained athletes: a comparison to population-based controls based on DXA, SXA, quantitative ultrasound, and biochemical markers. *Calcif Tissue Int* 1997;61:448-54.
- [4] Maimoun L, Galy O, Manetta J, Coste O, Peruchon E, Micallef JP, Mariano-Goulart D, Couret I, Sultan C, Rossi M. Competitive season of triathlon does not alter bone metabolism and bone mineral status in male triathletes. *International journal of sports medicine* 2004;25:230-4.
- [5] Cooper LA, Joy EA. Osteoporosis in a female cross-country runner with femoral neck stress fracture. *Current sports medicine reports* 2005;4:321-2.
- [6] Fredericson M, Kent K. Normalization of bone density in a previously amenorrheic runner with osteoporosis. *Medicine and science in sports and exercise* 2005;37:1481-6.
- [7] Prather H, Hunt D. Issues unique to the female runner. *Physical medicine and rehabilitation clinics of North America* 2005;16:691-709.
- [8] Wilson JH, Wolman RL. Osteoporosis and fracture complications in an amenorrhoeic athlete. *British journal of rheumatology* 1994;33:480-1.
- [9] Mudd LM, Fornetti W, Pivarnik JM. Bone mineral density in collegiate female athletes: comparisons among sports. *Journal of athletic training* 2007;42:403-8.
- [10] Frost HM. Bone "mass" and the "mechanostat": a proposal. *The Anatomical record* 1987;219:1-9.
- [11] Jurimae T, Soot T, Jurimae J. Relationships of anthropometrical parameters and body composition with bone mineral content or density in young women with different levels of physical activity. *Journal of physiological anthropology and applied human science* 2005;24:579-87.
- [12] Grimston SK, Tanguay KE, Gundberg CM, Hanley DA. The calciotropic hormone response to changes in serum calcium during exercise in female long distance runners. *The Journal of clinical endocrinology and metabolism* 1993;76:867-72.
- [13] Robinson TL, Snow-Harter C, Taaffe DR, Gillis D, Shaw J, Marcus R. Gymnasts exhibit higher bone mass than runners despite similar prevalence of amenorrhea and oligomenorrhea. *J Bone Miner Res* 1995;10:26-35.
- [14] Taaffe DR, Robinson TL, Snow CM, Marcus R. High-impact exercise promotes bone gain in well-trained female athletes. *J Bone Miner Res* 1997;12:255-60.
- [15] MacDougall JD, Webber CE, Martin J, Ormerod S, Chesley A, Younglai EV, Gordon CL, Blimkie CJ. Relationship among running mileage, bone density, and serum testosterone in male runners. *J Appl Physiol* 1992;73:1165-70.
- [16] Greene DA, Naughton GA, Briody JN, Kemp A, Woodhead H, Farpour-Lambert N. Musculoskeletal health in elite male adolescent middle-distance runners. *J Sci Med Sport* 2004;7:373-83.

- [17] Emslander HC, Sinaki M, Muhs JM, Chao EY, Wahner HW, Bryant SC, Riggs BL, Eastell R. Bone mass and muscle strength in female college athletes (runners and swimmers). *Mayo Clinic proceedings* 1998;73:1151-60.
- [18] Duncan CS, Blimkie CJ, Kemp A, Higgs W, Cowell CT, Woodhead H, Briody JN, Howman-Giles R. Mid-femur geometry and biomechanical properties in 15- to 18-yr-old female athletes. *Medicine and science in sports and exercise* 2002;34:673-81.
- [19] Egan E, Reilly T, Giacomoni M, Redmond L, Turner C. Bone mineral density among female sports participants. *Bone* 2006;38:227-33.
- [20] Greene DA, Naughton GA, Briody JN, Kemp A, Woodhead H, Corrigan L. Bone strength index in adolescent girls: does physical activity make a difference? *British journal of sports medicine* 2005;39:622-7; discussion 7.
- [21] Fredericson M, Chew K, Ngo J, Cleek T, Kiratli J, Cobb K. Regional bone mineral density in male athletes: a comparison of soccer players, runners and controls. *British journal of sports medicine* 2007;41:664-8; discussion 8.
- [22] Duncan CS, Blimkie CJ, Cowell CT, Burke ST, Briody JN, Howman-Giles R. Bone mineral density in adolescent female athletes: relationship to exercise type and muscle strength. *Medicine and science in sports and exercise* 2002;34:286-94.
- [23] Kemmler W, Engelke K, Baumann H, Beeskow C, von Stengel S, Weineck J, Kalender WA. Bone status in elite male runners. *Eur J Appl Physiol* 2006;96:78-85.
- [24] Stewart AD, Hannan J. Total and regional bone density in male runners, cyclists, and controls. *Medicine and science in sports and exercise* 2000;32:1373-7.
- [25] Moen SM, Sanborn CF, DiMarco NM, Gench B, Bonnick SL, Keizer HA, Menheere PP. Lumbar bone mineral density in adolescent female runners. *The Journal of sports medicine and physical fitness* 1998;38:234-9.
- [26] Kraut JA. The role of metabolic acidosis in the pathogenesis of renal osteodystrophy. *Advances in renal replacement therapy* 1995;2:40-51.
- [27] Fahey TD, Baldwin KM, Brooks GA. *Exercise Physiology: Human Bioenergetics and Its Applications*: McGraw-Hill; 2005.
- [28] Aoi W, Iwashita S, Fujie M, Suzuki M. Sustained swimming increases erythrocyte MCT1 during erythropoiesis and ability to regulate pH homeostasis in rat. *International journal of sports medicine* 2004;25:339-44.
- [29] Ashizawa N, Fujimura R, Tokuyama K, Suzuki M. A bout of resistance exercise increases urinary calcium independently of osteoclastic activation in men. *J Appl Physiol* 1997;83:1159-63.
- [30] Ashizawa N, Ouchi G, Fujimura R, Yoshida Y, Tokuyama K, Suzuki M. Effects of a single bout of resistance exercise on calcium and bone metabolism in untrained young males. *Calcified tissue international* 1998;62:104-8.
- [31] Zanker CL, Swaine IL. Relation between bone turnover, oestradiol, and energy balance in women distance runners. *British journal of sports medicine* 1998;32:167-71.
- [32] Zanker CL, Swaine IL. The relationship between serum oestradiol concentration and energy balance in young women distance runners. *Int J Sports Med* 1998;19:104-8.
- [33] Zanker CL, Swaine IL. Bone turnover in amenorrhoeic and eumenorrhoeic women distance runners. *Scandinavian journal of medicine & science in sports* 1998;8:20-6.
- [34] Zanker CL. Bone metabolism in exercise associated amenorrhoea: the importance of nutrition. *British journal of sports medicine* 1999;33:228-9.

- [35] Smith R, Rutherford OM. Spine and total body bone mineral density and serum testosterone levels in male athletes. *Eur J Appl Physiol Occup Physiol* 1993;67:330-4.
- [36] Cummings SR, Bates D, Black DM. Clinical use of bone densitometry - Scientific review. *Jama-Journal of the American Medical Association* 2002;288:1889-97.
- [37] Rico H, Revilla M, Hernandez ER, Villa LF, Alvarez del Buergo M, Lopez Alonso A. Age- and weight-related changes in total body bone mineral in men. *Mineral and electrolyte metabolism* 1991;17:321-3.
- [38] Siemon NJ, Moodie EW. Body weight as a criterion in judging bone mineral adequacy. *Nature* 1973;243:541-3.
- [39] Soot T, Jurimae T, Jurimae J, Gapeyeva H, Paasuke M. Relationship between leg bone mineral values and muscle strength in women with different physical activity. *J Bone Miner Metab* 2005;23:401-6.
- [40] Osteoporosis prevention, diagnosis, and therapy. *Jama* 2001;285:785-95.
- [41] Viguier-Carrin S, Garnero P, Delmas PD. The role of collagen in bone strength. *Osteoporos Int* 2006;17:319-36.
- [42] Ferreira LG, De Toledo Bergamaschi C, Lazaretti-Castro M, Heilberg IP. Effects of creatine supplementation on body composition and renal function in rats. *Medicine and science in sports and exercise* 2005;37:1525-9.
- [43] Joo YI, Sone T, Fukunaga M, Lim SG, Onodera S. Effects of endurance exercise on three-dimensional trabecular bone microarchitecture in young growing rats. *Bone* 2003;33:485-93.
- [44] Kiuchi A, Arai Y, Katsuta S. Detraining effects on bone mass in young male rats. *International journal of sports medicine* 1998;19:245-9.
- [45] Newhall KM, Rodnick KJ, van der Meulen MC, Carter DR, Marcus R. Effects of voluntary exercise on bone mineral content in rats. *J Bone Miner Res* 1991;6:289-96.
- [46] Notomi T, Okazaki Y, Okimoto N, Saitoh S, Nakamura T, Suzuki M. A comparison of resistance and aerobic training for mass, strength and turnover of bone in growing rats. *Eur J Appl Physiol* 2000;83:469-74.
- [47] Sakamoto K, Grunewald KK. Beneficial effects of exercise on growth of rats during intermittent fasting. *J Nutr* 1987;117:390-5.
- [48] Banu MJ, Orhii PB, Mejia W, McCarter RJ, Mosekilde L, Thomsen JS, Kalu DN. Analysis of the effects of growth hormone, voluntary exercise, and food restriction on diaphyseal bone in female F344 rats. *Bone* 1999;25:469-80.
- [49] Mosekilde L, Thomsen JS, Orhii PB, McCarter RJ, Mejia W, Kalu DN. Additive effect of voluntary exercise and growth hormone treatment on bone strength assessed at four different skeletal sites in an aged rat model. *Bone* 1999;24:71-80.
- [50] Bourrin S, Palle S, Pupier R, Vico L, Alexandre C. Effect of physical training on bone adaptation in three zones of the rat tibia. *J Bone Miner Res* 1995;10:1745-52.
- [51] Horcajada-Molteni MN, Davicco MJ, Collignon H, Lebecque P, Coxam V, Barlet JP. Does endurance running before orchidectomy prevent osteopenia in rats? *Eur J Appl Physiol Occup Physiol* 1999;80:344-52.
- [52] Huang TH, Lin SC, Chang FL, Hsieh SS, Liu SH, Yang RS. Effects of different exercise modes on mineralization, structure, and biomechanical properties of growing bone. *J Appl Physiol* 2003;95:300-7.

- [53] Nordsletten L, Kaastad TS, Skjeldal S, Kirkeby OJ, Reikeras O, Ekeland A. Training increases the in vivo strength of the lower leg: an experimental study in the rat. *J Bone Miner Res* 1993;8:1089-95.
- [54] Huang TH, Yang RS, Hsieh SS, Liu SH. Effects of caffeine and exercise on the development of bone: A densitometric and histomorphometric study in young Wistar rats. *Bone* 2002;30:293-9.
- [55] Huang TH, Chang FL, Lin SC, Liu SH, Hsieh SS, Yang RS. Endurance treadmill running training benefits the biomaterial quality of bone in growing male Wistar rats. *J Bone Miner Metab* 2008;26:350-7.
- [56] Iwamoto J, Yeh JK, Aloia JF. Differential effect of treadmill exercise on three cancellous bone sites in the young growing rat. *Bone* 1999;24:163-9.
- [57] Iwamoto J, Shimamura C, Takeda T, Abe H, Ichimura S, Sato Y, Toyama Y. Effects of treadmill exercise on bone mass, bone metabolism, and calciotropic hormones in young growing rats. *J Bone Miner Metab* 2004;22:26-31.
- [58] Hagihara Y, Fukuda S, Goto S, Iida H, Yamazaki M, Moriya H. How many days per week should rats undergo running exercise to increase BMD? *J Bone Miner Metab* 2005;23:289-94.
- [59] Wheeler DL, Graves JE, Miller GJ, Vander Griend RE, Wronski TJ, Powers SK, Park HM. Effects of running on the torsional strength, morphometry, and bone mass of the rat skeleton. *Medicine and science in sports and exercise* 1995;27:520-9.
- [60] Raab DM, Smith EL, Crenshaw TD, Thomas DP. Bone mechanical properties after exercise training in young and old rats. *J Appl Physiol* 1990;68:130-4.
- [61] Hou JC, Salem GJ, Zernicke RF, Barnard RJ. Structural and mechanical adaptations of immature trabecular bone to strenuous exercise. *J Appl Physiol* 1990;69:1309-14.
- [62] Shimamura C, Iwamoto J, Takeda T, Ichimura S, Abe H, Toyama Y. Effect of decreased physical activity on bone mass in exercise-trained young rats. *J Orthop Sci* 2002;7:358-63.
- [63] van der Wiel HE, Lips P, Graafmans WC, Danielsen CC, Nauta J, van Lingen A, Mosekilde L. Additional weight-bearing during exercise is more important than duration of exercise for anabolic stimulus of bone: a study of running exercise in female rats. *Bone* 1995;16:73-80.
- [64] Salem GJ, Zernicke RF, Martinez DA, Vailas AC. Adaptations of immature trabecular bone to moderate exercise: geometrical, biochemical, and biomechanical correlates. *Bone* 1993;14:647-54.
- [65] Cortright RN, Chandler MP, Lemon PW, DiCarlo SE. Daily exercise reduces fat, protein and body mass in male but not female rats. *Physiol Behav* 1997;62:105-11.
- [66] Lamb DR, van Huss WD, Carrow RE, Heusner WW, Weber JC, Kertzer R. Effects of prepubertal physical training on growth, voluntary exercise, cholesterol and basal metabolism in rats. *Research quarterly* 1969;40:123-33.
- [67] Afonso VM, Eikelboom R. Relationship between wheel running, feeding, drinking, and body weight in male rats. *Physiology & behavior* 2003;80:19-26.
- [68] Tokuyama K, Saito M, Okuda H. Effects of wheel running on food intake and weight gain of male and female rats. *Physiology & behavior* 1982;28:899-903.
- [69] Dohm GL, Louis TM. Changes in androstenedione, testosterone and protein metabolism as a result of exercise. *Proceedings of the Society for Experimental*

- Biology and Medicine Society for Experimental Biology and Medicine (New York, NY 1978;158:622-5.
- [70] Dudley SD, Gentry RT, Silverman BS, Wade GN. Estradiol and insulin: independent effects on eating and body weight in rats. *Physiology & behavior* 1979;22:63-7.
- [71] Gavin ML, Gray JM, Johnson PR. Estrogen-induced effects on food intake and body weight in ovariectomized, partially lipectomized rats. *Physiology & behavior* 1984;32:55-9.
- [72] Guyard B, Fricker J, Brigant L, Betoulle D, Apfelbaum M. Effects of ovarian steroids on energy balance in rats fed a highly palatable diet. *Metabolism: clinical and experimental* 1991;40:529-33.
- [73] Hervey E, Hervey GR. The effects of progesterone on body weight and composition in the rat. *The Journal of endocrinology* 1967;37:361-81.
- [74] Chatterton RT, Jr., Hrycyk L, Hickson RC. Effect of endurance exercise on ovulation in the rat. *Medicine and science in sports and exercise* 1995;27:1509-15.
- [75] Turner CH, Burr DB. Basic biomechanical measurements of bone: a tutorial. *Bone* 1993;14:595-608.
- [76] Chen HI, Chiang IP. Chronic exercise decreases adrenergic agonist-induced vasoconstriction in spontaneously hypertensive rats. *The American journal of physiology* 1996;271:H977-83.
- [77] Huang TH, Hsieh SS, Liu SH, Chang FL, Lin SC, Yang RS. Swimming training increases the post-yield energy of bone in young male rats. *Calcif Tissue Int* 2010;86:142-53.
- [78] Wallace JM, Ron MS, Kohn DH. Short-term exercise in mice increases tibial post-yield mechanical properties while two weeks of latency following exercise increases tissue-level strength. *Calcif Tissue Int* 2009;84:297-304.
- [79] Lin HS, Huang TH, Mao SW, Tai YS, Chiu HT, Cheng KYB, Yang RS. A short-term free-fall landing enhances bone formation and bone material properties. *Journal of Mechanics in Medicine and Biology* (In press) 2011.
- [80] Currey JD. The effect of porosity and mineral content on the Young's modulus of elasticity of compact bone. *J Biomech* 1988;21:131-9.
- [81] Currey JD. Changes in the impact energy absorption of bone with age. *J Biomech* 1979;12:459-69.
- [82] Boskey AL, Wright TM, Blank RD. Collagen and bone strength. *J Bone Miner Res* 1999;14:330-5.
- [83] Wang X, Bank RA, TeKoppele JM, Agrawal CM. The role of collagen in determining bone mechanical properties. *J Orthop Res* 2001;19:1021-6.
- [84] Skedros JG, Dayton MR, Sybrowsky CL, Bloebaum RD, Bachus KN. The influence of collagen fiber orientation and other histocompositional characteristics on the mechanical properties of equine cortical bone. *Journal of Experimental Biology* 2006;209:3025-42.
- [85] Burr DB. The contribution of the organic matrix to bone's material properties. *Bone* 2002;31:8-11.
- [86] Zioupos P, Currey JD. Changes in the stiffness, strength, and toughness of human cortical bone with age. *Bone* 1998;22:57-66.
- [87] Puustjarvi K, Nieminen J, Rasanen T, Hyttinen M, Helminen HJ, Kroger H, Huuskonen J, Alhava E, Kovanen V. Do more highly organized collagen fibrils increase bone

- mechanical strength in loss of mineral density after one-year running training? *Journal of Bone and Mineral Research* 1999;14:321-9.
- [88] Martin RB, Lau ST, Mathews PV, Gibson VA, Stover SM. Collagen fiber organization is related to mechanical properties and remodeling in equine bone. A comparison of two methods. *J Biomech* 1996;29:1515-21.
- [89] Skedros JG, Mason MW, Nelson MC, Bloebaum RD. Evidence of structural and material adaptation to specific strain features in cortical bone. *Anat Rec* 1996;246:47-63.
- [90] Martiniakova M, Grosskopf B, Omelka R, Vondrakova M, Bauerova M. Differences among species in compact bone tissue microstructure of mammalian skeleton: use of a discriminant function analysis for species identification. *Journal of forensic sciences* 2006;51:1235-9.
- [91] Ruth EB. Bone studies. II. An experimental study of the Haversian-type vascular channels. *The American journal of anatomy* 1953;93:429-55.
- [92] Garnero P, Borel O, Gineyts E, Duboeuf F, Solberg H, Bouxsein ML, Christiansen C, Delmas PD. Extracellular post-translational modifications of collagen are major determinants of biomechanical properties of fetal bovine cortical bone. *Bone* 2006;38:300-9.
- [93] Kohn DH, Sahar ND, Wallace JM, Golcuk K, Morris MD. Exercise alters mineral and matrix composition in the absence of adding new bone. *Cells Tissues Organs* 2009;189:33-7.
- [94] Augat P, Schorlemmer S. The role of cortical bone and its microstructure in bone strength. *Age Ageing* 2006;35 Suppl 2:ii27-ii31.



# Effect of the Er, Cr: YSGG Laser Parameters on Shear Bond Strength and Microstructure on Human Dentin Surface

Eun Mi Rhim<sup>1</sup>, Sungyoon Huh<sup>2</sup>, Duck Su Kim<sup>3</sup>, Sun-Young Kim<sup>4</sup>,  
Su-Jin Ahn<sup>5</sup>, Kyung Lhi Kang<sup>6</sup> and Sang Hyuk Park<sup>4,7</sup>

<sup>1</sup>*The Catholic University of Korea, St. Paul's Hospital,  
Dept. of Conservative Dentistry, Seoul,*

<sup>2</sup>*Shingu University, Dept. of Dental Hygiene, Seongnam,*

<sup>3</sup>*Kyung Hee University, Dental Hospital, Dept. of Conservative Dentistry, Seoul*

<sup>4</sup>*Kyung Hee University, Dept. of Conservative Dentistry, Seoul,*

<sup>5</sup>*Kyung Hee University, Dental Hospital at Gandong,  
Dept. of Biomaterials & Prosthodontics,*

<sup>6</sup>*Kyung Hee University, Dental Hospital at Gandong, Dept. of Periodontology,*

<sup>7</sup>*Kyung Hee University Dental Hospital at Gandong, Dept. of Conservative Dentistry  
Korea*

## 1. Introduction

The developments of laser technology have enabled their use in multiple dental procedures, such as soft tissue operations, composite restorations, tooth bleaching, root canal irrigation, caries removal and tooth preparations with minimal pain and discomfort (Turkmen et al., 2010). Recently, the Er,Cr:YSGG laser was recommended for minimally invasive purposes due to its precise ablation of the enamel and dentin without side-effects to the pulp and surrounding tissues. It has a 2780-nm wavelength and absorbed strongly by both water and hydroxyapatite. The sudden evaporation of bound water causes micro-explosions that blast away tiny particles of the tooth (Obeidi et al., 2010).

Previous studies reported that irregularities and the crater-shaped appearance of ablated dentin was comparable to the dentine surface after acid etching, which might promote micromechanical interlocking between dental restorative materials and the tooth surface (Visuri et al., 1996; Armengol et al., 1999; Martínez-Insua et al., 2000; Carrieri et al., 2007; Gurgan et al., 2008). Despite its efficiency, reports on the bond strengths of composite resin to a tooth substrate prepared by a laser are often confusing and contradictory. Some studies reported higher bond strengths to laser-prepared dentin than to acid-etched dentin (Visuri et al., 1996; Carrieri et al., 2007). Others have reported significantly lower bond strengths on laser preparation (Armengol et al., 1999; Martínez-Insua da Silva Dominguez et al. 2000; Gurgan Kiremitci et al. 2008) and others have reported no significant differences (Abdalla & Davidson, 1998).

Generally there are three adhesive systems. The first uses 30–40% phosphoric acid to remove the smear layer (etch-and-rinse (ER) technique). This bonding mechanism to dentin

depends on the hybridization of the resin within the exposed collagen mesh as well as to the dentin tubules (Abdalla & Davidson, 1998), creating a micromechanical interlocking of the resin within the exposed collagen fibril scaffold. The second is the “self-etch” adhesives (SEA) which employs acidic monomers that simultaneously condition and prime dentin. The smear layer remains partially but is used to hybridize with the underlying dentin (Perdigao et al., 2000). The last is an all-in-one system, but the stability of the bond strength decreases with time because it contains many hydrophilic monomers.

According to previous reports, a tiny flake surface formed by the laser irradiation of dentin can be removed with 30-40 % acid etching, but the primer of SEA cannot. This study hypothesized that the primer of SEA cannot improve the free surface energy of irradiated dentin. Therefore, it is unable to make a proper environment for sufficient bond strength. The null hypothesis was that the shear bond strength with “self-etch” adhesives (SEA) did not show a difference from that with the etch-and-rinse (ER) technique after a pretreatment with a laser in dentin.

This study examined the shear bond strength of a hybrid composite resin bonded with two different adhesive systems to the dentin surfaces prepared with Er,Cr:YSGG laser etching, and evaluated the morphologic structure of de-bonded dentin surface after Shear Bond Strength (SBS) Test by scanning electron microscopy.

## 2. Materials and methods

### 2.1 Tooth preparation

Tables 1 and 2 list the materials used in this study and the study design, respectively. Twenty four freshly extracted caries and restoration-free permanent human molars stored in distilled water were used. The teeth were embedded in improved stone with the occlusal surface of the crown exposed and parallel to the base of the stone, and the embedded teeth were sectioned at one third of the occlusal surfaces to expose the dentin surface. Each tooth was wet-ground with 320-grit silicon carbide paper and polished with 1200-grit to obtain a flat dentin surface. The specimens were stored in distilled water at 37 °C. The teeth were divided randomly into two groups, control and laser irradiated groups. The control groups without laser irradiation were divided randomly into two subgroups (SE bond and Single bond), and the laser irradiated groups were divided into four subgroups (SE bond with 1.4 W, 2.25 W and Single bond with 1.4W, 2.25W).

### 2.2 Laser irradiation

The Er,Cr:YSGG laser (Waterlase, BioLase Technology, Inc., San Clemente, CA) with a 2780 nm wavelength and 20 Hz of power with a sapphire tip was used. Laser irradiation was performed on the dentin surface with either 1.4 W or 2.25 W. The flattened dentin surfaces of the teeth were irradiated at 90° in non-contact mode with a fixed distance of 6 mm away from the laser tip in a sweeping motion to achieve an even surface coverage by overlapping the laser impact. The laser handpiece was attached to a modified surveyor to ensure a consistent energy density, spot size, distance and handpiece angle.

### 2.3 Bonding procedures

In all groups, including laser irradiated groups and control groups, the bonding procedures recommended by the manufacturer's instruction were followed strictly. In the single bond

adhesive system, etching procedures were conducted using 37 % phosphoric acid (3M ESPE, St. Paul, MN, USA) for 15 seconds followed by rinsing with a water spray for 15 seconds, and blot dried, and bonded and light curing for 15 seconds. In the Clearfil SE bond system, a primer was applied to the dentin surface for 10 seconds followed by bonding and light curing, as shown table 1.

After light curing the bonding resin, a Teflon tube (GI tech, Seoul, Korea) with an inner diameter of 2 mm and a height of 2 mm was attached to each dentin surface and filled with A3 Body Shade of the hybrid composite Resin (Filtek Supreme Plus 3 M ESPE, MN, USA) followed by light curing for 40 s. After light curing, the teeth were stored in water at 37°C for 24h before the Shear Bond Strength (SBS) Test.

Brand name	Manufacturer	Material type	Composition	Application procedure
Clearfil SE bond	Kuraray, Tokyo, Japan	Self etching adhesive system	Primer: MDP, HEMA, N,N-Diethanol p-toluidine, water Bonding resin: Bis-GMA, CQ, HEMA, MDP, Micro filler	Apply primer and leave 20 seconds, air blow, apply bonding system
Single bond	3M ESPE, St. Paul MN, USA	Etch and rinse adhesive system	Bis-GMA, HEMA, Water, UDMA, Ethanol, Polyalkenoic acid copolymer	Acid-etch for 15 seconds, rinse, apply adhesive, gentle air blow, light curing for 10 seconds.

Table 1. Materials used in this study.

Laser intensity	Adhesive system	
	Single bond	SE bond
Control (no laser)	Group A	Group D
1.4W	Group B	Group E
2.25W	Group C	Group F

Table 2. Classification of the experimental groups.

### 2.4 Shear Bond Strength (SBS) test

Before loading, the tube mold was removed carefully with a sharp blade and the specimens were then placed in a custom-made fixture mounted on a Universal Testing Machine (INSTRON Model 5562, Norwood, MA). The specimens were loaded to failure under

compression using a knife-edge loading head at a cross-head speed of 1 mm/min. The investigator, who was blinded to the group treatment, performed the load testing procedure. The maximum load to failure was recorded for each sample and the Shear bond strength (SBS) was expressed in megapascals (MPa), which was derived by dividing the imposed force (Newtons) by the bonded area (mm<sup>2</sup>).

### 2.5 SEM evaluation

To evaluate the surface (treated with Etching, Laser, and Laser + Etching) before bonding and the fractured surface between the composite resin and dentin side after measuring shear bond strength, the representative dentin specimens were selected randomly and mounted on aluminum stubs. The samples were then sputter-coated with gold palladium and examined by scanning electron microscopy (SEM) (ISI SX-30 Cambridge, MA, USA) with 1000X magnification.

### 2.6 Statistical analysis

The obtained shear bond strength data were analyzed by two way ANOVA with a level of significance of  $P < 0.05$ .

## 3. Results

### 3.1 Shear Bond Strength (SBS) evaluation

The Mean SBS±SD (MPa) of each group followed by a Single bond was 7.35±1.65, 7.61±1.50 and 6.34±1.39, respectively, and the Mean SBS±SD (MPa) for each group followed by a SE bond was 7.73±1.17, 7.88±2.77, and 6.48±1.77, respectively (Table 3), but there were no significant differences between the groups. The maximum and minimum SBS was observed in groups E and C, respectively. The maximum and minimum SBS in the Single Bond group was observed in groups B and C, respectively. The maximum and minimum SBS in the SE Bond group was observed in group E and F, respectively (Figure 1). Some samples dislodged and de-bonded during preparation for the shear bond test due to the uneven samples distribution.

Adhesive system	Single bond			SE bond		
	Control	1.4 W	2.25 W	Control	1.4 W	2.25 W
Laser intensity(W)						
Sample	Group A	Group B	Group C	Group D	Group E	Group F
Mean (MPa)	7.35	7.61	6.34	7.73	7.88	6.48
SD	1.65	1.50	1.39	1.17	2.77	1.77

Table 3. Comparison of the mean shear bond strength of the control and laser irradiated groups (Single bond and SE bond). Mean value (MPa) and standard deviation (SD) of the Shear Bond Strength (SBS) Test for the specimens treated with the Er,Cr:YSGG laser are shown but there were no significant differences between the groups ( $P > 0.05$ ).

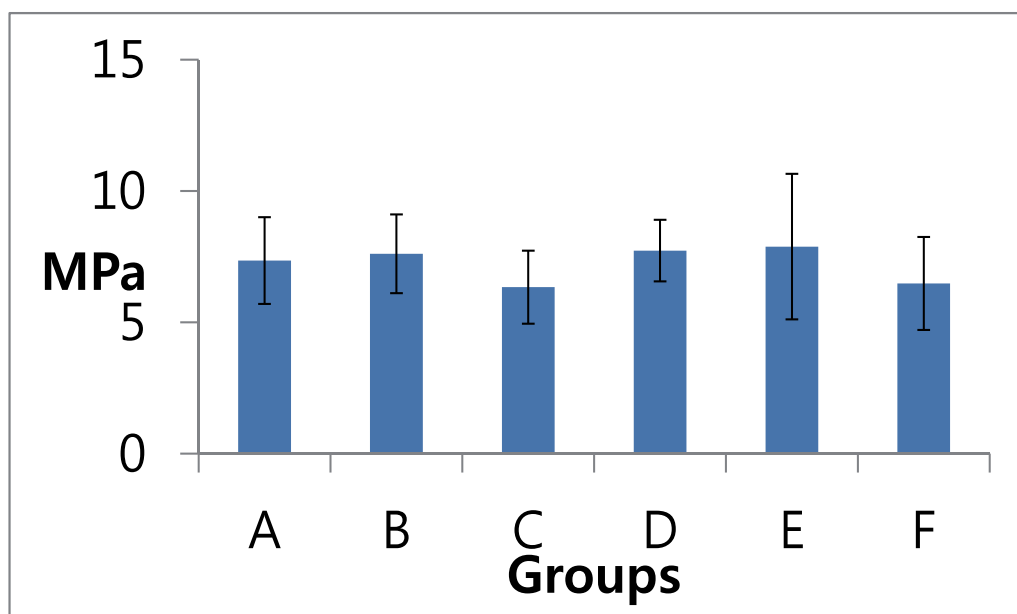


Fig. 1. Shear bond strength between the experimental groups.

### 3.2 SEM (Scanning Electronic Microscopy)

SEM revealed the fractured surface between the composite resin and dentin side, as shown in Figure 2. The representative SEM evaluation showed that thick layers of the adhesives were found on the fractured de-bonded surface of the composite resin (Figure 2-B, D, F). On the other hand, the fractured bonded surface of the dentin by the Clearfil SE bond adhesive treatment, as a result of the shear bond strength test followed by 37% phosphoric acid etching of some of the residues of the adhesives remaining on the surface of dentin side after the shear bond test (Figure 2-A, C, E).

Regarding the failure mode of the control group in the types of adhesive system, some residual chips were found (A) on the surface of dentin side fractured after 37% phosphoric acid etching and single bond adhesion but the fractured bonded surface of dentin by the Clearfil SE bond adhesive treatment as a result of the shear bond strength test followed by 37% phosphoric acid etching showed thick layers of composite resin attached to the dentin after the failure test (D).

In the irradiation groups, 1.4 W of irradiation followed by the Single bond procedure left the fractured dentin surface with small particles after the failure test (B). On the other hand, the fractured dentin surface irradiated with a power intensity of 2.25 W had exposed dentinal tubules after the test (C). On the other hand, 1.4 W of power intensity irradiation followed by the SE bond procedure revealed exposed dentinal tubules after the failure test (E), whereas 2.25 W of power intensity irradiation followed by the SE bond procedure resulted in a thick layer of composite resin fractured cohesively on the dentin side of the fractured surface (F).

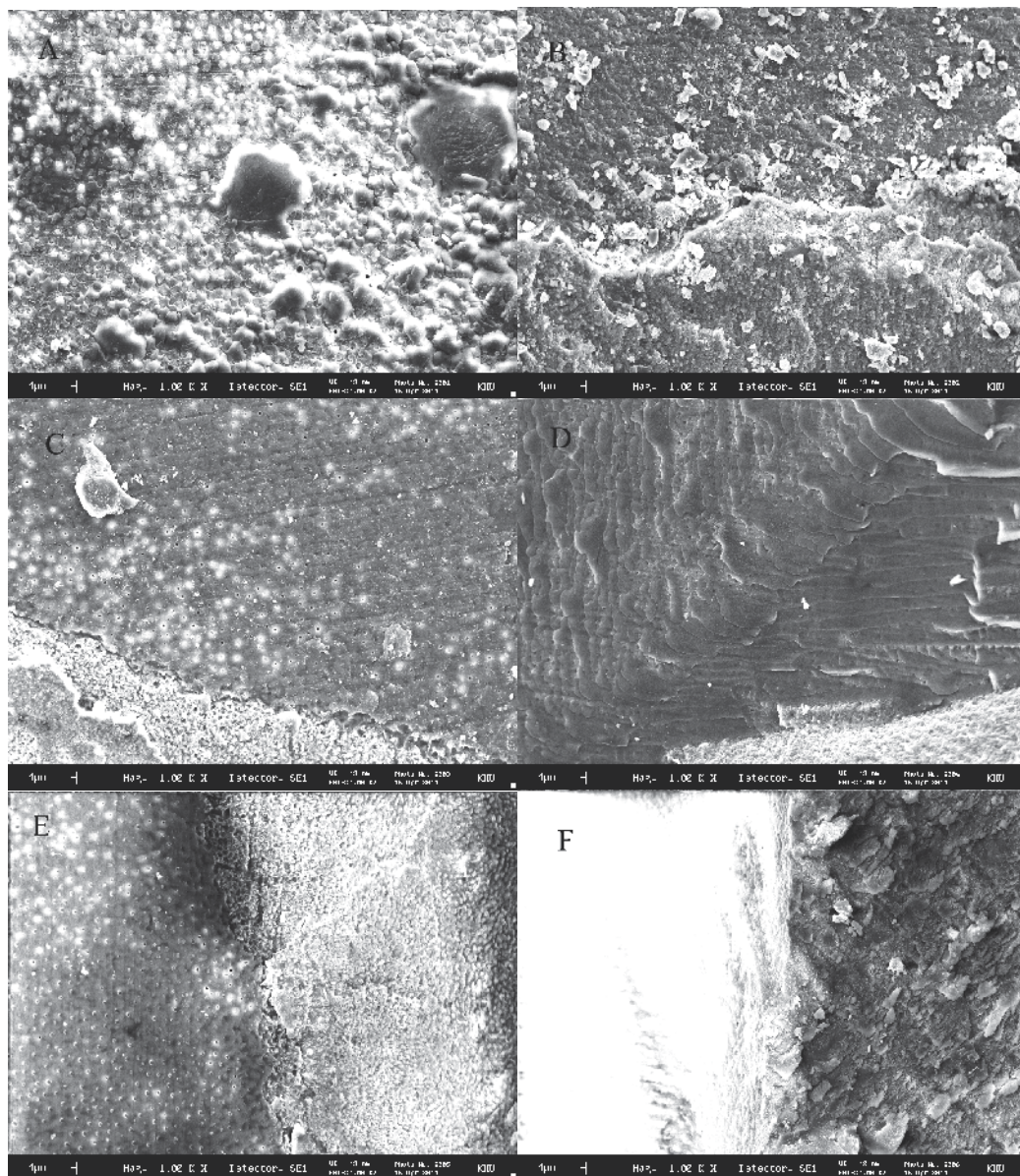


Fig. 2. SEM images (X1000) showing the fractured surface between the composite resin and dentin side. The fractured bonded surface of dentin by the single bond adhesive treatment as a result of the shear bond strength test followed by 37% phosphoric acid etching (A), and 1.4 W of power intensity irradiation followed by a Single bond procedure (B), and 2.25 W of power intensity irradiation followed by a Single bond procedure (C) were evaluated by SEM. The fractured bonded surface of the dentin by Clearfil SE bond adhesive treatment as a result of the shear bond strength test followed by 37% phosphoric acid etching (D), and 1.4 W of power intensity irradiation followed by the SE bond procedure (E), and 2.25 W of power intensity irradiation followed by the SE bond procedure (F) were evaluated by SEM.

#### 4. Discussion

Recently, Er:YAG and Cr:YSGG lasers were introduced in dentistry. For physical and medical reasons, they are used for the treatment of hard tissue. The advantage of an Erbium wave is that it is well absorbed by water and dental hard tissue. Although dentin contains a high proportion of water, the depth is shallow for laser transmission. The strong absorption of water reduces the level of heat during tooth preparation. As water absorbs laser radiation better than dental hard tissue, it reduces the increasing temperature of the tissue during the preparation. Water reaches the boiling point and causes microexposure of the tooth. This action breaks up the surrounding tissue into small pieces and dissipates them at the same time. As this explosion occurs in water, it is so-called a preparation induced by water. Although most radiation is absorbed in water, a certain amount of heat transmission is unavoidable. Therefore, a water spray is used for cooling. The proper amount of water spray prevents pulpal damage. As heat transmission normally depends on the pulse shape and pulse maintenance time, the amount of water varies according to the laser system and treatment itself. A lack of enough water spray causes pulpal damage.

In contrast to initial studies, there was no immunological difference between the laser system and conventional etching method. Moreover, the positive effect of the laser to regenerate pulp was discussed. Essentially, cavity preparation should be performed with the proper instruments with the "method of minimal pulse energy" according to the manufacturer's protocol. This is because the preparation should be performed with the capability to minimize additional damage.

The bond strength of the adhesive system is one of the major factors for the success of restorations. Therefore, this restoration parameter can be measured accurately by the bonding test. The bonding of resin composite material to the tooth structure prepared with different types of lasers has been reported (Visuri et al., 1996; Armengol et al., 1999; Martínez-Insua et al., 2000; Carrieri et al., 2007; Ekworapoj et al., 2007; Lee et al., 2007; de Carvalho et al., 2008; Gurgan et al., 2008; Chou et al., 2009). These studies reported variable results comparing the bond strengths of composite resin to a laser-prepared and acid etched dentin surface, and suggested that the laser preparation is more effective than etching in bonding strength of the composite resin to the tooth structure (Obeidi et al., 2010; Turkmen et al., 2010; Navimipour et al., 2011). This study compared the *in vitro* SBS of two different adhesive systems to dentin treated with an Er,Cr:YSGG laser. These results showed that the type of adhesive system had no effect on SBS, whereas the laser intensity was a criterion to be considered.

Generally, the manufacturer of Er,Cr:YSGG lasers recommended 2.25 to 2.5 W for laser etching but other studies used 2 to 3 W referring from their results of a pilot study to obtain the proper effects (Çalışkan et al., 2010). The data from this study showed that the shear bond strength (SBS) of dentin treated with 1.4 W, was higher than that of SBS with 2.25 W, which was recommended by the manufacturer. These results were different from other study results showing that the shear bond strength of laser etching (1.25 W or 3 W) was higher than the diamond bur (Gurgan et al., 2008). The distance between the laser tip and laser irradiated dentin surface may not be strict in this kinds of study designs. On the other hand, in this experiment, the sweeping motion of the laser irradiation 6 mm away from the dentin surface was used before the application of adhesive procedures to employ consistent defocused irradiation with lower intensity. Therefore, the difference in the effect between

the distance and irradiation time of the laser could not be performed and compared with other studies in this study (Chou et al., 2009; Obeidi et al., 2009; Obeidi et al., 2010).

Based on previous studies using Er,Cr:YSGG laser irradiation on the tooth structure, normal range of power intensity (2.5 W) was utilized on the surface of dentin while high power intensity of the laser (higher than 3 W) was more effective on the bonding strength of the enamel surface (Obeidi et al., 2010), (Dunn et al., 2005). On the other hand, Tagami *et al.* reported that 70mJ (1.75 W) of low laser intensity irradiation on the dentin surface followed by SE bond showed a higher micro shear bond strength than with 150mJ (3 W) (de Carvalho et al., 2008), which is similar to the present experiments. According to the manufacturer's recommendation for laser etching on dentin surface, it was decided to follow the laser protocol mode using two power intensities (2.5 W and 1.25 W). If a power intensity of 2.25 W and 1.4 W are converted to the mJ scale, they could be approximately 112.5 mJ and 70 mJ, respectively. In the present study, 1.4 W of laser intensity irradiation showed the highest shear bond strength between the composite resin and bonded dentin surface with the two types of adhesive systems (Single bond and Clearfil SE bond). Consequently, the SE primer of the SE bond probably could not remove the superficial layers of the irradiated dentin completely. On the other hand, phosphoric acid of three steps adhesive or two steps adhesive could remove most of the superficial layers of the irradiated dentin. In addition, one study reported the advantages of mechanical instruments or combining acid etching and mechanical instruments in removing the superficial layers (Obeidi et al., 2009).

With the respect to the micromorphological changes after acid etching and laser etching, SEM revealed different characteristic features from those found in conventional acid etched surfaces. The dentin surfaces irradiated with the Er,Cr:YSGG laser had a scaly, irregular, and rugged appearance compared to the acid etched dentin surface (Chou et al., 2009). In addition, with the higher laser intensity or longer irradiation time, the condition was worse in terms of the irregularity of the dentin surface, which has a close relationship with the bonding strength of the composite resin to dentin.

The control groups showed a higher SBS than the 2.25 W of laser irradiated groups in all bonding systems, but, SEM evaluation revealed more adhesive chips remaining on the control group than on the 2.25 W laser irradiated group. On the other hand, thick, rough, and irregular collapsed composite resins were estimated on both the control and 2.25 W laser irradiated groups. SEM examinations of the two kinds of laser intensity irradiation (1.4 W and 2.25 W) revealed that the 1.4 W laser intensity group had more adhesive chips remaining on the dentin than the 2.25 W laser group in the Single bond adhesive system, which is opposite to that observed in the Clearfil SE bond system.

One possible explanation is that the thermomechanical effects of higher laser intensity probably have extended into the subsurface dentin and undermined the integrity of the resin–dentin interface resulting in a lower bond strength. The formation of fissures or cracks in the subsurface dentin might be a start point for the failure of resin–dentin adhesion. Obviously, all irradiated groups were affected by thermo-mechanical effect, but 1.4 W and 2.25W were all affected by thermomechanical effects. On the other hand, 1.4 W laser intensity might not be seriously affected. Laser irradiation with a high intensity may obstruct the dentinal tubules by melting and fail to produce a good hybrid layer. Whereas, laser irradiation with a low intensity may leave the dentinal tubule open and facilitate the infiltration of bonding agent. This may account for the lower SBS values with 2.25 W irradiated dentin than with 1.4 W laser intensity.



These results suggest that the acid etching of lased dentin can reinforce the hybrid layer and formation of resin tags, but the acidic monomer of SE bonds cannot function at its best due to the obstruction of dentinal tubules and denatured collagen fibrils network and the absence of smear layer. These results were not the same as expected. A self etching adhesive system and two steps adhesive system showed a similar SBS because the resin tags only contribute to the bond strength in small portions (15%) and the poorer quality of the hybrid layer appears to be the main reason for the lower bond strength.

## 5. Conclusion

An Er,Cr:YSGG laser was used to determine if the laser can increase the shear bond strength between the composite resin and surface treated dentine surfaces. On the other hand, the pretreatment of dentin with an Er,Cr:YSGG laser does not affect the shear bond strength of the two different adhesive systems under these experimental conditions. In addition, the shear bond strength of two different adhesive systems in dentin treated with a 1.4W laser intensity was higher than that treated with 2.25W but the difference was not significant.

## 6. Acknowledgment

This study was supported in part by a grant from Kyung Hee University in 2006 (KHU-20060930) and by the Basic Science Research Program through the National Research Foundation of Korea (NRF) funded by the Ministry of Education, Science and Technology (NRF-20100023448).

## 7. References

- Abdalla AI, Davidson CL (1998) Bonding efficiency and interfacial morphology of one-bottle adhesives to contaminated dentin surfaces. *Am J Dent*, Vol. 11, No. 6, pp. 281-285, ISSN 0894-8275
- Armengol V, Jean A, Rohanizadeh R, Hamel H (1999) Scanning electron microscopic analysis of diseased and healthy dental hard tissues after Er: YAG laser irradiation: in vitro study. *J Endod*, Vol. 25, No. 8, pp. 543-546, ISSN 0099-2399
- Çalışkan MK, Parlar NK, Oruçoğlu H, Aydın B (2010) Apical microleakage of root-end cavities prepared by Er, Cr: YSGG laser. *Lasers in Medical Science*, Vol. 25, No. 1, pp. 145-150, ISSN 0268-8921
- Carrieri TCD, Freitas PM, Navarro RS, P. Eduardo C, Mori M (2007) Adhesion of composite luting cement to Er:YAG-laser-treated dentin. *Lasers in Medical Science*, Vol. 22, No. 3, pp. 165-170, ISSN 0268-8921
- Chou JC, Chen CC, Ding SJ (2009) Effect of Er, Cr: YSGG laser parameters on shear bond strength and microstructure of dentine. *Photomedicine and Laser Surgery*, Vol. 27, No. 3, pp. 481-486, ISSN 1549-5418
- de Carvalho RCR, de Freitas PM, Otsuki M, de Eduardo CP, Tagami J (2008) Micro-shear bond strength of Er: YAG-laser-treated dentin. *Lasers in Medical Science*, Vol. 23, No. 2, pp. 117-124, ISSN 0268-8921
- Dunn WJ, Davis JT, Bush AC (2005) Shear bond strength and SEM evaluation of composite bonded to Er:YAG laser-prepared dentin and enamel. *Dent Mater*, Vol. 21, No. 7, pp. 616-624, ISSN 0287-4547

- Ekworapoj P, Sidhu SK, McCabe JF (2007) Effect of different power parameters of Er, Cr: YSGG laser on human dentine. *Lasers in Medical Science*, Vol. 22, No. 3, pp. 175-182, ISSN 0268-8921
- Gurgan S, Kiremitci A, Cakir FY *et al.* (2008) Shear Bond Strength of Composite Bonded to Er,Cr:YSGG Laser-Prepared Dentin. *Photomedicine and Laser Surgery*, Vol. 26, No. 5, pp. 495-500, ISSN 1549-5418
- Lee BS, Lin PY, Chen MH *et al.* (2007) Tensile bond strength of Er, Cr: YSGG laser-irradiated human dentin and analysis of dentin-resin interface. *Dental Materials*, Vol. 23, No. 5, pp. 570-578, ISSN 0109-5641
- Martínez-Insua A, da Silva Dominguez L, Rivera FG, Santana-Penín UA (2000) Differences in bonding to acid-etched or Er: YAG-laser-treated enamel and dentin surfaces. *The Journal of prosthetic dentistry*, Vol. 84, No. 3, pp. 280-288, ISSN 1097-6841
- Navimipour EJ, Oskoe SS, Oskoe PA, Bahari M, Rikhtegaran S, Ghojzadeh M (2011) Effect of acid and laser etching on shear bond strength of conventional and resin-modified glass-ionomer cements to composite resin. *Lasers in Medical Science*, pp. 1-7, ISSN 0268-8921
- Obeidi A, Liu P-R, Ramp LC, Beck P, Gutknecht N (2010) Acid-etch interval and shear bond strength of Er,Cr:YSGG laser-prepared enamel and dentin. *Lasers in Medical Science*, Vol. 25, No. 3, pp. 363-369, ISSN 0268-8921
- Obeidi A, McCracken MS, Liu PR, Litaker MS, Beck P, Rahemtulla F (2009) Enhancement of bonding to enamel and dentin prepared by Er,Cr:YSGG laser. *Lasers Surg Med*, Vol. 41, No. 6, pp. 454-462, ISSN 1096-9101
- Perdigao J, May KN, Jr., Wilder AD, Jr., Lopes M (2000) The effect of depth of dentin demineralization on bond strengths and morphology of the hybrid layer. *Oper Dent*, Vol. 25, No. 3, pp. 186-194, ISSN 0361-7734
- Turkmen C, Sazak-Ovecoglu H, Gunday M, Gungor G, Durkan M, Oksuz M (2010) Shear Bond Strength Of Composite Bonded With Three Adhesives To Er, Cr: YSGG Laser-Prepared Enamel. *Quintessence International*, Vol.41, pp. e119-e124, ISSN 0033-6572
- Visuri SR, Gilbert JL, Wright DD, Wigdor HA, Walsh JT (1996) Shear Strength of Composite Bonded to Er:YAG Laser-prepared Dentin. *Journal of Dental Research*, Vol. 75, No. 1, pp. 599-605, ISSN 1544-0591

# Elaboration and Characterization of Calcium Phosphate Biomaterial for Biomedical Applications

Foued Ben Ayed

*Laboratory of Industrial Chemistry, National School of Engineering, Box 1173, 3038 Sfax  
Tunisia*

## 1. Introduction

Calcium phosphates constitute an important family of biomaterials resembling the part of calcified tissues. This study is based on calcium phosphate such as hydroxyapatite ( $\text{Ca}_{10}(\text{PO}_4)_6(\text{OH})_2$ , Hap), fluorapatite ( $\text{Ca}_{10}(\text{PO}_4)_6\text{F}_2$ , Fap) and tricalcium phosphate ( $\text{Ca}_3(\text{PO}_4)_2$ , TCP) phases because their chemical composition is similar to that of bone mineral (Hench, 1991; Legeros, 1993; Uwe et al., 1993; Elliott, 1994; Landi et al., 2000; Varma et al., 2001; Destainville et al., 2003; Wang et al., 2004; Ben Ayed et al., 2000, 2001a, b; 2006a, b; 2007; 2008a, b; Bouslama et al., 2009; Chaari et al., 2009). The most frequent is  $\beta$ -TCP because it is resorbable and osteoinductive (Gaasbeek et al., 2005; Steffen et al., 2001).  $\beta$ -TCP is resorbed in vivo by osteoclasts and replaced by new bone (Schilling et al., 2004). The tricalcium phosphate has been used clinically to repair bone defects for many years. However, mechanical properties of calcium phosphates are generally inadequate for many load-carrying applications. The tricalcium phosphate has a low density decreasing the mechanical properties. But, the efficiency of bi-phasic calcium phosphate (BCP) has been fully importantly efficiency its clinical efficacy to combat the chronic osteomyelitis in the long term. To our knowledge, if it is possible to vary the composition of bioceramic materials (composed of Hap and  $\beta$ -TCP) with its inherent porosity, it could be a solution owing to the faster resorption of this BCP together with the sustained release of the antibiotic.

In the literature Hap,  $\beta$ -TCP or the combination of both (Hap/TCP) was the most commonly used synthetic augments in high tibial osteotomy (Haell et al., 2005; Koshino et al., 2003; Gaasbeek et al., 2005; Van Hemert et al., 2004; Gutierrez et al., 2007). The use of bone cement as a temporary spacer for bone defects has been described, but secondary biological reconstruction was performed after cement removal (DeSilva et al., 2007). However, permanent acrylic bone cement has been used as an interface in the postero-medial part of high tibial osteotomy to maintain the opening angle and good results have been achieved (Hernigou et al., 2001). However, due to the different biomechanical features between bone and bone cement and missing bony remodelling and incorporation, the use of bone cement as a permanent spacer was not recommended, if one aims to achieve biological regeneration. Recently, Jensen and colleagues described that rapid resorption of  $\beta$ -TCP might impair the regenerative ability of local bone, especially in the initial stage of bone healing (Jensen et al.,

2006). The microstructure of the used  $\beta$ -TCP has important influence on the osteogenic effects (Okuda et al., 2007). This has recently been confirmed by Fellah and colleagues (Fellah et al., 2008). They show that the Hap/TCP with different micropores was evaluated in a goat critical-defect model.

Several research studies dealt with the question where and how to perform the osteotomy and which fixation material is most beneficial (Brouwer et al., 2006; Agneskirchner et al., 2006). Aryee et al. demonstrate histologically and radiologically that the complete rebuilding of lamelliform bone in patients without synthetic augmentation, whilst bony in growth into the Hap/TCP wedge of augmented osteotomies just slowly progressed (Aryee et al., 2008). In contrast to diminished osteotomies, there was no advantage in using Hap/TCP wedges or the combination of Hap/TCP wedges and platelet rich plasma (PRP) as supporting material after 12 months. In cases where augmentation is performed, either autologous spongius iliac bone graft or an Hap/TCP wedge of appropriate size was inserted into the osteotomy opening and pushed laterally until it is firmly aligned to the tibial bone. The Hap/TCP wedge utilised by us consists of 60% micro-macroporous biphasic Hap and 40%  $\beta$ -TCP. The average total porosity is 65–75%, whilst two different sizes of porosity are found within this material. The microporous part consists of pores with a diameter less than 10 $\mu$ m. The macroporous part consists of pores with a diameter between 300 $\mu$ m and 600 $\mu$ m (same as autograft macropores).

As a result of limited autologous bone availability and to minimise the problem of donor-site morbidity, many efforts have been made to find adequate supporting material for augmentation after osteotomy (Bauer et al., 2000; De Long et al., 2007). In this context, we chose biomaterials on base of calcium phosphates as solution for the biomedical applications. Thus,  $\beta$ -TCP or Hap-TCP combination has been clinically used to repair bone defects for many years (Elliott, 1994). Whereas,  $\beta$ -TCP or Hap-TCP have poor mechanical properties (Elliott, 1994; Wang et al., 2004). The usage at high load bearing conditions was restricted due to its brittleness, poor fatigue resistance and strength. Hence, there was a need for improving the mechanical properties of these materials by suitable biomaterials for clinical applications. We offer the study of the mixtures of tricalcium phosphate ( $\beta$ -TCP) and synthetic Fap in order to obtain a bioceramic with better mechanical properties than Hap-TCP combination or  $\beta$ -TCP as separately used. In fact, Fap is an attractive material due to its similarity in structure and bone composition in addition to the benefit of fluorine release (Elliott, 1994; Ben Ayed et al., 2001a). In Vitro studies we have shown that Fap is biocompatible (Elliott, 1994). It also has better stability and provides fluorine release at a controlled rate to ensure the formation of a mechanically and functionally strong bone (Elliott, 1994; Ben Ayed et al., 2006b).

Most studies have been devoted to the knowledge of the mechanical properties and biomedical applications of TCP-Hap (Elliott, 1994; Landi et al., 2000; Gutierrez et al., 2007). On the contrary little work has been devoted to the sintering, mechanical properties and clinical applications of TCP-Fap (Ben Ayed et al., 2007). So, the aim of this study is to prepare a biphasic calcium phosphates composites (tricalcium phosphate and fluorapatite) at various temperatures (between 1100°C and 1450°C) with different percentages of fluorine (0.5 wt %; 0.75 wt %; 1 wt %; 1.25 wt % and 1.5 wt % respectively, to the mass Fap percentage: 13.26 wt %; 19.9 wt %; 26.52 wt %; 33.16 wt % and 40 wt %). It also aims to characterize the resulting composites with density, mechanical resistance, infrared spectroscopy, X-ray diffraction, nuclear magnetic resonance ( $^{31}$ P) and scanning electron microscopy measurements.

## 2. Materials and methods

In this study the main used materials are commercial tricalcium phosphate (Fluka) and synthesized fluorapatite. The Fap powder was synthesized by the precipitation method (Ben Ayed et al., 2000). A calcium nitrate ( $\text{Ca}(\text{NO}_3)_2 \cdot 4\text{H}_2\text{O}$ , Merck) solution was slowly added to a boiling solution containing diammonium hydrogenophosphate ( $(\text{NH}_4)_2\text{HPO}_4$ , Merck) and ammonium fluorine ( $\text{NH}_4\text{F}$ , Merck), with continuous magnetic stirring. During the reaction, pH was adjusted to the same level (pH 8-9) by adding ammonia. The obtained precipitate was filtered and washed with deionised water; it was then dried at  $70^\circ\text{C}$  for 12h.

Estimated quantities of each powder ( $\beta$ -TCP and Fap) were milled with absolute ethanol and treated by ultra-sound machine for 15 min. The milled powder was dried at  $120^\circ\text{C}$  in a steam room to remove the ethanol and produce a finely divided powder. Powder mixtures were moulded in a metal mould and uniaxially pressed at 150 MPa to form cylindrical compacts with a diameter of 20 mm and a thickness of about 6 mm. The green bodies were sintered without any applied pressure or air at various temperatures (between  $1100^\circ\text{C}$  and  $1450^\circ\text{C}$ ). The heating rate was  $10^\circ\text{C min}^{-1}$ . The green compacts were sintered in a vertical resistance furnace (Pyrox 2408). The relative densities of the sintered bodies were calculated by the dimensions and weight. The relative error of densification value was about 1%.

The received powder was analyzed by using X-ray diffraction (XRD). The X-rays have used the Seifert XRD 3000 TT diffractometer. The X radiance was produced by using  $\text{CuK}_\alpha$  radiation ( $\lambda = 1.54056 \text{ \AA}$ ). The crystalline phases were identified from powder diffraction files (PDF) of the International Center for Diffraction Data (ICDD).

The samples were also submitted to infrared spectrometric analysis (Perkin-Elmer 783) using KBr.

Linear shrinkage was determined by dilatometry (Setaram TMA 92 dilatometer). The heating and cooling rates were  $10^\circ\text{C min}^{-1}$  and  $20^\circ\text{C min}^{-1}$ , respectively.

Differential thermal analysis (DTA) was carried out using about 30 mg of powder (DTA-TG, Setaram Model). The heating rate was  $10^\circ\text{C min}^{-1}$ .

The  $^{31}\text{P}$  magic angle spinning nuclear magnetic resonance ( $^{31}\text{P}$  MAS NMR) spectra were run on a Bruker 300WB spectrometer. The  $^{31}\text{P}$  observational frequency was 121.49 MHz with 3.0  $\mu\text{s}$  pulse duration, spin speed 8000 Hz and delay 5 s with 2048 scans.  $^{31}\text{P}$  shift is given in parts per million (ppm) referenced to 85 wt%  $\text{H}_3\text{PO}_4$ .

The microstructure of the sintered compacts was investigated by scanning electron microscope (Philips XL 30) on fractured sample surfaces. Because calcium phosphates are insulating biomaterial, the sample was coated with gold for more electronic conduction.

The particle size dimension of the powder was measured by means of Micromeritics Sedigraph 5000. The specific surface area (SSA) was measured by the BET method using azotes ( $\text{N}_2$ ) as an adsorption gas (ASAP 2010) (Brunauer et al., 1938). The main particle size ( $D_{\text{BET}}$ ) was calculated by assuming that the primary particles are spherical (Ben Ayed et al., 2001b):

$$D_{\text{BET}} = \frac{6}{s \cdot \rho} \quad (1)$$

Where  $\rho$  is the theoretical density of  $\beta$ -TCP ( $3.07 \text{ g.cm}^{-3}$ ) or Fap ( $3.19 \text{ g.cm}^{-3}$ ) and  $s$  is the SSA. The Brazilian test was officially considered by the International Society for Rock Mechanics (ISRM) as a method for determining the tensile strength of rock materials (ISRM, 1978). The Brazilian test was also standardised by the American Society for testing materials (ASTM) to

obtain the tensile strength of concrete materials (ASTM, 1984). The diametrical compression test also called the Brazilian disc test or the diametrical tensile test was considered a reliable and accurate method to determine the strength of brittle and low strength material.

An interesting parameter is the tensile strength,  $\sigma_r$ , which is the maximum nominal tensile stress value of the material. What is defined here is the horizontal tensile stress at the initiation of the large vertical crack at the centre of the disc. For the calculation of the tensile stress in the middle of the disc, Eq. (2) was used, corresponding to a plane stress condition. The usual way in evaluating the tensile strength from diametral compression test is by substituting the maximum load value into Eq. (2).

$$\sigma_r = \frac{P}{S} = \frac{2 \cdot P}{\pi \cdot D \cdot t} \quad (2)$$

where P is the maximum applied load, D diameter, t thickness of the disc and  $\sigma_r$  the tensile strength (or mechanical strength).

The essays were realized by means of a device by using "LLOYD EZ50" on cylindrical samples of 6 mm approximately of thickness and 20 mm of diameter. At least six specimens were tested for each test condition. An average of the values was then calculated. The results dispersal is in the order of 15 %.

### 3. Results and discussion

#### 3.1 Characterization of powder

Table 1 shows the SSA of  $\beta$ -TCP powder, Fap powder and different  $\beta$ -TCP - Fap composites, the average grain size  $D_{BET}$  (calculated by equation (1)) and the particle size distribution data (measured by granulometric repartition). The difference between the value deducted by SSA and by granulometric repartition was probably due to the presence of agglomerates in the initial powder. The SSA of different  $\beta$ -TCP - Fap composites increases with the percentages of Fap whereas the average grain size decreases (Table 1). This result shows the effect of Fap additive in tricalcium phosphate matrix. Indeed, the grain of Fap has a dense morphology by report  $\beta$ -TCP, which was responsible of the increasing of different composites SSA.

Compound	SSA (m <sup>2</sup> /g) ± 1.00	$D_{BET}$ (μm) ± 0.20	$D_{50}$ (μm) <sup>(a)</sup> ± 0.20	$d^b$
Fap	29.00	0.07	6	3.190
$\beta$ -TCP	0.70	2.80	5	3.070 ( $\beta$ ) 2.860 ( $\alpha$ )
$\beta$ -TCP - 13.26 wt% Fap composites	2.90	0.67	-	3.086
$\beta$ -TCP - 19.90 wt% Fap composites	3.32	0.58	-	3.094
$\beta$ -TCP - 26.52 wt% Fap composites	3.80	0.51	-	3.101
$\beta$ -TCP - 33.16 wt% Fap composites	4.37	0.44	-	3.110
$\beta$ -TCP - 40 wt% Fap composites	5.24	0.36	-	3.118

<sup>a</sup> : Mean diameter, <sup>b</sup> : theoretical density.

Table 1. SSA and average grain size obtained by different analysis of various compounds.

Fig. 1 shows the dilatometric measurements of a different powder used in this study ( $\beta$ -TCP, Fap and different  $\beta$ -TCP-Fap composites). The sintering temperatures began at about

1180°C, 1154°C, 1145°C, 1100°C, 1052°C, 1045°C and 775°C for  $\beta$ -TCP,  $\beta$ -TCP - 13.26 wt% Fap composites,  $\beta$ -TCP - 19.90 wt% Fap composites,  $\beta$ -TCP - 26.52 wt% Fap composites,  $\beta$ -TCP - 33.16 wt% Fap composites,  $\beta$ -TCP - 40 wt% Fap composites and Fap, respectively. The addition to Fap additive in the matrix of  $\beta$ -TCP decreasing the sintering temperature of the pure tricalcium phosphate (Fig. 1b-1f). Indeed, the sintering temperature of  $\beta$ -TCP decreases when the percentage of Fap increases.

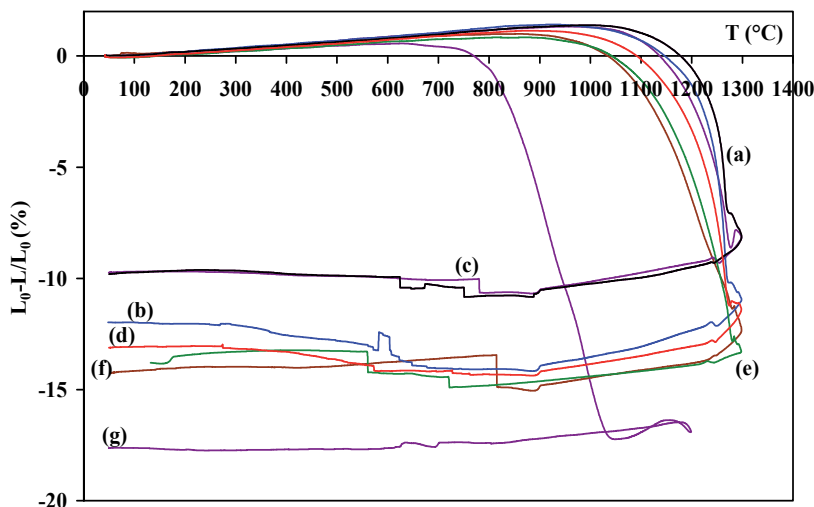
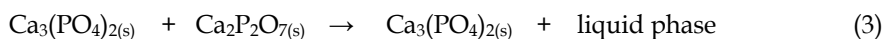


Fig. 1. Linear shrinkage versus temperature of: (a)  $\beta$ -TCP powder, (b)  $\beta$ -TCP - 13.26 wt% Fap composites, (c)  $\beta$ -TCP - 19.9 wt% Fap composites, (d)  $\beta$ -TCP - 26.52 wt% Fap composites, (e)  $\beta$ -TCP - 33.16 wt% Fap composites, (f)  $\beta$ -TCP - 40 wt% Fap composites, (g) Fap powder.

Differential thermal analysis studies detected out a potential phase change during the sintering of a different powder used in this study. Fig. 2a shows DTA curve of  $\beta$ -TCP. The DTA thermogramme shows 2 peaks relatives to the first and second endothermic allotropic transformation of  $\beta$ -TCP (1290°C and 1464°C). The last endothermic peak, at 1278°C, was related to a peritectic between  $\beta$ -TCP and pyrophosphate ( $\beta$ -Ca<sub>2</sub>P<sub>2</sub>O<sub>7</sub>). The chemical reaction was illustrated in the following:



This was similar to the result previously reported by Destainville and colleagues (Destainville et al., 2003).

Fig. 2b and Fig. 2g show the DTA curves of  $\beta$ -TCP - 13.26 wt% Fap composites and Fap powder, respectively. We notice one endothermic peak around 1180°C. This peak may be due to the formation of a liquid phase, formed from binary eutectic between CaF<sub>2</sub> and Fap (Ben Ayed et al., 2000). We can assume that fluorite (CaF<sub>2</sub>) was formed as a second phase during the powder preparation of Fap.

Fig. 2c, 2e and 2f illustrate the DTA curves of  $\beta$ -TCP - 19.9 wt% Fap composites,  $\beta$ -TCP - 33.16 wt% Fap composites and  $\beta$ -TCP - 40 wt% Fap composites, respectively. Fig. 2c and 2f are practically similar with the Fig. 2a. Indeed, DTA thermogramme of composites shows also 2 peaks of tricalcium phosphate allotropic transformations.

The DTA thermogramme of TCP - 26.52 wt% Fap composites shows 3 endothermic peaks at 1268°C, at 1280°C and at 1444°C, which are two peaks related with two allotropic transformations of tricalcium phosphate (Fig. 2d). The temperatures of allotropic transformations have been decreased about 10°C (1280°C in the place 1290°C) and 20°C (1444°C in the place 1464°C) with that of the pure  $\beta$ -TCP. This result has been explained probably by the Fap effect in  $\beta$ -CTCP matrix.

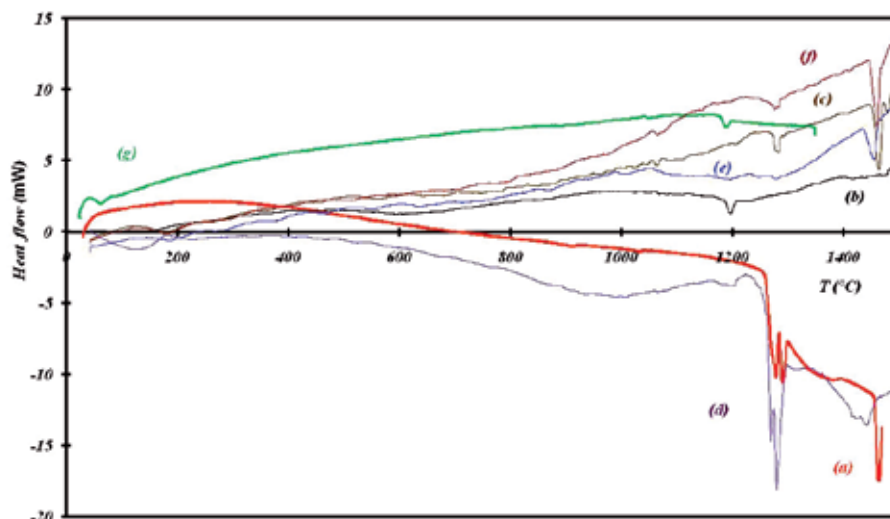


Fig. 2. DTA curves of: (a)  $\beta$ -TCP powder, (b)  $\beta$ -TCP - 13.26 wt% Fap composites, (c)  $\beta$ -TCP - 19.9 wt% Fap composites, (d)  $\beta$ -TCP - 26.52 wt% Fap composites, (e)  $\beta$ -TCP - 33.16 wt% Fap composites, (f)  $\beta$ -TCP - 40 wt% Fap composites, (g) Fap powder.

The DTA thermogrammes of  $\beta$ -TCP - 33.16 wt% Fap composites and  $\beta$ -TCP - 40 wt% Fap composites show only 2 endothermic peaks, which are relative to the allotropic transformations of tricalcium phosphate (Fig. 2e and 2f). In these curves, the endothermic peak relative to a peritectic between  $\beta$ -TCP and  $\beta$ -Ca<sub>2</sub>P<sub>2</sub>O<sub>7</sub> is practically disappeared. This chemical reaction between tricalcium phosphate and pyrophosphate was improved by the addition of 33.16 wt% or more Fap. Also, the temperatures of allotropic transformations decreased when the percentage of Fap increases (Fig. 2c-2f). This result has been explained probably by the Fap effect in  $\beta$ -TCP matrix.

### 3.2 Sintering and mechanical properties of tricalcium phosphate – fluorapatite composites

This Table 2 summarizes the mechanical strength of different  $\beta$ -TCP sintered at various temperatures (1100°C-1450°C) with different amounts of Fap (13.26 wt%, 19.9 wt%, 26.52 wt, 33.16 wt% and 40 wt%).

Fig. 3 illustrates the evolution of density and rupture strength of the composites sintered for 1h at various temperatures (between 1100°C and 1450°C) at different percentages of Fap (13.26 wt %; 19.9 wt %; 26.52 wt %; 33.16 wt % and 40 wt %). The densification and mechanical resistance varied as a function of Fap in the  $\beta$ -TCP matrix and sintering temperature.



wt% Fap	13.60	19.90	26.52	33.16	40.00
T (°C)	$\sigma_r$ (MPa)				
1100	0.25	1.68	2.00	2.53	0.23
1150	0.50	2.11	2.20	2.73	0.54
1200	0.90	2.55	3.00	3.01	0.85
1250	1.36	2.86	3.80	6.23	1.33
1300	2.31	3.41	6.00	8.74	1.80
1320	3.80	6.10	8.00	9.80	4.50
1350	6.00	6.45	9.20	13.20	10.10
1400	7.10	7.10	9.60	13.70	11.80
1450	3.60	5.33	8.00	5.70	6.20
Green	0.10	0.20	0.20	0.30	0.20

Table 2. Rupture strength versus temperature of different TCP-Fap composites.

Fig. 3A shows the relative density and mechanical resistance of  $\beta$ -TCP - 13.26 wt% Fap composites. The rupture strength and densification increase with sintering temperature. The optimum densification was obtained at 1350°C (87%). The maximum mechanical resistance reached 7.1MPa at 1400°C (Fig. 3A). This study shows that small additions of a Fap (13.26 wt %) can significantly enhance the sinterability and strength of  $\beta$ -TCP.

The evolution of  $\beta$ -TCP - 19.90 wt% Fap composites of densification and mechanical properties was practically similar to the  $\beta$ -TCP sintered with 13.26 wt% Fap (Fig. 3B). This curve illustrates a maximum densification at about 89% corresponding to the composites sintered at 1350°C. The mechanical resistance was similar to the  $\beta$ -TCP - 13.26 wt% Fap composites in value and sintering temperature (7.1 MPa at 1400°C).

Fig. 3C illustrates the evolution of the composites densification relative to the temperature between 1100°C and 1450°C. The densification was variable as a function of temperature. Between 1100°C and 1200°C, the samples relatives' densities were very small for any samples. An increase of density was shown between 1300°C and 1400°C, where the optimum densities are about 89.1 % at 1350°C. Fig. 3C shows the mechanical properties of the  $\beta$ -TCP - 26.52 wt% Fap composites samples according to the sintering temperature. Between 1100°C and 1250°C, the rupture strength of TCP - 26.52 wt% Fap composites samples was around 2-3 MPa. Above 1250°C, the rupture strength increases and reaches maximum value at 1400°C (9.6 MPa). Above 1400°C, the mechanicals properties of composites decrease during the sintering process. Indeed, the mechanical resistance of TCP - 26.52 wt % Fap composites reaches the 8 MPa at 1450°C. The evolution of mechanical properties of composites was considered a function of a sintering temperature. At 1350°C, the mechanical resistance optimum of  $\beta$ -TCP sintered without Fap additive reached 5.3 MPa (Bousslama et al., 2009), whereas the resistance increases to 9.4 MPa with 26.52 wt% Fap.

Fig. 3D shows the results of densification and mechanical properties of  $\beta$ -TCP - 33.16 wt% Fap composites. The ultimate densification was obtained at 1350°C (93.2%) and the maximum of mechanical resistance was approached at 1400°C (13.7 MPa). The  $\beta$ -TCP - Fap composites ratio was strongly dependent on the percentage Fap addition. The densification and mechanical properties remain low with 13.26 wt% Fap and 19.90 wt% Fap, when  $\beta$ -TCP sintered with 33.16 wt % Fap, the densification and mechanical resistance increase with the sintering temperature and reaches its maximum values.

With 40 wt % Fap, the densification and mechanical resistance decrease slowly with sintering temperature (Fig. 3E). The optimum relative density was obtained at 1350°C (92%) and the maximum mechanical resistance reached at 1400°C (11.8 MPa). As the amount of Fap increased (40 wt %), sinterability and mechanical properties considerably decreased. This result was clarified by the large (increase weight ratio) amounts of Fap used in the prepared composites. In fact the microstructure and thermal properties of Fap weren't stable at high temperature (after 1300°C) (Ben Ayed et al., 2000 and 2001b). Above 1400°C, the densification and the mechanical properties decrease with any  $\beta$ -TCP sintered with different percentages of Fap (Fig. 3).

Table 3 summarizes the optimum values of density and mechanical resistance of  $\beta$ -TCP sintered for 1h with different percentages of Fap. Whatever the content of Fap, the maximum of densification was obtained at 1350°C, whereas the optimum of rupture strength was reached at 1400°C (Table 3). The optimum values were obtained for  $\beta$ -TCP sintered with 33.16 wt% Fap (93.2% and 13.7 MPa).

wt % Fap	13.26	19.90	26.52	33.16	40
Optimum density (%)	87.87	89.00	89.10	93.20	92.62
Optimum strength (MPa)	7.1	7.1	9.6	13.7	11.8

Table 3. Optimum values of density (at 1350°C) and mechanical resistance (at 1400°C) of different  $\beta$ -TCP-Fap composites.

An increase of  $\beta$ -TCP- Fap density was shown between 1300°C and 1400°C, where the optimum densities were obtained at 1350°C with 33.16 wt % Fap. The used temperatures are similar to the densification of tricalcium phosphate when singly used (Ben Ayed et al., 2006a). But, the temperatures are relatively higher in comparison to those used for densification of only Fap (Ben Ayed et al., 2000, 2001b and 2006b). Indeed, Fap presents a good sinterability in the temperature ranging at 900°C-1100°C (Ben Ayed et al., 2000 and 2001b). At 1450°C, the densities decrease at different degrees of Fap additions. These results are similar to the previously reported by Ben Ayed et al. during the study of elaboration and characterization of calcium phosphate biomaterial (Ben Ayed et al., 2007).

This study shows the mechanical properties of the  $\beta$ -TCP-Fap composites samples according to the sintering temperature. At lower temperature (between 1100°C and 1200°C), the rupture strength of  $\beta$ -TCP-Fap composites was around 1 and 3 MPa (Fig. 3). When sintering temperature increase above 1200°C, the rupture strength increases slowly. These results are due to the increase of the densification caused by the growth of the grains size. Beyond 1300°C, the rupture strength increases and reaches maximum value at 1400°C. Between 1350°C and 1400°C, the increase in rupture strength was very clear for all samples with different weight ratio of Fap in the composites specimens. This is attributed to the influence and effect of Fap additive in relative densities and mechanical properties of the sintered composites. In fact, Ben Ayed et al. show that Fap has a good sinterability and mechanical

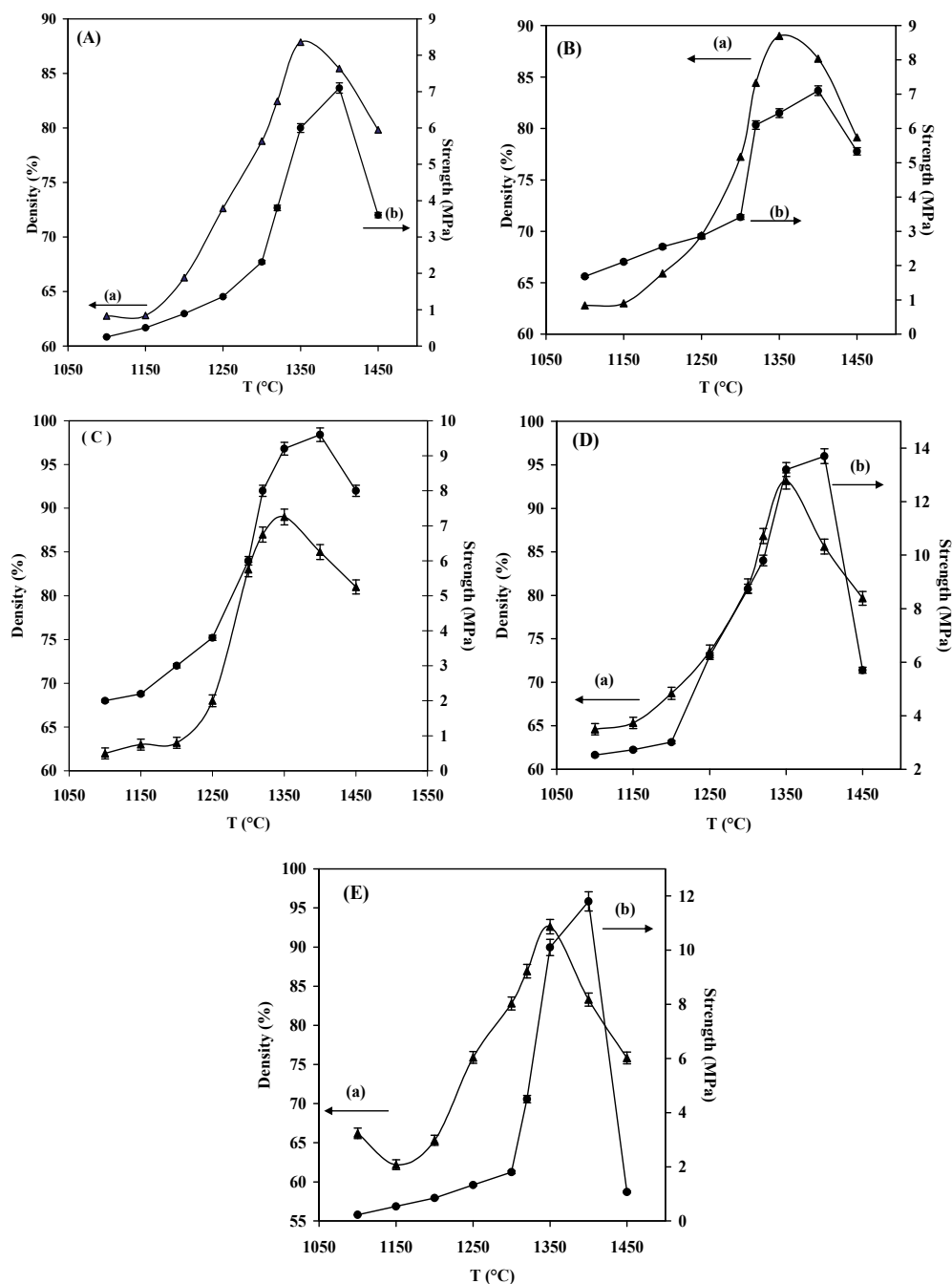


Fig. 3. Density and mechanical strength versus temperature of  $\beta$ -TCP sintered for one hour with different wt % of Fap: (A):  $\beta$ -TCP - 13.26 wt% Fap composites, (B)  $\beta$ -TCP - 19.90 wt% Fap composites, (C)  $\beta$ -TCP - 26.52 wt% Fap composites, (D)  $\beta$ -TCP - 33.16 wt% Fap composites, (E)  $\beta$ -TCP - 40 wt% Fap composites, ((a) : Density, (b): strength).

resistance (Ben Ayed et al., 2006b). It revealed that the mechanical resistance increases with temperature and reaches its maximum value about 14 MPa (Ben Ayed et al., 2006b).

The mechanical properties of the  $\beta$ -TCP and different TCP - Fap composites depend directly on the properties of the departure powder (granulometric, crystallinity of the powder, chemical composition, origin of powder) and on the operative conditions of the sintering process (temperature, heating time, cycle of sintering, atmosphere) (Ben Ayed et al., 2006b). Each of these parameters has a direct effect on the final properties of the composite.

Resorbable beta-tricalcium phosphate bioceramic is known for its excellent biocompatibility. However, it exhibits poor tensile strength. Here, we improved tensile strength of  $\beta$ -TCP bioceramic without altering its biocompatibility by introducing Fap additives, in different quantities (13.26 wt %; 19.9 wt %; 26.52 wt %; 33.16 wt % and 40 wt %). In this study, we showed that the presence of Fap with different amounts in  $\beta$ -TCP matrix improves the mechanical properties of  $\beta$ -TCP-Fap composites. This result was similar to the previous report by Bouslama et al. (Bouslama et al., 2009).

Table 4 displays several examples of dense calcium phosphates composites mechanical properties. The values found by mechanical strength were unequalled with the values in Table 4, because the authors have used different mechanical modes others than the Brazilian test. Indeed, many factors influence the mechanical properties such as: initial materials, the process conditions and annealing treatment. So, it is difficult to compare the results of this study with those found in literature.

Materials	$\sigma_r$ (MPa) <sup>a</sup>	$\sigma_f$ (MPa) <sup>b</sup>	$\sigma_c$ (MPa) <sup>c</sup>	$K_{IC}$ (GPa) <sup>d</sup>	References
Fap	14.00	-	-	4.5	Ben Ayed et al., 2006b
$\beta$ -CTCP	5.30	-	-	-	Bouslama et al., 2009
$\beta$ -TCP	-	92.00	-	-	Kalita et al., 2008
$\beta$ -TCP- Fap composites	9.60	-	-	-	Bouslama et al., 2009
brushite	-	-	32.00	-	Hofmann et al., 2009
Hap	-	-	5.35	3.52	Balcik et al., 2007
TCP-Hap composites (40/60)	-	-	4.89	3.10	Balcik et al., 2007
Hap- poly-L-lactic acid composites	-	-	100.00	6.00	Gay et al., 2009

<sup>a</sup> $\sigma_r$ : Mechanical strength (Brazilian test), <sup>b</sup> $\sigma_f$ : Flexural strength, <sup>c</sup> $\sigma_c$ : Compressive strength, <sup>d</sup> $K_{IC}$ :Young's modulus.

Table 4. Literature examples of dense calcium phosphates composites mechanical properties.

### 3.3 Characterization of sintered tricalcium phosphate - fluorapatite composites

After sintering, different techniques characterized the samples: X rays diffraction (XRD), <sup>31</sup>P MAS-NMR, scanning electronic microscopy (SEM) and infrared spectroscopy (IR).

Composites of  $\beta$ -TCP with Fap were pressureless sintered at temperatures from 1100 to 1450°C. The reactions and transformations of phases were monitored with X-ray diffraction.

The XRD patterns of the  $\beta$ -TCP were sintered at various temperatures (1100°C, 1300°C and 1400°C) with different percentages of Fap (13.26 wt % and 40 wt %) were shown in Fig. 4. These spectra are identical to the initial powder ( $\beta$ -TCP and Fap). We conclude that  $\beta$ -TCP and the Fap were steady during the sintering process. But when left at 1300°C, the thermogrammes indicate the germination of  $\alpha$ -TCP phase. This phase is a proof of the fragility of samples because the absolute densities of  $\beta$ -TCP and  $\alpha$ -TCP were different. Besides, the incorporation of Fap in tricalcium phosphate does not seem to be in its right decomposition. Indeed, the XRD revealed only phases of departure ( $\beta$ -TCP and Fap) and  $\alpha$ -TCP.

The Nuclear magnetic resonance chemical shift spectra of the  $^{31}\text{P}$  of the  $\beta$ -TCP as sintered at various temperatures (1100°C; 1300°C and 1400°C) with different percentages of Fap (13.26 wt %; 33.16 wt % and 40 wt %) are shown in Fig. 5. The  $^{31}\text{P}$  MAS-NMR solid spectra of composites show the presence of three tetrahedral environments of the phosphorus. Indeed, the  $^{31}\text{P}$  MAS - NMR analysis reveals the presence of three tetrahedral P sites for the  $\beta$ -TCP whereas the Fap possesses only one. This was similar to the result previously reported by (Yashima et al., 2003). They show that the phosphorus of tricalcium phosphate is located in three crystallographic sites: P(1)O<sub>4</sub>, P(2)O<sub>4</sub>, P(3)O<sub>4</sub> (Yashima et al., 2003). There is no record of any phase modification of the  $\beta$ -TCP or Fap, which confirms that the two powders,  $\beta$ -TCP and Fap were thermally steady between 1100°C and 1450°C.

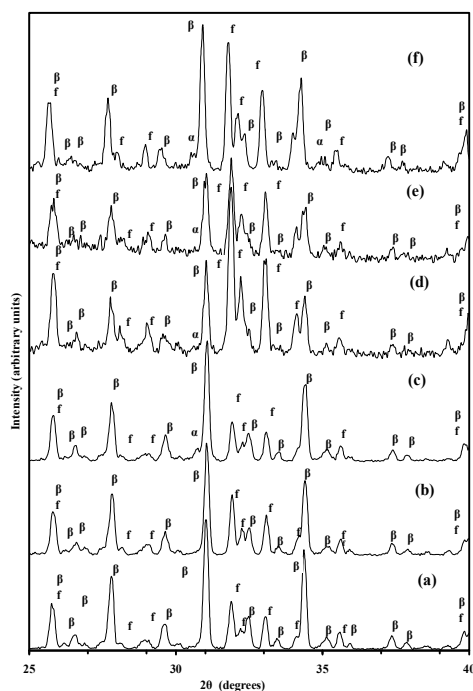


Fig. 4. XRD patterns of  $\beta$ -TCP-Fap composites sintered for one hour at various temperatures with different wt % of Fap: (a) 13.26 wt %, 1100°C; (b) 13.26 wt %, 1300°C; (c) 13.26 wt %, 1400°C; (d) 40 wt %, 1100°C; (e) 40 wt %, 1300°C and (f) 40 wt %, 1400°C ( $\beta$  :  $\beta$ -TCP; f : Fap;  $\alpha$  :  $\alpha$ -TCP).

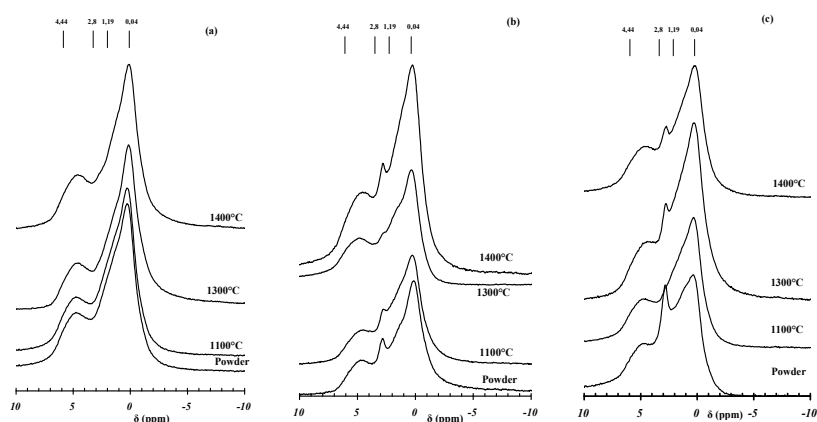
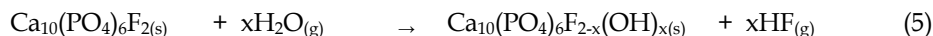


Fig. 5.  $^{31}\text{P}$  NMR spectra of  $\beta$ -TCP-Fap composites sintered for one hour at various temperatures with different wt % of Fap : (a) 13.26 wt %; (b) 33.16 wt % and (c) 40 wt % ( $\beta$  :  $\beta$ -TCP; f: Fap).

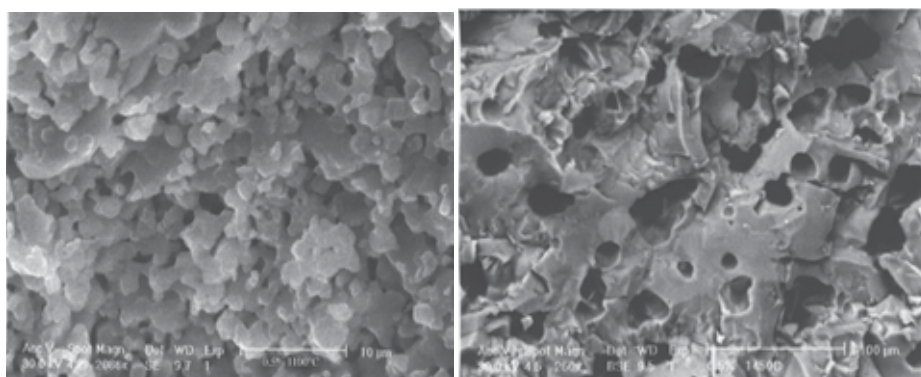
Fig. 6 and Fig. 7 show the SEM micrographs of  $\beta$ -TCP-Fap composites. This technique helps to investigate the texture and porosity of the biphasic bioceramic. The fracture surfaces clearly show the composite as sintered at various temperatures (1100°C, 1300°C, 1400°C and 1450°C) with different percentages of Fap (13.26 wt %; 19.9 wt %; 33.16 wt % and 40 wt %) revealing the influence of the temperature of microstructural developments during the sintering process (Fig. 6). These effects increased along the sintering temperature and the percentage of Fap.

The results of microstructural investigations of  $\beta$ -TCP-Fap composites sintered at various temperatures (1100°C and 1450°C) with 13.26 wt % Fap are shown in Fig. 6a and b. At 1100°C, the sample presents an important intergranular porosity (Fig. 6a). At higher temperatures (1450°C), the densification was hindered by the formation of large pores (Fig. 6b). During the sintering of Fap and TCP-Fap composites, Ben Ayed et al. also observed the formation of large pores at these temperatures (Ben Ayed et al., 2001b). They are attributed to the hydrolysis of Fap and  $\text{CaF}_2$ , as expressed by the following equation:



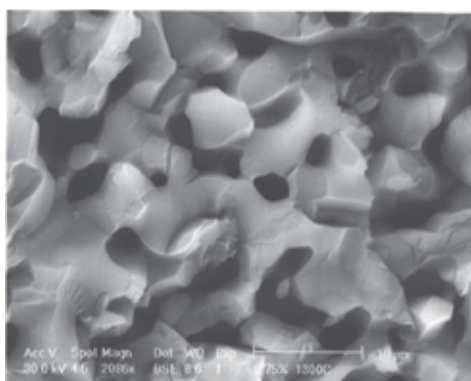
The increase of percentages of Fap from 13.26 wt % to 19.9 wt % did not show a significant change of the microstructure. When temperature increases, the microstructure of  $\beta$ -TCP-Fap composites was sintered at 1300°C with different percentages of Fap (19.90 wt %; and 33.16 wt %) reveals moderate grain growth (Fig. 6c and d). Indeed, we notice a partial reduction of the porosity and a presence of some closed pores (Fig. 6c and d).

At 1400°C, the microstructural analysis of  $\beta$ -TCP- 40 wt% Fap composites reveals the creation of a liquid phase (Fig. 6e). The outstanding modification on the microstructure of  $\beta$ -TCP-Fap composites takes place only due to the presence of a liquid phase that can occur by the increase of the sintering temperature or by an increase of the Fap content (Fig. 6e). At this temperature (1400°C), the fragility and the decrease of relative densities and mechanical properties were originated from the micro-crack formed by small expansion of the phase transformation samples due to the low density of  $\alpha$ -TCP (2.86 g/cm<sup>3</sup>) than that of  $\beta$ -TCP (3.07 g/cm<sup>3</sup>) (Fig. 6e). But also from the allotropic transformation from  $\beta$  to  $\alpha$  and from  $\alpha$  to  $\alpha'$ .

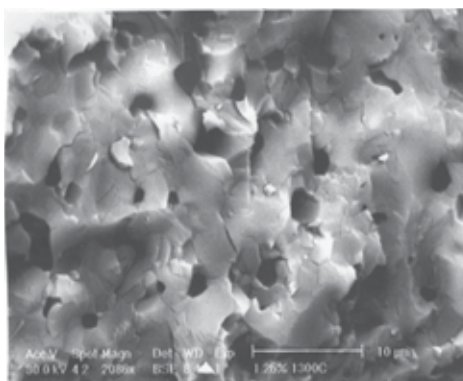


(a) \_\_\_\_\_ 10 $\mu$ m

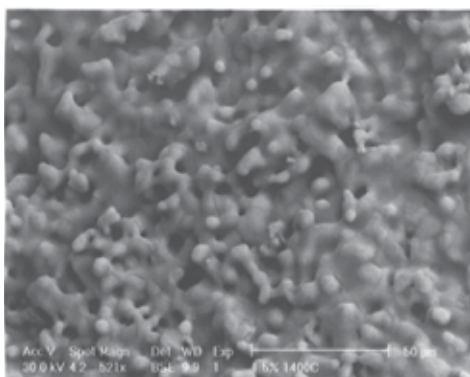
(b) \_\_\_\_\_ 100 $\mu$ m



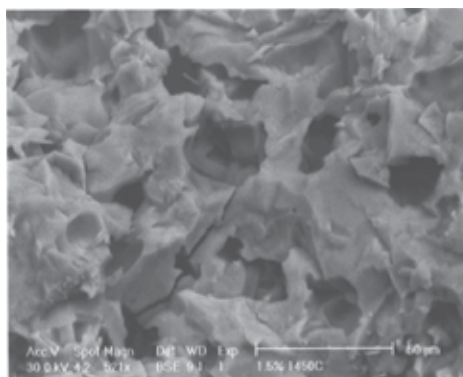
(c) \_\_\_\_\_ 10 $\mu$ m



(d) \_\_\_\_\_ 10 $\mu$ m



(e) \_\_\_\_\_ 50 $\mu$ m



(f) \_\_\_\_\_ 50 $\mu$ m

Fig. 6. SEM micrograph (fracture) of  $\beta$ -TCP-Fap composites sintered for one hour at various temperatures with different wt % of Fap: (a) 13.26 wt %, 1100°C; (b) 13.26 wt %, 1450°C; (c) 19.9 wt %, 1300°C; (d) 33.16 wt %, 1300°C; (e) 40 wt %, 1400°C and (f) 40 wt %, 1450°C.

Above 1400°C, the microstructure of  $\beta$ -TCP sintered at 1450°C with different percentages of Fap (13.26 wt % and 40 wt %) was totally modified (Fig. 6b and f). In fact, we observe two

types of microstructures; the first was characterized by the creation of large pores engendering the reaction of hydrolysis of Fap and the second was characterized by the exaggerated coarsening of grains (Fig. 6b and f). The microstructural analysis of the composite shows a larger amount of pores, preferentially located on the grain boundaries. In Fig. 7, the fracture surfaces show clearly the  $\beta$ -TCP-26.52 wt% Fap composite as sintered for 1 h at various temperatures (1300, 1350, 1400 and 1450°C) revealing the influence of the temperature of microstructural developments during the sintering process. These effects increased along the sintering temperature. The results of microstructural investigations of  $\beta$ -TCP-26.52 wt% Fap composites show that the morphology of the samples was completely transformed (Fig. 7a-d).

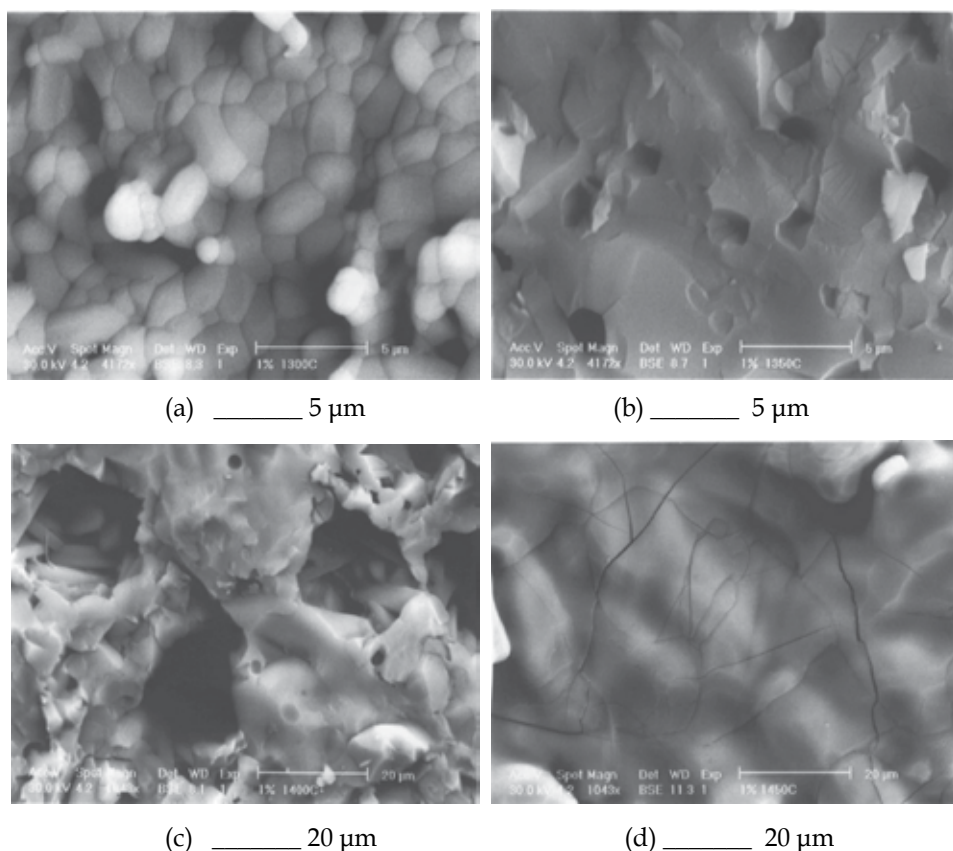


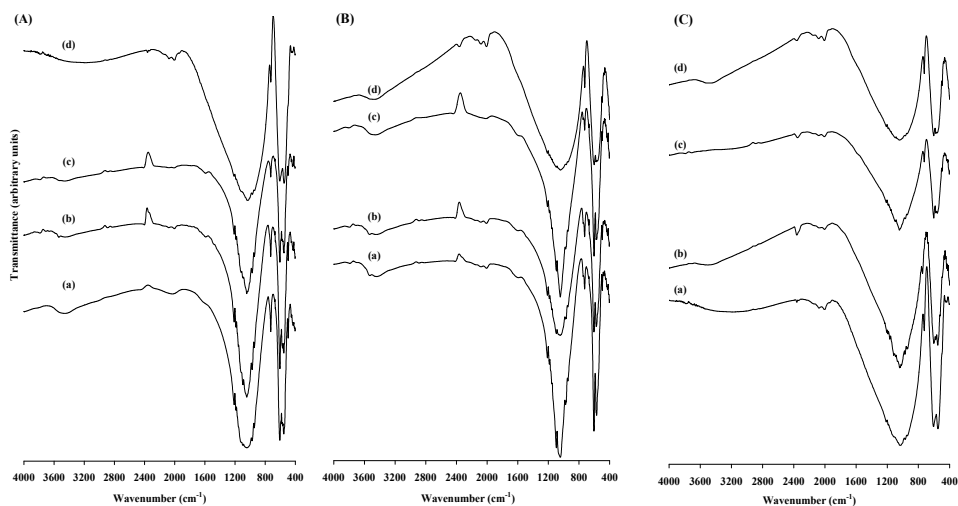
Fig. 7. SEM micrograph of  $\beta$ -TCP - 26.52 wt% Fap composites sintered for 1h at: (a) 1300°C, (b) 1350°C, (c) 1400°C, (d) 1450°C.

At 1300°C, the SEM micrographs of samples show liquid phase relative to the binary peritectic between pyrophosphate with the tricalcium phosphate (Fig. 7a). At 1350°C, one notices a partial reduction of the porosity (Fig. 7b). At higher temperatures (1400-1450°C), the densification was hindered by the formation of both large pores and many cracks (Fig. 7c and d).

Fig. 8A-8B show typical IR spectra of  $\beta$ -TCP sintered for one hour at various temperatures (1100°C, 1200°C, 1300°C and 1400°C) with 13.26 wt% and 40 wt% Fap, respectively. Most



bands were characteristic of phosphate group of  $\beta$ -TCP and Fap (at 540-600  $\text{cm}^{-1}$  and 920-1120  $\text{cm}^{-1}$ ). The peaks at 920  $\text{cm}^{-1}$  and 1120  $\text{cm}^{-1}$  are assigned to the stretching vibration of  $\text{PO}_4^{3-}$  ions and the peaks at 540  $\text{cm}^{-1}$  and 600  $\text{cm}^{-1}$  are assigned to the deformation vibration of  $\text{PO}_4^{3-}$  ions. The bands at 3500  $\text{cm}^{-1}$  and at 1640  $\text{cm}^{-1}$  were assigned to the adsorbed water molecule.



(A) with 13.26 wt% Fap at various temperatures: (a) 1100°C, (b) 1200°C, (c) 1300°C and (d) 1400°C.  
(B) with 40 wt% Fap at various temperatures: (a) 1100°C, (b) 1200°C, (c) 1300°C and (d) 1400°C.  
(C) at 1400°C with different percentages of Fap: (a) 13.26 wt %; (b) 19.9 wt %; (c) 33.16 wt % and (d) 40 wt %.

Fig. 8. IR of  $\beta$ -TCP sintered for one hour

Figs. 8A(a-b), 8B(a-b) show the IR spectra of the  $\beta$ -TCP-Fap composites sintered at 1100°C and 1200°C, respectively. In the spectra absorptions assigned to OH group, are detected at 3510  $\text{cm}^{-1}$  and 747  $\text{cm}^{-1}$ . Those absorptions indicate that the OH group substitutes F in the Fap structure, thus leading to the formation of hydroxyfluorapatite ( $\text{Ca}_{10}(\text{PO}_4)_6\text{F}_{2-x}(\text{OH})_x$ : FOHap). This compound may be the result of the reaction between Fap and water vapour traces (Ben Ayed et al., 2001b). This reaction was illustrated by Eq. 5. At higher temperature (1300°C-1400°C), the intensity of these bands decreases but does not completely vanish supposing that the amount of fluoride in the samples decreases when the temperature increases (Figs. 8A(c-d), 8B(c-d)). IR spectra of different composites sintered at 1400°C with different percentages of Fap (13.26 wt %; 19.9 wt %; 33.16 wt % and 40 wt %) were practically similar to the Figs. 8A-8B. Indeed, the typical IR spectra show the characteristics of the phosphate group of calcium phosphates (at 500-600  $\text{cm}^{-1}$ , 1019  $\text{cm}^{-1}$ , 1034  $\text{cm}^{-1}$ , 1105  $\text{cm}^{-1}$ ).

At higher temperatures, the  $\beta$ -TCP-Fap composites densification and mechanical properties were hindered by the exaggerated grain growth, the effect of the allotropic transformation of  $\beta$ -TCP and the formation of intragranular porosity. The SEM micrograph illustrated the change of microstructure at 1450°C. These results are similar to the previously obtained by Ben Ayed et al. during the sintering process of TCP-Fap composites (Ben Ayed et al., 2007).

The preliminary results obtained in this study have shown that the  $\beta$ -TCP-Fap composites have a potential of further development into an alternative system to produce denser  $\beta$ -TCP bodies. Further investigations are still under way to investigate the influence of Fap on the density, microstructure and mechanical properties of  $\beta$ -TCP-Fap biomaterials.

#### 4. Conclusion

Tricalcium phosphate and fluorapatite powder were mixed in order to elaborate biphasic composites. The influence of Fap substitution on the  $\beta$ -TCP matrix was detected in the mechanical properties of the sintered composites. The characterization of samples was investigated by using X-Ray diffraction, differential thermal analysis, scanning electronic microscopy and by an analysis using  $^{31}\text{P}$  nuclear magnetic resonance. The sintering of tricalcium phosphate with different percentages of fluorapatite indicates the evolution of the microstructure, densification and mechanical properties. The Brazilian test was used to measure the rupture strength of biphasic composites biomaterials. The mechanical properties increase with the sintered temperature and with fluorapatite additive. The mechanical resistance of  $\beta$  tricalcium phosphate - 33.16 wt % fluorapatite composites reached its maximum value (13.7MPa) at 1400°C, whereas the optimum densification was obtained at 1350°C (93.2%). Above 1400°C, the densification and mechanical properties were hindered by the tricalcium phosphate allotropic transformation and the formation of both intragranular porosity and cracks.

#### 5. Acknowledgment

The author thanks the Professor Bouaziz Jamel and Doctor Bouslama Nadhem for their assistances in this work.

#### 6. References

- Aryee, S., Imhoff, A. B., Rose, T., Tischer, T., 2008. *Biomaterials*, 29, 3497-3502.
- Agneskirchner, J.D., Freiling, D., Hurschler, C., Lobenhoffer, P., 2006. *Knee Surg. Sports Traumatol Arthrosc*, 14, 291-300.
- ASTM C496, *Standard test method for splitting tensile strength of cylindrical concrete specimens Annual Book of ASTM, Standards*, vol. 0.042, ASTM, Philadelphia, 1984, p. 336.
- Brouwer, R.W., Bierma-Zeinstra, S.M., van Raaij, T.M., Verhaar, J.A., 2006. *J. Bone Joint. Br.*, 454-9.
- Bauer, T.W., Muschler, G.F., Bone graft materials. An overview of the basic science, 2000. *Clin. Orthop. Relat. Res.*, 10-27.
- Balcik, C., Tokdemir, T., Senkoylo, A., Koc, N., Timucin, M., Akin, S., Korkusuz, P., Korkusuz, F., 2007. *Acta Biomaterialia*, 3, 985-996.
- Ben Ayed, F., Bouaziz, J., Bouzouita, K., 2000. *J. Eur. Ceram. Soc.* 20 (8), 1069.
- Ben Ayed, F., Bouaziz, J., Khattech, I., Bouzouita, K., 2001a. *Ann. Chim. Sci. Mater.* 26 (6), 75.
- Ben Ayed, F., Bouaziz, J., Bouzouita, K., 2001b. *J. Alloys Compd.* 322 (1-2), 238.
- Ben Ayed, F., Chaari, K., Bouaziz, J., Bouzouita, K., 2006a. *C. R. Physique* 7 (7), 825.
- Ben Ayed, F., Bouaziz, J., Bouzouita, K., 2006b. *Ann. Chim. Sci. Mater.* 31 (4), 393.

- Ben Ayed, F., Bouaziz, J., 2007. *C. R. Physique* 8 (1), 101-108.
- Ben Ayed, F., Bouaziz, J., 2008a. *Ceramics Int.* 34 (8), 1885-1892.
- Ben Ayed, F., Bouaziz, J. 2008b. *J. Eur. Ceram. Soc.* 28 (10), 1995-2002.
- Brunauer, S., Emmet, P. H., Teller, J., 1938. *Amer. Chem. Soc. J.* 60, 310.
- Bousslama, N., Ben Ayed F., Bouaziz, J., 2009. *Ceramics Int.* 35, 1909-1917.
- Chaari, K., Ben Ayed F., Bouaziz, J., Bouzouita, K., 2009. *Materials Chemistry and Physics*, 113, 219-226.
- Destainville, A., Champion E., Bernache - Assolant, D., 2003. *Mater. Chem. Phys.* 80, 69.
- De Long, Jr. W.G., Einhorn, T.A., Koval, K., McKee, M., Smith, W., Sanders, R., 2007. *J. Bone Joint. Am.*, 89, 49-58.
- DeSilva, G.L., Fritzler, A., DeSilva, S.P., 2007. *Tech. Hand Up Extrem Surg.*, 11,163-7.
- Elliott, J. C., 1994. *Structure and Chemistry of the Apatite and Other Calcium Orthophosphates*, Elsevier Science B.V., Amsterdam.
- Fellah, B.H., Gauthier, O., Weiss, P., Chappard, D., Layrolle, P., 2008. *Biomaterials*, 29, 1177-88.
- Gaasbeek, R.D., Toonen, H.G., van Heerwaarden, R.J., Buma, P., 2005. *Biomaterials*, 26, 6713-9.
- Gutierrez, M., Dias, A.G., Lopes, M.A., Hussain, N.S., Cabral, A.T., Almeida, L., 2007. *J. Mater. Sci. Mater. Med.*, 18, 2377-82.
- García-Leiva, M.C., Ocaña, I., Martín-Meizoso, A., Martínez-Esnaola, J.M., 2002. *Engineering Fracture Mechanics* 69, 1007-1013.
- Gay, S., Arostegui, S., Lemaitre, J., 2008. *Materials Science and Engineering C*, in press.
- Hench, L. L., 1991. *J. Am. Ceram. Soc.* 74 (7), 1487.
- Hofmann, M.P., Mohammed, A.R., Perrie, Y., Gbureck, U., Barralet, J.E., 2009. *Acta Biomaterialia*, 5, 43-49.
- Hernigou, P., Ma, W., 2001. *Knee*, 8, 103-10.
- Hoell, S., Suttmoeller, J., Stoll, V., Fuchs, S., Gosheger, G., 2005. *Arch. Trauma Surg.*, 125, 638-43.
- ISRM. Suggested methods for determining tensile strength of rock materials, *Int. J. Rock Mech. Min. Sci. Geomech. Abstr.* 1978. 15, 99.
- Jensen, S.S., Broggini, N., Hjorting-Hansen, E., Schenk, R., Buser, D. 2006. *Clin. Oral. Implants Res.*, 17, 237-43.
- Kalita, S.J., Fleming, R., Bhatt, H., Schanen, B., Chakrabarti, R., 2008. *Materials Science and Engineering C*, 28, 392 - 398.
- Landi, E., Tampieri, A., Celotti, G., Sprio, S., 2000. *J. Eur. Ceram. Soc.* 20, 2377.
- Legeros, R. Z., 1993. *Clinical Materials* 14, 65.
- Okuda, T., Ioku, K., Yonezawa, I., Minagi, H., Kawachi, G., Gonda, Y., 2007. *Biomaterials*, 28, 2612-21.
- Steffen, T., Stoll, T., Arvinte, T., Schenk, R.K., 2001. *Eur. Spine J.*, 10 (Suppl 2), 132-40.
- Schilling, A.F., Linhart, W., Filke, S., Gebauer, M., Schinke, T., Rueger, J.M., 2004. *Biomaterials*, 25, 3963-72.
- Uwe, P., Angela, E., Christian, R., 1993. *Mater. J. Sci.: Mate In Medicine* 4, 292.
- Varma, H. K., Sureshabu, S. 2001. *Materials letters* 49, 83.

Wang, C. X., Zhou, X., Wang, M. 2004. *Materials Characterization* 52, 301.

Yashima, M., Sakai, A. , Kamiyama, T., Hoshikawa, A., 2003. *J. Solid State Chemistry* 175, 272.

# Fracture Mechanisms of Biodegradable PLA and PLA/PCL Blends

Mitsugu Todo<sup>1</sup> and Tetsuo Takayama<sup>2</sup>

<sup>1</sup>*Research Institute for Applied Mechanics, Kyushu University*

<sup>2</sup>*Graduate School of Science and Engineering, Yamagata University  
Japan*

## 1. Introduction

Poly (lactic acid) (PLA), made from natural resources such as starch of plants, is one of typical biodegradable thermoplastic polymers and has extensively been used in medical fields such as orthopedics, neurosurgery and oral surgery as bone fixation devices mainly due to biocompatibility and bioabsorbability (Higashi et al., 1986; Ikada et al., 1996; Middleton & Tipton, 2000; Mohanty, 2000). Its importance has led to many studies on its mechanical properties and fracture behavior which found that the mode I fracture behavior of PLA is relatively brittle in nature (Todo et al., 2002; Park et al., 2004, 2005, 2006). Therefore, blending with a ductile biodegradable and bioabsorbable polymer such as poly ( $\epsilon$ -caprolacton) (PCL) has been adopted to improve the fracture energy of brittle PLA (Broz et al., 2003; Dell'Erba et al., 2001; Chen et al., 2003; Todo et al., 2007; Tsuji & Ikada, 1996, 1998; Tsuji & Ishizuka, 2001; Tsuji et al., 2003); however, it was also found that phase separation originated by immiscibility of PLA and PCL tends to degrade the mechanical properties of PLA/PCL blends (Todo et al., 2007). It has recently been found that such phase separation can dramatically be improved by using an isocyanate group, lysine tri-isocyanate (LTI) (Takayama et al., 2006; Takayama & Todo, 2006; Harada et al., 2007, 2008), and the fracture properties of PLA/PCL/LTI are much higher than those of PLA/PCL.

In this chapter, firstly the fracture behavior and micromechanism of pure PLA are summarized (Park et al., 2004, 2005, 2006; Todo et al., 2002). Effects of crystallization behavior and loading-rate on the mode I fracture behavior are discussed. Effect of unidirectional drawing on the fracture energy is also presented as one of the effective ways to improve the brittleness of PLA (Todo, 2007). Secondly, the fracture behavior of PLA/PCL blends is discussed on the basis of the relationship between the microstructure and the fracture property (Todo et al., 2007b). In the third section, improvement of microstructural morphology of PLA/PCL by using LTI is discussed (Takayama et al., 2006; Takayama & Todo, 2006; Todo & Takayama, 2007; Todo et al., 2007a). It has been found that addition of LTI effectively improves the phase morphology of PLA/PCL, resulting in dramatic improvement of fracture energy. Effects of annealing on the mechanical properties of PLA/PCL/LTI blend are discussed in the last section (Takayama et al., 2011). It has been found that a thermal annealing process can effectively improve the mechanical properties of the polymer blend, as a result of strengthened structures due to crystallization of PLA.

## 2. Fracture behavior of PLA

### 2.1 Effect of crystallization

The microstructure of crystalline PLA can be changed through annealing process from amorphous to highly crystallized states as shown in Fig.1. 70°C-3h indicates an annealing process that the specimens are kept in an oven at 70°C for three hours.

The annealing process of 70°C-3h results in an amorphous state, on the contrary, the 100°C-3h and 100°C-24h processes create highly crystallized states and longer annealing time tends to increase the size of crystals.

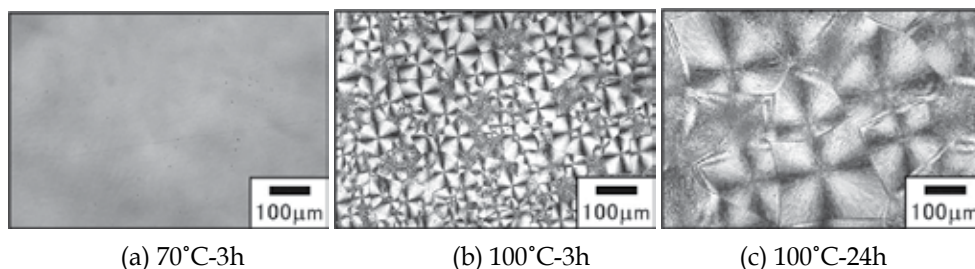


Fig. 1. Polarized micrographs of microstructures of PLA.

It has been found that such microstructure dramatically affects the fracture behavior of PLA. As an example, the critical energy release rate,  $G_{IC}$ , measured at a quasi-static rate, 1 mm/min, and an impact rate, 1 m/s, of loading is shown in Fig.2. as a function of crystallinity. At the quasi-static rate,  $G_{IC}$  slightly decreases with increase of crystallinity up to 48.3%, and kept constant up to 48.3%. Above 48.3%,  $G_{IC}$  rapidly decrease. On the other hand, at the impact rate,  $G_{IC}$  tends to increase with increase of crystallinity. As a result, the static  $G_{IC}$  is greater than the impact value up to 48.3%, and above 48.3%, on the contrary, the impact value becomes higher than the static value. This result suggests that the fracture mechanism at the static rate is different from that at the impact rate.

Fig. 3 shows polarized microphotographs of arrested cracks in the PLA specimens prepared under different annealing conditions, and tested under static and impact loading rates. For the amorphous specimen with the crystallinity,  $X_c=2.7\%$ , under the static loading-rate (Fig.3(a)), extensive multiple crazes were generated in the crack-tip region, while only a few crazes were observed under the impact loading-rate (Fig.3(b)). This kind of craze formation in crack-tip region is usually observed in amorphous polymers such as polystyrene in which craze formation is dominant rather than shear plastic deformation (Botsis, 1987). Disappearance of multiple craze formation observed at the impact rate corresponds to the reduction of additional energy dissipation in the crack-tip region compared to the static case where multiple crazes are formed, and therefore results in the decrease of  $G_{IC}$  as shown in Fig.2. On the contrary, for the highly crystallized specimen with  $X_c=55.8\%$  tested at the static rate (Fig.3(c)), a straight single crack without craze formation in the surroundings is observed. This type of crack growth usually corresponds to brittle fracture and lower  $G_{IC}$  than the amorphous dominant samples in which crazes are generated in crack-tip region. At the impact rate (Fig.3(d)), the main crack tends to be distorted and branched. These behaviors may be related to the increase of  $G_{IC}$  at the impact rate, although the detail of the mechanism is still unclear, and further study will be performed to elucidate such mechanism.

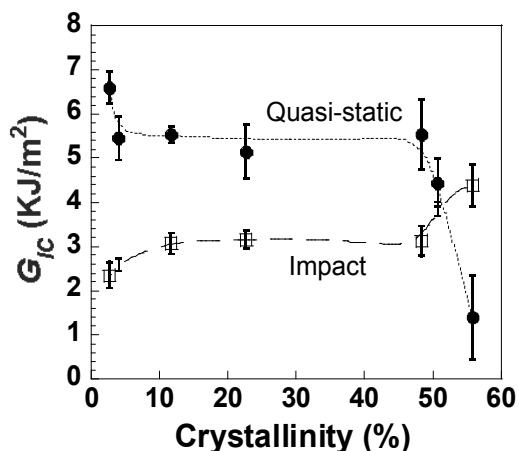


Fig. 2. Dependence of crystallinity on the critical energy release rate under a quasi-static and an impact loading conditions.

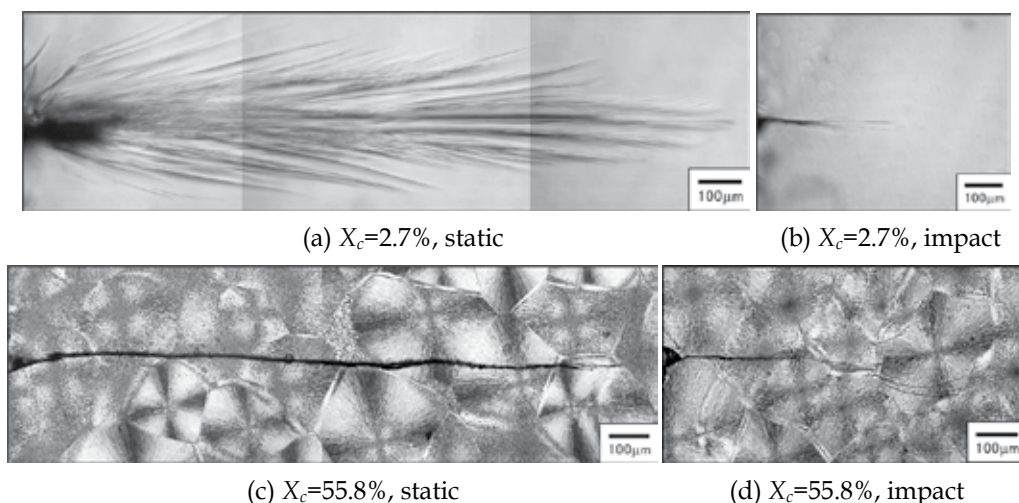


Fig. 3. Polarized micrographs of crack growth behavior.

Fig.4 shows FE-SEM micrographs of the fracture surfaces of the PLA samples. For the amorphous sample tested at the static rate, the fracture surface exhibits deep concavities and hackles due to multiple craze formation (Fig.4(a)). The fracture surfaces of the crystallized samples (Fig.4(c)) appears to be smoother than the amorphous one, corresponding to the decrease of the toughness values. The impact fracture surface of the amorphous sample (Fig.4(b)) is obviously smoother than the static one, corresponding to the decrease of  $G_{IC}$ . It is noted that drawing fibrils are also observed on the impact fracture surface, suggesting that effect of high strain-rate exists. Roughness of the impact fracture surface appears to increase with increase of crystallinity comparing the surfaces shown in Figs.4(b) and (d). For the impact surface of the highly crystallized sample (Fig.4(d)), relatively fine roughness exists suggesting the increase of  $G_{IC}$  as crystallinity increases.

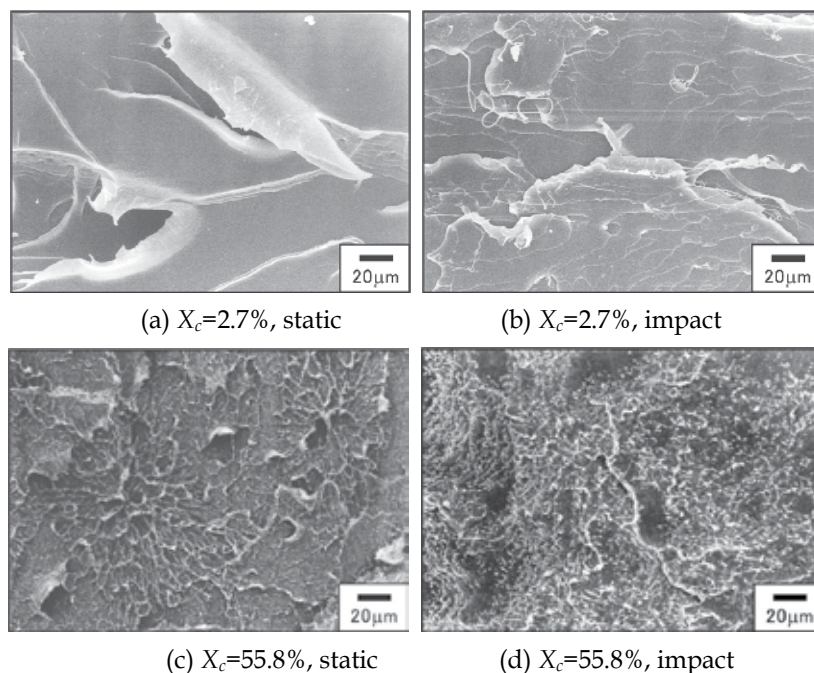


Fig. 4. FE-SEM micrographs of fracture surfaces.

## 2.2 Effect of unidirectional drawing process

Drawing process is known to be an effective way to improve the mechanical properties of thermoplastics, and effects of drawing on tensile and fracture properties of thermoplastics such as polypropylene (Mohanraj et al., 2003a, 2003b; Uehara et al., 1996), poly(acrylonitrile) (Sawai et al., 1999; Yamane et al., 1997) and PLA (Todo, 2007) have been studied. PLA is usually draw-processed when it is used for bone fixation devices, and therefore, fundamental effect of drawing on its fracture behavior needs to be characterized. As an example, dependence of draw ratio on the critical  $J$ -integral at crack initiation,  $J_{in}$ , is shown in Fig.5. In the fracture specimens, the initial notches were introduced in the direction perpendicular or parallel to the drawing direction. Therefore, the two different types of specimens are denoted as 'perpendicular' and 'parallel'. For the parallel,  $J_{in}$  decreased with increase of draw ratio, and  $J_{in}$  for draw ratio of 2.5 became about one fifth of the original. On the contrary, for the perpendicular,  $J_{in}$  increased as draw ratio increased, and  $J_{in}$  for draw ratio of 2.5 became five times greater than that of the original. Thus, greater energy is needed for crack propagation in the perpendicular than in the parallel. This is easily understood by considering the effect of drawing on the micromechanism of fracture. In draw-processed polymer, molecules are reoriented in the drawing direction. Therefore, energy dissipation during crack growth by elongation and scission of such oriented molecules is much greater in the perpendicular direction than in the parallel direction where such elongation and scission processes obviously decrease.

FE-SEM micrographs of fracture surfaces are shown in Fig. 6. The perpendicular with draw ratio 2.5 exhibited rougher surface with ductile deformation than the original (without drawing). It is interesting to note that crevices existed on the fracture surfaces that were thought to be cracks transversely propagated between the parallel fibrils reoriented in the



drawing direction. It is thus thought that the ductile deformation due to elongation of the oriented molecules and the transverse crack formation are primary mechanisms of toughening in draw-processed PLA. On the other hand, the fracture surface of the parallel were much smoother than that of the original, corresponding to the lower  $J_{in}$  value.  $J_{in}$  is contributed by energy dissipation through not only creation of fracture surface but also development of process zone. Polarized micrographs of notch-tip regions of the original and the perpendicular are shown in Fig.7. In the original, multiple crazes forming a fan shape were observed. They were initiated from the initial notch-tip and propagated almost perpendicularly to the tensile direction. For the perpendicular with draw ratio 2.5, crazes were much denser and the width of the damage region was much wider than the original. Transverse cracks generated in the drawing direction are observed, and these obviously correspond to the crevices observed on the fracture surfaces as shown in Fig.6(b). Larger damage region consisting of crazes and transverse cracks generated in crack-tip region indicates larger energy dissipation under crack initiation and propagation processes, and therefore, greater  $J_{in}$ .

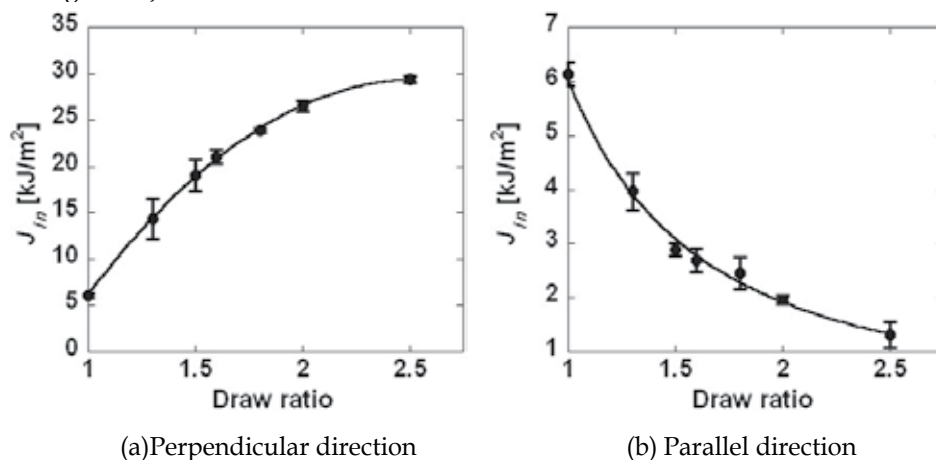


Fig. 5. Dependence of draw ratio on the critical  $J$ -integral at crack initiation.

In summary, it was shown that the crystallization behavior greatly affects the fracture behavior of PLA. Microstructure of PLA can easily be changed through annealing process by changing temperature and heating time. The static fracture energy tends to decrease as crystallinity increases, while the impact fracture energy increases.

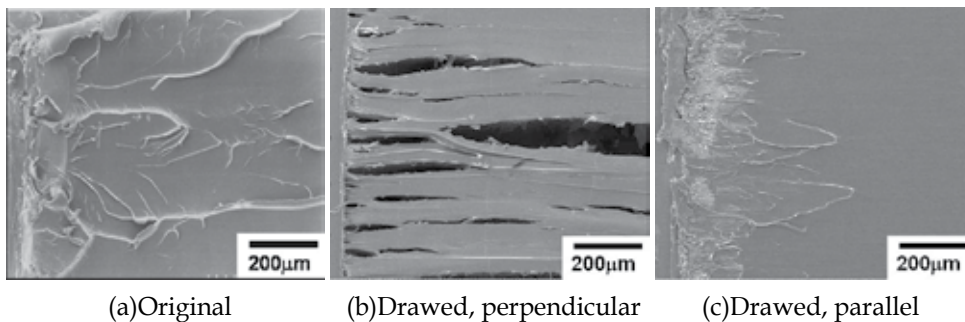


Fig. 6. FE-SEM micrographs of fracture surfaces (draw ratio=2.5).

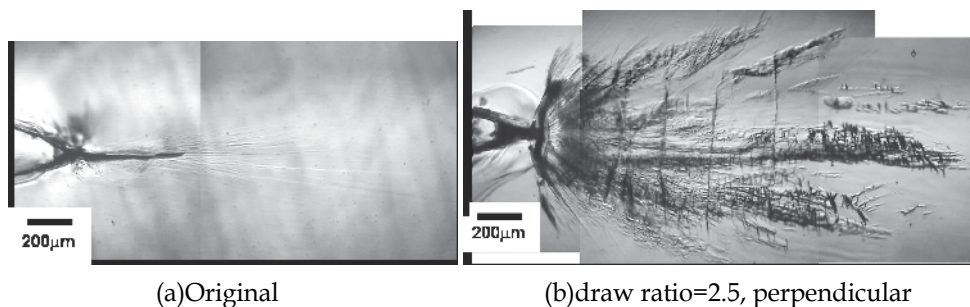


Fig. 7. Polarized micrographs of damage zones.

### 3. Fracture behavior of PLA/PCL blend

Blending with ductile biodegradable polymers such as PCL (Broz, 2003; Dell'Erba, 2001; Chen, 2003; Todo, 2007; Tsuji, 1996, 1998, 2001, 2003), poly(butylene succinate-co- $\epsilon$ -caprolactone) (PBSC) (Vannaladsaysy, 2010) and poly (butylene succinate-co-L-lactate) (PBSL) (Shibata, 2006, 2007; Vannaladsaysy, 2009; Vilay, 2009) has extensively been investigated in order to improve the fracture energy of PLA. Amongst them, PCL is known to be bioabsorbable and bioabsorbable, therefore has been applied in medical fields. In this paragraph, the Mode I fracture behavior of PLA/PCL blend is discussed.

FE-SEM micrographs of the cryo-fracture surfaces of PLA/PCL blends are shown in Fig.8. Phase separations indicated as spherulites of PCL are clearly observed. It is obvious that the size of the PCL spherulites increases with increase of PCL content. It is also seen that voids are created as a result of removal of the dispersed PCL droplets. In general, a blend of immiscible polymers such as PLLA and PCL creates macro-phase separation of the two components due to difference of solubility parameter. This kind of phase separation dramatically affects the physical and mechanical properties of the blend (Dell'Erba et al., 2001; Maglio et al., 1999; Tsuji et al., 2003).

Dependence of PCL content on the critical energy release rate at crack initiation,  $G_{in}$ , is shown in Fig.9.  $G_{in}$  increases with increase of PCL content up to 5wt%, and  $G_{in}$  becomes about 1.5 times greater than that of PLA.  $G_{in}$  slightly decreases as PCL content increases above 5wt%; however,  $G_{in}$  values of the blends with 10 and 15wt% of PCL are still higher than that of PLA.

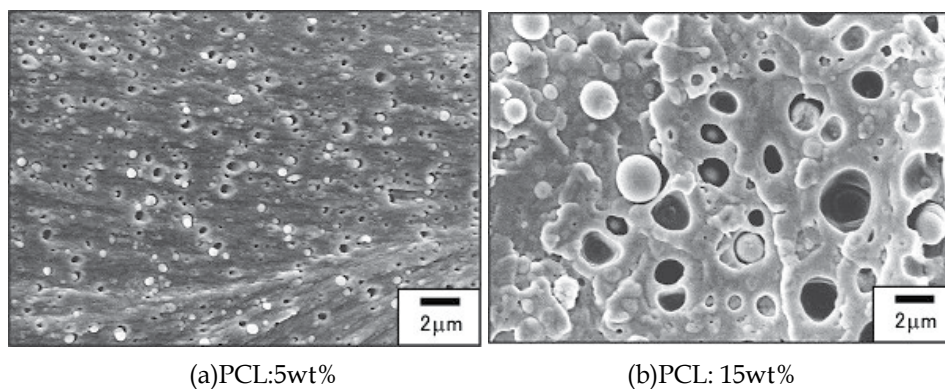


Fig. 8 Morphology of PLA/PCL blends

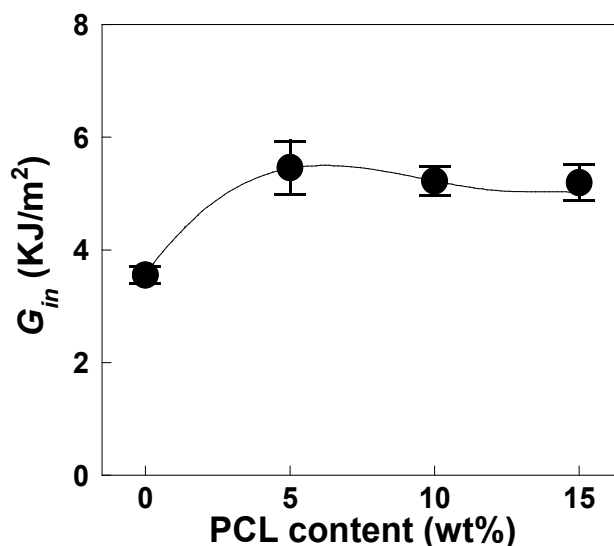


Fig. 9. Dependence of PCL content on the critical energy release rate at crack initiation.

Polarized micrograph of crack-tip region of PLA/PCL (PCL:15wt%) is shown in Fig.10. Craze-like damages similar to neat PLA shown in Fig.7(a) are created in the crack-tip region, and the size of the damage zone is much larger than that of PLA. FE-SEM micrographs of surface on the crack-tip region are also shown in Fig.11. The right-hand figure is a micrograph of the craze-like damages at higher magnification. The micrograph clearly indicates a typical structure of craze, consisting of voids and fibrils. The spherulites of PCL are also seen. The extended fibrils of the matrix PLA were found to be much longer than those of the neat PLA, suggesting that the existence of the dispersed PCL spherulites in PLA tends to enhance ductile deformation of PLA fibrils. It is thus clear that the dispersed PCL droplets play an important role in the formation of the craze-like damages in PLA/PCL blend. FE-SEM micrograph of the fracture surface is shown in Fig.12. Increased ductile deformation of the matrix PLA with appearance of porous structures is clearly observed on the surface. These holes are thought to be created by removal of PCL droplets.

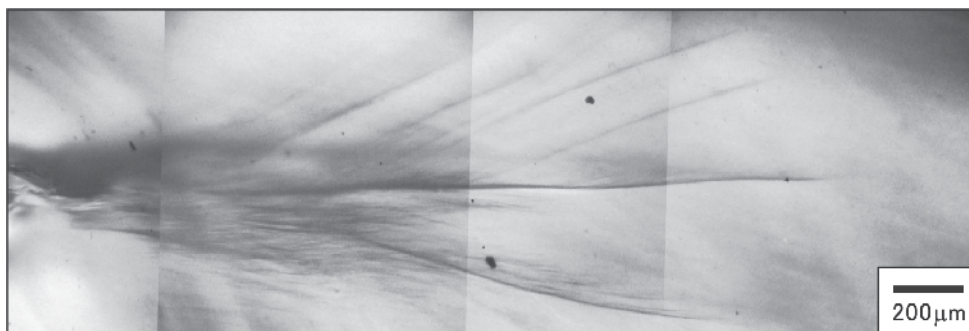


Fig. 10. Polarized micrograph of crack growth behavior in PLA/PCL.

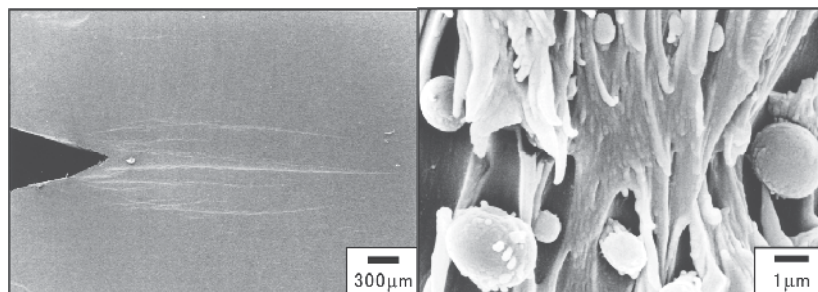


Fig. 11. FE-SEM micrographs of crack-tip region of PLA/PCL.

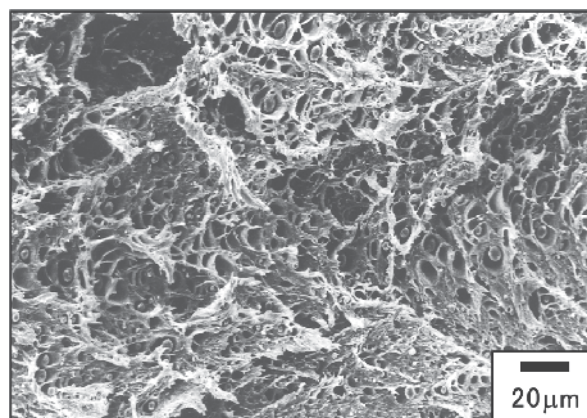


Fig. 12. FE-SEM micrograph of fracture surface of PLA/PCL.

In summary, it was shown that the fracture energy of PLA can be improved by blending with PCL with unchanged biocompatible and bioabsorbable characteristics. This improvement is considered to be achieved by stress relaxation and energy dissipation mechanisms such as extensive multiple craze formation of continuous phase and creation of extended fibril structures of dispersed phase. It is important to note that PLA/PCL exhibited phase separation due to incompatibility of two components, and created voids owing to removal of dispersed PCL phase. Those voids increased with increase of PCL content. PLA/PCL exhibited craze-like deformation of continuous phase similar to neat PLA during mode I fracture process, however, the size of the damage zone was much larger than the PLA, corresponding to the higher  $G_{in}$ . PLA/PCL also showed creation of voids by PCL phase separation within the fracture process region, and these voids were likely to be extended at lower stress level, and therefore, decrease  $G_{in}$  due to local stress concentration.

## 4. Toughness improvement of PLA/PCL blend

### 4.1 Effect of LTI

As shown in the above section, blending with PCL successfully improved the fracture energy of brittle PLA. It was, however, also found that the immiscibility of PLA and PCL causes phase separation, and tends to lower the fracture energy especially when PCL content increases. It has recently been found that the addition of lysine tri-isocyanate (LTI)

to PLA/PCL blends effectively improves their immiscibility (Takayama, 2006a, 2006b; Harada, 2007, 2008) and therefore the fracture energy (Takayama, 2006a, 2006b).

FE-SEM micrographs of cryo-fractured surfaces of PLA/PCL and PLA/PCL/LTI are shown in Fig.13. The content of PCL was 15wt% in these materials. Spherical features appeared on the micrograph are thought to be PCL-rich phases. These micrographs clearly showed that the size of the PCL-rich phase dramatically decreases by LTI addition. It is thus presumed that LTI addition effectively improves the miscibility of PLA and PCL. This is thought to be related to the following chemical reaction, that is, the hydroxyl group of PLA and the isocyanate group of LTI creates urethane bond:

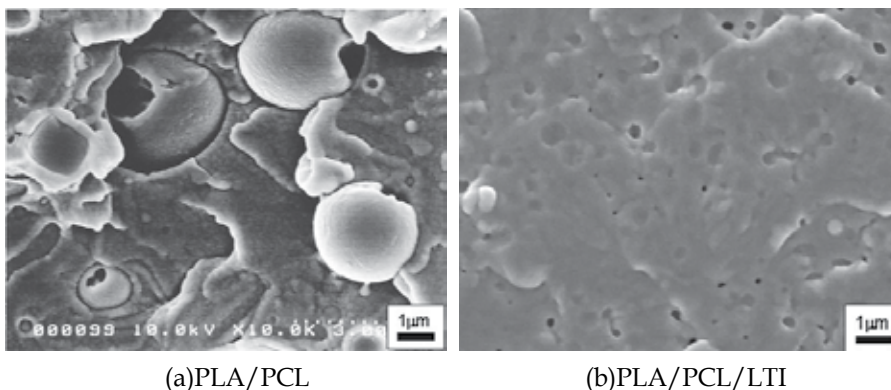
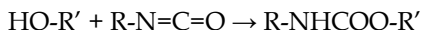


Fig. 13. FE-SEM micrographs of cryo-fracture surfaces of PLA/PCL and PLA/PCL/LTI.

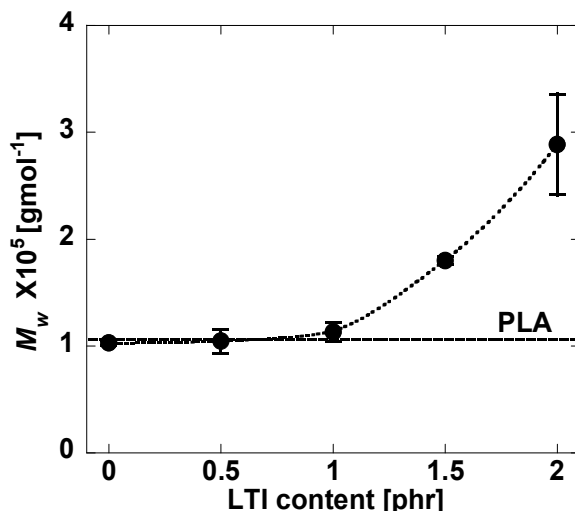


Fig. 14. Dependence of LTI content on the molecular weight.

Dependence of LTI content on the molecular weight,  $M_w$ , is shown in Fig.14. For comparison,  $M_w$  of neat PLA is also shown in the figure.  $M_w$  values of the blends tend to

keep unchanged up to 1phr of LTI content, and then rapidly increase up to 2phr, suggesting that the chemical reaction between the hydroxyl groups of PLA and PCL and the isocyanate groups of LTI was promoted by addition of LTI more than 1 phr. This microstructural change in molecular level due to LTI addition strongly support the macroscopic improvement of the fracture energy.

Dependence of LTI content on the crystallinity of PLA,  $x_{c,PLA}$ , is shown in Fig.15.  $x_{c,PLA}$  of PLA/PCL and PLA/PCL/LTI with 0.5phr of LTI are higher than that of PLA. It is considered that the crystallization of PLA in the blends was progressed actively more than in neat PLA. With increase of LTI content,  $x_{c,PLA}$  decreases rapidly at 1 phr and this value is slightly lower than that of neat PLA. These results support that the phase separation between PLA and PCL is improved dramatically at 1 phr. It is presumed that the chemical reaction between LTI and PLA/PCL during melt-mixing process results in the improvement of miscibility, and therefore the mobility of PLA and PCL molecules during solidification in cooling process is reduced, resulting in the reduction of crystallization.

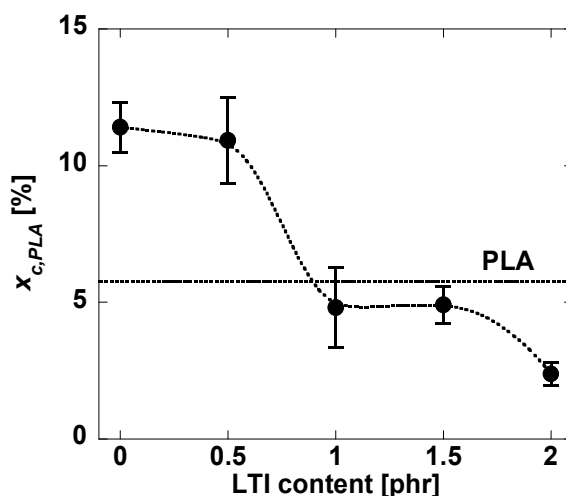


Fig. 15. Dependence of LTI content on crystallinity of PLA in PLA/PCL and PLA/PCL/LTI.

Dependence of LTI content on  $J_{in}$  is shown in Fig. 16. It is seen that  $J_{in}$  of PLA/PCL is a little larger than that of PLA, indicating the effectiveness of PCL blend on  $J_{in}$  is very low.  $J_{in}$  of PLA/PCL is effectively improved by LTI addition, and  $J_{in}$  increases with increase of LTI content up to 1.5 phr. There is no difference of  $J_{in}$  between 2 phr and 1 phr of LTI addition, suggesting that the improvement of  $J_{in}$  is saturated with about 1.5 phr of LTI.

Polarized micrographs of crack growth behaviors in PLA/PCL/LTI are shown in Fig.17. In PLA/PCL/LTI with 0.5 phr of LTI, craze-like features are still seen in the crack-tip region as also seen in neat PLA (Fig.7(a)) and PLA/PCL blend (Fig.10). The number of the craze-lines is obviously decreased due to LTI addition. With higher content of LTI, such craze-like feature is no longer generated, and instead, the crack-tip region is plastically deformed, very similar to the crack-tip deformation in ductile plastics and metal. It is known that this kind of plastic deformation dissipates more energy than the craze-like damage, resulting in the greater fracture energy. It is therefore thought that LTI addition to PLA/PCL dramatically changes the crack-tip deformation mechanism; as a result,  $J_{in}$  is greatly improved.

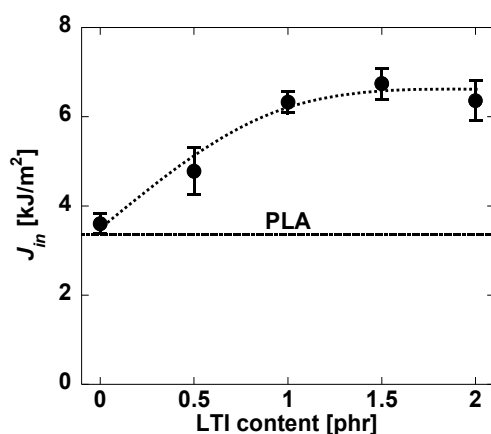
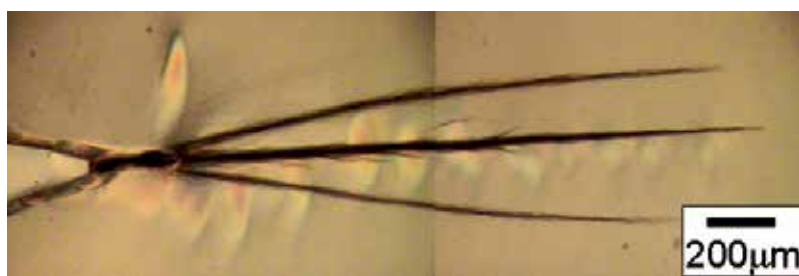


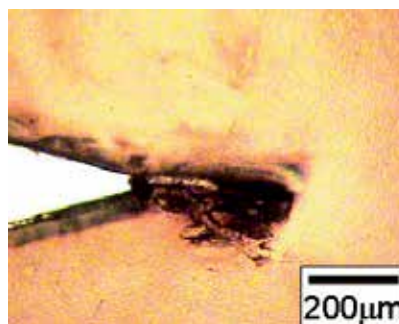
Fig. 16. Dependence of LTI content on the fracture energy,  $J_{in}$ .



(a) LTI: 0.5 phr



(b) LTI: 1 phr



(c) LTI: 2 phr

Fig. 17. Polarized micrographs of crack growth behaviors in PLA/PCL/LTI.

FE-SEM micrographs of fracture surfaces of PLA, PLA/PCL and PLA/PCL/LTI are shown in Fig. 18. The fracture surface of PLA is very smooth, corresponding to a brittle fracture behavior with low fracture energy. The surface roughness increases with the existence of elongated PCL and cavities by PCL blending. These cavities are thought to be created by debonding of the PCL-rich phases from the surrounding PLA matrix phase and usually cause local stress concentration in the surrounding regions. Thus, this kind of cavitation tends to lower the fracture energy because of the local stress concentration, and

compensates to the increase of fracture energy due to the ductile deformation of PCL. This is the reason for the slight improvement of  $J_{in}$  in PLA/PCL shown in Fig. 16. It is clearly seen from Fig. 18(c) that cavities do not exist on the fracture surface of PLA/PCL/LTI, indicating that the miscibility of PLA and PCL improves due to LTI addition. In addition, elongated structures are more on PLA/PCL/LTI than PLA/PCL. Thus, extensive ductile deformation associated with disappearance of cavitation is the primary mechanism of the dramatic improvement of  $J_{in}$ .

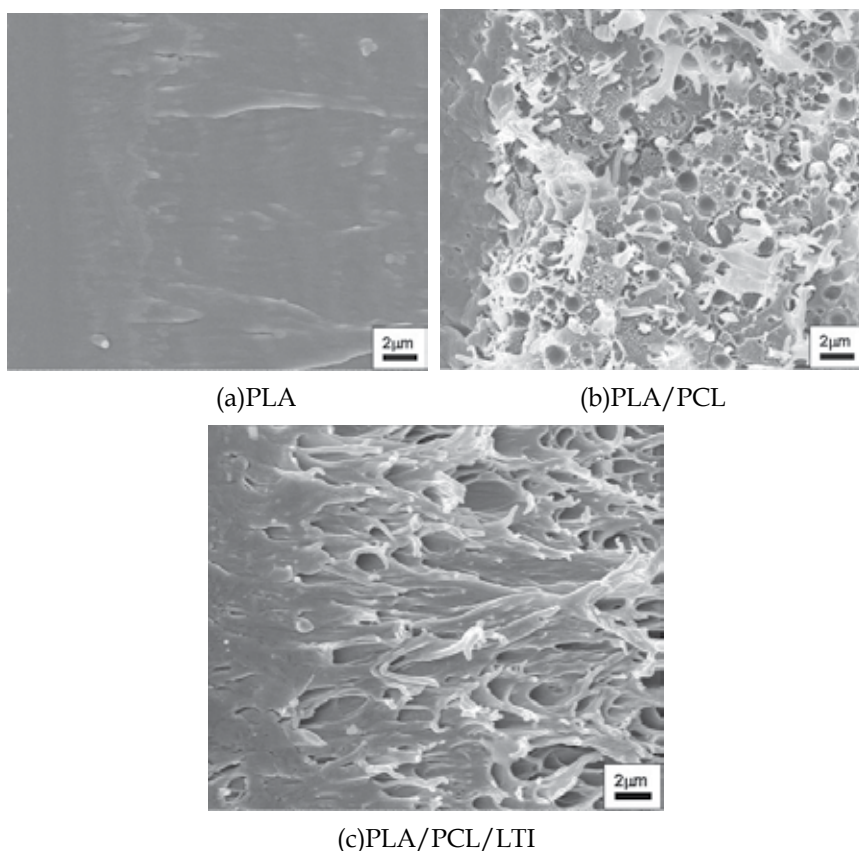


Fig. 18. FE-SEM micrographs of fracture surfaces of PLA, PLA/PCL and PLA/PCL/LTI.

In summary, the miscibility between PLA and PCL is dramatically improved by introducing LTI as an additive. The increase of molecular weight and the decrease of crystallinity with increase of LTI content clearly indicate that crosslinks are generated by urethane bonds in which the hydroxyl groups at the ends of PLA and PCL molecules react with the isocyanate groups of LTI during molding process. Such microstructural modification results in the dramatic improvement of the macroscopic fracture property,  $J_{in}$ .

#### 4.2 Effect of annealing process on PLA/PCL/LTI

As described in the previous section, the immiscibility of PLA/PCL can be improved by adding LTI as a compatibilizer, and as a result, the fracture energy of PLA/PCL is



effectively improved. However, blending of ductile PCL with PLA degrades another mechanical properties such as strength and elastic modulus of the base polymer PLA. Recently, Tsuji et al. found that the mechanical properties such as elastic modulus and tensile strength of PLA could be improved by annealing (Tsuji et al., 1995). It is thus expected that annealing process may also affect on the mechanical properties of PLA/PCL/LTI blend.

FE-SEM micrographs of cryo-fracture surfaces of quenched and annealed PLA/PCL and PLA/PCL/LTI are shown in Fig.19. Both the quenched and the annealed PLA/PCL show spherical structures of PCL. It is obviously seen that PCL spherulites in PLA/PCL/LTI are much smaller than those in PLA/PCL. The annealed blends exhibit rougher surfaces with spherical structures than the quenched samples. These spherical structures are thought to be the spherulites of PLA generated by crystallization during annealing process.

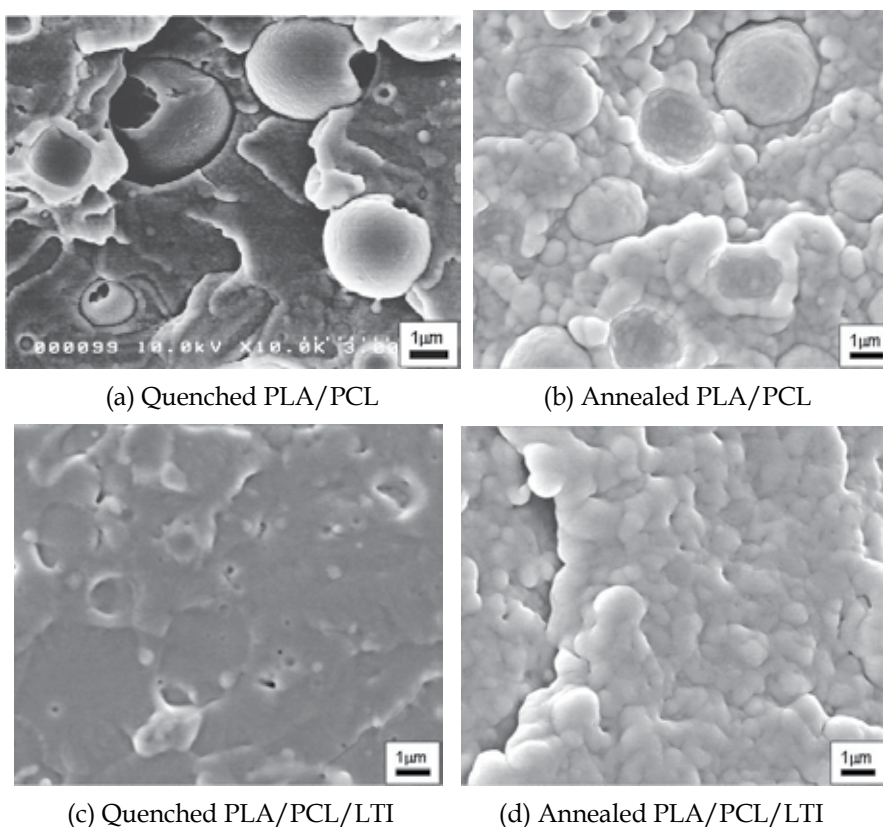


Fig. 19. FE-SEM micrographs of microstructures of PLA/PCL and PLA/PCL/LTI.

Effects of annealing on the elastic modulus,  $E$ , and the strength,  $\sigma_f$ , under three-point bending condition are shown in Fig.20. Both  $E$  and  $\sigma_f$  increase due to annealing. Effects of annealing on the crystallinity,  $x_{c,PLA}$ , and the molecular weight,  $M_w$ , are also shown in Table 1. It is clearly seen that  $x_{c,PLA}$  dramatically increases due to annealing. Thus, increasing  $x_{c,PLA}$  is likely to strengthen the structure of the polymer, resulting in the increase of  $E$  and  $\sigma_f$ .  $M_w$  of PLA/PCL increases slightly due to LTI, suggesting that LTI is thought to generate

additional polymerization with hydroxyl and carboxyl groups lying in the ends of PLA or PCL molecules. This polymerization results in the improvement of miscibility of PLA and PCL as shown in Fig.19(c). On the other hand,  $M_w$  of PLA/PCL decreases slightly due to annealing, indicating progression of thermal degradation in this blend. On the contrary,  $M_w$  of PLA/PCL/LTI slightly increases, suggesting that additional polymerization take place during annealing process.

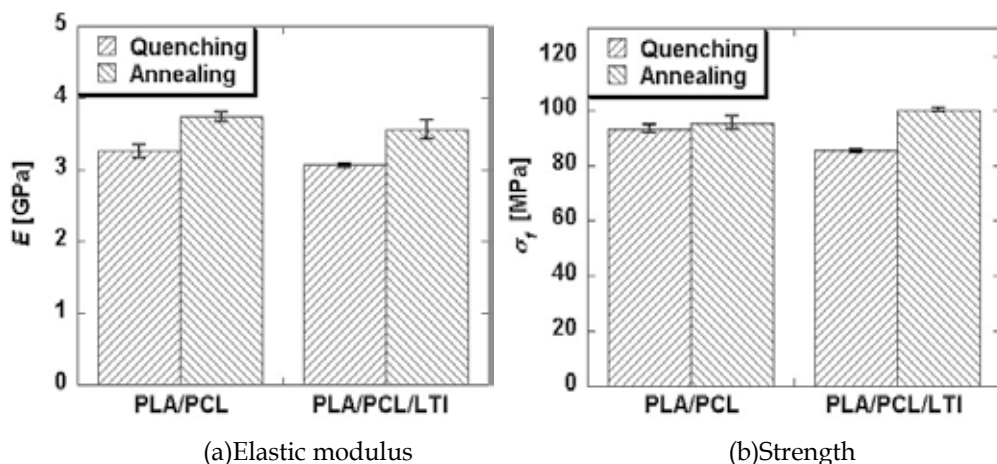


Fig. 20. Effects of annealing on bending mechanical properties.

Blend	$X_{c,PLA}$ (%)	$M_w$ (g/mol)
Quenched PLA/PCL	11.4	$1.03 \times 10^5$
Annealed PLA/PCL	45.6	$9.08 \times 10^4$
Quenched PLA/PCL/LTI	4.8	$1.13 \times 10^5$
Annealed PLA/PCL/LTI	36.6	$1.52 \times 10^5$

Table 1. Effects of annealing on the crystallinity and molecular weight.

Effects of annealing on the critical J-integral at crack initiation,  $J_{in}$ , are shown in Fig.21. It is clearly seen that  $J_{in}$  of PLA/PCL/LTI effectively increases due to annealing; on the contrary, PLA/PCL exhibits decrease of  $J_{in}$ .

FE-SEM micrographs of the fracture surfaces of the mode I fracture specimens are shown in Fig.22. By comparing Figs.22(a) and (b), it is clearly seen that ductile deformation of spherical PCL phase is suppressed by annealing. Cavities are also observed on the surface of PLA/PCL, as a result of removal of the spherical PCL phases. FE-SEM micrographs at higher magnification show that elongated structures of the spherical PCL phases are observed in the quenched PLA/PCL, while ruptured PLA fibrils and undeformed PCL spherulites are observed in the annealed PLA/PCL. It is also interesting to see in Fig.22(a) that some PCL fibrils are penetrated into the PLA phase and seem to be entangled with PLA fibrils. It is thought that the PLA phase creates a firm structure due to crystallization by annealing and therefore, entangled PCL fibrils with PLA fibrils are firmly trapped in the PLA phase. The PCL spherulites are thus surrounded by such firm crystallized PLA phase with entanglement of PLA and PCL fibrils, resulting in the rupture of the PCL fibrils and the

suppression of ductile deformation of the PCL spherulites. This is considered to be the primary reason for the degradation of  $J_{in}$  as shown in Fig.21.

It is clearly seen from Figs.22(c) and (d) that in the PLA/PCL/LTI blends, cavity formation is totally suppressed and as a result, ductile deformation is expanded due to the improved miscibility of PLA and PCL by LTI addition. This implies that the miscibility of PLA and PCL is improved by crosslinking of PLA and PCL macromolecules induced by the chemical reaction between the hydroxyl group of PLA and PCL and the isocyanate group of LTI. FE-SEM micrographs at higher magnification show that for both the quenched and annealed PLA/PCL/LTI blends, entangled fibril structures of PLA and PCL are observed. It is thus considered that this kind of structural transformation due to polymerization by LTI blending results in strengthening the structure of the PLA/PCL blends. The microstructure of PLA/PCL/LTI is thought to be further strengthened due to crystallization of PLA by annealing, resulting in the dramatic improvement of the mode I fracture energy  $J_{in}$  as shown in Fig.22.

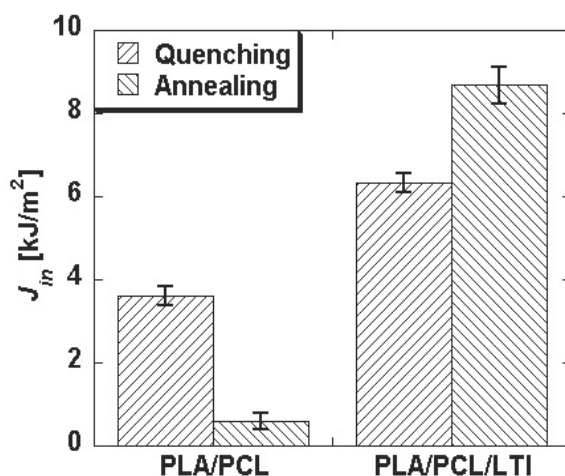
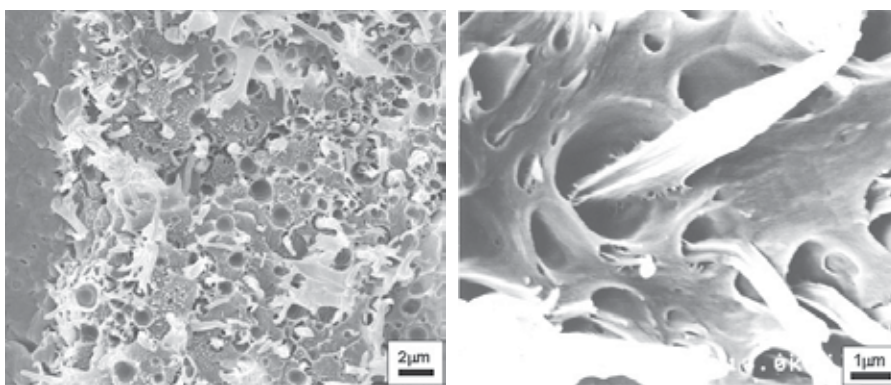
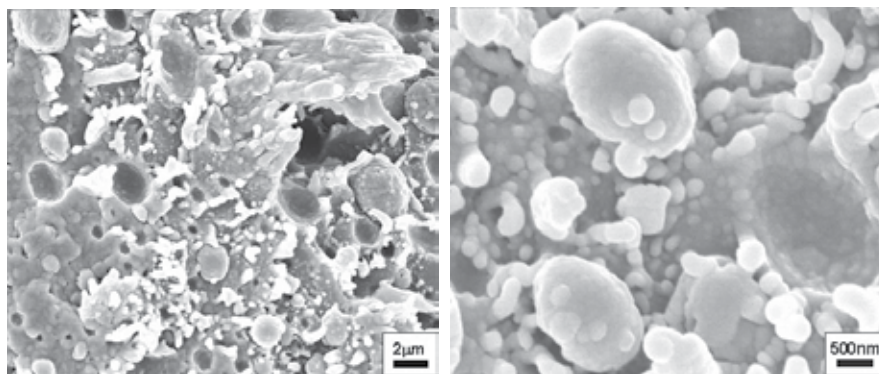


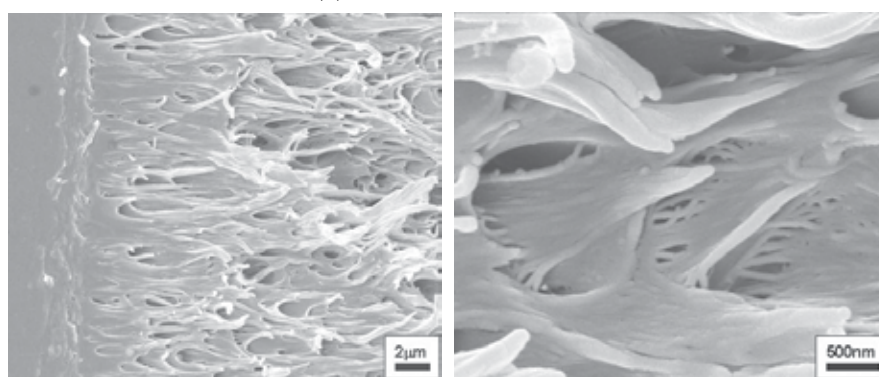
Fig. 21. Effects of annealing on the critical J-integral at crack initiation,  $J_{in}$ .



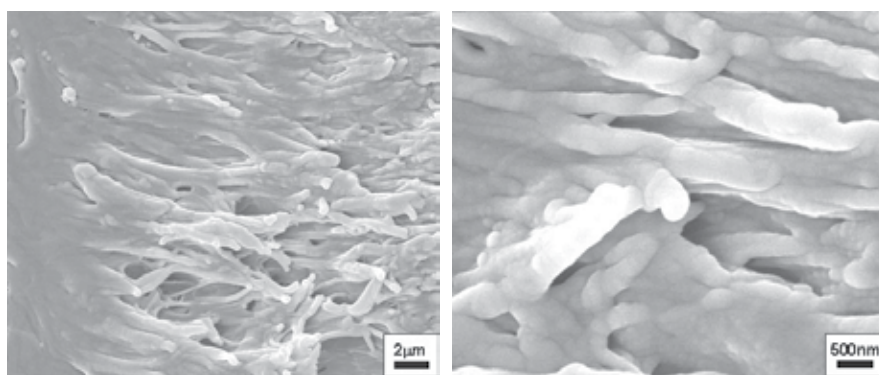
(a) Quenched PLA/PCL



(b) Annealed PLA/PCL



(c) Quenched PLA/PCL/LTI



(d) Annealed PLA/PCL/LTI

Fig. 22. FE-SEM micrographs of fracture surfaces of quenched and annealed samples.

In summary, the bending modulus and strength of both PLA/PCL and PLA/PCL/LTI are effectively improved by annealing. Crystallization of the PLA phase by annealing is thought to strengthen the structure of the PLA/PCL blend, resulting in increase of these properties. The mode I fracture energy of PLA/PCL significantly decreases by annealing mainly owing to embrittlement of the PLA phase. For the case of PLA/PCL/LTI, the structural transformation due to polymerization by LTI addition and crystallization by annealing

strengthen the microstructure, resulting in the dramatic improvement of the mode I fracture energy.

## 5. Conclusion

In this chapter, the fundamental fracture characteristics of bioabsorbable PLA were firstly discussed, and then as examples of toughening, effects of unidirectional drawing and blending with PCL on the fracture behavior were presented. Finally, microstructural modification for PLA/PCL blends using LTI additive was discussed. Thermal processes have great influences on the microstructure and the mechanical properties of PLA mainly due to crystallization behaviour during the heating process. Highly crystallized PLA tends to exhibit very brittle fracture behavior with low fracture energy. Amorphous PLA can generate multiple crazes at crack-tip region to dissipate more energy during fracture process than crystallized materials in which craze formation is suppressed. Drawing process can arrange molecules in one direction so that the fracture resistance in the perpendicular to the drawing direction is greatly improved, while the resistance in the drawing direction tends to degrade. Another effective way to improve the fracture energy is blending with ductile polymer such as PCL. PLA/PCL blends show higher fracture energy with extensive damage formation in crack-tip regions than neat PLA; however, the immiscibility of PLA and PCL results in phase separation morphology in which spherulites of PCL are dispersed in PLA matrix. Such morphological problem can effectively be improved by using LTI as an additive. The phase separation is almost disappeared and the fracture energy is greatly improved. The fracture micromechanism is changed from multiple craze-like damage formation to plastic deformation in crack-tip region. Furthermore, the mechanical properties including elastic modulus, strength and fracture energy of PLA/PCL/LTI blends can effectively be improved by introducing annealing process, although such process tends to degrade the fracture energy of PLA/PCL blends.

## 6. References

- Botsis, J., Chudnovsky, A., Moet, A. (1987). Fatigue crack layer propagation in polystyrene. 1. experimental observations. *International Journal of Fracture*, Vol.33, No.4, pp.263-276.
- Broz, M.E., VanderHart, D.L., Washburn, N.R. (2003). Structure and mechanical properties of poly(DmL-lactic acid)/poly( $\epsilon$ -caprolactone) blends. *Biomaterials*, Vol.24, pp.4181-4190.
- Chen, C.C., Chueh, J.Y., Tseng, H., Huang, H.M., Lee, S.Y. (2003). Preparation and characterization of PLA polymeric blends. *Biomaterials*, Vol.24, pp.1167-1173.
- Dell'Erba, R., Groeninckx, G., Maglio, G., Malinconico, M., Migliozzi, A. (2001). Immiscible polymer blends of semicrystalline biocompatible components: Thermal properties and phase morphology analysis of PLLA/PCL blends. *Polymer*, Vol.42, pp.7831-7840.
- Harada, M., Ohya, T., Iida, K., Hayashi, H., Hirano, K., Fukuda, H. (2007). Increased impact strength of biodegradable poly(lactic acid)/poly(butylene succinate) blend composites by using isocyanate as a reactive processing agent, *Journal of Applied Polymer Science*, Vol.106, No.3, pp.1813-11820.

- Harada, M., Iida, K., Okamoto, K., Hayashi, H., Hirano, K. (2008). Reactive compatibilization of biodegradable poly(lactic acid)/poly(epsilon-caprolactone) blends with reactive processing agents, *Polymer Engineering and Science*, Vol.48, No.7, pp.1359-1368.
- Higashi, S., Tamamoto, T., Nakamura, T., Ikada, Y., Hyon, S.H., Jamshidi, K. (1986). Polymer-hydroxyapatite composites for biodegradable bone fillers. *Biomaterials*, Vol.7, pp.183-187.
- Ikada, Y., Shikinami, Y., Hara, Y., Tagawa, M., Fukuda, E. (1996). Enhancement of bone formation by drawn poly(L-lactide). *Journal of Biomedical Materials Research*, Vol. 30, pp.553-558.
- Maglio, G., Migliozi, A., Palumbo, R., Immizi, B., Volpe, M.G. (1999). Compatibilized poly(epsilon-caprolactone)/poly(L-lactide) blends for biomedical uses. *Macromolecules Rapid Communication*, Vol.20, pp.236-238.
- Middleton, J.C., Tipton, A.J. (2000). Synthetic biodegradable polymers as orthopedic devices. *Biomaterials*, Vol.21, pp.2335-2346.
- Mohanraj, J., Chapleau, N., Aji, A., Duckett, R.A., Ward, I.M. (2003a). Fracture behavior of die-drawn toughened polypropylenes. *Journal of Applied Polymer Science*, Vol.88, pp.1336-1345.
- Mohanraj, J., Chapleau, N., Aji, A., Duckett, R.A., Ward, I.M. (2003b). Production, properties and impact toughness of die-drawn toughened polypropylenes. *Polymer Engineering Science*, Vol.43, No.6, pp.1317-1335.
- Mohanty, A.K., Misra, M., Hinrichsen, G. (2000). Biofibres, biodegradable polymers and biocomposites: An overview. *Macromolecular Materials and Engineering*, Vol.276/277, pp.1-24.
- Park, S.D., Todo, M., Arakawa, K. (2004). Effect of annealing on the fracture toughness of poly(lactic acid), *Journal of Materials Science*, Vol.39, pp.1113-1116.
- Park, S.D., Todo, M., Arakawa, K. (2005). Effects of isothermal crystallization on fracture toughness and crack growth behavior of poly(lactic acid), *Journal of Materials Science*, Vol.40, pp.1055-1058.
- Park, S.D., Todo, M., Arakawa, K., Koganemaru, M. (2006). Effect of crystallinity and loading-rate on mode I fracture behavior of poly(lactic acid). *Polymer*, Vol.47, pp.1357-1363.
- Sawai, D., Yamane, A., Kameda, T., Kanamoto, T., Ito, M., Yamazaki, M., Hisatani, K. (1999). Uniaxial drawing of isotactic poly(acrylonitrile): development of oriented structure and tensile properties. *Macromolecules*, Vol.32, No.17, pp.5622-5630.
- Shibata, M., Teramoto, N., Inoue Y. (2006). Mechanical properties, morphologies, and crystallization behavior of blends of poly(L-lactide) with poly(butylene succinate-co-L-lactate) and poly(butylene succinate). *Polymer*, Vol.47, pp.3557-3564.
- Shibata, M., Teramoto, N., Inoue Y. (2007). Mechanical properties, morphologies, and crystallization behavior of plasticized poly(L-lactide)/poly(butylene succinate-co-L-lactate) blends. *Polymer*, Vol.48, pp.2768-2777.
- Takayama, T., Todo, M. (2006). Improvement of impact fracture properties of PLA/PCL polymer blend due to LTI addition. *Journal of Materials Science*, Vol.41, No.15, pp.4989-4992.
- Takayama, T., Todo, M., Tsuji, H., Arakawa, K. (2006). Effect of LTI content on impact fracture property of PLA/PCL/LTI polymer blends. *Journal of Materials Science*, Vol.41, No.19, pp.6501-6504.

- Takayama, T., Todo, M., Tsuji, H. (2011). Effect of annealing on the mechanical properties of PLA/PCL and PLA/PCL/LTI polymer blends. *Journal of the Mechanical Behavior of Biomedical Materials*, Vol.4, pp.255-260.
- Todo, M., Shinohara, N., Arakawa, K. (2002). Effects of crystallization and loading-rate on the mode I fracture toughness of biodegradable poly(lactic acid). *Journal of Materials Science Letters*, Vol.21, pp.1203-1206.
- Todo, M., Kagawa, T., Takenoshita, Y., Myoui, A. (2008). Effect of press processing on fracture behavior of HA/PLLA biocomposite material. *Journal of Solid Mechanics and Materials Engineering*, Vol.2, No.1, pp.1-7.
- Todo, M., Takayama, T. (2007). Improvement of mechanical properties of poly(L-lactic acid) by blending of lysine triisocyanate. *Journal of Materials Science*, Vol.42, pp.4721-4724.
- Todo, M., Takayama, T., Tsuji, H., Arakawa, K. (2007a). Effect of LTI blending on fracture properties of PLA/PCL polymer blend. *Journal of Solid Mechanics and Materials Engineering*, Vol.1, No.9, pp.1157-1164.
- Todo, M., Park, S.D., Takayama, T., Arakawa, K. (2007b). Fracture micromechanisms of bioabsorbable PLLA/PCL polymer blends. *Engineering Fracture Mechanics*, Vol.74, pp. 1872-1883.
- Todo, M. (2007). Effect of unidirectional drawing process on fracture behavior of poly(L-lactide). *Journal of Materials Science*, Vol.42, No.4, pp.1393-1396.
- Tsuji, H., Ikada, Y. (1995). Properties and morphologies of poly (L-lactide): 1. Annealing condition effects on properties and morphologies of poly (L-lactide). *Polymer*, Vol.36, pp.2709-2716.
- Tsuji, H., Ikada, Y. (1996). Blends of aliphatic polyesters. I. Physical properties and morphologies of solution-cast blends from poly(DL-lactide) and poly( $\epsilon$ -caprolactone). *Journal of Applied Polymer Science*, Vol.60, pp.2367-2375.
- Tsuji, H., Ikada, Y. (1997). Blends of aliphatic polyesters. II. Hydrolysis of solution-cast blends from poly(L-lactide) and poly( $\epsilon$ -caprolactone) in phosphate-buffered solution. *Journal of Applied Polymer Science*, Vol.67, pp.405-415.
- Tsuji, H., Ishizuka, T. (2001). Porous biodegradable polyesters, 3 Preparation of porous poly( $\epsilon$ -caprolactone) films from blends by selective enzymatic removal of poly(L-lactide). *Macromolecular Bioscience*, Vol.1, No.2, pp.59-65.
- Tsuji, H., Yamada, T., Suzuki, M., Itsuno, S. (2003). Blends of aliphatic polyesters. part 7. effects of poly(L-lactide-co- $\epsilon$ -caprolactone) on morphology, structure, crystallization, and physical properties of blends of poly(L-lactide) and poly( $\epsilon$ -caprolactone). *Polymer Journal*, Vol.52, pp.269-275.
- Uehara, H., Yamazaki, Y., Kanamoto, T. (1996). Tensile properties of highly syndiotactic polypropylene. *Polymer*, Vol.37, No.1, pp.57-64.
- Vannaladsaysy, V., Todo, M., Takayama, T., Jaafar, M., Zulkifli, A., Pasomsouk, K. (2009). Effect of lysine triisocyanate on the mode I fracture behavior of polymer blend of poly(L-lactic acid) and poly(butylene succinate-co-L-lactide). *Journal of Materials Science*, Vol.44, No.11, pp.3006-3009.
- Vannaladsaysy, V., Todo, M., Jaafar, M., Ahmad, Z. (2010). Characterization of microstructure and mechanical properties of biodegradable polymer blends of poly(L-lactic acid) and poly(butylene succinate-co- $\epsilon$ -caprolactone) with lysine triisocyanate. *Polymer Engineering and Science*, Vol.50, No.7, pp.1485-1491.

- Vilay, V., Mariatti, M., Ahmad, Z., Pasomsouk, K., Todo, M. (2010). Improvement of microstructures and properties of biodegradable PLLA and PCL blends compatibilized with a triblock copolymer. *Materials Science and Engineering A*, Vol.527, No.26, pp.6930 - 6937.
- Vilay, V., Mariatti, M., Ahmad, Z., Pasomsouk, K., Todo, M. (2009). Characterization of the mechanical and thermal properties and morphological behavior of biodegradable poly(L-lactide)/poly( $\epsilon$ -caprolactone) and poly(L-lactide)/poly(butylenes succinate-co-L-lactide) polymer blends. *Journal of Applied Polymer Science*, Vol.114, pp.1784-1792.
- Vilay, V., Mariatti, M., Ahmad, Z., Pasomsouk, K., Todo, M.(2010). Improvement of microstructure and fractured property of poly(L-lactic acid) and poly(butylene succinate-co- $\epsilon$ -caprolactone) blend compatibilized with lysine triisocyanate. *Engineering Letters*, Vol.18, No.3, pp.303-307.
- Yamane, A., Sawai, D., Kameda, T., Kanamoto, T., Ito, M., Porter, R.S. (1997). Development of high ductility and tensile properties upon two-stage draw of ultrahigh molecular weight poly(acrylonitrile). *Macromolecules*, Vol.30, No.14, pp.4170-4178.



## **Part 3**

# **Evaluation of the Interaction and Compatibility of Biomaterials with Biological Media**



# Cell Adhesion and Spreading on an Intrinsically Anti-Adhesive PEG Biomaterial

Marga C. Lensen<sup>1,2</sup>, Vera A. Schulte<sup>1</sup> and Mar Diez<sup>1</sup>

<sup>1</sup>*DWI e.V. and Institute of Technical and Macromolecular Chemistry, RWTH Aachen*

<sup>2</sup>*Technische Universität Berlin, Institut für Chemie, Nanostrukturierte Biomaterialien  
Germany*

## 1. Introduction

This Chapter deals with bulk hydrogels consisting of a widely used biomaterial: poly(ethylene) glycol (PEG). PEG is renowned for its bio-inertness; it is very effective in suppressing non-specific protein adsorption (NSPA) and thereby preventing cell adhesion. However, we have observed unexpected adhesion of fibroblast cells to the surface of bulk PEG hydrogels when the surface was decorated with micrometer-sized, topographic patterns. This Chapter describes the aim of our investigations to unravel the biophysical, biochemical and biomechanical reasons why these cells do adhere to the intrinsically anti-adhesive PEG material when it is topographically patterned.

### 1.1 Application of hydrogels in biomaterial science

Amongst the different classes of materials which find use in the field of medicine and biology, hydrophilic polymers have demonstrated great potential. Networks formed from hydrophilic polymer often exhibit a high affinity for water, yet they do not dissolve due to their chemically or physically crosslinked network. Water can penetrate in between the chains of the polymer network, leading to swelling and the formation of a hydrogel (Langer & Peppas, 2003; Peppas et al., 2000; Wichterle & Lim, 1960). Generally such polymer networks can be formed via chemical bonds, ionic interactions, hydrogen bonds, hydrophobic interactions, or physical bonds (Hoffman, 2002; Peppas, 1986). Hydrogels have found numerous applications in drug delivery as well as in tissue engineering where they are used as scaffolds for the cultivation of cells to enable the formation of new tissues (Jen et al. 1996; Krsko & Libera, 2005; Langer & Tirrell, 2004; Peppas et al., 2006). Hydrogels are especially attractive for this purpose as they meet numerous characteristics of the architecture and mechanics of most soft tissues and many are considered biocompatible (Jhon & Andrade, 1973; Saha et al., 2007). Furthermore, concerning the intended purpose of cell encapsulation and delivery, hydrogels support sufficient transport of oxygen, nutrients and wastes (Fedorovich et al., 2007; Lee & Mooney, 2001; Nguyen & West, 2002).

In general, hydrogel matrices can be prepared from a variety of naturally derived proteins and polysaccharides, as well as from synthetic polymers (Peppas et al., 2006). Depending on their origin and composition, natural polymers have specific utilities and properties. Hydrogels from natural sources have for example been fabricated from collagen, hyaluronic acid (HA), fibrin, alginate and agarose (Hoffman, 2002). Collagen, HA and fibrin are

components which are in vivo present in the extracellular matrix (ECM) of mammalian cells. Since they are derived from natural sources, hydrogels formed from these polymers are inherently cytocompatible and bioactive. They can promote many cellular functions due to a diversity of endogenous factors present. However, scaffolds fabricated from natural sources are rather complex and often ill-defined, making it difficult to determine exactly which signals are promoting the cellular outcome (Cushing & Anseth, 2007). Furthermore they can possess an inherent batch-to-batch variability which can affect sensitive cells in their viability, proliferation, and development (Cushing & Anseth, 2007). Due to these limitations of gels formed from natural polymers, a wide range of synthetic polymers has been found suitable regarding their chemical and physical properties (Hoffman, 2002). The advantages of synthetic gels include their consistent composition and predictable manipulation of properties.

A few examples of synthetic hydrogel building blocks are given in **Figure 1**, including neutral (upper row) and ionic (bottom row) monomers (Peppas et al., 2006).

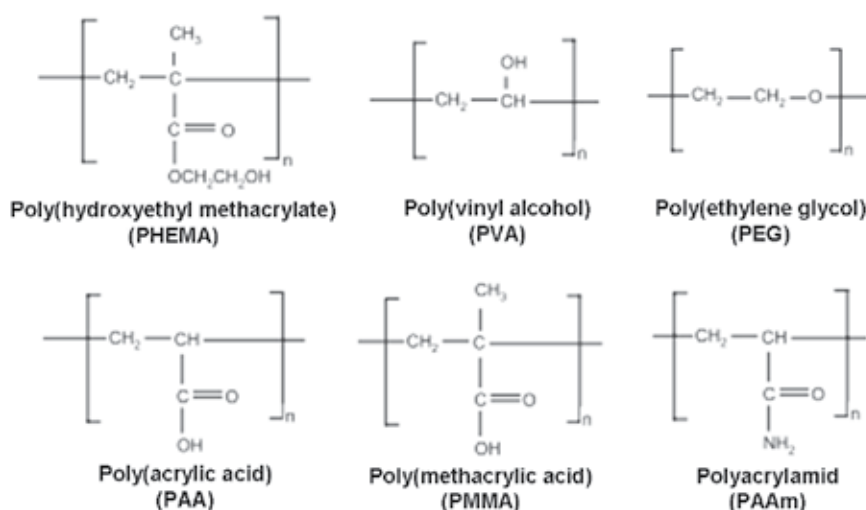


Fig. 1. Some examples of synthetic hydrogels that are used in biomedical applications. Reproduced with permission from Peppas et al., *Adv. Mater.*, 18, 1345-60. Copyright 2006 John Wiley and Sons.

Proteins are molecules, which often adsorb unspecifically from solution at biomaterial interfaces, a phenomenon that has been documented in a wealth of publications, e.g. references: (Andrade & Hlady, 1986; Andrade et al., 1992; Wahlgren & Arnebrant, 1991). Almost any material, when exposed to a physiological, protein-containing solution, becomes coated with proteins within seconds. As widely recognized, this adsorption of proteins to synthetic material surfaces is of great importance in the field of biomaterials as it plays a determining role for the subsequent cellular responses. Failure of most implant materials stems from an inability to predict and control the process of protein adsorption and cell interaction, resulting in an inappropriate host response to the material (Castner & Ratner, 2002; Hlady & Buijs, 1996; Tsai et al., 2002). Biomaterial surface-induced thrombosis, for example, one of the major problems in clinical applications of materials in contact with

circulating blood, begins with the unspecific adsorption of plasma proteins (Andrade & Hlady, 1986; Harris, 1992; Horbett, 1993).

Not only with regards to tissue engineering and implant design unspecific protein adsorption is a highly critical process, also different devices in diagnostics (e.g. protein arrays) and biosensors are based on specific receptor-ligand binding, demanding a non-interacting background. Therefore, much effort has been focused on the development of inert, protein resistant materials and coatings (Chapman et al., 2000; Elbert & Hubbell, 1996). Many synthetic hydrophilic polymers, including PAA, PHEMA, PVA, PEG and poly(ethylene oxide) (PEO) have been applied for this purpose (see Figure 1) (Castillo et al., 1985).

## 1.2 Biomedical applications of PEG- or PEO-based hydrogels

Some of the earliest work on the use of PEG and PEO as hydrophilic biomaterials showed that PEO adsorption onto glass surfaces prevented protein adsorption (Merrill et al., 1982). Several subsequent studies confirmed that PEO, or its low molecular weight ( $M_w < 10$  kDa) equivalent, PEG, were showing the most effective protein-repellent properties (Harris, 1992). PEG-modified surfaces are non-permissive to protein adsorption, bacterial adhesion and eukaryotic cell adhesion (Zhang et al., 1998; Desai et al., 1992; Drumheller et al., 1995; Krsko et al., 2009).

Based on these properties, PEG hydrogels are one of the most widely studied and used materials for a variety of biomedical applications such as tissue engineering, coating of implants, biosensors, and drug delivery systems (Langer & Peppas, 2003; Langer & Tirell, 2004; Krsko & Libera, 2005; Tessmar & Gopferich, 2007; Veronese & Mero, 2008; Harris & Zalipsky, 1997). PEG substrates have also been used to generate patterns of proteins or cells using for example the technique of microcontact printing (Whitesides et al., 2001; Mrksich & Whitesides, 1996; Mrksich et al., 1997). PEG hydrogels are approved by the US Food and Drug Administration (FDA) for oral and topical application; they are little immunogenic and non-toxic at molecular weights above 400 Da. Since PEG itself is not degradable by simple hydrolysis and undergoes only limited metabolism in the body, the whole polymer chains are eliminated through the kidneys or eventually through the liver ( $M_w < 30$  kDa) (Harris, 1992; Knauf et al., 1988).

Many groups have investigated surface coverings of PEG or PEO in order to try to elucidate why PEG has such remarkably effective properties and different theories have been proposed (Jeon et al., 1991; Prime & Whitesides, 1993). First, there are generally only weak attractive interactions between the PEG-coatings and a wide range of proteins, as protein adsorption is generally known to be more pronounced on hydrophobic surfaces in comparison to hydrophilic ones (Morra, 2000). Furthermore, as the interaction between water and PEG via hydrogen bonds is more favorable and surpasses possible attractive interactions of proteins with the surfaces, a repulsion force is created. Therefore the hydration of the layer, i.e. the binding of interfacial water is of high relevance for the exclusion of other molecules coming near the polymer surface (Harris, 1992; Harder et al., 1998). Additionally, molecules approaching the rather flexible, loosely crosslinked PEG hydrogel from the surrounding medium initiate the compression of the extended PEG molecules inducing a steric repulsion effect (Jeon et al., 1991; Morra, 2000). More specifically, a loosely crosslinked gel has relatively long segments between the crosslinks, which can take a relatively large number of conformations. The number of segment conformations would be substantially restricted by the binding of a protein molecule to the gel surface. This

would lead to a relatively large unfavorable entropic change, making the process of protein adsorption very unfavorable for thermodynamic reasons. Additionally, the high mobility of PEG chains allows little time for proteins to form durable attachments.

Many techniques have been developed to create PEG or PEO-bearing surfaces, e.g. exploiting physical adsorption, chemical coupling, and graft polymerization (Harris, 1992; Harris & Zalipsky, 1997; Prime & Whitesides, 1993; Fujimoto et al., 1993; Prime & Whitesides, 1991). Whitesides and co-workers have studied covalent coatings of oligo(ethylene glycol)s, so-called self-assembled monolayers (SAMs) and found that the resistance to protein adsorption increased with the chain length of the oligomers (Prime & Whitesides, 1991 and 1993). Furthermore, it has been demonstrated that the adhesion resistance of PEG increases with chain packing density (Sofia et al., 1998; Malmsten et al., 1998).

In recent years the versatility of star-shaped PEG molecules has been recognized, as they present a high number of end-groups per molecule allowing interconnectivity and functionalization (Groll et al., 2005a & 2005b; Lutolf et al., 2003). Some star polymers have been shown to achieve a high surface coverage and localization of the end-groups near the top of the star polymer (Irvine et al., 1996). Therefore, star-shaped PEG molecules are an interesting and promising alternative to linear PEG.

### **1.3 PEG-based hydrogels formed by UV-curing: patternable biomaterials**

We have been using PEG hydrogels that are prepared by UV-based radical crosslinking of six-armed star-shaped macromonomers via acrylate (Acr) end-groups. The polymer backbone consists of a statistical copolymer of 85 % ethylene oxide and 15 % propylene oxide (P(EO-stat-PO)) and each star molecule bears 6 reactive Acr end-groups. The formal notation of the precursor polymer would thus be Acr sP(EO stat PO). Nevertheless, in the following the resulting, crosslinked network will be denoted PEG-based (hydro)gel, even though the arms of the precursors do not consist of pure PEG, but contain a fraction (15%) of propylene glycol units in the copolymer. These PO-units give the prepolymer its unique and very useful property of being a liquid at room temperature, before crosslinking. The crosslinking reaction was initiated by a UV-based radical reaction with benzoin methyl ether as photoinitiator (PI) and an additional crosslinker (CL) (pentaerythritol triacrylate). Further experimental details concerning the synthesis and the curing conditions can be found in our recent publications (Lensen et al., 2007; Diez et al., 2009).

The hydrogel substrates were applied as free-standing bulk gels for 2D cell culture studies. Due to the fact that the prepolymer Acr-sP(EO-stat-PO) is liquid before crosslinking, the precursor mixture can be molded in any shape, which has enabled us to imprint desired micro- and nanometer topographic patterns into the hydrogel surface (Lensen et al., 2007; Diez et al., 2009). In the following, the properties of this hydrogel system in view of its use in biomedical applications will be evaluated, e.g. the cytotoxicity and cytocompatibility will be assessed, and the cell behavior on the surface of the hydrogels will be demonstrated. Finally, the remarkable effect of surface topography and substrate elasticity on protein adsorption, cell adhesion and cell spreading will be discussed.

## **2. Fabrication and properties of PEG-based substrates**

### **2.1 Synthesis of PEG-based hydrogels from Acr-sP(EO-stat-PO) macromonomers**

Hydrogels fabricated for the application in cell culture studies were crosslinked from Acr-sP(EO-stat-PO) prepolymers. UV-irradiation was used to initiate radical polymerization of the macromonomer mixture with added photoinitiator (PI) and crosslinking agent (CL) (Figure 2).

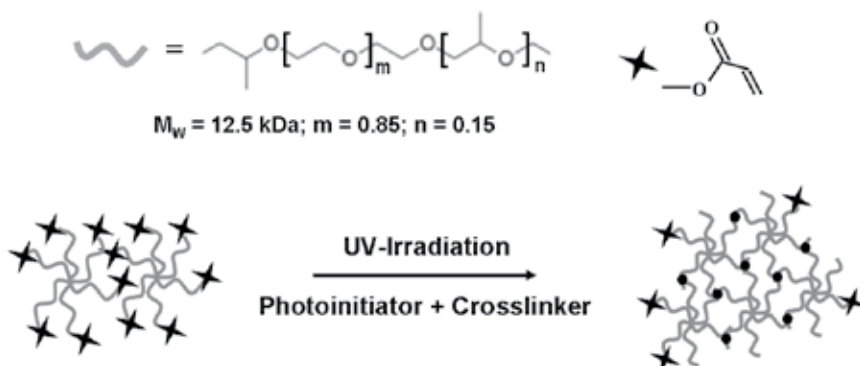


Fig. 2. Fabrication of bulk PEG-based hydrogels by means of UV-curing.

To ensure a complete reaction of the acrylate end-groups which could otherwise undergo undesired reactions with the biological system, the curing kinetics of the system were monitored. It was confirmed that after 10 min more than 90 % of the C-C double bonds of the acrylate end-groups had been consumed. After 60 min only 2.3 % of unreacted end-groups were left. Based on these observations it was decided to apply 60 min of UV-irradiation to the samples in order to achieve virtually complete crosslinking. Bulk PEG-based substrates were fabricated by casting the prepolymer mixture against a smooth silicon surface.

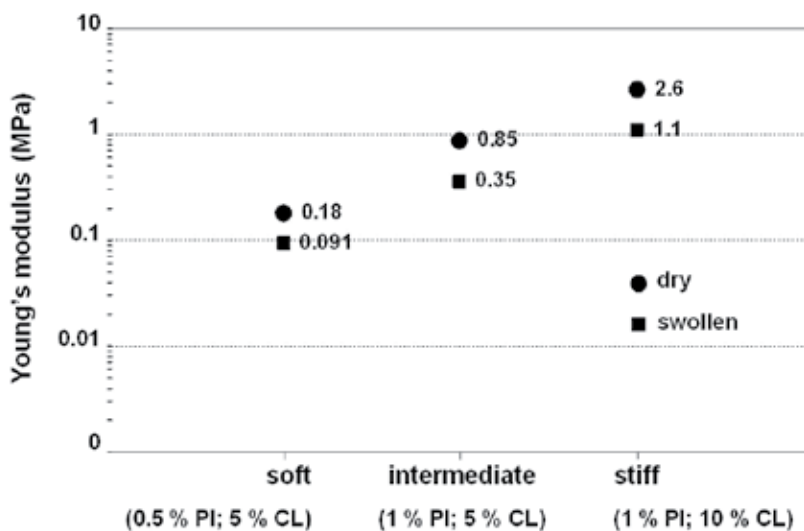


Fig. 3. Young's modulus (MPa) of bulk PEG-based hydrogel samples in dry and swollen state; gels were fabricated from three precursor mixtures with different percentages (w/v) of photoinitiator (PI) and crosslinking agent (CL). Reprinted with permission from: Schulte et al. *Biomacromolecules*, 11, 3375-83. Copyright 2010 American Chemical Society.

The UV-photopolymerization via the acrylate end-groups on the sP(EO-stat-PO) arms does not only allow topographic patterning of the hydrogel's surface, but also enables tuning of the crosslinking density, hence stiffness. Thus, varying the amount of added photoinitiator (PI) and crosslinker (CL) represents a practical approach to controlling the mechanical properties of PEG-based hydrogels (**Figure 3**). This is of high relevance for biomedical applications, as it is well known that cells feel and respond to the stiffness of the underlying substrate (Discher et al., 2005; Engler et al., 2006; Yeung et al., 2005). PEG-based hydrogels with distinctly different mechanical properties were fabricated; the resulting hydrogels from 3 different formulations are denoted as soft, intermediate and stiff (Schulte et al., 2010; Diez et al., 2011).

The stiffness in the swollen state, which is obviously the most relevant for cell culture, was shown to be approximately half of that measured in the dry state, ranging from ~100 kPa for the softest to 1 MPa for the stiffest, thus covering one order of magnitude in elastic modulus (Figure 3).

## 2.2 Cytotoxicity assessment of PEG-based substrates

As the material has not been used in this exact composition before, cytotoxicity tests were conducted to prove that possible traces of unreacted acrylate end-groups, photoinitiator or crosslinker did not interfere with cell viability. The impact of the material on the viability of L929 fibroblasts was tested with an indirect cell test. Cell membrane integrity as an important indicator for cell viability was tested with a commercially available enzymatic assay. Values shown in **Figure 4** were derived by comparison with a control sample of mortalized cells (incubation with DMSO), which was set to 100 % cytotoxicity. It should be noted that no direct test was possible as PEG is known to be anti-adhesive and the majority of the seeded cells would not stay attached to the PEG-substrate and could therefore not be used for quantitative studies.

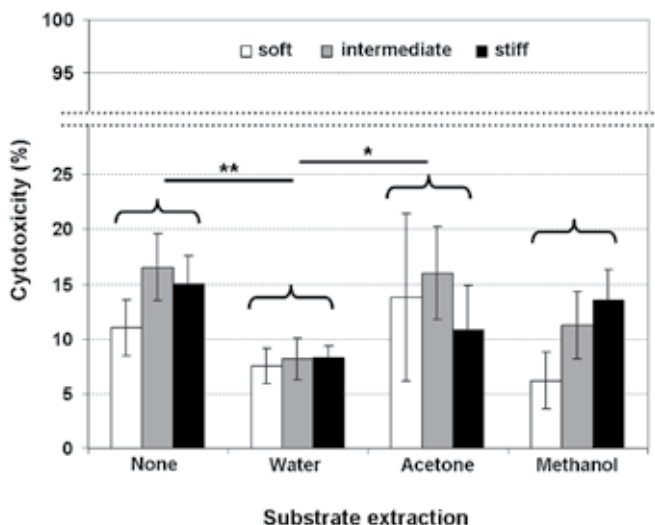


Fig. 4. Cytotoxicity of bulk PEG samples; shown are the results of an indirect cytotoxicity test with L929 cultured for 24 h in PEG conditioned (72 h) medium. The PEG samples had before been extracted in water, acetone or methanol for 24 h. The test was performed in triplicate with substrates of three different crosslinking densities. Statistical significance indicated by \*\*:  $p < 0.01$ ; \*:  $p < 0.05$ .



The percentage of dead cells after 24 h in the indirect cell test with medium that had been conditioned with PEG samples gave values between 7 % and 16 % depending on the sample composition (variations in the amount of PI and CL) and the solvent used for previous extraction of the samples. No significant difference in cytotoxicity could be observed comparing soft, intermediate and stiff samples. Looking at the impact of sample extraction medium, substrates which had been incubated in water for 24 h prior to the test showed the lowest cytotoxic effect. Compared with results gained by extraction with organic solvents (acetone) or without any treatment, the cytotoxicity level detected for the water washed samples was significantly lower ( $p < 0.05$  and  $p < 0.01$ , respectively). As a consequence of these test results PEG samples were stored in sterile water for at least 24 h after the crosslinking process prior to in vitro application.

### 2.3 Fibroblast culture on smooth PEG hydrogel substrates

In order to assess the cytocompatibility of the PEG-based hydrogels in direct contact with cells, L929 cells were cultured directly on the surface of bulk free-standing substrates. Samples of the three introduced elasticities were applied and cell morphology was documented by live imaging after 24 h and 48 h in culture (**Figure 5**). Subsequently, fixed and dried cells were further evaluated by means of electron microscopy (FESEM).

As can be seen in Figure 5, the cell morphology on the three different PEG substrates did not vary significantly, all cells displayed a round shape and only little or no stable cell adhesion was evident. This clearly confirms the cell-repulsive properties of the PEG-based material. Electron microscopy further showed that the rinsing and fixation of the samples led to the removal of a large number of cells. This observation underlines that only a negligible amount of cells was able to establish a contact to the surface. The majority of the cells tended to form aggregates after longer cultivation times. The number of cells visible on the images of the different samples cannot be compared directly as a slight shaking of the medium led to an immediate re-distribution of the cells above the surface.

Based on the observation that the cells were not able to build stable contacts to the surface the consequences for intracellular processes were studied as well. Many anchorage-dependent cell types stop to proliferate or can undergo a programmed cell death (apoptosis) without the presence of integrin-mediated cell-surface contacts (Frisch & Francis, 1994; Gilmore, 2005). The amount of the apoptotic markers caspase-3 and caspase-7 after 48 h of cultivation time on the three different PEG substrates and polystyrene (PS) was assessed with a commercially available assay and compared to a culture where apoptosis was specifically induced by staurosporin addition (values set to 100 %). The results are depicted in **Figure 6**.

As seen in Figure 6, cells cultured on the three different sP(EO-stat-PO) hydrogels did not show an enhanced level of apoptotic activity compared to those seeded on the control substrate PS. This observation is in accordance with results from other groups showing that fibroblasts are not very sensitive to lack of adhesions to a solid substrate if serum is present in the medium (Ishizaki et al., 1995; McGill et al., 1997). There was also no significant difference between the samples with the three different crosslinking degrees. Cell adhesion to PS after 48 h was confirmed by light microscopy.

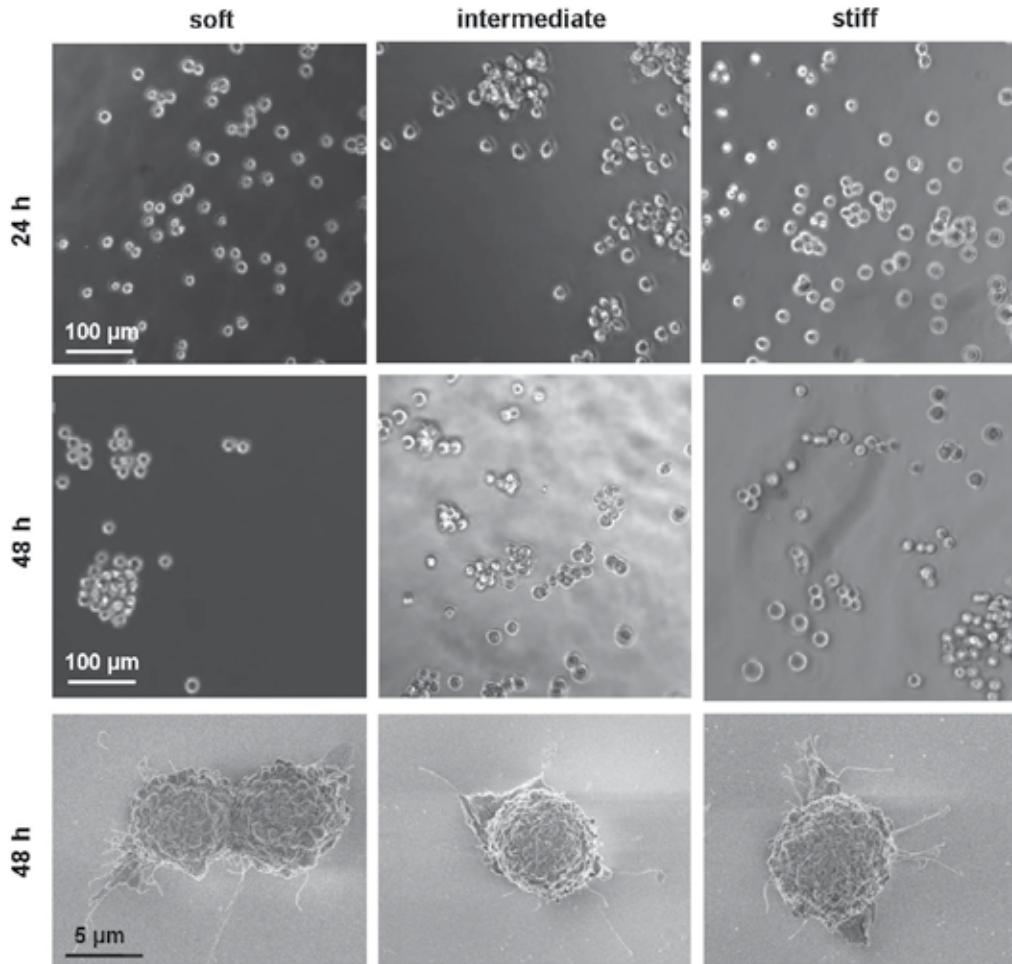


Fig. 5. Microscopic investigation of cytocompatibility of PEG-based hydrogels. L929 fibroblasts were cultured on smooth, bulk PEG samples that were fabricated with different percentages (w/v) of photoinitiator (PI) and crosslinking agent (CL); resulting in different mechanical properties. Cell morphology was monitored by light microscopy at different time points (24 h and 48 h) after initial cell seeding. Electron microscopy images (FESEM) of cells which were fixed and dried after 48 h are shown in the bottom row.

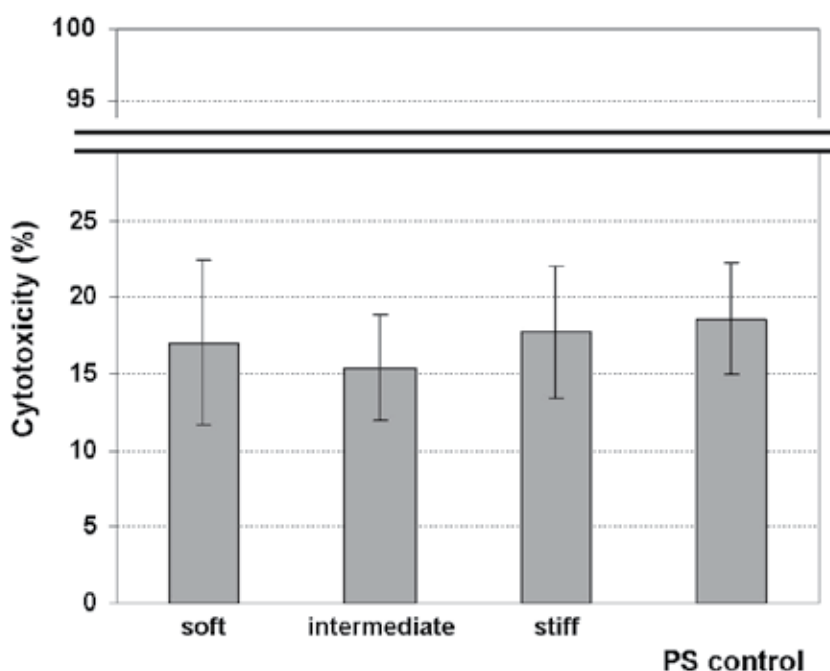


Fig. 6. Apoptotic level of fibroblasts cultured on PEG-based samples. The induction of apoptosis in L929 cells after 48 h cultivation time on smooth PEG samples was quantified with a caspase-3/-7 assay. The samples had before been extracted in water for 24 h. The test was performed in triplicate with substrates of three different crosslinking densities.

#### 2.4 Fibroblast culture on micropatterned PEG hydrogel substrates

While no cell adhesion was observed on the smooth surface of the PEG-based hydrogels, we have discovered that cells do adhere to bulk PEG hydrogels when they are topographically patterned (Lensen et al., 2008; Schulte et al., 2009). **Figure 7** depicts some representative images of fibroblasts adhering to the micropatterned surface of the PEG hydrogels.

In order to explain this observation we have considered that proteins may adsorb to the physically patterned gels and/or that the cells themselves 'feel' the physical pattern and respond on the level of cytoskeletal adaptations. In two follow-up studies we investigated those two (biochemical and biophysical) arguments in more detail. Thus, we examined the possibility of protein adsorption to the gels and we explored the effect of systematic variations of geometry and stiffness of the hydrogels on the enabled cell adhesion.

The first investigation concerned the systematic variation of the deformability of the topographic structures that the cells are assumed to perceive. Although it is unlikely that the cells are able to really deform the micrometer-sized bars, we did envisage that the deformability of the surface structures to depend on the groove width, on the aspect ratio of the bars, and on the inherent mechanical properties of the gels. Thus we prepared line patterns with different groove width (5, 10, 25 and 50  $\mu\text{m}$ ) and depth (5, 10 and 15  $\mu\text{m}$ ). Also we prepared hydrogel formulations resulting in gels with three different stiffnesses, denoted soft ( $\sim 90$  kPa), intermediate ( $\sim 350$  kPa) and stiff ( $\sim 1$  MPa).

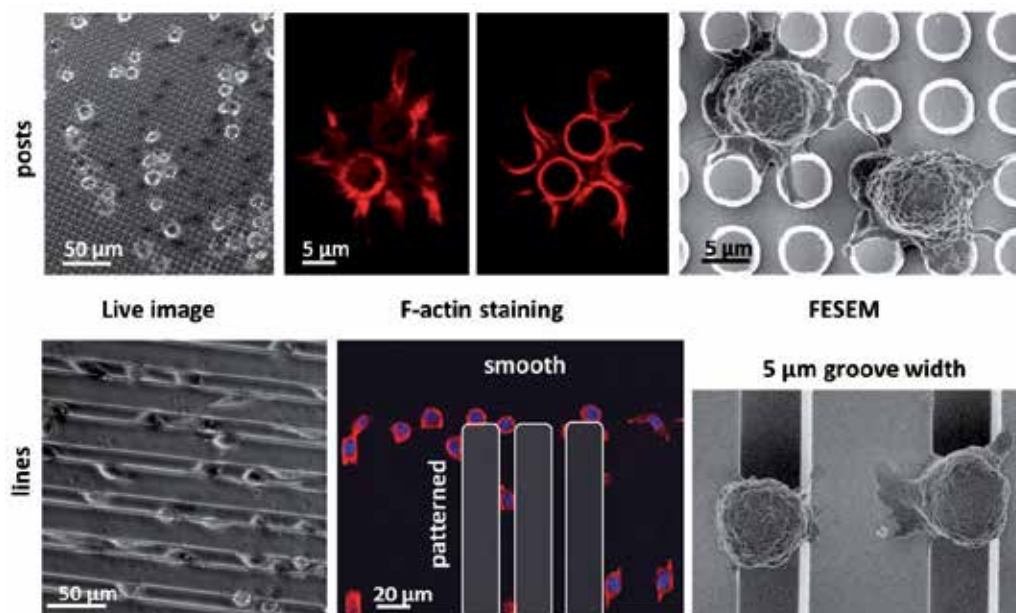


Fig. 7. Reprinted with permission from: Schulte et al., *Biomacromolecules*, 10, 2795–2801. Copyright 2009 American Chemical Society.

We have examined the effect of geometric parameters and of mechanical properties of the hydrogels and found that cells prefer to bind inside of grooves that are of comparable size as their cell body, i.e. 10  $\mu\text{m}$  wide and notably when those 10  $\mu\text{m}$  wide grooves were shallow (5  $\mu\text{m}$  deep). The effect of stiffness variations was only evident in combination with topography, and increased cell adhesion and spreading was observed on the softer gels (Figure 8; Schulte et al., 2010).

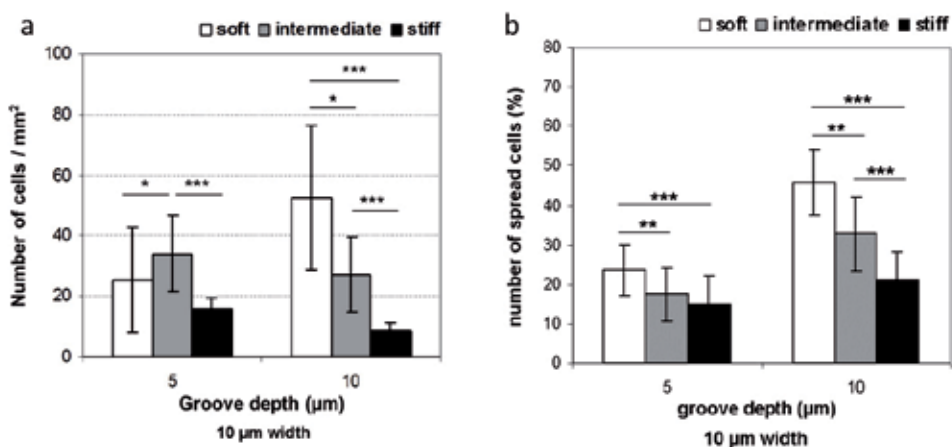


Fig. 8. Cell adhesion (a) and spreading (b) on topographically patterned PEG hydrogels with varied pattern geometries and stiffness. Reprinted with permission from: Schulte et al. *Biomacromolecules*, 11, 3375–83. Copyright 2010 American Chemical Society.

The cells were found to adhere inside the grooves and form adhesion contacts with the side walls as well as to the bottom of the shallower grooves. They were able to adhere to the narrower (5  $\mu\text{m}$  wide) grooves as well, but had to undergo tremendous shape adaptations, including deformation of the cell nucleus, as observed from fluorescence microscopy using selective staining agents for the actin cytoskeleton and for the nucleus (Figure 9, right image). The cells apparently like to snug into well-fitting grooves in a more compliant hydrogel material. No visual deformation of the hydrogels was found; the cells rather adapted their shape to fit into too narrow grooves (i.e. 5  $\mu\text{m}$  wide; Schulte et al., 2010).

Second, we investigated whether proteins could adsorb non-specifically to the gels and if so, if they would adsorb differently on the topographic structures, e.g. preferentially on the walls of the grooves, or on the convex (outer) or concave (inner) corners, since the eventually adherent cells were found to be located inside of the grooves and aligned along the ridges. We incubated the patterned hydrogel samples in protein solutions of three selected extracellular matrix (ECM) proteins, i.e. Fibronectin (FN), Vitronectin (VN) and bovine serum albumin (BSA). The former two are cell adhesion mediating proteins, while BSA does not facilitate cell adhesion. BSA is the most abundant protein in serum, and besides its abundance it is also a small protein, which diffuses fast and reaches the surface faster than the larger proteins FN and VN and finally the cells.

With help of immunological staining using fluorescently labeled antibodies we could demonstrate that from pure protein solutions all three proteins were able to adsorb to the PEG surfaces to a certain extent (Schulte et al., 2011). The fluorescence was homogeneously distributed over the surface; there was no detectable difference between for example the vertical walls or the horizontal planes between the grooves. Finally, it seemed that BSA was able to diffuse into the PEG hydrogels, since the fluorescence was not restricted to the surface (Schulte et al., 2011).

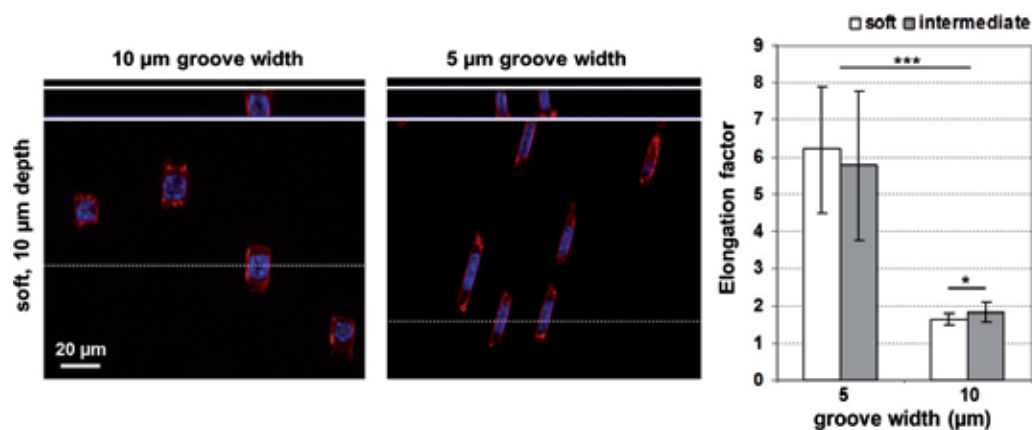


Fig. 9. Elongated cell morphology on topographically patterned PEG hydrogels with 10 or 5  $\mu\text{m}$  wide grooves. Reprinted with permission from: Schulte et al. *Biomacromolecules*, 11, 3375-83. Copyright 2010 American Chemical Society.

Notwithstanding the ability of all three proteins to adsorb to the PEG hydrogel, only VN was observed to adsorb in a detectable amount under competitive conditions, i.e. from a mixture of VN and FN and when serum, a complex mixture of proteins, was supplemented (Table 1; Schulte et al., 2011). This result was rather unexpected, since BSA is usually

observed to adsorb to virtually any surface, and because FN is generally considered to be the most important cell adhesion mediating protein in serum and consequently has been much more studied than VN.

Solution for Incubation		Protein detected by antibody staining	
		VN	FN
FBS	10 % in PBS	+++	
FBS	100 %	+++	
VN	5 µg/ml in PBS	+	+
FN	50 µg/ml in PBS		
VN	5 µg/ml in PBS	++	+
FN	20 µg/ml in PBS		
VN	10 µg/ml in PBS	++	
FN	20 µg/ml in PBS		
VN	10 µg/ml in PBS	+	
FN	50 µg/ml in PBS		

Table 1. Protein adsorption to the surface of the (topographically patterned) PEG-based hydrogel; qualitative results are given for samples that were incubated with serum (100% or 10% in buffer solution) or with buffer solutions containing a mixture of the pure proteins Vitronectin (VN) and Fibronectin (FN) in various ratios. Reproduced from: Schulte et al., (2011) *Macromol. Biosci.* (in press). Copyright 2011 John Wiley and Sons.

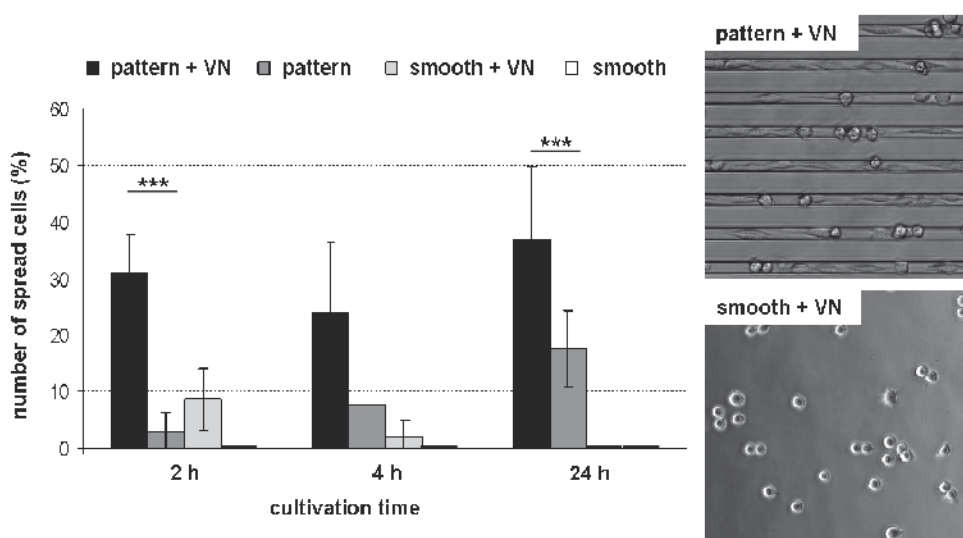


Fig. 10. Cell adhesion on PEG hydrogels enabled by surface topography and/or pre-incubation with the cell adhesion-mediating protein VN. Reproduced from: Schulte et al., *Macromol. Biosci.* (in press). Copyright 2011 John Wiley and Sons.

In order to verify whether this small but significant amount of adsorption of VN to the PEG surface is responsible for the observed cell adhesion on topographically patterned hydrogels we investigated the pre-incubated hydrogels (both smooth and patterned) in cell culture.

We analyzed the number of adherent cells and found an increased number of cells on the VN-incubated hydrogels. This effect was also found for the unpatterned, smooth hydrogels; after VN-incubation a very small but significant number of cells were able to adhere to the PEG surface. In **Figure 10** these results are depicted; comparing smooth and patterned hydrogels with and without VN-incubation.

It can be seen that compared to the effect of topography alone, the VN-incubation alone was less effective in enabling cell adhesion. Remarkably, the effect of VN on cell adhesion was only evident at early time points; after 24 hours the enabling effect was completely lost. Finally, a striking synergistic effect was observed from the combination of VN-incubation and topography; the number of adherent and spread cells was larger than the sum of the individual contributions (Schulte et al., 2011). Taking into account the apparent difference in the effect of topography and VN with time, we tentatively conclude that the cell adhesion protein VN facilitates the initial cell adhesion, while the adhesion-enabling effect of surface topography becomes dominant at longer times and is necessary for the development of durable and stable adhesion complexes.

### 3. Conclusion

Hydrogels are of high relevance for several biomedical applications. We have described the fabrication of a hydrogel system based on poly(ethylene glycol) and evaluated the potential of this PEG-based gel as a patternable biomaterial. PEG-based polymers are of great importance as biomaterials for applications in cell and tissue engineering, as coating of implants or biosensors, and as drug delivery systems. In particular, PEG coatings have been used to minimize surface biofouling by plasma proteins to create surfaces that are “invisible” to cells. Cell biological studies with murine fibroblasts (NIH L929) confirmed the expected non-adhesive nature of the smooth hydrogel surfaces and furthermore ruled out any toxic effect of the material. Alterations of the mechanical properties could easily be achieved by varying the crosslinking density.

The most striking result from our studies is that the very popular and versatile PEG biomaterial is not cell-repellent per se. Only when the surface of the bulk PEG hydrogels is smooth it is anti-adhesive to cells, and this applies to all hydrogels we have investigated with a stiffness ranging from 0.1 to 1 MPa. However, we have discovered that on the same PEG hydrogels when decorated with micropatterns of topography, cells are able to adhere and spread. We have explored several underlying biochemical, biophysical and biomechanical factors that could attribute to this phenomenon and found that these factors do have an effect indeed, and notably the combination of these parameters, e.g. protein adsorption, surface topography and substrate compliance, work together to enable cell adhesion to the intrinsically anti-adhesive PEG biomaterial.

More specifically, three investigated PEG-based hydrogels with different stiffness were all cell anti-adhesive when smooth. However, in combination with topography, the softer gels were clearly more attractive for the cells; on softer gels with the same pattern geometry, significantly more cells adhered and spread than on the intermediate or stiffer gels. It seems that the compliance of the softer gels enables the cells to ‘squeeze’ into the grooves, although the cells apparently deform their own cytoskeleton rather than the topographic features.

We also discovered that a slight but significant amount of the ECM-protein Vitronectin is able to adsorb to the PEG surface and that this leads to an increase in initial cell adhesion during the first 4 hours of cell culture. However, this effect rapidly falls off. The effect of

topography is a more durable effect that dominates at longer time scales, suggesting its role in the enabling of stable adhesion complexes, which is a process that occurs during more than several hours. We consider that the topographic features may provide shelter to the cells and prolong their residence time inside of the grooves. Added to this, the 'pulling' of the cells on the weakly bound cell adhesion proteins may be less effective when they are confined between the vertical walls than when the surface is smooth; as a consequence focal adhesion contacts can develop into stable focal adhesion complexes.

Thus, the combination of different (bio)chemical, physical and mechanical properties of the PEG hydrogels results in the observed cell adhesion on this intrinsically anti-adhesive biomaterial. The effects are difficult to disentangle, and marked synergistic effects were observed for example when using topographically patterned hydrogels that were incubated with Vitronectin prior to cell culture.

As PEG is generally well known for its anti-adhesive properties and is widely applied in biomedical applications, it is important to take into consideration what our study has shown: physical and mechanical surface properties can impede the anti-adhesive characteristics of PEG. On the other hand it also opens new opportunities for biomimetic material design which does not rely on complicated and expensive biochemical surface functionalization for manipulating cellular responses.

#### 4. Acknowledgment

The author gratefully acknowledge funding from the Alexander von Humboldt Foundation and the Federal Ministry for Education and Research (BMBF) in the form of a Sofja Kovalevskaja Award (M. C. L.) and from the DFG Graduate School "Biointerface" (GRK 1035).

#### 5. References

- Andrade, J. D. & Hlady, V. (1986) Protein adsorption and materials biocompatibility - a tutorial review and suggested hypotheses. *Adv. Polym. Sci.*, 79, 1-63.
- Andrade, J. D.; Hlady, V.; Wei, A. P.; Ho, C. H.; Lea, A. S.; Jeon, S. I.; Lin, Y. S. & Stroup, E. (1992) Proteins at interfaces principles multivariate aspects protein resistant surfaces and direct imaging and manipulation of adsorbed proteins. *Clin. Mater.*, 11, 67-84.
- Baroli, B. (2006) Photopolymerization of biomaterials: Issues and potentialities in drug delivery, tissue engineering, and cell encapsulation applications. *J. Chem. Technol. Biot.*, 81, 491-9.
- Castner, D. G. & Ratner, B. D. (2002) Biomedical surface science: Foundations to frontiers. *Surf. Sci.*, 500, 28-60.
- Castillo, E. J.; Koenig, J. L.; Anderson, J. M. & Lo, J. (1985) Protein adsorption on hydrogels. 2. Reversible and irreversible interactions between lysozyme and soft contact-lens surfaces. *Biomaterials*, 6, 338-45.
- Chapman, R. G.; Ostuni, E.; Takayama, S.; Holmlin, R. E.; Yan, L. & Whitesides, G. M. (2000) Surveying for surfaces that resist the adsorption of proteins. *J. Am. Chem. Soc.*, 122, 8303-4.
- Cushing, M. C. & Anseth, K. S. (2007) Hydrogel cell cultures. *Science*, 316, 1133-4.



- Desai, N. P.; Hossainy, S. F. A. & Hubbell, J. A. (1992) Surface-immobilized polyethylene oxide for bacterial repellence. *Biomaterials*, 13, 417-20.
- Diez, M.; Mela, P.; Seshan, V.; Möller, M.; Lensen, M. C. Nanomolding of PEG-based hydrogels with sub-10-nm resolution. *Small* 2009, 5, 2756-60.
- Diez, M.; Schulte, V. A.; Stefanoni, F.; Natale, C. F.; Mollica, F.; Cesa, C. M.; Chen, Y.; Möller, M.; Netti, P. A.; Ventre, M. & Lensen, M. C. (2011) Molding Micropatterns of Elasticity on PEG-based Hydrogels to Control Cell Adhesion and Migration *Adv. Eng. Mater. (Adv. Biomater.)*, 13 (4): n/a. doi: 10.1002/adem.201080122, in press.
- Discher, D. E.; Janmey, P. & Wang, Y. L. (2005) Tissue cells feel and respond to the stiffness of their substrate. *Science*, 310, 1139-43.
- Drumheller, P. D. & Hubbell, J. A. (1995) Densely cross-linked polymer networks of poly(ethylene glycol) in trimethylolpropane triacrylate for cell-adhesion-resistant surfaces. *J. Biomed. Mater. Res.*, 29, 207-15.
- Elbert, D. L. & Hubbell, J. A. (1996) Surface treatments of polymers for biocompatibility. *Annu. Rev. Mater. Sci.*, 26, 365-94.
- Engler, A. J.; Sen, S.; Sweeney, H. L. & Discher, D. E. (2006) Matrix elasticity directs stem cell lineage specification. *Cell*, 126, 677-89.
- Fedorovich, N. E.; Alblas, J.; de Wijn, J. R.; Hennink, W. E.; Verbout, A. J. & Dhert, W. J. A. (2007) Hydrogels as extracellular matrices for skeletal tissue engineering: State-of-the-art and novel application in organ printing. *Tissue Eng.*, 13, 1905-25.
- Fisher, J. P.; Dean, D.; Engel, P. S. & Mikos, A. G. (2001) Photoinitiated polymerization of biomaterials. *Ann. Rev. Mater. Res.*, 31, 171-81.
- Frisch, S. M. & Francis, H. (1994) Disruption of epithelial cell-matrix interactions induces apoptosis. *J. Cell Biol.* 124, 619-26.
- Fujimoto, K.; Inoue, H. & Ikada, Y. (1993) Protein adsorption and platelet-adhesion onto polyurethane grafted with methoxy-poly(ethylene glycol) methacrylate by plasma technique. *J. Biomed. Mater. Res.*, 27, 1559-67.
- Gilmore, A. P. (2005) Anoikis. *Cell Death Differ.* 12, 1473-7.
- Groll, J.; Ameringer, T.; Spatz, J. P. & Möller, M. (2005a) Ultrathin coatings from isocyanate-terminated star PEG prepolymers: Layer formation and characterization. *Langmuir*, 21, 1991-9.
- Groll, J.; Fiedler, J.; Engelhard, E.; Ameringer, T.; Tugulu, S.; Klok, H. A.; Brenner, R. E. & Möller, M. (2005b) A novel star PEG-derived surface coating for specific cell adhesion. *J. Biomed. Mater. Res. Part A*, 74A, 607-17.
- Harder, P.; Grunze, M.; Dahint, R.; Whitesides, G. M. & Laibinis, P. E. (1998) Molecular conformation in oligo(ethylene glycol)-terminated self-assembled monolayers on gold and silver surfaces determines their ability to resist protein adsorption. *J. Phys. Chem. B*, 102, 426-36.
- Harris, J. H. (1992) *Poly(ethylene glycol) chemistry: Biotechnical and biomedical applications*. Plenum Press: New York.
- Harris, J. H. & Zalipsky, S. (1997) *Poly(ethylene glycol) chemistry: Chemistry and biomedical applications*. Am. Chem. Soc.: Washington D.C.
- Hlady, V. & Buijs, J. (1996) Protein adsorption on solid surfaces. *Curr. Opin. Biotech.*, 7, 72-7.
- Hoffman, A. S. (2002) Hydrogels for biomedical applications. *Adv. Drug Deliv. Rev.*, 54, 3-12.

- Horbett, T. A. (1993) Principles underlying the role of adsorbed plasma-proteins in blood interactions with foreign materials. *Cardiovasc. Pathol.*, 2, S137-S48.
- Irvine, D. J.; Mayes, A. M. & Griffiths, L. (1996) Self-consistent field analysis of grafted star polymers. *Macromolecules*, 29, 6037-43.
- Ishizaki, Y.; Cheng, L.; Mudge, A. W. & Raff, M. C. (1995) Programmed cell-death by default in embryonic-cells, fibroblasts, and cancer-cells. *Mol. Biol. Cell*, 6, 1443-58.
- Jen, A. C.; Wake, M. C. & Mikos, A. G. (1996) Review: Hydrogels for cell immobilization. *Biotechnol. Bioeng.*, 50, 357-64.
- Jeon, S. I.; Lee, J. H.; Andrade, J. D. & Degennes, P. G. (1991) Protein surface interactions in the presence of polyethylene oxide .1. Simplified theory. *J. Colloid Interface Sci.*, 142, 149-58.
- Jhon, M. S. & Andrade, J. D. (1973) Water and hydrogels. *J. Biomed. Mater. Res.*, 7, 509-22.
- Knauf, M. J.; Bell, D. P.; Hirtzer, P.; Luo, Z. P.; Young, J. D. & Katre, N. V. (1988) Relationship of effective molecular-size to systemic clearance in rats of recombinant interleukin-2 chemically modified with water-soluble polymers. *J. Biol. Chem.*, 263, 15064-70.
- Krsko, P. & Libera, M. (2005) Biointeractive hydrogels. *Materials today*, 8, 36-44.
- Krsko, P.; Kaplan, J. B. & Libera, M. (2009) Spatially controlled bacterial adhesion using surface-patterned poly(ethylene glycol) hydrogels. *Acta Biomater.*, 5, 589-96.
- Langer, R. & Peppas, N. A. (2003) Advances in biomaterials, drug delivery, and bionanotechnology. *AIChE J.*, 49, 2990-3006.
- Langer, R. & Tirrell, D. A. (2004) Designing materials for biology and medicine. *Nature*, 428, 487-92.
- Lee, K. Y. & Mooney, D. J. (2001) Hydrogels for tissue engineering. *Chem. Rev.*, 101, 1869-79.
- Lensen, M. C.; Mela, P.; Mourran, A.; Groll, J.; Heuts, J.; Rong, H. T. & Möller, M. (2007) Micro- and nanopatterned star poly(ethylene glycol) (PEG) materials prepared by UV-based imprint lithography. *Langmuir*, 23, 7841-6.
- Lensen, M. C.; Schulte, V. A.; Salber, J.; Díez, M.; Menges, F. R. & Möller, M. (2008) Cellular responses to novel, micro-patterned biomaterials *Pure Appl. Chem.* 11, 2479-2487.
- Lutolf, M. P.; Raeber, G. P.; Zisch, A. H.; Tirelli, N. & Hubbell, J. A. (2003) Cell-responsive synthetic hydrogels. *Adv. Mater.*, 15, 888-92.
- Malmsten, M.; Emoto, K. & Van Alstine, J. M. (1998) Effect of chain density on inhibition of protein adsorption by poly(ethylene glycol) based coatings. *J. Colloid Interface Sci.*, 202, 507-17.
- McGill, G.; Shimamura, A.; Bates, R. C.; Savage, R. E. & Fisher, D. E. (1997) Loss of matrix adhesion triggers rapid transformation-selective apoptosis in fibroblasts. *J. Cell Biol.*, 138, 901-11.
- Merrill, E. W.; Salzman, E. W.; Wan, S.; Mahmud, N.; Kushner, L.; Lindon, J. N. & Curme, J. (1982) Platelet-compatible hydrophilic segmented polyurethanes from polyethylene glycols and cyclohexane diisocyanate. *Trans. Am. Soc. Artif. Intern. Organs.*, 28, 482-7.
- Morra, M. (2000) On the molecular basis of fouling resistance. *J. Biomater. Sci.-Polym. E.*, 11, 547-69.

- Mrksich, M. & Whitesides, G. M. (1996) Using self-assembled monolayers to understand the interactions of man-made surfaces with proteins and cells. *Annu. Rev. Biophys. Biomolec. Struct.*, 25, 55-78.
- Mrksich, M.; Dike, L. E.; Tien, J.; Ingber, D. E. & Whitesides, G. M. (1997) Using microcontact printing to pattern the attachment of mammalian cells to self-assembled monolayers of alkanethiolates on transparent films of gold and silver. *Exp. Cell Res.*, 235, 305-13.
- Nguyen, K. T. & West, J. L. (2002) Photopolymerizable hydrogels for tissue engineering applications. *Biomaterials*, 23, 4307-14.
- Peppas, N. A. (1986) *Hydrogels in medicine and pharmacy: Fundamentals*. CRC Press: Boca Raton.
- Peppas, N. A.; Bures, P.; Leobandung, W. & Ichikawa, H. (2000) Hydrogels in pharmaceutical formulations. *Euro. J. Pharm. Biopharm.*, 50, 27-46.
- Peppas, N. A.; Hilt, J. Z.; Khademhosseini, A. & Langer, R. (2006) Hydrogels in biology and medicine: From molecular principles to bionanotechnology. *Adv. Mater.*, 18, 1345-60.
- Prime, K. L. & Whitesides, G. M. (1991) Self-assembled organic monolayers - model systems for studying adsorption of proteins at surfaces. *Science*, 252, 1164-7.
- Prime, K. L. & Whitesides, G. M. (1993) Adsorption of proteins onto surfaces containing end-attached oligo(ethylene oxide) - a model system using self-assembled monolayers. *J. Am. Chem. Soc.*, 115, 10714-21.
- Saha, K.; Pollock, J. F.; Schaffer, D. V. & Healy, K. E. (2007) Designing synthetic materials to control stem cell phenotype. *Curr. Opin. Chem. Biol.*, 11, 381-7.
- Schulte, V. A.; Diez, M.; Möller, M. & Lensen, M. C. (2009) Surface Topography induces Fibroblast Adhesion on intrinsically non-adhesive Poly(ethylene Glycol) Substrates *Biomacromolecules*, 10, 2795-2801.
- Schulte, V. A.; Diez, M.; Hu, Y.; Möller, M. & Lensen, M. C. (2010) The combined influence of substrate elasticity and surface topography on the anti-adhesive properties of poly(ethylene glycol). *Biomacromolecules*, 11, 3375-83.
- Schulte, V. A.; Diez, M.; Hu, Y.; Möller, M. & Lensen, M. C. (2011) Topography induced cell adhesion to Acr-sP(EO-stat-PO) hydrogels: the role of protein adsorption *Macromolecular Bioscience* in press
- Sofia, S. J.; Premnath, V. & Merrill, E. W. (1998) Poly(ethylene oxide) grafted to silicon surfaces: Grafting density and protein adsorption. *Macromolecules*, 31, 5059-70.
- Tessmar, J. K. & Gopferich, A. M. (2007) Customized PEG-derived copolymers for tissue-engineering applications. *Macromol. Biosci.*, 7, 23-39.
- Tsai, W.-B.; Grunkemeier, J. M.; McFarland, C. D. & Horbett, T. A. (2002) Platelet adhesion to polystyrene-based surfaces pre-adsorbed with plasmas selectively depleted in fibrinogen, fibronectin, vitronectin, or von willebrand's factor. *J. Biomed. Mater. Res.*, 60, 348-59.
- Wahlgren, M. & Arnebrant, T. (1991) Protein adsorption to solid-surfaces. *Trends Biotechnol.*, 9, 201-8.
- Veronese, F. M. & Mero, A. (2008) The impact of pegylation on biological therapies. *Biodrugs*, 22, 315-29.

- Whitesides, G. M.; Ostuni, E.; Takayama, S.; Jiang, X. Y. & Ingber, D. E. (2001) Soft lithography in biology and biochemistry. *Annu. Rev. Biomed. Eng.*, 3, 335-73.
- Wichterle, O. & Lim, D. (1960) Hydrophilic gels for biological use. *Nature*, 185, 117-8.
- Yeung, T.; Georges, P. C.; Flanagan, L. A.; Marg, B.; Ortiz, M.; Funaki, M.; Zahir, N.; Ming, W. Y.; Weaver, V. & Janmey, P. A. (2005) Effects of substrate stiffness on cell morphology, cytoskeletal structure, and adhesion. *Cell Motil. Cytoskeleton*, 60, 24-34.
- Zhang, M. Q.; Desai, T. & Ferrari, M. (1998) Proteins and cells on PEG immobilized silicon surfaces. *Biomaterials*, 19, 953-60.

# A Preliminary In Vivo Study on the Histocompatibility of Silk Fibroin

Lu Yan<sup>1</sup>, Zhao Xia<sup>1</sup>, Shao Zhengzhong<sup>2</sup>, Cao Zhengbing<sup>2</sup> and Cai Lihui<sup>1</sup>

<sup>1</sup>*Department of Otorhinolaryngology, Huashan Hospital, Fudan University, Shanghai*

<sup>2</sup>*Department of Macromolecule Science, Fudan University, Shanghai, China*

## 1. Introduction

Biomaterials used for tissue engineering should have the property of good histocompatibility, superb plasticity and desired degradability, so that it can be extensively applied for defect tissue repairing with excellent clinical outcome. In the past decade, silk fibroin has become one of the most favored biomaterials for its wide availability, superb performance and readiness to be shaped for different purposes in tissue engineering<sup>[1-14]</sup>. Porous scaffolds made by silk fibroin can be made into different pore size and porosity to serve for different needs of tissue repairing. The porous structure may contribute to the mass exchange in the scaffolds. However, the implanted protein scaffolds will degrade and can hardly be separated from host tissues. Therefore, little has been reported on histocompatibility experiment in vivo for silk fibroin<sup>[15-22]</sup>.

In this chapter, progress in study of silk fibroin scaffold in tissue engineering application and biocompatibility research will be introduced, then our histocompatibility experiment of porous scaffolds will be reported. In our experiment, porous scaffolds were made platy and buried in subcutaneous part of the back of SD rat. Tissue reaction was observed, and the value of silk fibroin as tissue engineering scaffold material was discussed.

## 2. The application of silk fibroin in tissue engineering

It is known to all that the application of silk production as un-absorb suture has many years of history. Along with the progress of tissue engineering techniques, scientists can extract natural polymeric materials- fibroin from silk and make it into different forms to fit various needs of tissue engineering<sup>[1]</sup>. Vitro studies show silk fibroin is biodegradable. The speed and degree of degradation can be adjusted through changing physicochemical property<sup>[2-4]</sup>. The product of degradation is mainly free amino acid and has no toxic side-effect on tissue.

Silk fibroin can be easily made into different forms to serve for various needs such as membrane, gelatum, knitting scaffold, porous scaffold and electrospinning scaffold. Therefore, it has been gradually utilized in various medical field such as drug delivery<sup>[5,6]</sup>, nerve regeneration<sup>[7-9]</sup>, dermis healing<sup>[10]</sup>, artificial ligament repair<sup>[11,12]</sup>, bone or cartilage healing<sup>[13,14]</sup>, vascular tissue engineering<sup>[15,16]</sup>, otology application<sup>[17]</sup> and so on.

### 3. Biocompatibility research of silk fibroin

Silk fibroin has been utilized as natural biomaterial in tissue engineering applications. Many researches have been made *in vitro* to reveal its attractive properties such as slow-controllable degradation, mechanical robustness, and inherent biocompatibility<sup>[18-21]</sup>.

For the silk fibroin scaffolds are made up of proteins, those materials which have been implanted will degrade and could hardly be separated from host tissues, that made the study of histocompatibility difficult. Therefore, few report can be found about research on biocompatibility and degradation of porous fibroin scaffolds *in vivo* <sup>[4,22]</sup>.

### 4. Our *in vivo* research on the histocompatibility of silk fibroin

#### 4.1 Materials and methods

**Laboratory animals:** 8 healthy female Sprague-Dawley rat, body weight 220g~250g, get from department of laboratory animal medicine, Fudan University

**Preparation method of porous silk fibroin scaffold:** After degummed, the raw silk was dissolved into aqueous solution of LiBr (lithium bromide). The silk fibroin solution was adjusted to the concentration of 20% after filtration and concentration. Then n-butyl alcohol was added into the solution as volume ratio of 2: 1. Mixed solution was added into self-made mould after low-speed agitation, and white porous scaffold was obtained after freeze drying. The average pore size of the scaffold was between 10 and 20um.

**Material preparation:** We cut the porous silk fibroin scaffolds to 1cm×1cm squares (about 1 mm thick), infused the material into 75% ethanol solution for 0.5 hour, then immersed the materials into 0.9% NaCl water for 24 hours.

**Technique:** After peritoneal injection anesthesia, we longitudinal incised the skin of back open, blunt dissected surrounding tissues, and buried the porous silk fibroin scaffolds subcutaneous. Then we sew up the incision and raised the animals in different captivities.

**Histological examination** The rats were executed 2,4,6,8 weeks after operation. General observation and hematoxylin and eosin stain histological examination was performed.

#### 4.2 Result and discussion

**General observation** Animals recovered well after operation. Throughout the period of implantation, all scaffolds were well tolerated by the host animals and immune responses to the implants were mild. No obvious systemic reaction, abnormal eating and sleeping behaviors were found. The implant sample in animals' back hunched mildly. The wounds and surrounding skin healed well when drawing materials at different times (figure 1). No obvious hyperemia, seepage or purulent exudates signs were found in surrounding skin and muscular tissue. The surface of the scaffolds was wrapped up by the thin, semitransparent fibrous membranes. There was no obvious change in shape and appearance after implanting (figure 2). The inflammatory reaction surrounding the tissue was slight. And no obvious granulation was found. (table 1)

**The second week:** Fibroin scaffold is eosinophilic staining. The surface is not regular while there are big or small pores inside. Hematoxylin-eosin staining microscopic examination (table 2). Fibroblast grows adherently on the surface of the material. The surrounding tissue hyperplasticly changes, inflammatory cell infiltrate is visible, most of which are lymphocytes and macrophages. No signs of tissue necrosis are found. (figure 3,4)



Fig. 1. The wound healed up well while taking samples



Fig. 2. Thin connective tissue wrap could be found on the scaffold, and the inflammatory reaction surrounding the tissue was slight.

Time(week)	Section number	inflammatory reaction	fibrous encapsulation	granulation formation
2	2	slight	yes	no
4	2	slight	yes	no
6	2	slight	yes	no
8	2	slight	yes	no

Table 1. general observation

**The fourth week:** There is few parts with eosinophilic staining inside the material disappears 4 weeks after operation, which shows crumbling phenomenon, while it's general structure remains (figure 5). Fibroblasts grow along the surface of the scaffold or into the pores. There are lymphocytes and macrophages infiltrate. Vessel hyperplasia is visible,

while new capillary vessel inside the material is obvious. No signs of tissue necrosis are (figure 6).

**The sixth week:** There are a few parts with eosinophilic staining inside the material disappears 6 weeks after operation, which shows crumbling phenomenon, while it's general structure remains. Inflammatory cell infiltrate is visible 6 weeks after operation. Histocytes gradually grow deep into the scaffold. No signs of tissue necrosis are. (figure 7,8)

**The eighth week:** Histocytes grow more deeply into the scaffold. Inflammatory cell infiltrate is visible, most of which are macrophages. Vessel hyperplasia reduces inside the tissue, while hyperblastosis still obvious. No signs of tissue necrosis are. (figure 9,10)

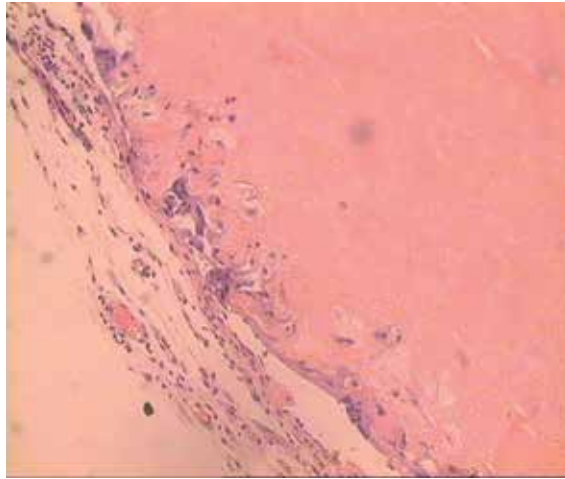


Fig. 3. Fibroblast grows adherently on the surface of the material two weeks after operation. The surrounding tissue hyperplasticly changes, inflammatory cell infiltrate is visible, most of which are lymphocytes and macrophages. No signs of tissue necrosis are found. ( $\times 200$ )

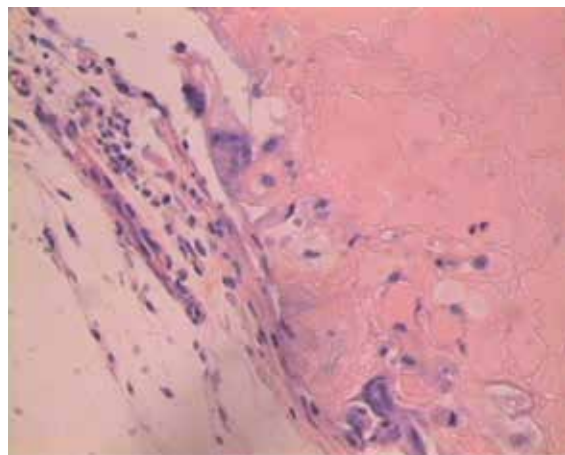


Fig. 4. Fibroin scaffold is eosinophilic staining. The surface is not regular while there are big or small pores inside. Fibroblasts grow adherently on the surface of the material. Inflammatory cell infiltrate is visible, most of which are lymphocytes and macrophages. ( $\times 400$ )



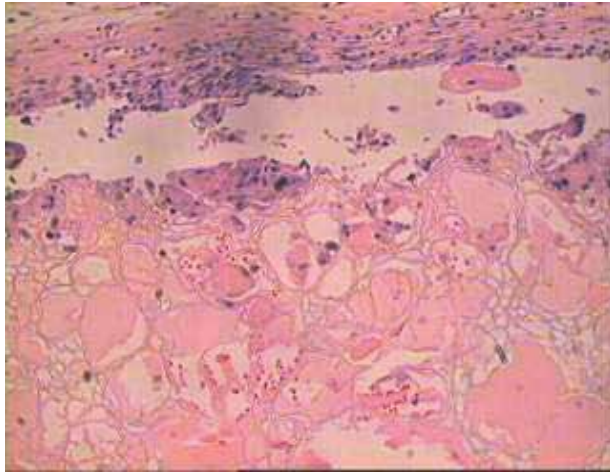


Fig. 5. There is few parts with eosinophilic staining inside the material disappears 4 weeks after operation, which shows disaggregation phenomenon, while it's general structure remains. ( $\times 200$ )

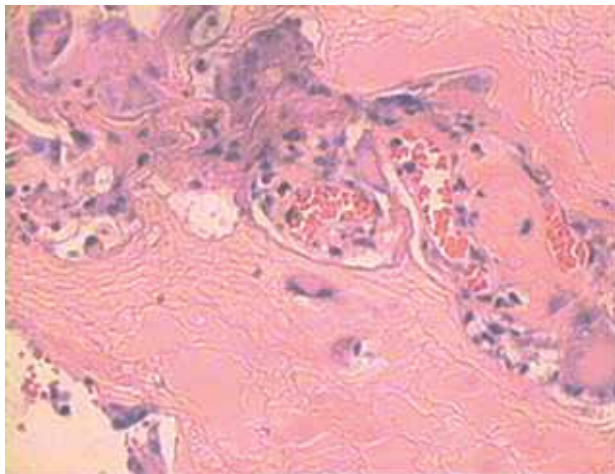


Fig. 6. Fibroblasts grow along the surface of the scaffold or into the pores. There are lymphocytes and macrophages infiltrate. Vessel hyperplasia is visible, while new capillary vessel inside the material is obvious. No signs of tissue necrosis are found. ( $\times 400$ )

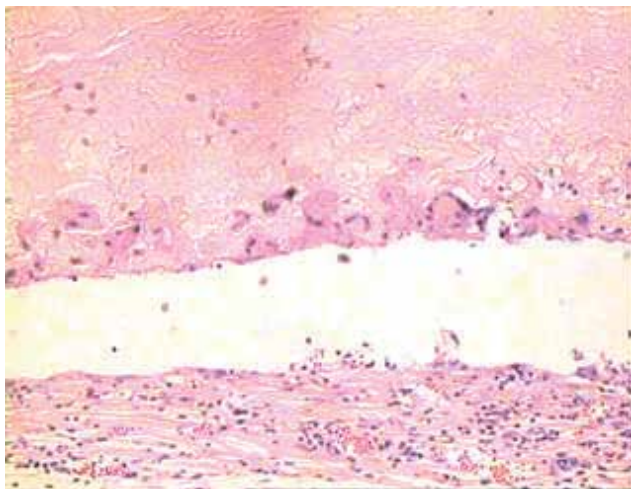


Fig. 7. Inflammatory cell infiltrate is visible 6 weeks after operation. Histiocytes gradually grow deep into the scaffold. No signs of tissue necrosis are found. ( $\times 200$ )

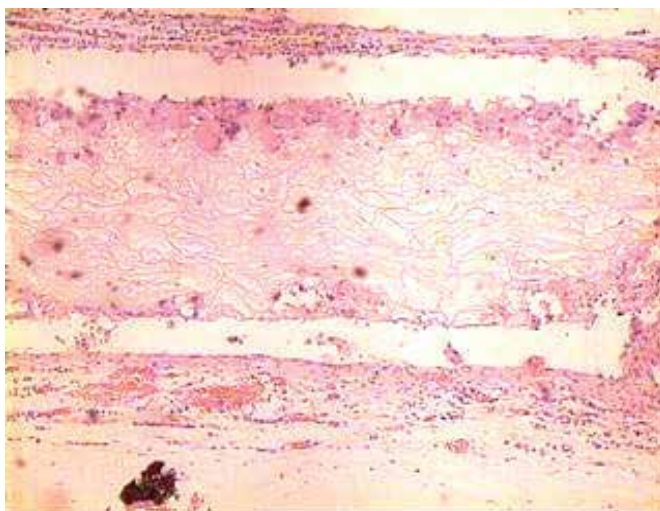


Fig. 8. There are a few parts with eosinophilic staining inside the material disappears 6 weeks postoperatively, which shows disaggregation phenomenon, while it's general structure remains. ( $\times 200$ )

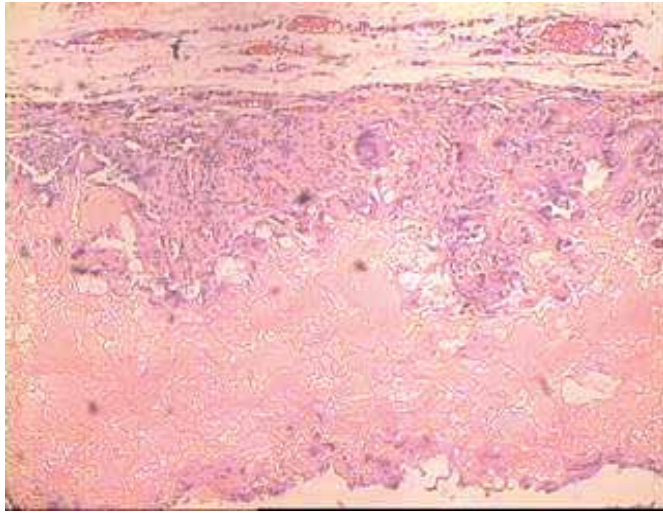


Fig. 9. Histocytes grow more deeply into the scaffold. Inflammatory cell infiltrate is visible, most of which are macrophages. Vessel hyperplasia reduces inside the tissue, while hyperblastosis still obvious. No sign of tissue necrosis is found. ( $\times 200$ )

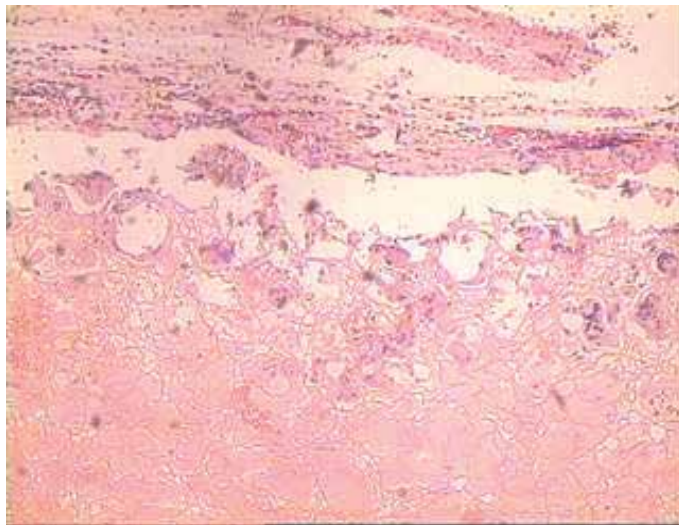


Fig. 10. The border of the scaffold break down at some part 8 weeks postoperatively, while the inside part remains as it was. ( $\times 200$ )

Time section (week)number	fibration	inflammatory cell type	Scaffold disaggregation	tissue necrosis	tissue ingrowth
2	2	yes	lymphocyte and macrophage	no	yes
4	2	yes	lymphocyte and macrophage	yes	no
6	2	yes	lymphocyte and macrophage	yes	no
8	2	yes	mostly macrophage	yes	no

Table 2. histopathology observation

Porous scaffolds made by silk fibroin can be formed into different pore size and porosity, which could meet the needs of different histocytes during repairing process. Porous structure is also helpful to the exchange of nutrient substance among different parts of scaffolds. So we choose the porous silk fibroin scaffold as the research object.

Biological material will be treated as foreign matter when implanted in the body, even if its biocompatibility is perfectly good. Therefore, foreign body reaction will be inevitable surrounding the material. The strength and extent of foreign body reaction are closely related to its biocompatibility and biodegradability. So, we evaluate the tissue reaction and material change after implantation by fibrous encapsulation, granulation formation · tissue fibrosis, type of inflammatory cells, tissue necrosis and tissue ingrowth, morphological changes and disaggregation of the scaffolds.

We found that wet porous fibroin scaffold was soft in texture, and could be easily cut into different forms to fit the need of implantation while the operation was performed. Tissue reaction around the materials was slight when we removed the scaffold, and the surface of the material was wrapped up by semitransparent fibrous membranes. The porous fibroin scaffolds were eosinophilic stained by HE. Its surface was irregular. And there are lacunes of different size inside the material. Chronic inflammation reaction occurred, mainly lymphocytes and macrophages could be found around the material. And fibrous capsule could be observed. After two weeks of implantation, blood capillary could be found proliferate into the lacuna of the material, and the fibroblasts also attached to the irregular surface of the material. These phenomena became more and more obvious as time went by, which showed that the surface texture of porous fibroin was favourable for interstitial cell to grow on. Moreover, the porous structure of the scaffold made the material permeable, which could probably cause the exchange of the nutrition and metabolite through the scaffold that lead to active tissue ingrowth. This may also be a plus factor for tissue regeneration.

Because the fibroin scaffolds were formed by protein and could hardly be separated from surrounding tissues, histopathology observation was performed after experiment instead of quantitative determination. During eight-weeks' observation, the scaffold disintegration started from the fourth week. But there was still no obvious change inside the scaffold structure until the eighth week, which indicated to us that we should set the observation period much longer to get more information about the degradation of fibroin porous scaffold in further research. We didn't make effective statistical analysis about the quantity and type of inflammatory cells surrounding the scaffold for the number of samples was too small. Moreover, according to the requirements of different tissue repair, the pore size and porosity of porous scaffolds should be different. And materials with different structure may cause different result in tissue reaction, tissue regeneration and material degradation. These are also challenging questions that need to be considered in further experiment.

## 5. Conclusion

To sum up, porous silk fibroin scaffold shows good histocyte attachment and has good histocompatibility. The Porous silk fibroin scaffold can degrade in vivo, but more study should be made on the mechanism and degradation products.

## 6. References

- Murphy AR, Kaplan DL. Biomedical applications of chemically-modified silk fibroin. *J Mater Chem*. 2009 Jun 23;19(36):6443-6450.
- Rebecca L. Horan, Kathryn Antle, Adam L. Collette, etc. In vitro degradation of silk fibroin. *Biomaterials*, Volume 26, Issue 17, June 2005, Pages 3385-3393
- Cao Y, Wang B. Biodegradation of silk biomaterials. *Int J Mol Sci*. 2009 Mar 31;10(4):1514-24.
- Wang Y, Rudym DD, Walsh A, etc. In vivo degradation of three-dimensional silk fibroin scaffolds. *Biomaterials*. 2008 Aug-Sep;29(24-25):3415-28.
- Lammel AS, Hu X, Park SH, etc. Controlling silk fibroin particle features for drug delivery. *Biomaterials*. 2010 Jun;31(16):4583-91.
- Wang X, Yucel T, Lu Q, etc. Silk nanospheres and microspheres from silk/pva blend films for drug delivery. *Biomaterials*. 2010 Feb;31(6):1025-35.
- Lu yan, Chi fang-lu, Zhao Xia, etc. Experimental study on facial nerve regeneration by porous silk fibroin conduit. *Zhonghua Er Bi Yan Hou Tou Jing Wai Ke Za Zhi*. 2006, 41(8),603-606.
- Yang Y, Ding F, Wu J, Development and evaluation of silk fibroin-based nerve grafts used for peripheral nerve regeneration. *Biomaterials*. 2007 Dec;28(36):5526-35.
- Tang X, Ding F, Yang Y, etc. Evaluation on in vitro biocompatibility of silk fibroin-based biomaterials with primarily cultured hippocampal neurons. *J Biomed Mater Res A*. 2009 Oct;91(1):166-74.
- Guan G, Bai L, Zuo B, etc. Promoted dermis healing from full-thickness skin defect by porous silk fibroin scaffolds (PSFSs). *Biomed Mater Eng*. 2010;20(5):295-308.
- Bosetti M, Boccafosci F, Calarco A, etc. Behaviour of human mesenchymal stem cells on a polyelectrolyte-modified HEMA hydrogel for silk-based ligament tissue engineering. *J Biomater Sci Polym Ed*. 2008;19(9):1111-23.
- Altman GH, Horan RL, Lu HH, et al . Silk matrix for tissue engineered anterior cruciate ligaments. *Biomaterials*, 2002, 23(20): 4131-4141.
- Meinel L, Fajardo R, Hofmanna S, et al . Silk implants for the healing of critical size bone defects. *Bone*, 2005, 37(5): 688-698.
- Hofmann S, Hagenmuller H, Koch AM, et al . Control of in vitro tissue-engineered bone-like structures using human mesenchymal stem cells and porous silk scaffolds. *Biomaterials*, 2007, 28(6): 1152-1162.
- Zhou J, Cao C, Ma X, etc. Electrospinning of silk fibroin and collagen for vascular tissue engineering. *Int J Biol Macromol*. 2010 Nov 1;47(4):514-9.
- Tamada Y. Sulfation of silk fibroin by chlorosulfonic acid and the anticoagulant activity. *Biomaterials*, 2004, 25(3): 377-383.
- Levin B, Redmond SL, Rajkhowa R, etc. Preliminary results of the application of a silk fibroin scaffold to otology. *Otolaryngol Head Neck Surg*. 2010 Mar;142(3 Suppl 1):S33-5.

- Ghanaati S, Orth C, Unger RE, etc. Fine-tuning scaffolds for tissue regeneration: effects of formic acid processing on tissue reaction to silk fibroin. *J Tissue Eng Regen Med.* 2010 Aug;4(6):464-72.
- Mandal BB, Das T, Kundu SC. Non-bioengineered silk gland fibroin micromolded matrices to study cell-surface interactions. *Biomed Microdevices.* 2009 Apr;11(2):467-76.
- Acharya C, Ghosh SK, Kundu SC. Silk fibroin protein from mulberry and non-mulberry silkworms: cytotoxicity, biocompatibility and kinetics of L929 murine fibroblast adhesion. *J Mater Sci Mater Med.* 2008 Aug;19(8):2827-36.
- Yang Y, Chen X, Ding F, etc. Biocompatibility evaluation of silk fibroin with peripheral nerve tissues and cells in vitro. *Biomaterials.* 2007 Mar;28(9):1643-52.
- Etienne O, Schneider A, Kluge JA, etc. Soft tissue augmentation using silk gels: an in vitro and in vivo study. *J Periodontol.* 2009 Nov;80(11):1852-8.

# Histopathological Effect Characteristics of Various Biomaterials and Monomers Used in Polymeric Biomaterial Production

Serpil Ünver Saraydin<sup>1</sup> and Dursun Saraydin<sup>2</sup>

<sup>1</sup>*Cumhuriyet University, Faculty of Medicine, Department of Histology and Embryology Sivas,*

<sup>2</sup>*Cumhuriyet University, Faculty of Science, Department of Chemistry Sivas, Turkey*

## 1. Introduction

When a synthetic material is placed within the human body, tissue reacts towards the implant in a variety of ways depending on the material type. The mechanism of tissue interaction (if any) depends on the tissue response to the implant surface. In general, there are three terms in which a biomaterial may be described in or classified into representing the tissues responses. These are bioinert, bioresorbable, and bioactive.

Biomaterials are often used and/or adapted for a medical application, thus comprises whole or part of living structures or biomedical devices which performs, augments, or replaces biological functions. Biomaterials are used in dental and surgical applications, in controlled drug delivery applications. A biomaterial may be an autograft, an allograft or a xenograft used as a transplant material.

Biomaterials are mostly polymers produced by monomers, and are used in artificial organ production in contemporary medicine. They are prepared by the polymerization reaction of certain monomers.

In several previous studies, we investigated whether acrylamide, methacrylamide, N-isopropylacrylamide, acrylic acid, 2-hydroxyethyl methacrylate, 1-vinyl-2-pyrrolidone and ethylene glycol had cytotoxic effects and induced apoptosis or not in spinal cord. Immunolocalization of glial fibrillary acidic protein (GFAP) was also determined, and it was evaluated by using semi-quantitative morphometrical techniques. The cytotoxicity of monomers on cultured fibroblastic cell lines was also examined *in vitro*.

Acrylic acid had the most cytotoxic effect when compared to the methacrylamide and the ethylene glycol groups. GFAP immunoreactivity was found to be rather stronger in the methacrylamide than the other monomers application groups. The methacrylamide, acrylic acid, N-vinyl pyrrolidone, acrylamide, N-isopropylacrylamide and 2-hydroxyethyl methacrylate application groups had TUNEL positive cells when compared to the other groups. While some monomers used in biomaterial production seemed not to affect the cell viability and GFAP immunoreactivity, some other monomers had adverse effects on those features. This in turn may contribute to the pathological changes associated to the monomer type.

In our previous other works, *in vitro* swelling and *in vivo* biocompatibility of radiation crosslinked acrylamide and its co-polymers such as acrylamide (AAM) and acrylamide/crotonic acid (AAM/CA), acrylamide/itaconic acid (AAM/IA), and acrylamide/maleic acid (AAM/MA) hydrogels were investigated.

The radiation crosslinked AAM, AAM/CA, AAM/IA and (AAM/MA) co-polymers were found to be well tolerated, non-toxic and highly biocompatible.

On the other hand, calcium phosphate ceramics and xenografts have been used in different fields of medicine and dentistry. We demonstrated the effects of calcium phosphate ceramics (Ceraform) and xenograft (Unilab Surgibone) in the field of experimentally created critical size parietal bone defects in rats. Although Ceraform was less resorptive and not osteoconductive properties, it could be considered as a biocompatible bone defect filling material having a limited application alternative in dentistry and medicine. However, xenograft seems biocompatible, osteoconductive, and could be used in a limited manner as a filling material in osseous defects in clinical practice.

## 2. Toxicological effect of the water-soluble monomers

### 2.1 Monomers

Monomer is a molecule of any of a class of compounds, mostly organic, that can react with other molecules of the same or other compound to form very large molecules, or polymers. The essential feature of a monomer is polyfunctionality, the capacity to form chemical bonds to at least two other monomer molecules. Bifunctional monomers can form only linear, chainlike polymers, but monomers of higher functionality yield cross-linked, network polymeric products. Toxicological effects of the monomers are changing from very low (zero) to very high.

Some polymeric biomaterials such as hydrogels are produced by the effect of initiator such as chemical initiator, heat, light or high energy radiation from the water soluble-monomers.

### 2.2 Cytotoxic effects

Biomaterial suitable for a biomedical application must be biocompatible at least on its surface. In several previous studies, we investigated whether acrylamide, methacrylamide, N-isopropylacrylamide, acrylic acid, 2-hydroxyethyl methacrylate, 1-vinyl-2-pyrrolidone and ethylene glycol used in polymeric biomaterial production had cytotoxic effects (Unver Saraydin et al., 2011). The cytotoxicity of xenograft (one of the alternative graft materials) was also examined *in vitro* (Unver Saraydin et al., 2011).

The viability of cultured fibroblastic cell lines following all monomer applications except for the ethylene glycol group were found to be decreased in all time intervals (Figure 1, 2), and differences were statistically significant ( $p < 0.05$ ). In addition, the cell viability was significantly ( $p < 0.05$ ) lower in the acrylamid application group when compared to the control group. Acrylic acid demonstrated the maximum cytotoxic effect when compared to the methacrylamide and ethylene glycol groups. On the other hand, the ethylene glycol group showed no cytotoxicity for cells (Graphic 1).

In our study of the xenograft cytotoxic activities, the xenograft showed no cytotoxicity for the cells (Figure 3). There was no decolorization zone around the samples. Although the cells were directly in contact with the xenograft in the culture media, they did not show any signs of injury and preserved their morphological characteristics and wholeness like those seen in the controls.





Fig. 1. Fibroblast viability %100 after 12 h incubation period with ethylene glycol

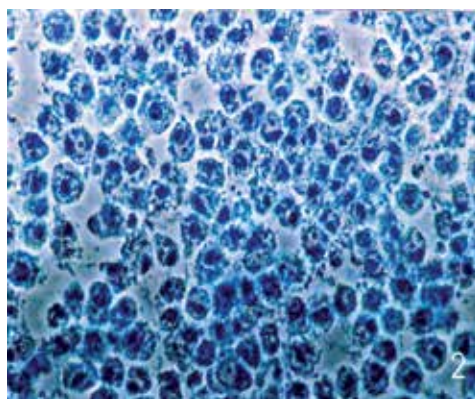
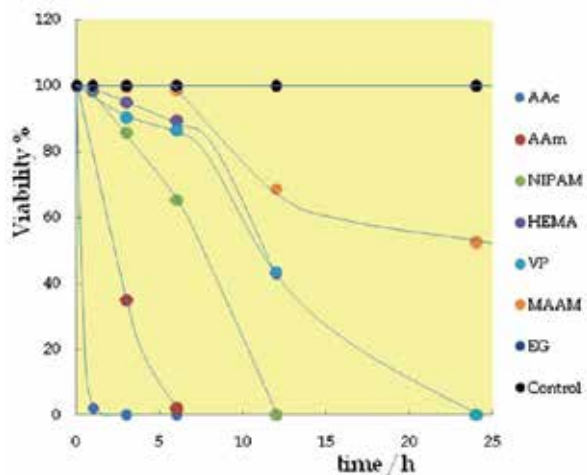


Fig. 2. Fibroblast viability % 0 after 12h incubation period with N-isopropyl acrylamide



Graphic 1. Shows the cell viability alterations between time groups in the fibroblastic cell lines by the time.

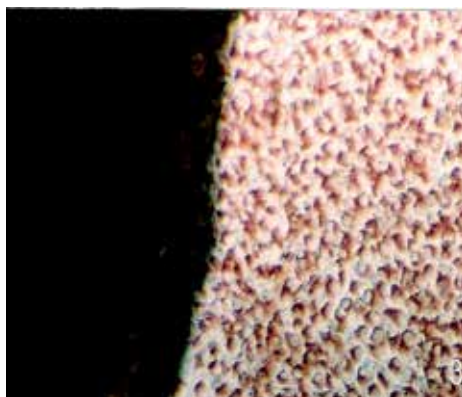


Fig. 3. There is no cytotoxicity for the cells.

### 2.3 Neurotoxic effects

Several studies revealed neurotoxic effects as well as ataxia and muscle weakness caused by biomaterials on humans and on laboratory animals. It has been suggested that they cause axonal degeneration in central and peripheral nervous system (Barber et al., 2001).

Astrocytes are the stellate glial cells in the central nervous system, which play a major role in supporting neurons, scar formation and development and maintenance of the blood-brain barrier. The physiological and metabolic properties of astrocytes indicate that those cells are involved in the regulation of water, ions, neurotransmitters, and pH of the neuronal milieu (Montgomery 1994). They are also implicated in protection against toxic insults such as excitotoxicity and oxidative stress (Lamigeon et al., 2001). Glial fibrillary acidic protein (GFAP) is an intermediate filament protein found predominantly in astrocytes (McLendon 1994). Therefore it is important to determine the glial fibrillary acidic protein (GFAP) immunoreactivity in astrocytes for the evaluation of biomaterials.

In our study, immunolocalization of glial fibrillary acidic protein (GFAP) was determined, and it was evaluated by using semi-quantitative morphometrical techniques (Unver Saraydin et al., 2011). GFAP immunoreactivity was found to be very strong in the methacrylamide, N-isopropylacrylamide, ethylene glycol and N-vinyl pyrrolidone application groups whereas it was weak in acrylic acid, acrylamide and 2-hydroxyethyl methacrylate applied groups (Table 1, Figure 4-10). Changes in GFAP immunoreactivity could be due to following conditions; astrocyte dysfunction, astrocyte loss accompanied by astroglial cell proliferation, de-differentiation, and changes in functional state of neuronal cell types, thus altering the neuron-glial homeostasis. The over-expression of GFAP could probably indicate the protective strategy of these tissues.

Although the neurotoxicity of acrylamide and many monomers has been known since 1950s, its mechanisms have remained obscure (Lee et al., 2005, Gold and Schaumburg, 2000). Acrylamide increases p53 protein (Okuno et al., 2006), recent studies indicate that it plays a role in apoptotic cell death in neurons (Morrison et al., 2003). Acrylamide can activate caspase-3 and cause apoptosis in neuronal cells (Sumizawa and Igisu, 2007). The cellular process of apoptosis is an important component of tissue and organ development as well as the natural response to disease and injury (David et al., 2003). DNA fragmentation in neurons was characterized by double staining with terminal deoxynucleotidyl transferase-mediated deoxyuridine triphosphate-biotin nick end labeling (TUNEL) (Bao and Liu, 2004). To our knowledge, however, it has not been determined whether acrylamide and other

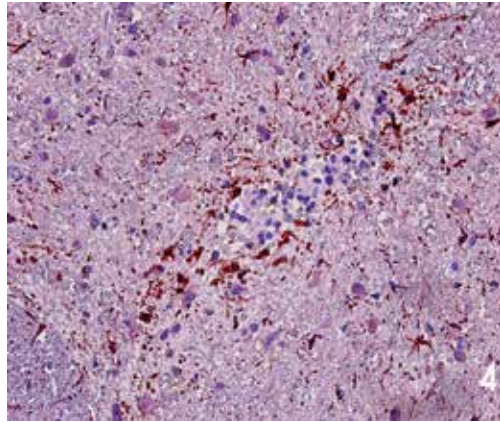


Fig. 4. Control group GFAP immunoreactivity. GFAP40X

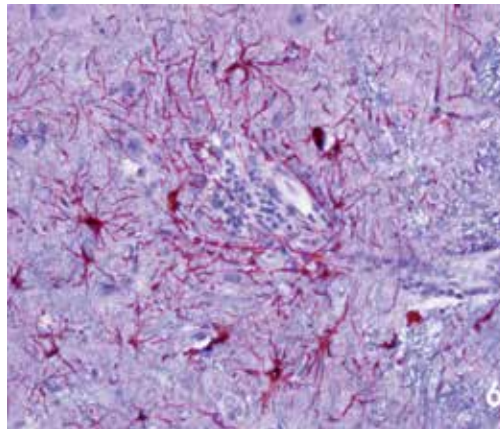


Fig. 5. GFAP immunoreactivity 6 week after Acrylic acid exposure. GFAP 40X

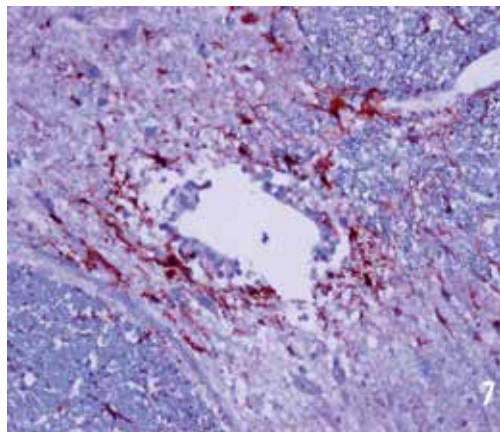


Fig. 6. GFAP immunoreactivity 2 week after Acrylamide exposure. GFAP 40X

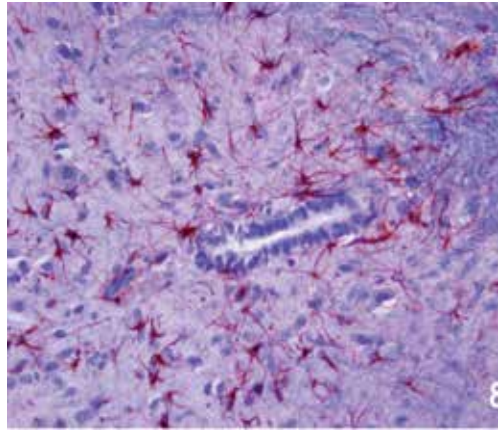


Fig. 7. GFAP immunoreactivity 6 week after 2-hydroxyethyl methacrylate exposure GFAP 40X

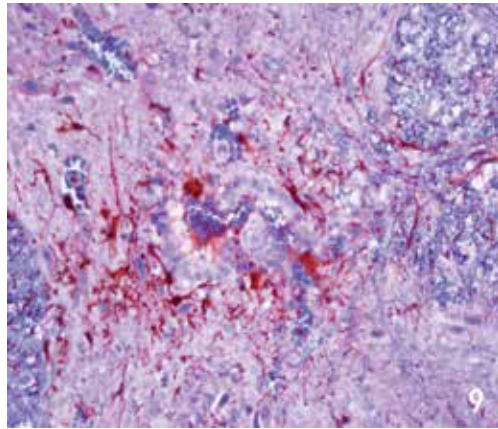


Fig. 8. GFAP immunoreactivity 4 week after methacrylamide exposure GFAP 40X

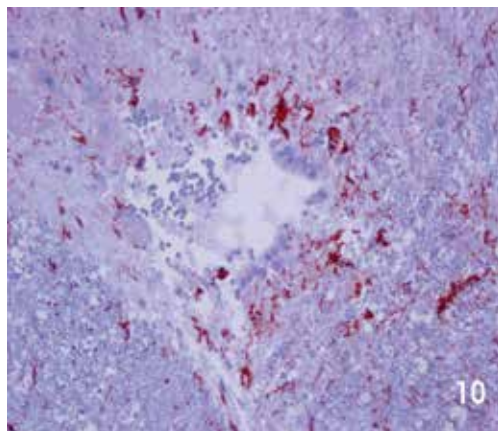


Fig. 9. GFAP immunoreactivity 6 week after N-isopropylacrylamide exposure GFAP 40X

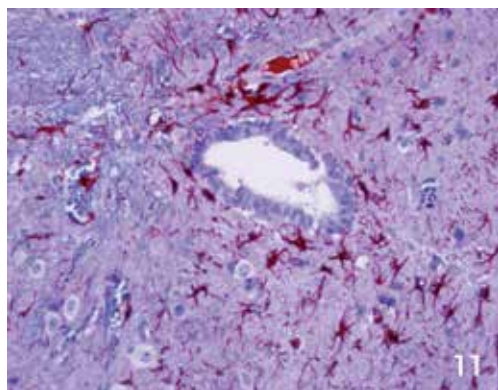


Fig. 10. GFAP immunoreactivity 4 week after N-vinyl pyrrolidone exposure. GFAP 40X

Monomer	1st week	2nd week	4th week	6 th week	12 th week
Ethylene glycol	++	++	+++	++	++
N-vinyl pyrrolidone	+++	+++	+++	+++	++
2-hydroxyethyl methacrylate	+	++	+++	++	++
Acrylamide	++	++			
Methacrylamide	+++	+++	++	++	+
N-isopropylacrylamide	+++	+++	+++	+++	
Acrylic acid	+	++		++	++
Control	+++	+++	+++	+++	+++

Table 1. Demonstrates the semi-quantitative scoring findings of GFAP immunolocalization in rat medullaspinalis following 1, 2, 4, 6 and 12 weeks of particular monomer applications

monomers cause apoptosis in neuronal cells. We therefore examined apoptosis by using terminal deoxynucleotidyl transferase dUTP nick and labelling (TUNEL) method in spinal cord (Unver Saraydin et al., 2011).

While TUNEL positive cells has been detected rarely in the control and in the ethylen glycol application groups, numerous TUNEL positive cells were intensively observed in the spinal cord of the methacrylamide, acrylic acid, N-vinyl pyrrolidine, acrylamide, N-isopropylacrylamide and 2-hydroxyethyl metacrylate application groups (Figure 11-14).

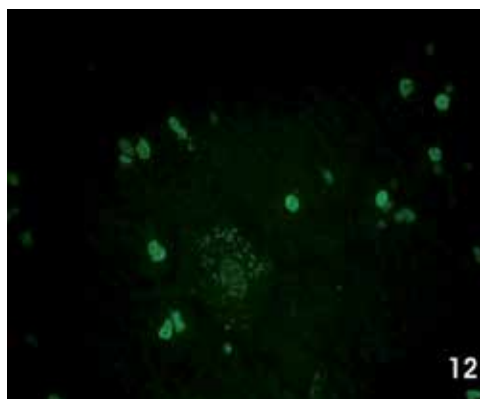


Fig. 11. TUNEL-positive apoptotic cells in the control group. TUNEL 100X

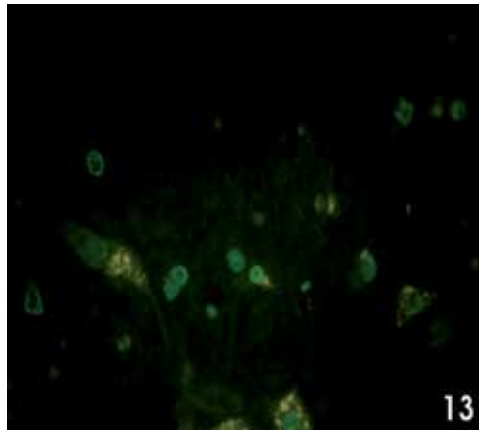


Fig. 12. TUNEL positive cells 6 week after 2-hydroxyethyl methacrylate. TUNEL 100X

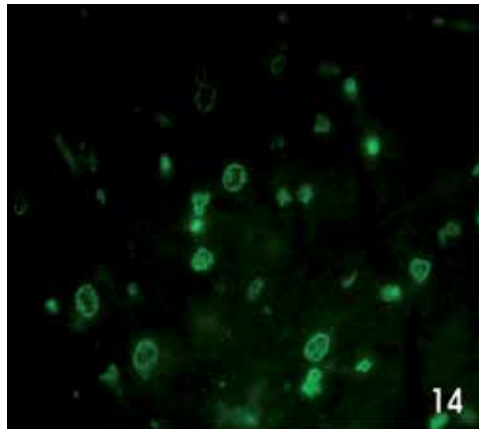


Fig. 13. TUNEL positive cells 6 week after N-isopropylacrylamide. TUNEL 100X

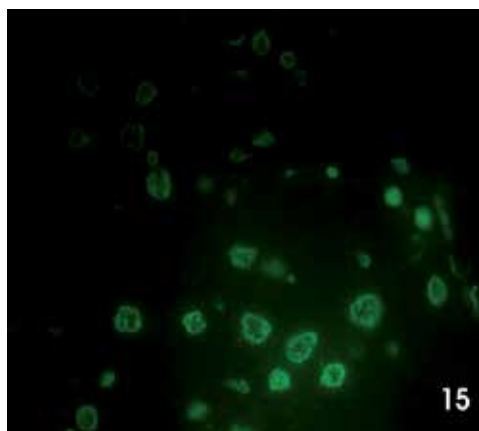


Fig. 14. TUNEL positive cells 6 week after N-vinyl pyrrolidone. TUNEL 100X

### 3. Polymeric biomaterials

Some polymeric biomaterials such as hydrogels are made of water-soluble molecules, connected usually by covalent bonds, forming a three-dimensional insoluble network. The space between chains is accessible for diffusion of solutes and this space is controllable by the level of cross-linked (connected) molecules. They usually show good biocompatibility in contact with blood, body fluids, and tissues. Therefore, they are very often used as biomaterials for medical purposes, for instance contact lenses, coating of catheters, etc.

Biomaterials are defined as materials that can be interfaced with biological systems in order to evaluate, treat, augment, or replace any tissue, organ, or function of the body.

The clinical application of a biomaterial should not cause any adverse reaction in the organism and should not endanger the life of the patient; any material to be used as part of a biomaterial device has to be biocompatible. The definition of biocompatibility includes that the material has to be nontoxic, non-allergenic, noncarcinogenic, and non-mutagenic, and that it does not influence the fertility of a given patient. Preliminary use of *in vitro* methods is encouraged as screening tests prior to animal testing. In order to reduce the number of animals used, these standards use a step-wise approach with review and analysis of test results at each stage. Appropriate *in vitro* investigations can be used for screening prospective biomaterials for estimations of toxic effect. Cytotoxicity *in vitro* assay is the first test to evaluate the biocompatibility of any material for use in biomedical devices (Rogero et.al. 2003).

Hydrogels can be synthesized by accomplishing crosslinking via  $\gamma$ -irradiation (Güven, O; et.al. 1999, Saraydın et.al. 1995, 2002, Karadağ et. al. 2004). However, little work is done on the biomedical applications of the hydrogels prepared by crosslinking of a homo- or copolymer in solution with  $\gamma$ -irradiation. It is well known that the presence of an initiator and a crosslinking agent affects the macromolecular structure and phase behavior of hydrophilic polymers in solution and contributes to inhomogeneity of the network structure. It is argued that more homogeneous network structures can be synthesized, if crosslinking is accomplished with  $\gamma$ -irradiation in the absence of an initiator and a crosslinking agent. The structural homogeneity of the network affects the swelling behavior and mechanical properties that improved the biological response of materials and subsequently the performance of many medical devices (Benson 2002). Thus, looking to the significant consequences of biocompatibility of biomaterials, we, in the present study, are reporting the results on the biocompatibility with the copolymeric hydrogels prepared with acrylamide (AAm) and crotonic acid (CA) or itaconic acid (IA) or maleic acid (MA) via radiation technique. The selection of AAm as a hydrophilic monomer for synthesizing hydrogel rests upon the fact that it has low cost, water soluble, neutral and biocompatible, and has been extensively employed in biotechnical and biomedical fields. On the other hand, CA monomer consists of single carboxyl group, while IA and MA monomers are consisting of double carboxyl groups. These carboxylic acids could provide the different functional characteristics to acrylamide-based hydrogels. So, these monomers were selected for the preparation of the hydrogels and their biocompatibility studies.

In our previous other works, *in vitro* swelling and biocompatibility of blood *in vivo* biocompatibility of radiation crosslinked acrylamide co-polymers such as acrylamide (AAm), acrylamide/crotonic acid (AAm/CA), acrylamide/itaconic acid (AAm/IA) and

acrylamide/maleic acid (AAM/MA) hydrogels were investigated (Saraydin et al., 1995, Karadağ et. al. 1996, Saraydin et al., 2001, 2004).

### 3.1 In vitro swelling of the hydrogels in the simulated body fluids

In this stage of the study, the swelling of the hydrogels in the simulated physiological body fluids was investigated (Saraydin et al., 1995, Karadağ et. al. 1996).

The phosphate buffer at pH 7.4 (pH of cell fluid, plasma, edema fluid, synovial fluid, cerebrospinal fluid, aqueous humour, tears, gastric mucus, and jejunal fluid), glycine-HCl buffer at pH 1.1 (pH of gastric juice), human sera, physiological saline and distilled water intake of initially dry hydrogels were followed for a long time until equilibrium (Saraydin et al., 2001, 2002).

The fluid absorbed by the gel network is quantitatively represented by the EFC (equilibrium body fluids content), where:  $EFC\% = [\text{mass of fluid in the gel} / \text{mass of hydrogel}] \times 100$ . EFCs of the hydrogels for all physiologically fluids were calculated. The values of EFC% of the hydrogels are tabulated in Table 2.

Simulated body fluid	AAM	AAM /CA	AAM /MA	AAM /IA
Distilled Water	86.3	93.9	94,7	92.0
Isoosmotic phosphate buffer	87.5	93.8	89,7	92.2
Gastric fluid	87.7	93.6	92,4	88.7
physiological saline	87.8	92.9	89,7	88.7
Human Sera	88.6	92.5	89.8	86.4
In rat	89.0	93.1	91.9	91.7

Table 2. EFC values of the hydrogels

All EFC values of the hydrogels were greater than the percent water content values of the body about 60%. Thus, the AAM and AAM/CA, AAM/MA and AAM/IA hydrogels were exhibit similarity of the fluid contents with those of living tissues.

### 3.2 In vitro blood biocompatibility

In the second stage of this study, the biocompatibility of the hydrogels was investigated against some biochemical parameters of human sera at 25 °C.

The mean and standard deviation values of control and test groups for biochemical parameters of human sera are listed in Table 3.

Table 3 shows that the values of means of control and test groups are in the range of normal values and there is no significant difference in values before and after contacting these sera with the hydrogels. On the other hand, Student's t-test is applied to control and test groups. No significant difference in values of biochemical parameters was found.

### 3.3 In vivo tissue biocompatibility

In this part, hydrogels based on copolymer of AAM, AAM/MA, AAM/CA and AAM/IA with capacity of absorbing a high water content in biocompatibility with subcutaneous tissues of rats were examined. After one week implantation, no pathology such as necrosis, tumorigenesis or infection were observed in the excised tissue surrounding the hydrogels and in skin, superficial fascia and muscle tissues in distant sites. After 2–4 weeks, thin fibrous capsules were thickened. A few macrophage and lymphocyte were observed in



Biochemical parameters of Normal human serum / Unit	Normal values	Control	AAm	AAm/CA	AAm/MA	AAm/IA
Glucose/mg dl <sup>-1</sup>	70-110	87.0±8.2	91.0± 6.1	88.1±3.99	88.8±6.0	88.4±5.30
Triglyceride/mg dl <sup>-1</sup>	40-160	127.3±24.6	127.0±25.8	130.6±19.9	127.2±25.1	125.6±20.7
Cholesterol/mg dl <sup>-1</sup>	125-350	158.6±10.9	160.6±14.3	159.8±11.3	157.8±10.8	160.6±14.3
BUN/mg dl <sup>-1</sup>	8-25	14.8±1.27	15.2±4.56	14.6±3.73	15.2±4.10	15.6±3.84
Creatinin/mg dl <sup>-1</sup>	0.8-1.6	0.98±0.14	1.06±0.17	1.02±0.14	0.98±0.18	1.00±0.18
Total protein/g dl <sup>-1</sup>	6.0-8.4	6.52±0.15	6.72±0.15	6.70±0.13	6.60±0.22	6.48±0.30
Albumin/mg dl <sup>-1</sup>	3.5-5.6	4.02±0.15	3.88±0.15	3.98±0.18	3.96±0.20	3.94±0.10
Alkaline phosphatase/U	35-125	53.6± 13.1	54.5±12.3	54.0±14.9	52.6±12.6	52.6± 10.3
Alanine transaminase/U	7-56	14.6±2.12	16.0±2.63	15.7±3.23	15.9±2.47	16.0±2.63
Aspartate transaminase/U	5-40	16.2±5.33	15.2±3.19	16.5±3.03	17.2±5.16	15.2±3.19
Direct bilirubin/mg dl <sup>-1</sup>	0.0-0.3	0.12±0.04	0.12±0.04	0.11±0.03	0.11±0.03	0.12±0.04
Indirect bilirubin/mg dl <sup>-1</sup>	0.1-1.1	0.45±0.05	0.35±0.09	0.35±0.09	0.45±0.05	0.40±0.07
Chlorine/meq dl <sup>-1</sup>	95-107	98.5±2.17	98.8±2.3	98.6±2.12	97.8±1.75	98.2±2.10
Sodium/meq dl <sup>-1</sup>	137-146	142.7±1.4	142.8± 0.9	143.0±1.6	142.7±1.4	142.0±1.6
Potassium/meq dl <sup>-1</sup>	3.5-5.5	4.80±0.28	4.68±0.36	4.94±0.39	4.87±0.35	4.70±0.35
Calcium/mg dl <sup>-1</sup>	8.5-10.8	9.40±0.39	9.47±0.28	9.42±0.28	9.63±0.42	9.47±0.28
Phosphorus/mg dl <sup>-1</sup>	2.5-4.5	3.60±0.41	3.60±0.32	3.68±0.42	3.60±0.36	3.56±0.38

Table 3. Means and standard deviations of biochemical parameters of human sera

these fibrous capsules consisting of fibroblasts, and a grouped mast cells and lymphocyte were observed between tissues and capsule in the some samples (Figure 15, 16).

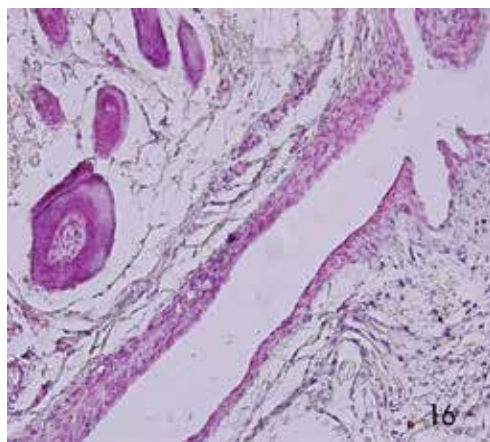


Fig. 15. After one week, the implan-tation site of AAm hydrogel, H-E, 20X

After 6–10 weeks, the adverse tissue reaction, giant cells and necrosis of cells, inflammatory reaction such as deposition of foamed macrophage were not observed in the implant site, however, it is observed to increase in the collagen fibrils due to proliferation and activation of fibroblasts (Fig. 17). No chronic and acute inflammation, adverse tissue reaction were observed in the all test groups. It is no determination related to the loss of activation and liveliness of cells in the capsule cells and in distant sites. No pathology were observed in the skin and the tissues of straight muscle in the close to implant sites.

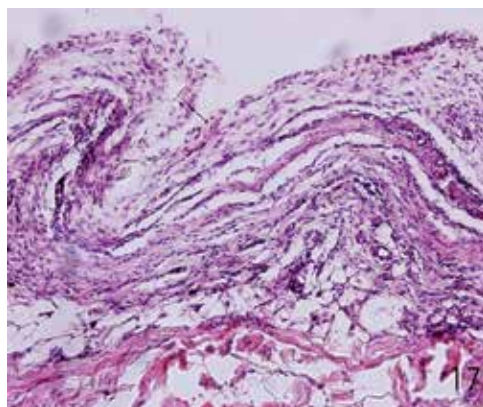


Fig. 16. After 4 week, the implantation site of AAm hydrogel, H-E, 20X

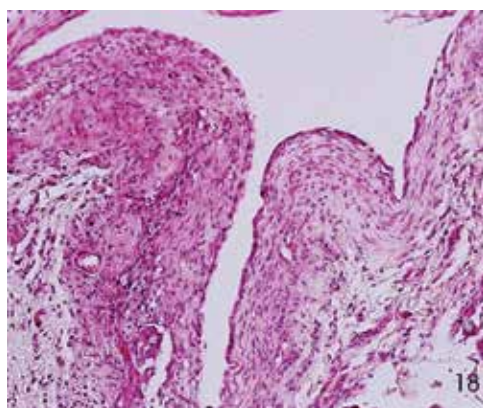
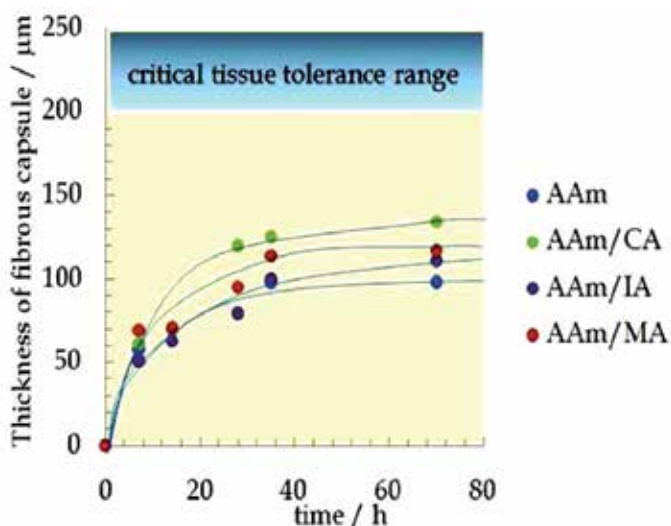


Fig. 17. 10 week postimplantation of AAm/CA hydrogel. H-E, 20X

The thickness of the fibrous capsules were measured in the optical microscope using a micrometer scale. The means of five measurements for each the sample and each time point were calculated. The thickness of fibrous capsules are gradually increased to 6 weeks, and then these values are becomed a constant value. The thickness of fibrous capsule occurred due to AAm/CA, AAm/MA and AAm/IA hydrogels implant are high from the values of AAm and hydrogels. The carboxyl groups on the chemical structure and ionogenic character of AAm/CA, AAm/MA and AAm/IA hydrogels can be caused to the high thickness of the fibrous capsule (Smetana et al., 1990). The thickness of the fibrous capsules were measured in the optical microscope using a micrometer scale. The means of five measurements for each the sample and each time point were calculated and shown in Graphic 2. The thickness of fibrous capsules are gradually increased to 6 weeks, and then these values are becomed a constant value. The thickness of fibrous capsule occurred due to AAm/CA, AAm/MA and AAm/IA hydrogels implant are high from the values of AAm and hydrogels. The carboxyl groups on the chemical structure and ionogenic character of AAm/CA, AAm/MA and AAm/IA hydrogels can be caused to the high thickness of the fibrous capsule (Smetana et al., 1990). On the other hand, Student's *t* test was applied to the all constant values of thickness of fibrous capsules of the hydrogels, and no significant differences ( $p > 0.05$ ) was

found. These thickness of fibrous capsule indicated well within the critical tissue tolerance range. It was given by the some reporters that the threshold capsule thickness should not exceed 200–250  $\mu\text{m}$  for an implanted biomaterial (Jeyanthi and Rao, 1990). Our results clearly indicated that the capsule thickness of the excised tissue were well within these stipulated threshold limits. On the basis of the findings we can conclude that the biological response against the tested hydrogels was very similar to the biocompatibility of very low swollen of poly(2-hydroxyethyl methacrylate) hydrogel, which considered as a biologically inert polymer (Smetana et al., 1990). However, it is important that the swelling of acrylamide based hydrogels are very high than the swelling of poly(2-hydroxyethyl methacrylate) hydrogels for the biomedical uses.



Graphic 2. The curves of thickness of fibrous capsule – implantation time.

#### 4. Bioactive ceramic biomaterials

Bioactive refers to a material, which upon being placed within the human body interacts with the surrounding bone and in some cases, even soft tissue. This occurs through a time - dependent kinetic modification of the surface, triggered by their implantation within the living bone. An ion - exchange reaction between the bioactive implant and surrounding body fluids - results in the formation of a biologically active carbonate apatite (CHAp) layer on the implant that is chemically and crystallographically equivalent to the mineral phase in bone. Prime examples of these materials are synthetic hydroxyapatite, glass ceramic and bioglass.

Calcium phosphate ceramics and xenografts have been used in different fields of medicine and dentistry. We demonstrated the effects of calcium phosphate ceramics (Ceraform) and xenograft (Unilab Surgibone) in the field of experimentally created critical size parietal and mandibular bone defects in rats (Develioglu et al., 2006, 2007, 2009, 2010).

Many researches are currently conducted to find out the ideal material to support bone repair or regeneration. The limitations of autogenous grafts and allogeneic bankbone have led to a search for synthetic alloplast alternatives. Calcium phosphate ceramics have been

widely used because the mineral composition of these implants materials does fully biocompatible (Rey C. 1990, LeGeros. 2002). The porous structure of the ceramics is claimed to enhance bone deposition and implant stabilization in the recipient bone. The optimal pore size is still debated to be ranging from 50 and 565  $\mu\text{m}$  (Gauthier et al., 1998, Chang et al., 2000). However, porosity of the material is inversely proportional to the mechanical stability of these calcium phosphate based ceramics (Le Huec et al., 1995). This loss of stability is often cited as a limitation in the use of calcium phosphate-based ceramics in clinical practice. A convenient compromise to overcome this problem is to use a biphasic ceramic, which maintains its mechanical resistance until the resorption is achieved (Gauthier et al., 1998).

Various types of xenografts are used in medicine, dentistry, and also in periodontology. One of the xenografts is Unilab Surgibone, which is currently being used successfully in medicine and implantology. Moreover, osteoconductive properties are also known (Zhao et al., 1999). Unilab Surgibone is obtained from freshly sacrificed calves which is partially deproteinized and processed by the manufacturers. It is available in various shapes like tapered pins, blocks, cubes, granules, circular discs and pegs (Balakrishnan et al., 2000). Xenograft materials, bovine bones have been the most preferred ones, basically because they are easily obtainable and there are no great ethical considerations. Additionally they have the great advantage of practically unlimited availability of source/raw material. Partially deproteinized and defatted preparations (e.g. Unilab Surgibone) was indicated reduce antigenity and mild immune response (William et al., 2008).

Generally, xenografts are one of the alternative graft materials used in different fields for filling osseous defects Slotte and Lundgren, 1999, Salama 1983). Nonetheless, an interesting alternative to xenografts is Biocoral® (natural coral), which has been shown to exhibit osteoconductive and biocompatible properties whereby gradual replacement with newly formed bone occurred after its resorption (Guillemin et al., 1989, Doherty et al., 1994, Yilmaz and Kuru, 1996, Yukna Ra and Yukna CN, 1998).

Another xenogeneic, bone-derived implant material is Bio-Oss, which is similar to the xenograft investigated in our studies (Develioglu et al. 2009, 2010). Bio-Oss has been proposed as a biocompatible graft material for bony defects for it has shown osteoconductive properties – that is, it was replaced with newly formed bone after grafting (Yildirim et al, 2001, Sculean et al., 2002, Carmagnola et al., 2002). However, regarding the resorption of Bio-Oss, contradicting reports have emerged. On one hand, a previous study revealed that the bovine bone mineral underwent resorption (Pinholt et al., 1991). On the other hand, numerous researchers claimed that the resorption process of Bio-Oss® was very slow (Skoglund et al., 1997, Jensen et al 1996, Klinge et al., 1992).

In our previous studies with Ceraform (calcium phosphate ceramics) and xenograft (Unilab Surgibone), multinuclear giant cells (MNGC) were observed in the implantation region on 1<sup>st</sup>, 3<sup>rd</sup>, 6<sup>th</sup> ve 18<sup>th</sup> months.

The observed MNGCs are featured morphologic characteristics of foreign body giant cell (FBGC). These cells are osteoclast-like cells. Both cell types develop from a common precursor (Anderson, 2000) Since foreign body giant cell (FBGC) are the fusion products of monocytic precursors, which are also the precursors of macrophages, (Brodbeck et al., 2002, Matheson et al., 2004) the presence of such leukocytes in the wound healing compartment may be of central importance in driving the tissue reaction to the material. No necrosis, tumorigenesis, or infection was observed at the implant site up to 18 months (Figure 18-20).

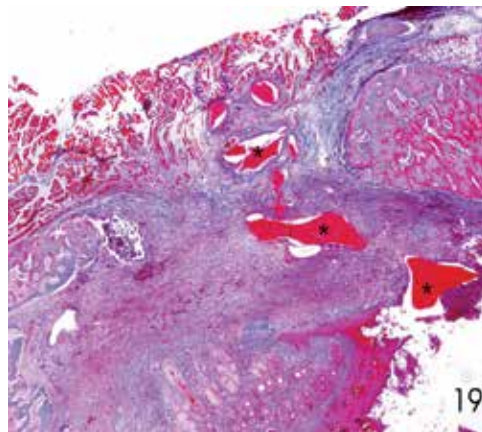


Fig. 18. Remnants of the Xenograft (\*) surrounded by fibrous tissue at 30 days. A-T 4X.

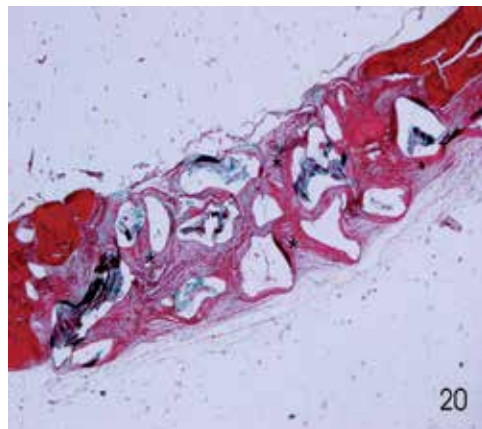


Fig. 19. A dense, fibrovascular tissue (\*) in the side of ceraform implantation at 12th month M-T, 4X.

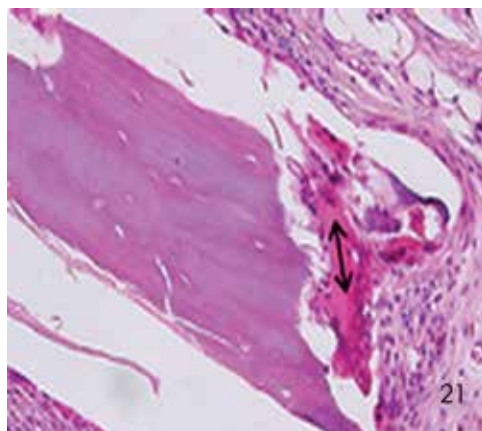


Fig. 20. Multinuclear giant cell (↔) in the implantation site. H-E, 40X

A long-term study would be useful to evaluate the biological degradation behavior of the material utilized in this study. BCP ceramics are well known to be biodegradable due both to body fluid dissolution and bioresorption cellular activity Nery et al., 1990, Piatelli et al., 1996). It might indicate that the implants utilized in our studies are progressively resorbed, but the size of the particle might be big (Handschel et al., 2002) The studies reveal that Ceraform and xenograft are biocompatible. However, the materials did not promote bone formation.

## 5. Conclusion

In conclusion, while some vinyl monomers had cytotoxic effects on tissues, their polymers, Ceraform and Unilab Surgibone were found to be biocompatible in soft and hard tissues and they seem only to be beneficial bone filler materials in treatment of the bone defects. Unilab Surgibone and xenograft could be used as bone filler materials in the treatment of traumatic and post-traumatic skeletal complications (e.g delayed unions, non-unions), defects due to bone removal (e.g. bone tumors, congenital diseases) or low bone quality (e.g. osteoporosis, osteopenia) and in other medical fields.

## 6. References

- Anderson JM. (2000). Multinucleated giant cells. *Current Opinion in Hematology*, Vol. 7, pp. 40–47, ISSN 1065-6251.
- Balakrishnan, M.; Agarwal DC, Kumar SA (2000). Study of efficacy of heterogeneous bone graft (Surgibone) in orthopaedic surgery. *Medical Journal Armed Forces India*, Vol. 56, pp. 21-23, ISSN 0377-1237.
- Bao F., Liu D. (2004). Hydroxyl radicals generated in the rat spinal cord at the level produced by impact injury induce cell death by necrosis and apoptosis: Protection by a metalloporphyrin. *Neuroscience*, Vol. 126, pp. 285-295, ISSN 0306-4522.
- Barber DS, Hunt JR, Ehrich MF, Lehning EJ, Lo-Pachin RM (2001). Metabolism, Toxicokinetics and Hemoglobin Adduct Formation in Rats Following Subacute and Subchronic Acrylamide Dosing. *Neuro Toxicology*, Vol. 22, pp. 341-353, ISSN 0161-813.
- Benson RS. (2002) . Use of radiation in biomaterials science. *Nuclear Instruments & Methods In Physics Research Section B-Beam Interactions With Materials And Atoms*; Vol. 191, pp. 752-757, ISSN 0168-583.
- Brodbeck WG, Nakayama Y, Matsuda T, Colton E, Ziats NP, Anderson JM. (2002). Biomaterial surface chemistry dictates adherent monocyte/macrophage cytokine expression *in vitro*. *Cytokine*, Vol. 18, pp. 311–319, ISSN 1043-4666.
- Carmagnola D, Berglundh T, Lindhe J. (2002). The effect of a fibrin glue on the integration of Bio-Oss with bone tissue. An experimental study in Labrador dogs. *Journal of Clinical Periodontology*, Vol. 29, pp. 377-383, ISSN 1600-051.
- Chang BS, Lee CK, Hong KS, Youn HJ, Ryu HS, Chung SS, Park KW. (2000). Osteoconduction at porous hydroxyapatite with various pore configurations. *Biomaterials*, Vol. 21, pp. 1291–1298, ISSN 0142-9612.
- David H. Kim, Alexander R. Vaccaro, Fraser C. Henderson, Edward C. Benzel. (2003). Molecular biology of cervical myelopathy and spinal cord injury: role of oligodendrocyte apoptosis. *The Spine Journal*. Vol. 3, pp. 510-519, ISSN 1529-9430.

- Develioğlu H, Ünver Saraydın S, G. Bolayır, L. Dupoirieux. (2006). Assessment of the effect of a biphasic ceramic on bone response in a rat calvarial defect model. *Journal of Biomedical Materials Research*, Vol. 77, pp. 627-631, ISSN 1549-3296.
- Develioğlu H, Ünver Saraydın S, Laurent Duopoirieux, Zeynep Deniz Şahin. (2007). Histological findings of long-term healing of the experimental defects by application of a synthetic biphasic ceramic in rats. *Journal of Biomedical Materials Research*, Vol. 80, pp. 505-508, ISSN 1549-3296.
- Develioğlu H, Ünver Saraydın S, Ünal Kartal. (2009). The bone healing effect of a xenograft in arat calvarial defect model. *Dental Materials Journal*, Vol. 28, pp. 396-400, ISSN 0287-4547.
- Develioğlu H, Ünver Saraydın S, Ünal Kartal, Levent Taner. (2010). Evaluation of the long term results of rat cranial bone repair using a particular xenograft. *Journal of Oral Implantology*. Vol. 36, pp. 167-173, ISSN 0160-6972.
- Doherty MJ, Schlag G, Schwarz N, Mollan RA, Nolan PC, Wilson DJ. (1994). Biocompatibility of xenogeneic bone, commercially available coral, a bioceramic and tissue sealant for human osteoblasts. *Biomaterials* Vol. 15, pp. 601-608, ISSN 0142-9612.
- Gauthier O, Bouler JM, Aguado E, Pilet P, Daculsi G. (1998). Macroporous biphasic calcium phosphate ceramics: Influence of macropore diameter and macroporosity percentage on bone ingrowth. *Biomaterials*; Vol. 19, pp. 133-139, ISSN 0142-9612.
- Gold BG, Schaumburg HH. (2000). Acrylamide. In: Spencer PS, Schaumburg HH (eds) *Experimental and clinical neurotoxicology*, 2nd edn. ISBN 0195084772, Oxford University Pres, New York pp 124-132.
- Guillemin G, Meunier A, Dallant P, Christel P, Pouliquet JC, Sedel L. (1989). Comparison of corals resorption and bone apposition with two natural corals of different porosities. *Journal of Biomedical Materials Research*, Vol. 23, pp. 767-779, ISSN 1549-3296.
- Güven O, Sen M, Karadağ E, Saraydın D. (1999). A review on the radiation synthesis of copolymeric hydrogels for adsorption and separation purposes. *Radiation Physics And Chemistry*, Vol. 56, No. 4, pp. 381-386, ISSN 0969-806.
- Handschelel J, Wiesmann HP, Sratmann U, Kleinheinz J, Meyer U, Joos U. (2002). TCP is hardly resorbed and not osteoconductive in a nonloading calvarial model. *Biomaterials*; Vol. 23, pp. 1689 -1695, ISSN 0142-9612.
- Jensen SS, Aaboe M, Pinholt EM, Hjorting-Hansen E, Melsen F, Ruyter IE. (1996). Tissue reaction and material characteristics of four bone substitutes. *The International Journal of Oral & Maxillofacial Implants*, Vol. 11, pp. 55-56, ISSN 0882-2786.
- Jeyanthi R., Rao KP. (1990). *In vivo* biocompatibility of collagen poly(hydroxyethyl methacrylate) hydrogels. *Biomaterials*, Vol. 11, pp. 238-243, ISSN 0142-9612.
- Karadağ, E; Saraydın, D; Cetinkaya, S; Güven, O. (1996). In vitro swelling studies and preliminary biocompatibility evaluation of acrylamide-based hydrogels *Biomaterials*, Vol. 17, pp. 67-70, ISSN 0142-9612.
- Karadağ, E; Saraydın, D; Güven, O. (2004). Water absorbency studies of gamma-radiation crosslinked poly (acrylamide-co-2,3-dihydroxybutanedioic acid) hydrogels. *Nuclear Instruments & Methods In Physics Research Section B-Beam Interactions With Materials And Atoms*. Vol. 225, No. 4, pp. 489-496, ISSN 0168-583.

- Klinge B, Alberius P, Isaksson S, Jönsson J. (1992). Osseous response to implanted natural bone mineral and synthetic hydroxyapatite ceramic in the repair of experimental skull bone defects. *Journal Oral Maxillofacial Surgery* Vol. 50, pp. 241-249, ISSN 02782391.
- Lamigeon C, Bellier JP, Sacchettoni S, Rujano M, Jacquemont B. (2001). Enhanced neuronal protection from oxidative stress by coculture with glutamic acid decarboxylase-expressing astrocytes. *Journal of Neurochemistry*, Vol. 77, pp. 598–606, ISSN 1471-4159.
- LeGeros RZ. (2002). Properties of osteoconductive biomaterials: Calcium phosphates. *Clinical Orthopaedics*, Vol. 395, pp. 81–98, ISSN 0009-921.
- Le Huec JC, Schaeferbeke T, Clement D, Faber J, Le Rebeller A. (1995). Influence of porosity on the mechanical resistance of hydroxyapatite ceramics under compressive stress. *Biomaterials*, Vol. 16, pp. 113–118, ISSN 0142-9612.
- Lee K-Y, Shibutani M, Kuroiwa K, Takagi H, Inoue K, Nishikawa H, Miki T, Hirose M. (2005). Chemoprevention of acrylamide toxicity by antioxidative agents in rats-effective suppression of testicular toxicity by phenylethyl isothiocyanate. *Arch Toxicol*, Vol. 79, pp. 531-541, ISSN 0340-5761.
- Matheson MA, Santerre JP, Labow RS. (2004). Changes in macrophage function and morphology due to biomedical polyurethane surface undergoing biodegradation. *Journal of Cell Physiology*, Vol. 199, pp. 8 –19, ISSN 0021-9541.
- McLendon, R.E, Bigner, D.D. (1994). Immunohistochemistry of the glial fibrillary acidic protein: basic and applied considerations. *Brain Pathology*, Vol. 4, pp. 221-228, ISSN 1015-6305.
- Montgomery D. L. (1994). Astrocytes: form, functions, and roles in disease. *Veterinary Pathology*, Vol. 31, pp. 145-167, ISSN 0300-9858.
- Morrison RS, Kinoshita Y, Johnson MD, Guo W, Garden GA. (2003). P53-Dependent cell death signaling in neurons. *Neurochemistry Research*, Vol. 28, pp. 15-27, ISSN 0364-3190.
- Nery EB, Eslami A, Van SR. (1990). Biphasic calcium phosphate ceramic combined with fibrillar collagen with and without citric acid conditioning in the treatment of periodontal osseous defects. *Journal of Periodontology*, Vol. 61, pp. 166 –172, ISSN 0022-3492.
- Okuno T, Matsuoka M, Sumizawa T, Igisu H. (2006). Involvement of the extracellular signal-regulated protein kinase pathway in phosphorylation of p53 protein and exerting cytotoxicity in human neuroblastoma cells (SH-SY5Y) exposed to acrylamide. *Archives of Toxicology*, Vol. 80, pp. 146-153, ISSN 0340-5761.
- Piatelli A, Scarano A, Mangano C. (1996). Clinical and histologic aspects of biphasic calcium phosphate ceramic (BCP) used in connection with implant placement. *Biomaterials*, Vol. 17, pp. 1767–1770, ISSN 0142-9612.
- Pinholt EM, Bang G, Haanes HR. (1991). Alveolar ridge augmentation in rats by Bio-Oss. *Scandinavian Journal of Dental Research*, Vol. 99, pp. 154-161, ISSN 0029-845.
- Rey C. (1990). Calcium phosphate biomaterials and bone mineral. Differences in composition, structures and properties. *Biomaterials*, Vol. 11, pp. 13–15, ISSN 0142-9612.



- Rogero S. O., Malmonge S. M., Lugão A. B., Ikeda T. I., Miyamaru L., and Cruz Á. S. (2003). Biocompatibility Study of Polymeric Biomaterials. *Artificial Organs*, Vol. 27, No. 5, pp. 424-427, ISSN 1525-1594.
- Salama R. (1983). Xenogenic bone grafting in humans. *Clinical Orthopaedics and Related Research*, Vol. 174, pp. 113-121, ISSN 0009-921.
- Saraydın, D; Karadag, E; Guven, O. (1995). Acrylamide/maleic acid hydrogels. *Polymers For Advanced Technologies*, Vol. 6, No. 12, pp. 719-726, ISSN 1042-7147.
- Saraydın, D; Karadag, E; Çetinkaya, S; Guven, O. (1995). Preparation of acrylamide maleic-acid hydrogels and their biocompatibility with some biochemical parameters of human serum. *Radiation Physics And Chemistry*, Vol. 46, No. 4-6, pp. 1049-1052, ISSN 969-806.
- Saraydın, D; Koptagel, E; Unver-Saraydın, S; Karadag, E; Guven, O. (2001). In vivo biocompatibility of radiation induced acrylamide and acrylamide/maleic acid hydrogels. *Journal of Materials Science* Vol. 36, No. 10, pp. 2473-2481, ISSN 0022-2461.
- Saraydın, D; Caldıran, Y. (2001). In vitro dynamic swelling behaviors of polyhydroxamic acid hydrogels in the simulated physiological body fluids. *Polymer Bulletin* Vol. 46, No. 1, pp. 91-98, ISSN 0170-0839.
- Saraydın, D; Isikver, Y; Karadag, E; Sahiner, N; Guven, O. (2002). In vitro dynamic swelling behaviors of radiation synthesized polyacrylamide with crosslinkers in the simulated physiological body fluids. *Nuclear Instruments & Methods In Physics Research Section B-Beam Interactions With Materials And Atoms*, Vol. 187, No. 3, pp. 340-344, ISSN 0168-583.
- Saraydın, D; Karadag, E; Sahiner, N; Guven, O. (2002). Incorporation of malonic acid into acrylamide hydrogel by radiation technique and its effect on swelling behaviour. *Journal Of Materials Science* Vol. 37, No. 15, pp. 3217-3223, ISSN 0022-2461.
- Saraydın, D; Unver-Saraydın, S; Karadag, E; Koptagel, E; Guven, O. (2004). In vivo biocompatibility of radiation crosslinked acrylamide copolymers. *Nuclear Instruments & Methods In Physics Research Section B-Beam Interactions With Materials And Atoms* Vol. 217, No. 2, pp. 281-292, ISSN 0168-583.
- Sculean A, Chiantella GC, Windisch P, Gera I, Reich E. (2002). Clinical evaluation of an enamel matrix protein derivate (Emdogain®) combined with a bovine-derived xenograft (Bio-Oss®) for the treatment of intrabony periodontal defects in humans. *International Journal of Periodontics Restorative Dentistry*, Vol. 22, pp. 259-267, ISSN 0198-7569.
- Skoglund A, Hising P, Young C. (1997). A clinical and histologic examination in humans of the osseous response to implanted natural bone mineral. *International Journal of Oral Maxillofacial Implants* Vol. 12, pp. 194-199, ISSN; 0882-2786.
- Slotte C, Lundgren D. (1999). Augmentation of calvarial tissue using non-permeable silicone domes and bovine bone mineral. An experimental study in the rat. *Clinical Oral Implants Research*, Vol. 10, pp. 468-476, ISSN 0905-7161.
- Smetana Jr. K, Vacík J., Součková D., Krčová Z., Šulc J. (1990). The influence of hydrogel functional groups on cell behavior *Journal of Biomedical Materials Research*, Vol. 24, pp. 463-470, ISSN 1549-3296.
- Sumizawa T, Igisu H. (2007). Apoptosis induced by acrylamide in SH-SY5Y cells. *Archives of Toxicology*, Vol. 81, pp. 279-282, ISSN 0340-5761.

- Ünver Saraydın S, Develioğlu H. (2011). Evaluation of the bone repair capacity and the cytotoxic properties of a particular xenograft: An Experimental study in rats *Turkiye Klinikleri Journal of Medical Sciences*, Vol.31, No.3, pp.541-547, ISSN 1300-0292.
- Ünver Saraydın S, H. Eray Bulut, Ünal Özüm, Z. Deniz Şahin İnan, Zübeyde Akın Polat, Yücel Yalman, Dursun Saraydın. (2011). Evaluation of the Cytotoxic effects of various monomers, In vitro also their effects on Apoptosis and GFAP immunolocalization in rat spinal cord In vivo. *HealthMED*. Vol. 5, No. 1, pp. 17-28, ISSN 1840-2291.
- William S. Pietrzak, Charles A. Vacanti, (2008). *Musculoskeletal Tissue Regeneration: Biological Materials and Methods*, Publisher: Totowa, NJ : Humana Press, p:121, ISSN 0895-8696.
- Yılmaz S, Kuru B. (1996). A regenerative approach to the treatment of severe osseous defects: report of an early onset periodontitis case. *Periodontal Clinical Investigation* Vol. 18, pp. 13-16, ISSN 1065-2418.
- Yukna RA, Yukna CN. (1998). A 5-year follow-up of 16 patients treated with coralline calcium carbonate (BIOCORAL®) bone replacement grafts in infrabony defects. *Journal of Clinical Periodontology*, Vol. 25, pp. 1036-1040, ISSN 0303-6979.
- Yıldırım M, Spiekermann H, Handt S, Edelhoff D. (2001). Maxillary sinus augmentation with the xenograft Bio-Oss® and autogenous intraoral bone for qualitative improvement of the implant site: a histologic and histomorphometric clinical study in humans. *International Journal of Oral Maxillofacial Implants*, Vol. 16, pp. 23-33, ISSN 0882-2786.
- Zhao YF, Mendes M, Symington JM, Listrom RD, Pritzker KP. (1999) Experimental study of bone growth around a dental implant after Surgibone grafting. *International Journal of Oral Maxillofacial Implants*, Vol. 14, pp. 889-897, ISSN 0882-2786.

# Facial Remodelling and Biomaterial

G. Fini, L.M. Moricca, A. Leonardi, S. Buonaccorsi and V. Pellacchia  
*La Sapienza/ Roma  
Italy*

## 1. Introduction

Facial remodelling comprises all the surgical techniques able to reconstruct the correct proportion between soft and hard tissues of the face. In order to obtain facial harmony maxillo-facial surgeons have at disposal many surgical techniques such as reconstructive, orthognatic, aesthetic surgery and camouflage. In the study of a patient who presents facial asymmetry two base evaluations are necessary: aesthetic analysis and cephalometric analysis. The first is an evaluation of the skeleton in association to the evaluation of the soft tissues according to the harmonic proportions of the face, while the second consists in the evaluation of the skeletal relationships with respect to the basicranium through the identification of specific craniometrical points. It is possible to establish a specific therapeutic plan for the specific facial

asymmetry by means of the combination of these analyses and the addition of the radiographies study. There are various pathologies that need facial remodelling: acquired syndromes, congenital syndrome such as the Hemifacial Microsomiae, autoimmune disorder or atrophic disease such as Perry-Romberg Syndrome, traumas, demolitive surgery and infectious pathologies. In these clinical conditions the choice of a therapeutic treatment of camouflage instead of corollary surgery and conventional aesthetics techniques is made when there is a specific request from patients. This decision is also made when there is an increased operative risk and the deficits to fill are not massive. The described surgical treatments present the advantage of being not invasive, easy to position, not much traumatic and with immediate results. The complications can be the following: shifting of the biomaterial, chronic inflammation, quick reabsorption of the used materials, infections and reject. The camouflage is growing as a surgical technique for the continuous scientific studies, on the new bio-materials. The studied filling bio material are the porous polyethylene and the bio-bone for the hard tissues, the Polyalkylimide and Polyacrylamide for the soft tissues. Some representative clinical cases are presented.

During our experience, patients have been treated with the following bio materials: porous polyethylene, bio-bone, polialkylimide, polyacrylamide, and with a combined treatment with polyacrylamide and porous polyethylene. The patients treated with porous polyethylene presented pathologies deriving 50% from traumas, 40% from malformation and a 10% from congenital asymmetries. The patients treated with bio-bone (7% of the total patients) of the total were presented in all cases the bony atrophy of the jaw.

Patients suffering from infectious pathologies (HIV) were included among the patients treated with polialkylimide, others with autoimmune pathologies (PRS) and with malformative syndromes were included too. The treatment with polyacrylamide was

carried out in patients with autoimmune syndrome (Scl and PRS), LPS results people, HIV affected, and patients with congenital malformation (HMF). We have a diagnostic and therapeutic procedure uniform for all the patients; the first clinical evaluation concerns radiographic and laboratory examination, such as head and neck Dimensional Computed Tomography, Magnetic Resonance, Ultrasonography, Orthopantomographic x-rays, searches for ANA-ENA-Anti Cardiolipina anticorpal; specialized infective and immunologic consultation relating to the single patient has been committed. The 7% of the patients has been treated with a replenishment composed of the combination with porous polyethylene and polyacrylamide because of the wide loss of both skeleton and soft tissues. Some other representative clinical cases are presented:

## 2. Biomaterials

**Polyacrylamide - Clinical Case 1:** CC, a female of 17 years old, came in our center for hemifacial asymmetry. This anomaly was characterized by a progressive atrophy of the left hemiface. The patient did not present diplopia. The objective examination we observed the presence of slight atrophy of the left middle and inferior third of the face, including nasolabial region and the omolateral upper lip. A nasal pyramid deviation also appeared and confirmed by the anterior rhinoscopy, which also showed a left-convex deviation of the nasal septum. A Dimensional Computed Tomography scan was performed. This exam confirmed a maxillo-mandibular fault. Then an orthotic evaluation was performed to value muscular structures. We adopted a surgical approach which primarily provided an improvement of the respiratory activity. Then, we planned a filling of the atrophic soft tissues through infiltrations of Polyacrylamide. The infiltrations have been performed after 2 months from the septorhinoplasty surgery. Biomaterial (5ml) in the left nasolabial fold was filled. After 1 month from the beginning of the treatment, we noticed an evident reduction of the pre-existing deficit of the soft tissues. The clinical and Ultrasonography checks after 2, 6, 12 and 24 months confirmed a correct integration of the used biomaterial.



Fig. 1. Lateral view of the patient before treatment

**Clinical case 2:** E.M, female of 45 years referred about the appearance of a progressive facial asymmetry alterations interesting the lower third of the face in particular in the last 3 years. The tissue deficit was becoming clearer without any symptoms or alterations in the facial motility. (FIGURE 1) Therefore a Computed Tomography Scan of the face was performed, in order to evaluate the entity of such deficit. It shows marked deficit of the soft tissue, which was extending partially to the skeletal structures<sup>11</sup>. During the objective exam conducted even with a photographic study, the loss of the symmetry was appreciating, in particular to the third lower of the hemiface. Problems related to the function of the facial nerve, were not noticed, and the patient did not refer facial hypoesthesia.

Therefore the patient underwent to fill of the facial soft tissues with biomaterial. The biomaterial was implanted in the left middle and inferior third of the hemiface; moreover it has been noticed a partial resorption of the biomaterial at the end of treatment. A total of 3 infiltrations has been performed for a tot of 8ml of infiltrated biomaterial. (FIGURE 2)



Fig. 2. Lateral view of the patient after treatment

**Clinical Case 3:** E.D.E, male of 55 years old, immuno-compromised patient, affected by HIV from 20 year. He had underwent to the Highly Active Anti-Retroviral Therapy treatment (HAART) from about ten years. The patient referred the appearance of an atrophy in the middle third of face, he had developed a lypodistrophy lesion of soft tissues. (FIGURE 3)



Fig. 3. Particular of the lypodistrophy area

The patient was stable from clinical and infective point of view, confirmed by hematologic exams; so that we decided to underwent the patient to biomaterial infiltration with Polyacrylamide. The sites of treatment were the areas where the atrophy and the lypodistrophy are happened. Clinical-aesthetic and infective results in six years of follow-up were good. (FIGURE 4)



Fig. 4. Particular of the the lypodistrophy area after treatment

**Polyalkylimide - Clinical case 4:** D.L.B, a male of 30 years old, showed an atrophy of the middle and inferior third of the face. The patient eight years before, referred a not treated facial trauma. The objective exam showed the presence of a moderate atrophy of the righthemiface, associated to aesthetic and functional alterations. In particular, a combination of the right orbital-malar asymmetry complex, and a righth orbital oenophtalmo was noticed as well. 7. The patient referred about the appearance of dyplopia. It has not been well clarifiyed. The patient underwent before further clinical and radiological checks exams to study the soft tissues, and to evaluate the ocular motility, so as a Perry Romberg Syndrome was suggested for diagnosis. A surgical treatment was planned to correct the oenophtalmo and to restore the ocular motility correcting the dyplopia dysfunction. On the other hand, this surgery has been performed with the goal of resolving the atrophy and the face's deformity through the use of porous polyetilene. Afterwards, a treatment of polyackylimide infiltrations has been planned. The patient, after 1 week from the treatment with biomaterial, presented a good tolerance and a total restoration of the facial eurytmia. An ultrasonographic evaluation was performed to value the integration of the biomaterial after 6,12 and 24 months; this exam showed a compartment of the biomaterial implanted, associated to fibrotyc branches compatible with the basal pathology.

**Porous polyethylene - Clinical Case 5:** S.B, a female of 40 years old, referred facial asymmetry. The objective exam showed a skletal deformity of mandibular and maxillary component, associated to mycrogenia.(FIGURE 5)

The patient presented a congenital nose deformity too. The surgical treatment was planned with mandibular promotion by means graft of porous polietylene. Then in the same surgical step a graft "on lay" of septal cartilage was positionated on the nasal dorsum. Ultrasonographic checks after 1 month, 23 months and 6 months were optimal; radiologic exams were performed to check the planted biomaterial. These investigations verified a good tolerance and a well fixed of the biomaterial. (FIGURE 6)



Fig. 5. Frontal view of the patient before treatment



Fig. 6. Frontal view of the patient after treatment

**Bio-bone - Clinical case 6:** ML, 19 years old female, came up to our attention for a mandibular lesion. It was an occasionally finding of a Magnetic Resonance carried out previously after a lipothymia event. This mandibular 8 lesion was an osteolytic one, positioned in the left ramous under 3.6 to 3.8 roots. Patient had not symptoms, and the clinical exam didn't show any visible or touchable lesion in the fornix gum, or at the corresponding teeth. Patient only referred a mononucleosis infection six months before. Computed Tomography of the Head and Neck and Orthopantomographic x-rays were carried out (FIGURE 7) .



Fig. 7. Pre operative Orthopantomographic x-rays

These images were likely suggestive for adamantinoma. That hypothesis led to a particular operative intervention with the aim of a definitive diagnosis and treatment. In fact the histologic exam would have led, or not, to a mandibular resection. So left mucous fornix section was performed in order to uncover the mandibular bone from 3.6 to 3.8 dental elements and to dissect the bone through osteotribe, as long as the lesion was found. Strangely enough the surgical finding was a rarefaction of the bone, no capsular structure or any other elements that could help with the diagnosis were observed as well. Consequently a conservative surgical technique was carried on, such as cutting out the bone box with 3.7 and 3.8 because of their roots inclusion in the osteolytic lesion as well. The missing bony part was filled with a demineralized bone matrix, in order to prevent iatrogenic fracture. So before performing a mandibular ramous resection, we have been waiting for the definitive histologic diagnosis. Unfortunately, against every expectation, it resulted as a follicular cyst within *Candida A.* yeasts. It was performed a bacteriologic exam that resulted positive for *C. Albicans* too and for *Hafnia alveii*. Antibiotic and antimicotic therapies were carried out for a long period. After three months patient underwent to a Orthopantomographic x-rays, that revealed the biomaterial integration but a surgical intervention of removing bio-bone it was necessary in order to assure the complete eradication of the *Candida* infection. (FIGURE 8)



Fig. 8. Post operative Orthopantomographic x-rays

**Porouse polyethylene and Polyacrylamide - Clinical case 7:** R.A, a male of 40 years old, affected by the Goldenhar syndrome, he underwent to different reconstructive surgical treatments, to restore the normal symmetry of the face soft tissues. The patient showed a facial asymmetry characterized by an atrophy of the right hemifacial soft tissues, associated to auricular agenesys, and a behind-positioning of the left auricle. (FIGURE 9)



Fig. 9. Frontal view of the patient before treatment



Radiological and clinical exams with Computer Tomography Dental Scan and Telecranium x ray in two projections with cephalometric study were performed to evaluate bony and soft tissues. After 1 month surgery was performed: two fixtures with abutment have been positioned in the right mastoid bone, Then the left auricular was positioned to reestablish the normal structures of the face. In the same surgical time, two porous polyethylene prosthesis were implanted in the malar region, to restore the sagittal diameter of the middle third of the face; other two porous polyethylene prosthesis were implanted on the mandibular angle and one more prosthesis was implated on the sinphisis, to restore the transversal and sagittal diameter of the thrid inferior of face. After three mounths an auricular prosthesis associated to Polyacrylamide implant, was positioned in bilateral pre-auricular area (**FIGURE 10**). Clinical and radiological follow-up demonstrated a good integration of implants and the biomaterial.



Fig. 10. Frontal view of the patient after treatment

### 3. Ultrasonography monitor follow-up

The ideal biomaterial should be easy to implant and to remove, and simple to be identified by a low-dose radiation and low-cost radiologic technique. Authors wanted to evaluate ultrasonography (US) as a technique in monitoring biomaterial status after operation. Ultrasonography has been shown as an excellent way to visualize clinical features and a possible pathologic process of an implanted biomaterial; it is a non-invasive, low-radiation and low-cost dose radiologic technique. Reconstruction in facial deficit diseases needs adequate biomaterial to implant and a careful patients observation, that is, both clinical and radiologic. Ultrasonography is a fundamental component of the follow up of implanted biomaterial patients. the use of synthetic materials instead of an autolog tissue is codified from years and is widely diffused. In the last years, maxillofacial surgery has adopted poliacrilamide for the soft tissue, which is already used in esthetic surgery such as “last generation filler” to overwhelm the defects of the time such as wrinkles and furrows. Such material has replaced paraffin and silicone fluid used in the 1960s, and collagen and analogs used in the 1980s. In the same years, Conley and Baker experienced some slow-resorption synthetic materials that, when inserted in the derma, overwhelmed cutaneous imperfections. The biomaterials used until that moment were all very well tolerated, but they introduced the disadvantage of being “statics” materials, concrete, and above all, temporary. In the last few years, poliacrilamide has replaced, in part, the use of these

materials. It does not have these common disadvantages, such as being concrete, visible during activation of mimics muscles, and having a temporary effect. For what concerns the skeletal tissue, for years we have used autologous bone grafts and cartilaginous tissues similar to many prosthetic materials. They showed plastic phenomenon and they were easy to infections and resorption instead of esthetic and functional aspects. In these years, porous polyethylene results to be a suitable material for bony integration; it is easy to use and has great reconstructive quality and low susceptibility to infections. A general problem of the same biomaterials is a lack of visibility on conventional radiographs; they can be seen using magnetic resonance imaging or computed tomography. These investigations are not suitable for the frequent examinations, because magnetic resonance imaging is a high-priced procedure and computed tomography has a high radiation dose. During the follow-up, we encountered some difficulties for their radiotransparency; therefore, in our study, we used a noninvasive technique such as ultrasonography (US) to estimate the filling conditions and eventually to characterize an eventual pathologic process during the early phase. The aim of this study was to examine the use of ultrasound imaging in detecting the changes in biomaterials.

All patients were grouped according to different kinds of diseases: malformative pathologies (patients with hemifacial microsomia), degenerative pathologies (patients with scleroderma and with Romberg syndrome), results of skull-facial traumas, and pure aesthetic problems such as senile alopecia. They have been examined using US (in early and late postsurgical courses) with a high-resolution probe (7.5-13 MHz, Astro; Esaote Biomedica, Genoa, Italy). The protocol of the study has foreseen almost 3 ultrasound controls; with a variable follow-up of 7 days to 36 months. After 7 days of implantation, we made the first ultrasound control.

Porous polyethylene, being a semirigid material that needs rigid internal fixture, decreased migration and stabilization problems. The polyacrylamide is introduced as a gel. If it is not well positioned, it could migrate. Integration and migration progress can be studied by US investigations, such as object examination. Initially, in both treated groups, transplants may show a light inflammatory state that will disappear in the succeeding days. Correct evaluation to appraise for the stabilization of the materials is composed of evaluating clinical and US parameters. The clinical parameters were as follows: the alteration absence of the impending fabrics, the graft, the edema absence, manque' mobilization, or migration of the implantation. The US parameters were as follows: absence of massive harvests of liquidate, inflammatory reactions of the surrounding fabrics, and good visualization of the implantation and the surrounding tissue. With this worktop, we have been able to appraise the diverged characteristics of the biomaterial and visualize the tissues reactions. In our results porous polyethylene showed strong ecogenic features such as the bone and vanishing margins; however, the implantation (like a titanium screw) appears as a reverberated ultrasound bundle. We could evidence the stability of the biomaterials, namely, its integration, eventual nearby tissue alterations, in the early and late phases. Therefore, polyacrylamide appears anecogenous with a water-like aspect in the recent implants and corpuscolated in the older ones. Sometimes, such as in connective tissue degenerative pathologies (such as scleroderma) with an increase of the fibrotic component, we can visualize more vacuolized structures not for a lack of fibrotic integration but for the pathologic fibrotic beams. Although the implant seemed to be surrounded by a fibrotic tissue envelope, US technique can be considered an excellent way to visualize the clinical

features and the pathologic process of implanted biomaterials. It represents a low-cost and low-radiation dose technique for a careful follow-up of patients affected by facial deficit disease after biomaterial implantation. The US technique shows a high radiologic sensibility in evaluating the features of the biomaterials. For its use, the limited cost and lack of investigation on harmful US is the key for studying of the biomaterials. (18)

#### 4. Discussion

A biomaterial is defined as a several composed structure, able to interface with the biological systems in order to increase the volume, to give support or to replace a tissue. The performances of the installed materials are evaluated on the basis of bio-functionality and bio-availability therefore bio-compatibility (1).

The bio-functionality is the property of a bio-material to produce a determinate function from the physical and mechanical point of view while the bio-availability is the capacity of a bio-material to develop a determinate function during all the useful life of the plant (2). The final properties of a material depend both on the intrinsic molecular structure of the polymer and on the chemical and physiques processes to which it is exposed and can be widely manipulated intervening on the 10 operating conditions of such processes and on the polymerization's reaction. The immediate answers of the human body to the action of a bio-material is divided in two phases: an inflammation is initially developed because of the first defensive reaction of the organism to an foreign body; subsequently there is a restorative process of the damage. In general if the installed material is toxic, this causes the necrosis of the surrounding tissues; if it is not toxic and inert under the biological point of view a fibrous capsule around to the plant is formed (this answer is quite rare because the biomaterial is usually not completely inert); if, at last, the material is bioactive, it stimulates a precise biological answer and it is progressively supplemented with the surrounding tissue .

In most cases the material undergone some degradation form and the products of such process are released in the tissues. Such products, if they are not biologically active and they are not toxic, are removed with the normal metabolic processes, if however their concentration reaches high values they can locally accumulate and give an acute or chronic pathologies .In case, instead, of toxic products, a persistent inflammation developed; the products of the degradation processes, can stay in the releasing zone, with only local effects, or they can spread in the vascolare system and have so effects also on organs and tissues far from the releasing zone. The progress of the medical research has allowed the perfecting and the development of new biomaterial in the reconstructive surgery, that has aesthetic licence to obtain excellent results by no much invasive surgical techniques and immediate results. An ideal bio-material presents these characteristics: absence of toxicities, anti-allergic properties, bio-compatibility (2), biofunctionality, easy to use and easy to remove. In our study the porous polyethylene and the bio bone have been analysed as substitutive of the hard tissues and the polyacrylamide and polialkylimide for the soft tissues (3). The bony reintegration is a complex and multi-factory process studied end analyzes in the time (4). At present several substitutive alternatives of the bone by autologus and eterologus bone, biomaterial are possible. Since the past what better choice was considered the allograft bone (5-6) which was useful for replacement of big bony deficits even if with difficult 11 vascularization (16-50% of fractures)(7). The bone-conductive, mechanical and

immunological properties were good but correlated to the seat of the withdrawal and to the type of bone processing (5-7-8-9). The Demineralized Bone Matrix can be easily extracted with 0.5 or 0.6 NHCL (10-11)

from the allograft bone so as to obtain an increase in the bone-inductive capacities, the loss of the immunological power and an increase in his supplementary effectiveness (12). One of the limits of the Demineralized Bone Matrix is his malleable consistency which makes him suitable for the bony filling most than to the bony replacement, above all in districts of the face that is not subject to the traction of the soft tissues (13). Everybody notice the porous polyethylene, used for the reconstruction of the hard tissues of the face; This material presents bio-compatibility with the human organism and easy malleability (14). This includes that the surgical time are considerably reduced and the surgical procedure are not much invasive. One of the advantages of this material is his property to restore big bony deficits, contributing to give volume to the absent structures . It is fixed by screws, which contribute to the maintenance of a fixes position in the time, as it is also taken back in literature (15). His utilization can be corollary of the orthognathic surgery in the restoration of the facial harmony or in the treatment of facial asymmetries from pathologies. Sharpen for this big variety of applications the porous polyethylene exists in various forms concerning the various facial places to restore: orbital margin (15), nasal dorsum, mandibular ramus. The injectable filler are very commonly used for the treatment of soft alterations of the tissues of the face; these can be of different nature and composition. Are commonly divided in temporary and permanent; in our work take the permanent filler into consideration like the plyacrylamide and polialkylimide. These are also defined of the "hidrogel", for the high water content; their use has prevalently aimed at the filling of soft tissues, whit satisfactory results. Their principal properties are: elasticity, permeability and high bio-compatibility with the organism. Of these we remember the polialkylimide, injective bio-material formed by 2.5% of synthetic polymer of polyalkylimide and for 97.5% from a pirogen water. Studies have been also executed in 12 vitro and they have shown a low toxicity and cutaneous sensibilization, following prolonged treatment. The polyacrilyamide (16- 17) is an injectable bio- material, formed by 3% of reticulate polymer of polyacrylamide and 97% from not pirogenic water. It is an hydrophilus absorbent gel, what comes infiltrated in deficit of the soft tissue. His mechanism of action is to add volume to the soft tissues, restoring the normal structures of the face. This bio material has an easy applicability also in different pathologies; important is not to use in post herpetic phase. It needs several applications for the partial absorption which can verify.

## 5. Results and conclusion

The study's results, based on our experience, have been more than satisfactory. The 290 treated patients, have given optimum results to a 6 year follow up. And also true that the experience acquired during the years about the porous polyethylene is previous of 12 years from the beginning of our study, that is happened in 2000. The justify for which in such work we considered the patient treated from this date, is due to the fact that before we did not have a sufficient sample of patient treated with other filling biomaterial to compare with porous polyethylene already mentioned. In aesthetics surgery the new fillers got rich of greater biological qualities and of easy utilization and their application has made possible for various infectious, malformativ or post-traumatic pathologies. This comparison has been optimum, in the perspective of a patient's better management and treatment of the deficits

of the facial soft tissue: in order to choose the biomaterial as much as more suitable and bio-compatible with the host organism. To a careful evaluation of every single case, the results have not been completely uniform; in the patients treated with polyalkylimide, adverse reactions have happened: in two cases has verified a multi-capsule formations around the biomaterial, with relative capsule formation and in only one case the rejection, with adverse cutaneous reaction. In particular the case of rejection has verified in subject with Hemi-facial atrophy. The phenomenon of compartmentalization was verified in only two cases, it was not due to the absence of integration of the biomaterial with the organism but it was consequent to the 13 autoimmune pathology. For the subjects treated with polyacrylamide adverse reactions have not happened; the material has shown a good integration in patients with various pathologies. This biomaterial turns out to be of easier utilization and provided with greater fluidity injection. For what concerns the patients affected with infectious pathologies like HIV, their treatment with filling biomaterial has given both recent and after 3 year distance good results; rejection events have not happened. Such patients are constantly evaluated by the infective point of view; we have experiences of biomaterial's utilization in HIV+ patients with HAART treatment which present lipodystrophy lesions. The malleability and easy application of the hydrogel, an utilization of theirs has made possible in combination to other biomaterials. The use of different biomaterials in the same patient is necessary when the deficit to fill was high and when the simple application of an only one biomaterial was turning out insufficient. The treated cases have given good results and good tolerance between the installed material. Porous polyethylene, bio-bone, Polyalkylimide, Polyacrylamide offer a good alternative in selected cases to the traditional reconstructive surgery, for the immediate results and easy way of application. A follow up of at last six years through echography and Computed Tomography exams shows their biocompatibility, stability and inactivity, The restoring of symmetry and harmony of a face can be reached through both traditional surgery and also using biomaterials, that can substitute tissues graft or osteotomy with an easy way of application, their stability and their long lasting, not last a good esthetic result.<sup>14</sup>

## 6. References

- Bulbulian AH. Maxillofacial prosthetics: evolution and practical application in patient rehabilitation. *J Prosthet Dent* 1965; 15:554Y569
- Fini Hatzikiriakos G. Uno sguardo al passato, curiosita` sulle protesi nasali. *Il Valsala* 1985;61:61Y64
- Tjellstrom A. Osteointegrated implants for replacement of absent or defective ears. *Clin Plast Surg* 1990;17:355Y366
- Tjellstrom A, Granstrom G. One stage procedure to establish osteointegration: a zero to five years follow-up report. *J Laryngol Otol* 1995;109:593Y598
- Schaaf NG. Maxillofacial prosthetics and the head and neck cancer patients. *Cancer* 1984;54:2682Y2690
- Labbe´ D, Be´nateau H, Compe`re JF, et al. Implants extra-oraux: indications et contre-indications. *Rev Stomatol Chir Maxillofac* 2001;102:239Y242
- Be´nateau H, Crasson F, Labbe´ D, et al. Implants extra-oraux et irradiation: tendances actuelles. *Rev Stomatol Chir Maxillofac* 2001;102:266Y269
- Granstrom G, Jacobsson M, Tjellstrom A. Titanium implants in irradiated tissue: benefits from hyperbaric oxygenation. *Int J Oral Maxillofac Implants* 1992;7:15Y25

- Markt JC, Lemon JC. Extraoral maxillofacial prosthetic rehabilitation at the M.D. Anderson Cancer Center: a survey of patient attitudes and opinions. *J Prosthet Dent* 2001;85:608Y613
- Tjellstrom A, Granstrom G. One-stage procedure to establish osteointegration: a zero to five years follow-up report. *J Laryngol Otol* 1995;109:593Y598
- Ramires PA, Miccoli MA, Panzarini E, Dini L, Protopapa C. In vitro and in vivo biocompatibility of a Polykymide Hydrogel for soft tissue augmentation. *J.Biomed.Mater.Res.Part*.2004; 72: 230-238. 2004.
- Christensen LC, Breiting VB, Aasted A, Jorgensen A, Kebuladze I. Long-Term effects of polyacrylamide hydrogel in human breast tissue. *Plast.Reconstr.Surg*.2003; 11:1883-1890
- Rees TD, Ashlet FL, Delgado JP. Silicone fluid injectons for facial atrophy: a 10 years study.*Plast.Reconstr.Surgery*. 1985;52: 118-125.
- Greenwald AS,bBoden SD, goldberg VM et al.Bone graft substitutes: Facts, fictions and applications. *J. Bone Joint Surg Am* 2001; 83-A:S98-S103
- Bauer TW, Muschler GF. Bone Graft Materials. An overview of The basic scienze. *Clin Orthop*. 2000; 371:10-27.
- Oka Y, Ikeda M. Treatment of severe osteochondritis dissecans of the elbow using osteochondral grafts from a rib. *J Bone Joint Surg Am*. 2001 83-b: 738-739
- Stevenson S. Biology of bone grafts. *Orthoped Clin North Am*. 1999; 30:543-552.
- Skowronski PP, An Yh. Bone graft materials in orthopaedics.MUSC Orthopaed J. 2003;6:58-66
- Betz RR. Limitation of autograft and allograft: new synthetic solutions. *Orthopedics* 2002;25(Suppl):S561-S560
- Hollinger JO, Mark DE, Goco P, et al. A comparison of four particulate bone derivatives. *Clin*
- Pietrzak WS, MillervSD, Kucharzyk DW, et al. Demineralized bone graftvformulations: Design, development, and a novel exemple. Proceedings of the Pittsburg BonevSymposium, Pittsburgh, PA, August 19-23,"003,557-575.
- Davy DT.Biomechanical issues in bone transplantation. *Orthop Clin North Am*.1999;30:553-56 science and technology for the Craniomaxillofacial Surgeon.*J Craniofac. Surg*. 005(16);6:981-988.15
- Mauriello JA, McShane R, Voglino J. Use Vicryl( Polyglactina 910) mesh implant for correcting enophtalmos A study of 16 patients. *Ophthal Plast Reconstr Surg* 1990; 6:247-251.
- S. Ozturk, M Sengezer, S Isik et all. Long Term Outcomes of Ultra Thin Porous Polyethylene Implants used for Reconstruction of Orbital Floor Defects. *J Craniofac Surg*. 2005 (16) 6:973-977.
- S. Buelow, D Heimburg, N. Pallua. Efficacy ad Safety of Polycrylamide Hydrogel for Facial Soft-Tissue Augmentation. *Plast Reconstr Surg* 2005 (15);1137-1146. KW Broder, SR Cohen. An Overview of Permanent and Semipermanent Fillers. *Plast Reconstr Surg* 2006 118(3 suppl.) S7\_S14 Biomaterial Implantation in Facial Esthetic Diseases: Ultrasonography Monitor Follow-Up
- Elena Indrizzi, MDS, Luca Maria Moricca, MD, Valentina Pellacchia, MD, Alessandra Leonardi, MD, Sara Buonaccorsi, MD, Giuseppina Fini, MDS, PhD. The Journal of Craniofacial Surgery -Vol.19, N. 4 -July 2008

## **Part 4**

# **Prevention and Management of Biological Phenomena at Biomaterial/Cell Surfaces**





# Biomaterials in Urology - Beyond Drug Eluting and Degradable - A Rational Approach to Ureteral Stent Design

Dirk Lange, Chelsea N. Elwood and Ben H. Chew  
*The Stone Centre at Vancouver General Hospital, University of British Columbia  
Canada*

## 1. Introduction

Ureteral stents are commonly used in urology to provide urinary drainage of the upper tracts, particularly following treatment of urolithiasis. Stents are commonly plagued with infections and encrustation, particularly in stone-forming patients (Denstedt and Cadieux 2009). This involves a multistep process outlined in Figure 1. The first step is formation of a conditioning film comprised of urinary proteins, ions, and crystals that are deposited at the stent surface (Tieszer, Reid et al. 1998). The conditioning film becomes an attractive surface for bacteria to adhere to and forms a biofilm which can lead to a urinary tract infection or encrustation (Wollin, Tieszer et al. 1998; Choong and Whitfield 2000; Choong, Wood et al. 2001; Shaw, Choong et al. 2005). Bacteria have been demonstrated to adhere to the stent surface in up to 90% of indwelling stents, which in 27% of cases leads to a positive urine culture (Reid, Denstedt et al. 1992).

Ideally, ureteral stent biomaterials would be able to limit or completely prevent the processes shown in Figure 1. Various attempts have been made to reduce the deposition of crystals, bacteria, and protein on stent surfaces including using low surface energy biomaterials (Tieszer, Reid et al. 1998), heparin coating (Cauda, Cauda et al. 2008), antimicrobial eluting biomaterials (Cadieux, Chew et al. 2006; Chew, Cadieux et al. 2006; Wignall, Goneau et al. 2008; Cadieux, Chew et al. 2009), diamond-like carbon coatings (Laube, Kleinen et al. 2007), polyethylene glycol and marine mussel adhesive proteins (Pechey, Elwood et al. 2009) to name just a few. Most have limited effectiveness and some have even shown increased bacterial adhesion compared to controls in the case of heparin coating (Lange, Elwood et al. 2009). While drug-eluting technology of biomaterials is both readily available and used clinically in other fields, its role in urology has been limited. Triclosan was used recently in ureteral stents. It held promise in *in vitro* (Chew, Cadieux et al. 2006) and animal infection models (Cadieux, Chew et al. 2006) but it fared poorly in those patients requiring chronic ureteral stents (Cadieux, Chew et al. 2009). The current methodology of technological implementation surrounding ureteral stent coating and design have come from trial and error or are borrowed technologies from coronary and vascular stenting. The time has come for the urological world to apply the same types of scientific discovery and development to problems specific to urinary devices rather than just applying the end product from other areas of medicine. What works in vascular stenting may not be directly applicable to the urinary environment.

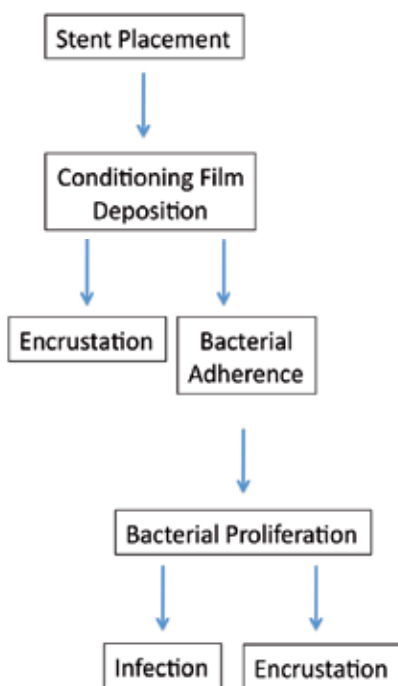


Fig. 1. The processes following stent insertion that lead to bacterial adhesion, infection, and encrustation. Following stent insertion, urinary components deposit on the surface, forming anchor points for both bacteria as well as ions/minerals. Subsequent bacterial colonization and proliferation leads to the formation of a resistant biofilm that leads to subsequent infection. In addition the interaction of ions/minerals with conditioning film components and bacterial induced crystallization will facilitate encrustation of the device. Inhibition of the common step of conditioning film deposition is a potential step in preventing patient symptoms associated with indwelling ureteral stents.

## 2. Problems arising from stents

Stents have been associated with increased morbidity causing infection,(Riedl, Plas et al. 1999) encrustation,(Paick, Park et al. 2003) hematuria,(Damiano, Oliva et al. 2002; Joshi, Newns et al. 2003; Joshi, Chitale et al. 2005) and discomfort (Joshi, Stainthorpe et al. 2001; Joshi, Okeke et al. 2002). The Ureteral Stent Symptom Questionnaire (USSQ) looks at different facets of life including sexual function which has been shown to be negatively affected by the presence of a stent (Sighinolfi, Micali et al. 2007). In fact, ureteroscopes, intracorporeal lithotriptors, and ureteroscopic techniques have improved to the point that the major morbidity of ureteroscopy has become the stent left *in situ* postoperatively. Studies evaluating differences in postoperative complications and stone-free rates in stented compared to non-stented patients have shown that stents are not a routine requirement following uncomplicated ureteroscopy (Hosking, McColm et al. 1999; Borboroglu, Amling et al. 2001; Denstedt, Wollin et al. 2001). The uncommon, but most severe problem arising from stents is the “forgotten stent” that is left in place for several months to years. These stents become encrusted and create difficulty for both patient and urologist, especially since their

removal involves multiple surgical procedures (Rana and Sabooh 2007) and may result in loss of the renal unit or potentially even death (Singh, Srinivastava et al. 2005).

### **3. Current stent biomaterials**

The synthetic polymer, polyethylene, was previously used in stent construction, but was abandoned due to its stiffness, brittleness, and tendency to fragment. Blends of polyethylene and other polymers, such as polyurethane, have been shown to resist encrustation (Gorman, Tunney et al. 1998; Gomha, Sheir et al. 2004). Silicone is currently the most biocompatible stent material as it is the most resistant to biofilm formation, infection and encrustation (Watterson, Cadieux et al. 2003), and is one of the most lubricious materials available (Jones, Garvin et al. 2004); however, its softness and elasticity make it difficult to handle, particularly through tortuous or tight ureters. In addition, the low tensile strength of silicone makes it susceptible to extrinsic compression. The development of new stent materials aimed to meld the flexible and elastic properties of silicone with the rigidity of polyethylene which resulted in the development of polyurethane, the most common class of polymer currently used in stents. Polyurethane, however, is a stiff material that causes patient discomfort and significant ureteral ulceration and erosion have been reported in an animal model (Marx, Bettmann et al. 1988). New proprietary materials and combinations are softer, more comfortable, and easier to maneuver within the urinary tract. Examples of commonly used materials in stents include Percuflex® (Boston Scientific Corporation, Natick, MA), Silitek® (Surgitek, Medical Engineering Corporation, Racine, WI, USA), C-Flex® (Consolidated Polymer Technologies, Clearwater, FL, USA), Tecoflex® (Thermedics, Wilmington, MA, USA), and ethylene-vinyl-acetate (from the polyefin family of which polyethylene is a member). They have been designed to provide rigidity to facilitate handling by the surgeon and to provide adequate drainage while being soft enough to limit patient discomfort.

### **4. New materials**

New materials include metal stents that are designed to keep the ureter open despite extrinsic ureteral compression secondary to lymphadenopathy due to malignancy. Ureteric obstruction may result in decreased renal function, pain, or infection requiring urinary diversion (Chitale, Scott-Barrett et al. 2002; Allen, Longhorn et al. 2010). As these stents must remain in place for long periods of time, they require frequent exchanges because they are susceptible to infection and encrustation with increased indwelling time. The goal in this patient population is to develop a stent that maintains ureteral patency during extrinsic compression, is soft to minimize discomfort, and is resistant to encrustation and infection.

### **5. Metal ureteral stents**

Metal ureteral stents were introduced by Pauer in 1992 (Pauer and Lugmayr 1992) and have been utilized in the treatment of malignant ureteric obstruction (Kulkarni and Bellamy 2001; Liatsikos, Karnabatidis et al. 2009; Masood, Papatsoris et al. 2010; Papatsoris and Buchholz 2010; Sountoulides, Kaplan et al. 2010), ureteral strictures (Daskalopoulos, Hatzidakis et al. 2001; Papatsoris and Buchholz 2010), and ureteropelvic junction obstruction (Barbalias, Liatsikos et al. 2002; Masood, Papatsoris et al. 2010; Benson, Taylor et al. 2011). Current

problems associated with metallic stents include biofilm formation, infection, migration, and tissue hyperplasia leading to luminal obstruction (Barbalias, Liatsikos et al. 2002; Wah, Irving et al. 2007; Liatsikos, Karnabatidis et al. 2009; Sountoulides, Kaplan et al. 2010).

Metal stents were originally used for the relief of end-stage malignant disease, where the ureteral stricture was either directly caused by the tumor or indirectly via pressure of a tumor on the ureter. Pauer and Lugmayr used metallic ureteral stents in 1996 (Pauer and Lugmayr 1996) to treat 54 malignant stenoses of the ureter in 40 patients via the implantation of a self-expandable permanent endoluminal stent (SPES), the Wallstent™. During a follow-up period of 10.5 months, 51 ureters maintained adequate patency. Of these, 51% needed no further intervention, while 49% needed intervention to re-establish patency. In comparison insufficiency was noted at a mean 4.3 weeks in control patients with an indwelling Double-J catheter. One of the drawbacks of metal stents is, however, that they induce local urothelial hyperplasia, with ingrowth of tissue through the struts that may result in recurrent obstruction during long term placement. Recently, a nickel-cobalt-chromium-molybdenum-alloy stent double pig-tailed stent (Resonance™ Stent, Cook Urological, Spencer, IN, USA) has been developed to provide long-term urinary drainage in patients with malignant ureteric strictures (Blaschko, Deane et al. 2007; Wah, Irving et al. 2007; Lopez-Huertas, Polcari et al. 2010; Wang, Lee et al. 2010). The tight winding of this metal stent helps to maintain stent flexibility and movement, while resisting in-growth of tissue. In addition to this, the movement of the stent causes opening of the coils, allowing the fluid to access the lumen. In a study of 15 patients, this metal stent provided adequate long-term (up to 12 months) urinary drainage in patients with malignant ureteric obstruction without significant bulky pelvic disease. These stents were also found to have minimal encrustation (Wah, Irving et al. 2007). An *in vitro* study has shown that this metal stent provides its best drainage when the ureter is tightly compressed onto its outer surface which is likely due to the result of increased flow between the coils of the metal stent. It was this feature that makes the Resonance™ stent useful in patients in which the ureter is obstructed due to malignancy (Blaschko, Deane et al. 2007; Liatsikos, Karnabatidis et al. 2009; Masood, Papatsoris et al. 2010; Sountoulides, Kaplan et al. 2010; Wang, Lee et al. 2010; Benson, Taylor et al. 2011).

## 6. Biodegradable stents

Despite the fact that the biocompatible materials and stent designs have improved over the years, they have one key disadvantage, which is the fact that they have to be removed via a separate procedure unless the retention suture is left on the stent. Avoiding a secondary procedure for ureteral stent removal would decrease patient morbidity and make this technology attractive. More recent research has focused on the design of stents that do not need to be removed and are biodegradable. The design of a biodegradable stent must take into consideration the biocompatibility properties of the material, as well as the degree of expansion and degradation rates, and most importantly it must be able to fulfill the basic requirement of a stent in that it must be able to guarantee urinary flow from the renal pelvis through the ureter and into the bladder for the desired period of time. Degradable materials also must retain their properties after sterilization and be able to withstand a long shelf-life before use. One of the challenges involved in designing a biodegradable stent is the control of the rate and direction of degradation. Schlick and Planz (Schlick and Planz 1997; Schlick and Planz 1998) designed a stent composed of plastic, the degradation of which was

dependent upon the urine pH. In vitro experiments with artificial urine showed that the stents were stable at urine pH less than 7.0 for at least 30 days, while they dissolved completely within 48 hours at pH greater or equal to 7.0. The principle behind this stent is that it would remain stable at physiological urine pH of 5-6, but can be triggered to dissolve by medically altering urinary pH. Although very promising, this technology remains at an experimental stage and awaits animal trials. An additional factor that may need to be taken into consideration is the influence of encrustation protein deposition as it can form a platform for bacterial adherence and infection. The influence of encrustation and protein deposition must also be considered as it can form a platform for bacterial adherence, all of which may influence urine pH. Uropathogens in general are known to increase urine pH, and may have an effect *in vivo*. In addition to this, medically increasing the urinary pH may introduce an additional risk for infection as more alkaline pH favours bacterial survival and some increased stone formation (calcium phosphate and struvite stones). In addition, encrustation of the stent may also prevent its exposure to the altered pH environment, environment and the altered pH, thus limiting its rate of decomposition.

A spiral stent (Spirastent<sup>®</sup>, Urosurge Medical, Coralville, IA) is a polyurethane stent with metal helical ridges designed to prevent kinking and compression in chronically obstructed patients. In *in vitro* studies, this stent increased flow and theoretically increased the space between stent and ureter to facilitate passage of stone fragments.(Stoller, Schwartz et al. 2000) The spiral design has been incorporated into biodegradable materials for urethral stents.(Isotalo, Talja et al. 2002; Laaksovirta, Isotalo et al. 2002) Laaksovirta et al used a self-reinforced poly-L-lactic and poly-L-glycolic acid (SR-PLGA) copolymer spiral urethral stent (SpiroFlow stent, Bionx Implants Ltd, Tampere, Finland) following prostatic laser coagulation.(Laaksovirta, Isotalo et al. 2002) This stent degraded in 6–8 weeks and resisted encrustation at 4 weeks in artificial urine. After 8 weeks, the SpiroFlow<sup>®</sup> stent was significantly less encrusted than the metal urethral stents Prostakath<sup>®</sup> (Engineers and Doctors A/S, Copenhagen, Denmark) and Memokath<sup>®</sup> 028 (Engineers and Doctors A/S). SR-PLGA is the most commonly utilized material for prostatic stents, but it has also been developed as a ureteral stent and may be incorporated into new degradable, encrustation-resistant ureteral stents in the future.(Olweny, Landman et al. 2002)

An alginate based ureteral stent was designed to stay in place for at least 48 hours after uncomplicated ureteroscopy.(Lingeman, Preminger et al. 2003; Lingeman, Schulsinger et al. 2003) Of 87 patients, 80.5% of patients retained their stents greater than 48 hours. Seventeen patients had early stent passage (earlier than 48 hours), but did not require any supplemental procedures to insert another stent. Although these results were promising, several patients (14) still had stent fragments remaining at 30 days, while 3 patients had stent fragments remaining after 90 days. All three of these patients underwent shockwave lithotripsy and two went on to have endoscopic ureteroscopy to remove the fragments from the kidney. Because of the lack of all stents to degrade by 3 months, this stent is no longer commercially available. (Lingeman, Preminger et al. 2003)

The authors are currently involved in developing a new biodegradable stent (Poly-Med Inc., Anderson, SC) that dissolves within 1 to 4 weeks in a porcine model. The animals stented with degradable stents displayed less histologic inflammation than animals stented with control polyurethane biostable Double J stents (Chew, Lange et al. 2010). Weekly intravenous pyelograms displayed less hydronephrosis in the degradable stent group. All stents degraded by 4 weeks and degradation began after 1 week in a very controlled fashion

and no animal had a distal obstructed ureter Due to retained stent pieces. Properties such as stent softness from these biodegradable stents may improve patient comfort. Clinical studies will be necessary to determine if biodegradable stents are more comfortable.

## 7. Stent coatings

One of the most common stent coatings is hydrogel, which consists of hydrophilic polymers that absorb water and increase lubricity and elasticity. (Marmieri, Pettenati et al. 1996; John, Rajpurkar et al. 2007) These properties facilitate stent placement, making the device rigid and easily maneuverable in its dry state, but once exposed to urine, the hydrogel begins to absorb and trap water in its polyanionic structure, causing it to soften and theoretically increase patient comfort. Data on encrustation and infection are less convincing, as hydrogel has been shown to both reduce (Gorman, Tunney et al. 1998) and increase encrustation and biofilm formation (Desgrandchamps, Moulinier et al. 1997). Hydrogels have been used in an attempt to soak and retain antibiotics but an *in vitro* study did not show increased efficacy of bacterial killing compared to non-antibiotic soaked hydrogel coated stents (John, Rajpurkar et al. 2007).

Glycosaminoglycan (GAG), a normal constituent of urine, is a natural inhibitor of crystallization. Other novel stent coatings include pentosan polysulfate (Zupkas, Parsons et al. 2000) (a member of the Glycosaminoglycan family a normal constituent of urine and a natural inhibitor of crystallization), phosphorylcholine (Stickler, Evans et al. 2002) (a constituent of human erythrocytes that mimics a natural lipid membrane), and polyvinyl pyrrolidone (Tunney and Gorman 2002) (a hydrophilic coating, similar to hydrogel, that absorbs water).

Attempts to reduce encrustation have included other stent coatings, such as the bacterial enzyme, oxalate decarboxylase, which has been shown to decrease encrustation in silicone discs placed in rabbit bladders. (Watterson, Cadieux et al. 2003) A novel coating of mPEG-DOPA<sub>3</sub>, a natural constituent produced by mussels that produces strong adhesive properties, also has the ability to avoid biofouling in the environment. The polyethylene (PEG) component provides the antifouling property while the DOPA<sub>3</sub> provides the adherence that PEG lacks on its own. Adherence of these combined compounds on silicone disks has resulted in a strong ability to resist bacterial adherence and growth *in vitro*. (Ko 2007) Further development of this type of coating was studied *in vivo* using a rabbit *E. coli* cystitis model (Pechey, Elwood et al. 2009). This study showed that the anti-adhesive coating was successful at inhibiting bacterial adhesion and decreased the incidence of infection, however it was unable to prevent non-bacterial mediated encrustation.

Plasma deposited diamond like carbon coatings have been used to coat stents in an attempt to prevent encrustation (Laube, Kleinen et al. 2007). *In vitro* experiments have shown a 30% decrease in encrustation of these stents in artificial urine compared to the non-coated controls. Ongoing clinical trials appear to indicate a further enhancement of these results *in vivo*, however a mechanism for this needs to be elucidated. Encrustation of ureteral stents remains one of the most common problems associated with ureteral stenting and more research will need to be done for an optimal stent design which resists the deposition of bacteria, minerals and proteins.

In vascular medicine, the anticoagulant heparin has been shown to inhibit bacterial attachment to venous catheters (Ruggieri, Hanno et al. 1987; Appelgren, Ransjo et al. 1996), which has been attributed to its highly negative charge. Similarly, effects of heparin have

also been observed for ureteral stents. Riedl *et al.* (Riedl, Witkowski *et al.* 2002) used heparin-coated and uncoated polyurethane ureteral stents and inserted them into obstructed ureters with indwelling times between 2 and 6 weeks. Electron microscopy showed that the uncoated control stents were covered with amorphous anorganic deposits and bacterial biofilms as early as 2 weeks following stent insertion, while the heparin-coated stents remained unaffected by encrustation following 6 weeks of indwelling time. Cauda *et al.* (Cauda, Cauda *et al.* 2008) performed a long term study involving patients with bilateral ureteral obstructions treated via the insertion of a heparin-coated stent into one ureter, and an uncoated control stent into the other ureter. Overall, the uncoated control stents were found to be encrusted with amorphous, crystalline inorganic deposits and bacterial biofilm as early as 1 month post-insertion, while the heparin-coated stents remained visibly free of encrustation as long as 10 months post-insertion. Biofilm encrustation was evident only on the external surface of the coated stent after 1 year of being in place. Heparin coated ureteral stents (Radiance Stent, Cook Urological) were tested in an *in vitro* model of infected urine and did not display any reduction in bacterial adherence compared to control stents (Lange, Elwood *et al.* 2009). These preliminary results are somewhat promising, but clinical trials involving a larger number of patients are needed to ensure that heparin coating of stents is effective across a broader patient range.

## 8. Drug eluting stents

The most serious complications of long term stenting involve infection triggered by bacterial adherence and biofilm formation on the surfaces of stents as well as patient discomfort due to stent placement. Much research has gone into the prevention of infection, and the most promising results have come from drug eluting stents. Triclosan is an antimicrobial used in many products including soap, surgical scrub, toothpaste, and mouthwash. It inhibits the highly conserved bacterial enoyl-ACP reductase, which is responsible for fatty acid synthesis and cell growth. Cadieux *et al.* reported that, compared to control stents, triclosan-loaded stents implanted in rabbit bladders infected with *Proteus mirabilis* were associated with significantly fewer urinary tract infections. (Cadieux, Chew *et al.* 2006) Chew *et al.* have shown that bacterial adherence to triclosan eluting stents is markedly reduced compared to regular stents. (Chew, Cadieux *et al.* 2006) These studies indicate that human clinical trials involving these stents are warranted.

Ureteral stents may also be loaded with pharmaceuticals to aid patient comfort, and to prevent encrustation. Irritative and painful stent symptoms have traditionally been managed with oral medications such as anticholinergics and analgesics, or even by stent removal. Drug-eluting stents release a medication that acts locally on the bladder to decrease irritation and pain. In an attempt to determine which medication might improve stent-related symptoms, Beiko *et al.* intravesically instilled 3 different medications into the bladder of 40 patients who received a ureteral stent at the time of shockwave lithotripsy. (Beiko, Watterson *et al.* 2004) Intravesical ketorolac significantly reduced flank pain scores following stent insertion compared to lidocaine or oxybutynin following SWL. A ketorolac-eluting ureteral stent was designed and shown to produce the highest levels of ketorolac in the ureteral tissues in a porcine model (Chew, Davoudi *et al.* 2010). The levels of ketorolac in the ureter were 11 fold of that found in the serum thereby reducing potential systemic side effects while delivering medication directly to the target area. The stent was biocompatible and systemic levels of ketorolac were negligible. A double-blinded prospective randomized controlled trial comparing ketorolac-eluting ureteral stents to

controls showed no difference in pain scores except in young males who had less symptoms with the ketorolac eluting stent (Krambeck, Walsh et al. 2010).

Liatsikos *et al* have tested paclitaxel eluting metal stents in the pig ureter to examine the tissue effects and stricture formation. (Liatsikos, Karnabatidis et al. 2007) Paclitaxel eluting stents produced less ureteral inflammation and hyperplasia of the surrounding tissue compared to the bare metal stents. Ureteral patency was lost in the control stents and maintained by the Paclitaxel eluting stents. These studies were carried out over a 21 day period and require further validation via long term animal trials.

Stent encrustation worsens with increased indwelling time and concurrent infection with urease-producing organisms. Oxalate is normally broken down in the gastrointestinal tract by the enzyme oxalate decarboxylase, which is found in a commensal organism *Oxalobacter formigenes*. Oxalate that escapes degradation and fecal excretion is absorbed into the bloodstream and filtered in the kidneys where, under certain conditions, it can combine with calcium to form calcium oxalate stones. Watterson *et al.* coated silicone disks with oxalate decarboxylase and implanted these into rabbit bladders. (Watterson, Cadieux et al. 2003) After 30 days, the oxalate decarboxylase-coated disks were significantly less encrusted than control disks. Coating ureteral stents with such an enzyme could theoretically prevent encrustation as the stent would elute an enzyme to degrade urinary oxalate.

## 9. Identifying potential targets in stent design

When considering the design of new indwelling ureteral devices such as stents or catheters, the sequential steps triggering a given side effect should be taken into consideration, however this has been complicated by the complexity of mechanisms involved. Rational drug design hypothesizes that the alteration of a biological target has therapeutic value and forms the basis for the invention of new medications predicated on the identification and knowledge of a specific biological target. The first step involves turning to basic science and considering the molecular and biochemical pathways involved in the condition to identify specific targets for drug design. Once a target has been identified, its molecular structure is determined and a suitable drug that will alter it in a favorable manner is designed. Usually the target is a key molecule in a metabolic or signaling pathway specific to a disease condition or pathology (Mandal, Moudgil et al. 2009).

We believe that the same principals can also be applied to the design of ureteral stents, as the current stent designs have failed to live up to their expectations in the complex environment of the urinary tract. Given the fact that the mechanisms causing stent symptoms are unknown makes it difficult to identify a key target in the context of rational drug design to relieve patient symptoms. The identification of such a target in the urinary tract would be beneficial, as it will allow for the reduction or elimination of stent symptoms by targeting a single mechanism. However, in order for that to become a possibility, key steps in the mechanisms surrounding stent-related symptoms need to be identified to allow for their inhibition.

Although identifying a single receptor or enzyme target in the development of stent encrustation and infection is unlikely, a more solid understanding of the mechanism involved in this process is required. Several processes occur following stent insertion and the cumulative effect can result in stent associated symptoms suffered by the patient. It has been well documented that a urinary conditioning film deposits on the stent surface shortly following device insertion that consists of urinary components (Tieszer, Reid et al. 1998).



These components are believed to facilitate bacterial adhesion leading to bacterial colonization, proliferation, and biofilm formation with subsequent infection. Once a biofilm has formed, this environment facilitates recurrent infection and eradication of bacteria is difficult. Bacteria embedded within the biofilm change to a low metabolic state and undergo a low replication rate, thus rendering antibiotics (which are most effective against bacteria in high metabolic states and undergoing replication) ineffective. In many cases, embedded bacteria are also protected since antibiotics cannot penetrate the biofilm and the protecting exopolysaccharide layer excreted by the bacteria onto its surface. Thirdly, bacteria can upregulate resistance genes once inside the biofilm (Lewis 2005).

Aside from biofilm formation and infection, another symptom associated with patient morbidity caused by indwelling ureteral stents is device encrustation. Stent encrustation can be idiopathic and caused by calcium oxalate crystals. In other instances, stent encrustation can be attributed to the presence of urease producing bacteria, which break down urinary ammonia into ammonium (thus effectively taking a hydrogen ion), which results in a rise in urinary pH and crystallization of magnesium, ammonium and phosphate ions. These crystals then adhere to the surface of the stent via the interaction with components of the conditioning film. The conditioning film on the stent surface is considered to be a great contributor to bacterial associated encrustation because it facilitates bacterial adhesion and crystal adhesion to the stent surface. In addition to this, the conditioning film has also been implicated in idiopathic encrustation (in the absence of bacteria) of the stent with calcium oxalate crystals. As such, certain conditioning film components have been proposed to be able to bind minerals from the urine, forming a nidus for crystal growth and device encrustation. To date, we have identified 3 potential targets to interrupt the sequence of events involved in the evolution of stent encrustation and infection: 1) preventing conditioning film formation, 2) preventing initial adherence and encrustation and 3) inhibition of further bacterial proliferation.

## 10. Current stent biomaterial design

Over the years, attempts have been made at preventing stent associated symptoms by targeting either bacterial adhesion and encrustation or inhibition of bacterial proliferation. Drug eluting technology to prevent bacterial adhesion has previously been used in a triclosan-eluting ureteral stent. Triclosan is an antimicrobial found in over 800 commercially available products such as soaps, hand scrubs, and toothpaste. This stent proved to be successful at eliminating bacterial loads *in vitro* (Chew, Cadieux et al. 2006) as well as a *Proteus mirabilis* urinary tract infection in a rabbit model (Cadieux, Chew et al. 2006), but did not show any significant differences in long term clinical trials (Cadieux, Chew et al. 2009). Similarly a heparin-coated stent was designed to prevent bacterial adhesion given the material's highly negative charge. This stent was shown to decrease encrustation in patients (Hildebrandt, Sayyad et al. 2001; Riedl, Witkowski et al. 2002; Cauda, Cauda et al. 2008), however was unable to prevent bacterial adhesion (Lange, Elwood et al. 2009). The use of diamond-like amorphous carbon as a coating on stents is a new technology that has shown some promise in terms of inhibiting encrustation (Laube, Bradenahl et al. 2006; Laube, Kleinen et al. 2007), however experiments aimed at determining its ability to inhibit bacterial adhesion is lacking. One of the drawbacks of these new technologies is the fact that they are susceptible to blockage by the deposition of the urinary conditioning film, which covers any coating and blocks elution of drugs from the stent, rendering it ineffective and promoting bacterial adhesion and encrustation via mechanisms discussed above.

## 11. Seeking novel targets in the pursuit of rational stent design.

Given the fact that the urinary conditioning film has been directly implicated in causing both bacterial adhesion and associated/non-associated encrustation, it becomes important to switch our focus from designing a biomaterial that inhibits direct bacterial and ion/mineral deposition to one that inhibits conditioning film components. It is important to focus on understanding this biological target further and the first step is to identify components of the conditioning film. Santin et al have previously identified human serum albumin as well as Tamm-Horsfall Protein (THP) as major conditioning film components found on four stents removed from patients (Santin, Motta et al. 1999). More recently, Canales et al have studied the conditioning films of stents removed from 27 patients, identifying hemoglobin alpha and beta chain, albumin, calgranulin B, fibrinogen beta chain, vitronectin, annexin A1, calgranulin A, fibrinogen gamma chain, and THP as the ten most common adherent components (Canales, Higgins et al. 2009). In addition, this group also hypothesized that the presence of histones likely contribute to stent encrustation given their unique net positive charge. Despite the fact that these papers have contributed to a large extent to the identification of conditioning film components, it still needs to be determined whether urinary conditioning films differ between stent types or patients, as the molecules targeted in stent design should be “universal” and need to be common between patients and stent types.

Our group has recently compared the composition of conditioning films found on certain stents from Boston Scientific (Polaris) to those on Bard stents (InLay) after they have been removed from patients (Lange et al, unpublished data). Both of these stents differ in their biomaterials, as the Polaris stent is made of an olefinic copolymer, while the InLay stent is made of polyurethane. To date, there does not appear to be a significant difference in the conditioning film composition from patients with the same stent type or between the two different stent types, indicating that conditioning film deposition is not affected by different stent biomaterials or patients. Similar results have also been obtained by Tieszer et al, who showed via X-ray photoelectron spectroscopy that the elemental composition of conditioning film components was unaffected by stent biomaterial or patient characteristics (Tieszer, Reid et al. 1998). Our study found that the fifteen most common proteins include cytokeratins, serum albumin, hemoglobin subunits alpha and beta, THP, fibrinogen gamma chain, protein S100A9, vitronectin and apolipoprotein. Interestingly, the majority of the fifteen most commonly found proteins are binding sites for bacteria and thus facilitate bacterial adhesion and biofilm formation. In addition to this, the presence of calcium binding proteins such as the S100 proteins or THP may act as a nidus for encrustation. We found that significantly less Polaris stents contained THP and fibrinogen gamma chain compared to the InLay stent, eliminating these two proteins as potential targets. Overall these results validate specific conditioning film components as targets for future stent biomaterial design as they appear to play a role in stent associated infection and encrustation. Further analysis will have to be performed to determine whether commonalities exist between the physical characteristics of these components and whether they can be targeted to inhibit their deposition.

Our current experiments are aimed at studying the temporal deposition of urinary components onto the surface of stent pieces, as some proteins such as serum albumin are known to bind to other proteins rather than the surfaces themselves. In the context of urinary component deposition, it is possible that certain proteins with a higher affinity to

the stent surface form a base layer to which other proteins such as serum albumin attach. Such a mechanism of deposition would be favorable for the purpose of rational stent design, as the proteins forming the base layer would make excellent targets for adhesion prevention. If temporal aspects can be determined in addition to the various layers of proteins, potential targets could be identified to prevent the initiating events of encrustation and infection.

## 12. Conclusions

We propose that the principles used by our colleagues in pharmaceutical research in the pursuit of rational drug design can be transferred to the design of novel ureteral stent biomaterials: 1) To understand the potential targets in ureteral stent encrustation and infection and 2) Develop biomaterials to limit these processes. Current research to date has focused on the prevention of bacterial adherence and encrustation; however, we propose that research interests should shift to the initial primary steps in conditioning film formation, thus perhaps preventing the whole cascade of events from occurring. Once these processes have been more clearly defined, the pursuit of highly specific engineered biomaterials can be started. Identification of specific targets would help direct the development of new materials and hopefully succeed where previous work has failed.

## 13. References

- Allen, D. J., S. E. Longhorn, et al. (2010). "Percutaneous urinary drainage and ureteric stenting in malignant disease." *Clin Oncol (R Coll Radiol)* 22(9): 733-739.
- Appelgren, P., U. Ransjo, et al. (1996). "Surface heparinization of central venous catheters reduces microbial colonization in vitro and in vivo: results from a prospective, randomized trial." *Crit Care Med* 24(9): 1482-1489.
- Barbalias, G. A., E. N. Liatsikos, et al. (2002). "Ureteropelvic junction obstruction: an innovative approach combining metallic stenting and virtual endoscopy." *J Urol* 168(6): 2383-2386; discussion 2386.
- Barbalias, G. A., E. N. Liatsikos, et al. (2002). "Externally coated ureteral metallic stents: an unfavorable clinical experience." *Eur Urol* 42(3): 276-280.
- Beiko, D. T., J. D. Watterson, et al. (2004). "Double-blind randomized controlled trial assessing the safety and efficacy of intravesical agents for ureteral stent symptoms after extracorporeal shockwave lithotripsy." *J Endourol* 18(8): 723-730.
- Benson, A. D., E. R. Taylor, et al. (2011). "Metal ureteral stent for benign and malignant ureteral obstruction." *J Urol* 185(6): 2217-2222.
- Blaschko, S. D., L. A. Deane, et al. (2007). "In-vivo evaluation of flow characteristics of novel metal ureteral stent." *J Endourol* 21(7): 780-783.
- Borboroglu, P. G., C. L. Amling, et al. (2001). "Ureteral stenting after ureteroscopy for distal ureteral calculi: a multi-institutional prospective randomized controlled study assessing pain, outcomes and complications." *J Urol* 166(5): 1651-1657.
- Borin, J. F., O. Melamud, et al. (2006). "Initial experience with full-length metal stent to relieve malignant ureteral obstruction." *J Endourol* 20(5): 300-304.

- Cadieux, P. A., B. H. Chew, et al. (2006). "Triclosan loaded ureteral stents decrease proteus mirabilis 296 infection in a rabbit urinary tract infection model." *J Urol* 175(6): 2331-2335.
- Cadieux, P. A., B. H. Chew, et al. (2009). "Use of triclosan-eluting ureteral stents in patients with long-term stents." *J Endourol* 23(7): 1187-1194.
- Canales, B. K., L. Higgins, et al. (2009). "Presence of five conditioning film proteins are highly associated with early stent encrustation." *J Endourol* 23(9): 1437-1442.
- Cauda, F., V. Cauda, et al. (2008). "Heparin coating on ureteral Double J stents prevents encrustations: an in vivo case study." *J Endourol* 22(3): 465-472.
- Chew, B. H., P. A. Cadieux, et al. (2006). "In-vitro activity of triclosan-eluting ureteral stents against common bacterial uropathogens." *J Endourol* 20(11): 949-958.
- Chew, B. H., H. Davoudi, et al. (2010). "An in vivo porcine evaluation of the safety, bioavailability, and tissue penetration of a ketorolac drug-eluting ureteral stent designed to improve comfort." *J Endourol* 24(6): 1023-1029.
- Chew, B. H., D. Lange, et al. (2010). "Next generation biodegradable ureteral stent in a yucatan pig model." *J Urol* 183(2): 765-771.
- Chitale, S. V., S. Scott-Barrett, et al. (2002). "The management of ureteric obstruction secondary to malignant pelvic disease." *Clin Radiol* 57(12): 1118-1121.
- Choong, S. and H. Whitfield (2000). "Biofilms and their role in infections in urology." *BJU Int* 86(8): 935-941.
- Choong, S., S. Wood, et al. (2001). "Catheter associated urinary tract infection and encrustation." *Int J Antimicrob Agents* 17(4): 305-310.
- Damiano, R., A. Oliva, et al. (2002). "Early and late complications of double pigtail ureteral stent." *Urol Int* 69(2): 136-140.
- Daskalopoulos, G., A. Hatzidakis, et al. (2001). "Intraureteral metallic endoprosthesis in the treatment of ureteral strictures." *Eur J Radiol* 39(3): 194-200.
- Denstedt, J. D. and P. A. Cadieux (2009). "Eliminating biofilm from ureteral stents: the Holy Grail." *Curr Opin Urol* 19(2): 205-210.
- Denstedt, J. D., T. A. Wollin, et al. (2001). "A prospective randomized controlled trial comparing nonstented versus stented ureteroscopic lithotripsy." *J Urol* 165(5): 1419-1422.
- Desgrandchamps, F., F. Moulinier, et al. (1997). "An in vitro comparison of urease-induced encrustation of JJ stents in human urine." *Br J Urol* 79(1): 24-27.
- Gomha, M. A., K. Z. Sheir, et al. (2004). "Can we improve the prediction of stone-free status after extracorporeal shock wave lithotripsy for ureteral stones? A neural network or a statistical model?" *J Urol* 172(1): 175-179.
- Gorman, S. P., M. M. Tunney, et al. (1998). "Characterization and assessment of a novel poly(ethylene oxide)/polyurethane composite hydrogel (Aquavene) as a ureteral stent biomaterial." *J Biomed Mater Res* 39(4): 642-649.
- Hildebrandt, P., M. Sayyad, et al. (2001). "Prevention of surface encrustation of urological implants by coating with inhibitors." *Biomaterials* 22(5): 503-507.
- Hosking, D. H., S. E. McColm, et al. (1999). "Is stenting following ureteroscopy for removal of distal ureteral calculi necessary?" *J Urol* 161(1): 48-50.

- Isotalo, T., M. Talja, et al. (2002). "A bioabsorbable self-expandable, self-reinforced poly-L-lactic acid urethral stent for recurrent urethral strictures: long-term results." *J Endourol* 16(10): 759-762.
- John, T., A. Rajpurkar, et al. (2007). "Antibiotic pretreatment of hydrogel ureteral stent." *J Endourol* 21(10): 1211-1216.
- Jones, D. S., C. P. Garvin, et al. (2004). "Relationship between biomedical catheter surface properties and lubricity as determined using textural analysis and multiple regression analysis." *Biomaterials* 25(7-8): 1421-1428.
- Joshi, H. B., S. V. Chitale, et al. (2005). "A prospective randomized single-blind comparison of ureteral stents composed of firm and soft polymer." *J Urol* 174(6): 2303-2306.
- Joshi, H. B., N. Newns, et al. (2003). "Ureteral stent symptom questionnaire: development and validation of a multidimensional quality of life measure." *J Urol* 169(3): 1060-1064.
- Joshi, H. B., A. Okeke, et al. (2002). "Characterization of urinary symptoms in patients with ureteral stents." *Urology* 59(4): 511-516.
- Joshi, H. B., A. Stainthorpe, et al. (2001). "Indwelling ureteral stents: evaluation of quality of life to aid outcome analysis." *J Endourol* 15(2): 151-154.
- Ko, R. C., PA; Dalsin, JL; Lee, BP; Elwood, CN, Razvi, H (2007). "Novel Uropathogen-Resistant Coatings Inspired by Marine Mussels." *Journal of Endourology* 21(Supplement No. 1): A5.
- Krambeck, A. E., R. S. Walsh, et al. (2010). "A novel drug eluting ureteral stent: a prospective, randomized, multicenter clinical trial to evaluate the safety and effectiveness of a ketorolac loaded ureteral stent." *J Urol* 183(3): 1037-1042.
- Kulkarni, R. and E. Bellamy (2001). "Nickel-titanium shape memory alloy Memokath 051 ureteral stent for managing long-term ureteral obstruction: 4-year experience." *J Urol* 166(5): 1750-1754.
- Laaksovirta, S., T. Isotalo, et al. (2002). "Interstitial laser coagulation and biodegradable self-expandable, self-reinforced poly-L-lactic and poly-L-glycolic copolymer spiral stent in the treatment of benign prostatic enlargement." *J Endourol* 16(5): 311-315.
- Lange, D., C. N. Elwood, et al. (2009). "Uropathogen interaction with the surface of urological stents using different surface properties." *J Urol* 182(3): 1194-1200.
- Laube, N., J. Bradenahl, et al. (2006). "[Plasma-deposited carbon coating on urological indwelling catheters: Preventing formation of encrustations and consecutive complications]." *Urologe A* 45(9): 1163-1164, 1166-1169.
- Laube, N., L. Kleinen, et al. (2007). "Diamond-like carbon coatings on ureteral stents--a new strategy for decreasing the formation of crystalline bacterial biofilms?" *J Urol* 177(5): 1923-1927.
- Lewis, K. (2005). "Persister cells and the riddle of biofilm survival." *Biochemistry (Mosc)* 70(2): 267-274.
- Li, X., Z. He, et al. (2007). "Long-term results of permanent metallic stent implantation in the treatment of benign upper urinary tract occlusion." *Int J Urol* 14(8): 693-698.
- Liatsikos, E. N., G. C. Kagadis, et al. (2007). "Application of self-expandable metal stents for ureteroileal anastomotic strictures: long-term results." *J Urol* 178(1): 169-173.

- Liatsikos, E. N., D. Karnabatidis, et al. (2007). "Application of paclitaxel-eluting metal mesh stents within the pig ureter: an experimental study." *Eur Urol* 51(1): 217-223.
- Liatsikos, E. N., D. Karnabatidis, et al. (2009). "Ureteral metal stents: 10-year experience with malignant ureteral obstruction treatment." *J Urol* 182(6): 2613-2617.
- Lingeman, J. E., G. M. Preminger, et al. (2003). "Use of a temporary ureteral drainage stent after uncomplicated ureteroscopy: results from a phase II clinical trial." *J Urol* 169(5): 1682-1688.
- Lingeman, J. E., D. A. Schulsinger, et al. (2003). "Phase I trial of a temporary ureteral drainage stent." *J Endourol* 17(3): 169-171.
- Lopez-Huertas, H. L., A. J. Polcari, et al. (2010). "Metallic ureteral stents: a cost-effective method of managing benign upper tract obstruction." *J Endourol* 24(3): 483-485.
- Mandal, S., M. Moudgil, et al. (2009). "Rational drug design." *Eur J Pharmacol* 625(1-3): 90-100.
- Marmieri, G., M. Pettenati, et al. (1996). "Evaluation of slipperiness of catheter surfaces." *J Biomed Mater Res* 33(1): 29-33.
- Marx, M., M. A. Bettmann, et al. (1988). "The effects of various indwelling ureteral catheter materials on the normal canine ureter." *J Urol* 139(1): 180-185.
- Masood, J., A. Papatsoris, et al. (2010). "Dual expansion nickel-titanium alloy metal ureteric stent: novel use of a metallic stent to bridge the ureter in the minimally invasive management of complex ureteric and pelviureteric junction strictures." *Urol Int* 84(4): 477-478.
- Minghetti, P., F. Cilurzo, et al. (2009). "Sculptured drug-eluting stent for the on-site delivery of tacrolimus." *Eur J Pharm Biopharm* 73(3): 331-336.
- Olweny, E. O., J. Landman, et al. (2002). "Evaluation of the use of a biodegradable ureteral stent after retrograde endopyelotomy in a porcine model." *J Urol* 167(5): 2198-2202.
- Paick, S. H., H. K. Park, et al. (2003). "Characteristics of bacterial colonization and urinary tract infection after indwelling of double-J ureteral stent." *Urology* 62(2): 214-217.
- Papatsoris, A. G. and N. Buchholz (2010). "A novel thermo-expandable ureteral metal stent for the minimally invasive management of ureteral strictures." *J Endourol* 24(3): 487-491.
- Pauer, W. and H. Lugmayr (1992). "Metallic Wallstents: a new therapy for extrinsic ureteral obstruction." *J Urol* 148(2 Pt 1): 281-284.
- Pauer, W. and H. Lugmayr (1996). "[Self-expanding permanent endoluminal stents in the ureter. 5 years results and critical evaluation]." *Urologe A* 35(6): 485-489.
- Pechey, A., C. N. Elwood, et al. (2009). "Anti-adhesive coating and clearance of device associated uropathogenic *Escherichia coli* cystitis." *J Urol* 182(4): 1628-1636.
- Rana, A. M. and A. Sabooh (2007). "Management strategies and results for severely encrusted retained ureteral stents." *J Endourol* 21(6): 628-632.
- Reid, G., J. D. Denstedt, et al. (1992). "Microbial adhesion and biofilm formation on ureteral stents in vitro and in vivo." *J Urol* 148(5): 1592-1594.

- Riedl, C. R., E. Plas, et al. (1999). "Bacterial colonization of ureteral stents." *Eur Urol* 36(1): 53-59.
- Riedl, C. R., M. Witkowski, et al. (2002). "Heparin coating reduces encrustation of ureteral stents: a preliminary report." *Int J Antimicrob Agents* 19(6): 507-510.
- Ruggieri, M. R., P. M. Hanno, et al. (1987). "Reduction of bacterial adherence to catheter surface with heparin." *J Urol* 138(2): 423-426.
- Santin, M., A. Motta, et al. (1999). "Effect of the urine conditioning film on ureteral stent encrustation and characterization of its protein composition." *Biomaterials* 20(13): 1245-1251.
- Schlick, R. W. and K. Planz (1997). "Potentially useful materials for biodegradable ureteric stents." *Br J Urol* 80(6): 908-910.
- Schlick, R. W. and K. Planz (1998). "In vitro results with special plastics for biodegradable endoureteral stents." *J Endourol* 12(5): 451-455.
- Shaw, G. L., S. K. Choong, et al. (2005). "Encrustation of biomaterials in the urinary tract." *Urol Res* 33(1): 17-22.
- Sighinolfi, M. C., S. Micali, et al. (2007). "Indwelling ureteral stents and sexual health: a prospective, multivariate analysis." *J Urol* 178(1): 229-231.
- Singh, V., A. Srinivastava, et al. (2005). "Can the complicated forgotten indwelling ureteric stents be lethal?" *Int Urol Nephrol* 37(3): 541-546.
- Sountoulides, P., A. Kaplan, et al. (2010). "Current status of metal stents for managing malignant ureteric obstruction." *BJU Int*.
- Stickler, D. J., A. Evans, et al. (2002). "Strategies for the control of catheter encrustation." *Int J Antimicrob Agents* 19(6): 499-506.
- Stoller, M. L., B. F. Schwartz, et al. (2000). "An in vitro assessment of the flow characteristics of spiral-ridged and smooth-walled JJ ureteric stents." *BJU Int* 85(6): 628-631.
- Tieszer, C., G. Reid, et al. (1998). "Conditioning film deposition on ureteral stents after implantation." *J Urol* 160(3 Pt 1): 876-881.
- Tieszer, C., G. Reid, et al. (1998). "XPS and SEM detection of surface changes on 64 ureteral stents after human usage." *J Biomed Mater Res* 43(3): 321-330.
- Tunney, M. M. and S. P. Gorman (2002). "Evaluation of a poly(vinyl pyrrolidone)-coated biomaterial for urological use." *Biomaterials* 23(23): 4601-4608.
- Wah, T. M., H. C. Irving, et al. (2007). "Initial experience with the resonance metallic stent for antegrade ureteric stenting." *Cardiovasc Intervent Radiol* 30(4): 705-710.
- Wang, H. J., T. Y. Lee, et al. (2010). "Application of resonance metallic stents for ureteral obstruction." *BJU Int*.
- Watterson, J. D., P. A. Cadieux, et al. (2003). "Oxalate-degrading enzymes from *Oxalobacter formigenes*: a novel device coating to reduce urinary tract biomaterial-related encrustation." *J Endourol* 17(5): 269-274.
- Watterson, J. D., P. A. Cadieux, et al. (2003). "Swarming of *Proteus mirabilis* over ureteral stents: a comparative assessment." *J Endourol* 17(7): 523-527.
- Wignall, G. R., L. W. Goneau, et al. (2008). "The effects of triclosan on uropathogen susceptibility to clinically relevant antibiotics." *J Endourol* 22(10): 2349-2356.

- 
- Wollin, T. A., C. Tieszer, et al. (1998). "Bacterial biofilm formation, encrustation, and antibiotic adsorption to ureteral stents indwelling in humans." *J Endourol* 12(2): 101-111.
- Zupkas, P., C. L. Parsons, et al. (2000). "Pentosanpolysulfate coating of silicone reduces encrustation." *J Endourol* 14(6): 483-488.



# ***Candida* Biofilms on Oral Biomaterials**

Philippe Courtois  
*Université Libre de Bruxelles, Brussels*  
*Belgium*

## **1. Introduction**

Biological as well as inert surfaces of the oral cavity are exposed to an abundant microflora that is able to initiate the formation of biofilms. Yeasts are frequently involved, such as *Candida* (especially *albicans*), a low-level commensal of oral, gastrointestinal, and genitourinary mucosae in humans. *In vivo* and *in vitro* studies have shown *Candida* incorporation into biofilms covering different biomaterials used in the oral cavity for the manufacturing of dentures, orthodontic appliances, etc. Yeast (*Candida* genus) biofilms can then induce device-related infections mainly in the elderly and in medically-compromised patients with subsequent morbidity and occasional mortality, all bearing high social and financial costs. Generally, scientific literature does not integrate all aspects of material/tissue interfaces: mechanisms of *Candida* biofilm development and biomaterial maintenance, the welfare of patients, and prevention of candidosis. *In vitro* investigations were mainly undertaken with mono-species biofilms whereas *Candida* incorporation into biofilms on oral surfaces tends to correspond with an increase in the yeast/bacteria ratio. This illustrates the need for interdisciplinary insight. This chapter will review 1) the literature data concerning material surfaces in support of *Candida* biofilms in the oral environment, 2) the *in vitro* approaches to understanding the mechanisms of *Candida* biofilm formation on materials, 3) the interfaced manipulations in order to prevent *Candida* biofilm onset, and 4) the precautions when testing new devices *in vivo* in the oral cavity.

## **2. Materials as a support of *Candida* biofilm in the oral environment**

Biomaterials placed in the oral environment offer new surfaces prone to biofilm formation. Rough surfaces allow more biofilms to develop than smooth ones. In contrast with free microorganisms in suspension (defined as planktonic), which are able to grow in liquid, biofilm development is theoretically divided into three stages: 1) attachment to the surface (Figure 1), 2) proliferation into a monolayer of anchoring cells, and 3) growth into several layers of budding cells (blastoconidia) with filamentous structures as hyphae or pseudohyphae (Figure 2).

Numerous studies indicated the presence of *Candida* on oral dentures (Vandenbussche & Swinne, 1984; Abu-Elteen & Abu-Elteen, 1998; Busscher et al., 2010) and other oral devices such as orthodontic appliances (Addy et al., 1982; Hägg et al., 2004). Some authors (Arendorf & Addy, 1985; Jewtuchowicz et al., 2007) demonstrated an effect of *Candida* carriage in the oral environment caused by wearing devices. Indeed, orthodontic appliances

have been shown to increase *Candida* counts in the mouth (Arendorf & Addy, 1985) and in the periodontal pockets of dental device wearers with gingivitis (Jewtuchowicz et al., 2007). Inserted devices act as new reservoirs able to imbalance oral microflora. In a healthy mouth, saliva protects oral mucosa against candidosis; in contrast, dry mouth is associated with increased yeast counts and candidosis risk. *In vitro*, cigarette smoke condensates increased adhesion of *Candida albicans* on orthodontic material surfaces such as bands, brackets, elastics, and acrylic resin (Baboni et al., 2010).

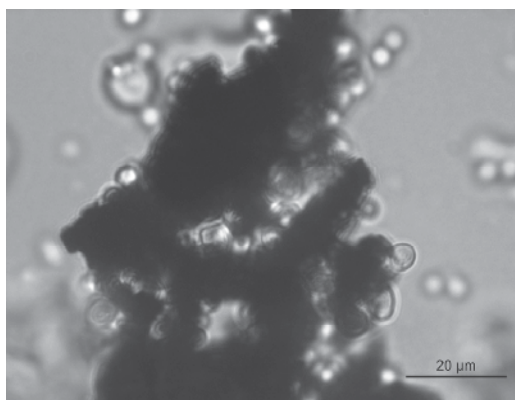


Fig. 1. *Candida albicans* suspension mixed with titanium powder directly observed on microscope in the absence of any stain procedure. Some blastoconidia are already adherent to material (attachment can be attested by MTT test after 3 washings). Magnification: x1000.

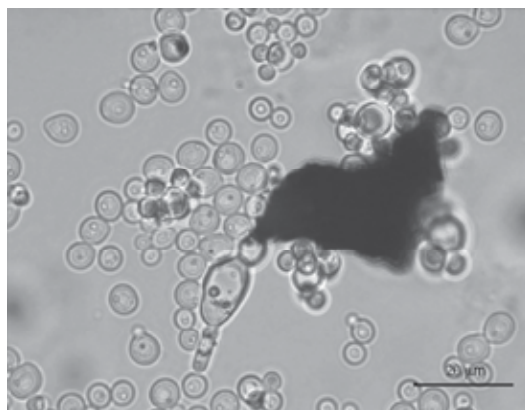


Fig. 2. Titanium grain surrounded by blastoconidia clusters and filamentous structure (pseudohyphae) after a two-week incubation. Magnification: x1000.

### 2.1 *Candida* on dentures

*Candida albicans* is often detected on methyl methacrylate polymers or acrylic resins from dentures. Biofilm formation on dentures results from complex interactions among yeast, bacteria, nutrients, and saliva or even serum proteins (Nikawa et al., 1997; Nikawa et al., 2000). *Candida* carriage on acrylic resin has been reported in the literature as varying up to more than 80% of the investigated dentures. For instance, yeasts were found in 14% of

isolates from previously worn dentures in the Northeast and Southwest regions of the United States (Glass, 2010); in their conclusions, the authors pointed out frequent denture use without appropriate disinfection and biofilm formation within the pores of the material. In a previous study (Vanden Abbeele et al., 2008), authors reported *Candida* contamination of upper prosthesis in 76% of denture wearers hospitalized for long-term care in geriatric units. The most frequently isolated species were *C. albicans* (78%), *C. glabrata* (44%) and *C. tropicalis* (19%). Carriage of more than one yeast species was found in 49% of the contaminated dentures. There was a significant association between denture contamination and palatal mucosa colonization, making *ex vivo* denture decontamination mandatory, together with *in vivo* mucosa disinfection. *Candida* carriage has been observed in different types of dentures, both with and without soft liner fittings (Bulad et al., 2004; Mutluay et al., 2010).

Adhesion of *Candida* to the base materials of the dentures is associated with denture plaque (i.e. denture biofilm) and denture-related stomatitis. Even if many observations support the presence of *Candida albicans* in the biofilms on dentures, insufficient data are available to assess the etiology and to understand the pathogenesis of *Candida*-associated denture stomatitis. Review of the literature (Radford et al., 1999; Pereira-Cenci et al., 2008) does not permit settling specific and non-specific plaque hypotheses. Indeed, denture plaque comprises an ill-defined mixture of bacteria (such as *Streptococcus spp.*, *Lactobacillus spp.*, *Staphylococcus aureus*, and Gram-negative anaerobic bacteria) with *Candida spp.* also apt to cause mucosa inflammation.

## 2.2 *Candida* on other materials inserted in the oral cavity

*Candida spp.* was detected in low proportions at peri-implantitis sites and in failing implants associated with periodontopathogenic bacteria such as *Porphyromonas spp.*, *Prevotella spp.* and *Actinobacillus actinomycetemcomitans* (Alcoforado et al., 1991; Leonhardt et al., 1999; Pye et al., 2009), but ecological relationships with their surrounding and eventual pathological roles are yet to be understood. *In vitro*, *Candida albicans* may also adhere to pieces of biodegradable membranes used for periodontal tissue regeneration (Molgatini et al., 1998) and to tissue-conditioning materials for denture relining (Kulak & Kazazoglu, 1998). Additionally, presence of *Candida albicans* has been documented on obturator prostheses (whatever the material may be: silicone, polymethyl methacrylate, or titanium) in patients with maxillary defects (suffering from congenital malformation, tumors, or trauma), and on the mucosa adjacent to the prosthesis (Depprich et al., 2008; Mattos et al., 2009); these patients can present prosthesis-induced stomatitis. Finally, the use of orthodontic appliances leads to an increased carriage rate during the appliance-wearing time, with a significant fall of salivary pH and an increase of *Candida* count observed at different oral sites through various sampling techniques (Hibino et al., 2009).

## 2.3 *Candida* on devices used outside the oral cavity

Materials inserted in other sites can be colonized by yeasts as well, causing device-related infections (Cauda, 2009): articular prosthesis, cardiac devices (Falcone et al., 2009), catheters, vascular access devices (Brouns et al., 2006), and voice prostheses (Kania et al., 2010). These infections require prolonged antifungal therapy and often device removal.

## 3. Experimental approach

A better understanding of interface biology and material surface treatments requires experimental models to produce *in vitro* biofilms on supports that are easy to manipulate in

the laboratory (Chandra et al., 2001) and the ability to investigate *in vivo* biofilm growth or drug susceptibility. Different studies have already described such models, mainly addressing procedures that are able to limit yeast adherence and biofilm formation. Some of these technologies were originally proposed as artificial dental plaque biofilm model systems (reviewed by Sissons, 1997), especially for plaque biology studies in caries and periodontitis research. This section will report on the experimental models producing *Candida* biofilms onto biomaterials. Table 1 summarizes some contributions from literature.

design	reference	material
<b><i>in vitro</i> models</b>		
<i>static culture models</i>		
- material dived in solution	Chandra et al., 2001	acrylic, silicone
- poloxamer gel in Petri dish	Percival et al., 2007	material covered by gel
- 96-well culture microtiter plate	Peeters et al., 2008	polystyrene
- titanium powder	Ahariz & Courtois, 2010	titanium powder
<i>continuous culture models</i>		
- continuous flow culture system	Uppuluri et al., 2009	silicon elastomer
- Modified Robbins Device	Coenye et al., 2008	
- constant depth film fermenter	Lamfon et al., 2003	enamel, dentine, acrylic
<b><i>in vivo</i> models</b>		
- animal models	Andes et al., 2004 Nett et al., 2010 Rიცოვ et al., 2010	central venous catheter acrylic denture subcutaneous catheter
- human models	Budtz-Jrgensen et al., 1981	tape or acrylic disk

Table 1. Experimental designs reported in the literature to produce *Candida*-biofilms.

*Candida albicans* can be grown with or without the addition of saliva on different materials used in dentistry including acrylic resins, denture-lining material, porcelain, composite, amalgam, hydroxyapatite, silicone, and polystyrene.

### 3.1 *In vitro* models

*In vitro* models consist of static cultures or continuous cultures.

#### 3.1.1 Static culture models

Mono-species biofilms can be experimentally grown on pieces of materials currently used in dentistry, such as polymethylmethacrylate strips or silicone elastomer disks (Chandra et al., 2001). Some surfaces prepared from mucosa (epithelial cell cultures) or hard tooth tissues (enamel, dentine) were used as well. The materials are immersed in assay tubes or in multi-well culture plates containing a contaminated solution similar to saliva for a predefined incubation period. The polystyrene wall of the container itself has been used as an adherent surface for biofilm formation: 96-well plates allow management of experiments with numerous replications in various conditions (Peeters et al., 2008). Specific studies of the adhesion phase require an intermediate washing step to remove non-adherent yeast cells. Evaluation of the biofilm growth phase is generally based on microbial cell staining (crystal violet, among others), metabolic activities (tetrazolium test), biomass determination (dry weight, incorporation of radioactive tracer such as amino acids), or microscopic examination.

Poloxamer hydrogel, being liquid at low temperatures and solid at cultivation temperatures, has been proposed (Percival et al., 2007) as a culture support in the Petri dish to induce bacteria and yeast biofilm-like aggregates. The thermoreversible gelation makes the preparation and the recovery of biofilm samples easy and reproducible but still requires further confirmation for use in biofilm biology. Powder material, such as titanium powder, provides increasing support surfaces that are similar to cell culture on beads; moreover, it allows the anchored phase to be easily separated from the planktonic phase by simple sedimentation (Ahariz & Courtois, 2010). The titanium surface is not antimicrobial by itself, so it can be used as support for *Candida* biofilm. Titanium is widely employed for implant manufacturing due to its good biocompatibility and mechanical properties, but infection remains as a primary cause for failure, leading to removal. *Candida albicans* biofilms on titanium powder could offer a simple and reliable model for further investigation of new antimicrobial strategies; moreover, the model could be extendable to other microorganisms contaminating implanted materials. Making implant surfaces resistant to microbial colonization should reduce infectious complications; however, such developments need an *in vitro* model that allows the effect of surface modification and coatings on biofilm production to be studied. This aspect will be detailed in the next section.

The approach by means of static cultures simplifies the *in vivo* complexity to interactions between one single species and one single support without considering the numerous salivary compounds and abundant oral microflora in the real oral environment. Microorganisms in biofilms *in vivo* display properties different from those observed under laboratory conditions. The single-species procedures can be extended to a two-membered microbial co-culture or a characterized microbial consortium in order to reconstitute a medium for approaching oral microcosm and containing sterilized or artificial saliva. Multi-species biofilms have already been investigated on various dental materials such as enamel, amalgam, composite, and acrylic to assess the role of surface roughness (foremost in the first steps of biofilm formation) and impact of (pre)conditioning by saliva (Dezelic et al., 2009). Diffusion of drugs through biofilms, including *Candida* biofilms, can be documented by an experimental perfusion system superposing disk, filters, biofilm, and agar containing the drug under evaluation (Samaranayake et al., 2005). Perfusion of drugs in biofilms allows the putative factors that lead to biofilm antimycotic resistance to be evaluated.

### 3.1.2 Continuous culture models

Contrary to static cultures, continuous culture models (flow cells, Modified Robbins Device, chemostats, artificial mouths, and constant depth film fermenter) take into account oral flow and oral bathing conditions as shear forces and nutrient supplies (Bernhardt et al., 1999; Ramage et al., 2008). Indeed, oral biofilms on prosthetic materials are exposed to salivary fluxes conveying water and nutrients to the aggregated microorganisms in the saliva. For instance, liquid flow has been shown to influence the production of an extracellular matrix by *Candida albicans* biofilms *in vitro* (Hawser et al., 1998). Taking extracellular material produced in static cultures as a basal value, a gentle stirring significantly multiplied this by ~1.25, while a more intense stirring led to complete inhibition. Other data (Biswas & Chaffin, 2005) reported the absence of *Candida albicans* biofilm formation in anaerobiosis even if this yeast can grow in anaerobic environment. Yeast retention against a continuous flow of medium has been used as a marker for yeast adhesion to a surface in the same manner as the retention after liquid washes (Cannon et al., 2010). Cultures under continuous flow conditions facilitated the penetration of *Candida albicans* into silicone elastomers when

compared to static conditions, especially when pure cultures were tested. The presence of *Streptococci* reduced material invasion by the yeast, thereby revealing the importance of testing materials in a biological environment (Rodger et al., 2010).

A continuous flow culture (CFC) aims at cultivating microorganisms in a continuous flow of fresh medium to mimic physiological conditions and to avoid the decline of the culture by nutrient depletion. Such instrumentation is easy to assemble in a microbiology laboratory equipped with an incubator, peristaltic pump, fresh medium flask, tubing, and chamber(s) where the material of interest, on which biofilm was already initialized, is inserted (Uppulari et al., 2009). Serial chambers allow independent samples to be produced under similar conditions (nutrients, flow rate, temperature, and incubation time). *Candida albicans* biofilms have been reported to grow more rapidly under continuous flow than in static culture (Uppulari et al., 2009).

Specific devices have been developed for continuous flow studies. The Modified Robbins Device (MRD) is a small channel-shaped chamber with different openings in which biomaterial discs could be inserted when the instrument is mounted to form the channel wall. These devices are provided with a liquid circulator for low-pressure applications. Microorganisms introduced into the fluid stream can adhere to the plugs and generate a biofilm that is easy to remove for analysis. This instrumentation was used to evaluate some maintenance protocols for oral devices (Coenye et al., 2008), as well as for other purposes.

The constant depth film fermenter (CDFF) is an instrument that is able to generate standardized biofilms on any materials that can thereafter be removed for subsequent investigations; the advantages of such a device includes controlled experimental conditions for growth that mimic the oral environment. Some authors (Lamfon et al., 2003) used the CDFF to produce *Candida* biofilms in the presence of artificial saliva on enamel, dentine, and denture acrylic disks. Their data demonstrated that the roughness of the material influences formation and development of *Candida* biofilms.

### 3.2. *In vivo* models

The rat catheter biofilm infection model (Andes et al., 2004; Lazzell et al., 2009; Rídicová et al., 2010) allows evaluation *in vivo* of the compartment of one microorganism that is exposed to host proteins and immune factors. Other animal models have been utilized to monitor materials and devices that are placed in the bathing conditions of the oral cavity and to mimic denture stomatitis with fungal invasion and neutrophil infiltration of the adjacent mucosa. The rodent acrylic denture model was developed for such purposes (Nett et al., 2010). In humans, abraded pieces of self-adhesive (Budtz-Jørgensen et al., 1981) or acrylic resin disk (Avon et al., 2007) were fixed on dentures to gain some information *in vivo* concerning biofilm formation in the oral cavity.

## 4. Surface treatment to control *Candida* biofilms

*Candida* in biofilms on prosthetic materials is difficult to remove. If it is absurd to eradicate a commensal of the oral environment, it is important to consider the prosthesis and the patient simultaneously because the prosthesis is a nest for *Candida* growth and a possible source of infection for the oral mucosa. Daily brushing should be encouraged in all denture-wearers; in denture stomatitis, decontamination of the denture becomes a mandatory part of treatment. Often, the family or professional caregivers must compensate for the difficulties that the elderly face due to loss of independence, dexterity, or memory. Thus, antifungals

(azoles, nystatin) should be reserved for patient treatment and are less active against biofilms on dentures (see *infra*); moreover, they may cause the emergence of resistant strains. Use of antiphlogistic solutions has been highly successful; as many of them are fungicidal. However, there are no comparative studies that examine all aspects of the problem.

Rarely, if ever, do study authors take into account the views of all professionals involved in denture care, not only the opinions of the dentist who treats the patient, but also those of the prosthetist who sees the potential deleterious effects of some decontaminating procedures and the microbiologist who isolates and studies yeast *in vitro*. Microbiologists are able to determine the minimum inhibitory concentrations of antifungals on *Candida* growth in suspensions, or better (but less often), on *Candida* biofilms produced in the laboratory. Dental technicians are involved in the relationship with the materials they provide, biofilms, and the decontamination procedures. Clinicians' decisions cannot rely on evidence-based studies alone since they lack data from large-scale clinical trials (i.e., *in vivo* studies).

#### 4.1 Anti-biofilm agents

Many molecules that are embedded in antiseptic mouthwash or in effervescent tablets are candidacidal. Sodium hypochlorite, a major component of bleach that is also produced *in vivo* by myeloperoxidase from the neutrophils, has an anti-*Candida* effect. Ozonated water with or without ultrasound reduces yeasts' adherence to the resin. The use of ultrasound reduces the concentration required for effectiveness of most antiseptics or fungicide antimycotics. The use of a microwave oven is not recommended because the conditions that suppress the yeasts are too close to those that damage some prosthesis materials. When misused, some products can damage the materials: the repeated use of chlorhexidine colors resins brown; hypochlorite at a high dose bleaches them. Hydrogen peroxide is active only at a very high concentration that is close to the mucosal toxicity level; moreover, in the presence of hydrogen peroxide, *Candida* over-expresses catalase and glutathione oxidase, which in turn reduces the concentration of hydrogen peroxide and protects the yeast cells against oxidation.

An alternative to prevent biofilm formation could involve a reduction of microorganism adherence to materials by anti-adhesive/anti-microbial coatings, with or without drug release. Indeed, the anchoring of microorganisms to surfaces such as mucosa, teeth, or biomaterial is a pivotal step in initiating biofilms into the oral cavity. Adhesion can be quantified by measurement of the microorganisms' retention after fixed incubation periods and washings or by the microorganisms' retention against a continuous flow of medium (Cannon et al., 2010). Many protocols have been proposed to limit biofilm formation on various materials used in dentistry (recently reviewed by Busscher et al., 2010): antibiotic and peptide coatings, silver and polymer-brush coatings, and quaternary ammonium couplings. *In vitro*, titanium dioxide coating inhibits *Candida* adhesion to the denture's base in acrylic resin (Arai et al., 2009). Surface protection from bacteria and yeast by chitosan coating is also worthy of further pharmacologic and clinical studies (Carlson et al., 2008). Surface treatment must solve numerous challenges before clinical implementation: the amount of bioavailable drug on the material's surface, kinetic and safety of the released compounds, interferences with the oral environment, and the quest for multifunctional effects such as biofilm control, tissue integration, and/or tissue regeneration.

#### 4.2 New strategies based on research in *Candida*-biofilm biology

The decreased susceptibility of yeast biofilms to classical antifungal drugs encouraged scientists to explore other means to inhibit *Candida* and to limit the deleterious effects of its biofilm. Knowledge of interactions between *Candida* and oral tissues and between *Candida* and oral bacteria should present new perspectives for therapy. Microorganisms in biofilms (yeast included) are less sensitive to antimicrobial agents than free microorganisms in suspension. Authors (Thurnheer et al., 2003) have shown a decreased drug diffusion rate through polyspecies biofilms, containing *Candida* among others, proportional to the cubic root of the drug's marker molecular weight, suggesting the deviousness of the diffusion route through biofilm depth as the cause of delay in molecule penetration. Nevertheless, drug resistance could also be attributed to metabolic properties and gene expression induced by microorganisms living in the community and to the production of an extracellular matrix.

Other *in vitro* studies (reviewed by Nobile et al., 2006) suggest several molecular factors that explain biofilm development and biofilm drug resistance, such as specific biofilm phenotypes (Finkel & Mitchell, 2011), adhesins, cell to cell communication, and quorum sensing (Deveau & Hogan, 2011). The link between hyphae production and *Candida* biofilm development *in vitro* and between hyphae production and pathological conditions *in vivo* led to the investigation of the genetic regulation of hyphal morphogenesis. The rapid initiation of biofilm in the presence of new surfaces available for anchoring oriented the genetic analysis towards a gene expression distinct from that found in the planktonic state.

Quorum sensing pathways that allow microorganism colonies (including yeast) to sense their cell density involve small molecules such as farnesol and tyrosol. The former is known to promote resistance against oxidative stress and inhibit hyphal morphogenesis and biofilm formation, whereas the latter is a putative biofilm facilitator. The (over)expression and polysaccharidic matrix production of adhesins is also linked to biofilm formation. All of these biological characteristics contribute to make *Candida* biofilms "a well-designed protected environment" (Mukherjee P. et al., 2005). A better knowledge of molecular events in *Candida* biofilm formation could present new strategies to prevent oral candidiasis contracted from biomaterials inserted in the oral cavity.

#### 4.3 New strategies based on research in exocrine biology

Antimicrobial molecules/systems derived from exocrine secretions are interesting topics of research. Studies *in vitro* have already shown the benefits of lysozyme, lactoferrin, histatin (Pusateri et al., 2009), and peroxidase systems with thiocyanate, chloride, and especially iodide. However, transferring such data to *in vivo* studies hasn't yet provided the expected results because of the immense complexity of the oral environment. Again, the publication of large clinical studies is still being awaited.

Research in peroxidase biology is an illustrative example of the multiple facets of knowledge transfer from fundamental sciences to clinical applications. In the presence of hydrogen peroxide, for example, peroxidases in exocrine secretions are able to catalyze the production of hypohalous compounds that carry an antimicrobial effect: hypiodite *in vitro* and hypothiocyanite in saliva. Previous studies have shown that a 30-minute exposure to hypiodite was sufficient to inhibit planktonic growth *in vitro* (Majerus & Courtois, 1992). Moreover, the development of *Candida* biofilm on material surfaces could be reduced or even suppressed by lactoperoxidase-generated hypiodite and hypothiocyanite. This was



the case not only when peroxidase and substrates system were dissolved in the liquid phase into which the material was immersed, but also when peroxidase precoated on material was activated by simple addition of the substrates to the liquid surrounding this material. Those data also demonstrated the efficiency of peroxidase systems against a *Candida* strain during a three-week incubation period and concomitantly suggested a possible interest in coating the material with peroxidase.

Other investigations demonstrated 1) that lactoperoxidase activity was not modified by coating onto titanium, 2) that lactoperoxidase incorporated in oral gel maintained its activity for at least one year, and 3) that the substrate exhaust (namely hydrogen peroxide and iodide) was the true limiting factor (Bosch et al., 2000; Ahariz et al., 2000). Previous investigations indicated an antibacterial effect on Gram-positive and Gram-negative bacteria, which suggests a non-specific inhibitory effect of hypoiodite on microbial metabolism and growth (Courtois et al., 1995). The ability to transfer this knowledge from bench to clinic is questionable. Indeed, the immunogenicity of a material surface coated with lactoperoxidase should restrict the applications of this system to *ex vivo* conditions. Besides the toxicity of oxidant products on host cells, the competition between iodide and thiocyanate is another limiting factor for *in vivo* use. Thiocyanate is not only present in several exocrine secretions (e.g., human saliva) but is also the preferential substrate of lactoperoxidase. Simultaneous incorporation of iodide and thiocyanate in the same gel decreased the beneficial effect of 2 mM iodide in the presence of increasing concentrations of thiocyanate ranging from 0.25 to 4 mM, which correspond to the normal range of this ion in saliva.

## 5. Precautions for testing new devices *in vivo*

Finally, the investigators must be aware of the biases frequently encountered in clinical trials that evaluate microbial contamination and colonization of oral devices and prosthesis. Recommendations and guidelines to evaluate the benefits of prophylactic anti-*Candida* procedures are similar to these advocated for any oral care product. Two important biases that must be taken into account are the influence of investigators on patients' hygiene behavior (Grimoud et al., 2005) and the galenic formulation of products lacking the active molecule. Evaluation of dentifrice efficiency for denture hygiene also needs other controls: one testing the product without brushing and one testing the mechanical brushing alone. The abrasive effect of the product must be evaluated, and the abrasiveness of saliva itself is another concern to be considered.

Quantification of the *Candida* biomass that is adherent to the device is difficult in practice. Yeast samples from the oral environment can be collected by rinsing, imprinting, or swabbing. Swabs and imprints are more suitable for gathering yeasts attached to surfaces, and swabbing is easier for clinical studies on a larger scale. Procedures to quantify yeast biomass *in vitro* are not applicable *in vivo* for epidemiological studies and hygiene purposes, particularly since denture-wearers are not always compliant. Dentures can be rinsed in saline and brushed in standard condition to harvest microbial cells. The suspension is thereafter serially diluted for counting (Panzeri et al., 2009).

Another study (Vanden Abbeele et al., 2008) documented the reliability of oral swabbing to investigate yeast carriage on denture. Sampling dentures for *Candida* is more than just a diagnostic tool: it could present an opportunity to verify the patient's compliance with hygiene advice as well as the efficiency of new topical antifungals. Yeast counts after swab

culture reflect the biomass present on the oral surfaces, but this is not the number of yeast cells included in oral biofilms. Colony forming units (CFU) counted on the agar medium represented only a small part of the cells harvested by the cotton, as assessed by three successive spreadings of the same cotton that provided similar data (in the range interval of 0.1 logarithmic units). Furthermore, two successive swabs of the same oral surface yielded similar quantities of yeast cells (in the range interval of 0.5 logarithmic units).

Finally, investigators themselves can influence the hygiene behavior of the subjects under study. The study previously quoted (Vanden Abbeele et al., 2008) also analyzes the effect of the oral care program. In the absence of any hygiene advice, a second denture swabbing taken in 46 patients after an interval of one week demonstrated only minor variations, thus minimizing the hygiene-stimulation effect produced by pursuing the collection of samples. Repeated sampling (at one-week intervals) of 46 different healthy denture-wearers demonstrated yeast counts remaining in the same range ( $\pm 1$  logarithmic unit) for more than 85% of the denture swabs and mucosa samples. Values below the lower limit ( $-1$  logarithmic unit) occurred in less than 15% of denture and mucosa swabs. This was attributed to behavioral changes in hygiene practice following the investigators' first visit. By contrast, a hygiene program including a placebo oral gel (tested to be inactive *in vitro*) led to a decrease of yeast carriage after two weeks.

## 6. Conclusion

Yeasts belonging to the *Candida* genus usually colonize the human oral cavity. *In vivo* and *in vitro* studies have shown *Candida* incorporation into biofilms covering different biomaterials and devices such as dentures. These biofilms may indicate an increased risk factor for invasive candidosis when the host immune system is compromised. Daily denture brushing is recommended to all denture (and other device) wearers in order to prevent the development of *Candida* biofilm. Family members and healthcare workers must assume this task when there is a deficiency in dexterity and/or a loss of autonomy, especially in elderly and disabled persons. In case of candidosis in denture-wearers, decontamination of dentures is mandatory. Antimycotics such as azoles or nystatin must be reserved for curative treatment of infected patients; they are less active against *Candida* biofilms on dentures and could lead to emergent resistance if applied daily to dentures in order to prevent yeast colonization. Nevertheless, few studies, if any, integrate all aspects of denture care: welfare of denture-wearers, prevention of candidosis, biomaterial defects after decontamination processing, and possible *Candida* biofilm development. Daily brushing of dentures remains the key recommendation. A better understanding of *Candida* biology in the oral environment will provide new tools to control *Candida* biofilms, the possible development of more appropriate biomaterials for dentistry (or surface improvements), and better management of biomaterial use in the oral cavity. Further investigations in this field will require cooperation among dentists, biologists, and engineers.

## 7. Acknowledgment

The author reports no conflicts of interest in this work. The author wishes to thank the students from the *Haute Ecole Francisco Ferrer* (Medical Biology section) and the *Université Libre de Bruxelles* (Faculty of Medicine, Dentistry section) in Brussels who enthusiastically participated in studies on biofilm biology in the frame of their final memory or doctorate.

The author also thanks Pr M. Stas, MD PhD for her helpful advice and review of the manuscript.

## 8. References

- Abu-Elteen, K. & Abu-Elteen, R. (1998). The prevalence of *Candida albicans* populations in the mouths of complete denture wearers. *The New Microbiologica*, Vol.21, No.1, (January 1998), pp. 41-48, ISSN 1121-7138
- Addy, M.; Shaw, W.; Hansford, P. & Hopkins, M. (1982). The effect of orthodontic appliances on the distribution of *Candida* and plaque in adolescents. *British journal of orthodontics*, Vol.9, No.3, (July 1982), pp. 158-163, ISSN 0301-228X
- Ahariz, M.; Mouhyi, J.; Louette, P.; Van Reck, J.; Malevez, C. & Courtois, P. (2000). Adsorption of peroxidase on titanium surfaces: a pilot study. *Journal of biomedical materials research*, Vol.52, No.3, (December 2000), pp. 567-571, ISSN 0021-9304
- Ahariz, M. & Courtois, P. (2010). *Candida albicans* susceptibility to lactoperoxidase-generated hypiodite. In: *Clinical, cosmetic and investigational dentistry*, , Vol.2010, No.2, (August 2010), pp. 69-78, ISSN 1179-1353, Available from <http://www.dovepress.com/candida-albicans-susceptibility-to-lactoperoxidase-generated-hypiodite-peer-reviewed-article-CCIDEN>
- Ahariz, M. & Courtois, P. (2010). *Candida albicans* biofilm onto titanium : effect of peroxidase precoating. In: *Medical Devices: Evidence and Research*, Vol.2010, No.3, (August 2010), pp. 33-40, ISSN 1179-1470, Available from <http://www.dovepress.com/candida-albicans-biofilm-on-titanium-effect-of-peroxidase-precoating-peer-reviewed-article-MDER>
- Alcoforado, G.; Rams, T.; Feik, D. & Slots, J. (1991). Microbial aspects of failing osseointegrated dental implants in humans. *Journal de parodontologie*, Vol.10, No.1, (February 1991), pp. 11-18, ISSN 0750-1838
- Andes, D.; Nett, J.; Oschel, P.; Albrecht, R.; Marchillo, K. & Pitula A. (2004). Development and characterization of an *in vivo* central venous catheter *Candida albicans* biofilm model. *Infection and immunity*, Vol. 72, No.10, (October 2004), ISSN 0019-9567
- Arai, T.; Ueda, T.; Sugiyama, T. & Sakurai, K. (2009). Inhibiting microbial adhesion to denture base acrylic resin by titanium dioxide coating. *Journal of oral rehabilitation*, Vol.36, No.12, (December 2009), pp. 902-908, ISSN 0305-182X
- Arendorf, T. & Addy, M. (1985). Candidal carriage and plaque distribution before, during and after removable orthodontic appliance therapy. *Journal of clinical periodontology*, Vol.12, No.5, (May 1985), pp. 360-368, ISSN 0303-6979
- Avon, S.; Goulet, J. & Deslauriers, N. (2007). Removable acrylic resin disk as a sampling system for the study of denture biofilms *in vivo*. *Journal of prosthetic dentistry*, Vol.97, No.1, (January 2007), pp.32-38, ISSN 0022-3913
- Baboni, F.; Guariza Filho, O., Moreno, A. & Rosa, E. (2010). Influence of cigarette smoke condensate on cariogenic and candidal biofilm formation on orthodontic materials. *American journal of orthodontics and dentofacial orthopedics*, Vol.138, No.4, (October 2010), pp. 427-434, ISSN 0889-5406

- Bernhardt, H.; Zimmermann, K. & Knoke, M. (1999). The continuous flow culture as an *in vitro* model in experimental mycology. *Mycoses*, Vol.42, Suppl.2, (1999), pp.29-32, ISSN 0933-7407
- Biswas, S. & Chaffin, W. (2005). Anaerobic growth of *Candida albicans* does not support biofilm formation under similar conditions used for aerobic biofilm. *Current microbiology*, Vol.51, No.2, (August 2005), pp. 100-104, ISSN 0343-8651
- Bosch, E.; Van Doorne, H. & De Vries S. (2000). The lactoperoxidase system: the influence of iodide and the chemical and antimicrobial stability over the period of about 18 months. *Journal of applied microbiology*, Vol.89, No.2, (August 2000), pp. 215-224, ISSN 1364-5072
- Brouns, F.; Schuermans, A.; Verhaegen, J.; De Wever, I. & Stas, M. (2006). Infection assessment of totally implanted long-term venous access devices. *Journal of vascular access*, Vol.7, No.1, (January-February, 2006), pp. 24-28, ISSN 1129-7298
- Budtz-Jørgensen, E.; Theilade, E.; Theilade, J. & Zander, H. (1981). Method for studying the development, structure and microflora of denture plaque. *Scandinavian journal of dental research*, Vol.89, No.2, (April 1981), pp. 149-156, ISSN 0029-845X
- Bulad, K.; Taylor, R.; Verran, J. & McCord, J. (2004). Colonization and penetration of denture soft lining materials by *Candida albicans*. *Dental materials*, Vol.20, No.2, (February 2004), pp. 167-175, ISSN 0109-5641
- Busscher, H.; Rinastiti, M.; Siswomihardjo, W. & van der Mei H. (2010). Biofilm formation on dental restorative and implant materials. *Journal of dental research*, Vol.89, No.7, (July 2010), pp. 657-665, ISSN 0022-0345
- Cannon, R.; Lyons, K.; Chong, K. & Holmes, A. (2010). Adhesion of yeast and bacteria to oral surfaces. *Methods in molecular biology*, Vol.666, (2010), pp. 103-124, ISSN 0164-3745
- Carlson, R.; Taffs, R.; Davison, W. & Stewart, P. (2008). Anti-biofilm properties of chitosan-coated surfaces. *Journal of biomaterials science. Polymer edition*, Vol.19, No.8, (August 2008), pp. 1035-1046, ISSN 0920-5063
- Cauda, R. (2009). Candidaemia in patients with an inserted medical device. *Drugs*, Vol.69, Suppl.1, (November 2009), pp. 33-38, ISSN 0012-6667
- Chandra, J.; Mukherjee, P., Leidich S.; Faddoul, F.; Hoyer, L.; Douglas, L. & Ghannoum, M. (2001). Antifungal resistance of candidal biofilms formed on denture acrylic *in vitro*. *Journal of dental research*, Vol.80, No.3, (March 2001), pp. 903-908, ISSN 0022-0345
- Chandra, J.; Kuhn, D.; Mukherjee, P.; Hoyer, L.; McCormick, T. & Ghannoum M. (2001). Biofilm formation by the fungal pathogen *Candida albicans*: development, architecture, and drug resistance. *Journal of bacteriology*, Vol.183, No.18, (September 2001), pp. 5385-5394, ISSN 0021-9193
- Coenye, T.; De Prijck, K., De Wever, B. & Nelis, H. (2008). Use of the modified Robbins device to study the *in vitro* biofilm removal efficacy of NitrAdine, a novel disinfecting formula for the maintenance of oral medical devices. *Journal of applied bacteriology*, Vol.105, No.3, (September 2008), pp. 733-740, ISSN 1364-5072
- Courtois, P.; Vanden Abbeele, A.; Amrani, N. & Pourtois, M. (1995). *Streptococcus sanguis* survival rates in the presence of lactoperoxidase-produced OSCN<sup>-</sup> and OI<sup>-</sup>. *Medical sciences research*, Vol.23, No.3, (1995), pp. 195-197, ISSN 0269-8951

- Depprich, R.; Handschel, J.; Meyer, U. & Meissner, G. (2008). Comparison of prevalence of microorganisms on titanium and silicone/polymethyl methacrylate obturators used for rehabilitation of maxillary defects. *Journal of prosthetic dentistry*, Vol.99, No.5, (May 2008), pp. 400-405, ISSN 0022-3913
- Deveau, A. & Hogan, D. (2011). Linking *quorum sensing* regulation and biofilm formation by *Candida albicans*. *Methods in molecular biology*, Vol. 692, (2011), pp. 219-233, ISSN 1064-3745
- Dezelic, T.; Guggenheim, B. & Schmidlin, P. (2009). Multi-species biofilm formation on dental materials and an adhesive patch. *Oral health and preventive dentistry*, Vol.7, No.1, (March 2009), pp. 47-53, ISSN 1602-1622
- Falcone, M.; Barzaghi, N.; Carosi, G.; Grossi, P.; Minoli, L.; Ravasio, V.; Rizzi, M.; Suter, F.; Utili, R.; Viscoli, C.; Venditti, M. & Italian Study on Endocarditis. (2009). *Candida* infective endocarditis: report of 15 cases from a prospective multicenter study. *Medicine*, Vol.88, No.3, (May 2009), pp. 160-168, ISSN 0025-7974
- Finkel, J. & Mitchell, A. (2011). Genetic control of *Candida albicans* biofilm development. *Nature reviews - microbiology*, Vol.9, No.2, (February 2011), pp. 109-118, ISSN 1740-1526
- Glass, R.; Conrad, R.; Bullard, J.; Goodson, L.; Metha, N.; Lech S. & Loewy, Z. (2010). Evaluation of microbial flora found in previously worn prostheses from the Northeast and Southwest regions of the United States. *Journal of prosthetic dentistry*, Vol.103, No.6, (June 2010), pp. 384-389, ISSN 0022-3913
- Grimoud, A.; Lodter, J.; Marty, N.; Andrieu, S.; Bocquet, H.; Linas, M.; Rumeau, M. & Cazard, J. (2005). Improved oral hygiene and *Candida* species colonization level in geriatric patients. *Oral diseases*, Vol.11, No.3, (May 2005), pp. 163-169, ISSN 1354-523X
- Hägg, U.; Kaveewatcharanont, P.; Samaranayake, Y.; Samaranayake L. (2004). The effect of fixed orthodontic appliances on the oral carriage of *Candida* species and Enterobacteriaceae. *European journal of orthodontics*, Vol.26, No.6, (December 2004), pp. 623-629, ISSN 0141-5387
- Hawser, S.; Baillie, G. & Douglas, L. (1998). Production of extracellular matrix by *Candida albicans* biofilms. *Journal of medical microbiology*, Vol.47, No.3, (March 1998), pp. 253-256, ISSN 0022-2615
- Hibino, K.; Wong, R.; Hägg, U. & Samaranayake, L. (2009). The effects of orthodontic appliances on *Candida* in the human mouth. *International journal of paediatric dentistry*, Vol.19, No.5, (September 2009), pp. 301-308, ISSN 0960-7439
- Jewtuchowicz, V.; Brusca, M.; Mujica, M.; Gliosca, L.; Finqueliévich, J.; Lovannitti, C. & Rosa, A. (2007). Subgingival distribution of yeast and their antifungal susceptibility in immunocompetent subjects with and without dental devices. *Acta odontológica latinoamericana*, Vol.20, No.1, (July 2007), pp. 17-22, ISSN 0326-4815
- Kania, R.; Lamers, G.; van de Laar, N.; Dijkhuizen, M.; Lagendijk, E.; Huy, P.; Herman, P.; Hiemstra, P.; Grote, J.; Frijns, J. & Bloemberg, G. (2010). Biofilms on tracheoesophageal voice prostheses: a confocal laser scanning microscopy demonstration of mixed bacterial and yeast biofilm. *Biofouling*, Vol.26, No.5, (July 2010), pp. 519-526, ISSN 0892-7014

- Kulak, Y. & Kazazoglu, E. (1998). *In vivo* and *in vitro* study of fungal presence and growth on three tissue-conditioning materials on implant supported complete denture wearers. *Journal of oral rehabilitation*, Vol.25, No.2, (February 1998), pp. 135-138, ISSN 0305-182X
- Lamfon, H.; Porter S.; McCullough, M. & Pratten J. (2003). Formation of *Candida albicans* biofilms on non-shedding oral surfaces. *European journal of oral sciences*, Vol.111, No.6, (December 2003), pp. 465-471, ISSN 0909-8836
- Lazzell, A.; Chaturvedi, A.; Pierce, C.; Prasad, D.; Uppuluri, P. & Lopez-Ribot, J. Treatment and prevention of *Candida albicans* biofilms with caspofungin in a novel central venous catheter murine model of candidiasis. *Journal of antimicrobial chemotherapy*, Vol.64, No.3, (September 2009), pp.567-570, ISSN 0305-7453
- Leonhardt, A.; Renvert, S. & Dahlén, G. (1999). Microbial findings at failing implants. *Clinical oral implants research*, Vol.10, No.5, (October 1999), pp. 339-345, ISSN 0905-7161
- Majerus, P. & Courtois, P. (1992). Susceptibility of *Candida albicans* to peroxidase-catalyzed oxidation products of thiocyanate, iodide and bromide. *Journal de biologie buccale*, Vol.20, No.4, (December 1992), pp. 241-245, ISSN 0301-3952.
- Mattos, B.; Soussa, A.; Magalhães, M.; André, M.; Brito, E.; Dias, R. (2009). *Candida albicans* in patients with oronasal communication and obturator prostheses. *Brazilian dental journal*, Vol.20, No.4, (2009), pp. 336-340, ISSN 0103-6440
- Molgatini, S.; González, M.; Rosa, A.; Negroni, M. (1988). Oral microbiota and implant type membranes. *Journal of oral implantology*, Vol.24, No.1, (January 1998), pp. 38-43, ISSN 0160-6972
- Mukherjee, P.; Zhou, G.; Munyon, R. & Ghannoum, M. (2005). *Candida* biofilm: a well-designed protected environment. *Medical mycology*, Vol.43, No.3, (May 2005), pp. 191-208, ISSN 1369-3786
- Mutluay, M.; Oğuz, S.; Ørstavik, D.; Fløystrand, F.; Doğan, A; Söderling, E. ;Närhi, T. & Olsen, I. (2010). Experiments on *in vivo* biofilm formation and *in vitro* adhesion of *Candida* species on polysiloxane liners. *Gerodontology*, Vol.27, No.4, (December 2010), pp. 283-291, ISSN 0734-0664
- Nett, J.; Lepak, A.; Marchillo, K. & Andes, D. (2009). Time course global gene expression analysis of an *in vivo* *Candida* biofilm. *Journal of infectious diseases*, Vol.200, No.2, (July 2009), pp. 307-313, ISSN 0022-1899
- Nett, J.; Marchillo, K.; Spiegel, C. & Andes, D. (2010). Development and validation of an *in vivo* *Candida albicans* biofilm denture model. *Infection and immunity*, Vol.78, No.9, (September 2010), pp.3650-3659, ISSN 0019-9567
- Nikawa, H.; Nishimura, H.; Hamada, T.; Kumagai, H. & Samaranayake, L. (1997). Effects of dietary sugars and, saliva and serum on *Candida* biofilm formation on acrylic surfaces. *Mycopathologia*, Vol.139, No.2, (August 1997), pp. 87-91, ISSN 0301-486X
- Nikawa, H.; Nishimura, H.; Makihira, S.; Hamada, T.; Sadamori, S. & Samaranayake, L. (2000). Effects of serum concentration on *Candida* biofilm formation on acrylic surfaces. *Mycoses*, Vol.43, No.3-4, (May 2000), pp. 139-143, ISSN 0933-7407

- Nobile, C. & Mitchell, A. (2006). Genetics and genomics of *Candida albicans* biofilm formation. *Cellular microbiology*, Vol.8, No.9, (September 2006), pp. 1382-1391, ISSN 1462-5814
- Panzeri, H.; Lara, E.; Paranhos, H.; Lovato da Silva, C.; de Souza, R.; de Souza Gugelmin, M.; Tirapelli, C.; Cruz, P. & de Andrade, I. (2009). *In vitro* and clinical evaluation of specific dentifrices for complete denture hygiene. *Gerodontology*, Vol.26, No.1, (March 2009), pp. 26-33, ISSN 0734-0664
- Peeters, E.; Nelis, H. & Coenye, T. (2008). Comparison of multiple methods for quantification of microbial biofilms grown in microtiter plates. *Journal of microbiological methods*, Vol.72, No.2, (February 2008), pp. 157-165, ISSN 0167-7012
- Percival, S.; Bowler, P. & Dolman, J. (2007). Antimicrobial activity of silver-containing dressings on wound microorganisms using an *in vitro* biofilm model. *International wound journal*, Vol.4, No.2, (June 2007), pp. 186-191, ISSN 1742-4801
- Pereira-Cenci, T.; Del Bel Cury, A.; Crielaard, W. & Ten Cate, J. (2008). Development of *Candida*-associated denture stomatitis: new insights. *Journal of applied oral science*, Vol.16, No.2, (March-April 2008), pp. 86-94, ISSN 1678-7757
- Pusateri, C.; Monaco, E. & Edgerton, M. (2009). Sensitivity of *Candida albicans* biofilm cells grown on denture acrylic to antifungal proteins and chlorhexidine. *Archives of oral biology*, Vol.54, No.6, (June 2009), pp. 588-594, ISSN 0003-9969
- Pye, A.; Lockhart, D.; Dawson, M.; Murray, C. & Smith, A. (2009). A review of dental implants and infection. *Journal of hospital infection*, Vol.72, No.2, (June 2009), pp. 104-110, ISSN 0195-6701
- Radford, D.; Challacombe, S. & Walter J. (1999). Denture plaque and adherence of *Candida albicans* to denture-base materials *in vivo* and *in vitro*. *Critical reviews in oral biology and medicine*, Vol.10, No.1, (February 1999), pp. 99-116, ISSN 1045-4411
- Ramage, G.; Wickes, B. & López-Ribot, J. (2008). A seed and feed model for the formation of *Candida albicans* biofilms under flow conditions using an improved modified Robbins device. *Revista iboamericana de micologia*, Vol.25, No.1, (March 2008), pp. 37-40, ISSN 1130-1406
- Ricicová, M.; Kucharíková, S.; Tournu, H.; Hendrix, J.; Bujdáková, H.; Van Eldere, J.; Lagrou, K. & Van Dijck, P. (2010). *Candida albicans* biofilm formation in a new *in vivo* rat model. *Microbiology*, Vol.156, No.3, (March 2010), pp. 909-919, ISSN 1350-0872
- Rodger, G.; Taylor, R.; Pearson, G. & Verran, J. (2010). *In vitro* colonization of an experimental silicone by *Candida albicans*. *Journal of biomedical materials research. Part B, applied biomaterials*, Vol.92, No.1, (January 2010), pp. 226-235, ISSN 1552-4973
- Samaranayake, Y.; Ye, J.; Yau, J.; Cheung, B. & Samaranayake, L. (2005). *In vitro* method to study antifungal perfusion in *Candida* biofilms. *Journal of clinical microbiology*, Vol.43, No.2, (February 2005), pp. 818-825, ISSN 0095-1137
- Sissons, C. (1997). Artificial dental plaque biofilm model systems. *Advances in dental research*, Vol.11, No.1, (April 1997), pp. 110-126, ISSN 0895-9374
- Thurnheer, T.; Gmür, R.; Shapiro, S. & Guggenheim, B. (2003). Mass transport of macromolecules within an *in vitro* model of supragingival plaque. *Applied and environmental microbiology*, Vol.69, No.3, (March 2003), pp. 1702-1709, ISSN 0099-2240

- Uppulari, P.; Chaturvedi, A. & Lopez-Ribot, J. (2009). Design of a simple model of *Candida albicans* biofilms formed under conditions of flow: development, architecture, and drug resistance. *Mycopathologia*, Vol.168, No.3, (September 2009), pp. 101-109, ISSN 0301-486X
- Vanden Abbeele, A.; de Meel, H.; Ahariz, M.; Perraudin, J.-P.; Beyer, I. & Courtois, Ph. (2008). Denture contamination by yeasts in the elderly. *Gerodontology*, Vol.25, No.4, (December 2008), pp. 222-228, ISSN 0734-0664
- Vandenbussche, M. & Swinne, D. (1984). Yeasts oral carriage in denture wearers. *Mykosen*, Vol.27, No.9, (September 1984), pp. 431-435, ISSN 0027-5557





*Edited by Rosario Pignatello*

These contribution books collect reviews and original articles from eminent experts working in the interdisciplinary arena of biomaterial development and use. From their direct and recent experience, the readers can achieve a wide vision on the new and ongoing potentialities of different synthetic and engineered biomaterials. Contributions were selected not based on a direct market or clinical interest, but based on results coming from very fundamental studies. This too will allow to gain a more general view of what and how the various biomaterials can do and work for, along with the methodologies necessary to design, develop and characterize them, without the restrictions necessarily imposed by industrial or profit concerns. The chapters have been arranged to give readers an organized view of this research area.

In particular, this book contains 25 chapters related to recent researches on new and known materials, with a particular attention to their physical, mechanical and chemical characterization, along with biocompatibility and hystopathological studies. Readers will be guided inside the range of disciplines and design methodologies used to develop biomaterials possessing the physical and biological properties needed for specific medical and clinical applications.

Photo by Petrovich9 / iStock

**IntechOpen**

